Laboratory Directed Research and Development

FY1999

Annual Report

Lawrence Livermore National Laboratory

DISCLAIMER

Laboratory Directed Research and Development

FY1999 Annual Report

Lawrence Livermore National Laboratory

UCRL-LR-113717-99

Acknowledgments

Contents

Section 2 Atmospheric and Geosciences

Section 3 **Biotechnology and Health Care Technologies**

Section 4 **Computing/Modeling/Simulation**

Section 5 **Energy and Environmental Technologies**

Section 6 **Lasers/Electro-optics/Beams**

Section 7 Manufacturing Processes and Technologies

Section 8 Materials Synthesis and Characterization

Section 9 Nuclear/Atomic Science and Technology

Section 10 Space Science and Technology

Appendix

Overview of FY1999 LDRD Program at LLNL

The Lawrence Livermore National Laboratory (LLNL) was founded in 1952 and has been managed since its inception by the University of California (UC) for the U.S. Department of Energy (DOE). Because of this long association with UC, the Laboratory has been able to recruit a world-class workforce, establish an atmosphere of intellectual freedom and innovation, and achieve recognition in relevant fields of knowledge as a scientific and technological leader. This environment and reputation are essential for sustained scientific and technical excellence. As a DOE national laboratory with about 7,000 employees, LLNL has an essential and compelling primary mission to ensure that the nation's nuclear weapons remain safe, secure, and reliable and to prevent the spread and use of nuclear weapons worldwide. The Laboratory receives funding from the DOE Assistant Secretary for Defense Programs, whose focus is stewardship of our nuclear weapons stockpile. Funding is also provided by the Deputy Administrator for Defense Nuclear Nonproliferation, many Department of Defense sponsors, other federal agencies, and the private sector. As a multidisciplinary laboratory, LLNL has applied its considerable skills in high-performance computing, advanced engineering, and the management of large research and development projects to become the science and technology leader in those areas of its mission responsibility.

The Laboratory Directed Research and Development (LDRD) Program was authorized by the U.S. Congress in 1984. The Program allows the Director of each DOE laboratory to fund advanced, creative, and innovative research and development (R&D) activities that will ensure scientific and technical vitality in the continually evolving mission areas at DOE and the Laboratory. In addition, the LDRD Program provides LLNL with the flexibility to nurture and enrich essential scientific and technical competencies, which attract the most qualified scientists and engineers. The LDRD Program also enables many collaborations with the scientific community in academia, national and international laboratories, and industry.

The projects in the FY1999 LDRD portfolio were carefully selected to continue vigorous support of the strategic vision and the long-term goals of DOE and the Laboratory. Projects chosen for LDRD funding undergo stringent selection processes, which look for high-potential scientific return, emphasize strategic relevance, and feature technical peer reviews by external and internal experts. The FY1999 projects described in this annual report focus on supporting the Laboratory's national security needs: stewardship of the U.S. nuclear weapons stockpile, responsibility for the counter- and nonproliferation of weapons of mass destruction, development of high-performance computing, and support of DOE environmental research and waste management programs. In the past, LDRD investments have significantly enhanced LLNL scientific capabilities and greatly contributed to the Laboratory's ability to meet its national security programmatic requirements. Examples of past investments include technical precursors to the Accelerated Strategic Computing Initiative (ASCI), special-materials processing and characterization, and biodefense. Our analysis of the FY1999 portfolio shows that it strongly supports the Laboratory's national security mission. About 95% of the LDRD dollars have directly supported LLNL's national security activities in FY1999, which far exceeds the portion of LLNL's overall budget supported by National Security Programs, which is 63% for FY1999.

Components of the LDRD Program at LLNL

In FY1999, the Laboratory continued to invest in important areas supporting national security efforts within the LDRD Program's three major components: *Strategic Initiatives* (SI), *Exploratory Research* (ER) projects, and the *Laboratory-Wide* (LW) Competition. (The LDRD Program also funds a few projects in a fourth category called *Feasibility Studies*.)

Strategic Initiatives. The SI component focuses on innovative research and development activities that are likely to set new directions for existing programs, may help develop new programmatic areas within LLNL mission responsibilities, and enhance the Laboratory's science and technology base. Projects in this category are usually larger and more technically challenging than those funded in the other categories. An SI project must be aligned with the articulated strategic R&D priorities of at least one of the four Laboratory strategic councils: (1) the Council on Bioscience and Biotechnology, (2) the Council on Energy and Environmental Systems, (3) the Council on National Security, and (4) the Council on Strategic Science and Technology. Although many deserving SI proposals are considered, less than one-third are funded.

In FY1999, the LDRD Program funded ten SI projects that included detailed studies of special-materials under high strain rates for defense programs, innovative methods of using weapons computer codes in new applications and science explorations, computational biology research and radiation/chemical mutagen studies for bio-defense. Other efforts addressed global and regional climate simulations, and the Sustained Spheromak Physics Experiment that, if successful, could potentially reduce the cost of fusion energy. Many of the ten diverse research projects in this category take advantage of ASCI's high performance computing capability at LLNL.

Exploratory Research. The ER component of LDRD aligns with a Laboratory directorate's strategic R&D needs. Examples include exploration of proton radiography; development of faster algorithms for highly parallel processing computers, such as those used in ASCI; and improved understanding of high explosive safety. Typically, fewer than half the proposals submitted to the directorate are forwarded to the ER Oversight Committee for further review and selection. Over 65% of LDRD funds are in this ER category—in FY1999, 142 of the 184 projects funded were ER proposals.

Laboratory-Wide Competition. Projects in the third LDRD component—the LW competition—emphasize innovative and creative research concepts and ideas that are subject to limited management filtering. Hoping to encourage participation of individual researchers, the competition is open to all LLNL staff in programmatic, scientific, engineering, technical support, or administrative areas. In FY1999, we funded 23 LW projects from the 77 proposals submitted.

The LDRD Program also funds a few projects in a fourth category called Feasibility Studies (FS). This special category of LDRD projects provides flexibility to develop better definition for potential research in any category. In FY1999, we funded 11 projects in the FS category.

Highlights of FY1999 LDRD Projects in the SI, ER, and LW Categories

Below we highlight six LDRD projects funded in FY1999—two projects each from the SI, ER, and LW categories. Although hardly a comprehensive list, these six projects do illustrate the diverse scope of LDRD research. Further, the list demonstrates the LDRD Program's emphasis on science and technology needs of DOE's national security mission.

One of the ten SI's funded in FY1999, which is relevant to improving predictive capabilities for weapon safety, performance, and aging effects in the U.S. nuclear weapons stockpile, is the LDRD project in *Dislocation Dynamics, micro3D Simulations and Experiments.* David Lassila and his team of researchers are addressing the mechanical behavior of metals. This SI focuses on the development of microscale simula-

tions to predict strength properties (referred to as "dislocation dynamics"). Dislocations are the fundamental crystalline features associated with strength properties of metals and their performance under strain, especially very high rates of strain encountered in nuclear explosions. The movement and interactions of large numbers of dislocations caused by an applied load give rise to plastic deformation. Dislocation-dynamics simulations can be used to study the forces required for these movements and interactions—in essence, the fundamental strength properties.

This dislocation dynamics and simulations project is investigating the development of multiscale modeling approaches that can be used to rigorously "link" information from atomistic simulations to the models used in continuum computer code simulations. The overall objective of this multiscale modeling research is to provide predictive strength models for polycrystalline body-centered cubic metals and to establish a fully integrated predictive modeling capability for strength properties of metals under extreme conditions of pressure and temperature. This project has attracted the best minds in the U.S. and Europe to participate in this effort. See page 4-5 for further discussion of FY1999 accomplishments for LDRD Project 97-SI-010.

A second SI funded in FY1999 addresses global interconnectivity in the United States, which is highly vulnerable to attacks on its critical national infrastructure. Currently, there is little capability to simulate such attacks, evaluate the consequences, and assess the effectiveness of preventive measures. The goal of this LDRD research on the *Modeling and Simulation for Critical Infrastructure Protection* is to meet these national security needs.

The objective of this SI is to develop a modeling and simulation environment for the Information Operations, Warfare, and Assurance (IOWA) initiative. IOWA is being developed as an integrated suite of simulation engines, computer visualization tools, analysis techniques, and assessment methods for understanding and evaluating information operations issues. The IOWA environment is created to determine how information systems may be vulnerable to intrusion, what actions can be taken to successfully defend against these intrusions, and what are the consequences of such intrusions if they do occur. In FY1999, J. Smart and his team used LLNL's Open LabNet as a pilot application and expanded their research into simulation of Internet Protocol (IP) networks and telecommunication infrastructure and are generating an overall simulation environment and capability. In FY2000, this SI effort will address the characterization of computer and network vulnerabilities. This work is attracting a great deal of attention, and key members of the team have been asked to support major U.S. government initiatives in this area. For further information about this SI and more detail about its accomplishments in FY1999, see page 4-29.

In the ER category, one of the projects funded in FY1999 is entitled *Fundamental Aspects of Radiation-Induced Microstructural Evolution in Plutonium–Gallium Alloys.* This ER project focuses on radiation-damage accumulation, which leads to microstructural evolution that can have an adverse impact on a nuclear weapon's performance. The scientific and technological challenge of predicting plutonium microstructural evolution is essential to the security and reliability of our nation's nuclear weapons stockpile. In this project, Michael Fluss and his team of researchers are developing predictive molecular-dynamics modeling of radiation-induced microstructural changes. The goals of this project's research are to advance model validation and to determine the critical parameters for mass-transport kinetics and the behavior of radioactive materials under conditions of very long storage times.

An experimental sample of Pu–Ga is irradiated to produce stable, but non-interacting, defect pairs, then annealed using various time and temperature prescriptions. As the changes in defect concentration are tracked, the annealing process exhibits distinct stages. By measuring the temperature dependence of the annealing kinetics, activation energies for mass transport can be deduced. These deductions are essential to model the defect kinetics leading to microstructural changes brought on by more complex self-irradiation in Pu metals.

During the final year of this project, LLNL scientists will measure the annealing curves for proton irradiated Pu–Ga as a function of radiation dose. The experimental data generated in this project will be used in materials-modeling codes to predict those microstructural changes. This predictive capability is essential to ensure the reliability of our nuclear weapons stockpile and will provide a basis for interpreting engineering testing related to surveillance and safeguards. The intimate connection between theory and experiment should result in a systematic investigation of radiation damage in metals by the presence of helium, which applies to the mission challenges raised by Pu alloys in science-based stewardship of our nuclear weapons stockpile. See page 8-9 for further information on FY1999 accomplishments of LDRD Project 98-ERD-028.

In the second ER project highlighted here, *Novel Parallel Numerical Methods for Radiation and Neutron Transport*, Peter Brown and his team are developing advanced solution methods for the equations that model the transport of photons and neutrons through materials. In many of the multi-physics codes at the Laboratory, transport generally comprises anywhere from 30–50% of the time for a simulation. When using Monte Carlo methods, the percentage can be as high as 80%. The goal of this research is to reduce the transport solve time in these simulations by means of more advanced numerical methods. In particular, scalable methods are a necessity. By scalability, we generally mean that the time to

solution remains constant as the problem size grows and additional computer resources are used. In lieu of nuclear testing, scalable solution methods are relevant to address numerical problems arising in transport modeling of terascale weapons simulations.

Photon and neutron transport are physical processes that must be adequately represented in high-temperature hydrodynamics simulations to properly account for their effects on the fluid dynamics and to correlate the calculations with experimental diagnostic data. Prototype LLNL neutron transport codes have been executed on the IBM ASCI Blue Pacific SST to simulate the flux of fusion neutrons that comes out of an LLNL laser target chamber during an actual experiment. Experimental results from this research have demonstrated unprecedented detail in the total neutron scalar flux distribution, providing the two largest deterministic transport calculations ever performed. Both simulations provided the LLNL researchers the opportunity to investigate the scalability of the prototype code on problems requiring thousands of processors and billions of unknowns, with features similar to those that will be encountered in the nuclear weapons stockpile security effort. See page 4-7 for more information about FY1999 accomplishments for LDRD Project 98-ERD-022.

Next, we highlight two current LDRD projects in the LW category. The goal of the first project, entitled *Three-Dimensional Simulations of Scenario Earthquakes along the Hayward Fault*, is to determine the geographical distribution of high-amplitude seismic ground motion in the Bay Area. The Hayward fault runs through some of the most densely populated regions of the San Francisco Bay Area, and is expected to experience a Richter magnitude 6.8 to 7.5 earthquake within the next 30 years. It is estimated that such an earthquake will cause 1,000 to 10,000 fatalities and $50B to $500B in damages. Regions where high-amplitude seismic ground motion is expected must be identified so that appropriate engineering improvements can be made.

Shawn Larsen and his team are combining the seismic ground motions predicted from three-dimensional (3-D) simulations of scenario earthquakes along regional faults with a 3-D geological model of the Bay Area developed at UC, Berkeley. The simulations are computed using E3D, an LLNL-developed, sophisticated, 3-D seismic-wave-propagation code that is implemented on high-performance, massively parallel computers.

The 3-D seismic-modeling techniques used in this study are gaining acceptance inside and outside the Laboratory. For example, this team is participating in collaborative efforts with outside organizations to investigate seismic hazard in the Santa Clara Valley. The parallel-processing capabilities in E3D and the Laboratory's high-performance computers enable them to perform the largest and most sophisticated simulations in the world. See page 2-9 for more information about FY1999 accomplishments for LDRD Project 98-LW-028.

In a second LW research effort for FY1999, entitled *New Si-Based Compound Clusters and Their Application in Field Emission Devices*, LDRD researchers address the work function of materials, defined as the minimum energy required to remove an electron from the material into the vacuum, which plays a major role in the efficiency, durability, and economic viability of field emission devices. (Field emission is defined as the emission of electrons from the surface of a condensed phase into a vacuum under high electrostatic fields.) The purpose of this research is to produce and investigate the properties of the silicon/alkali metal/oxygen compounds films, consisting of small clusters with low work function (down to 1.2 eV). The small radii of curvature inherent to these clusters provide an easy path for emission of electrons in an electrostatic field. This, in turn, means that the conventional gated field emission structures could be drastically simplified, and the required sharp "tips," which are extremely difficult to make, could either be relaxed or eliminated.

Mehdi Balooch and his team using transmission electron microscopy and electron diffraction showed that under certain deposition conditions the Cs/Si/O nanoclusters are crystallites and have random orientation. They successfully built field-emission diode displays that exhibited turn-on voltage in the range of 10–20 V and did not require the fabrication of any complicated sharp structure. This technique, which could significantly reduce the manufacturing cost of field-emission display, has been applied on microchannel plate and used as a diagnostic tool for x-ray detection. The team has filed three patent applications and published their results in *Physical Review B* and the *Journal of Applied Physics.* For a summary of their accomplishments in FY1999, see page 8-14.

LDRD Funding for FY1999

In FY1999, the LDRD Program was authorized by DOE to fund $57.8M for projects in three categories: roughly 70% for ER, 24% for SI, and 6% for LW (see Fig. 1).
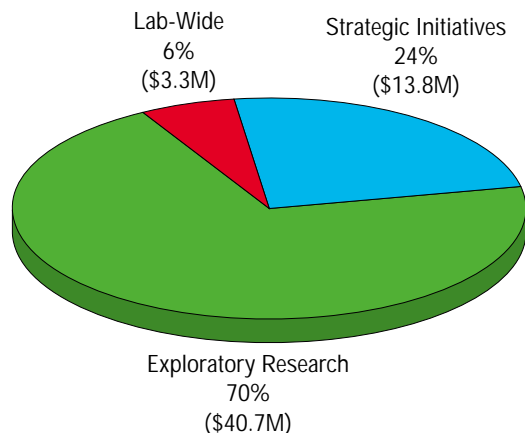
Figure 1. Distribution of FY1999 dollars among the three components of the Laboratory's LDRD Program.

The LDRD projects vary in size: 34 projects were funded at less than $100K, while 8 were funded at more than $1M; the average funding for an LDRD project in FY1999 was $306K. Figure 2 shows the distribution of funds for the FY1999 portfolio of projects.
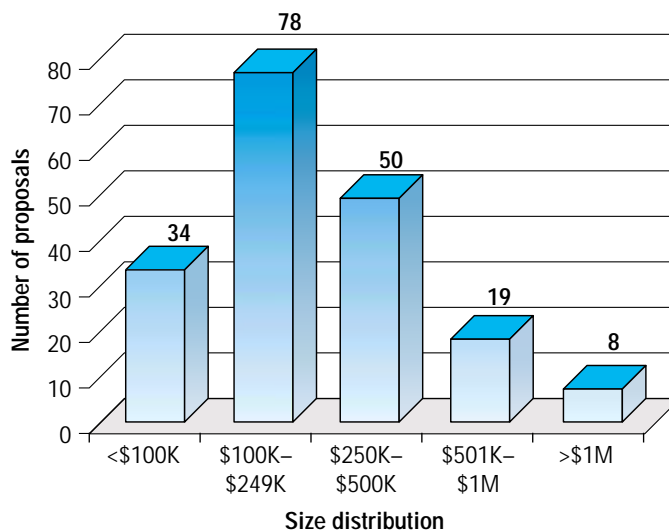
Figure 2. Distribution of FY1999 funding dollars among the Laboratory's 189 LDRD projects.

Projects are categorized into ten competency areas. Although projects often address more than one competency area, this report classifies each project in the most appropriate category. Figure 3 shows the FY1999 funding distribution among these competency areas.
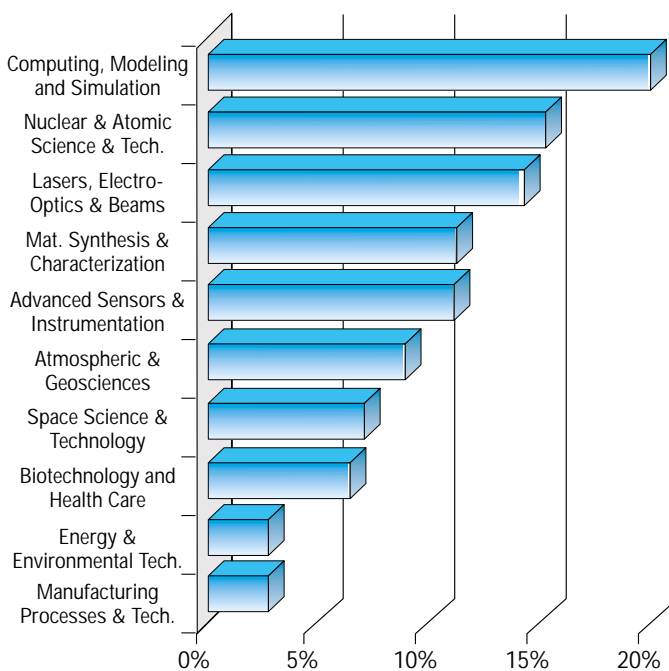
Figure 3. Distribution of FY1999 funding among the ten competency areas.

Recent LDRD Program Accomplishments

In compiling statistics on publications, patents, staff-member hires, and national awards, we find the LDRD Program is extremely productive. For example, in 1998, LDRD-based research accounted for 39 of 78 patents issued to LLNL. Similar performance statistics apply to publications and awards based on LDRD research.

Below, we highlight a few of the achievements of recent and successful LLNL projects. These projects also illustrate the diversity of the LDRD-funded research.

- **Demonstration of the feasibility of proton radiography for hydrodynamic testing.** An LLNL team, in collaboration with Los Alamos National Laboratory scientists and engineers, made significant progress in demonstrating the feasibility of using high-energy protons for dynamic radiography of thick objects that are of interest to the Stockpile Stewardship Program. They have also successfully identified a cost-efficient path leading to the timely development of a proton radiography experimental test-bed which would provide 3-D views of objects undergoing hydrodynamic testing.

- **Demonstration of the world's brightest laser.** After accomplishing a string of laser-physics "firsts," an LLNL team demonstrated near-diffraction limited focussing of a 100-fs, 15-J, Ti:Sapphire laser. The resulting intensity on target was greater than 10^{21} W/cm^2, a world record.

- **Creation of antimatter with laser light.** Using a high intensity laser, LLNL scientists demonstrated that the interaction of high intensity laser light with solids could induce nuclear processes, including relativistic electron generation, positron production, and photonuclear fission. The work was presented as an invited talk at the Centennial meeting of the APS, and was featured prominently in the *AIP Physics News Update* of March 31, 1999.

- **Discovery of quartz-like solid CO_2.** By subjecting CO_2 gas to high pressures and heating it with a laser, LLNL scientists created a new polymerized form of the substance. The solid CO_2 is optically active, which means it changes the frequency of light that passes through. The discovery was reported at the Centennial meeting of the APS and covered by the *New York Times* on March 23, 1999 ("Carbon dioxide . . . has assumed an astonishing new form . . .").

- **New computer code for simulating the x-ray spectra from cosmic sources**. Using special LLNL expertise in modeling atomic processes in high temperature laboratory plasmas, LLNL scientists have developed and tested a new computer code for calculating the x-ray spectra emitted by astronomical objects such as main sequence stars, x-ray binaries, supernova remnants, quasars, and black holes. This code will enable the analysis and interpretation of high-resolution x-ray spectra taken with instruments aboard the Chandra X-ray Telescope, which was launched into space by NASA's space shuttle Columbia in July 1999.

Moreover, the LDRD Program enables many collaborations with the scientific community at universities, national and international laboratories, and industry. Below is a list a few collaborative accomplishments.

- **Discovery of Element 114.** In collaboration with scientists from Dubna, Russia, LLNL researchers believe that they have discovered Element 114, which lasted 30 seconds before decaying, a longevity that could verify predictions of "an island of stability" beyond the lighter, less stable nuclei observed earlier.

- **Highest Redshift Quasar.** In another collaboration with six institutions, LLNL researchers discovered a quasar with one of the most luminous starbursts on record—an achievement that was featured on CNN.

- **The B Factory was completed and began its data-taking phase.** The accelerator built by scientists from Stanford Linear Accelerator (SLAC), Lawrence Berkeley National Laboratory (LBNL) and LLNL was commissioned in the summer of 1998 and formally dedicated in October 1998 by the Secretary of Energy. In early 1999, the BaBar detector was completed and commissioned, and the B Factory began high luminosity operation in May 1999. All LLNL accelerator and detector systems were successfully delivered and are working to specification. Laboratory physicists are fully involved in exploiting the science of the B Factory, which is aimed at explaining the observed asymmetry between matter and antimatter in the Universe.

- **Sonoluminescence.** Another LDRD-funded project has helped explain the phenomena of sonoluminescence, which was first detected ten years ago when experimenters observed that ultrasonically driven bubbles of gas within water emitted tiny flashes of light, lasting a mere trillionth of a second. Through experiments and modeling, LLNL researchers and their university collaborators explained the phenomena purely in the context of conventional hydrodynamics, chemistry, and plasma physics.

R&D 100 Award Winners in FY1999

Laboratory scientists and their LDRD-funded research continue to garner national recognition. In recent years, many *R&D 100 Awards* from R&D Magazine have been earned for innovative technologies developed through LDRD-funded research. In FY1999, three of the six *R&D 100 Awards* received by LLNL scientists were based on their LDRD research. The first project to earn an *R&D 100 Award* is entitled *Diode-Pumped Solid State Green Lasers for Industrial Material Processing*—a high-powered replacement to lamp-pumped solid state lasers for variety of applications,

including precision laser machining and laser isotope separation (see Fig. 4).

Figure 4. Diode-Pumped Solid State Green Lasers for Industrial Material Processing. Jim Chang and his team developed a cost-effective, high-powered replacement to lamp-pumped solid-state lasers.

A second *R&D 100 Award* went to the LDRD project *Gamma Watermarking*—a revolutionary method of identifying and authenticating material objects (see Fig. 5).

Figure 5. Gamma Watermarking can help law enforcement officers establish indisputable links between owners and their property. See pages 9-15 and 9-16.

A third *R&D 100 Award* in FY1999 was earned by the research team developing PEREGRINE™—a 3-D Monte Carlo radiation dose calculation system that includes both hardware and software for calculating accurate radiation therapy dosage using fundamental physics principles (see Fig. 6). Moreover, in addition to winning the *R&D 100 Award*, LLNL has reached a milestone by finalizing licensing negotiations for PEREGRINE™ radiation treatment planning.
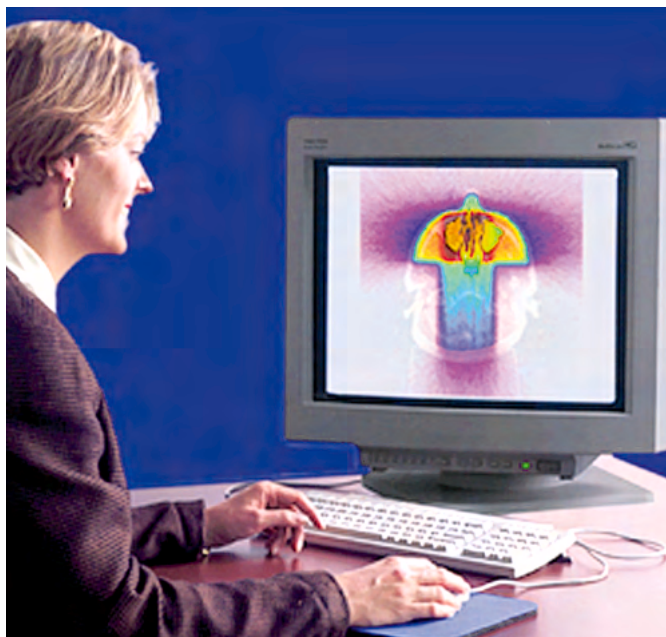
Figure 6. Through the PEREGRINE™ radiation dose calculation system, cancer patients can receive the highest accuracy dose calculations for radiation therapy. See page 4-21.

The FY1999 LDRD Annual Report

This *Lawrence Livermore National Laboratory FY1999 Laboratory Directed Research and Development Annual Report* compiles one-page articles submitted by the principal investigators of their LDRD-funded projects. Each article summarizes an unclassified project and discusses its motivation, scope, and progress for FY1999. This annual report also includes several appendices, including a compilation of LDRD publications, an index of principal investigators, and an index of the projects according to their LDRD tracking codes.

The LDRD-funded projects described in the articles that follow are arranged in sections by competency areas and assigned a unique tracking code, which consists of three elements (e.g., 98-SI-010). The first element is the year the project began (1998); the second is the LDRD component in which the project is funded (Strategic Initiative), and the third identifies the order in which the proposal was received.

Advanced Sensors and Instrumentation

1

Advanced Sensors and Instrumentation

Eyeglass: A Large-Aperture Space Telescope

R. A. Hyde, F. G. Patterson, S. N. Dixit, I. M. Barton, M. C. Rushford

The Eyeglass is a novel form of large-aperture space telescope, utilizing a diffractive lens as its primary optical element. This diffractive lens, fabricated on a thin membrane, provides a lightweight, easily deployable, method of fielding a very large (tens of meters in diameter) aperture optic. Because its primary aperture is a high f-number transmissive element, the Eyeglass virtually eliminates the stringent surface figure requirements faced by reflective telescopes.

The major optical challenge when using diffractive telescopes is chromatic correction. The focal length of a Fresnel lens varies inversely with wavelength so that diffractive optics are generally useful only for monochromatic (i.e., laser) applications. In principle, one can eliminate these chromatic problems by using a relay telescope to re-image the first diffractive lens onto a second diffractive lens, which then corrects the aberrations. Our major effort this year was to quantitatively investigate this form of chromatic correction with a diffractive telescope based upon our Eyeglass designs.

We built a prototype diffractive telescope based upon a 20-cm, $f/100$ lens. The lens was fabricated by a lithographic process, generating a 4-level, digitally blazed, phase profile. In order to chromatically correct this diffractive lens, we combined it with a 4-cm relay lens (a refractive achromat) and a 2.2-cm, $f/11$, inverse diffractive lens.

This experiment successfully demonstrated our ability both to chromatically correct diffractive telescopes, and to do so with diffraction-limited performance. In the figure, we show the telescope's point-spread function (PSF) for 633-nm laser light and for broadband (470- to 700-nm) white-light. The broadband light is clearly focused into a tight spot, which has the predicted 95-mm Airy width. We have also used this telescope (piping in light via turning mirrors) to look at real astronomical objects, taking pictures of the Moon, Saturn, Jupiter, and the Sun.

A full-sized space-based Eyeglass must use a thin-film diffractive lens, not a conventional, thick silica one. To demonstrate that thin-film lenses can be made and will function, we built a binary-profile, 20-cm polymer lens and successfully tested it in the color-correcting telescope. We made this lens using a replication technique developed the previous year; we made and used a silica master as one face of a mold, in which a photo-polymer was placed and cured. This process resulted in a 40-mm thin-film lens, which also gave color-corrected, diffraction-limited optical performance.

One major problem for large space optics is how they can be stowed in a small launch fairing for delivery to space. Origami is a promising approach to compactly fold-up a large Eyeglass lens, since it can generate patterns using only single-layer-folds in known locations. We have found (and computer-simulated) several fold-patterns, which are suitable for packaging large, rotationally symmetric thin-film lenses.

Our full-scale Eyeglass designs have to date been based upon large 2-D membranes. We have explored a new approach to implementing large diffractive lenses, based upon a net of optical fibers (or ribbons). A 1-D diffractive lens can potentially be fabricated by an array of separated straight ribbons, each built with optical-fiber technology; a truss orthogonally holding two such lenses would then create a large 2-D lens. We have analyzed the static and vibrational behavior of such lenses and have shown that they are feasible for Eyeglass. The greatest challenge appears to be that the fabrication tolerances achieved by the optical fiber industry are not tight enough for Eyeglass use; therefore, this does not represent an off-the-shelf fabrication route.
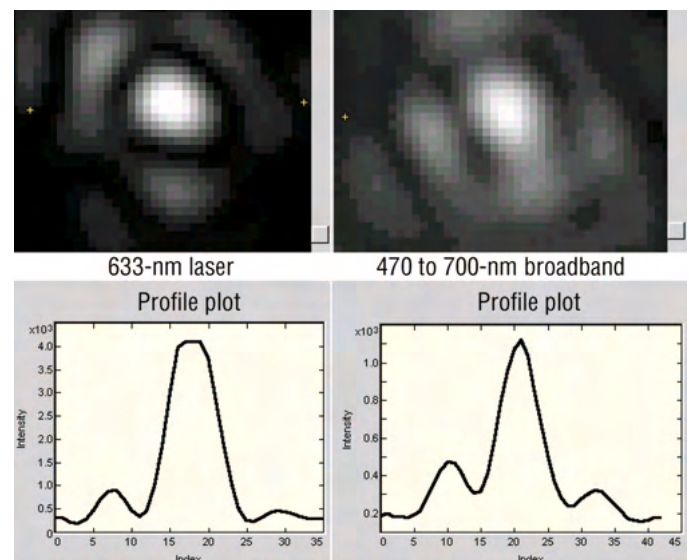
Focused spots from a diffractive telescope, showing the PSF for 633-nm laser light and for broadband white-light.

LANDMARC Radar Mine Detection

S. G. Azevedo, J. M. Brase, E. T. Rosenbury

97-SI-013

Antipersonal (AP) mines are the most numerous mines worldwide, and their small size and low metal content make them difficult to find. Because of serious technical challenges, no radar mine detectors are yet deployed for finding AP mines. Our goals in the LANDMARC project have been to (1) investigate the feasibility of using radar to detect mines, (2) identify and characterize the key parameters for radar detection of AP mines, (3) develop and experimentally validate models of the radar and clutter signatures, and (4) develop relationships within the user and sponsoring agencies.

LLNL's micropower impulse radar (MIR) is a natural choice for this application because the ultrawideband nature of its signal (also, small size, low cost, and low power) makes it ideal for ground penetration (the low frequencies) and imaging resolution (the high frequencies). In past years, we have also shown how diffraction tomographic imaging from synthetic-aperture or real arrays provides image enhancement to reduce clutter.

In FY1999, we addressed three major problems affecting MIR mine detection: clutter from the ground-surface echo, clutter from rough surface, and inaccurate subsurface imaging.

The ground presents a large dielectric interface; it produces a reflected signal (ground clutter) that can overshadow the relatively small mine signal. Our earlier attempts to minimize this effect only served to increase ground clutter along with the mine signature.

In FY1999, we found an alternative configuration through modeling [Fig. 1(a)]. In collaboration with Northeastern University (NU), we found that a parabolic reflector canted at a 45-degree angle produced a near-plane wave whose energy could be reflected away from the detectors, while the scattered energy from the mine would be measured. We fabricated a parabolic-section reflector, using an array of MIR receivers [Fig. 1(b)], and measured the returns from mines in three soil types at various depths. In all cases, the surface echo was significantly reduced and detection was improved over the 85% probability of detection measured last year. Where the ground surface is not smooth, the parabolic reflector also improved detection [Fig. 1(c)], as predicted by the model.

Subsurface imaging is also affected by inaccurate models of soil dielectric properties. Optimal imaging of the subsurface allows the deminer to discriminate between a mine and a rock on the basis of shape. A key parameter on which the imaging is based is the dielectric constant or velocity of electromagnetic waves in soils. Small inconsistencies in this parameter can significantly change the object's shape and contrast in the image. In FY1999, we developed an iterative method for determining radar velocity in the soil, thereby sharpening the image. In addition, we developed theoretical support for a new image-reconstruction algorithm that makes use of evanescent wave phenomena. Fast algorithms and advances in computer technology will allow the data to be analyzed rapidly enough for humanitarian scenarios.

LANDMARC technology has shown that even small AP mines can be detected by radar under certain conditions; probabilities of detection can be predicted for those cases.

Nationwide, there is less support for new mine-detection technologies than 3 years ago, and much of the available research funding is now directed at promising methods for detecting the chemical signatures of high explosives (sniffers, nuclear quadrapole resonance, etc.). However, LANDMARC technologies have made an impact; we anticipate that future mine-detection systems will include radar sensors, perhaps MIR.

Now that the LANDMARC project is complete, we are exploring ways to perform further tests through university collaborations, and we are employing the outcomes of this research on other subsurface imaging and detection problems.

Figure 1. Application of micropower impulse radar (MIR) receivers to improved mine detection: (a) simulation of microwave field over ground-plus-mine, (b) array of MIR receivers arranged on a portable, parabolic dish for developmental testing, and (c) image of mine with minimal first-surface echo.
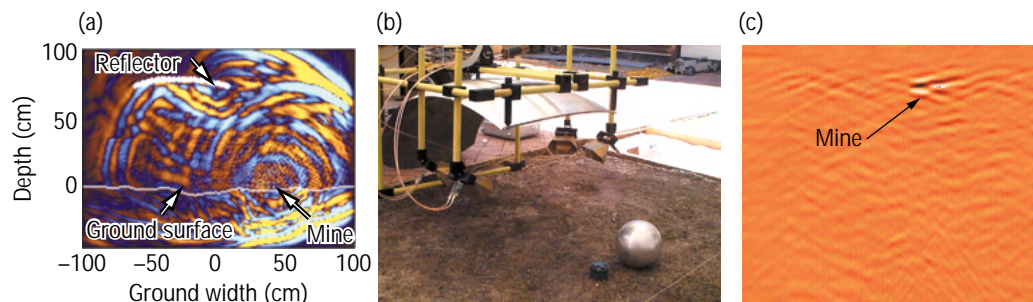
Wireless Microsensor Modules for Distributed Network Sensing

C. F. McConaghy, J. N. Simon, A. P. Lee, J. Trevino, L. Jones

98-ERD-017

Sensors and supporting electronics used in wireless sensor networks must be small, low power, and capable of operating continuously over long lifetimes. Our goal in this project has been to develop a prototype wireless sensor with reasonably low power to preserve battery life as well as a very small package that is easily deployed in distributed networks.

Our sensor is a unique, miniature system that combines wireless electronics, sensors based on microelectro-mechanical systems (MEMS), signal processing, control electronics, and a battery within a very small module. The modules are designed to communicate over distances on the order of 30 m, and networks can be built by combining a number of these modules. A key feature of this network is the ability to process data within each module and minimize the amount of raw data propagated in the network.

The result of our first year's work was a module in the form of a 2-in. (50.8 mm) cube. During FY1999, we built a 1- by 2- by 2-in. (25.4 by 50.8 mm) module that (1) uses one third the power of the original module, and (2) can be configured to use as little as one tenth the power required by certain other network configurations that allow duty cycling of the radio-frequency (rf) receiver.

The sensor must be small enough and low enough in power to allow incorporation in such a package. During FY1999, we continued the development of a sensitive accelerometer that we began last year. This particular accelerometer is based on a silicon proof mass that is held to a supporting silicon wafer with very small 3- by 3-μm tethers. Unlike off-the-shelf MEMS accelerometers, this device is designed for low-frequency work and has a predicted resonance near 50 Hz. The large proof mass is formed by state-of-the-art, deep, reactive-ion-etching a dumbbell-shaped structure through the entire 380-μm thickness of a silicon wafer while maintaining a 16 to 1 depth to width ratio. Figure 1(a) shows the proof mass after etching; Fig. 1(b) shows the tethers that support the proof mass. We are continuing to fully develop and test this accelerometer.

During FY1999, we also demonstrated the previously designed 2-in. (50.8 mm) cube in a link to a host base station. The rf electronics in the base station were similar to those in the wireless sensor, with the addition of an interface to a laptop computer running a Labview control program. The MEMS-based accelerometer used in the sensor module is very sensitive to movement. When shaken, the module produced a waveform that was captured, transmitted to the host, and displayed.

In FY1999, we also built a new module consisting of four, 30- by 50-mm, multilayer boards interconnected using elastomeric connectors on all four edges. The space between each board is 4 mm. The connectors allow every other pin to be grounded and also form a shielded structure around each layer. Figure 1(c) shows the board stack held in a plastic housing. The top board in the stack is an LLNL-designed, single-conversion, 900-MHz receiver designed to demodulate binary-phase shift-keyed (BPSK) data. Because the demodulation is achieved using an inductor-capacitor differential delay line, data recovery is simplified by avoiding more complex control loops. The other boards are a direct-sequence, spread-spectrum modem board; a signal processor/controller board; and the sensor board. The modem, which is based on a state-of-the-art, field-programmable gate array (FPGA), can be programmed to give process gains of 11 or 127 with data rates of either 100 or 8 Kbits/s.

Some of the rf work was done in collaboration with the University of California, Los Angeles.

In the future, we will focus on linking multiple modules, including a second sensor within each module, and shrinking the overall size of the module to a 1-in.[3] package.
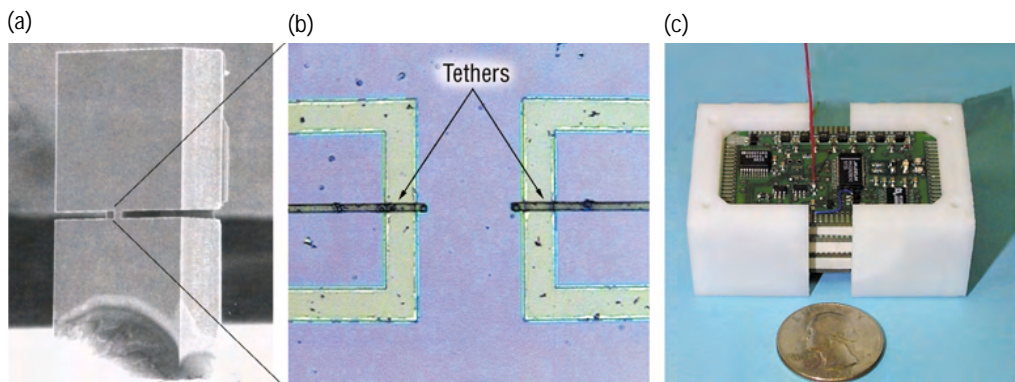
Figure 1. Our micromachined accelerometer consists of (a) the dumbbell-shaped, 380-μm-thick proof mass supported by (b) 3- by 3-μm polysilicon tethers. The accelerometer (c) is contained within the wireless sensor, which is a stack of four 30- by 50-mm boards spaced 4 mm apart.

True Gamma-Ray Imaging Technologies

K. P. Ziock, D. Archer, D. Beckedahl, J. Blair, A. Dougan, J. Kammeraad, J. Luke, B. Pohl, G. Schmid

98-ERD-025

Smuggling of special nuclear material (SNM) is of overwhelming concern because the potential devastation by the successful delivery of even one nuclear device is staggering. We are developing full-volume gamma-ray detectors to detect and counter this threat. Through the use of imaging, our detectors will achieve unsurpassed sensitivity to the gamma radiation emitted by SNM. The instruments will allow us to determine the direction of origin of each detected gamma ray. With this information, background radiation impinging from all directions can be rejected in favor of the spatially localized signal from the materials one is seeking. Smuggled materials will appear as a localized "hot-spot" on a distributed sea of radiation. Current systems perform no imaging at all.

To achieve images at the gamma-ray energies of interest (~0.2 to 2.0 MeV), we use the fact that these photons "bounce off" electrons (i.e., Compton scattering). By measuring the energy of the recoiling electron and the energy and direction of travel of the recoiling gamma ray, we can reduce the incident direction of the initial gamma ray to a narrow ring that is a small fraction of the area of all possible incident directions. A point source appears as the location where rings in the image overlap.

Taking full advantage of Compton scattering requires a detector that (1) is sensitive throughout its volume to the energy deposited by the recoiling electron and gamma ray, and (2) provides the location and energy of each interaction site. We are working on prototypes of two detectors that take advantage of this physics. One—utilizing high-purity germanium (HPGe) as the detection medium—would provide an efficient, man-portable instrument. The other—based on high-pressure noble gas—is envisioned as a large fixed or vehicle-mounted instrument.

Our efforts on the HPGe detector during FY1999 were concentrated on verifying earlier calculations and measurements (which we had made on a 1-D, position-sensitive system) on a fully 3-D, position-sensitive device. We worked in close collaboration with a group at Lawrence Berkeley National Laboratory—where there is a detector of suitable configuration to demonstrate our goals. An apparatus based on the Compton-scattering process allowed us to deposit a known amount of energy in small-volume elements within the detector. The signal generated by these depositions was used to measure the position-response function of the detector. Preliminary results show that we can achieve a position resolution in all three dimensions that is better than 1 mm for energy depositions as small as 300 keV. We achieved this performance with electronic noise levels that can be significantly reduced in a custom unit, thereby further improving our performance.

During FY1999, we directed our work on the noble-gas detector towards developing an apparatus with which to experimentally verify our earlier calculations. We focused on the rigorous gas-purity requirements (impurities levels of parts per billion) and the detector working pressure of 50 atm (5 MPa). We (1) constructed a gas-handling system to purify and maintain the gas at these purity levels, and (2) designed and constructed experimental chambers to verify the gas purity and perform the gamma-ray detection measurements.

We also worked on understanding the structure of the radioactive background at degree angular scales. Because of local changes in manmade and natural features, the world's background radioactivity varies from place-to-place by several times its size. With our imaging techniques, we look for localized sources. To understand our sensitivity to such sources, we must understand the structure of the ambient radiation background on the resolution scale of our images. This is an area that has previously not been investigated. Lacking an imaging detector, it is hard to measure this background—we are developing models of the real world to try to understand this. Our goal is to build a 3-D world populated with structures comprised of materials with realistic emission spectra. The response of our detector can be placed in this world and the images obtained used to predict and understand what we will see when our systems become operational.

In FY2000, our goal is to demonstrate both the energy and 3-D position resolution required to generate useful Compton images using the completed noble-gas detector system. These results will be used to optimize the design of a full-sized prototype.

FemtoScope: Ultrahigh Bandwidth Single-Transient Optical Signal Recorder

M. E. Lowry, C. V. Bennett, H. W. H. Lee, T. C. Bond, P. A. Thielen

Many national security missions and stockpile stewardship, in particular, will require advancement in high-speed signal recording and analysis. For instance, if one performs a simple spatial scaling from the geometries of weapons physics experiments carried out at the Nevada Test Site to capsule geometries at the National Ignition Facility, a conclusion might be drawn that measurement bandwidths in excess of 1 THz could be required. It is the objective of this research to investigate technologies that will lead to single-transient data recorders with temporal resolutions in the 100-fs to 1-ps range and in dynamic ranges greater than 100. Our technical approach has two complementary development tracks. Our first track is to develop novel all-optical gating technology that will enable high fidelity, single-transient samplers. All-optical switching gates are used to switch out sequential short-time slices of the single-transient signal. Multiple low-bandwidth detectors then record the switched time slices in parallel, thereby sampling the optical signal. Our second approach is to develop a high performance time-lens that expands the time-scale of the optical signal beam. This temporal magnification of the signal will allow the use of slower sampler technology.

In FY1999, in the all-optical gating track, we demonstrated the first all-optical Fullerene sampling gate in a tabletop Sagnac interferometer with temporal resolution of 100 fs. The test waveform was two 4-ps pulses spaced apart by 6 ps. The time-domain-sampled data was compared to an autocorrelation measurement and found to be in excellent agreement. We also conducted detailed modeling of our non-linear directional coupler sampling design and determined the materials to use for its implementation. Further, for this approach, contamination of the signal beam with the pump beam is a significant source of noise; however, we have determined that the nonlinear material exhibits significant switching behavior even with the pump beam displaced spectrally by 20 nm. With this spectral separation, we can optically filter any pump contamination from the signal. In future research, we will fabricate and test Fullerene samplers with at least 10 gates, based upon the nonlinear directional coupler design.

In the time-lens track, we completed construction of the ×100 time-lens, which we designed in FY1998. We carried out detailed evaluations of this time-lens, some of which is illustrated in the figure. In this measurement, an input test pattern containing two optical pulses of width (87 fs) are generated with

systematically variable time delay (667-fs increments). The pulse doublets are passed through the time lens and recorded with a high-speed photodiode and a sampling scope. The output time from the sampling scope is shown on the bottom axis. The centroids of the second pulses are connected by a line, the slope of which demonstrates a temporal magnification (output time verses input time) of 103. We used this magnification factor to generate the equivalent input time on the top axis. This system is currently limited in bandwidth and dynamic range by the response of the photodiode (note ringing in traces of the figure). Deconvolving the response of the photodiode shows that this time lens has a temporal resolution better than 130 fs. We also successfully used streak camera recording with the time-lens in single-transient operation, improving overall system temporal response. Our next step is to miniaturize this time-lens by using all waveguided and optical fiber components leading to a greatly improved signal-to-noise ratio for single-transient measurements and a system that can be fielded.
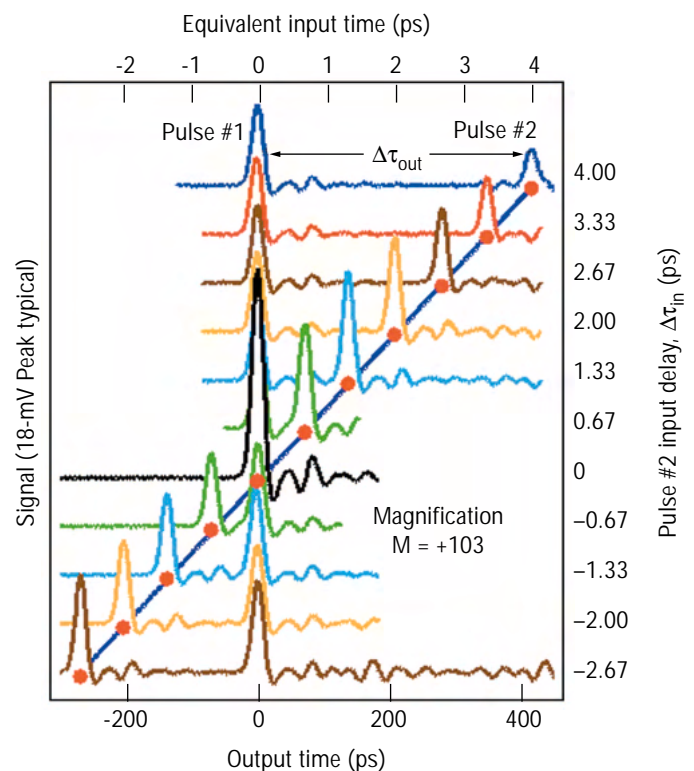
A series of temporal images recorded with a changing input delay for pulse #2. The output time vs. input time demonstrates a temporal magnification of 103.

Qualification of Computer-Based Components for Safety-Critical Applications

J. D. Lawrence

The developers of safety-critical instrumentation and control (I&C) systems must qualify the design of the components used in these systems; in fact, this qualification may be a legal requirement. Examples of safety-critical I&C systems include protection systems for nuclear power plants, monitors for hazardous areas, and medical devices. For computer-based components, design qualification is required for the embedded software—it confirms that a component can be trusted to perform its safety functions under the full range of operating conditions.

Currently, design qualification of computer-based systems is based upon developing confidence in the developer's design, verification, and validation activities. However, this approach has several undesirable characteristics; that is, it (1) does not directly measure the safety of the product, but draws an inference about safety from observation of the development process; (2) requires labor-intensive inspections of development processes and records; and (3) often cannot be applied to existing systems because the appropriate records are not available.

We have been exploring an alternative approach that allows qualification for an important subset of I&C components used in safety-critical applications: computer-based I&C components for safety applications. Our goal is to determine if a combination of static analysis and limited testing can be used for qualification by identifying design constraints that enable meaningful analysis and testing. Once we identify such design constraints, either digital systems can be designed to allow for testing, or existing systems can be tested for conformance to the design constraints as a first step in a qualification process. Our approach will (1) significantly reduce the cost and monetary risk involved in qualifying commercial components for safety-critical service; and (2) permit more rapid introduction of new technology into safety service, thus reducing costs and increasing safety margins.

In FY1998, we chose methods for abstracting and analyzing computer programs in I&C components (using flowgraph and testing theories) and created a list of design constraints that we believed would enable the analysis. In FY1999, we completed the analysis, wrote a prototype analysis program, and demonstrated the approach on several small problems.

Our analysis program operates on a subject program through five steps: (1) create a flowgraph from the program, (2) verify that the design constraints have been met by the program, (3) transform the flowgraph into a tree form, (4) analyze the paths in the tree, and (5) construct a safety argument from the analysis and limited testing.

Our prototype analysis program is directed primarily at the fourth step, because the other steps do not require new research. The analysis starts from the flowgraph, and first transforms it into tree form. There is one branch in the tree for each potential execution path in the subject program. These paths are determined by the conditional branch statements in the subject program. The analysis program first determines the branch predicate for each branch, which consists of the concatenation of all the predicates on the branch with internal variables replaced by functions of the input variables. Then, logically impossible branches are eliminated. As a by-product of this analysis, a branch function is determined, which yields the result calculation for each branch in terms of input variables.

The analysis program then analyzes each remaining branch to determine if faults exist. (We had determined these fault categories during FY1998.) For example, the analysis can determine if any timing constraints have been violated by any branch. When this analysis is completed, the analysis program reports results— either that the subject program has one or more potential faults, or that it is fault-free.

Ultrahigh-Contrast Imaging

C. Max, S. Olivier, B. Macintosh, C. Carrano, D. Gavel, J. Brase

98-ERD-036

The recent indirect detection of 29 planets around 27 nearby stars affords an unprecedented opportunity to characterize these new solar systems from the ground by developing new techniques for ultrahigh-contrast imaging.

In this project, we are exploring techniques that use adaptive optics (AO) to detect very faint objects close to very bright ones. Our long-term goal is to use the Keck Telescope in Hawaii for direct detection of planets and faint companions around nearby stars.

The technologies needed for this ultrahigh-contrast imaging are closely related to those used by LLNL's Laser Program for precision beam control and high-fidelity measurements of optical systems. They include (1) suppression of scattered light; (2) new modes of operation for detectors; (3) high-accuracy calibration techniques for AO systems; and (4) new, "high-finesse" AO systems to reduce light scattered by inhomogeneities in the telescope's primary mirror. We are using LLNL's existing AO system at the University of California's Lick Observatory, together with simulations and laboratory demonstrations, to prototype these technologies for subsequent full implementation at the Keck Telescope.

Our major accomplishment during FY1999 was a search for structure and companions around bright nearby stars using the Lick Observatory AO system. Early in FY1999, we implemented two new methods for characterizing and reducing low-frequency errors on the Lick AO system. We also re-engineered the Lick AO system to attain high optomechanical stability.

Our initial search for structure and companions around nearby stars yielded several successes. The figure shows a low-mass companion to a young star discovered in July 1999 using the AO system at Lick Observatory.

Data on the star HD210277 from high-contrast AO observations at Lick were analyzed by M. Liu, a graduate student at the University of California, Berkeley (UCB). G. Marcy and R. Butler (also at UCB) had—using radial-velocity methods—detected a planetary companion with a high-eccentricity orbit around this star. The presence of a stellar companion was a popular explanations for the high measured eccentricity of the planet's orbit. However, our AO images were used to rule out this stellar companion. A paper describing this work has been published.

One of the major goals of planet-formation studies is to characterize the environments of extrasolar planetary systems. Given the high frequency of stellar companions, secondary stars are an important factor: companions may inhibit planetary formation or significantly alter planetary orbits. We have conducted a high-resolution stellar companion search of nine known extrasolar planetary systems. No new close companions were detected, although several wider visual binary stars (e.g., 16 Cyg A/B) are known. Our preliminary analysis implies that at separations greater than 0.75 arcsec, the AO detection limits exclude any companion stars down to the hydrogen-burning limit.

The long-term goal of this project is to use the new AO system on the 10-m Keck Telescope for even higher-sensitivity planet searches. Following engineering tests of the Keck AO system late in FY1999, it became fully operational.

In FY2000, we will use the precision measurement techniques developed on the Lick AO system to measure high-spatial frequency aberrations and enable prediction of the sensitivity of Keck for planet searches. We will also (1) deploy a coronagraph to further increase the dynamic range of our observations, (2) broaden our search for substellar companions to a large sample of nearby stars, and (3) utilize both the Lick and Keck Observatory AO systems for ultrahigh-contrast imaging.
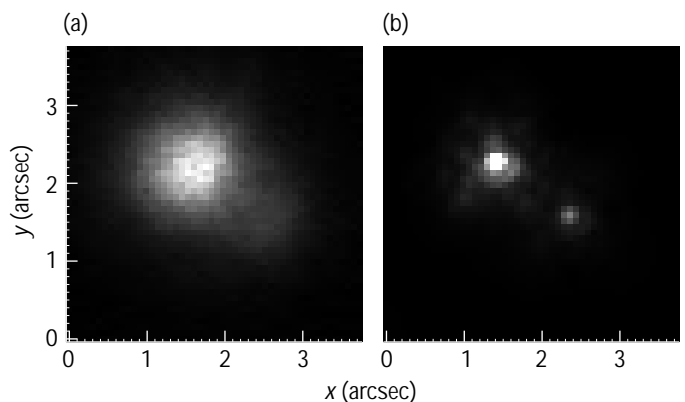
Figure 1. Low-mass companion to a young star (GL808) discovered in July 1999 using LLNL's adaptive optics (AO) system at Lick Observatory: (a) image without AO and (b) image with AO. Adaptive optics allows companions located near bright stars to be detected with high contrast ratio.

RadSensor: An Optical Dielectric Modulation Approach for Prompt Sensing of Ionizing Radiation

M. E. Lowry, H. W. H. Lee, M. C. Larson, H. E. Petersen, G. R. Delgado, S. K. Ault, P. A. Thielen

98-ERD-095

Ultrahigh speed detectors of ionizing radiation will have several important applications in weapons physics and inertial confinement fusion experiments. Examples include diagnostics for fusion burn at the National Ignition Facility and gamma detectors for weapons radiography. We are developing a novel class of ionizing radiation detector that will modulate the intensity of an optical beam in proportion to the intensity of an impinging ionizing radiation beam. Our approach holds the promise of sub-picosecond (ps) temporal response with single-x-ray photon sensitivity. With the temporal history of the ionizing radiation beam so encoded unto an optical carrier beam, the information can be conveniently transported to a remote location for recording (see the related LDRD progress report on FemtoScope, p. 1-5).

As the x-ray photon passes through the material, a large fraction of the deposited energy is stored temporarily as electron-hole (e-h) pair excitations. Rapid relaxation to the band edge alters the absorption spectra of the material by "band filling." A blue-shift in the absorption edge occurs, effectively modulating the imaginary part of the index of refraction. The Kramers-Kronig sum-rule governs these modulations of the dielectric function, dictating that this absorption change will also modulate the real part of the complex optical index. This modulation of the dielectric function can now be used to modulate an optical carrier beam that is also passing through the material.

The e-h pair relaxation processes leading to the band-filling absorption shift are known to be fast (~100 fs) when optical excitation is used. Studying the dynamics of the shift with ionizing radiation is an essential element of this project. However, to develop a radiation detector that accurately tracks the temporal profile of a x-ray beam, the band-filling must also relax to equilibrium rapidly after it is formed. In FY1998, we demonstrated that low-temperature gallium arsenide (LT-GaAs) does exhibit this fast relaxation with optical excitation.

The band edge of LT-GaAs is at too long an optical wavelength for the optically modulated signal to be detected by the streak camera photocathode. Consequently, in FY1999 we initiated the development of alternative semiconductor materials with a blue-shifted band edge compatible with streak camera recording. To achieve this wavelength shift and high-speed operation, we evaluated several classes of molecular beam epitaxy-grown material, including AlGaAs quantum wells, AlGaAs digital alloys, and bulk low-temperature AlGaAs—all at various deposition and anneal temperatures. To evaluate these materials, we developed sophisticated pump-probe spectroscopy tools, including differential transmission spectroscopy (DTS), where an optical pump beam excites e-h pairs in the material under test (see Fig. 1). A "white light," short-pulse probe is then transmitted through the sample and the transmission spectra are measured. This pump-probe combination is repeated systematically for different temporal delays between the pump and probe; the probe spectrum is also measured in the absence of the pump beam. The difference spectrum is then generated for each of the pump-probe temporal delay values. Using this technique, we determined that the band edge was blue-shifted to 780 nm, excellent for streak camera recording. Furthermore, by analyzing these pump-probe signals near the band edge as a function of annealing temperature we have determined that lower-temperature annealing will decrease both the rise-time and fall-time of the DTS signal. We have also developed a laser driven electron source that produces a short pulse of 8×10^6 10-keV electrons. In FY2000, we will progress to e-beam characterization of RadSensor devices and develop a streak camera-based system suitable for fielding.
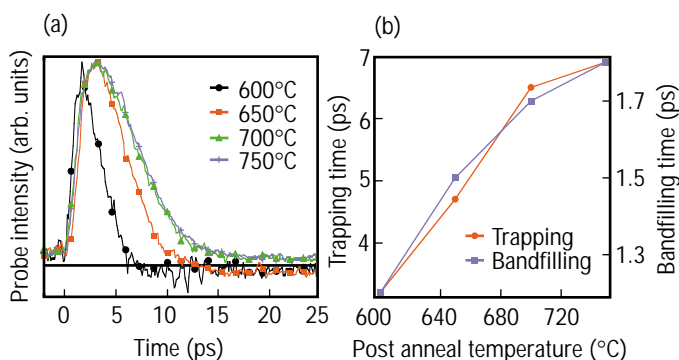
Figure 1. (a) shows pump-probe differential transmissions measurements for LT-AlGaAs for various anneal temperature, while (b) shows rise-times and fall times from (a) vs. anneal time.

Real-Time Detection and Identification of Biological Aerosols with Mass Spectrometry

K. Langry, S. Labov, M. Frank, E. Gard, J. Horn, F. Magnotta, J. Ullom, H. Benner

98-ERD-097

Recent bombings in American cities, the discovery of Iraq's aggressive biological warfare (BW) program, and the release of sarin in a Tokyo subway have all caused government officials and military planners to re-evaluate our ability to defend ourselves against a catastrophic BW attack on a major metropolitan area. Experiments with surrogate agents during the late 1960s, along with recent atmospheric modeling studies, suggest that we could sustain massive casualties and deaths. If an attack with BW agents occurs, early detection and agent identification will be paramount in the effort to save lives.

Our research effort is directed at developing the capability for real-time analysis of biological aerosols in rural and urban environments. The goal of our project is to show that biological aerosol particles exhibit a characteristic molecular signature that can be developed using a combination of laser thermolysis and time-of-flight (TOF) mass spectrometry. To achieve our goal, we are exploring laser-based methods for dislodging major identifying proteins from the surfaces of bacterial spores. Proteins liberated with this technique will be analyzed as they are displaced from the spore using a TOF spectrometer equipped with a superconducting tunnel junction (STJ) detector. This combination of laser thermolysis, TOF mass spectrometry, and high molecular mass (>MD) detection with the STJ detector represents a new, sophisticated approach to the real-time analysis of biological aerosols. With this capability, we will be able to build autonomous detection systems that will sample the atmosphere and identify biological aerosols ranging from warfare agents to other pathogenic agents of medical and agricultural concern.

In FY1999, we cultured three species from the genus *Bacillus* (*cereus, thuringiensis*, and *subtilis* var. *Niger*) and prepared clean spores of each species [see Fig 1(a)]. These spores were evaluated using the matrix-assisted, laser-desorption/ionization (MALDI) technique on a TOF mass spectrometer—as whole spores, and as their extracted protein coats. The whole-spore spectra [see Fig. 1(b)] show that each of the three species yields a unique molecular signature in the 10- to 100-kD mass range. We compared this mass spectral data with mass data collected by electrophoresis—the two techniques show remarkably similar distribution of molecules with corresponding masses. We used electrophoresis and column-chromatographic techniques to purify some of the individual proteins that comprise the spore coats.

In collaboration with Lawrence Berkeley National Laboratory (LBNL), we compared the mass range sensitivity for LLNL's STJ detector with the microchannel plate detector, a standard detector used in mass spectrometry. The STJ detector showed almost an order of magnitude greater sensitivity in the mass range of 20- to 100-kD. There were also other areas where the STJ detector was superior to the microchannel plate.

Generation of mass spectra at infrared (IR) frequencies with the optical parametric oscillator (OPO), which we constructed in FY1998, was delayed when the Nd:YAG pump laser was found to be too unstable; however, we replaced this laser and modified the optics of the OPO. The result was substantially improved output in the 2.7- to 3.5-µm spectral region that corresponds to the hydrogen-heteroatom stretching frequencies of peptides and proteins.

To complement the spectral range of the OPO system, we assembled a Raman-shifted dye laser (RSL) that will provide tunable laser output between 5 and 7 µm, which corresponds to the intense carbonyl absorption frequencies of amino acids, peptides, and proteins. We will begin testing and operating these IR laser systems as soon as safety procedures have been implemented.

In FY2000, we will use the OPO and RSL to generate mass spectra from matrix-free spores and purified spore proteins.
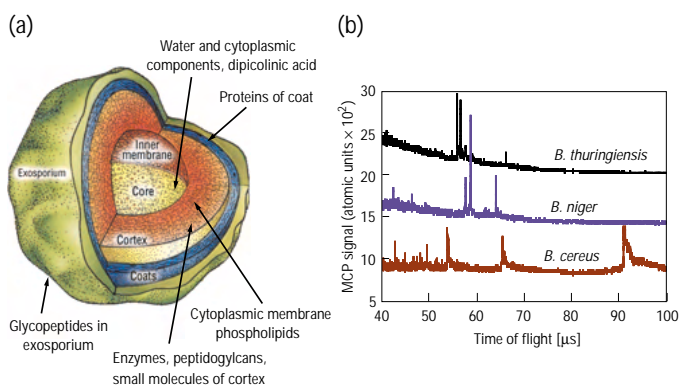
Figure 1. The stratigraphy of a typical spore of the genus *Bacillus* and the location of signature molecules that potentially could be elicited with pulsed infrared laser irradiation are shown in (a); (b) shows mass spectra of spores obtained from three species of *Bacillus* (*thuringiensis, subtilis* var. *Niger*, and *cereus*) using the MALDI (matrix-assisted laser desorption/ionization) mass-spectrometry technique. Matrices of sinipinic acid containing spores of the different species were irradiated with a pulsed nitrogen laser (357 nm).

Development of AMS Capability for Plutonium and Other Actinides

J. E. McAninch, T. F. Hamilton, T. A. Jokela

98-ERD-100

Low-level actinide measurements have important application throughout the DOE complex—in areas such as civilian and worker exposures, environmental levels and transport, radioactive waste, and nonproliferation and national security. Many present-day applications require a combination of sensitivity and throughput beyond that possible with currently available techniques. Development of a robust, high-throughput, and cost-effective analytical tool with the sensitivity to detect these prominent products of the nuclear fuel cycle at environmental levels will have a broad impact in many of these core DOE mission areas.

The main focus of this project is the development of an actinide measurement capability within LLNL's Center for Accelerator Mass Spectrometry (CAMS). Specifically, this project will result in a capability for the quantitation of plutonium concentrations and isotope ratios in urine bioassays. The technical goals are (1) sensitivity $<1 \times 10^6$ atoms per sample, (2) initial throughput of several hundred samples per year, and (3) a cost per sample similar to that of standard alpha-spectrometry measurements.

Our efforts during FY1999 consisted of addressing basic technical issues related to achieving these goals—such as sample form, detection efficiency, backgrounds, and interferences.

The work within this project capitalizes on a series of hardware upgrades to the CAMS spectrometer, which center around the construction of a heavy-element beamline that will include a 4.4-m radius, 45° electrostatic analyzer (ESA) for removal of interferences, primarily ^{238}U interference at mass 239. Our LDRD-funded capability development during FY1999 was performed on a prototype version of this beamline, in which a Wien filter provided limited rejection of interferences. The figure shows the prototype and planned beamlines.

During FY1999, we demonstrated the basic components of our capability. Sample preparation was based—with only minor modifications—on standard alpha-spectrometry protocols. Backgrounds at masses 237 and 239 were about 1 to 2×10^7 atoms per sample and were dominated by remaining interference from ^{238}U. Backgrounds at masses 240 and 241 were less than 1×10^7 atoms per sample. Precision, at about 10 to 20%, was limited by the relatively long time (~30 s) required to switch between isotopes on the prototype beamline.

We successfully applied our preliminary capability to a set of soil samples that included International Atomic Energy Agency (IAEA) reference materials. Measured $^{239+240}$Pu concentrations showed reasonable agreement with the IAEA reference value; ^{240}Pu/^{239}Pu isotope ratios matched recently published inductively coupled plasma-mass spectrometry (ICP–MS) results for the same samples. Measurements of ^{241}Pu, a difficult-to-detect beta emitter that could provide an important additional isotopic signature, were also made in these samples. Though not a primary focus of this project, measurements of ^{241}Pu come with no added cost. Similarly, we expect capabilities for other isotopes, such as ^{237}Np, as direct byproducts of the present project.

Our work during FY1999 forms the basis for development of the full capability during FY2000. The final heavy-element beamline is expected to be operational in early FY2000. The ESA is expected to improve rejection of ^{238}U by a factor of 10 to 100, which will allow us to reach the target sensitivity while simultaneously reducing the demands on the sample-preparation chemistry. Faster isotope switching will reduce measurement time and improve isotope-ratio precision to about 1 to 2%. During FY2000, we will emphasize (1) demonstrating the routine application of this capability, and (2) optimizing the sample preparation to minimize cost and maximize throughput.

Once complete, our AMS capability will provide ultratrace sensitivity for Pu isotopes with high rejection of interferences and low susceptibility to other elements and compounds in the sample (matrix components). These advantages will lead to reduced demands on the sample-preparation chemistry, to high throughput, to rapid turn around of results, and—ultimately—to larger, more reliable, and more complete data sets.

Diagram of the accelerator mass spectrometer used for measurements of Pu concentrations and isotope ratios. We conducted our FY1999 development work on the prototype beamline; we expect improved sensitivity and precision with the final heavy-element beamline.
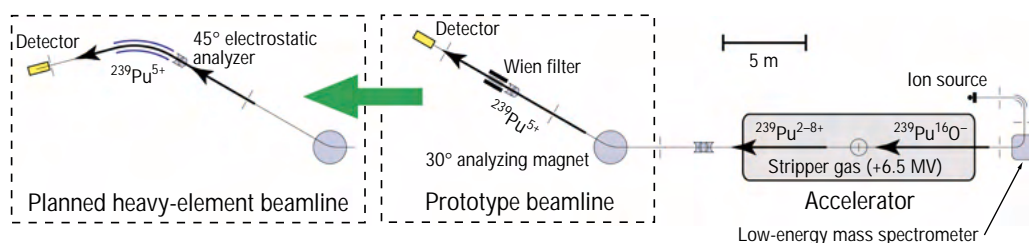
Novel Ultrasound Scintillator

J. S. Kallman, A. E. Ashby, D. Ciarlo, G. H. Thomas

98-LW-035

Nondestructive evaluation (NDE) is important for evaluating materials and processes without causing any damage. The primary imaging technologies at the Laboratory utilize either x-rays or ultrasound. X-ray imaging is very useful, but sometimes a subject is either difficult to penetrate, has low x-ray contrast, or might be damaged by radiation. Ultrasound has different penetration and contrast characteristics from x-rays and eliminates the subject's exposure to ionizing radiation. One of the ultrasound modalities used at LLNL is transmission ultrasound imaging, which is best suited to imaging subjects that are lossy—such as high explosives and ceramics important in the nuclear weapons stockpile stewardship effort. In this modality, the subject is placed in an ultrasound medium bath, and the resultant output acoustic field is mechanically scanned with an ultrasound sensor. This imaging modality, although useful, is very time consuming, taking approximately 20 minutes to collect the data from small objects.

In an effort to speed the acquisition of transmission ultrasound data and to make feasible the routine use of volumetric ultrasound imaging, we developed the Optically Parallel Ultrasound Sensor (OPUS). This sensor uses the phenomenon of frustrated total internal reflection to make the acoustic field modulate an optical beam. The OPUS allows the acquisition of an entire plane of acoustic field data all at once and could reduce the time of data acquisition by up to four orders of magnitude.

In FY1999, we extended our proof-of-principle research on the OPUS and produced prototype acoustic field sensors, which we used to acquire transmission ultrasound data over a planar region. These sensors will also be used to transmit ultrasound imaging and ultrasonic tomography.

The sensor consists of a planar silicon nitride membrane supported on micromachined gold walls over a glass substrate. The membrane is divided into 70-μm square cells. The deflection of the membrane by ultrasonic waves causes a reflected optical beam to be modulated, which is captured by a charge-coupled device camera. Strobing the illumination and capturing a sequence of images allows us to extract the phase and amplitude of the acoustic wave at any point on the sensor.

Working from the proof-of-principle system and data collected in FY1998, we constructed the OPUS data acquisition system shown in the figure and built several sensors. Over the course of the year, we experimented with the sensors, collecting data and making refinements to the sensor designs in both microstructure and macrostructure. We discovered that the membranes must be very carefully cleaned prior to sensor assembly, as any contamination larger than 0.2 μm was large enough to cause the membrane to deform around it—consequently, concentrating stress and eventually breaking the membrane under the hydrostatic load of being immersed into the operating fluid. We also found that the nonplanarity of the silicon wafers on which the membranes are grown can accentuate the membrane fragility. We are now constructing low-stress membranes on flatter wafers, with more compulsive cleaning to remove debris. The result has been much higher quality, durable sensors. Another aspect of our work this year was the start of automating the acquisition of data. We began the modifications to the computer program that acquires the data to automate sequence acquisition.
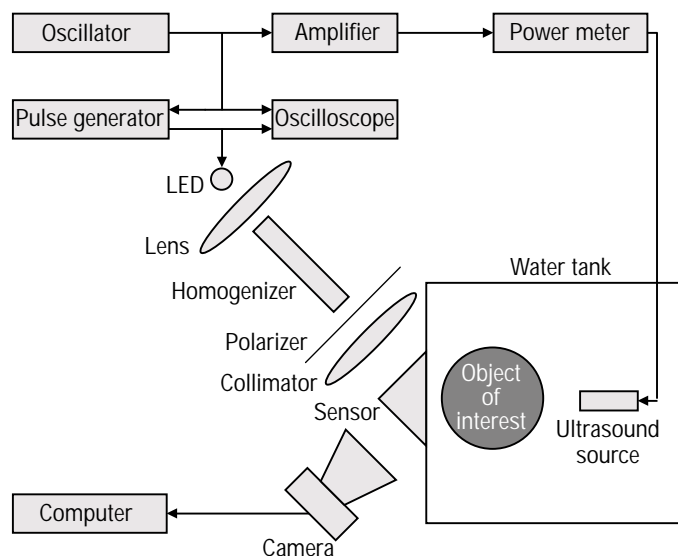
Schematic of transmission ultrasound data acquisition system. The LED is synchronized to a specific phase in the acoustic cycle by the pulse generator.

Remotely Interrogated, Gbit/s, Free-Space-Laser Communications Link

A. J. Ruggiero, J. D. Cooke, R. P. Ratowsky

99-ERD-011

The evolving sophistication of remote-sensing systems for military and intelligence applications has led to an increasing demand for high-data-rate communications links (comlinks). Distributed microsensor networks incorporating satellites and unmanned aerial vehicles (UAVs) are merging with terrestrial sensor networks to provide unprecedented, multisensor data-fusion capabilities. Increasingly large data volumes, along with mission requirements for low-weight, high-reliability, insensitivity to electromagnetic interference (EMI), low cost, and low probability of interception/detection (LPI/LPD)—all place additional stress on future tactical communications systems.

Comlinks using retromodulator phase-conjugate (RMPC) mirrors provide a potential solution to the problem. Initially proposed in the late 1980s, RMPC mirrors are all-optical devices that receive an incident optical beam, encode temporal information on the beam, and then return the encoded information to the point of origin in a manner in which the wavefront is reversed (i.e., phase conjugated). Phase conjugation of an optical beam creates a reflected beam that precisely retraces the optical path of the incident beam. Data are encoded by modulating the phase-conjugation process. Phase conjugation removes optical distortions caused by atmospherics and permits establishment of a high signal-to-noise comlink. In addition, because the phase-conjugation process precisely returns the probe or beacon beam to its origin, it provides an automatic pointing and tracking function. Previous attempts to employ nonlinear optical phase conjugation in comlinks have met with limited success—primarily because of the inherent limitations associated with the materials used as optical phase conjugators. These systems often required either high levels of system complexity and optical power, or if implemented under low power conditions, exhibited severe range limitations.

In this project, we are developing an alternative RMPC mirror based on intracavity, nondegenerate, four-wave mixing in broad-area semiconductor laser structures. This novel class of microphase conjugator takes full advantage of semiconductor engineering and processing technology to produce phase-conjugation devices that can be economically packaged and easily interfaced with a variety of sensor heads by simple current encoding. Data rates of Gbit/s or greater are feasible in our approach, which circumvents the issues that plagued deployment of previous comlinks that were based on nonlinear optical phase conjugation. A possible deployment scenario is shown in the figure.

Our efforts in FY1999 focused on exploring the general feasibility of the approach and gaining an understanding of the key issues involved in actually making the proposed comlink a reality. We generated phase-conjugate signals via intracavity, nondegenerate, four-wave mixing using less than 100 nW of injected probe power and intracavity powers in the tens of milliwatts. These experiments were done in a novel, broad-area laser structure known as an alpha-distributed feedback laser (DFB) for the first time; they demonstrated the feasibility of efficient phase conjugation of low-power signals in these systems. Our experiments on the effects of frequency detuning of the beacon or probe laser revealed strong cavity-resonance effects that we exploited to produce conjugate powers one thousand times greater than the probe beam. We also demonstrated that high-speed modulation of the conjugate signals and the simultaneous conjugation of different-frequency probe beams. Our results were in good agreement with the first-order theoretical models of intracavity, diode-laser, four-wave mixing that were also developed as part of this preliminary work. Using the knowledge gained during this effort, we developed a conceptual design for an optimal 2-D microphase conjugator. We are currently pursuing patent positions on this technology, and have partnered with a major diode laser manufacturer for its development. In FY2000, we plan to finish our laboratory feasibility experiments and modeling.
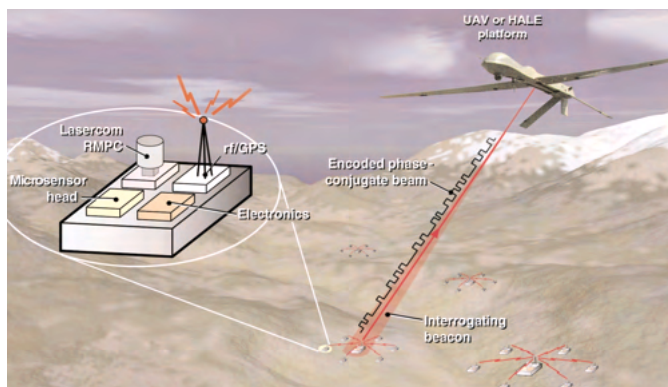
High-data-rate, interrogated communications links based on semiconductor-laser, retromodulator, microphase-conjugator technology can be used for data uplinks and downlinks between air and ground assets. Illustrated as a data uplink from an unattended ground sensor to an unmanned aerial vehicle (UAV) or high altitude long endurance (HALE) platform, the link is initiated by irradiation of the sensor system with a laser beacon. The sensor system responds by returning an encoded phase conjugate beam. The ground system consists of the microsensor head, interface electronics, retromodulator phase conjugator (RMPC), and a low-power radio-frequency global-positioning system (rf/GPS) for initial sensor location.

Stand-Off Detection and Tracking of Bioaerosol Clouds

F. Magnotta, W. M. Pfenninger, D. C. Johnson, W. E. Conaway

99-ERD-013

The military use of biological weapons (BW) is considered a very real threat on today's battlefield. The potential for devastating losses and the increase in the accessibility of the production technology make BW proliferation and use primary concerns. U.S. military planners are under pressure to provide tools to the war fighters in the field that diminish the impact of such an attack through early detection and rapid, effective response. Early detection is perhaps the critical factor in limiting casualties. Exposure to low levels of agent (less than 10 agent-containing particles per liter of air in the case of anthrax) over the period of several minutes can be fatal. Stand-off sensing could be used to provide significant advanced warning of an attack by detecting a cloud well in advance of its reaching a protected area. Several approaches have been proposed to provide standoff detection of a biological agent attack, including short-range laser-induced-fluorescence and a long-range, non-discriminating, single laser wavelength-scattering technique. We are investigating a technique that has not been considered previously and represents a novel approach to the long-range, stand-off BW detection problem.

The paradigm tested in this LDRD project expands on the use of simple single wavelength scattering; it attempts to recover spectral information from a released bio-cloud by invoking differential scattering and absorption using a frequency agile, mid-wave infrared laser system. The mid-wave infrared is reasonably well-matched for efficient Mie scattering from bioaerosol particle sizes and can provide access to the C–H, N–H, and O–H stretching signature region for organic and biological materials. The LDRD builds on DOE investment in advanced laser technology development at LLNL under the CALIOPE Program. The Portable Lidar Laboratory (PLL) developed by that program is a high repetition rate, frequency agile, and continuously tunable solid-state laser transmitter system operating in the optimal mid-wave infrared wavelength region. Previous modeling studies and laboratory measurements at LLNL indicated that laser radiation scattered from an agent-containing cloud should display a spectral signature that is characteristic of the cloud's contents. The calculations also indicated that this technique can provide adequate signal levels from plumes located at stand-off distances from close-in to several tens of kilometers. The purpose of this LDRD is to test these predictions by performing a field experiment utilizing the CALIOPE PLL.

In FY1999, we performed a five-week field test at the Aberdeen Proving Ground in collaboration with the Army's Chem-Bio Center. The samples tested were *Bacillus Globigii, Bacillus Thuringiensis, Ovalbumin, Kaolin* and two types of Arizona road dust. The materials were dispersed into quantitatively measured aerosol clouds downrange of the PLL. Mie scattering returns were collected using 16 transmitted wavelengths chosen to optimally interrogate the spectral features of the bio simulant materials. The results of the field test demonstrated that all six materials could be discriminated from one another. The absolute scattering and extinction cross-sections for all of the samples were measured. The minimum detectable particle density/path length product was also determined and was comparable to that calculated in the modeling studies.

This project demonstrated for the first time the ability to detect and discriminate various bio-simulant aerosol clouds from one another and from common dust clouds. In FY2000, we will continue to pursue our modeling efforts in an attempt to understand the detailed nature of the observed scattering returns. In addition, we will undertake a second field test using the newly built CALIOPE Apex Lidar system, which will demonstrate the enhanced detection capabilities of that platform.

Large-Scale, Wireless Sensor Networks with Distributed Data Interpretation

R. M. Bryant, F. U. Dowla, C. T. Cunningham, S. G. Peglow

99-ERD-014

Intelligent and easily deployable sensor systems are important for many national security applications, particularly those relating to nonproliferation and tactical systems. Current wireless sensor platforms are characterized by large size and weight, high battery-energy needs, and limited intelligence and network scalability. In these systems, sensor information is communicated to a central node, where it is fused with other sensor information. As the number of sensor nodes and the area of coverage increase, communication energy and latency increase, requiring larger and heavier platforms—which are cumbersome to deploy and not feasible for covert applications. The goal of this project is to addresses these issues through the development of distributed data-interpretation algorithms and energy-efficient hopping network protocols—thus allowing networks with hundreds of nodes. The application being addressed is recognition and tracking of target vehicles using both seismic and magnetic sensors.

In FY1999, we focused on (1) evaluating and selecting the distributed algorithms for target detection, (2) determining and analyzing energy-efficient network communication protocols, (3) defining the microsensor processing requirements, and (4) prototyping and field testing using an existing sensor platform.
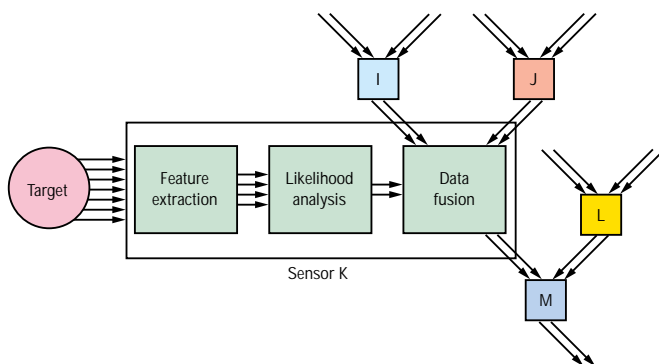
A scalable, self-configuring sensor network based on Bayesian algorithms. Each sensor node (Sensor K) extracts features from the sensor signal, calculates the probability of a target match, and fuses probabilities with neighboring sensor nodes (Sensors I, J, L, and M).

We considered two approaches for distributed decision making—one based on neural-network concepts and the other using Bayesian algorithms. The concept of distributing a neural network across multiple sensor nodes was not feasible because (1) training a distributed neural network is problematic due to unknown sensor positioning, and (2) communication between sensor nodes would be excessive because all nodes must share information throughout the network. The Bayesian approach does not require training and is energy efficient because communication occurs only when there is sufficient probability that a target has been detected. In this approach (see figure), each sensor node independently extracts features from its raw sensor signals, compares these features with the targets, calculates a detection likelihood, fuses likelihoods received from neighboring nodes, and communicates only the likelihoods to its neighboring nodes.

During FY1999, we defined an efficient, scalable, self-configuring network approach that forms a tree-structured topology based at a user or gateway node. Our simulations using the commercial Opnet Modeler network-simulation package showed that the network can configure in a time proportional to the diameter of the network rather than in proportion to the number of nodes—this greatly improves network scalability. The communication protocol is contention-based, with link-level acknowledgments to protect against collisions and bit-errors. We also designed a wake-up signaling mechanism that allows receivers to reduce overall energy usage.

We used the existing LLNL tactical, unattended, ground-sensor (TUGS) platform for developing prototype software and for collecting vehicular seismic signals. Five units were integrated for developing and testing the networking software, signal-processing algorithms, and Bayesian data-fusion and target-recognition algorithms. Results of the field tests indicate the importance of both low-frequency seismic signals in distinguishing different vehicle sizes and the synergy with other sensor types, such as magnetic sensors.

In FY2000, we plan to develop a small network of wireless sensor platforms capable of recognizing and tracking a target vehicle.

Speckle Reduction for LIDAR using Optical Phase Conjugation

M. W. Bowers, J. J. Benterou, J. B. Cooke

99-ERD-024

Remote detection systems can be used to monitor the production and use of chemical, biological, and nuclear weapons as well as environmental conditions around the world. LIDAR (light detection and ranging) is well suited for these applications. In a LIDAR system, a laser beam is transmitted out towards the area to be probed; the return scatter from the aerosol itself or the topographic background is detected and measured.

Practical LIDAR systems are complicated by noise sources such as speckle, which results from the light scattering off a diffuse surface and interfering with itself to create light and dark spots at the detector plane. Optical phase conjugation is a nonlinear optical method of removing the destructive interference of the diffuse rays of light, which results in a uniform illumination of the detector and a reduction in the associated noise. We intend to show that it is possible, under most normal LIDAR operating conditions, to use optical phase conjugation to mitigate the effects of speckle.

Our goal for FY1999 was to demonstrate the technical feasibility of using optical phase conjugation to reduce the undesirable effects of speckle. The first step towards this goal was to perform a numerical study to show what regimes would benefit from this new technology. We planned a laboratory experiment that would approximate an outdoor field LIDAR system. The results of this experiment demonstrated that the phase conjugation process improved the quality of the scattered light by an order of magnitude (see figure). Although good, the results were less than expected through the numerical studies performed earlier. The problem was found to be in the geometry of the stimulated Brillouin scattering (SBS) phase conjugator. The geometry prevented light rays that were entering at extreme angles from participating in the phase conjugation process. We found that waveguides, which can capture the light rays that enter at extreme angles, were the solution to this problem, and we tested liquid- and solid-filled waveguides for their applicability. Although the liquid-filled waveguides did have good phase conjugation properties, they suffered from heat buildup near the entrance that created bubbles after several minutes of operation. The bubbles would be drawn into the waveguide, stopping the SBS process. This problem can be corrected by flowing the liquid continuously through the waveguide, removing bubbles whenever they form. The solid waveguides are essentially optical fibers that are specially shaped to enhance the SBS process. These waveguides have similar phase conjugation properties to those of the liquid filled counterparts, but do not suffer from the bubble formation.

We undertook a collaborative effort, funded through this LDRD project, with the University of Rochester, to search for appropriate materials for the SBS process in wavelength regions of interest to most commercial LIDAR systems. A table of more than 100 suitable materials was narrowed down to the best candidates. We determined that commercially available infrared (IR) fibers would be suitable candidates because of their availability in a waveguide form.

We will move our speckle reduction system to the portable LIDAR laboratory for field testing in FY2000. We plan to test the noise reduction capabilities at a range of 1-km using a variety of diffuse and specular targets. An increase in the signal to noise of just three in this test will prove to be an order of magnitude reduction in the averaging time needed for this LIDAR to perform its intended functions.
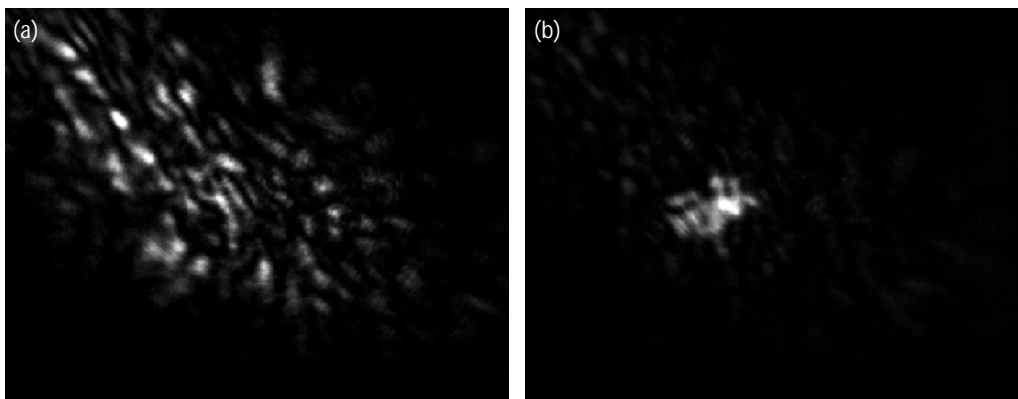
The experimental results show speckle (a) for a LIDAR return signal and significantly better signal quality (b) after the incorporation of the optical phase conjugation.

Fast Gate: Subnanosecond Gated Detectors for Laser Radiography

J. Trebes, M. Feit, S. Hatchett, M. Key, M. Perry, T. Phillips, J. Sefcik, R. Snavely, M. Weber

99-ERD-035

X-ray radiography is used as a principal diagnostic in a wide range of hydrodynamic tests relevant to the weapons program and also for basic materials and equation-of-state science studies. The quality of the x-ray radiograph can be significantly degraded by the scattering of x rays within the object and by the test system itself. Elimination of these scattered x rays from the recorded images could either substantially improve the image contrast and signal-to-noise or allow smaller, lower-cost x-ray sources to be used. The scattered x rays could be minimized through the use of a much shorter-duration x-ray pulse and a fast, gated detector. Intense, laser-driven hard-x-ray sources such as produced by the Petawatt laser offer a new, short-pulse source of x rays for x-ray radiography. The combination of the existing short-duration, Petawatt-produced x-ray pulses and an x-ray detector with sub-100-ps gate times could eliminate most of the scattered x rays from the radiograph image and allow highly improved radiography.

Our goal in this project was to develop a new class of high-speed, high-energy x-ray detectors for flash-x-ray radiography applications. These detectors would have a detection time of 100 ps or less and would be sensitive to x rays up to 10 MeV.

During FY1999, we evaluated several detector concepts through detailed analysis and modeling. These included detectors based on Cherenkov emission, on resonance transistion radiation, and on the use of the electric fields produced by Compton electrons to provide a polarization rotation in a laser-probed, electro-optic crystal. These detector concepts, while having the potential for sub-100-ps time response, were shown to have insufficient x-ray detection sensitivity at MeV x-ray energies of interest.

We also investigated a new scintillator crystal and fabricated and tested prototype detector elements. This crystal, barium lutetium floride ($BaLu_2F_8$), has a density of 7.14 g/cm^3, which allows for good x-ray stopping power at high x-ray energies and for submillimeter spatial resolution. The crystal has a fast, ultraviolet fluoresence emission band at 300 nm because of core valence transitions.

We worked with a commercial company to manufacture the first ever long-crystal samples of $BaLu_2F_8$. These crystals measured 20 by 1 by 1 mm and were appropriate for use in high-energy detection systems. We measured the time response of the fast emission band when sample crystals were irradiated with 90-ps x rays produced from a laser-plasma x-ray source. The risetime was less than 30 ps, with a decay time of less than 800 ps. The fluorescence efficiency was measured relative to a commonly available barium floored crystal of identical size. The $BaLu_2F_8$ crystal was found to be 5 times less efficient than the barium fluoride crystal.

We investigated possible uses of the new $BaLu_2F_8$ crystals in practical high-energy high detection and found that (1) the $BaLu_2F_8$ crystals can be packaged into an array; (2) the high-speed fluorescence produced by x-ray irradation of the $BaLu_2F_8$ crystals in the radiography process can be imaged with an ultraviolet lens onto a gated, microchannel plated detector; and (3) the combination of the extremely fast risetime of the ultraviolet fluorescence from $BaLu_2F_8$ and the sub-100-ps gating times for micochannel plate detectors will allow an efficient MeV x-ray detector to be built with sub-100-ps gating times.

Defect Inspection of Heterodyne Mask Blank

G. E. Sommargren

99-ERD-060

The U.S. dominance of the semiconductor industry is vital to national security as well as to the overall health of our economy. To meet the needs of advanced semiconductor design, each generation of lithography demands smaller critical dimensions (CDs). This in turn puts a tremendous burden on the fabrication of the masks that contain the master patterns —specifically, on the detection of defects—because a mask defect as small as one-eighth the CD may cause the failure of a semiconductor chip.

If we assume (1) 3-year intervals between generations, (2) a lithography tool with a de-magnification between the mask and wafer of 0.25, (3) a maximum mask defect of half the CD, and (4) a starting point in 1999 of a CD equal to 180 nm and a maximum mask defect of 90 nm—then, by 2014 we can expect a CD of 35 nm and a maximum mask defect of 18 nm. A new infrastructure for mask inspection will be required to keep pace with this aggressive schedule; mask blanks will require a 100% inspection.

The detection of defects smaller than 100 nm is not commercially available, nor is the ability to inspect transparent substrates (a prime candidate for future mask blanks). As masks become a significant factor in the cost of ownership of lithography tools, defect detection becomes a critical technology.

Defects scatter light; however, scatter from defects smaller than the wavelength of light is weak, falling off as the sixth power of the defect size. Conventional scattering methods that use direct detection of this scattered light become quite inaccurate for defects smaller than 100 nm, particularly in the presence of background scatter from the inherent roughness and inhomogeneity of the mask blank as well as ambient light scattered from surfaces within the instrument.

Our goal in this project has been to address defect detection using a heterodyne interference/synchronous detection technique that can amplify the scattered light from small defects by as much as six orders of magnitude.

During FY1999, we explored the use of heterodyne techniques to enhance the detection of the scattered light while simultaneously rejecting background scatter. In this approach, shown schematically in the accompanying figure, two laser beams with slightly different frequencies are focused onto the surface of the mask blank at different angles of incidence. Weak scatter from a defect in the probe beam mixes with the strong, specularly reflected reference beam on a high-speed photodetector. The sinusoidal output at the difference frequency has a magnitude proportional to the product of the weak scattered field and the strong specular field. Bandpass filtering removes electronic noise. Optical noise is significantly reduced because background scatter originating outside the coherent probe volume does not contribute to the detected sinusoidal signal. Electromagnetic modeling of the scatter from defects of varying size and refractive index and from inherent surface roughness determines the exact geometry of the illumination and probe beams that is necessary to maximize the signal-to-noise ratio.

Controlled beam mixing and optical heterodyne detection experiments indicate that defects as small as 15 nm can be detected under typical background-noise conditions. These initial results led to the construction of a prototype instrument that, at year's end, was being interfaced to a computer for data acquisition. To characterize the instrument, we fabricated mask blanks that are sparsely covered with calibrated, 20- to 100-nm-diam gold spheres.

By the close of FY1999, we had initiated technology-transfer efforts. We have had several meetings with users and suppliers of defect-detection equipment. Intel has been briefed on this work; KLA-Tencor and ADE have expressed a strong interest in working with us and are currently comparing their direct-scatter measurement methods to our heterodyne approach.
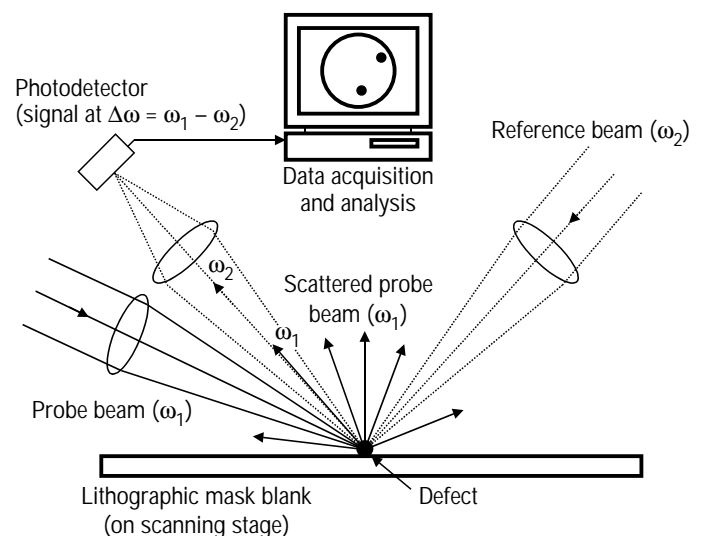
Experimental layout of the probe, reference, and scattered beams for detecting a defect on a lithographic mask blank using optical heterodyne detection.

Single Fluorescent Molecule Confocal Microscopy: A New Tool for Molecular Biology Research and Biosensor Development

C. Darrow, R. Balhorn, K. Campos, T. Huser, S. Lane, T. Peyser, M. Yan

99-ERD-067

This project seeks to exploit the use of single-molecule detection (SMD) in the development of ultra-sensitive assays for medical, biological, and national security applications. A relatively new technology, SMD allows the isolation, detection, and characterization of individual fluorescent molecules. Because fluorescent molecules (e.g., rhodamine) can be chemically attached to antibodies, they can be used to tag or label a target species (e.g., a toxin) in an assay sample. The ability to then detect and identify single rhodamine labels leads to theoretically unprecedented sensitivities for such an assay. Our goal is to demonstrate the sensitivity of a specific SMD assay, namely an assay for *botulinum* neuro toxin. This particular toxin is an ideal candidate because of (1) its extreme toxicity to humans, (2) the low contamination levels at which it is harmful, and (3) the possibilities of exposure through contaminated food products or terrorist activities.

Funding of the project began in April FY1999, with the intent of pursuing continued funding for FY2000. The goals for FY1999 were to reconfigure and upgrade existing laboratory equipment and to demonstrate SMD at LLNL. We have achieved both of these goals as described below.

We fiber-coupled an existing Zeiss Axiovert 135 to a continuous-wave argon ion laser, which would serve as a fluorescence excitation source. This excitation light is delivered to the sample at the focus of a 100× oil-emersion objective (see Fig. 1a). Using a dichroic beam splitter and bandpass filter, we directed fluorescence light to an avalanche photodiode detector (APD). The microscope was further modified to accommodate an extremely high-precision, active-feedback piezo-electric *x-y* scanning stage upon which samples were placed. The detector and *x-y* scanner were interfaced to a desktop computer and data was recorded as photon counts at each *x-y* location (pixel). Data were presented as 2-D scanned images of fluorescence intensity of a (usually square) region of the sample from 10^2 to 10^4 μm^2. So far, we have performed measurements on dried samples of rhodamine or rhodamine-labeled DNA fragments. Precautions in sample preparation include ultrasonically cleaning sample slides, the use of ultra-pure solvent, and fresh glass-surface-treating reagents. We studied various samples, both to benchmark the instrument and in executing our plan to develop ultra-sensitive assays. For our first demonstration of SMD, 10^{-11} molar solutions of rhodamine in MeOH were spun coat on cleaned glass slides. Such low concentrations were required to assure that only one molecule of rhodamine would be present in any pixel (i.e., focal volume). These samples were excited with the 514-nm line of the argon-ion laser and scanned in *x-y* as described above. These experiments verified operation of the SMD microscope and data collection system. In addition, photo-bleaching and temporary transition to "dark states" were evident in repeatedly recorded images of the same region of the sample.

In FY2000, we intend to chemically assemble molecular structures that will allow us to create many unique fluorescent labels for high-multiplicity assays for medical and drug-discovery applications. These labels will require us to attach varying numbers of several different fluorophores to a molecular scaffolding that can then be used to tag a specific antibody associated with that unique combination of distinguishable dye molecules. Our approach is to use synthetic DNA for this scaffolding. At the end of FY1999, we successfully imaged single rhodamine molecules attached to strands of DNA (see Fig. 1b). Using short, complementary strands of labeled synthetic DNA, we will next investigate from a dual-fluorophore and record its signature after the addition of a second wavelength channel to the SMD microscope.

(a) (b)
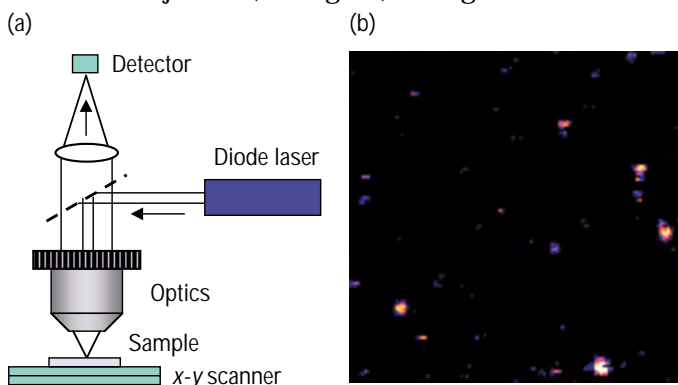
Figure 1 (a) A schematic of confocal SMD microscope apparatus; (b) a scanned image of single, rhodamine-labeled DNA strands.

Demonstration of a Radiation-Hard Magnetic Random Access Memory Cell

T. W. Sigmon

99-ERD-079

Although the phenomenon of magneto-resistance has been known since the beginning of the century, its application to practical magnetic devices has only recently been achieved. As the terminology implies, magneto-resistance is the change in the resistance of a conducting material with the introduction of an external magnetic field. This effect is nearly negligible in most materials—at best, it induces about a 2% resistance change in bulk materials—so that the outstanding technical difficulty confronting device applications is this unacceptably small field-sensitivity.

This situation changed dramatically in 1989 with the discovery of the so-called giant magneto-resistive (GMR) materials, which are typically very thin, alternating layers of magnetic and non-magnetic materials. Some of these materials had measured relative resistance changes of 100% or greater making them clear candidates for a variety of sensing and storage applications. One exciting application of these new materials is to non-volatile memory storage, the so-called magnetic random access memory (MRAM) cell. Storage cells based upon GMR materials have many attractive features. Some of these properties include (1) the intrinsic non-volatility of the stored memory, since no electric field application is required to maintain or refresh the bit information; (2) intrinsic radiation-hardness, since these cells are simply metals and not semi-conductors; and (3) the fabrication process is compatible with existing interconnect technology. There is a growing realization in the storage industry that MRAM cells have the potential to replace static random access memory (SRAM), dynamic random access memory (DRAM), and electrically erasable, programmable, read-only memory (EE-PROM), all of which are essential to the personal computer industry.

Non-volatile memory is critically important for DOE/Defense Program (DOE/DP) weapons systems, where they are used for code storage and for circumvention. DOE non-volatile memory technologies must retain information even in the presence of ionizing radiation. The use of magnetic elements to store information could solve ionizing radiation and electromagnetic pulse (EMP) memory vulnerability problems.

This research project was a joint effort with Sandia National Laboratories (SNL) in Albuquerque, New Mexico to investigate the feasibility of developing a useful radiation-hard MRAM design. Specifically, the proposal relied upon the different strengths of the two laboratories to integrate LLNL's MRAM cell design into SNL's radiation-hard complementary metal-oxide semiconductor (CMOS) process. In broad outline, LLNL personnel deposited GMR films upon SNL-supplied patterned wafers, which were subsequently tested for radiation-hardness. Furthermore, LLNL personnel developed an important process integration step that introduced a non-linear element (a diode) independently of the underlying CMOS circuitry. Building the nonlinear element on top of the patterned interconnect layer is a unique approach that permits post-processing integration of the memory cell onto otherwise fabricated integrated circuits.

Two important aspects of the research were successfully completed in FY1999. An LLNL-developed material combination with high (8%) GMR response was deposited upon SNL-supplied wafers and the radiation hardness of these materials was confirmed. An initial problem with corrosion was uncovered early in the project and eliminated by a careful experimental study that identified which surface material was causing the corrosion. With suitable replacement of this material, there was no measurable degradation in any of the magnetic properties at the highest radiation levels tested.

Even more importantly, the nonlinear element was successfully fabricated using pulsed-excimer-laser processing to directly convert amorphous silicon deposited onto the word line into doped polycrystalline silicon without damage to the underlying CMOS circuits. This demonstration has important consequences for the existing EE-PROM market and possibly the SRAM and DRAM markets. We will seek funding from both industry and government for future development.

Analysis of Active Sensor Discrimination Requirements for Various Missile Defense Scenarios

A. Ledebuhr, E. English

99-ERD-080

During FY1999, we explored and analyzed a combined passive/active sensor concept to support the advanced discrimination requirements for various missile defense scenarios. The idea is to combine multiple infrared (IR) spectral channels with an imaging LIDAR (light detection and ranging system) behind a common optical system, as shown in Fig. 1(a). The imaging LIDAR would itself consist of at least two channels: one channel at the fundamental laser wavelength (e.g., the 1064 nm for Nd:YAG) and one channel at the frequency doubled (at 532 nm for Nd:YAG). For example, a two-color laser output would allow the longer wavelength for a direct detection time of flight ranger and an active imaging channel at the shorter wavelength. The LIDAR can function as a high-resolution 2-D spatial image either passively or actively with laser illumination. Advances in laser design also offer three-color (frequency tripled) systems, high rep-rate operation, better pumping efficiencies that can provide longer distance acquisition, and ranging for enhanced discrimination phenomenology. New detector developments can enhance the performance and operation of both LIDAR channels. A real time data fusion approach that combines multi-spectral IR phenomenology with LIDAR imagery can improve both discrimination and aim-point selection capability.

We also acquired the Satellite Tool Kit (STK) developed by the Analytical Graphics, Inc. in FY1999. The STK software is a recognized simulation tool used by the aerospace industry for high fidelity satellite orbital simulation. It also contains modules that can model various missile flight trajectories and global target tracking from both ground and space assets. Figure 1(b) shows a simulation of close by inspection maneuvers around an orbiting satellite. Figure 1(c) shows a realistic ballistic missile engagement using a Navy asset. With this tool, we have developed several engagement scenarios demonstrating a ballistic missile defense capability by intercepting an inter-continental ballistic missile (ICBM) originating from a potential rogue state. We have also analyzed several ICBM intercept scenarios and showed the potential defense footprint for ship deployment at several potential hot spots. The simulation, developed to show the role that the Navy could play in ballistic missile defense, was demonstrated and successfully showcased the capability of this analytic tool. We are continuing our effort to build high fidelity satellite and ballistic missile defense simulation capabilities, using the capabilities acquired in this LDRD project. In addition, some laser measurements were conducted to support the development of advanced discriminating LIDAR sensors for ballistic missile defense applications.

Figure 1. Various aspects of this project: (a) discriminating sensors combine both passive IR and active imaging LIDAR in integrated package; (b) a satellite proximity maneuver simulation; and (c) a ballistic missile defense simulation.

1–20

Laboratory Directed Research & Development • FY1999
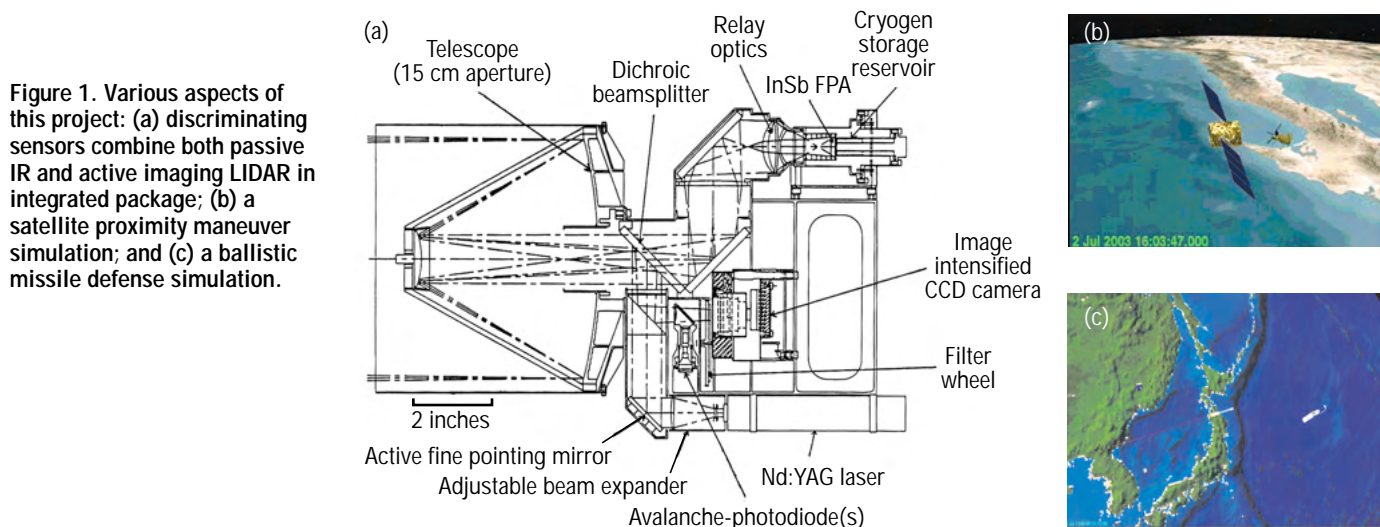
Evaluation of a New, Noncontact, Object-Identification System

G. C. Burnett

99-ERD-081

Many objects of importance to defense and related security applications are difficult to identify using conventional observational techniques because the object is hidden or requires identification from a distance. In earlier work, we had observed that small, homodyne radars can measure very low-amplitude vibrations of many objects that either generate acoustic signals or that respond to acoustic signals. These objects include buried land mines, objects behind walls or underground, and even the human vocal system.

The purpose of this project is to validate the concept of using radar vibration sensors to identify the uniqueness of vibration modes in several different types of objects and under several different conditions. Our results will provide data for evaluating the use of radar systems for (1) identifying buried land mines [including antipersonnel (AP) mines], (2) detecting micromotions in deep underground tunnels and bunkers, and (3) measuring the response of human tissue to the acoustic vibrations of the human voice. The last could be used in personnel-verification applications.

Our plan was to perform three experiments. Two experiments would use LLNL's vibration laboratory to generate known vibration amplitudes in two different systems. In the first, we would force vibrations in AP-mine surrogates buried under several inches of sand and soil and detect their responses. In the second, we would—using modulated antennas as surrogate sources—measure the attenuation of the source and the sensitivity of our equipment to the motions of objects buried under layers of rock, sand, and soil.

In the third experiment, we and our collaborators at the University of California, Davis (UCD), Voice/Speech/Swallowing Center would use LLNL's optical-sensor facilities to calibrate the motions of tissues in the human mouth against low-power radar signals. We would compare the amplitudes of vibrations measured with calibrated mechanical or optical techniques to those measured with low-power electromagnetic sensors used in the field-disturbance mode.

During FY1999, we completed the first in the series of experiments. The specific goal of this initial experiment was to determine if various objects could be distinguished from one another on the basis of their response to forced vibrations in the 10- to 300-Hz range. Several mine surrogates (a polyvinylchloride pipe, a metal pipe, and a inert AP mine) were vibrated with a small shaker and measured with the radar in a variety of positions at a distance of about 2 mm in air. The results were inconclusive. The objects responded to the vibrations in a variety of ways, which differed between objects (which is good) but also differed with respect to the orientation of the same object (not so good). The frequency responses also exhibited large, flat peaks that make comparison quite difficult. Although the radar vibration sensor could detect the vibration of the objects quite well, from the available data it was clear that recognition of the objects was not feasible.

During FY1999, we assembled the equipment and wrote the data-taking algorithms for the third experiment; we and our collaborators at UCD agreed on an experimental protocol and submitted the results to our respective review boards. However, we cannot begin the experiment until our protocols have been reviewed and approved by the Human Subjects Internal Review Board (IRB). We hope to receive IRB approval early in FY2000, and will proceed with the third experiment at that time.

High-Power, Pulsed-Fiber Amplifier Scaling for Ultracompact, Long-Range, Mid- and Long-Wave-Infrared DIAL Systems

A. J. Ruggiero, M. W. Bowers, W. A. Neuman

99-ERD-082

A crucial issue in the practical deployment and use of active, remote-sensing systems for proliferation detection is their overall system size and level of complexity. Conventional DIAL transmitters developed for these applications are typically large and complex. (DIAL stands for differential absorption LIDAR, where LIDAR stands for light-intensity detection and ranging.) Reducing the weight, volume, and power requirements of these systems is essential if they are to be used on realistic surveillance platforms. Technologies based on integrated optical and fiber-optic devices, which are inherently compact and robust, provide a potentially revolutionary pathway to deployable, infrared DIAL transmitters. Significant advances in high-power, doped fiber-amplifier systems capable of delivering tens of watts of output power at millijoule pulse energies are becoming a reality. Laser sources for DIAL transmitters require sufficient pulse energy and also high spectral fidelity, good spatial-beam quality, and high polarization purity. However, applying energy scaling to fiber-amplifier technology is difficult because of the need to balance these requirements with the nonlinear effects and energy-storage considerations that drive the amplifier designs toward large fiber cores, where these parameters are hard to control.

We investigated the use of low-power, fiber phase conjugation for polarization and spatial-mode control in large-core, erbium-doped fiber amplifiers (EDFAs). The phase-conjugation process uses nonlinear effects to produce a time-reversed replica (phase conjugate) of the amplified beam. If the laser beam is distorted during amplification, then its phase conjugate—reflected back through the same distortion—can be restored to its original state. The correction of spatial and polarization distortions in large-core fibers using stimulated Brillouin scattering (SBS) phase conjugation is well known. Low-power phase conjugators based on SBS in tapered fibers have also been demonstrated. We focused on the subtleties of applying these approaches to microjoule-level phase conjugation and aberration correction of EDFA pulses propagated through large-core fibers.

We used the method developed by N. G. Basov and his associates in Moscow. In this method, the beam is divided into two orthogonal polarizations. One polarization is rotated to be parallel to the other; they are recombined just before phase conjugation. Figure 1(b,c) shows some of the data from a tapered, SBS, fiber conjugator [Fig. 1(a)]. We have demonstrated [Fig. 1(d)] that (1) an SBS threshold can be achieved in the energy regime of interest using silica-based fiber, and (2) a tapered design can increase its useful range. We also demonstrated pulse-shaping techniques using a semiconductor optical amplifier to precondition the input to the fiber amplifier so that the temporal profile of the output was optimized for phase conjugation. Input-pulse shaping appears to be crucial in managing the temporal instabilities inherent in the SBS process.

On the basis of this study, we believe that fiber phase conjugation can provide a viable route to high-power, large-core fiber amplifiers with good spatial beam quality and polarization purity.

Figure 1. Stimulated Brillouin scattering experiment for studying microjoule-level phase conjugation and aberration correction: (a) vector phase conjugator for large-core, polarized, fiber-amplifier operation; (c) aberrated laser-beam output from a large-core fiber; (b) restored output after the phase-conjugate return; and (d) nonlinear reflectivity data (showing efficiency of the phase-conjugate process).
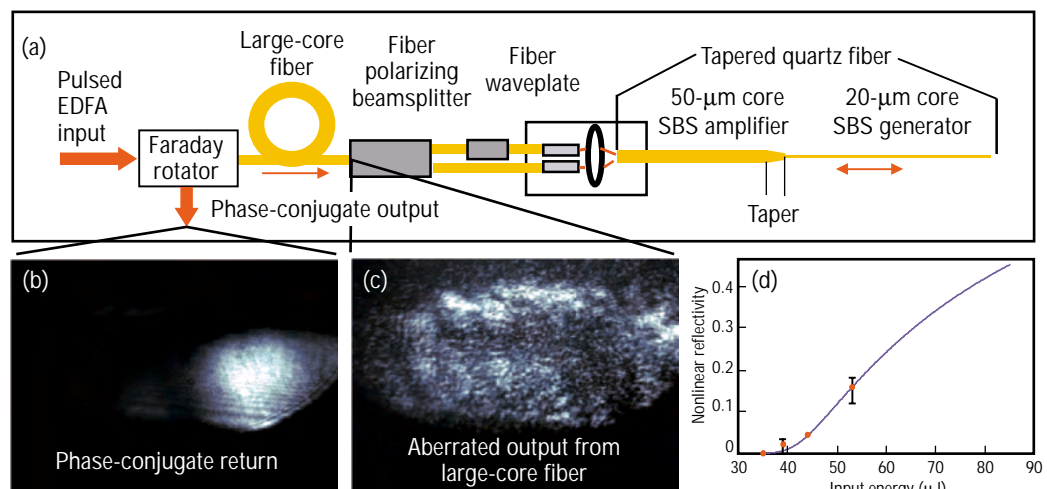
Broad-Band Acoustic Velocimetry

D. H. Chambers

99-FS-011

Conventional methods for estimating the velocity of an object using acoustic pulses require long pulse lengths of pure tones so that Doppler frequency shifts can be easily measured. However, accurate range estimates require short pulses that make propagation times easy to measure. This tradeoff between remote measurements of the range and velocity of a moving object has usually been resolved by choosing which quantity is more important for a particular application. For naval applications, active sonar systems are built to estimate range. Velocity is inferred by tracking the object. Similarly, for medical ultrasound systems the pulses are designed to determine range to various internal structures. However, there is increased interest in measuring velocity to estimate blood flow for cancer detection. Adding this capability to medical ultrasound machines requires a redesign of the system to emit long pulses at the expense of resolution.

The recent development of white-light velocimetry by David Erskine at LLNL showed that, by proper preconditioning of short pulses, both range and velocity can be estimated with comparable resolution.

In this feasibility study, our goal was to demonstrate that Erskine's technique for preconditioning pulses for velocity and range estimation would work with acoustic pulses and would also have possible application to medical ultrasound systems and sonar.

To apply the white-light velocimetry technique to ultrasound, during FY1999 we formulated a general mathematical description of the technique. Erskine's original approach used two interferometers to apply a known time delay to the incoherent illumination and to check for changes in the delay in the reflected light. In acoustics, the pulses that are typically generated are coherent short pulses. Our new mathematical formulation showed that the two-interferometer technique would apply to coherent pulses. This guided a series of experiments where a sphere was towed at known speeds through a tank of water and in front of an acoustic array. Pulses emitted by the array were reflected from the moving sphere and then received by the array. Various pulse shapes were chosen to determine the variation of accuracy with pulse shape.

Our results showed that speeds as slow as 0.5 m/s were measurable using short Gaussian pulses. The measurements become easier for faster speeds up to 1 m/s. This demonstrates that long pulses are not necessary to obtain good estimates of velocity.

In sum, we demonstrated that Erskine's technique would work as predicated. We are now considering how this technique could be used in sonar systems and medical Doppler imaging. In addition, this technique could be used for estimating radar range and velocity.

A New Ultraspecific Optical Method for Sensing Biological Agents: Direct Detection of Biological Activity

J. H. Satcher, Jr., R. L. Balhorn, C. B. Darrow, D. R. Cary, J. P. Bearinger

We are investigating the development of sensors that would utilize a detection method which (1) require little or no processing, (2) significantly lower background, and (3) be capable of quickly reporting the presence of infectious airborne, waterborne, or blood-borne microorganisms or microorganism-produced toxins (e.g., HIV, hepatitis, emerging virulent influenzas (viruses); *Clostridium, Anthracis, E. coli, Salmonella* (bacteria); malaria, Cryptosporidium (parasites); and ricin, botulinum (toxins). This new detection scheme would distinguish between live and inactive viral particles, which no current detection method is capable of making.

The elimination of non-specific binding, using techniques proposed here, would greatly improve the performance of existing sensors. The system we are investigating to demonstrate this principle is a protein coat portion of the HIV virus. This virus uses two protein receptors (CD4 and a chemokine, CXCR4 or CCR5), which bind at specific sites on the surface coat protein GP120 of HIV that elicits a conformational change in the protein structure. Once the sites on the viral surface are occupied, the virus is known to physically pull together or to co-localize the two-receptor proteins.

Initial demonstration experiments in FY1999 were performed with specially designed receptors free in solution. Efforts then focused on working out the experimental details of the technique using the avidin–biotin interaction as a model system. The binding of tagged biotins to the avidin protein and the signal produced as a result of the binding provided a good model of the high specificity and unequivocal detection of biological activity. This work demonstrated positive response only in cases where the avidin protein bound at least two biotins. Experiments involving a surface protein GP120 in solution—a substantially larger protein than avidin—are currently underway.

Efforts for FY2000 are aimed at immobilizing one or both of a labeled protein pair onto a surface. One possible sensing design uses a single labeled receptor affixed to a substrate and a second labeled receptor that is free in solution. Another scheme requires that the bound receptors be attached in a flexible manner to a sensor surface enabling them to be physically pulled together and co-localized. The first approach (single tether) may require a washing step in order to minimize background signal. The latter scheme embodies a detection method that uses only the particles collected in the sample and requires no additional processing.

Dynamic Focusing of Acoustic Energy for Nondestructive Evaluation

J. V. Candy, D. H. Chambers, R. D. Huber, G. H. Thomas

99-LW-045

The ability to detect and separate multiple, acoustic-energy scatterers embedded in a background medium or within another object offers a wide variety of applications, ranging from detecting and destroying kidney stones, to using underwater acoustics for active target detection, to detecting flaws in critical parts during nondestructive evaluation (NDE). The last is critical, for example, for inspecting mirrors employed in the National Ignition Facility (NIF) and for enhanced surveillance for stockpile stewardship. Not only will the development of this technology provide the Laboratory with an ultrasonic test bed, it will also enable us to improve and enhance our flaw-detection capability.

Dynamic-focusing techniques are based on the concept of time-reversal (T/R) processing of noisy, ultrasonic sensor array measurements—it is a technique for focusing energy in both homogeneous and inhomogeneous media. Because of its optical analog—the phase-conjugate mirror (PCM)—the T/R focusing processor is usually called a "time-reversal mirror" in the literature. However, the T/R mirror is a dynamic, broadband (multiple frequency) analog of the PCM that is used to focus narrowband (single frequency) monochromatic waves. Thus, the T/R mirror can effectively be used to detect flaws (or scatterers) by utilizing its primary attribute—the ability to iteratively focus on the strongest flaw. A T/R processor simply receives the multichannel time series radiated from the region under investigation, collects and digitizes the array data, and then time-reverses the sensor-array signals and retransmits them back through the medium to the focus [see Fig. 1(a)].

Our goal in this project is to develop techniques for dynamically focusing acoustic energy for the detection and identification of flaws for the NDE of critical parts under ultrasonic test. Using the T/R focusing property as the core, we are developing new algorithms to iteratively decompose the received field into its constituent scatterers, even when they overlap in time. This type of processing offers a unique contribution in its own right.

Our approach includes a detailed simulation, algorithm development, a proof-of-principle experiment, and the design of a viable flaw-detection and localization system. Through simulation, we will determine the feasibility of flaw detection in critical materials. Through experiments, we will incorporate the effects of hardware limitations and noise into the simulator, thereby revealing any "show stoppers" in the process.

During FY1999, we developed a flaw-detection algorithm capable of "deciding" when the T/R processor has focused on the dominant flaw. Once detected, that particular flaw must be removed from the measured data so that we can focus on the next strongest flaw. We can continue until all flaws have been detected and removed from the measured data.

By assuming independent, decoupled flaws with no mutual interactions, we demonstrated—on synthesized data sets—a recursive decomposition algorithm. To (1) verify the successful performance of the algorithm, and (2) demonstrate the focusing capability of the T/R processor, we simulated flaws in aluminum and conducted basic, proof-of-concept acoustic experiments in a water tank. This experiment demonstrates the focusing capability of the T/R processor, where we observe a dominant scatterer along with weaker scatterers (left-hand picture) during the initial excitation. Focusing is accomplished through the iteration process described above and results in just the dominant scatterer [right-hand picture in Fig. 1(b)].

In FY2000, we plan to (1) theoretically develop a processing algorithm that removes the assumption of independent flaws with no mutual interactions; (2) implement and test the algorithm on synthesized data; (3) select, acquire/develop, and operate an NDE hardware system capable of leading to the final performance experiments and an inspection system.
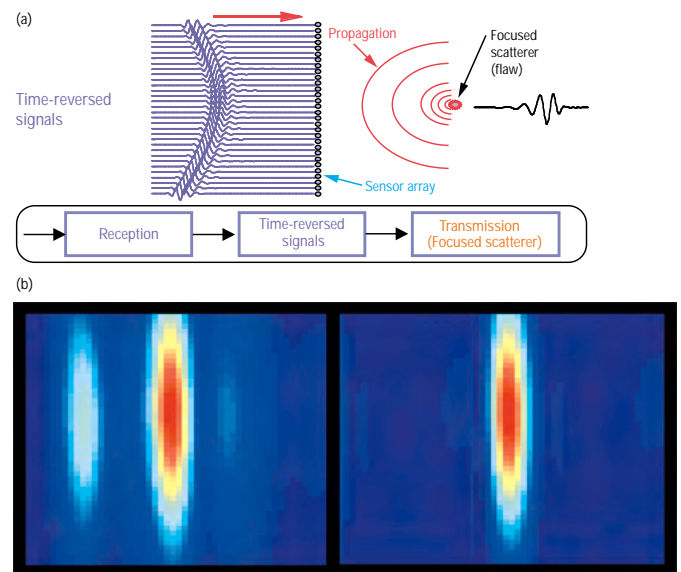
Figure 1. Time-reversal (T/R) processing for detecting and separating multiple scatterers. T/R processing (a) provides a means to focus on a scatterer (flaw) through a homogeneous or inhomogeneous medium. (b) A proof-of-principle experiment demonstrates dominant-scatterer focusing through a homogeneous water medium using the T/R processor. The left-hand picture in (b) shows three flaws; however, after T/R processing only the dominant flaw is shown (right-hand picture).
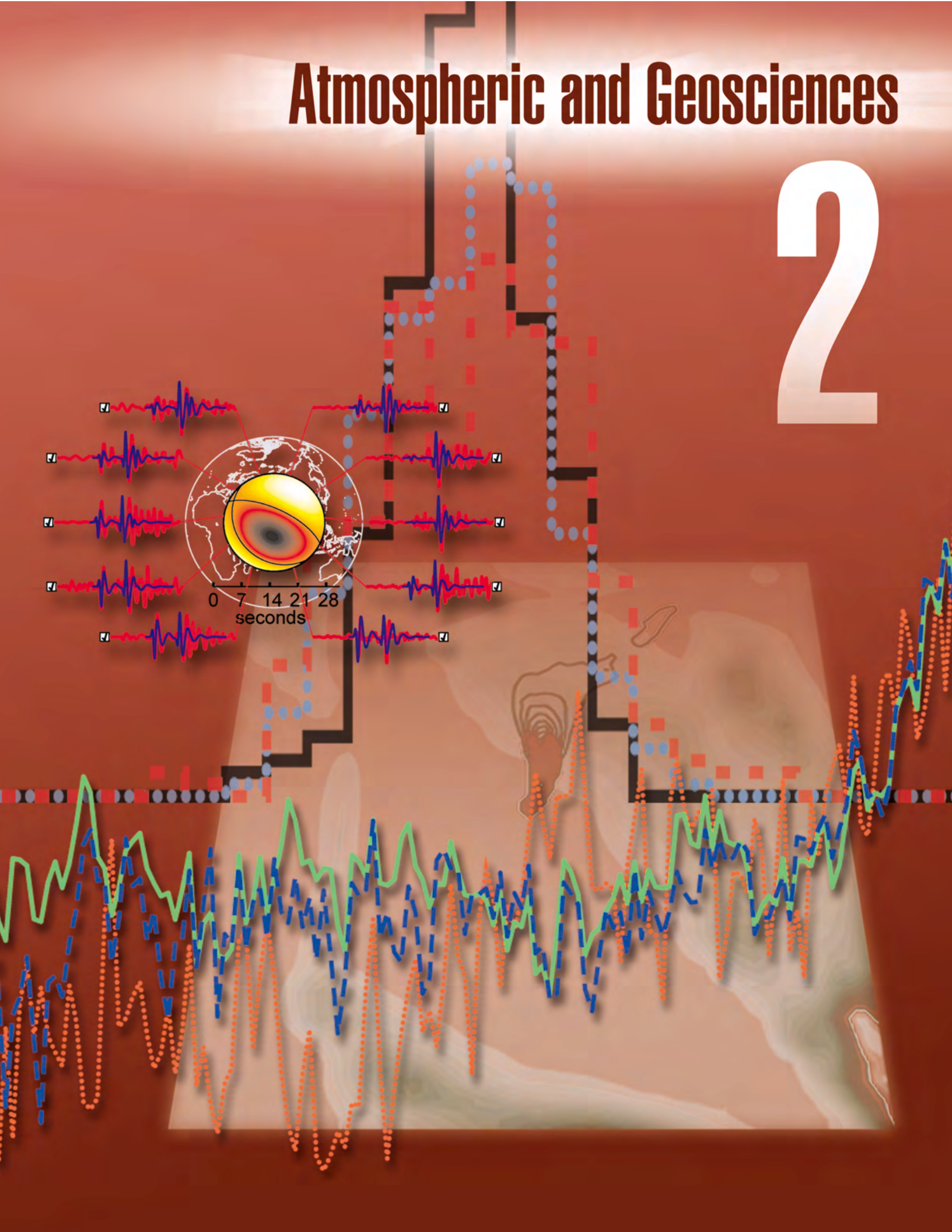
Section 2

Atmospheric and Geosciences

Measurements of Past ^{14}C Levels and ^{13}C/^{12}C Ratios in the Surface Waters of the World's Subpolar Oceans

T. A. Brown

97-ERD-052

In collaboration with the University of Washington, the National Marine Mammal Laboratory, and the University of Massachusetts, Amherst, we continued developing unique biological archives that allow the determination of past ^{14}C concentrations and ^{13}C/^{12}C ratios in the surface waters of the world's subpolar oceans. Such carbon isotope time-histories provide strong constraints on global-scale ocean general circulation models (OGCMs), and thereby, will lead to improvements in the quantification of the global carbon cycle. The overall goal of our research is to reduce current uncertainty in the oceanic uptake of anthropogenic CO_2, and to elucidate the role of the world's oceans as the most important global sink of fossil-fuel CO_2.

During FY1999, we completed ^{14}C measurements of archived scales from subpolar north Pacific Ocean sockeye salmon. The measurement of these scales has allowed the development of ^{14}C time-histories for the eastern, central, and western regions of the subpolar north Pacific that extend back to the mid-1940s. Comparison with time–series from the OGCM at LLNL indicates that ^{14}C in the subpolar north Pacific is transported downwards out of the surface waters and through the thermocline faster than predicted by the model. This result suggests that the LLNL model, and similar OGCMs operated at other institutions, underestimate the rate at which anthropogenic carbon is transferred to the deeper ocean, and may be underestimating oceanic uptake of anthropogenic CO_2.

We also measured the ^{14}C contents of sub-sectioned scales from salmon that were caught off West Greenland in 1981. These Labrador Sea salmon came from both European and North American stocks, and there are significant differences in the migration routes the stocks follow to arrive in the Labrador Sea during their second year of open-ocean life. The ^{14}C results obtained for the outer scale sections, which grew during the summer that all the salmon spent in the Labrador Sea, are consistent between salmon and are consistent with ^{14}C results obtained by direct water sampling in the region during the 1981 Transient Tracers in the Ocean Program. For the scale sections that grew during the periods in which the European and North American stocks occupied different regions, our ^{14}C results suggest that subsectioning of the scales may provide ^{14}C time-histories for each of the regions.

In FY1999, we also completed exploratory measurements on two other archived records of surface water carbon isotope contents. Our ^{14}C measurements on fractions from three Antarctic crabeater seal teeth demonstrated the development of appropriate techniques for preparing samples from such archived teeth. The ^{14}C results we obtained for the 1989 tooth from the western side of the Antarctic Peninsula are in reasonable agreement with direct open-ocean sampling results obtained for regional waters in 1992. The ^{14}C results obtained for the two teeth collected on the eastern side of the Antarctic Peninsula showed an increasing trend in ^{14}C content between 1986 and 1990. While preliminary, this result suggests that ^{14}C time-histories derived from archived seal teeth may provide strong constraints on the underlying circulation patterns of the Weddell and Bellingshausen Seas.

The ^{14}C time-series obtained from our subpolar north Pacific salmon scales have demonstrated the utility of our scales-based carbon isotope time-histories in constraining and validating the OGCMs being used in efforts to predict the effects of climate change over the next hundred years. We have been successful in our initial exploration of the existing archives of north Atlantic salmon scales and Antarctic crabeater seal teeth. We will continue our efforts to develop time-series for the surface waters of the world's subpolar ocean from these and other biological archives.

Geospeedometry: Application of Cosmic-Ray Surface Exposure Dating to Problems in Active Tectonics

F. J. Ryerson, R. C. Finkel, M. W. Caffee, P. Tapponier, G. Peltzer, A. Yin

97-ERI-003

Since its initiation 50–60 million years ago, the ongoing collision between India and Asia has led to the formation of the Himalayas, the Pamir, and the Tibet plateau. Well-defined active fault zones make this an ideal region in which to study the response of continental lithospheres to tectonic forces. Whether deformation of the continental lithosphere is localized on major fault zones or homogeneously distributed remains a fundamental question in continental geodynamics. The goal of this project is to develop kinematic constraints on models by determining the slip-rates on active faults throughout Asia. Slip-rates are determined through satellite- and field-based measurements of tectonic offsets combined with cosmic-ray surface exposure dating, which are facilitated by LLNL's Center for Accelerator Mass Spectrometry. This research is (1) establishing the methodology and reliability of the application of cosmic-ray exposure age dating to depositional surfaces in remote areas, (2) developing new isotopic methods at LLNL, and (3) advancing the utility of satellite-based imagery and morphological analysis in the investigation of active tectonics and climate change.

In collaboration with colleagues at UCLA, the Institut de Physique du Globe de Paris, and the Chinese Seismological Bureau, we concentrated on the Altyn Tagh Fault (ATF) and the associated features that define the northern edge of Tibet. Study areas include (1) the Kunlun Fault, a left-lateral strike-slip fault to which a portion of the displacement along the ATF is transferred; (2) the Karakax Valley segment of the ATF in western Tibet; (3) the eastern terminus of the ATF in the Tang He Nan Shan, where strike-slip movement is transferred to thrusting, thickening, and uplift; and (4) the Aksai segment of the ATF near the eastern terminus of the fault. At each site surface, we dated sample constraining lateral or vertical offsets using ^{10}Be, ^{26}Al, and radiocarbon.

Results on the main segment of the ATF indicate that the slip-rate along the fault decreases from rates as high as 20–25 mm/y at its western end, decreasing to >5 mm/y at its eastern terminus. The variation in slip-rate is consistent with the behavior of an eastward propagating fault that transfers motion to sub-parallel strike-slip faults and sub-perpendicular thrust faults. Near Subei, we measured a 5 mm/y decrease in the ATF slip-rate across its junction with one such feature—the Tang He Nan Shan thrust belt. In contrast, we measured the rate of slip Kunlun Fault over 800 km of its length—yielding a uniform slip-rate of 12 ± 2 mm/y integrated over 40,000 years (see figure). This is the first time a major strike-slip fault has been observed over such an extended spatial and temporal scale. The constant slip-rate along the Kunlun Fault is consistent with the absence of connected features that could redistribute its motion. Together with the absence of any clearly related crustal thickening at its eastern terminus, the constant slip-rate suggests that, unlike the ATF, the Kunlun Fault is a "mature" feature, which is no longer propagating eastward.

The ATF is the major feature responsible for the eastward displacement of Tibet relative to Siberia. The high slip-rates we observe are in agreement with the localized deformation in which the Asian lithosphere approximates a collection of rigid blocks. The association of the eastward extrusion of Tibet, and the presence of young mountain belts at the propagating end of the ATF indicates a causal relationship between strike-slip faulting and crustal thickening and uplift in northern Tibet. Simply put, the northern part of Tibet was constructed through the propagation and growth of lithospheric strike-slip faults, in contrast to the southern boundary, which was uplifted by simple convergence and crustal shortening. The contrasting behavior of northern and southern Tibet requires a strain discontinuity within the central plateau. In the future, we will evaluate the kinematic compatibility of several recognized features that may constitute such a discontinuity.
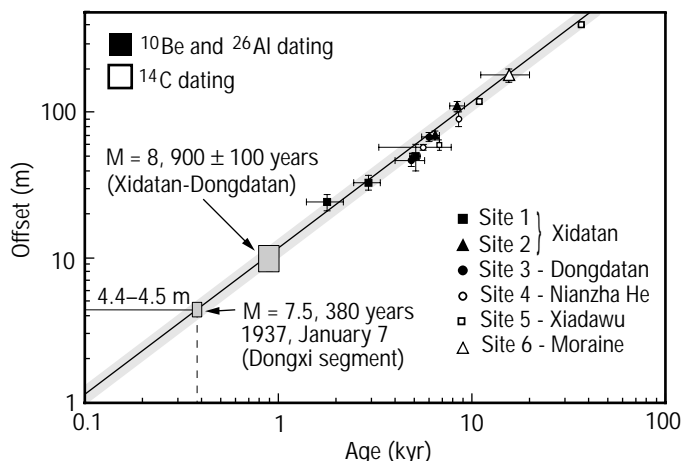
Slip-rates over 800 km of the Kunlun Fault, determined through cosmic-ray exposure and radiocarbon dating—yielding a uniform slip-rate of 12 ± 2 mm/y integrated over 40,000 years.

Investigations of Paleoclimatic Variations using Accelerator Mass Spectrometry

J. R. Southon, M. K. Kashgarian, T. A. Brown

97-ERI-009

The aims of this project are two-fold: to provide data sets for testing carbon-cycle and climatic models under conditions different from those of today, and to develop basic insights into climatic processes by studying past climatic change on time scales of hundreds or thousands of years. The real-world climatic-regime data that we are collecting will complement and strengthen LLNL's modeling work and will increase our confidence in predicting future climatic change.

We use radiocarbon dating by accelerator mass spectrometry (AMS) as a chronometer for climatic variations; ^{14}C also acts as a natural tracer for the carbon cycle of the past. In this project, we are contributing LLNL's ^{14}C expertise in major collaborations with earth scientists and oceanographers at several University of California campuses, other U.S. universities, the U.S. Geological Survey, and overseas institutions. A major outcome of the project has been an increasing realization that climatic changes are strongly correlated over large areas of the Northern Hemisphere. This suggests that while such changes may be initiated by changes in oceanic circulation, they are primarily propagated through major (rapid) reorganizations of atmospheric circulation patterns—rather than slowly through the oceans.

Because of a lack of bioturbation, anoxic sediments preserve uniquely high-resolution paleoclimatic records. During FY1999, we sampled cores from an anoxic fjord site on the west coast of Vancouver Island to look for faunal changes, changes in oceanic–atmospheric ^{14}C offsets, or other indications of variations in oceanic upwelling over the past several hundred years. Over the past year, we also developed the first radiocarbon chronology for these cores by dating terrestrial material such as twigs, conifer needles, etc. Previous LDRD-funded work on sediments from the Santa Barbara Basin (Central California) showed centennial upwelling fluctuations plus a systematic drop over the past 1600 years. Our new time scale allows us to correlate changes in these two regions and thus test different possible forcing mechanisms for climatic change in the North Pacific.

A major challenge for paleoclimatology is to explain why and how climate switches between glacial and deglacial states. During FY1999, we produced a detailed ^{14}C calibration curve for the period of deglaciation—earlier than the present tree-ring calibration—by dating foraminifera (calcareous skeletons of plankton) preserved in annually layered marine sediments from an anoxic basin off Venezuela (see figure). This calibration has two benefits: (1) it allows us to tie together radiocarbon-dated paleoclimatic records and calendric archives such as ice cores; and (2) fluctuations in the calibration curve give insight into carbon-cycle variations. Our new results confirm previous radiocarbon data showing large fluctuations in the carbon cycle during the Younger Dryas cold period (12,900 to 11,600 before the present—BP), when large areas around the North Atlantic returned to almost full-glacial conditions. Our data show that these changes were almost certainly driven by changes in oceanic circulation. They also suggest that a similar sequence occurred in the Older Dryas–early Allerod period about 1000 years earlier and—for the first time—document the effect of this earlier reversal on the carbon cycle. Preliminary work on a deeper Ocean Drilling Project (ODP) core from the same site shows that similar but larger fluctuations also occurred 25,000 to 30,000 BP.

A spin-off from this work has been new insights into differences in the chronologies of major Greenland ice-core projects (GISP2 and GRIP)—two critically important paleoclimatic archives. Our work shows that "slippage" between the two chronologies occurs in restricted regions of the cores, not as a distributed slow drift as previously thought. This might point the way to future work on reconciling the two time scales and providing a unified chronology for the deglacial period.
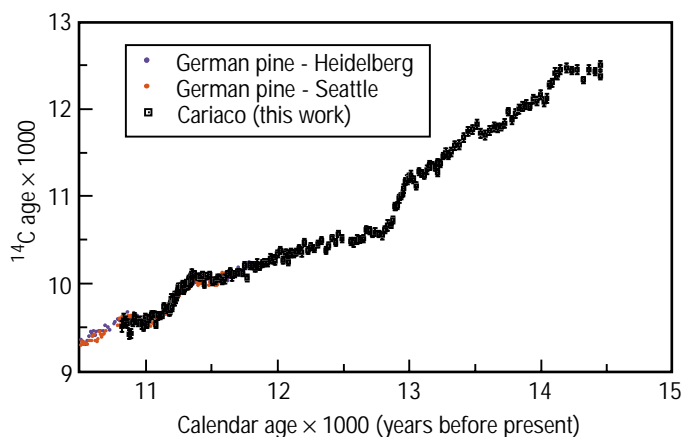
Radiocarbon calibration curve, showing the end of the tree-ring data (results from two laboratories) and our new extension. Departures from linearity show the effects of large changes in the carbon cycle during deglaciation.

Geologically Precise Hydrogeological Models Enhanced by Geophysical Data

S. F. Carle, A. L. Ramirez, W. D. Dailey, R. L. Newmark, A. F. B. Tompson

98-ERD-005

Accurate and geologically realistic hydrogeological models are needed for design of effective remediation systems. An oversimplified model that does not resolve preferential pathways and traps for contaminant migration will yield overly optimistic predictions of remediation success. Permeability in the alluvial aquifer system underlying LLNL varies more than four orders of magnitude within a 5-m lateral and 1-m vertical distance, producing a high degree of uncertainty in contaminant fate and transport. The traditional characterization approach of drilling and sampling simply cannot resolve this heterogeneity in a cost-effective manner.

In this project, we have been improving the accuracy and realism of subsurface characterization by integrating prior geological knowledge with three unique LLNL capabilities: geostatistics; electrical resistance tomography (ERT); and the parallel flow modeling code, *ParFlow*.

Traditionally, geologists visualize subsurface heterogeneity by drawing 2-D cross sections. Alternatively, we have developed unique geostatistical methods that integrate both borehole data and subjective geological insight to quantify description of detailed and realistic 3-D geological heterogeneity. Our geostatistical simulation codes produce multiple, geologically plausible interpretations or "realizations" constrained by borehole data.

ERT images subsurface electrical resistivity variations from voltages induced by currents applied over strings of downhole electrode pairs. Electrical resistivity correlates with clay content, which controls permeability. Thus, ERT detects variations in subsurface permeability. However, prior to this study we could not verify the accuracy of 3-D ERT in heterogeneous geological settings. To address this problem, in FY1998 we used ParFlow to generate 3-D, synthetic ERT data sets from geostatistical realizations of the alluvial aquifer system beneath LLNL. Comparing ERT images to the realizations, we found that ERT could indeed resolve major interborehole heterogeneities.

Having established the imaging capabilities of ERT, in FY1999 we formulated a method to integrate ERT as "soft conditioning" into the geostatistical simulation process—to produce realizations that more closely approximate the true subsurface heterogeneity. For example, Fig. 1(a) shows a sliced view of the true distribution of high-permeability zones for an LLNL site, Fig. 1(b) shows a geostatistical probability estimate of locating a high-permeability zone, and Fig. 1(c) shows a geostatistical probability estimate enhanced by ERT. The integration of ERT clearly improves these geostatistical probability estimates.

Our ability to generate realistic, synthetic ERT data enables us to evaluate the efficacy of ERT at different geological settings and electrode configurations before field experiments are deployed. In future applications such as the Hanford DOE site, this new capability will help us optimize electrode configurations and tune inversion parameters to maximize resolution. Moreover, the flexibility of our geostatistical approach permits integration of sparse subsurface data sets and geophysics with LLNL's advanced transport modeling capabilities.
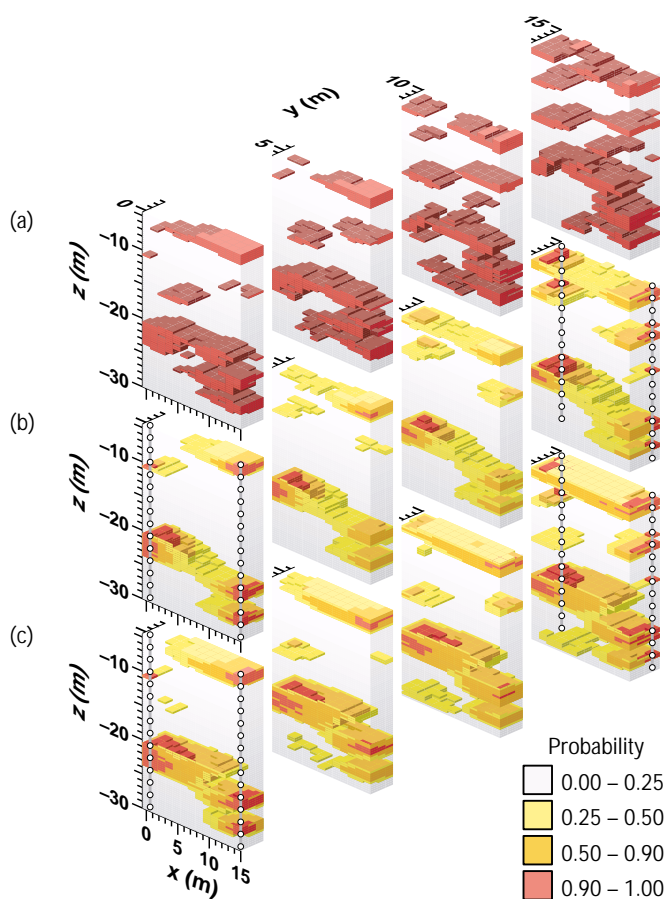
Figure 1. Sliced, 3-D probability estimates of the location of high-permeability zones for a subsurface site at LLNL, comparing (a) the true spatial distribution, (b) a geostatistical estimate, and (c) a geostatistical estimate enhanced by electrical resistance tomography. Note the close correlation between (a) and (c).

Martian Carbonates: Hot or Cold?

I. D. Hutcheon, A. J. R. Kent, F. J. Ryerson

98-ERD-042

In 1996, when scientists working for the National Aeronautics and Space Administration (NASA) announced the possibility of fossil life in a Martian meteorite, they caused a major stir in both scientific and non-scientific circles. Numerous studies have examined ALH 84001, the meteorite that contains the possible fossil remnants. In particular, the carbonate minerals that host the microscopic, fossil-like structures have been subject to intense scrutiny. Much of this work has centered on the formation temperature of these minerals. As terrestrial life is only viable over a relatively narrow and well-defined range of temperatures (~0 to 150°C), knowledge of the formation temperature and thermal history of the carbonate minerals in ALH 84001 would provide a direct constraint on the possibility that this meteorite hosts the fossil remains of ancient, Martian biogenic activity.

We have used the rates of cation diffusion in carbonate minerals to assess the formation temperature of ALH84001 carbonates. Previous studies have shown that the carbonate minerals in ALH 84001 vary significantly in chemical composition over short distances—changes of up to 10% in the mole fraction of Ca, Fe, and Mg are apparent over distances of only 1–2 microns. Over time, diffusion will act to homogenize such chemical zoning and, since diffusion is a temperature-driven process, we can use diffusion-based models to constrain the thermal history of the carbonate minerals. The main requirement for this modeling is an accurate knowledge of the diffusion coefficients for cations in the carbonate minerals found in ALH 84001. In FY1998, we developed a simple powder-source technique for measuring cation diffusion rates at the temperatures of interest; in FY1999, we applied this technique to successfully measure the cation diffusion rate of Ca and Mg in calcite and magnesite (two carbonate minerals found in ALH84001). We measured diffusion rates at the lowest possible temperatures because these data will provide the strongest constraints on the low-temperature processes believed to have occurred on Mars.

Measured log D_0 values for diffusion of Mg in calcite and Ca in magnesite at temperatures between 600–400°C are − 15.8 ± 0.9 and –8.6 ± 3.7 m^2/s and the activation energies are 76 ± 14 and 202 ± 51 kJ/mol, respectively. The diffusion rate of Mg in magnesite at temperatures between 400–550°C is substantially faster than expected from extrapolation of existing higher-temperature data, suggesting that different mechanisms may govern diffusion of Mg at temperatures above and below ~550°C. This new discovery highlights the value in our strategy of measuring diffusion rates at the lowest possible temperatures. Calculations based on our new results indicate that the carbonate minerals in ALH 84001 most plausibly formed at temperatures below 200°C. Carbonates are thus unlikely to have formed by high temperature fluid or melt-related processes.

We presented our latest results at the *30th Lunar and Planetary Science Conference*, and we have completed a manuscript for submittal to *Earth and Planetary Science Letters.* In FY2000, we will concentrate on measuring the diffusion rates of Fe and Mn in calcite and magnesite and attempt to measure Ca and Fe diffusivities in the Fe-rich carbonate, ankerite. By the end of FY2000, we should have cation diffusivities for the full suite of carbonate minerals in ALH 84001, which we will use to develop a multi-component diffusion model to constrain the thermal history of ALH84001. Our research is related to on-going, NASA-supported studies of primitive meteorites and provided the basis for a new proposal to DOE's Office of Basic Energy Sciences to investigate trace element fluid-mineral partitioning and diffusion in terrestrial carbonate minerals.

Diagnostic Systems Approach to Watershed Management

M. L. Davisson, J. E. Moran, G. B. Hudson

98-ERD-046

Agricultural activities, sewage discharge, urban/industrial runoff, and habitat change adversely affect the potability of rivers, streams, and shallow groundwater. For example, total organic carbon (TOC) in raw drinking water, which form halogenated carcinogens during chlorination, rises with increasing land use. Another example is increased dissolved salt levels in surface and ground water, which have affected many drinking water supplies in California. While drinking water regulations are currently implemented only on the user end, management of the watershed is a newly recognized method for regulating water quality at the source end. However, by its very nature, sources of non-point-source pollution (NPSP) are difficult to diagnose with traditional water quality investigations, limiting the effectiveness of watershed management strategies.

Isotopic measurements offer a new tool for delineating sources of NPSP. Natural isotopic abundances of dissolved and suspended constituents in surface and groundwater are intrinsic to their geographic origins and the process of their generation. In addition, accurate measurement of water-quality parameters below drinking water limits provides a basis for discerning contaminant generation and removal.

The goal of this project is to develop and demonstrate new measurement and investigative approaches in environmental studies of surface water and groundwater by utilizing these isotopic and geochemical measurements. The particular focus is to relate our results to contaminant transport and their applicability to DOE programs and watershed management agencies and consortia.

In FY1999, we measured ^{13}C and ^{14}C of total organic carbon (TOC) in drinking water to delineate respectively, the source and mean age of the TOC. Our preliminary results show that isotopic abundances of TOC vary seasonally and distinguish sources. We have also shown that dissolved TOC is different from TOC sorbed to suspended sediments in the water column, demonstrating both short and long-range transport of TOC in rivers. Work is ongoing to show whether these isotope variations are inherently different between reactively labile and refractory components of the TOC.

We also completed work in the San Joaquin River, where the upper watershed is an alpine area and the mid to lower reaches are semi-arid regions dominated by intense agricultural irrigation. The river terminates in the Sacramento-San Joaquin Delta, which is a critical junction for water transfers to southern California. During the summer, the river flow in the lower watershed comprises entirely agricultural irrigation return flows with high salt loads. Soils and shallow groundwater in these areas are known for their saltiness.

We collected isotopic and geochemical samples during baseflow (July to October) along the 200-mile stretch of San Joaquin River. Dissolved metal and salt concentrations in the alpine upper watershed were very dilute. This contrasted with river water in the agricultural areas where concentrations of nitrogen, chloride, molybdenum, and uranium were high. Further downstream in the Delta, these high concentrations decreased due to dilution from other rivers and scavenging processes. We measured isotopes of uranium ($^{234}U/^{238}U$) to distinguish the source of the high uranium concentration (see figure). They could have been derived from phosphate fertilizers applied in irrigated areas adjacent to the river, and as such the $^{234}U/^{238}U$ activity ratio would be approximately one, characteristic of their primary uranium ore source. Alternatively, most natural water has higher activity ratios due to alpha recoil affects of thorium decay and the slightly higher solubility of the ^{234}U. Although uranium concentration varied by greater than four times, isotopic analyses had essentially the same $^{234}U/^{238}U$ activity ratios, which were greater than one. These results suggest that the higher uranium concentrations are due to natural sources rather than from fertilizers, and were simply leached during irrigation.
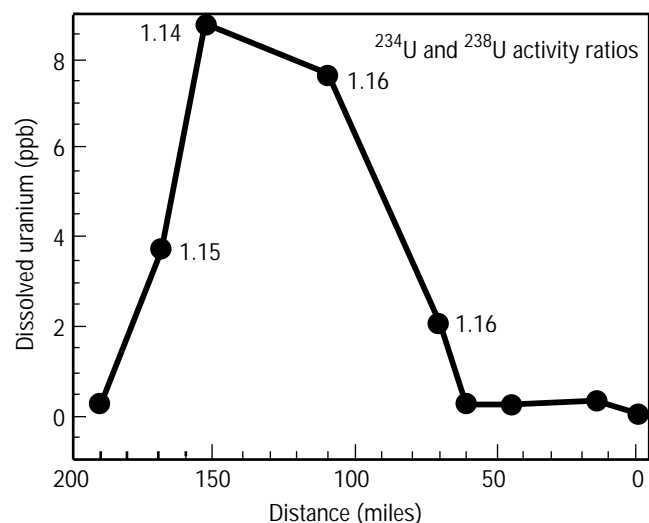
Isotopic ratios of 234U/238U in the San Joaquin River indicating natural sources because of similarity at different concentrations and their value of greater than one.

Seasonal to Decadal Variability in Pacific Circulation using Δ^{14}C in Corals

M. Kashgarian, T. P. Guilderson

98-ERI-002

We are investigating the circulation of the tropical Pacific surface ocean by measuring radiocarbon (^{14}C) at monthly resolution in massive corals. Since radiocarbon is a highly sensitive indicator of water mass movement, results of this research have a direct impact on the understanding of global climate events such as the El Niño-Southern Oscillation (ENSO) and are used as a key diagnostic of tracing anthropogenic CO_2 in the ocean. We are collecting and integrating ^{14}C data into high-resolution ocean circulation models. Our work uses an integrated approach to oceanography and climatology and involves collaboration with researchers and resources at LLNL and from several universities.

Our research addresses two questions: (1) How does the shallow circulation of the tropical Pacific vary on seasonal to decadal time scales? and (2) Which dynamic processes determine the mean vertical structure of the equatorial Pacific thermocline? These high-resolution Δ^{14}C time series provide a powerful constraint on the rate of surface ocean mixing and fundamental information about the shallow circulation of the Pacific. They can also be used as a benchmark for the next generation of high-resolution ocean models that predict climate.

While previous coral Δ^{14}C studies have demonstrated the utility of ^{14}C time series to study the dynamics of ocean circulation over multi-decadal time scales, our objective is (1) to document ^{14}C variability in the surface ocean in the Pacific and (2) to determine how that variability relates to shallow circulation and mean vertical structure of the thermocline. In FY1998, we completed post-bomb (~1950 to present) time series from Nauru (166°E, 0.5°S) and Guadalcanal (167°E, 7°S) in the western tropical Pacific and a partial multi-decadal record from the Galapagos (90°W, 0°). In FY1999, we generated high resolution coral Δ^{14}C records from Rarotonga (21°S,160°W) in the southern sub-tropics (as shown in the figure) and the island of Hawaii in the northern sub-tropics; these are two Pacific source regions of subsurface water masses that impact the vertical structure of the tropical thermocline. In general, these sub-tropical sites (Rarotonga, Hawaii) have relatively high Δ^{14}C because of longer mean residence time of surface water in the gyres and higher air-sea exchange of CO_2. The Δ^{14}C in eastern equatorial Pacific surface waters (Galapagos) is lower because of the subsurface pathway of the Equatorial Undercurrent and entrainment of deep thermocline waters that upwell into this region. These Δ^{14}C values in the warm pool region (Nauru, Guadalcanal) are dominated by advective processes and thus are intermediate between the subtropics and eastern region.

Our high-resolution coral data show (1) the long-term increase in Δ^{14}C reflecting oceanic uptake of bomb-derived ^{14}C and (2) high amplitude seasonal-to-interannual variations associated with changes in circulation, which can be used as a diagnostic in ocean general circulation and climate models. Although there may be offsets with respect to observed absolute Δ^{14}C values, matching the timing and amplitude of the post-bomb peak and the shape of the response function is an essential test of any model trying to predict the uptake and redistribution of anthropogenic CO_2. A model peak that occurs "earlier" than the observed bomb peak indicates an overly stratified upper-ocean; whereas a later peak suggests problems in modeling advective processes. In areas of downwelling, such as Rarotonga (see figure), the simulated surface ocean bomb ^{14}C maxima occur too early and with too much amplitude. This indicates inadequate vertical mixing and coupling between the wind-driven and interior regions of the ocean in the model, which results in a piling-up of ^{14}C and CO_2 in the upper ocean. Our coral data sets allow modelers to discover inadequacies that could hamper efforts to predict ocean CO_2 uptake on decadal to centennial timescales.

In FY2000, we plan to complete our post-bomb Galapagos record and develop records from Bali and Langkai in Indonesia and Fanning Island in the central equatorial Pacific.
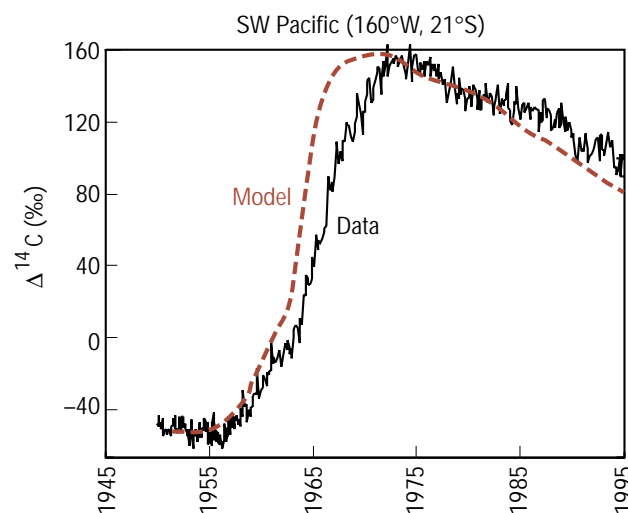
High-resolution Rarotonga Δ^{14}C coral data (thin line) and that simulated in the LLNL general circulation model (dashed line).

Assessing Changes in Solar Activity using Cosmogenic Radionuclides

R. Finkel, M. W. Caffee

98-ERI-013

In this project, we have been focusing on three aspects of the earth sciences that are of concern to DOE: (1) energy use as affected by potential climatic change (i.e., solar effects on climate), (2) landform stability as it relates to the assessment of natural and man-made hazards (i.e., the chronology of geomorphic processes), and (3) global atmospheric mixing as it influences problems related to the ozone hole and to emissions by jet aircraft (e.g., chemical and radiative characteristics of the upper troposphere and stratosphere). Work conducted during FY1999 on each aspect of this project will be discussed in turn.

The amount of solar radiation received by the earth changes in step with the 11-year sunspot cycle and also over longer time scales. Solar effects on climate are important because potential human influences via greenhouse gases or atmospheric aerosols are superimposed on a background of natural climatic change that must be considered during the construction of scenarios describing future climate. We are using cosmogenic ^{10}Be and ^{36}Cl in polar ice cores to develop a proxy record for solar activity during the Holocene and Late Pleistocene. By the close of FY1999, we were completing continuous measurements of ^{10}Be and ^{36}Cl in samples from the 3-km-deep Greenland Ice Sheet Project 2 (GISP2) ice core from central Greenland. Our results show the effects of changes in solar activity, climate, and geomagnetic fields.

Our study of landform stability is important because the interactions among various elements of the landscape influence the harshness of floods, the danger of earthquakes, the severity of landslides, the potential for soil erosion of croplands, the reliability of water supplies, and other factors that directly affect the daily lives of human populations. Landscape, however, constantly evolves through the forces of tectonics, weathering, hydrology, and climate. We are using cosmogenic-nuclide surface-exposure dating to determine the rates of these processes in relatively young landscapes. During FY1999, we (1) assembled an extraction line for determining in-situ ^{14}C in rocks and began optimizing its performance, (2) reduced blanks to less than the minimum required for the determination of in-situ ^{14}C from rocks, (3) developed a heating protocol that ensures the removal of ^{14}C contamination derived from meteoric sources, and (4) installed a system for introducing carrier carbon so as to ensure quantitative tracing of the in-situ ^{14}C.

As part of our study of atmospheric mixing, during FY1999 we obtained initial insight into global-scale transport in the stratosphere and stratosphere–troposphere exchange. Our data were derived from distributions of the radioactive tracers ^{10}Be/^{7}Be that are produced in the atmosphere by cosmic rays. For our measurements, we obtained 150 high-altitude air-filter samples from NASA-sponsored flights.

Our work during FY1999 was strongly experimental, emphasizing sample measurement and technique development. In FY2000, we plan to emphasize data analysis and modeling. For the solar-variability part of our study, we will compare our ice-core data with environmental records—including those relating to climatic change. For the landform stability study, we will begin measuring in-situ ^{14}C. To understand the processes controlling the global distribution of ^{10}Be/^{7}Be, we will analyze our measurements using NASA's Goddard Institute of Space Science (GISS) global climate model (GCM).

Three-Dimensional Simulations of Scenario Earthquakes along the Hayward Fault

S. C. Larsen, D. Dreger, C. Stidham, M. Antolik

98-LW-028

The Hayward fault, which runs through some of the most densely populated regions of the San Francisco Bay Area, is expected to experience a magnitude 6.8 to 7.5 earthquake within the next 30 years. It is estimated that such an earthquake will cause 1,000 to 10,000 fatalities and $50B to $500B in damages. It is important to identify regions where high amplitude seismic ground motions are expected so that appropriate engineering improvements can be made.

The goal of this project is to determine the geographical distribution of high-amplitude seismic ground motions in the San Francisco Bay Area. To do this, we combine the ground motions predicted from 3-D simulations of scenario earthquakes along regional faults with a 3-D geological model of the Bay Area developed at the University of California, Berkeley. These simulations are computed using E3D, a sophisticated 3-D seismic-wave propagation code implemented on high-performance and massively parallel computers. In addition, we integrated our ground motion predictions with finite-element models of the San Francisco Bay Bridge to determine how large, engineered structures will respond during seismic events.

In FY1999, we validated our methodology by performing 3-D simulations of the 1989 Loma Prieta and 1994 Northridge earthquakes, then compared these results to observed seismic data. Unlike traditional approaches for modeling earthquake data, our 3-D simulations fit the observations extremely well. In addition, we implemented 3-D attenuation algorithms into the E3D code and found that seismic attenuation has some influence but does not significantly affect our calculations. These results confirm our ability to accurately simulate earthquake ground motions, and indicate that 3-D simulations are needed to make reliable predictions of seismic shaking.

We simulated a suite of 20 Magnitude 7 earthquake scenarios for the Hayward fault, selected to characterize typical fault rupture parameters expected for large events. These 3-D simulations reveal strong levels of ground shaking along the Hayward fault and in nearby large sedimentary basins (e.g., San Pablo Bay, Santa Clara Valley, and Livermore Valley). These simulations are being used to generate probabilistic earthquake ground motion maps for the San Francisco Bay Area, which show the 30-year likelihood that a specified level of seismic shaking will occur.

One of the most important scientific results was our demonstration of the significant influence 3-D geologic structure has on seismic wave propagation. For example,

the 3-D simulations reveal that the geologic contrast across both sides of the San Andreas fault causes seismic energy to be refracted or refocused back into the populated regions of the Bay Area. This refocusing of seismic energy is not predicted by traditional earthquake modeling techniques.

The ground motion simulations were integrated with finite-element models of the San Francisco-Oakland Bay Bridge to predict how this structure will respond during large earthquakes. These simulations indicate that there are some earthquake scenarios that will cause significant damage to this bridge.

Our modeling efforts have received significant visibility, including local and national news coverage. Future efforts include an assessment of high amplitude seismic shaking that may impact the Laboratory site and research funded by the Pacific Gas and Electric Company to model seismic ground motions in the Santa Clara Valley. In addition, our 3-D modeling techniques are being applied to a diverse set of non-earthquake projects important to LLNL and DOE. These include research in nuclear nonproliferation, fossil energy exploration, hydroacoustics modeling, underground structure detection, medical imaging, and National Ignition Facility glass inspection.
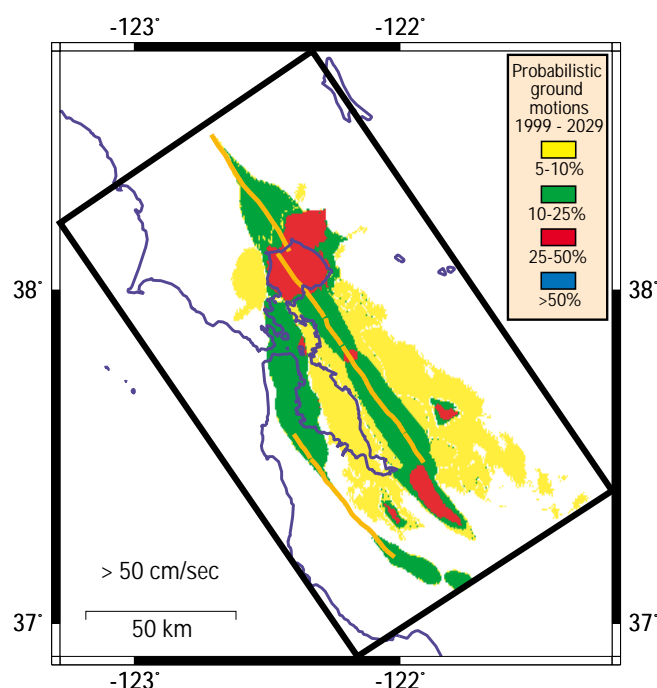
Ground motion map indicating probability that horizontal ground velocities will exceed 50 cm/s during next 30 years.

Performance Prediction for Large-Scale, Nuclear-Waste Repositories

W. E. Glassley, J. J. Nitao, T. Bulous, M. Gokoffsky, C. W. Grant, J. W. Johnson, J. Kercher, J. A. Levatin, C. I. Steefel

The success of many major DOE and U.S. nuclear programs ultimately depends on safely and securely disposing of high-level nuclear waste. Yucca Mountain, Nevada, is seen as a potentially suitable repository site because of its arid climate and remote location. Although the present-day characteristics of Yucca Mountain are important, we must be able to simulate how such a potential nuclear-waste repository will evolve over its 10,000-year lifetime.

Rock at Yucca Mountain contains a small volume of water in its microscopic pores. Heat from the repository will heat the water in the near vicinity of the nuclear waste. The resulting water vapor will migrate to cooler areas, where it will condense—changing the structure of pores and fractures by dissolving or precipitating minerals. These processes affect the movement of water, since they modify the spaces through which the water must migrate. A realistic simulation of a repository must accurately account for these various feedback loops over thousands of years at high spatial resolution—of great importance because these interactions determine where, when, and how much water might reach waste containers. A single simulation to model these coupled processes would require many years to complete on standard work stations; many such simulations are required to evaluate various "what if" scenarios for repository behavior.

The purpose of our work is to use the massively parallel processor (MPP) computers available at LLNL to greatly reduce simulation time, while also (1) increasing the reliability, accuracy, complexity, and resolution of the models; and (2) constructing a new computer simulation capability that will allow us to acquire new insights into how the Yucca Mountain repository might evolve.

Last year, we solved some of the important conceptual problems of how to mathematically couple the thermal, hydrological, and chemical processes and applied our new code (a greatly modified and extended version of an earlier code called NUFT) to simple models of the potential repository. During FY1999, we improved code efficiency, evaluated improved strategies for solving the equations in this complex mathematical system, and greatly expanded the code's chemical capabilities. Now, using approximately 400 to 600 central processing units, we can (1) simulate much more complex problems involving realistic geometries for the layout of the potential repository; and (2) evaluate how different heat outputs of multiple waste containers, heterogeneity of the geology, etc. affect repository performance. These results show, among other things, that the acidity in the vicinity of waste packages can vary over several orders of magnitude, over distances of a few meters, depending upon the local initial environmental conditions and the heat outputs of the waste packages. By employing this computational tool, we will be able to determine the sensitivity of the geological system and the engineered properties of the environment around waste packages to these and other variables of repository design.

By simulating repository evolution during the first few decades of operation, we can also predict where specific changes may occur, and thus guide a monitoring program designed to establish at an early time whether the repository evolves as predicted. Such information can provide an additional means for safeguarding the integrity of the waste containers.

In FY2000, we will focus on adding capabilities that will describe the evolution of the physical properties of the system, particularly of mechanical changes in the rock. This will bring us to our stated goal of achieving a fully coupled model by the end of FY2000. Also—to analyze the many gigabytes of data each simulation generates—we will continue working with other groups at the Laboratory to employ high-resolution visualization capabilities.

Multiscale Dispersion and Uncertainty Prediction using Terascale Computing Capabilities

M. J. Leach, H.-N. Chin, D. J. Larson

Any numerical meteorological forecast is sensitive to small uncertainties in the initial data. A practical approach to quantifying these uncertainties and to providing a best estimate of the evolution of the atmosphere is to run an ensemble of forecasts from slightly perturbed initial conditions. Ensemble forecasts with global models are typically used at national weather centers to estimate extratropical storm tracks or storm intensification and, recently, to predict hurricanes.

LLNL's National Atmospheric Release Advisory Center (NARAC) provides forecasts and guidance for a variety of different release types, including accidental spills of chemical and toxic gases, accidental releases from nuclear power plants, and terrorist releases of chemical or biological agents. Depending on the sensitivity to the released materials, predictions of the path or location of the dispersing material may be needed for several hours or even days. However, as the duration of the forecast increases, the predictability decreases, and the uncertainty of the forecast increases.

In this project, our objectives have been to (1) develop a real-time computer-modeling system for multiscale atmospheric flow and dispersion prediction using state-of-the-science models running on a terascale computing platform, and (2) apply this modeling system to the development of an ensemble forecasting methodology to estimate quantitatively the major uncertainties in dispersion predictions.

During FY1999, we created parallel versions of the Lagrangian particle-dispersion (LODI) code (where many particles are used to create a plume) and the coupled oceanic–atmospheric mesoscale prediction system (COAMPS) code. By parallelizing the codes, we can perform the simulations necessary to create the ensembles and estimate the uncertainty in the dispersion predictions. The LODI parallelization has been completed. COAMPS parallelization, being done in collaboration with the Naval Research Laboratory, is nearly complete. The parallelization is very efficient—the speedup is nearly linear relative to the number of processors.

To meet our second objective, we used COAMPS and LODI to create an ensemble of dispersion forecasts. First, it is necessary to create initial conditions that adequately sample probability space. Two popular methods are used for global-scale models: (1) the so-called "breeding" method—which does not work on the regional scale—where we have combined initial- and boundary-value problems; and (2) the singular-vector approach, which requires an additional huge investment in software

development beyond the scale of this project. We took the approach of getting initial conditions and boundary conditions for our ensemble by using different data sources for the initial conditions; that is, we used three different large-scale models (the Aviation model and Eta model from the National Weather Service and the Navy's NOGAPS model) to drive COAMPS. In addition, we introduced a Monte Carlo perturbation to the large-scale fields, giving us a six-member ensemble.

Results from our ensemble, 36 hours into a meteorological forecast, are reproduced in the figure. Besides showing that there can be large differences in the dispersion forecast, the results illustrate an interesting meteorological phenomenon; that is, half the trajectories traverse the underlying terrain, whereas the rest are blocked by the terrain and go around to the northwest. This is a classic scale interaction, where the interaction between small-scale terrain and the large-scale forcing depends on wind speed and atmospheric stability. Using an ensemble yields the range of possible solutions. A large ensemble containing an adequate number of simulations would yield the probability of each solution occurring.

We completed the tasks we outlined for FY1999, parallelizing COAMPS and LODI and creating an ensemble dispersion forecast—and demonstrated the utility of ensemble forecasts for dispersion predictions.
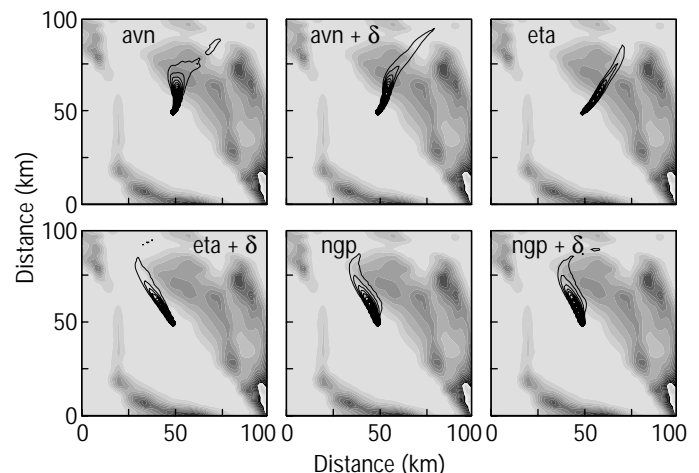
Individual simulations in an ensemble created by COAMPS and LODI codes. Each simulation is identified by the large-scale model used for initial conditions: [avn = the Aviation model; eta = Eta model; and ngp = NOGAPS model]. Those simulations that included random perturbations are labeled with a δ. The concentration of the dispersed particles is shown by black contour lines; the topography is in a gray scale, with elevations ranging from sea level (lightest tone) to 500 m (darkest tone).

Using High-Performance Computing to Develop Transportable Seismic Identification and Modeling Techniques

P. Goldstein

99-ERD-034

We are developing new capabilities for identifying small magnitude seismic events that utilize high-performance computing to account for realistic seismic source and wave propagation phenomena. The ability to accurately identify small magnitude seismic events and nuclear explosions is essential for monitoring of low-yield or comprehensive nuclear test ban treaties. These capabilities can also play an important role in assessing nuclear weapons development efforts and capabilities in other countries.

Despite decades of research, attempts to identify such small magnitude seismic events have met with limited success. Thus far, the most successful approaches are empirically based. A fundamental problem with these empirical approaches is that they require large data sets of events with known source type so that a technique can be calibrated to account for regional geologic structure. Also, these empirical techniques do not account for realistic source properties. For example, there are significant differences in the type and relative amount of energy radiated in different directions (the radiation pattern) by an earthquake and an explosion, which are not accounted for by conventional empirical methods.

We are developing a model-based approach to seismic identification that accounts for realistic source and propagation phenomena. Our initial research focussed on the development of a technique that models the first part of an event's seismic waveforms in terms of an explosive source or earthquake fault and propagation through relatively simple geologic structures. We have shown (Goldstein and Dodge, 1999) that this technique can be used to determine accurate high-resolution estimates of the depth of such sources relative to the surface of the earth. Accurate estimates of the depth of an event are particularly relevant for identification and monitoring purposes because of the extreme technological and economical challenges of emplacing a device at depths greater than a few kilometers. This technique also provides estimates of source orientation and radiation pattern, which also constrain event type. The figure shows the utility of this approach by comparing the depth and radiation pattern parameters estimated for the May 11, 1998 India nuclear explosion and a nearby earthquake in 1991. Based on our analysis, the May 11, 1998 event is constrained by the seismic data to be very shallow and to have radiated energy, similar to an explosion, nearly uniformly in all directions. In contrast, the nearby event was found to be approximately 19 km deep and had a much more complex, earthquake-like angular distribution of radiated energy.

The results described above are significant because they demonstrate the potential of a model-based approach and provide useful event identification information. However, the results are limited because they only utilize a small portion of the seismic waveforms and do not account for the effects of complex geologic structure. In FY2000, we intend to develop techniques to utilize a much greater portion of the seismic waveforms by incorporating the effects of complex geologic structure. Preliminary results from this work suggest that we should be able to model much larger portions of the seismic waveforms at a greater range of distances and smaller magnitudes, even if the source or receiver is located in complex geologic structure.

Comparison of observed and predicted synthetic waveforms, angular distribution of radiated energy, and source parameters of a 1998 India nuclear explosion and those of a nearby earthquake in 1991. The explosion is very shallow and radiates energy uniformly.
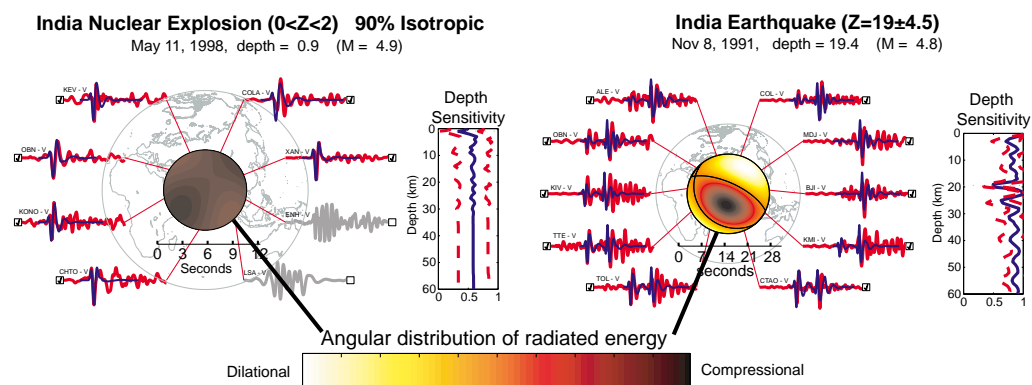
Multivariate Climate Change Detection

B. D. Santer, K. E. Taylor, C. Doutriaux

99-ERD-056

The aim of this project is to investigate whether the identification of human effects on climate can be facilitated by examining the joint behavior of a number of different climate variables rather than a single variable only (typically surface temperature).

Much of our research in FY1999 was spent obtaining results from climate model experiments that have been performed at the Max-Planck Institute for Meteorology (MPI) in Hamburg, Germany, at the National Center for Atmospheric Research (NCAR) in Boulder, Colorado, and at the Los Alamos National Laboratory. Our initial analysis has involved computing climatic indices that provide information on large-scale features of the atmospheric and oceanic general circulation. We then investigated the variability between different climatic indices.

One particular relationship—the covariability between temperatures at the Earth's surface and in the lower troposphere (LT)—has been of particular interest. It has been noted that there is an apparent difference between the thermometer-estimated surface warming of roughly 0.2°C per decade since 1979 and the much smaller temperature trend in the lower troposphere estimated from satellites and radiosondes. This difference has received considerable scientific and political attention.

Our research suggests that this difference may be largely real, and not simply an artifact of data quality problems in the satellite and surface data. We find that the temperature-trend differences between the surface and lower troposphere are reduced from 0.2 to 0.1°C per decade by accounting for differences in the coverage (the satellite data have global coverage, whereas the surface data do not). This residual difference cannot be completely explained by natural variability of the climate system, as represented in three state-of-the-art climate models (see figure).

Our analysis of experiments performed with a state-of-the-art climate model demonstrates that the cooling effect of Mt. Pinatubo and stratospheric ozone depletion is probably greater in the troposphere than at the surface. In contrast, experiments that consider changes in greenhouse gases alone tend to produce warming of the troposphere relative to the surface. The closest match between modeled and observed surface-troposphere trend differences occurs in an experiment with a combination of human-induced atmospheric composition changes and the volcanic aerosols from the eruption of Mt. Pinatubo. Our work refutes recent claims that modeled and observed tropospheric temperature trends over the last two decades are fundamentally inconsistent. Such claims are based on experiments that consider changes in greenhouse gases alone.

Our paper describing this research on modeled and observed atmospheric temperature changes has been accepted for publication in *Science* magazine. It describes a highly successful collaboration between scientists at five research institutes in three different countries. The Director of MPI (Prof. Lennart Bengtsson) has invited LLNL's Program for Climate Model Diagnosis and Intercomparison (PCMDI) to participate in the design and analysis of new model experiments directed towards improving our understanding of the nature and causes of recent atmospheric temperature changes.

In addition, two other papers on basic observational uncertainties have been published or accepted by the *Journal of Geophysical Research*. In FY1999, we presented our findings at two prominent international scientific meetings in Birmingham, England and in Hamburg, Germany. Our expertise in the analysis of modeled and observed temperature changes has resulted in the nomination of the principal investigator of this LDRD project (B. D. Santer) to a U.S. National Academy panel charged with reconciling temperature measurements from different observing systems.

In FY2000, we will expand and complete the multivariate detection part of our project. The expansion will involve looking at climate index data from two additional models so that we will have results from at least five state-of-the-art climate models. The aims of the planned work are to learn something useful about model-predicted "multi-variable" climate-change signals, to search for these signals in observed climate data, and to see how well models capture the observed covariability between different elements of the climate system.
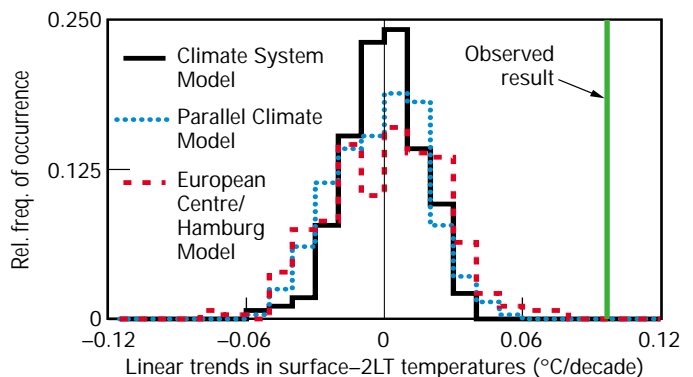
Observed temperature-trend differences between the surface and lower troposphere cannot be explained by the natural variability simulated in three climate models. The x-axis shows the trend difference between the surface and the lower troposphere, on timescales of 20 years. The green line indicates that the Earth's surface has warmed by roughly 0.1°C per decade more than the lower troposphere (since 1979).

Mantle Dehydration and the Global Water Cycle

K. Putirka, H. F. Shaw, M. W. Caffee, F. J. Ryerson

The composition of the Earth's mantle records the processes of core, crust, and atmosphere formation. Isotope ratios are used to define mantle components because they are unaffected by melting or crystallization; thus, they reflect long-term changes in geochemistry. The Earth's mantle contains several isotopically distinct components. However, the spatial distribution of these components, although critical to our understanding of mantle dynamics, is largely unknown. Geophysical techniques appear unable to resolve these components. As such, geochemical variations are needed to elucidate their depths. The strategy employed here is to develop, through experiments at high temperatures and pressures, depth-sensitive compositional parameters that can be used to map the depth distribution of these mantle sources.

It has recently been observed that isotopic ratios at many oceanic islands converge to a narrow range of values, termed the focus zone (FOZO). Such observations have fueled speculation regarding the nature and placement of FOZO and other mantle components. Since FOZO appears to be common to most plume-related volcanoes, it has been proposed that FOZO represents the composition of the deep mantle. Alternatively, FOZO might represent an intimate mixture of depleted-mantle (DM) and enriched-mantle (EM) components that resides at shallow depths. Isotopic ratios themselves cannot be used to differentiate these hypotheses because they do not carry intrinsic depth information.

Our only recourse for locating the depths of such components is through geochemistry. The strategy here is to determine whether isotopic ratios correlate with variations in depth-sensitive, major-element chemistry. Our experimental data on the partitioning of Na and Ti between basaltic melts indicates that TiO_2/Na_2O increases systematically with the depth of melting. If the concentration of an isotopic component is correlated with a melting-depth indicator such as TiO_2/Na_2O, then its concentration varies with depth; scatter, on the other hand, would indicate a component that is vertically dispersed. To perform such comparisons, we have compiled a global oceanic database that includes compositional data for over 2000 basalts.

When TiO_2/Na_2O is compared to $^{87}Sr/^{86}Sr$ and $^{144}Nd/^{143}Nd$, some remarkable patterns are apparent [Fig. 1(a,b)]. First, lavas from Atlantic islands plot within a coherent field, where $^{87}Sr/^{86}Sr$ and $^{144}Nd/^{143}Nd$ ratios begin near DM at low TiO_2/Na_2O and trend toward FOZO-like values as TiO_2/Na_2O increases. Second, lavas from islands in the Pacific and Indian Oceans appear to originate either near a DM or an EM position, and similarly converge toward FOZO-like isotopic ratios with increased TiO_2/Na_2O. As part of this pattern, Pacific and Indian Ocean lavas exhibit negative slopes when $^{87}Sr/^{86}Sr$ is greater than 0.7035 to 0.7040 and $^{144}Nd/^{143}Nd$ is greater than 0.51285 to 0.51290, near-vertical slopes when isotopic ratios are largely confined to these values, and positive slopes at lower ratios.

This compositional convergence suggests that mantle plumes from all oceanic basins tap a common, deep-seated source, similar to FOZO. In addition, DM appears to be the dominant component for melts produced at the most shallow levels in the mantle. The coherence of Atlantic Ocean islands would further suggest that the Atlantic's upper mantle is considerably less heterogeneous compared to mantle-source regions in either the Pacific or Indian Oceans. It would thus appear that the sub-Atlantic mantle has a much smaller admixture of enriched components such as EM, and that these components in the Atlantic are highly localized beneath the Azores. That EM components appear to be dispersed in the mantle on a global scale indicates that vertical mixing during mantle convection is efficient.

Figure 1. TiO_2/Na_2O vs $^{87}Sr/^{86}Sr$ and $^{144}Nd/^{143}Nd$ for the global oceanic database. Approximate positions of depleted mantle (DM), enriched mantle (EM), and the focus zone (FOZO) are indicated.
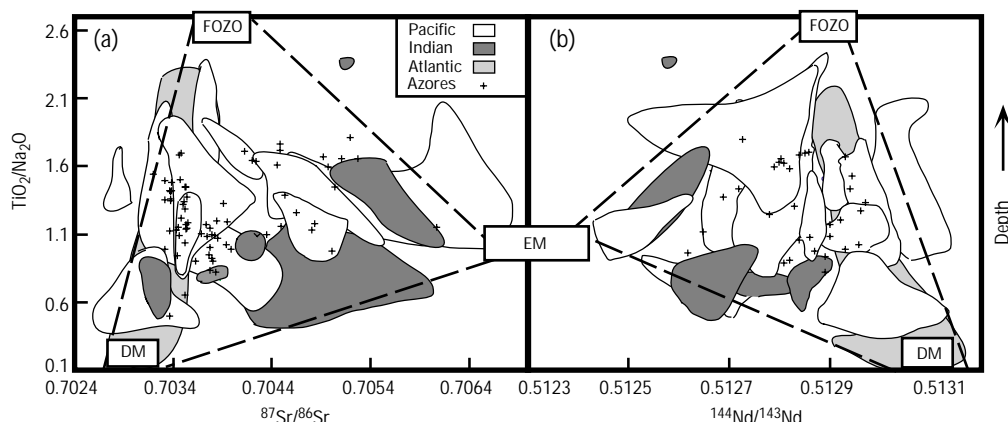
Determination of the Pre-Bomb Southern (Antarctic) Ocean Radiocarbon in Organic Matter

T. P. Guilderson

99-ERI-015

The Southern Hemisphere is an important and unique region of the world's oceans for water-mass formation and mixing, upwelling, nutrient utilization, and carbon export. In fact, one of the primary interests of the oceanographic community is to decipher the climatic record of these processes in the source or sink terms for Southern Ocean surface waters in the CO_2 balance of the atmosphere. Current coupled ocean–atmosphere modeling efforts to trace the input of CO_2 into the ocean imply a strong sink of anthropogenic CO_2 in the Southern Ocean. However, because of its relative inaccessibility and the difficulty in directly measuring CO_2 fluxes in the Southern Ocean, these results are controversial at best.

An accepted diagnostic of the exchange of CO_2 between the atmosphere and ocean is the prebomb distribution of radiocarbon in the ocean and its time-history since atmospheric nuclear testing. Such histories of ^{14}C in the surface waters of the Southern Ocean do not currently exist, primarily because there are no continuous biological archives (e.g., in corals) such as those that have been used to monitor the ^{14}C history of the tropics and subtropics.

One potential exploitable archive is the store of organisms collected over the last approximately 100 years as part of biological surveys and "routine" oceanographic surveys in the Southern Ocean. Most of these samples are preserved with formaldehyde, which acts to "harden" the organic matrix by cross-linking to proteins at an amine group. Since formaldehyde (usually as formalin) is a hydrocarbon product, the carbon isotopic chemistry is "dead" (no ^{14}C) and thus has the potential to contaminate the original radiocarbon signature. To accurately recover the ^{14}C of the water, it is thus not possible to simply combust the specimens and convert the resulting CO to graphite for standard radiocarbon analysis. Rather, to recover the "natural" ^{14}C signal embedded in these samples it is necessary to analyze only carbon atoms fixed by the organisms themselves.

The goal of this project is therefore to develop a consistent methodology for recovering the natural ^{14}C signal in organic material collected from the Southern Ocean. Comparison of sediment-trap bulk organic material preserved with formalin, mercuric chloride, and sodium azide indicate that—at least for recently recovered (early 1990s) material—contamination in the formalin-preserved samples is not an issue. An alternative explanation is that the amount of "formalin-fixed" amino acids in the trap material is insufficient to influence bulk analysis.

To test the effect of long-term storage on radiocarbon signatures, in FY1999 we acquired (from the Auckland Museum in New Zealand) formalin-preserved mollusk samples (tissue and shell or carbonate) that had been collected (alive) in 1929 and 1930. Our analysis of carbonate and bulk tissue in these samples documents a shift of nearly –100‰ in the bulk tissue samples relative to the carbonate (barring contamination, the values should be similar). This indicates that bulk ^{14}C analysis of samples stored for a significant amount of time (in this case about 70 years) is compromised.

In FY2000, we will utilize a newly upgraded sample-preparation laboratory to make compound-class organic extractions (lipid, carbohydrate, etc.) from the same tissue samples to assess if specific compounds are immune to the influence of ^{14}C contamination by formalin. An ultimate test will be to clip specific carboxyl chain carbons off amino acids, releasing the carboxyl-carbon as CO_2 that can then be easily extracted and utilized for radiocarbon analyses. If successful—the extract compound class and/or carboxyl-chain ^{14}C content is similar to the shell material—we will obtain samples from the archives of organic specimens maintained by such museums as the Smithsonian Institution of Natural History and the American Museum of Natural History and begin mapping the prebomb distribution of radiocarbon in the surface waters of the Southern Ocean.

Application of Terascale Computing Capabilities to Simulations of Global and Regional Climate

P. B. Duffy

99-SI-001

We are applying DOE's unequaled computational resources to model simulations and scientific studies of climate and climatic change. A summary of the year's activities follows. One of the most significant studies is described more fully at the end of this article.

Our model-development work during FY1999 included (1) adapting the CICE (sea-ice) model to run on massively parallel computers, (2) adding advective transport of water vapor to the University of Victoria atmospheric-energy/moisture-balance model, (3) adding a representation of the ocean-carbon cycle to the parallel ocean program (POP) oceanic-circulation model, and (3) evaluating a new "reduced" computation mesh in an oceanic-climate model.

Our scientific studies included (1) performing an ensemble of simulations of the climate of the 20th century (in collaboration with scientists at the National Center for Atmospheric Research), (2) assessing a proposed geoengineering scheme for mitigating the effects of increased atmospheric greenhouse gases, (2) assessing the effects of explicitly representing "trace" greenhouse gases in climate models (as opposed to the "equivalent CO_2" approximation), (3) assessing the effects of "flux adjustments" on simulated temperature

Trends in the surface temperature of the Earth (1860 to present) from observations (dotted red line), globally complete model output (green line), and model output altered to match the coverage of the actual observations (dashed blue line).

variability in climatic models, (4) comparing observed temperature variability to that simulated in climatic models, (5) assessing the effects of incomplete observational coverage on Earth's apparent temperature trend, (6) assessing the robustness of the predicted slowdown in the circulation of oceanic thermohaline, and (7) comparing observed and simulated storage of fossil-fuel carbon in the ocean.

Our studies (3) and (4) above are slated for inclusion in the next report of the Intergovernmental Panel on Climate Change (IPCC). This panel is sponsored by the United Nations (UN) and is composed of scientists who provide a summary of the scientific understanding of climatic change for policy makers.

Much of present-day climatic research is based on the assumption that Earth's surface has apparently warmed by about 0.7°C since 1860. The validity of this result has been questioned, however, because it is based on measurements that cover only a small fraction (less than 20%) of Earth's surface at the start of the period in question. It is thus possible that the apparent temperature trend is significantly in error due to systematic increases in the spatial coverage of the observations during that period.

In one study [see (5) above], we are assessing this possibility using ten independent climatic-model simulations of the climate of the late 19th and 20th centuries. Since these simulations predict temperatures for the entire Earth, they allow us to assess the effects of incomplete observational coverage on Earth's apparent temperature trend.

We performed this assessment by deriving two temperature trends from each model simulation: the first is based on temperatures covering the entire Earth's surface; the second includes only locations where observations are available. We found that the error in the apparent temperature trend caused by incomplete temperature observations is at most about 0.1 or 0.2°C, a relatively small fraction of the apparent trend of 0.7°C (see the figure). Thus, our conclusion is that incomplete observational data probably causes relatively small errors in the apparent warming of the Earth since 1860.

In FY2000, we plan to (1) demonstrate our ability to perform climatic simulations using LLNL's terascale computing capabilities, and (2) continue the collaborative development of next-generation climatic models.

Biotechnology and Healthcare

3

Biotechnology and Health Care Technologies

Functional Characterization of DNA Repair Proteins

D. M. Wilson III

97-ERD-002

Genetic material (DNA) is susceptible to (1) spontaneous decomposition, (2) attack by reactive chemicals produced naturally in cells, and (3) assault by environmental and food mutagens. DNA modifications can lead to permanent genetic changes that promote human disease. To combat the deleterious effects of DNA damage, organisms are equipped with DNA repair systems. The focus of our investigations has been to elucidate the details of mammalian DNA repair. These studies have provided important insights into the relationship of DNA repair to human disease and a framework for designing more effective anti-cancer treatment schemes.

Sites of base loss (or AP sites) are frequently formed DNA lesions corrected by a multistep pathway that is initiated by an AP endonuclease. In mammals, the predominant AP endonuclease is Ape1. We used biochemical and structural approaches to elucidate the molecular detail of the Ape1-DNA complex. We used computer modeling techniques to elucidate which DNA elements influence Ape1 repair activity. Insights from these studies allow us to design inhibitor substrates that could prove useful in anti-cancer treatment schemes. We are also developing methods to isolate dominant-negative and increased-repair-capacity Ape1 proteins that may serve as radio-sensitizing or -protective agents when used with gene therapy approaches. In addition, we are generating mammalian cell lines deleted in Ape1. The complementary nature of the biochemical and genetic projects permits a thorough dissection of the biological contributions of Ape1. Finally, we have identified a second human protein with similarity to Ape1, termed Ape2, which will serve as a target for future investigations. Radicals are generated during normal oxygen metabolism or from exposure to ionizing radiation and attack chromosomal DNA to form oxidative damage, including 3'-blocking termini. The repair of 3'-damages is not understood. We are designing assays to identify repair factors involved in removing obstructive 3'-ends and are presently testing several candidate 3' to 5' exonuclease. Developed-in-vitro assays may also serve as a means for assessing individual repair capacity and for predicting one's sensitivity to ionizing radiation.

The process most involved in preventing the harmful effects of spontaneous, oxidative, and alkylation DNA damage is base excision repair (BER). A reduction in BER would therefore lead to an increased risk of developing disease. We identified variation among humans in proteins of BER (Ape1, Polymerase β, Xrcc1, and Ligase 3), and showed that variation in Ape1 leads to reduced repair activity. We are now employing biochemical assays (e.g., DNA binding and protein-protein interaction) to determine the impact of the observed variation on the integrated nature of BER. When combined with x-ray crystallography and computer molecular dynamics, these studies will (1) determine which population-observed BER variation imparts reduced repair capacity, (2) elucidate the mechanistic basis for the reduced activities, and (3) establish a foundation for defining the relationship of genetic differences in BER to human disease susceptibility.

Nucleases are central contributors to DNA repair, recombination, and replication. Defects in these processes have been associated with increased cancer risk, neurological disorders, and premature aging. We identified human (HEX1/hEXO1) and mouse (mExo1) genes that encode factors with homology to the RAD2 family of nucleases. Yeast genetic studies, mammalian expression analysis, DNA substrate specificity, and protein-protein interactions suggest that the mammalian Exo1 proteins function in recombination and mismatch repair. Since we have only a fundamental understanding of the biological roles of the mammalian Exo1 proteins, we are expanding our biochemical studies, our expression analysis, and have established a collaboration to generate a null mouse. In essence, we wish to generate a mouse mutated in the EXO1 gene, then examine the phenotype of the resulting animal, which is more prone to cancer development, etc. These investigations will help determine the functional contribution of this important mammalian nuclease and its relationship to human disease.

Incorporating Biomechanical and Clinical Data into Design of an Ergonomic Computer Pointing Device

P. Tittiranonda, S. R. Burastero

97-ERD-031

Work-related musculoskeletal disorders (MSDs) are a major public health problem at the Laboratory and nationwide. Within office settings, work-related MSDs have been reported to increase tenfold between 1991 and 1997. With a shift to a graphically based environment, computer use has become more oriented to pointing devices, where usage can account for two-thirds of the time spent on the computer. In addition, MSD risk factors such as repetition, force, contact stresses, and awkward postures have been associated with intensive mouse usage. However, very few studies have looked at upper limb biomechanics during pointing device operations. The goal of this project was to use LLNL's unique capabilities in field ergonomic studies, clinical biomechanics, and computational modeling to ultimately design a superior pointing device prototype.

These biomechanical exposure measurement techniques are being applied at LLNL to improve safety in field; in addition, the settings serve to change product design methods in industry. We are now leveraging application of ergonomic exposure assessment technologies into the development of clinical rehabilitation techniques for injured employees and "user friendly" exposure measurement tools for use by safety professionals.

This project addresses several important issues in ergonomic research of computer input devices including (1) identifying how current input device design features can affect upper extremity discomfort, (2) quantifying upper limb movement and force during pointing device operation, (3) predicting how the muscles and joints are affected with given pointing device design configurations, and (4) determining ergonomic

Surface electrodes attached to the forearm and index finger muscles to measure muscle load during mouse usage.

advantages of a "biomechanically rational" prototype design. This project provides new exposure measurement tools and product design paradigms for safer ergonomic products.

Previously, we developed a more accurate method for establishing wrist orientation using inverse kinematics and successfully validated its accuracy on a wrist phantom and human hands. Through this approach, we can accurately characterize the motion of the wrist, which has non-orthogonal and non-intersecting axes. The new computational method has helped us determine the effects of standard pointing devices on upper limb joint postures. In addition, we worked with computational modelers to generate a computational model to simulate the effects of a given input device configuration on the muscles and joints of the thumb. This research served to provide information we needed to build a prototype that potentially reduces MSD risks.

To demonstrate the biomechanical benefits of our pointing device prototype, we used surface electromyography to measure muscle loading when operating our prototype compared to other designs. In collaboration with the University of Michigan, we developed new techniques to obtain very sensitive measurement of muscle activity in the hand, wrist, and forearm.

During FY1999, we used the surface electromyography measurement technique that was validated in the previous year to characterize the loading patterns of the upper extremity when subjects use three different pointing devices and our prototype in their own work environment (see figure). Muscle activity results suggested that our prototype could significantly decrease finger and shoulder muscle load, when compared to other devices including subject's own mouse or trackball. The results of this study will be presented at several ergonomic conferences, including the International Ergonomic Association. As further evidence of the scientific relevance of our research, our results were presented at the National Academy of Sciences and at the DOE Medical Technology Exposition in Washington, D.C.

High Precision Short-Pulse Laser Ablation System for Medical Applications

B.-M. Kim, M. D. Feit, A. M. Rubenchik, J. E. Marion II

The energy of intense <1-ps ultrashort laser pulses (USLP) is mostly deposited near the surface within a thickness of less than 1 μm. Because of extremely localized and fast energy deposition, high-pressure and high-temperature plasma are generated. As the plasma is ejected from the surface, extremely high-pressure shock waves are at first generated. An initially strong shock wave propagates into the tissues, but weakens substantially by a distance on the order of a few microns. With the short pulse duration, the accompanying rarefaction wave causes this attenuation.

Other researchers have indirectly estimated the USLP-induced stress waves. We measured the pressure directly using the Mach-Zehnder interferometry technique. We monitored water ablation as a close approximation to soft tissue ablation; interferometric fringe shifts are directly related to density changes. We calculated the pressure by using a proper equation of state.

We obtained interferograms at threshold fluences for pulse widths of 130 fs, 500 fs, 1 ps, 5 ps, and 10 ps (see figures below). Interestingly, a transition occurred between 1 ps and 5 ps, in terms of stress wave patterns. For 130-fs to 1-ps pulses, surface-generated spherical wave was observed. On the other hand, for 5-ps and 10-ps pulses, a vertical channel was observed at the axis of the incident beam and cylindrical stress waves were generated. These phenomena might be explained as follows: High intensity USLP instantaneously produces plasma at the tissue surface by means of multiphoton ionization. This plasma efficiently absorbs laser pulse energy and shields tissue from the laser irradiation. Tissue shielding is indicated by surface initiated spherical shock. For long pulses, plasma buildup is much slower, and the initial part of the pulse penetrates deeply into the tissue. Distributed energy absorption initiates the cylindrical shock, implying that thermal damages may be extended to deeper region. This result is consistent with the results we obtained last year during hard tissue ablation studies.

We found that the speed of the stress wave is independent of pulse width or pulse intensity once the pressure is attenuated after traveling only tens of microns. We found that the higher energy results in more advanced wave propagation. The speed of the stress wave is close to that of the acoustic waves of 1.53 km/s. The measured pressure of the spherical waves is inversely proportional to the wave radius. This indicates that the initial shock waves quickly lose energy and become acoustic waves. The cylindrical waves decrease in amplitude inversely as the square root of radius initially. The cylindrical wave pressure drops little more slowly afterwards.

We realized considerable improvement in understanding the USLP ablation of biological tissues. We presented our results in seven international conferences and submitted two papers to peer-reviewed journals in FY1999. We are currently looking for industrial partner who will be manufacturing a small-sized, relatively inexpensive ultrashort pulse laser system for medical applications.

(a)
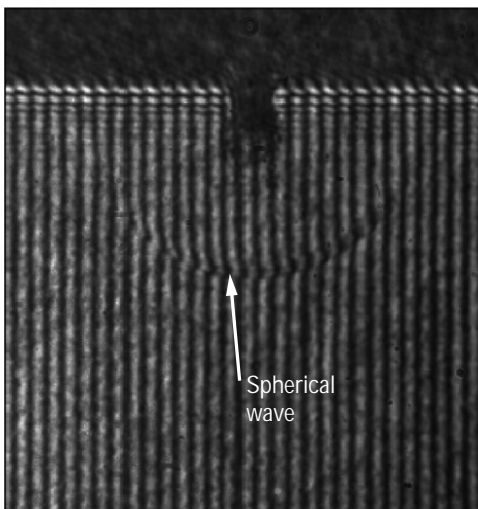
(b)
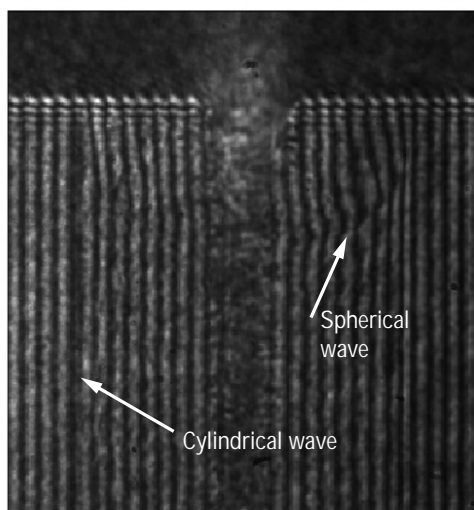
Comparison of the stress waves generated by (a) a 130-fs laser pulse and (b) a 10-ps laser pulse.

Spherical wave

Spherical wave

Cylindrical wave

Advanced Imaging Catheter

L. Da Silva, M. Everett, W. Colston, A. Wang, A. Lee, D. Schumann, R. London, P. Amendt

98-ERD-062

Catheter-based, minimally invasive surgery is performed by making a small incision in a main artery (e.g., the femoral artery in the thigh) and then inserting a long, thin, hollow tube and navigating it through the artery to the treatment area. The advantages of this technique—reduced patient trauma and fast recovery—make it one of the fastest growing surgical procedures. In the United States, over 700,000 catheter procedures are performed annually, and this number is rapidly increasing with improvements in catheter technology.

Catheter procedures now rely on radiography and manual manipulation for navigating and positioning the device. Our practicing-clinician contacts have repeatedly mentioned frustration at not being able to navigate and image at the catheter's tip. The difficulty can be appreciated when you consider that catheters are hollow, polymer tubes that can be as long as 2 m and that they are made soft and pliable to reduce the possibilities of perforating arteries or damaging the arterial wall. This makes the control problem similar to pushing on a string. Both the navigational and arterial-damage problems could be solved by a compact catheter that offers imaging and active-control capabilities to guide and position the distal end (i.e., the end in the body). Clinicians have emphasized that such a device would be a tremendous breakthrough.
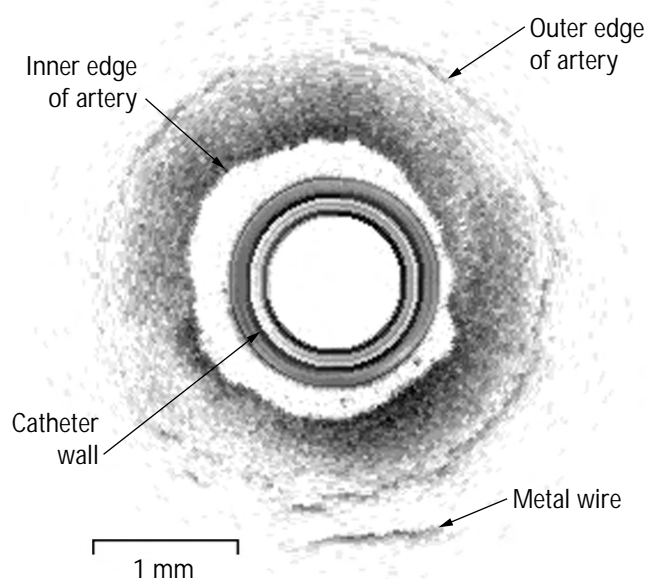
Optical coherence tomography (OCT) image of a porcine artery—generated from a 250-μm-diam probe embedded in the wall of a catheter.

Over the past two years, we have applied LLNL's expertise in optical imaging, microfabrication, and modeling to further the development of this next-generation catheter. As far as we know, we are the only group working on this concept. This technology also has the potential for noninvasive or minimally invasive imaging into explosives or weapons systems.

In FY1999, we demonstrated an OCT imaging system that operates at 50 scans/s, 10 times faster than our previous system. We also significantly improved the design of the optics at the distal end of the catheter, making 150-μm-diam probes feasible while significantly reducing manufacturing cost and enhancing robustness. OCT imaging has been demonstrated with 250-μm-diam probes deployed both through the center of a catheter and incorporated into the catheter wall. Incorporating the optical fiber in the wall leaves the central lumen of the catheter available for a medical device. An image obtained from a 250-μm-diam probe incorporated in the wall of a 1.6-mm-diam catheter tubing is shown in the figure. This figure demonstrates successful imaging of the artery's walls and of a metal wire outside the artery.

To increase our understanding of these images, we have also developed the capability to model OCT imaging. Specifically, we (1) modified existing Monte Carlo photon-transport codes to track the phase and path length of photons propagating through biological tissue, and (2) modeled the predicted OCT signal from a single imaging fiber in an artery filled with blood. The results showed the rapid decay in photon signal associated with the high scattering coefficient of blood and the jump in signal at the artery wall; these results were in good agreement with experimental data collected previously.

In addition, we tested catheter-tip actuation using a shape-memory alloy (SMA). SMAs undergo a reversible, temperature-dependent transformation between a low-temperature martensite phase and a high-temperature austenite phase. Upon being heated, these materials can recover large amounts of mechanical deformation (strain). We mechanically stretched nickel–titanium (Ni–Ti) wire and then threaded it up and down two adjacent lumens in the catheter wall. When resistively heated, the wire shrank to its original length and thereby caused the catheter tip to bend.

Several patents have been filed on this technology, and two have been issued. The catheter development and modeling efforts are continuing. Our long-term goal is to further develop this technology and transfer it to the medical community.

Highly Parallel µL-Scale Biochemical Processor

R. R. Miles, K. A. Bettencourt, C. K. Fuller, J. Hamilton

As part of this ongoing project, we are investigating methods of performing microscale biological assays. Our focus during FY1999 has been on producing a compact, parallizable device for preparing and amplifying "on-chip," polymerase chain reaction (PCR) samples. This device would use PCR to replicate DNA until the amount of DNA is sufficient to detect. This is a very specific test and can be used to detect the presence in the fluid of a biological pathogen such as anthrax or plague. The primary advantages of this technology are that (1) the devices could be used for automatically preparing biological samples, thereby reducing the manual handling of potentially pathogenic substances; and (2) testing costs are reduced and the number of tests performed in a given time increased. These attributes are very useful for any large-scale biological-testing program, whether it be testing for drug-discovery applications or assessing the extent of exposure following a biological terrorist event.

Our ultimate goal is to achieve a "PCR-on-a-chip." During FY1999, our emphasis has been on fabricating and testing prototype devices. We used standard microfabrication and microelectromechanical systems (MEMS) techniques to fabricate microdevices in silicon and glass with platinum electrodes. Following injection of a sample into the inlet port of the microdevice (using a syringe pump), a dielectrophoretic (DEP) force is used to collect and concentrate the biological particles of interest on a set of interdigitated electrodes. (A DEP force results when an electric dipole is induced in a particle so that the particle can be propelled toward areas of high electric-field gradients.)

In Fig. 1, we present typical results obtained from our prototype devices. In Fig. 1(a) *Bacillus globigii (B.g.)*

spores, a model for anthrax, are shown captured and concentrated on the edges of electrodes patterned at 30-mm intervals. We showed that *B.g.* can be captured easily from water moving at up to 1 cm/s. *Erwinia herbicola (E.h.)*, a model for plague, is also easily captured from a flowing stream. Captured *E.h.* can be lysed by introducing lysing solution into the flow stream. The cells were dissolved; the DNA freed from the cellular nuclei then moved with the flow stream to a second set of electrodes, where it was collected using the DEP force.

Figure l(b) shows captured *E.h.* DNA. We demonstrated that DNA is best captured from water if the applied voltage is less than 10 kHz and the flow rate is less than 1 mm/s. Reagents were introduced. A heater patterned on the glass surface of the PCR chip was used to cycle the temperature of the mixture to perform PCR replication of the DNA. With each thermal cycle, the amount of detectable DNA is doubled until the DNA reaches detectable amounts.

During FY1999, we also verified our ability to purify the DNA after its exposure to known inhibitors to PCR, such as humic acid.

In FY2000, we will add on-chip micro-magneto-hydrodynamic pumps; the result will be compact biological test devices that can be used in mobile test laboratories.

To our knowledge, no other researcher has performed PCR following DEP concentration. A provisional patent has been filed on this concept. The DOE's nonproliferation program has begun to fund the continuation of this work as part of a microbiological sample-preparation device for continuous-monitoring applications.
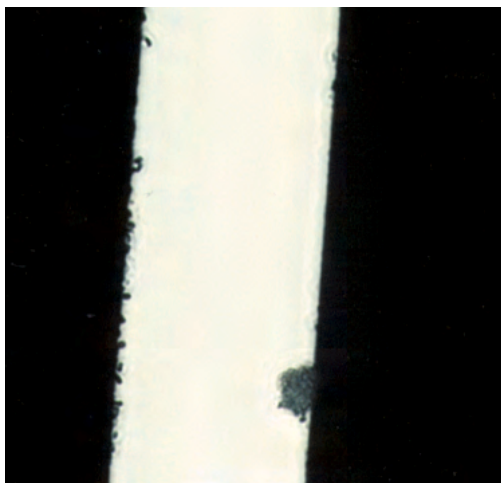
(a) (b)
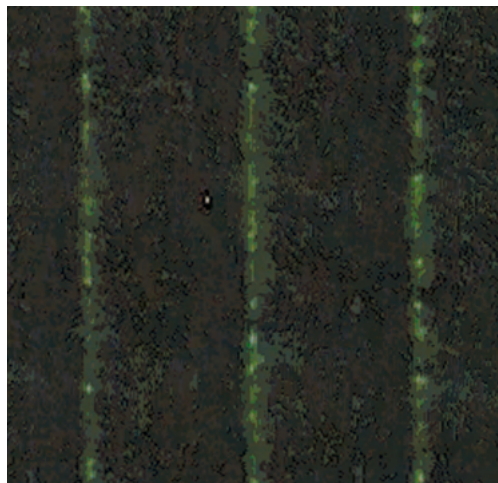
Figure 1. Biological particles (DNA) captured on electrodes using the dielectrophoretic force: (a) *Bacillus globigii,* and (b) *Erwinia herbicola* DNA.

Magnetohydrodynamic Pumps for Microfluidic Manifolds

A. V. Lemoff, A. P. Lee

98-ERD-089

Micro total analysis systems are one of the ultimate goals of today's microfluidic research. In such systems, all functions necessary to analyze a sample are integrated onto a single microfluidic substrate. One of the most critical components of a micro total analysis system is a microfluidic pump. On board pumping is required to transport samples and reagents for biological or chemical analysis from one point in a microfluidic system to another.

The AC magnetohydrodynamic (MHD) micropump demonstrated here produces a continuous flow and is suitable for solutions containing biological samples. In this pump, an alternating current (AC) flows across a fluidic channel between two electrodes, while a synchronous magnetic field, perpendicular to both the channel and the current, produces a pumping force along the channel. The voltage requirement of this micropump is lower than most other micropumps that are compatible with biological systems. Moreover, the design of the micropump allows for multiple, independently controlled pumps to be integrated on a single chip, thus enabling complex microfluidic systems.

In FY1999, we measured varying concentrations of NaCl solutions (1 M, 0.1 M, and 0.01 M) to determine the maximum current allowed in the microchannel before bubble formation is observed. In a practical system, this limit cannot be exceeded since bubbles impede flow and cause electrode degradation. Increasing the frequency allows higher currents to be achieved without bubble formation. All measurements were performed with a top channel width of 800 μm and an electrode area of 4 mm by 380 μm. For channels of different width but from the same electrode area, the same bubble current threshold is observed. For smaller widths, there is a lower voltage drop. For larger widths, there is a higher voltage drop across the solution because the resistance depends upon the length of the current path in the solution.

After determining the maximum current allowed in the microchannel before electrolysis occurs, we performed flow measurements on these solutions. Figure 1(a) shows a photograph of a fluidic chip in which liquid is pumped about a circular loop. The electromagnet is located underneath the fluidic chip. We mixed the conducting solutions with 5-μm polystyrene beads and used video capture software to record and track the particles frame by frame to determine flow rates. We also used other conductive solutions in the micropump, including 0.01-M NaOH, phosphate buffer solution (PBS pH = 7.2), and Lambda DNA in 5-mM NaCl solution. The highest flow rate achieved in this set-up using 1-M-NaCl solution is 18 μL/min.

For a given channel current, there are two ways to vary the flow speed in our micropump. The first method is to vary the magnetic field strength. The second method is to vary the relative phase between the channel current and the magnetic field. The maximum speed, with opposite directions, is seen at 0 deg. and 180-deg. relative phase, and no flow is observed at 90-deg. relative phase. Although all conducting solutions used had the same qualitative behavior, the bubble current thresholds, and hence the maximum flow rates, are different.

The ability to control the flow speed and flow direction enables the control of microfluidic manifolds. Figure 1(b) shows a photograph of an AC MHD fluidic manifold, a 2 by 1 switch. Flow in either input can be selected by controlling each MHD electrode pair by varying its current amplitude or phase with respect to one electromagnet located underneath the chip.

In FY2000, we plan to automate the controls of the MHD fluidic switch, which will increase the switching speed. We will also increase the complexity of the manifolds.

(a)

(b)

Figure 1. An AC magnetohydrodynamic micropump: (a) top view of the fluidic chip, where liquid is pumped about a circular loop; (b) top view of a fluidic switch.
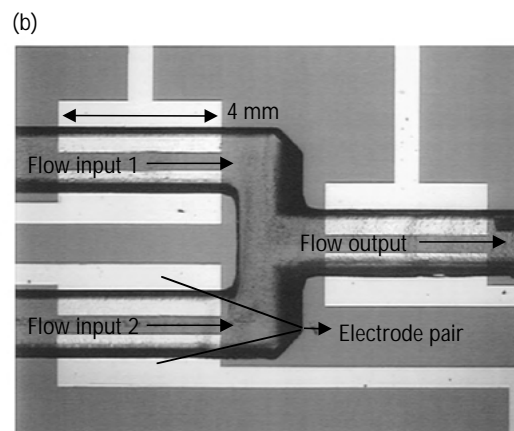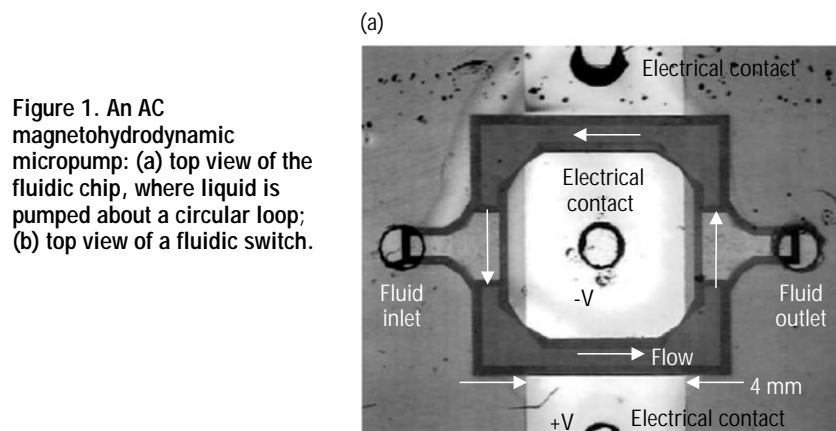
Low-Charge-State AMS for Biological Research

J. S. Vogel, T. Ognibene, M. Roberts

Living organisms use a wide variety of organic molecules with striking specificity at very low concentrations. Human health and well being depend on understanding these low-concentration chemical reactions. Even the nutrients we eat are digested to their component compounds before being restructured into our living cells. Therapeutic drugs must be tailored to interact properly with the specific biochemical pathway that they are expected to modify and to inflict as little harm as possible on biological components that are not the desired target. Low-level environmental contaminants are often capable of inflicting harm, and we must understand the levels at which these compounds become harmful and how to ameliorate their damage.

These areas of research—nutrition, pharmacy, and toxicology—depend on sensitive tools to discover chemical distribution and interactions within humans at natural or nontoxic levels. At LLNL, we have developed accelerator mass spectrometry (AMS) as a technology that enables tracing isotope-labeled chemicals in humans without exposing participants to toxic or radiative risks.

In this project, we are developing a high-throughput AMS system dedicated to biochemical research in nutrition, pharmacy, and toxicology that will be used by collaborating researchers throughout the University of California and also at other institutions. Many components of our AMS system are similar to other AMS spectrometers. However, because many more samples must be measured in biochemical research than in the well-established earth sciences, we have designed and built the components of our new spectrometer to achieve high throughput.

Specific accomplishments during FY1999 include (1) incorporating an ion source that produces relatively high ion currents (200 to 250 μA of negative carbon ions) that are a factor of 10 greater than the ion sources used with similar spectrometers, (2) using a "zoom lens" connection between source and spectrometer that optimizes the practical use of these high currents, (3) exploring the limitations imposed by using lower charge states for the accelerated ions that represent the AMS signal, and (4) establishing an operational strategy that permits direct use of the spectrometer by university researchers and students. We also performed and confirmed computer simulations that accurately model the ion paths at high currents. These models were used to determine optimal placement of spectrometer components.

During FY2000, we expect our spectrometer to reach full operation at high throughput. This project will now complete the research on the best operation mode and will begin use of the new spectrometer in several collaborative projects, including development of a new form of immunoassay for early detection of cancer signatures in human blood plasma and a new approach to identification of proteins.

Nutrition research will be one of the first high-throughput projects on the system. The variation in the response of humans to common nutrients is much greater than the variation seen among individuals from the highly inbred animal strains that are commonly used in biochemical research. This AMS project develops the techniques required to perform health-related research that is best done with human subjects. One such research program, which began during FY1999 at the University of California, Davis, is funded by the National Institutes of Health (NIH). We will use our high-throughput, low-charge-state equipment in a two-part study. In one part, we will trace the fate of folic acid in 30 people, with about 500 samples per person. Ten of these participants will have a common variation in folate metabolism that requires dietary modification for optimal health—we will find the underlying details of this condition. We are also studying 20 participants to determine how beta carotene provides vitamin A to tissues that depend on this potentially toxic nutrient. A large population suffers poor health and eyesight due to low metabolism of available carotene to vitamin A.

Such health-related research will continue at LLNL, but our demonstration of the value of low charge-state AMS in bioscience will make this technology an affordable analytical tool at medical research centers.

Computational Methods for Automatic Fitting of Proteins

B. Rupp, S. Ringhofer, A. Szoke, H. Szoke

98-LW-002

X-ray crystallography is the principal method for determining the 3-D structure of biological macromolecules—information that forms the basis for structural biology, drug design, and molecular medicine. However, x-ray diffraction patterns contain no phase information, and the reconstruction of the electron density requires additional phase information. A large part of this additional phase information is derived from the structural model, which is fitted into electron density using a priori chemical knowledge. Weak experimental phases produce only ill-defined electron density. In these cases, the resulting x-ray structures are therefore subject to severe model bias. Endeavors such as structural genomics and the study of potential bioterrorism agents require minimized model bias and the best possible experimental electron-density maps (phases). The key problem of high throughput structure determination lies in the time-consuming map refinement and iterative, manual, rebuilding procedures. With our automated fitting project, we are addressing this major throughput bottleneck.

In this project, we are concentrating on two related issues: (1) obtaining the best electron-density maps, and (2) building models with minimum manual interference and bias introduction.
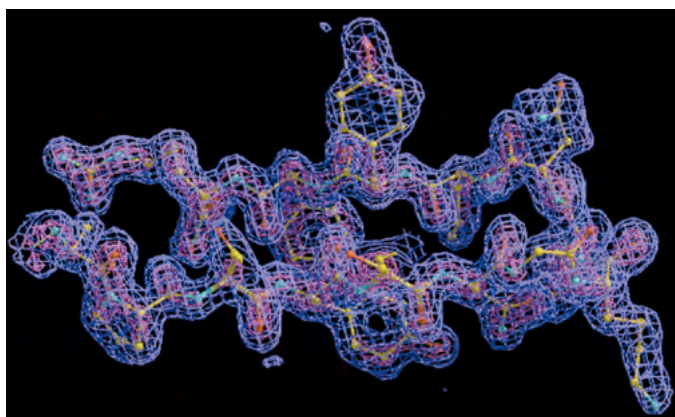
Map of *tetanus C* after iterative manual rebuilding of the protein model using the program wARP, which provides maps of excellent quality that are suitable for automatically building models. The entire loop is embedded in well-defined density of excellent quality.

To address the first issue, in FY1999 we critically assessed maps from real data by submitting them to a variety of map-generation methods: weighted automated refinement of proteins (wARP), electron density (EDEN), and sharp/solomon. The figure shows a loop of the *tetanus C* fragment in electron density created by wARP. Map quality is judged by the positive comparison of the electron density generated by the respective method with that of a "known model." However, because the known model itself would have been generated by a map-reconstruction method and could therefore be biased, we created reference-model data that accurately describe (using well-defined error models) experimental diffraction data. These reference-model data are mandatory for objective, bias-free, and consistent comparisons of map-generation methods. Starting from a known model, and using a program that we are developing, we can now calculate a set of structural factors that obey the same error statistics as real data. We will make the program accessible to the crystallographic community through our Web server.

During FY1999, we also investigated the potential strengths and weaknesses of our method at different stages of map improvement by applying it to the structure of the *tetanus C* fragment, which we have solved at 1.57Å (see figure). The tetanus neurotoxin is prototypical of the family of chlostridial neurotoxins, which are potential agents in bioterrorism. Exact structural information is therefore of major interest for the Chemical and Biological Nonproliferation Program (CBNP) being pursued at LLNL and nationwide.

Once the best possible map has been obtained by methods described above, a protein model must be built into the map. So far, this must be done mostly manually, which is a very time-consuming process. In FY1999, we developed two new computational algorithms that should improve automated model building. One is based on the fast computation of the local morphology of the protein; the second uses pseudo-electrostatic potentials. The latter should enable us to find correlations between electron-density maps and parts of protein structures (e.g., the protein backbone) rapidly.

Opto-Acoustic Enhancement of Drug Delivery

S. R. Visuri, L. B. Da Silva

98-LW-030

Significant benefits can be realized by locally delivering drugs and enhancing their uptake across cell barriers. Most medicines are administered orally or intravenously—neither is an effective way of targeting specific sites. We have developed a technique using optically generated ultrasound, termed opto-acoustics that (1) can greatly improve local drug efficiency, and (2) has the potential to decrease systemic dosages and side effects and to enable revolutionary therapies. The many applications of the opto-acoustic technique include delivery of thrombolytics to dissolve blood clots, delivery of drugs to prevent arterial restenosis, localized delivery of chemotherapeutics for cancer therapy, and delivery of vectors for gene therapies.

The concept is similar to transdermal ultrasound, which can increase drug transfer across the skin by up to 5000 times. Ultrasound is postulated to transiently disorder the cell membrane, creating channels through which compounds can enter. This temporary disruption of a cell's barrier can increase intracellular concentrations of compounds that normally are impermeable or have low diffusion rates.

Our initial research during FY1998 had demonstrated the concept of using opto-acoustics to permeate cells and also established thresholds for cellular necrosis caused by stress waves. In FY1999, we defined parameters for optimal permeation and explored pulse frequency, acoustic intensity, and treatment duration. We used a diode-pumped, frequency-doubled Nd:YAG laser operating at 0.5- to 20-kHz repetition rates to produce a series of acoustic pulses via thermoelastic expansion. These acoustic waves were propagated into cultured and plated cells in media that contained a selection of normally impermeable, fluorescent-labeled dextran dyes. Uptake of the dye was quantified via fluorescent microscopic analysis. Following treatment with the opto-acoustic technique, we noted cellular incorporation of dyes up to a molecular weight of 40,000; control cells that did not receive opto-acoustic treatment had unremarkable incorporation of the dye. The acoustically treated cells incorporated more than 16 times the amount of dye compared to untreated cells (see figure). Following treatment, the viability of the cells was confirmed by assays of membrane integrity and cellular activity.

Optimal results were obtained with pulse frequencies of 1 to 5 kHz; higher-frequency operation decreased the acoustic energy per pulse. Acoustic intensity in the range of 1 Mpa was required to make the cells permeable. Efficiency of producing acoustic energy was generally increased by using shorter laser pulses and shorter penetration depths. The thermal load into the samples was managed with a closed-loop continuous flow of the optical absorbent.

During FY1999, we also explored the use of ultrasound for gene-transfer applications. For this study, we used a 20-kHz ultrasound source emitting less than 1 W/cm^2 to transiently permeate mouse lymphoblast cells. A Beta-Galactosidase enzyme assay was used to monitor the transfection rate of the cells. Although higher ultrasound energies affected cell viability, these dosages often yielded higher transfection rates. Ultrasound approximately doubled the number of cells that were transfected compared to the control vector for specific parameters.

Our experiments have proven the efficacy of cell permeation using opto-acoustic techniques and provide the basis for developing a clinically viable drug-delivery device. This method of localized, enhanced, drug delivery has the potential to dramatically reduce required drug dosages and associated side effects and to enable revolutionary therapies. A patent application has been filed for this technology.

(a)

(b)
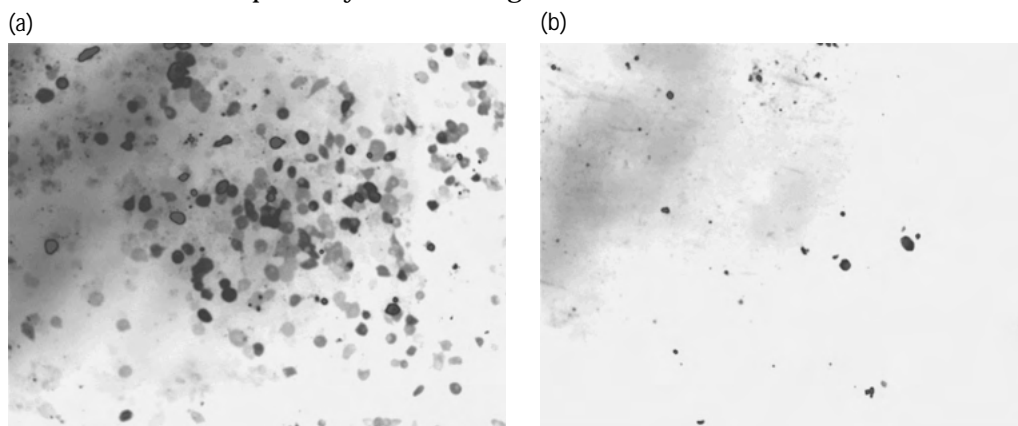
Figure 1. Incorporation of fluorescent-labeled dextran dye into (a) cells receiving opto-acoustic treatment, and (b) control cells. Equal numbers of cells are represented in fields (a) and (b), yet treated cells incorporated approximately 16 times more dye than control cells.

Beyond the DNA: A Prototype for Functional Genomics

J. S. Albala

99-ERD-039

The Human Genome Project has produced a vast amount of information about the sequence of each of the estimated 100,000 human genes. Future genomics efforts will focus on advancing our understanding of the function of newly identified genes, which must ultimately be examined at the protein level.

Protein–nucleic acid interactions are essential for gene expression, structural organization, replication, and DNA repair. One of the critical components of cellular biochemistry is the integrity of interactions between proteins and DNA. Understanding the details of these interactions is a fundamental step towards comprehending key aspects of disease biochemistry. The complexity of these interactions makes it necessary to analyze protein–DNA binding in vitro. Many techniques have been designed for this purpose such as filter binding studies, electrophoretic mobility shift assays, and footprinting technologies. However, these traditional techniques are laborious and time-consuming.

Our project is the first demonstration elucidating protein activity with DNA bound to a glass slide. These experiments have shown that protein–DNA interactions and enzymatic activity can be measured using our newly developed oligonucleotide *functional chip*. It is anticipated that this functional genomics screen can be utilized for assaying novel proteins in high-throughput.

The functional chip contains a variety of DNA fragments attached to a glass slide. The chip is used to screen individual proteins for their DNA substrate affinity. This interaction is then visualized using fluorescent immunocytochemical techniques for detection of the protein–DNA binding events or enzymatic activity. We used a glass slide in the design of the functional chip because it facilitates the analysis of proteins in a cheap and effective manner. This is a high-throughput functional genomics approach since hundreds of different oligonucleotides can be attached to the slide and analyzed against numerous proteins in parallel to determine DNA binding or enzymatic activity of the proteins.

DNA repair enzymes have been implicated in a variety of human cancers and are thus an area of great interest for novel protein discovery and analysis. In order to examine the functional activity of these enzymes, different types of oligonucleotides were synthesized and applied to the slide to represent different types of native and damaged DNA.

We selected the RecA enzyme as a prototype for study because it binds various forms of DNA in these processes. RecA is a DNA-dependent ATPase from *E. coli*, which functions in homologous recombination and DNA repair. We have demonstrated the binding of RecA to oligonucleotides on the functional chip paralleling similar results obtained by more traditional means (see figure).

We chose APE, a double-stranded DNA-specific human endonuclease, to demonstrate the utility of the functional chip to screen for enzymatic activity in a microarray format. APE specifically incises the DNA backbone of damaged double-stranded DNA, specifically having an apurinic site. Using the functional chip, we have shown that oligonucleotides on the functional chip can be enzymatically digested and the application of a mutant APE enzyme eliminates this activity. Future work will extend these studies to examine additional human DNA repair proteins produced using a high-throughput expression paradigm.

In FY2000, we will use the functional chip as a high-throughput screen for proteins defective or mutant in various aspects of DNA repair. Future effort will focus on automation of chip production and utility. We are in the process of submitting a record of invention to be completed early in FY2000.

Panel A	Panel B
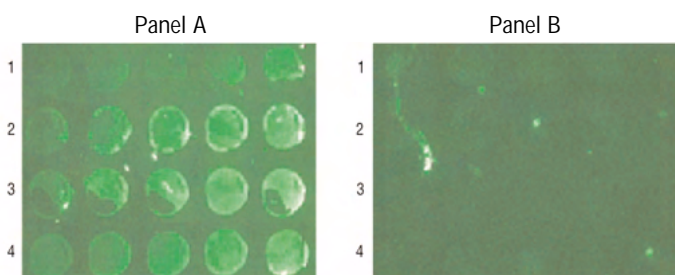
Panel A shows RecA binding single-stranded (row 1) and double-stranded oligonucleotides (rows 2–4). The RecA protein was prepared in buffer containing ATP-γ-S, which inhibits the dissociation of the protein from the DNA. Protein–DNA binding is demonstrated by the presence of the fluorescent spots.

Panel B shows oligonucleotides spotted as in Panel A. The RecA protein was prepared in buffer containing ATP, which allows the enzyme to bind and dissociate from the DNA. No fluorescent signal denotes a lack of captured protein–DNA interaction.

Analysis of the *Yersinia pestis* Genome: A Prototype for Functional Genomics

P. M. McCready, E. Garcia

There is an international effort currently underway to understand the genetic composition of the world around us, extending from the smallest virus through man. The largest investment from the public and private agencies is in the arena of DNA sequencing, a process that allows us to "read" the most elementary chemical sequence of the genetic material, DNA. Particular portions of the DNA or "genes" dictate what we are and how we respond to our environment. Many bacteria have been completely analyzed at this basic level and are awaiting more detailed functional characterization relating genes to a particular characteristic (e.g., the ability to cause disease in humans). Attention is now turning toward large scale "functional genomics," an area that is still in need of much development to fully exploit the enormous volume of sequence data being generated.

Yersinia pestis, the bacteria responsible for bubonic plague, is comprised of approximately 4.9 million DNA bases and 4,500 genes. When *Y. pestis* is grown at room temperature, it is not virulent to humans. However, growth at elevated temperatures yields a microbe that is capable of causing disease. Assay of certain molecules present in the bacteria at these two different temperatures tells us what genes are candidates for this change. The candidate gene(s) can then be used to make abundant amounts of the corresponding protein, providing the material needed to determine how that protein contributes to virulence.

Any information we reveal about virulence in *Y. pestis* will be applicable to several disease-causing microbes. We can therefore compare the candidate virulence genes with those in other bacteria to see what is unique to *Y. pestis*, what is common to other virulent bacteria, and what is shared with all microbes. *Y. pestis* is also a national security concern because of its potential use as a biological warfare agent. The identified virulence genes will also be used in the design and deployment of tools for the identification, detection, and neutralization of these organisms in the environment.

Our LDRD funding began in the last four months of FY1999. We constructed a relational database that contains the sequence composition of the *Y. pestis* DNA and may be queried. In collaboration with the DOE Genome Consortium at the Oak Ridge National Laboratory, these data were used to computationally predict where the 4,500 genes are located and which genes are of potential interest.

We synthesized chemical reagents to extract the first set of 96 known virulence-associated genes into dishes. We developed a protocol to extract the appropriate biological material from *Y. pestis* at the two different temperatures. This work resulted in substrate that will be used to identify important genes for virulence and their corresponding proteins.

We investigated bacterial and insect cells in order to identify which is more favorable for the upcoming generation of proteins and their subsequent purification. We programmed and tested a robotic workstation that is capable of handling thousands of samples a day to facilitate structural and functional determinations. Our research during the past four months resulted in the infrastructure needed to accomplish the following in FY2000: (1) to identify and synthesize all predicted genes in *Y. pestis*; (2) to generate and query expression arrays to understand which genes are contributing to virulence; (3) to make and purify the proteins that correspond to these genes; and (4) to carry out structural characterization of key proteins.

An Automated Approach for the Identification of Functionally Relevant Small Molecule Inhibitors

D. M. Wilson III

99-FS-010

Radiation induces the formation of genetic damages via direct ionization or through the production of reactive oxygen intermediates that chemically modify DNA. Radiation is thought to elicit its cytotoxicity by inducing the formation of lethal DNA damage, including modified bases, baseless sites, and strand breaks. To avert the deleterious effects of radiation, cells are equipped with DNA repair systems and cellular responses that function to amend genetic imperfections and to prevent the replication of damaged DNA. The focus of this feasibility study was to investigate the development of a novel, function-based technology for isolating inhibitors of proteins involved in radiation-protection. Such inhibitor molecules represent potential radiosensitizing agents, which could be used to increase the biological effectiveness of a given radiation dose.

We considered the combination of unique laboratory expertise in robotics, computational modeling, combinatorial chemistry, and DNA repair enzymology. We investigated a novel automated approach for the rapid identification of small molecule inhibitors of proteins. This capability could be applied to current laboratory research on proteins involved in the repair of radiation-damaged DNA. Inhibitors of proteins involved in cellular resistance to radiation have potential value as co-therapeutics in anti-cancer treatments and could be licensed to pharmaceutical companies for further testing. The developed technology could potentially be used to determine the functions of new proteins identified during the Human Genome Project. An invention disclosure has been filed for the base technology to be designed.

Two major repair pathways, base excision repair (BER) and recombinational repair (RR), exist to avert the deleterious effects of radiation-induced DNA damage. In the development of an automated system, we identified inhibitor molecules for two proteins that participate in such pathways, namely the Ape1 protein (the major human abasic endonuclease of BER) and Fen1 (a structure-specific endonuclease of RR). Since our experimentation revolves around isolating molecules that inhibit biochemical function (i.e., molecules that prevent DNA binding, polymerization, or nuclease activity), we would in essence be identifying functionally relevant inhibitors.

We identified potential inhibitor molecules for Ape1 using a "docking" approach (in which candidate ligands are examined for their fit into surface cavities of a known protein structure). These and related approaches provide a valuable pre-screen for experimental assays. A similar approach will be used for Fen1. Potential inhibitors (which can be purchased or synthesized) identified by such docking methods would serve as the initial targets in our search for effective inhibitor compounds. Computational approaches could also be used in follow-up studies to determine the binding sites of the chemical inhibitors, to develop more potent inhibitors, and to draw predictive conclusions about the structure-function mechanism of the target protein.

The screening technique would utilize a simple flow-based filter system operated by robotics. Commercial laboratory instrumentation and automation are available for creating a nearly hands-off system for inhibitor molecule screening. Specifically, a general purpose dispensing instrument (i.e., the Packard Multiprobe II), using opaque, filter-backed microtiter plates, would be combined with on-deck vacuum extraction to generate a rapid screening technology. System integration tools and experience from the LLNL Human Genome Project could be leveraged. In general, target proteins (e.g., Ape1 and Fen1) will be incubated with potential inhibitor compounds and the effectiveness at inactivating a specific biochemical activity assessed. Such experiments are presently being performed with Ape1. Identified inhibitors could subsequently be used to determine if they can effectively sensitize human cells in culture to radiation exposures.

Chimeric Proteins to Detect DNA Damage and Mismatches

S. L. McCutchen-Maloney, C. A. Giannecchini, I. R. McConnell, M. P. Thelen

99-LW-004

We are developing chimeric proteins to detect DNA damage and mismatches. This detection method could benefit both basic research as well as potentially lead to a diagnostic for DNA damage and mismatches including single nucleotide polymorphisms.

Our approach is unique from other detection methods that use DNA repair proteins to detect damage and mismatches in that we are producing chimeric proteins rather than using individual proteins. The chimeric proteins are produced by fusing two individual proteins into one, thereby generating a protein with a novel function. Our work integrates the protein structure/function and computational modeling efforts with the molecular toxicology and DNA repair interests at LLNL. This work may also fall into the category of proteomics research since it may be possible to design other chimeric proteins with novel functions, as more protein sequences become available.

If not repaired, DNA damage and mismatches can lead to mutations and eventually cancer. Therefore, methods to detect damage are useful not only in basic research but also in monitoring DNA mutations that could predispose an individual to cancer. Current methods to detect DNA damage often use radioactive labeling and rely on expensive instrumentation that is not readily available in many research settings. Our method to detect DNA damage and mismatches using chimeric proteins would alleviate the need for radioactive material and expensive equipment, and could potentially be performed using a simple gel electrophoresis apparatus.

In FY1999, we produced five chimeric proteins each of which is comprised of a nuclease (a protein that can degrade DNA) and either a damage or a mismatch recognition protein (a protein that can bind to DNA damage or mismatches). We used polymerase chain reaction (PCR) mutagenesis to fuse the two genes of interest to make the chimeric DNA sequences. We then engineered these DNA sequences into an expression system in order to produce the chimeric proteins in bacteria. The chimeric proteins were purified away from bacterial proteins by affinity and ion exchange chromatography. Characterization of the chimeric proteins is currently underway and preliminary results suggest that the chimeric proteins will be useful for detecting DNA damage and mismatches.

To date, we have shown that three of the chimeras that we produced possess greater affinity for damaged than for undamaged DNA. We detected this in an assay designed to look at degradation of DNA after addition of a chimeric protein. In this assay, one sample of DNA contains a site of damage and other sample (with the same sequence) does not contain damage. When a chimeric protein is added to the two DNA samples, the damage recognition protein should bind the sample containing DNA damage allowing the nuclease to degrade the DNA. Thus, the damaged DNA should be preferentially degraded. We observed this for three of the chimeric proteins; we are still characterizing the remaining two.

In FY2000, we will continue to optimize conditions for the detection of DNA damage and mismatches using our chimeric proteins. Next, we will investigate several DNA samples that contain different kinds of DNA damage and DNA mismatches. We are also in the process of designing the next generation of chimeric proteins based on the results we have obtained so far and on ongoing computational modeling. A patent application for this work is in progress. We hope to have enough data to publish a manuscript soon.

Polarized Light Imaging through Scattering Media

D. J. Maitland, V. Sankaran, R. London, D. Steich, G. Zimmerman

99-LW-011

Imaging through optically turbid media has a variety of applications, including medical diagnostics, underwater imaging, and atmospheric optics. The common goal in these applications is to discriminate weakly scattered photons—which have traveled a near-direct path through the medium—from highly scattered photons—which have traveled a more circuitous path through the medium.

The goals of this project are to (1) experimentally demonstrate that polarized light can be used to optically diagnose or image objects that are embedded in optically turbid media, and (2) increase the physical understanding of polarization propagation in scattering media by means of both experimental phantom studies and numerical simulations that use a Monte Carlo code that has been modified to include polarization. The Monte Carlo model is set up to use an electromagnetic (EM) scattering cross section to determine polarized photon propagation. In its simplest form, the EM cross section is specified by well-known analytic solutions. However, for many problems of interest, including complex particle shape and coherently scattering media, 2-D and 3-D Maxwell solvers are a good way to obtain the cross-section solution.

During FY1999, we constructed a low-noise Stokes polarimeter. Our experimental results have indicated that polarized light can indeed be used to image through optically turbid samples [Fig. 1(a,b)]. For example, our initial research suggests that it may be possible to use polarized light to discriminate cancerous tumors from the healthy tissue in which they are embedded. Our results show that (1) polarized light survives hundreds to thousands of scattering events in tissue and tissue phantoms (microspheres in water suspensions) for a 1- to 3-cm path length (depending on the type of tissue), and (2) embedded objects that have different polarization properties will locally disturb the polarization state.

Using measurements in myocardium, adipose tissue, and blood, we found that—in contrast to results obtained in tissue phantoms—linearly polarized light survives through longer propagation distances in biological tissue than does circularly polarized light.

We found that highly concentrated samples result in an increase in the amount of polarized light that is scattered in the forward direction relative to that in less-dense samples made up of the same scatterers. Since most biological samples are a collection of densely packed, 0.1 to 10-mm scatterers, our result is a significant step towards understanding why polarized light propagates as it does in tissue. We believe that this effect results from interference between the scattering elements in the sample.

We validated the polarization Monte Carlo/EM numerical model against our experimental results. The multiple-scattering model agrees well with the multiple scattering in the experiments. Early instrumentation simulations indicate novel detection schemes may improve the image resolution of the current system.

We have partially described our results to date in two published journal papers, two submitted journal papers, and one conference proceedings. The graduate student working on this project, Vanitha Sankaran, was honored with the Dekker award from the International Society for Optical Engineering for her thesis research, which was partially funded by this LDRD project. Dr. Sankaran has elected to continue her work on polarized light physics as a postdoctoral researcher at LLNL.

In FY2000, we will continue the basic science research and build a prototype experimental system that can be applied to cancer-detection research. Core LLNL technologies will allow us to tackle the polarization-propagation problem both experimentally and with current, LLNL-developed models.

(a) (b)

Figure 1. Imaging objects in optically turbid media with polarized light. A transparency slide with printed (black ink) letters was placed in the center of a 10-mm^2 glass cuvette. The cuvette was filled with intralipid such that the reduced optical path was $\tau' = 1.0$. The images shown measure 4 by 5 mm. In (a), the unpolarized-light image shows no indication of the embedded object; in (b) a polarization image clearly indicates the presence of the embedded object.
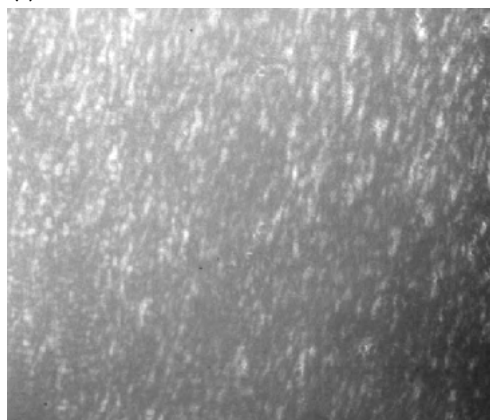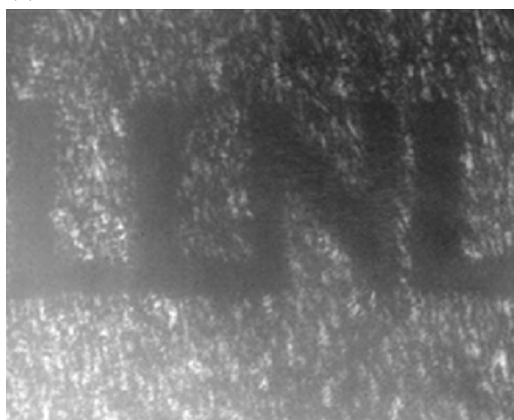
High-Efficiency Multilayer X-Ray Optics for X-Ray Crystallography

S. M. Lane, T. W. Barbee, B. Rupp

99-LW-013

X-ray crystal diffraction is the principal tool used to determine the detailed structure of macromolecules. Although high x-ray fluences can be obtained at synchrotron facilities, most structural determinations are made using smaller and more convenient systems that are based on rotating-anode x-ray generators. LLNL has several such systems, as do most other academic, biomedical, and pharmaceutical laboratories. With these small systems, for large macromolecules the typical time required to obtain a data set from one crystal sample is one week; it typically requires more than a day even to determine that a sample is unsuitable for measurement. This lack of a sufficiently intense laboratory x-ray source is a principal bottleneck in the rapidly growing field of protein-structure determinations, which is becoming an important tool in understanding, detecting, and developing vaccines for biological warfare agents.

At LLNL, we recently successfully developed a new class of x-ray optics for proximity-focused x-ray lithography. These optics are truncated paraboloids with mirrored inner surfaces that are made using optical replication techniques. (No other group that we know of is capable of making such x-ray optics.) In this project, we are extending this technology and using existing fabrication facilities at LLNL to develop x-ray optics capable of significantly improving ($>10\times$) the x-ray fluence delivered to a sample by current x-ray-diffraction systems.

During FY1999, we performed extensive ray-trace simulations to design a single-element, miniature, truncated-ellipsoidal x-ray optic. This optic will use multilayer resonance mirrors with graded layer thicknesses (graded-*d* spacing). Such mirrors provide wavelength selection and high reflectivities at relatively large reflection angles (up to 1.8 deg compared to 0.3 deg for grazing reflection at a 1.5 Å Cu–K wavelength). These larger reflection angles and the geometry of the optic provide a much larger collection solid-angle than present mirrors. Estimates indicate that at least a 10- to 100-fold improvement in x-rays delivered to a sample could be obtained, leading to a proportionally reduced measurement time.

Most mirrors fabricated for x-ray crystallography use grazing-incidence mirrors (mirrors using total external reflection). Mirrors made of alternating layers of low- and high-*Z* materials can efficiently reflect at much larger angles because they act as synthetic crystals and reflect by Bragg diffraction. These multilayer mirrors obey the Bragg diffraction law ($\lambda = 2d\sin\Theta$) where λ is the x-ray wavelength, *d* is the layer spacing, and Θ is the reflection angle. Because the average reflection angle varies with axial position on the optic, the *d*-spacing must also vary.

During the past year, we have obtained high-quality, ultrasmooth test mandrels for producing the first prototype graded-thickness multilayer optics. We have designed, fabricated, and tested a system for determining the deposition rate of the multilayers as a function of position on the surface of these complex, curved mandrels.

Our goal in the coming year is to (1) produce initial prototype optics, and then (2) perform crystallography measurements to demonstrate significantly increased x-ray fluence to sample.

The capability of producing multilayer optics using replication techniques will be important for a variety of other x-ray applications that benefit from increased x-ray fluences, including microradiography, x-ray microfluorescence analysis, microphotoelectron analysis, x-ray lithography, and x-ray microscopy.

Development of Nuclear Magnetic Resonance Pulse Sequences and Probes to Study Biomacromolecules

M. Cosman, V. V. Krishnan, R. Maxwell

99-LW-031

Nuclear magnetic resonance (NMR) spectroscopy is the only method that can determine the structure and dynamics of biomolecules in the solution state. However, NMR has inherently low sensitivity. Strategies addressing this problem include the development of NMR probes and pulse sequences. Probes are the hardware containing the radio frequency (rf) circuitry that excites and detects the NMR signals;

Figure 1. Newly designed NMR pulse sequence (a) and the corresponding 600-MHz, ^{1}H spectra of the proteins (b) basic pancreatic trypsin inhibitor (BPTI) and (c) lysozyme in limited-volume (250 μL) and concentration (0.5 mM). The time sequence of radio-frequency (rf) pulses (solid bars) and pulsed field gradients (hatched bars) is shown in (a). The pulses marked S are single-lobe, sinc-shaped pulses to selectively invert water magnetization. The various delays used in the sequence are $\tau = 0.1$ ms, $\delta/2 = 7$ ms, and $T = 130$ ms. The phase cycling ϕ_{1-4} and ϕ_r (receiver phase) are used to advantageously use the radiation-damping effects for water suppression. This allows us to dramatically increase the sensitivity of detection for limited amounts of biomolecules dissolved in water.

pulse sequences are composed of a series of rf pulses and delays that manipulate the nuclear spins.

During FY1999, we focused on using microfabrication techniques to design and construct a high-sensitivity microprobe. These techniques (1) enable fabrication of microcoils that increase the limits of detection of mass-limited samples by increasing the effective sample-to-coil ratio, and (2) provide a high degree of reproducibility and accuracy in design. With the University of California, Davis, we are using a three-mask process to construct two types of microcoils. The coils were used to compare the electrical characteristics of microcoils on glass vs. those on glass with anodic-bonded silicon. One prototype microcoil was a 200-mm inner diameter, 5-turn planar coil with a 20-mm spacing between the coils. The electromagnetic characteristics of this coil were close to those of the simulated results obtained using the commercially available Maxwell 3D Field Simulator program.

To study limited sample amounts, we designed pulse sequences to measure important physical properties such as self-diffusion coefficients. The pulse sequence and the corresponding experimental spectra obtained for two test proteins are shown in Fig. 1(a–c). This work has been published.

Our new pulse sequence will greatly aid optimization of our prototype microprobe. Our designs are further aided by the availability of unique DNA samples. In a typical 11-base-pair DNA duplex, 20 phosphorus signals are severely overlapped in the ^{31}P spectrum. This poor resolution has hindered the effective use of the phosphorus nucleus for determining details about the DNA backbone. Others have unsuccessfully tried to optimize both probes and pulse sequences for phosphorus detection by using small molecules in organic solvents and then extrapolating the results to large biomolecules in water. We, however, prepared modified DNA in which the phosphodiester backbone is severely distorted. Thus, we acquire better signal dispersions in the phosphorus spectra, which allows us to develop methods and probes using real biomolecules in water. Our probe development, pulse sequence design, and sample preparation are thus all interdependent.

During FY1999, we also worked on the expression of the membrane receptor, bradykinin, for the development of solid-state NMR prototype microprobes and new pulse sequences.

In FY2000, we expect to continue to (1) prepare our samples; (2) complete the optimization, construction, and testing of our prototype microprobe; and (3) develop new pulse sequences.

Systemic Administration of Bone Morphogenic Protein (BMP-7) for the Treatment of Osteoporosis

J. H. Kinney

99-LW-056

Because present treatments for osteoporosis do not recover trabecular connectivity, we have explored new agents, particularly bone morphogenic protein (BMP-7), for generating new bone tissue and rebuilding connectivity.

The ovariectomized rat is an important small-animal model for studying the effects of estrogen loss on trabecular bone architecture. Histomorphometry of the rat's proximal tibia has demonstrated that estrogen loss after an ovariectomy leads to a rapid decline in trabecular bone volume. In earlier work by our group, 3-D, in-vivo microtomography had shown that there is also an accompanying loss of trabecular connectivity that parallels this decrease in bone volume. By five days postovariectomy, we found a significant decrease in both bone volume and connectivity that progresses continuously before beginning to plateau at seven weeks postovariectomy.

It is now generally believed that the loss of connectivity in the proximal tibia is irreversible, even if trabecular bone volume can be restored by treatment with antiresorptives or anabolic agents. However, the clinical importance of this finding is not well established. Although the early clinical successes of bisphosphonate therapy may have given us cause to believe that connectivity was at best only a marginal contributor to bone strength, recent studies are now suggesting otherwise. First, a computational mechanics study of human vertebrae by our group suggested that reestablishing lost trabecular connections is important for recovering bone strength. Second, and more compelling, is a recent clinical finding that recurrence of vertebral fracture in patients treated with cyclic etidronate therapy was more frequent in patients with low trabecular connectivity based on iliac crest biopsy measurements. Thus, at least in cases of severe osteopenia, we must accept the possibility that connectivity plays an important role in treatment outcome.

Our research during FY1999 explored the relationship between trabecular microarchitecture and bone strength in the lumbar vertebrae prior to studying the systemic administration of BMP-7 to treat osteoporosis. Using synchrotron radiation microtomography, we quantified the structural parameters defining trabecular bone architecture; finite-element methods were used to explore the relationships between these parameters and the compressive elastic behavior of the vertebrae. We found that four months after ovariectomy, there was a 22% decrease in trabecular bone volume and a 19% decline in mean trabecular thickness. This was accompanied by a 150% increase in trabecular connectivity, a result of the perforation of trabecular plates. Finite-element analysis of the trabecular bone removed from the cortical shell showed a 37% decline in the Young's modulus in compression after ovariectomy with no appreciable change in the estrogen-treated group. The intact vertebrae (containing its trabecular bone) exhibited a 15% decrease in modulus with ovariectomy, but this decline lacked statistical significance. Ovariectomy-induced changes in the trabecular architecture were different from those that have been observed in the proximal tibia. This difference was a consequence of the much more plate-like structure of the trabecular bone in the vertebra. The cortical shell dominated the biomechanical behavior of the rat vertebra, and significant alterations in the trabecular architecture were not reflected by changes in the mechanical properties of the intact vertebra. This last observation, which needs further study, questions our ability to extrapolate the results of biomechanical testing of trabecular bone in small-animal models to human osteoporosis.

Biophysical Analysis of DNA–Protein Interactions using an Optical Trap to Manipulate Single DNA Molecules

J. Felton, R. Balhorn

99-LW-057

Many proteins bind to DNA and perform functions that are essential for normal cell growth and division. Some function by organizing the packing of the DNA into chromosomes, while others participate in regulating the activity of genes, repairing genetic damage, or replicating the genome prior to cell division. Until recently, methods for studying how proteins interact with DNA required the analysis of large numbers of molecules (10^{12} to 10^{17}), and the results could only provide information about the activities of ensembles of molecules.

In an earlier LDRD project, we combined the use of an optical trap to isolate and manipulate single DNA molecules with a microfabricated flow cell to provide the molecule with access to different well-resolved chemical environments. In this project, our goal was to develop a new experimental approach that can be used to monitor the binding of proteins to individual DNA molecules and to determine how their binding alters its structure.

In the successful approach developed during FY1999, individual DNA molecules attached to polystyrene beads are (1) trapped in a specially designed, bifurcated flow cell using a focused infrared laser; and (2) moved across the interface between two flowing solutions into a buffer stream containing a protein that binds to DNA [Fig. 1(a)]. Changes in the structure of the DNA molecule—which is made visible by the binding of the fluorescent dye YOYO-1—can be monitored using a video camera in real time as the protein binds.

Using this technique, we investigated how proteins synthesized by the developing sperm cell coil and condense the sperm's DNA into donut-shaped toroidal structures. Our experiments using individual DNA molecules have shown that all four spermatid proteins that participate in the restructuring of the spermatid genome as it matures into a fully functional sperm cell (protamine 1, protamine 2, TP1, and TP2) condense DNA into toroids when they bind [Fig. 1(b)]. Although the rate of DNA condensation was shown to be dependent on the concentration of protein (the condensation process is limited by the rate of protein binding to DNA), the two protamines were much more effective than the transition proteins in condensing DNA. At low protein concentrations, variations in the rate of DNA coiling/condensation could be observed along the length of the DNA molecule.

The rate at which the protein dissociated from DNA could also be measured simply by pulling the condensed DNA molecule back across the interface between the two solution into the buffer stream containing the DNA molecules and then measuring the length of time it took for the DNA molecule to re-extend.

These experiments not only provided new information about the process of sperm chromatin decondensation in the egg, but also they indicated how protamine-like peptides could be engineered for use in condensing and protecting genes to improve the efficiencies of gene integration in gene therapy. The off-rate (the rate at which the protein comes off the DNA after binding] for protamine was determined to be 0.72 molecules/s. At this rate, the sperm genome would take about 6 years to uncoil once it fertilized an egg. Our data strongly support the hypothesis that protamine must be actively removed from DNA once the sperm enters the egg, because the decondensation process is normally completed 5 to 15 min after fertilization.

Binding and dissociation experiments conducted with peptides corresponding to subsets of the protamine DNA binding domain also showed that the rate of peptide dissociation from DNA was directly related to the number of arginine residues in the peptide's sequence. Arg6, which contains only 30% of the arginines present in protamine's DNA binding domain, was observed to dissociate from DNA 18,000 times faster than protamine. This information, reported in a recent Science article, provided new information that can be used to engineer special peptides for use in packaging and protecting DNA for gene therapy.

(a)

(b)
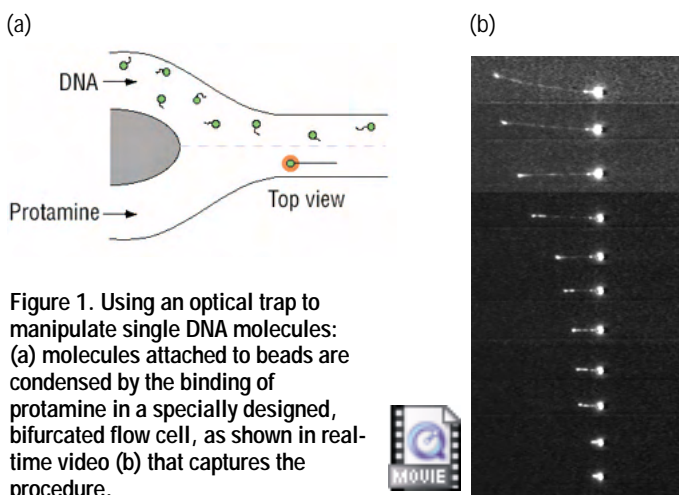
Figure 1. Using an optical trap to manipulate single DNA molecules: (a) molecules attached to beads are condensed by the binding of protamine in a specially designed, bifurcated flow cell, as shown in real-time video (b) that captures the procedure.

Broad Spectrum Biological Assays using Liquid-Based Detection Arrays

F. Milanovich, J. Albala, R. Langlois, K. Venkateswaren

99-SI-016

The release of a biological agent by terrorists represents one of the most serious threats to the safety of U.S. citizens. Richard Butler, head of the U.N. Special Commission's weapons inspection team in Iraq, remarked that "everyone wonders what kind of delivery systems Iraq may have for biological weapons, but it seems the best delivery system would be a suitcase left in the Washington subway." Detecting such an event and responding in a timely manner represents a grand challenge to developers of biodetection technology.

At present, there are over 30 pathogens and toxins on various agencies threats lists. Because most of the pathogens are rarely seen by public health personnel, the ability to rapidly identify their infection is waning. In addition, many pathogenic infections are not immediately symptomatic, with delays as long as several days, often compromising effective treatment. This translates into two major deficiencies in our ability to counter biological terrorism: (1) The lack of any credible technology to rapidly detect and identify all the pathogens or toxins on current threat lists; and (2) The lack of a credible means to rapidly diagnose thousands of potential victims. The biotechnology industry responded to this call by delivering generations of sophisticated instrumentation, capable of highly parallel chemical assays, characterized by complex sample handling schemes with sophisticated fluidic interconnects and arrays of sample reservoirs. Such devices have yet proved impractical for long-term monitoring of public environments.

We are developing a faster, more flexible, and less expensive high-throughput, parallel-assay technology. The technology, which we call the Liquid Array (LA), utilizes optical encoding of small diameter beads that serve as the templates for biological capture assays. Once exposed to a fluid sample these beads can be identified and probed for target pathogens at rates of several thousand beads per second. Since each bead can be separately identified, we can perform parallel assays by ascribing a different assay to each bead in the encoded set. In collaboration with Luminex Corp of Austin, Texas, we are currently reducing a 100-bead set to practice as a broad-spectrum biological pathogen/toxin identifier. The goal for this development is a detection technology capable of simultaneously identifying 30 different bioagents and of diagnosing several thousand individuals in less than six hours.

We are also exploring a major spin-off application in proteomics. The efforts of the Human Genome Project have yielded a mass of genetic information. The challenge now lies in determining the function of the proteins encoded by the newly discovered genes, specifically the interaction of these proteins with one another and with DNA. These interactions are responsible for cell metabolism, structural organization, and DNA replication and repair. Understanding the complexities of these interactions is a fundamental step towards comprehending essential aspects of disease biochemistry. The LA format provides a novel high-throughput screening approach for the functional analysis of protein–DNA and protein–protein interactions, and would greatly propel this area of research.

Although the project was initiated late in FY1999, we can report several significant accomplishments already. We demonstrated a 15-plex immunoassay, the results of which are shown and described in the figure below. We confirmed the participants of a complex protein–DNA repair mechanism that involves three proteins and a segment of DNA. This establishes the proof-of-principle for using the arrays in complex molecular interaction studies. In FY2000, we intend expand our efforts to include collaborations with the health science community in potentially high profile applications such as medical triage, rapid childhood disease diagnosis, and significant blood bank diagnostic throughput enhancements.
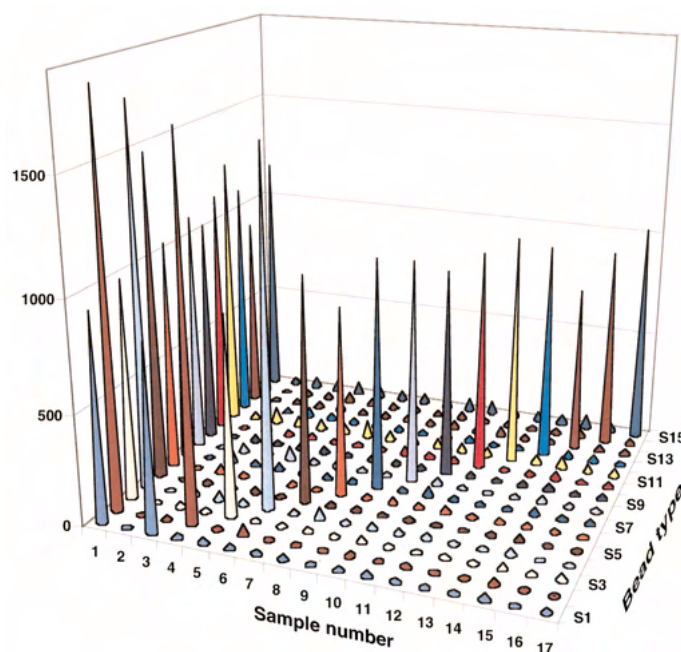
The results of 17 separate analyses (sample number) performed with a 15-bead set. The vertical axis represents concentration of analyte. Sample 1 demonstrates detection of 15 targets.

Computing/Modeling/Simulation

4
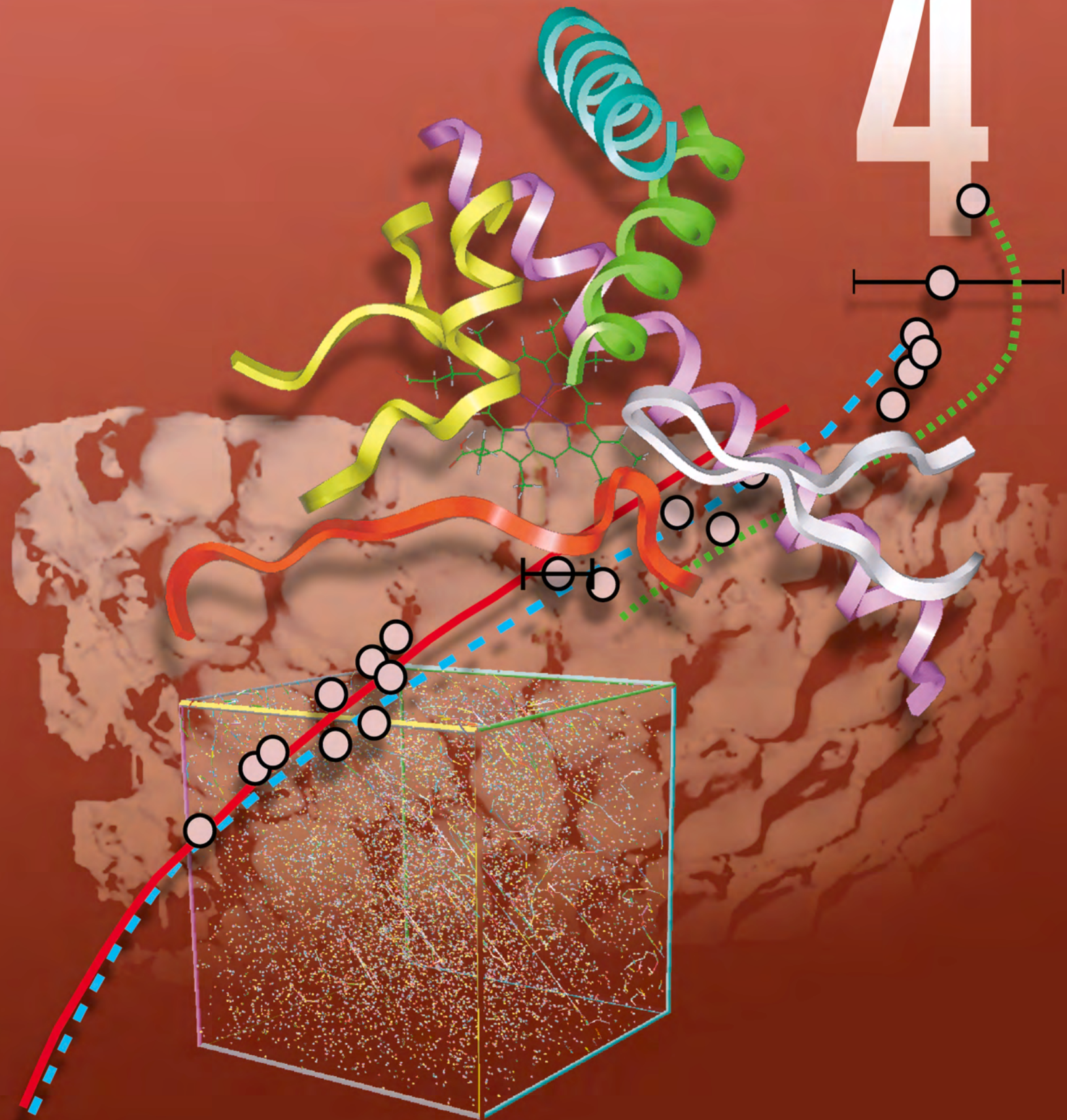
Computing/Modeling/Simulation

3-D Massively Parallel CEM Technologies for the Design of Advanced Accelerator Components

D. J. Steich, J. S. Kallman, D. A. White, S. T. Brugger

97-ERD-009

Significant need exists for more advanced time-domain computational electromagnetics modeling (CEM) in areas such as accelerator technologies. Bookkeeping details and modifying inflexible software constitute a vast majority of the effort required to address such needs. This effort escalates rapidly as problem complexity increases, e.g., hybrid meshes requiring hybrid numerics on massively parallel processors (MPPs). Our research attempts to alleviate the above limitations by investigating flexible abstractions for these numerical algorithms on MPPs using object-oriented methods—thus providing a programming environment that insulates physics from bookkeeping.

Previously, we built a prototype code that tested memory and meshing abstractions, tested a massively parallel implementation, added higher order wakefield physics, and began exploring hybrid mesh abstractions. When compared to earlier models, we achieved a 100-fold reduction in the cell count required to simulate wake potentials for kicker accelerator components.

In FY1999, we (1) tested the ability to add new physics, (2) implemented and tested a proof-of-principle for hybrid mesh types, (3) built three libraries encapsulating our key abstractions, (4) generalized and improved our abstractions by greatly simplifying design and implementation, (5) added a better memory management capability, and (6) significantly improved overall efficiency.

After building the code, we tested the ability to easily add new physics by implementing a generalized unstructured mesh current source. We successfully added new physics much faster than previously possible by modifying the original Fortran—but we wanted the process to be even simpler. This test case pointed to deficiencies in our abstractions requiring further generalization. Next, we designed and implemented hybrid mesh abstractions that included tests where any number of structured, unstructured, mixed-element, revolved, and extruded meshes were concatenated together, each with disparate overheads. Although we successfully implemented hybrid mesh abstractions that provided a simple interface hiding all the details, the complexity of implementation behind the interface raised concerns about long-term maintainability, flexibility, and performance.

By the second quarter of FY1999, we were achieving our milestones and discovered ways to significantly improve our abstractions. We decided to attempt a major redesign and re-implementation of our abstractions. This redesign was a huge undertaking so late in the project, even using the latest object-oriented software techniques. However, the expected increase in capability, flexibility, and performance and the expected decrease in complexity would dramatically improve this research effort. This new design consists of three libraries now in the final stages of completion. A majority of the infrastructure is in place and working. The two main tasks remaining are the re-implementation of hybrid meshes and transparent communication.

The first library consists of container, memory-management, and math utility classes specialized for scientific applications. The second library deals with data organization and unifies notions of equations, materials, and geometry. The third library abstracts the construction, topology, concatenation, and traversal of meshes. These low-level, highly extensible libraries represent a powerful set of abstractions that insulate physics from bookkeeping on MPP environments. Once completed, the libraries will allow implementation of fully 3-D MPP programs by writing hundreds, rather than tens of thousands, of lines of code. These libraries now have a unified memory model, are much more capable, much simpler (~5× code reduction), and are more efficient (~7× faster) than our previous version.

In the future, we intend to incorporate these libraries into a production level code. We have successfully demonstrated proof-of-concept for the key abstractions and have built a working code capable of modeling vital accelerator components.

DataFoundry: Data Warehousing and Integration for Scientific Data Management

C. R. Musick, Jr.

97-ERD-033

The *DataFoundry* project is a computer-science research effort focused on enhancing our ability to integrate and provide online functional access to data from external sources. Data warehousing is a set of techniques for gathering, and providing access to data from external sources into one location and one format for storage and analysis. Unfortunately, the content, representation, and interfaces typical of scientific data sources are highly dynamic, and standard warehousing approaches fail in dynamic environments.

The need for automating scientific data-management tasks is apparent in many applications, such as determining the type and level of detail of metadata needed to support code generation in the data-integration process. For example, with the sequencing of the human and multiple other species' genome well on the way to completion, genome scientists realize that the next phase of research will—of necessity—be focused on how to make effective use of all the new data. With contributions from well over 100,000 authors world-wide stored in over 500 unique public data sources, even the "simple" task of finding and applying relevant information is overwhelming.

The major challenge in keeping an integrated data collection updated and fully functional is cost: any change in the representation of the underlying data is very expensive to repair. It is also expensive to add a new source to the collection. The high cost comes from writing code to respond to the change, e.g., (1) read the new data format, (2) match concepts in the new data to those in the warehouse, and (3) load the new data into the warehouse. We addressed this issue with the use of highly structured metadata that captures domain-specific knowledge and represents it in a declarative,

standardized way. The metadata, an essential part of the software we developed, automatically generates much of the code previously built by hand. With this approach, we demonstrated a 50% reduction in the effort required to maintain a warehouse. In FY1999, we reiterated and formalized the metadata design to ease its transfer to other domains. The metadata design and related code-generation software are the subject of a DataFoundry patent, which has DOE approval and is well into the application process.

In FY1999, we applied the research concepts in a prototype warehouse for the Human Genome Project. We extended the prototype in several ways. We added an extensive genomic sequence data source, thus expanding our original focus on protein data. We incorporated automated update methods for the majority of the data and explored methods for fixing this code before it breaks by detecting when and how the underlying data changes. On the more theoretical side, this research led to a Ph.D. thesis for one of the students on the project. Finally, we extended the interface to the warehouse to support the types of exploration genomics researchers now carry out with data and algorithms, rather than with wet-lab experiments. Biologists at LLNL are currently using our prototype.

In FY2000, the research initiated in this LDRD project will continue through funding from the Accelerated Strategic Computing Initiative and the Human Genome Center at LLNL. The research emphasis will be on improving techniques for data integration and access. Specifically, we will explore scaling database-oriented queries to large, computational data, and will continue scaling data-integration approaches to work in highly dynamic Worldwide Web environments.

LATIS3D: The Gold Standard for Laser–Tissue Interaction Modeling

R. A. London, A. J. Makarewicz, B-M. Kim, T-S. B. Yang

We have developed a computer program for laser-tissue interaction modeling called LATIS3D to aid in the development of new instruments and procedures for laser medicine. This project has led to fundamental advances in the design of several laser medical therapies and to the establishment of LLNL as the top location for the application of computer modeling to laser medicine. In addition, our work has enhanced LLNL's core competency in radiation-hydrodynamics by pushing simulation codes into new parameter regimes. By applying our codes to current experiments and product development, we can contribute to their verification and validation. During FY1999, we made several advances to LATIS3D and applied it in two areas of medicine.

First, we designed laser protocols for photodynamic therapy for treating arthritis. We added a laser source and refraction boundary conditions to LATIS3D, then did several calculations of laser-transport applied in the knee. These first studies used simplified 3-D knee models composed of block-shaped regions. We performed Monte Carlo simulations of the distribution and absorption of light, examining the effect of source placement and the degree of inflammation of the synovial membrane (caused by arthritis). This study showed that it is desirable to deliver light energy directly to the synovial membrane using an optical fiber rather than by external means. We also found that the diseased synovial membrane limits light penetration.

To obtain a more realistic anatomical model, we obtained a public domain 3-D magnetic resonance image (MRI) of a human knee. We performed manual segmentation of the image and created a voxel-based mesh. The femur and tibia were manually separated in the vertical direction by 1 cm to model arthroscopic surgery, in which a fluid is injected into the joint. The fiber light source was placed along the x-axis ($z = 0$, $y = 0$) extending from $x = -2$ to $x = 2$. The mesh and light absorption are shown in the figure, where the absorption of light near the surface of the bones is evident. These results demonstrate (1) the capability to translate an anatomical model derived by segmentation into a mesh that can be imported into LATIS3D, and (2) the capability to perform a light transport calculation using the model.

In another study, we examined the effect of the smoothness of tissue boundaries on the reflection and transmission of light, which depends strongly on the angle at which the light hits the boundary between two materials. We performed calculations using both a jagged boundary between the synovial fluid and bone tissue and a smooth, tilted boundary. The results show that with the jagged boundary the relative error in the light intensity can be as high as 25%. This implies that using meshes with smooth tissue surfaces will produce more accurate light distribution results.

To develop more accurate and faster tissue segmentations, and smoother meshes, we began an automatic tissue segmentation and meshing effort, utilizing morphological image processing methods. We made preliminary efforts to segment the public domain MRI dataset discussed above. The morphological method was found to give results better than the manual segmentation—and more importantly, with less effort. This work will be pursued in the future.

In addition, we applied LATIS3D to the study of optoacoustic stress waves. These waves have several uses in medicine, including the destruction of blood clots, kidney stones, and gallstones, the regeneration of skin, and the induction of cell permeability changes for drug delivery. We modeled stress wave generation and propagation in an effort to optimize the design of instruments for these therapies. In particular, we have studied techniques to generate and focus the stress waves using optical fibers. The results of our simulations agree qualitatively with experimental data for both a flat-tipped fiber and a focusing lens. The results indicate that focusing tips at the ends of optical fibers will allow sharp focusing and enhance development of both compressive and tensile pressures. Our research is being extended under a DOE/OBER grant.
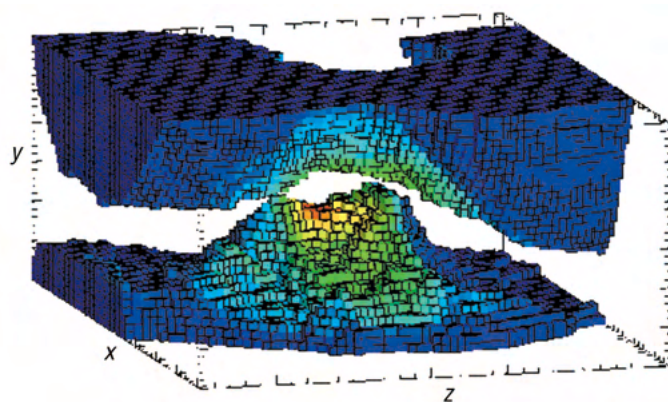
The mesh (black lines) and LATIS3D calculations of the light distribution (color scale) for the central region of the knee.

Enabling Computational Technologies for Terascale Scientific Simulations

S. F. Ashby

We are developing scalable algorithms and object-oriented code frameworks for terascale scientific simulations on massively parallel processors (MPPs). Our main research thrusts are in multigrid-based linear solvers and adaptive mesh refinement technology. This research will enable Laboratory programs to use the Accelerated Strategic Computing Initiative (ASCI) Blue-Pacific MPP to address important scientific issues. For example, our research is already benefiting the nation's Stockpile Stewardship Program by making practical highly resolved 3-D simulations.

The solution of a large linear system arises in many scientific applications, including radiation transport, structural dynamics, flow in porous media, and fusion energy. These systems result from discretizations of partial differential equations on computational meshes. Our first research objective is to develop multigrid preconditioned iterative methods for such problems and to demonstrate the scalability of these methods on MPPs with upwards of 10,000 processors.

Scalability describes the way in which total computational work grows with problem size; it is a measure of how effectively additional resources can be used to solve increasingly larger problems. Many factors contribute to scalability: computer architecture, parallel implementation, and choice of algorithm. Scalable algorithms can decrease simulation times several orders of magnitude.

Multigrid is an example of a scalable linear solver. It uses a relaxation method like Gauss-Seidel to damp high-frequency error, leaving only low-frequency (smooth) error, which can be accurately and efficiently solved for on

Embedded boundary capabilities enable Structured Adaptive Mesh Refinement Application Infrastructure (SAMRAI) to capture complex geometry in an efficient manner.

a coarser (smaller) grid. Recursive application of this technique to each consecutive system of coarse-grid equations leads to a multigrid V-cycle. If its components are defined properly, the algorithm's computational costs grow linearly with problem size.

There are two basic multigrid approaches, geometric and algebraic. Geometric multigrid is typically used for problems on structured meshes. Such an algorithm was used in a 3-D parallel inertial confinement fusion (ICF) simulation to speed up the overall simulation time by a factor of 6. The largest problem we have solved is a one-billion-zone anisotropic diffusion problem that took less than 80 seconds using 3,150 processors on the ASCI-Red MPPs platform. We have also developed a parallel algebraic multigrid (AMG) algorithm that has been integrated into two unstructured-grid ASCI simulation codes. Because the parallelization of AMG is not straightforward, it required new developments in the AMG coarsening algorithm. Preliminary testing has already shown significant speedups in linear system solution time in one of the ASCI codes using AMG over the solver previously used.

Our second research thrust is to develop an object-oriented code framework for structured adaptive mesh refinement (AMR) applications (see figure). AMR allows more efficient use of computing resources—central processing unit (CPU) time and memory—by focusing numerical effort locally within the computational domain with varying degrees of spatial and temporal resolution. This makes it practical to run simulations—especially those involving complex physics and large spatial domains—that would be prohibitively expensive on a uniform mesh. Our effort, called SAMRAI, provides general and extensible software support for rapid prototyping and development of parallel AMR applications.

In FY1999, we continued to develop the SAMRAI software framework and expand our application collaborations with LLNL, DOE, and academic efforts. Most major components of the parallel-structured AMR support framework are complete. Most future development will address specific needs of our application collaborators. The SAMRAI library is supported and used on all three ASCI machines and a wide range of development platforms belonging to our collaborators. The most notable application projects using SAMRAI are the Utah and Chicago ASCI Alliance Centers, an adaptive laser-plasma interaction simulation code at LLNL, and in an effort to apply AMR to arbitrary Lagrangian Eulerian (ALE) hydrodynamics methods at LLNL.
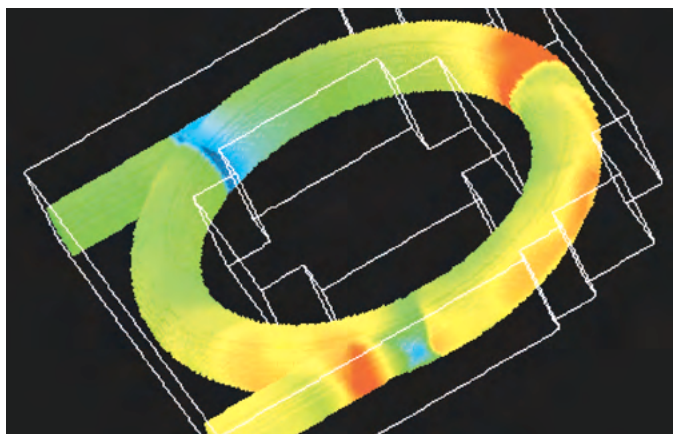
Dynamics at the Microscale: Experiment and Simulations

D. H. Lassila, T. Diaz de la Rubia, L. L. Hsiung, W. E. King

97-SI-010

The principal mechanism by which plastic deformation in metals occurs is the generation and motion of "dislocations." Dislocations are atomistic-scale defects in an ordered lattice (crystal structure); they are commonly referred to as "line defects." It is the aggregate behavior of millions of dislocations per cubic centimeter that results in interesting and important mechanical behaviors such as the ductile behavior of lead or the brittle-fracture behavior of iron at low temperatures. General relationships between the composition of a metal and its strength and fracture properties such as these have been established over decades of study; however, a detailed understanding of the effects of the composition and microstructure of a metal based on first principles is lacking. Such knowledge is relevant to improving predictions of the strength properties of metals under extreme conditions of pressure and temperature.

A multiscale modeling approach employing three key computer simulations —atomistic, dislocation-dynamics, and mesoscale/continuum scales, as shown in the figure—can be used to model and understand the effects of composition and microstructure on mechanical behavior. In this project, we have focused on developing an experimentally validated dislocation simulation that will (1) utilize information generated at the atomistic-length scale, and (2) predict strength properties needed at the mesoscale/continuum. In essence, dislocation dynamics is the critical link between information generated at the atomistic-length scale and the strength properties used in computer simulations at mesoscale/continuum lengths.

The simulation and experimental work is highly coupled and is focused on the mechanical behavior of molybdenum, which is representative of many body-centered-cubic (bcc) metals of interest to Laboratory programs.

The simulations of dislocation dynamics that we are developing are primarily in 3D. In the past year, we made significant progress in the implementation of the rules of physics that govern the mobility and interaction of dislocations. For example, we implemented algorithms that correctly account for the formation of dislocation junctions when two dislocations cross paths and react to form a third dislocation (this is an important hardening mechanism in bcc metals).

We also (1) completed numerous simulations that involved large numbers of dislocation segments and predicted strength properties of single crystals for a wide range of loading conditions; (2) began coupling a dislocation-dynamics simulation with a parallel multiphysics hydrodynamics code to enable the incorporation of phenomena such as the heat conduction associated with modeling adiabatic-shear instabilities; and (3) using single crystals of molybdenum, performed deformation experiments over a wide range of temperatures and deformation rates .

The deformation experiments are central to this work because they provide both strength properties and dislocation structures that are necessary to validate the simulations. The materials used for this experimental work must be of high quality and high purity, and they must also be free of low-angle grain boundaries. Therefore, during FY1999, we procured high-quality single crystals of molybdenum and developed purification equipment that enabled us to reduce interstitial impurities to minute levels.

At the close of the year, we were performing extensive characterizations of the test materials using state-of-the-art microscopy techniques to establish the relationships between microstructure properties. Specifically, we were using transmission electron microscopy (TEM) as the principal technique for characterizing dislocations. Such static observations of dislocations and dislocation structures can establish initial conditions for simulations and validate the structures predicted by dislocation-dynamics simulations.

Future efforts will focus on detailed and extensive comparisons between experimental data and the results of our simulation, with the goal of achieving a fully validated simulation capability. In the near future, simulations will be performed on LLNL's most powerful massively parallel processor (MPP) supercomputers in collaboration with individuals at IBM.
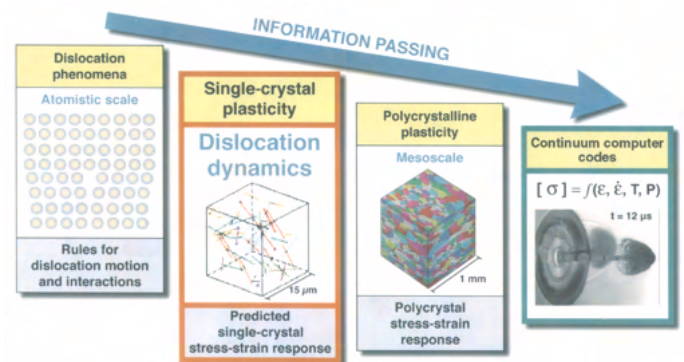
LLNL's multiscale modeling approach involves simulations at three length scales, where carefully defined "information passing" from the shorter- to longer-length scales enables "bridging of the length scales."

Modeling of Anisotropic Inelastic Behavior

D. J. Nikkel, A. A. Brown, D. S. Nath, J. Casey

98-ERD-020

Laboratory programs have a growing reliance upon the predictive quality of numerical simulations, especially in the areas of material processing, manufacturing, and Science-based Stockpile Stewardship. The ability of numerical simulation codes to predict the behavior of systems involving materials undergoing large deformations is contingent upon having a realistic model of the material behavior. Such models must be accurate in the full range of possible loading conditions to which the materials may be subjected. Use of overly simplified models in regimes where they are not well suited can seriously compromise the validity of a simulation. Many problems of engineering interest involve metals undergoing large deformation under multiaxial states of stress and the need for reliable models for these applications can hardly be overemphasized. Experimental data demonstrate that simple models of plasticity do not accurately represent material behavior under these conditions. The objective of our research is to develop better physical models of the anisotropic behavior of metals subjected to large inelastic deformations.

In this project, we combined novel experiments characterizing inelastic material behavior with an effort to develop better material models for implementation into numerical analysis codes. During FY1999, we further refined the experimental procedures developed in previous years for measuring yield surfaces and obtained some important new data. We made analytical representations of

Simulation of a Taylor impact experiment using a circular cylindrical tantalum specimen. Anisotropic behavior is seen in the ovaling of the impact footprint and the nonsymmetric distribution of plastic strain (fringes).

the yield surface data and developed a continuum model. We explored issues related to the implementation of anisotropic models into numerical codes, in the context of both purely Lagrangian and arbitrary Lagrangian-Eulerian (ALE) formulations. In particular, we developed a methodology to track and advect material directions within the context of an ALE formulation.

At a microstructural level, polycrystalline metals are composed of aggregates of individual crystals, each of which has its own orientation and properties. Annealed polycrystalline metals, as a consequence of having randomly distributed grain orientations, typically exhibit isotropic behavior with respect to a reference configuration; that is, at a given point in the material, the material response of a specimen in any direction is the same. However, significant processing of materials, or even moderate plastic deformations, can cause grains that were at first randomly oriented to become aligned, resulting in behavior that is anisotropic where material response in various directions is significantly different. Engineering models of polycrystalline metals generally omit microstructural details and describe the effective macroscopic behavior in terms of a phenomenological continuum model. The transition between elastic and plastic behavior is represented within the theory by the yield function. Viewed geometrically in stress (or strain) space, the yield criterion represents a surface bounding the region where only elastic behavior occurs (see figure). This project has produced an experimental capability to identify representative points on the multiaxial yield surface at a given elastic–plastic state. Using a single specimen, we can measure the yield surface at several states and can observe its evolution. We can use this data to develop and validate advanced constitutive models.

We also pursued an alternative strategy of constructing a macroscopic model by incorporating information from lower length scales. We obtained new analytical results for bounding the effective yield surface predicted by homogenizing models that include an explicit description of material microstructure and the statistical distribution of crystal orientations. Detailed orientation imaging microscope scans were also performed that provide a complete three-dimensional representation of a polycrystal, which can then be modeled numerically as a virtual test sample.

We have established a solid framework from which to pursue numerical developments of anisotropic plasticity while providing experiments for their verification. From this foundation, further work will continue under programmatic auspices, focusing on the development of improved material models for Accelerated Strategic Computing Initiative codes.
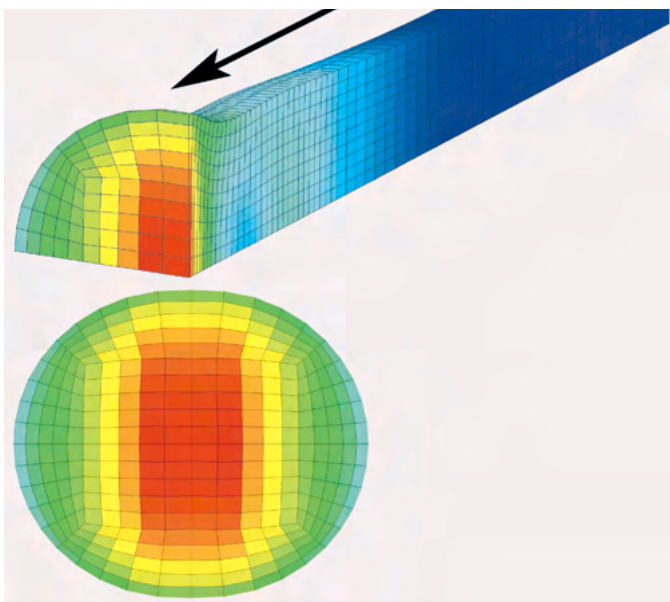
Novel Parallel Numerical Methods for Radiation and Neutron Transport

P. N. Brown, B. Chang, K. Grant, U. Hanebutte, C. S. Woodward

98-ERD-022

In many of the multi-physics simulations performed at LLNL, transport calculations can take up 30% to 50% of the total run time. When using Monte Carlo methods, the percentage can be as high as 80%. Thus, a significant core competence in the formulation, software implementation, and solution of the numerical problems arising in transport modeling is essential to Laboratory and DOE research. In this project, we are developing scalable solution methods for the equations that model the transport of photons and neutrons through materials. Our goal is to reduce the transport solve time in these simulations by means of more advanced numerical methods and their parallel implementations. It is essential that these methods are scalable, i.e., the time to solution remains constant as the problem size grows and additional computer resources are used. For iterative methods, scalability requires that the number of iterations to reach convergence is independent of, and that the computational cost grows linearly, with problem size.

We are focusing on deterministic approaches to transport, building on our earlier work in which we performed a new detailed analysis of some existing transport methods and developed new approaches. The Boltzmann equation, the underlying equation to be solved, and various solution methods have been developed over many years. Consequently, many production codes are based on these methods, which are in some cases decades old. For the transport of x-rays through partially ionized plasmas in local thermodynamic equilibrium, the transport equation is coupled to nonlinear diffusion equations for the electron and ion temperatures via the highly nonlinear Planck function. We are investigating the suitability of traditional solution approaches to transport on terascale architectures as well as designing new scalable algorithms, and in some cases hybrid approaches combining both.

During FY1999, we performed a full-system run of our neutron transport code on the IBM Accelerated Strategic Computing Initiative (ASCI) Blue Pacific SST (Stockpile Sustained Teraop) system. The purpose of this calculation was to simulate the flux of fusion neutrons discharged from LLNL's Nova Laser target chamber. The fusion neutrons can be very penetrating when they emerge from the target chamber because they are born at a very high energy (14.1 MeV), and can be dangerous if not absorbed in a shield. This calculation, which allowed us to show unprecedented detail in the total neutron scalar flux distribution, is arguably one of the largest deterministic transport calculations ever performed. We also demonstrated the ability of our spherical harmonics solution method to give a solution without ray effects, which pose difficulties on some ASCI applications, on a problem with widely varying spatial scales (4 orders of magnitude) and material properties (14 orders of magnitude). The source of neutrons was a point source at the center of the hohlraum in the target chamber. The colors on the isosurfaces in the figure below represent values of the total neutron scalar flux. The spatial mesh used roughly 160 million spatial zones; there were 23 energy groups with linearly anisotropic scattering in each group (requiring 4 moments per zone), for 15 billion unknowns. The multigroup solution took roughly 27 hours on two of the three sectors of the SST, using 960 nodes and 3,840 processors (with threads). We are currently working on acceleration methods and alternative solution approaches to reduce the run time. This run also gave us the opportunity to investigate the scalability of our methods on problems requiring thousands of processors and billions of unknowns. It also demonstrated a lack of scalability of our iterative solution method when using spherical harmonics.

In FY2000, we plan to develop scalable preconditioning approaches for our spherical harmonics solution method and structured adaptive mesh refinement capabilities for our radiation and neutron transport solvers.
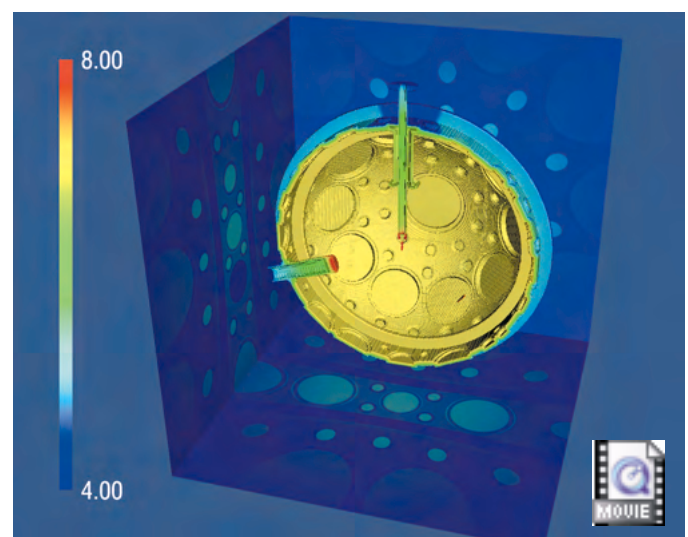
The isosurfaces display a cut-away view of the interior of the target chamber. In particular, the target assembly is shown along with the chamber interior geometry. The colors on the isosurfaces represent values of the total neutron scalar flux—red denotes the regions of highest flux and blue the lowest.

Computational Theory of Warm Condensed Matter

T. W. Barbee III, M. P. Surh, L. Benedict

98-ERD-052

Laboratory missions, such as science-based stockpile stewardship (SBSS), demand accurate materials-modeling capabilities, including calculations of the equation of state (EOS) and opacity. These SBSS programs require knowledge of these properties over an extreme range of densities and temperatures. In the low-density/high-temperature limit, models based on plasma physics are very accurate; whereas models based on condensed-matter physics perform best in the high-density/low-temperature regime. In this project, we are focusing on "warm" condensed matter, i.e., on the region of intermediate temperature and density where the high-temperature or low-temperature approximations may no longer be valid.

Current models for the EOS of warm, dense matter are primarily based on theoretical models that (1) are most accurate in the low-temperature limit and (2) treat the effect of finite temperature as a perturbation of the zero-temperature solution. These models are largely untested above the melting point—especially approaching the Fermi temperature T_{Fermi} (the characteristic energy scale for the interacting electrons in a material). Thus, the goal of the current project is to develop rigorous extensions of existing state-of-the-art condensed-matter techniques that are valid in this intermediate-temperature regime.

Our approach focuses on three areas: (1) improving theoretical treatments of the thermal contributions to the EOS; (2) calculating optical properties (e.g., opacity) at finite temperature; and (3) developing a new theoretical formalism that can be used to solve the quantum-mechanical, many-electron problem at finite temperature.

In FY1999, we included the effects of ion disorder on the EOS by performing molecular dynamics (MD) simulations at high temperatures. For all but the lightest elements, thermal excitation of core electrons must be included to obtain reliable results. We developed a new pseudopotential formalism, derived from photoemission calculations, which we have adapted to treat atom-electron scattering at extreme temperatures. The preliminary indications are that the calculations should be reliable for temperatures up to one million Kelvin. We employed this new formalism to calculate the shock Hugoniot of aluminum at temperatures up to 300,000 K. As shown in the figure, the results are in excellent agreement with experimental data, with the previous low-temperature calculations, and approach the high-temperature theory at high density and temperature.

A second line of inquiry focused on the effects of including a finite temperature quantum-mechanical description of the electron gas (as modeled by the exchange and correlation potential V_{xc}). We found that the predicted density of extremely strongly shocked beryllium (at $T>T_{Fermi}$) changed by several percent when a finite-T model was used for V_{xc}, indicating that inclusion of finite-T effects is needed for accurate results at $T>T_{Fermi}$. We also found that for $T<<T_{Fermi}$, finite-T effects were insignificant, as we expected.

We have also generalized our $T = 0$ computational approach for the calculation of linear optical constants to non-zero electron temperature, T_e. Computations of the imaginary part of the dielectric function, $\varepsilon_2(\omega)$, for ω in the visible/near-ultraviolet range have been done for crystalline Si at $T_e = 0 – 0.75$ eV, in order to predict the results of pump-probe experiments performed with short-pulsed lasers.

During FY2000, we plan to extend our MD-based EOS studies to heavier elements and larger systems, and use the output of our MD simulations to calculate optical properties of systems including thermal ion disorder as well as thermally excited electrons.
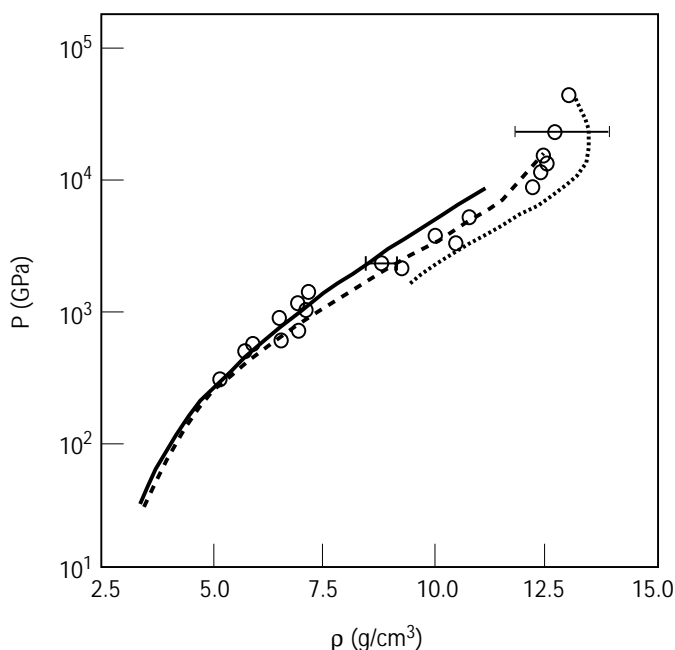
Principal Hugoniot of aluminum calculated as described in text (dotted line) is compared with experimental data (circles), condensed-matter-based (solid), and plasma-physics-based (dotted) theories.

LambdaConnect: Multi-wavelength Technologies for Ultrascale Computing

M. C. Larson, M. E. Lowry, S. W. Bond, M. D. Pocha, H. E. Garrett, R. R. Patel, H. E. Petersen, W. Goward, M. A. Emanuel

Ultrascale computing—the integration of large numbers of processors into a single, highly capable multiprocessor system—is of great interest to several national security programs. Fast data communications within such systems are essential to high performance. Such communication is currently hampered by the bandwidth, latency, and congestion characteristics of the electronic fabric used to interconnect the many system processing and memory elements. To alleviate these communication bottlenecks, we are leveraging the recent emergence of byte-wide optical interconnects that use linear arrays of multimode optical fibers in a ribbon cable assembly. We have shown that the addition of multiple wavelengths over this byte-wide medium can enable source-routed switching, which greatly relieves communications congestion and improves bandwidth.

Implementation of these wavelength source-routed communications fabrics require the development of novel components, including optical transmitters capable of fast wavelength tuning and fixed optical filters. All components must be compatible with existing multimode fiber ribbon cables. This project aims at developing prototypes of these components to investigate the feasibility of implementing byte-wide, multi-wavelength multi-mode optical interconnects for ultrascale computers.

Our original LambdaBus system concept relied on wavelength tunable transmitters that broadcast into an N×N optical splitter, in which optical signals at each of N input ports are combined and coupled to N output ports. At each of the output ports a filter in front of the receiver selected the correct wavelength. This approach is wasteful of the optical signal, incurring an automatic $1/N$ loss in the signal (as it is broadcast to all N output ports).

Recently, however, we conceived a power efficient wavelength routing fabric that routes a particular input port and wavelength to one particular output port rather than broadcasting to all output ports simultaneously. The device uses a blazed diffraction grating and broadband add/drop filters to provide wavelength re-use thus enabling fully non-blocking power-efficient N×N interconnection with only N wavelengths. Using a ferrule with 2 parallel arrays of 12 fibers each, we have demonstrated a 3-input by 3-output wavelength router where each input/output channel is two bits wide. The device provides fully non-blocking interconnection between all inputs and outputs and shows virtually no bit-to-bit crosstalk, paving the way to the implementation of an 8-port, multimode 12-fiber wide efficient routing

element. (Crosstalk is the unwanted presence of optical signal from one channel interfering with a second independent channel.)

We have performed extensive characterization of our 4-wavelength transmitter modules. Our 4-wavelength transmitter packages were modulated at 1.25 Gb/s and spectra were captured for 10 of the output. Further modulation experiments were conducted at 1 Gb/s that were aimed at exploring crosstalk issues in the interconnect. We measured bit-error rate (BER) as a function of optical power in two different crosstalk tests. In the first test, BER of a specific vertical cavity surface-emitting laser (VCSEL) was measured with and without the activation of neighboring VCSELs. The modulation of the neighboring VCSEL showed no degradation of the BER, demonstrating that our package succeeds in providing both electronic and optical isolation between bits in the byte-wide transmitter. Further, we investigated the wavelength crosstalk of our transmitter package by measuring the BER at one wavelength (825 nm) with and without a signal present on another wavelength (991 nm), as shown in the figure.

We have also developed the technology to process multi-wavelength VCSEL arrays monolithically at low cost. These developments are crucial for enabling us to scale our transmitter to higher wavelength count (8–16) and for manufacturing the technology at low cost. Finally, we have made significant progress in the area of long-wavelength VCSELs, by demonstrating a 1200-nm VCSEL.

Our plans for FY2000 focus on scaling this multiwavelength technology to enable both higher wavelength count (8–16) transmitter modules as well as physical-layer communications demonstrations.
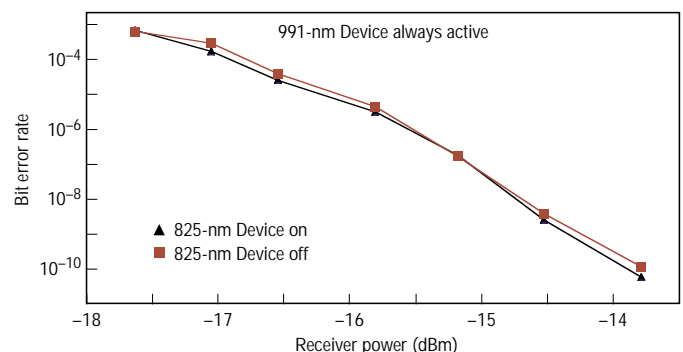
Wavelength to wavelength single fiber crosstalk BER measurements. The BER on a 991-nm VCSEL vs. optical power, with and without optical signals on the VCSEL at 825 nm.

A General Method for Coupling Atomistic to Continuum Mechanics Simulations with Application to Stress Corrosion Cracking

A. A. Quong, B. Sadigh, J. Shu, W. G. Wolfer

98-ERD-087

Scientists dealing with stockpile and nuclear materials stewardship are beginning to rely on scientific information for evaluating the lifetimes and predicting the behavior of materials in many systems. Increasingly, there is a need to study the failure of materials from an atomistic point of view. This is a very difficult problem because the number of atoms required to study a realistic system often exceeds the simulation size even using today's enormous massively parallel computers. Therefore, one often has to approximate the real system by simulating just a small piece.

Presently, we have a working 2-D version of the code that has been implemented with pair-potentials, and the elastic medium is taken as an isotropic. (Our preliminary results were presented at the *Fall Meeting of the Materials Research Society* in November 1998.) Numerical results obtained with this method compare well with much larger atomistic calculations. We ascribe numerical differences to the approximation of an isotropic elastic medium.

We developed a computational tool that embeds an atomistic region into a larger elastic continuum. By seamlessly coupling the atomistic region to the elastic continuum, the long-ranged stress and strain fields are allowed to interact with the region of interest. This is particularly important in many problems where the interaction of the elastic field with the atomistic defect must be included—specifically in the study of stress-corrosion cracking (SCC). Predicting failure due to SCC is often very difficult because the crack growth rates are very slow. In some cases, the rate of crack growth is on the order of a single broken atomic bond every few seconds. Not only do the atomic level processes that encompass the chemistry at the crack tip have to be explicitly included, but the analysis must also include environmental factors such as macroscopic stress fields and the corrosive environment.

Our new computational tool treats a realistic system by partitioning it into two regions. The first region is the region that undergoes large changes from the unperturbed-solid. This may be the introduction of a defect such as a crack or a dislocation, or a point defect such as a vacancy or interstitial. The second region is a continuum region that is taken as a linear-elastic medium. This elastic region can be finite or infinite in extent depending on the particular problem. Coupling the two regions seamlessly is the most difficult part of the problem. We do this by introducing quasi-atoms in the elastic region near the atomistic region. The quasi-atoms perform two roles. First, they couple the atomistic region to the strains in the elastic region since the positions of the quasi-atoms are determined from solving the elasticity equations of the continuum. Second, they provide the correct environment for the atoms near the atomistic-continuum boundary. Without the quasi-atoms, the atoms near the interface would behave as surface-like atoms rather than bulk-like atoms. The atoms on the boundary determine the boundary conditions for solving the linear elasticity equations. To solve the elasticity equations, we use the boundary element method, a Green's function method that is very efficient; we only need to perform numerical integration over the boundaries, rather than over the entire continuum.

We are currently studying how the interplay between applied stress and crack orientation effects atomic bond strength at crack tip. We are also implementing more advanced atomistic techniques (currently empirical potentials) based on electronic structure theory.

Effects of Radiation on the Mechanical Properties and Structural Integrity of Nuclear Materials

T. Diaz de la Rubia, E. Alonso, M. J. Caturla, B. D. Wirth

98-ERD-090

Under irradiation with energetic particles, metals often undergo plastic flow localization and a catastrophic degradation of their mechanical properties. This is manifested as hardening and results, among other things, in a significant upward shift in the ductile to brittle transition temperature. The effect limits the lifetime of the pressure vessel in most of the world's nuclear power plants and threatens to severely limit the choice of materials for the development of fusion-based alternative energy sources. While these phenomena have been known for many years, an explanation of the underlying fundamental mechanisms and their relation to the irradiation field is lacking. To provide a physically based description, a multiscale modeling approach is required.

Over the past few years, much progress has been made in describing the fundamental aspects of irradiation effects in solids. Our own molecular dynamics (MD) calculations for a 20-keV Cu recoil in a Cu matrix show that large vacancy and interstitial clusters are produced within a few tens of picoseconds as the cascade reaches its quiescent state. We have shown that in low stacking-fault energy metals, vacancies collapse to stacking-fault tetrahedra (SFT) within a few tens of picoseconds at room temperature. Interstitial clusters form glissile dislocation loops that migrate in one dimension by thermally activated glide. Based on this model, our kinetic Monte Carlo (KMC) simulations of neutron irradiated Cu near room temperature show that over 90% of the visible point defect clusters are vacancy SFT, in excellent agreement with experiments.

To investigate the relation between irradiation field and mechanical behavior, we have coupled the results of our atomistic calculations to our 3-D mesoscale dislocation dynamics (DD) simulation. The figures show the results of our simulations in Cu where cross slip/double cross slip takes place and defects are absorbed by sweeping dislocations based on criteria developed from linear elasticity and atomistic calculations. The figures clearly show localization of plastic flow in defect-free channels. The channel width is ~200 nm with a channel spacing of 1000 nm in agreement with experimental observations. Based on close examination of the simulation results, the mechanism of channel formation can be described as follows: As dislocations propagate from a Frank-Read source, a screw dislocation segment may be pinned by the defects and eventually cross slip from its primary plane as the stress is increased. This is followed by a double cross slip of the segment, thus creating a new dislocation source on a plane parallel to the initial primary plane. These two planes are not very far apart (100 to 200 nm), causing

dislocation segments of opposite signs to form dipoles and in turn pulling the segments together and limiting further spreading of the band.

In summary, we have developed a multiscale computer simulation that provides a physical description of the underlying mechanisms that govern plastic flow localization and mechanical failure in irradiated metals. Our MD simulations show that defect clusters are produced in displacement cascades. KMC calculations show that SFT and sessile interstitial clusters accumulate in the irradiated bulk, but glissile interstitial clusters glide in 1D to reach network dislocations and decorate them. Our DD simulation shows that flow localization results from a combination of dislocation pining by irradiation-induced defect clusters, unpinning by unfaulting and absorption of the defect clusters, and cross slip of the dislocation as the stress is increased. Double cross slip results in dipole formation, which in a natural way self-limits the width of the channels. The plastic instability results in catastrophic mechanical failure. Our results will be published in two papers accepted by the *Journal of Nuclear Materials*.

During FY2000, we will extend our calculations to investigate the kinetics of Cu precipitation in Fe and to elucidate the role of those precipitates on radiation hardening and the ductile-to-brittle transition temperature.
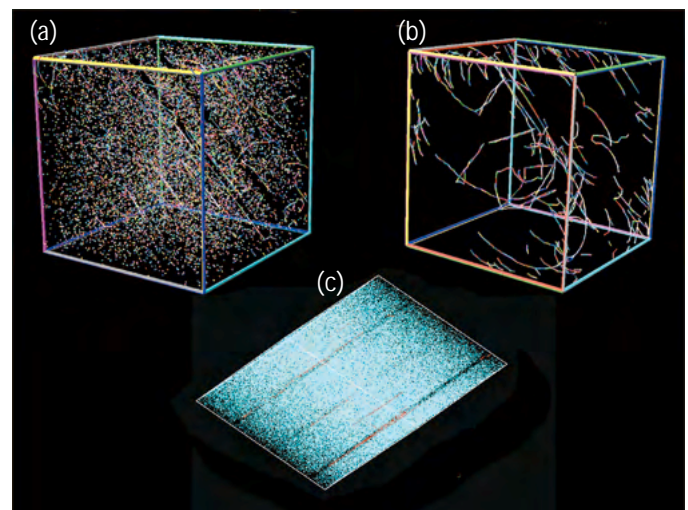
Figure 1(a) shows a 3-D representation of the dislocation dynamics box in which the defect-free channels (where plasticity is localized) are clearly visible. The point defect clusters are shown as small colored dots. For clarity, Fig. 1(b) shows the dislocation microstructure without the defect clusters. In Fig. 1(c), a 2-D projection of the glide plane on which the dislocation activity has localized is shown. Again, the defect-free channels are clearly visible.

Algorithm for Wave-Particle Resonances in Fluid Codes

N. Mattor

98-ERD-099

Historically, predicting wave–particle resonances in collisionless systems has required kinetic codes. These are difficult, because they require twice the dimensionality of fluid codes. Recent theoretical work has produced a collisionless closure term (CCT) that includes these resonances in much simpler fluid equations.

We are continuing work on calculating the CCT in a fluid code. Progress during FY1999 was significant. We wrote a 1-D electrostatic fluid code, es1f, intended to contain the same dynamics as the particle code es1. The code can switch between several forms of the CCT, including eikonal or exact, Fourier or real space, and Lagrangian or Eulerian in both space and phase velocity dimensions. Currently, the best success is with a "local CCT" that calculates the CCT from fluid variables local in time and space. With this closure, es1f now outperforms es1 on the damping of a Langmuir wave in a 1-D collisionless plasma, the classic "particle trapping problem." We are addressing the "two-stream instability"; es1f follows es1 dynamics up to the time of the first particle bounce. The current hurdle is that this particle bounce makes the density multivalued, which es1f cannot currently handle. We are looking at ways to circumvent this.

The most useful result of FY1999 has been a spinoff: analyzing fluctuations via the mathematics developed for the above closure theory. Specifically, the phase velocity transform (PVT) is an integral transform that divides a function of space and time into components propagating at constant phase velocities without distortion [Fig. 1a)] by grouping together appropriate Fourier modes. The PVT was used to decompose fluctuation data from the Sustained Spheromak Physics Experiment (SSPX) at LLNL, as an alternative to standard techniques such as Fourier or wavelet transforms, or singular-value decomposition. The PVT has distinct advantages, the main one being that the component waves more closely resemble propagating waves expected in fluid systems. Figure 1(b) shows a PVT spectrum obtained from SSPX probe data. Our results are being published.

(a)

(b)
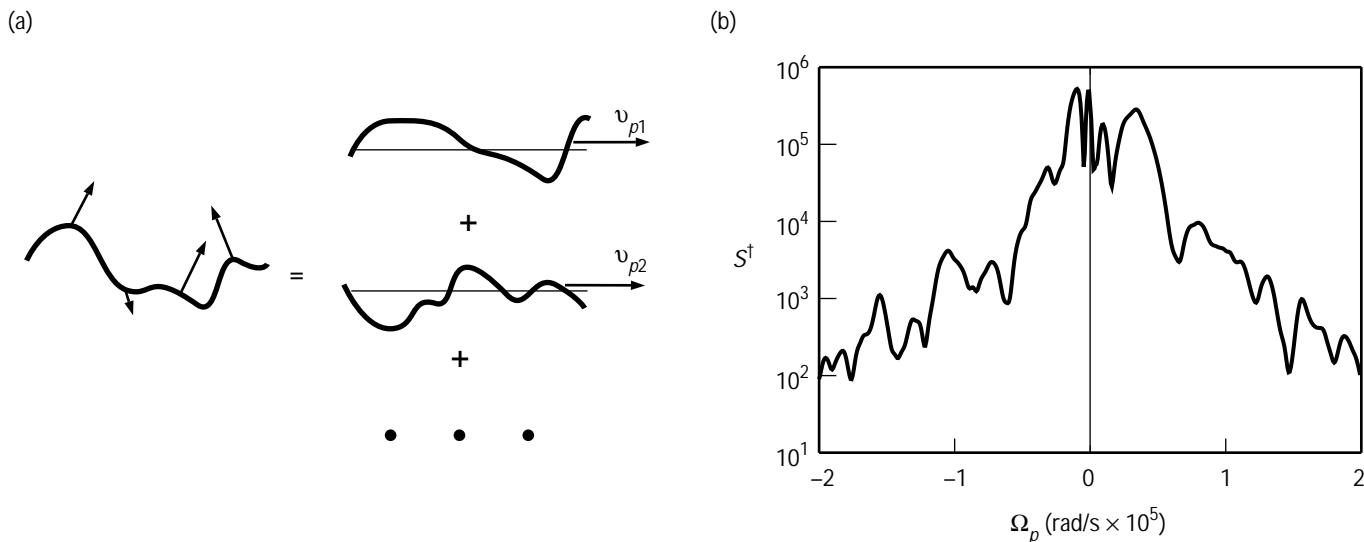
Figure 1. Analyzing fluctuations via our newly developed mathematics: (a) the phase velocity transform (PVT), which divides a spatiotemporal fluctuation into components υ_{p1}, υ_{p2}, etc., that propagate at constant phase velocity υ_p without distortion; and (b) PVT spectrum, $S^\dagger (\Omega_p)$, obtained from magnetic probe data on LLNL's Sustained Spheromak Physics Experiment. Each peak represents a coherent PVT mode traveling at angular phase velocity, Ω_p. Closer examination of each mode reveals details unavailable with other transforms, e.g., nonsinusoidal wave structure, nonlinear wave interaction, and spatial information about modes beyond the alias range.

Strategic Initiative in Computational Biology

M. E. Colvin, F. Gygi, G. Galli, K. A. Fidelis, D. Barsky, F. C. Lightstone,
J. C. Sasaki, R. Monaco, T. A. Kuczamarski

98-SI-008

By bringing together LLNL capabilities in parallel computing, computational chemistry, structural biology, and genome informatic, we are developing new modeling methods and applying them to problems in biology to establish a new state-of-the-art in biological simulation. This research, which is already proving valuable to existing LLNL research in molecular biology and genomics, will be critical to the emerging areas of biological defense and advanced sensors. Moreover, the modeling methods developed in this LDRD project are being applied to LLNL projects in combustion and explosives. In FY1999, we made good progress in developing new simulation methods and applying them to solve biological questions.

A central component of this initiative is the development of the first principles molecular dynamics (FPMD) method for parallel supercomputers. This method simulates the motion of molecules using nearly exact quantum mechanics, in contrast to the less accurate ball-and-spring models currently used. We applied this method to simulate pure water at an unprecedented level of accuracy using the Accelerated Strategic Computing Initiative (ACSI) computer; these calculations would have taken decades using conventional computers. Additionally, we used FPMD to determine the distribution of water around the DNA phosphodiester backbone, providing information necessary to understand the mechanism of enzymes that repair damaged DNA.

We continued our highly productive collaboration on the food mutagens, chemicals found in certain cooked foods that bind to DNA and initiate cancer. We have begun simulations of these mutagens bound to DNA double helices, which will help explain the wide range of cancer potencies observed within this class of chemicals. We also completed a computational study of the bioflavonoids, chemicals found in fruits and vegetables that reduce the risk from food mutagens.

This year, we began modeling the metabolic enzymes responsible for the chemical activation of the food mutagens. The first step in the pathway to cancer for these compounds is oxidation by a class of enzymes known as cytochrome P450. Although no structures are known for animal P450s, we are applying the advanced protein-modeling methods developed under this strategic initiative to predict the structure of human P450, using the structures of distantly related bacterial enzymes (see figure). This structure will be used to simulate the binding of both the food mutagens and the protective bioflavonoids to the P450 active site.

In collaboration with Duke University, we are studying a widely used anticancer drug, cyclophosphamide. We completed a simulation study of the chemical reaction that converts this drug to a form that binds DNA. This reaction is believed to be the rate-limiting step in the activation of this drug. Our ability to simulate this step provides a powerful tool in developing new anticancer drugs. This year we also published an invited review article on the roles for computer modeling in anticancer drug design.

Other important components of our strategic initiative are simulations to determine the fundamental factors determining DNA structure. In collaboration with Professor Eric Kool at Stanford University, we published the first complete model of DNA bases binding to DNA replication enzymes, which we used to explain the activity of non-polar base analogs. We also published a study of base pairing in parallel DNA, contradicting previous theories of guanine-cytosine DNA basepair stabilization and predicting that the greatest stability occurs through an unusual arrangement known as wobble-pairing.

Additionally, in FY1999, we worked on several other biological projects, including simulations of anti-freeze proteins, blood glucose sensors, and chemicals that will bind to bacterial toxins. We also used the ASCI Blue computer to discover major portions of more than 46,000 previously unknown genes in the human DNA sequence databases.

In FY2000, we will begin several new research projects, including the first full molecular dynamics simulations of a DNA repair enzyme. We will also perform quantum chemical simulations on the catalytic mechanism of P450 oxidation of food mutagens, and we will begin collaboration with U.C. Berkeley to run high accuracy calculations of the stacking interactions in DNA bases.
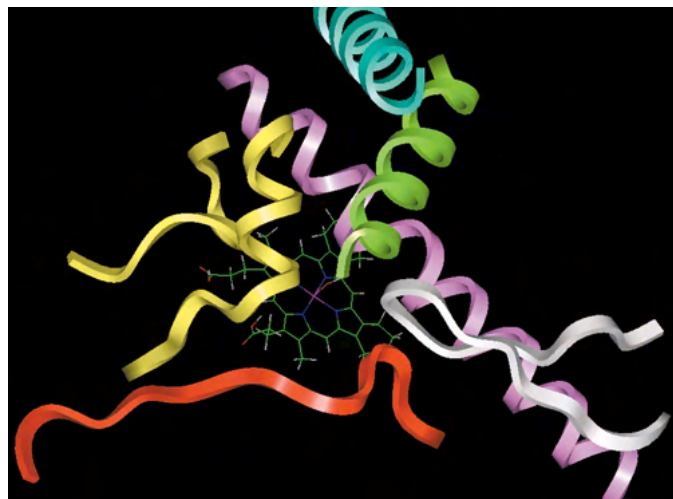
Model active site of the human P450 enzyme implicated in the activation of food mutagens is generated using sequence and structural information from distantly related proteins.

Computational Chemistry of Plasma Polymerization

C. K. Westbrook, A. Kubota, W. J. Pitz

99-ERD-006

Plasma polymerization involves a rich system of processes occurring over extremely disparate time and length scales. The process is important to many applications where thin films are required, including microelectronics, biotechnology, and protective coatings; however, there is little fundamental understanding of the process.

We are studying plasma polymerization, using interconnected computational models. Our goal is to integrate a reactor-scale plasma model with a detailed atomistic model of the surface chemistry, such that the properties of the deposited film can be custom-tailored by adjusting the reactor, precursor, and plasma conditions. The detailed plasma–surface interactions and surface chemistry are the most poorly understood aspect of plasma polymerization and are the main focus of our studies. Our results will establish a new computational chemistry expertise at LLNL and should also lead to models for chemical vapor deposition, catalytic combustion, aerosol kinetics, and other capabilities of potential importance. This work builds on LLNL's unique expertise in low-temperature plasma modeling and in detailed kinetic models of large-hydrocarbon combustion.

Plasma reactors have a length scale of meters; microfeatures on a wafer surface have length scales of 10 mm. Characteristic time scales are the residence time in the reactor (on the order of 1 s); plasma species (neutrals, ions, and electrons) have much smaller characteristic time scales (ms, ms, and ns, respectively). To account for the interaction of energetic ions with atoms on the substrate surface, we deal with the evolution of the collision cascade with time and with length scales on the order of picoseconds and angstroms, respectively. Splitting algorithms separate the fast and slow processes to allow dealing with these disparate time scales. However, surface reactions currently involve empirical rate expressions that ignore atomic-scale features and the details of the surface chemistry.

During FY1999, we developed a molecular dynamics (MD) code to simulate the subpicosecond dynamics of the collision cascade and the bond-breaking and bond-forming processes that are associated with energetic hydrocarbon fragments. The figure shows the computed result when 18 successive 25-eV CH_3^+ ions strike the surface at near-glancing angles. The primary effect is the efficient removal of H from the surface and the breaking of C–C bonds. With increasing connectivity of the C–C network structure, we expect a surface that is more resistant to erosion and that favors deposition and crosslinking.

To calculate over a representative surface area, we consider a 50- by 50-Å cell of about 6,000 atoms. Periodic boundary conditions are applied in the lateral x–y directions, with the bottom 2 Å fixed in space. A Langevin thermostat is applied to the bottom 6 Å of the cell. We are now using empirical, multiple-body potentials for the C–H systems; in future studies we will, by employing ab-initio techniques, develop accurate C–H and C–F potentials fit to reaction coordinates of important chemical reactions.

Our kinetic Monte Carlo (MC) code, also developed during FY1999, examines difficulties associated with surface-modification processes. In a study involving 5,000 to 25,000 atom cubic MC lattices, we found that only three simple reactions on a hydrocarbon surface were involved: (1) H-abstraction, (2) H-adsorption and (3) CH_3 attachment to a radical site. Including methyl radical addition requires our model to describe the site of the reaction in a much more complex manner than is needed for H atom reaction; therefore, we must use computationally expensive numerical methods.

In FY2000, we will complete a parallelized MD code, meanwhile adjusting the cutoff range, refresh rate, and other internal parameters. Our MC code will be modified to include surface reactions and their site dependencies. Using these codes in a hybrid MD–MC framework, we will study very large systems on LLNL's massively parallel supercomputers and look at surfaces on mesoscale features such as steps and trenches; we also hope to examine other surface systems (C–F, Si–O, C–F–Si–O, and Si–O–Cl).
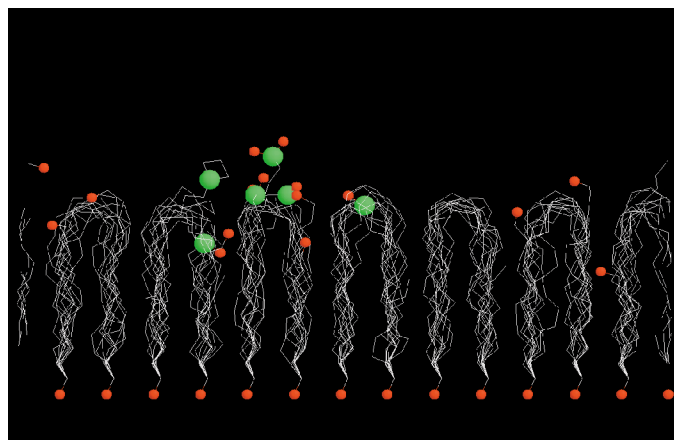
Simulation produced by our molecular dynamics code, showing how incident methyl ions can rearrange, damage, or add to an existing polymer layer.

Programming Models for Shared-Memory Clusters

J. M. May, B. R. de Supinski, S. R. Taylor

99-ERD-009

Parallel computer architectures traditionally fall into two categories, (1) shared-memory computers, which have multiple processors that communicate through a common pool of memory; and (2) distributed-memory computers, which have separate nodes in which each processor has its own private memory—and nodes exchange data by passing messages over a network. A shared-memory cluster is a hybrid architecture in which a network connects nodes, as in a distributed-memory computer, but each node contains two or more processors sharing memory. All of LLNL's large parallel computers are shared-memory clusters. These hybrids present special challenges to programmers, who must manage both shared and distributed memory.

Distributed-memory programs often use a standard programming library called MPI (message-passing interface) to pass messages between nodes. Shared-memory programs exploit multiple processors using either explicit threads, which are subprograms that run concurrently and can see each other's data, or compiler directives, which instruct the compiler to assign different loop iterations to different processors. Portable Operating System Interface (POSIX) threads (Pthreads) is a standard library for managing threads, and Open MP is a standard set of directives. In general, Pthreads programs are harder to write but more flexible than OpenMP programs.

In some shared-memory clusters, programs can use MPI exclusively, treating processors on the same node as if they could not communicate directly through shared memory. Alternatively, they can use a mixed-programming model, exchanging data between nodes with MPI and using either Pthreads or OpenMP to manage the parallelism within a node.

In this project, we explored the tradeoffs involved in choosing programming models for shared-memory-cluster parallel computers. Specifically, we investigated the performance and ease of use of these mixed-programming models by addressing three questions:

(1) What are the costs of basic operations in each model? (2) How do these costs affect the overall running time of applications? (3) How easy is each model to use?

We began in FY1999 by surveying eight codes at LLNL that already use mixed models. These included several large production codes. The codes all use MPI, and they manage shared memory using explicit threads, compiler directives, or (in one case) a commercial library of parallelized mathematical functions. We learned that several codes had initially used Pthreads, but developers abandoned that model because of its complexity. The codes were converted to OpenMP and performed about as well, and the directives were much easier to use. It took weeks or months to add Pthreads calls to existing MPI-based programs, but only days to add OpenMP directives. However, these directives work well only for certain parallel algorithms. OpenMP is appropriate when a program's work can be divided in advance into independent pieces. However, some programs generate new work continually, so a compiler cannot easily assign work to processors in advance. These "task queue" programs require the greater flexibility of explicit threading.

We also measured the performance of basic Pthread operations, such as sending and receiving synchronization signals. We found significant variations between different computers for the same operations, suggesting that some Pthreads implementations could be improved. We developed a program that is the first to measure the performance of Pthread operations, and we are releasing it to the public so that others can perform similar measurements on different machines.

On the basis of this work, we have advised developers of other LLNL codes on the tradeoffs between different mixed-programming models. Data from our Pthreads benchmark software will help us evaluate thread libraries provided by computer vendors. Our study of mixed programming models is continuing under the Accelerated Strategic Computing Initiative (ASCI) Problem Solving Environments program.

Quantitative Tomography Simulations and Reconstruction Algorithms

H. E. Martz, Jr., M. B. Aufderheids, III, D. Goodman, A. Schach von Wittenau, C. Logan, J. Hall, J. Jackson, D. Slone

99-ERD-015

X-ray-transmission radiography and computed tomography (CT) are important diagnostic tools that are at the heart of LLNL's effort to meet the goals of the DOE's Advanced Radiography Campaign. This campaign seeks to improve radiographic simulation and analysis so that radiography can be a useful quantitative diagnostic tool for stockpile stewardship.

Current radiographic accuracy does not allow satisfactory separation of experimental effects from the true features of an object's image when the image has been reconstructed after radiography or tomography. This can lead to difficult and sometimes incorrect interpretation of the radiographic and tomographic results. By improving our ability to simulate the whole radiographic and CT system, it will be possible to examine the contribution of system components to various experimental effects, with the goal of removing or reducing them. By merging this simulation capability with a maximum-likelihood, constrained-conjugate-gradient (CCG) reconstruction technique, we would have a physics-based, forward-model image-reconstruction code.

Current back-projection-construction tomographic methods used for reconstructing CT images make strong assumptions about the radiographic projection data. These assumptions include the presence of energy-independent, photon-attenuation cross sections and the absence of detector or source-spot blur, scattering, and noise and other artifacts. These assumptions are not strictly correct. Radiation-attenuation cross sections depend strongly on energy and material composition; detector and source-spot blur can and usually is significant; scattering is present; noise and artifacts are common. Some if not most of these assumptions can be treated in the forward model of a reconstruction algorithm. (In a simple sense, the forward projection is ray tracing through a 3-D object onto a 2-D plane, creating a radiograph or projection; the back-projection is creating a 3-D representation of the 3-D object from several 2-D radiographs or projections.)

In this project, we seek to improve the accuracy of computed tomography from transmission radiographs by studying what physics is needed in the forward model.

During FY1999, we decided to study eight test objects, which would help validate the performance of the radiographic simulation codes and tomographic image-reconstruction codes. First, we incorporated preliminary scattering models in LLNL's HADES (a straight-ray simulation code used to model the process of x-ray, neutron, and proton transmission radiography); this code was then used to simulate the radiography of the test objects. For radiographic and tomographic imaging, we used an amorphous-silicon array with a MinR scintillator at 9 MV. We measured the spatial response for this system and used Monte Carlo simulations to determine the energy spectrum for the source and the spatial response of the detector as a function of energy. We acquired experimental radiographs and HADES simulations for all the test objects, and detailed COG simulations for some of them. COG is another LLNL Monte Carlo simulation code that incorporates full physics and is used to model the process of x-ray, neutron, and proton transmission radiography.

At year's end, we had begun to validate our radiation models by comparing them with the experimental radiographs. Incorporation of both spectral information for the source and the detector point-spread function were required to improve HADES simulated radiographs to within 5% of the measured radiographs. This is better than a three-fold improvement over our previous method. Our results are encouraging; however, we need agreement to better than 1% before we can obtain high-accuracy (~1%) reconstructions of tomographic images. Towards this end, we have determined a method for merging the CCG and HADES codes into a new, improved image-reconstruction code. These codes will be run separately; information will be exchanged using shared memory.

In FY2000, we will (1) demonstrate accurate and fast radiographic-simulation tools by further investigating and refining our Monte Carlo and HADES models to improve the agreement with the measured radiographic results; (2) complete the merging of CCG and HADES; (3) study several performance tests with both simulated and experimental CT data; (4) demonstrate that our methods to reduce CT artifacts in simulated data work as well with experimental data; and (5) develop new methods for reconstructing images of objects with high-Z, high-density components.

Lattice-Boltzmann Simulation of Microfluidic Devices

D. S. Clague, P. Krulevitch, M. Garcia, P. J. Cornelius

99-ERD-016

In a manner resembling that which occurred in the electronics industry more than a decade ago, many fluid-based processes are making the transition from employing macroscopic, bench-scale laboratory instruments to employing microchip-based devices. This revolutionary transition represents the future in many important technologies (e.g., in the chemical and pharmaceutical industries), all of which involve the transport of complex fluids in micrometer- to millimeter-sized channels etched into microchip-like substrates. Instruments or devices that make use of such fluid processes are known as microfluidic devices.

A primary feature of these devices is the manipulation of macroscopic solutes within a suspending fluid. However, colloidal particles and macromolecules experience a number of physical forces that influence their transport and separation within microchannels. To achieve the desired functionality, the designer of these devices must therefore understand and be able to make creative use of these interactions and the resulting phenomena. In a practical sense, the device-manufacturing process from concept to prototype is increasingly more time consuming and expensive; hence, the modeling and simulation aspect of microfluidic-device design is now recognized by many as critical to current and future efforts in this area.

In this research effort, we are developing enhanced lattice-Boltzmann (LB) simulation capabilities to study these complex fluid systems. In the LB method, one solves a discrete form of the Boltzmann transport equation on a lattice. The beauty of the LB method is that incorporating bounding walls, stationary and mobile objects, and nearly any desired physics into the simulations is rather straightforward [Fig. 1(a)]. Furthermore, the LB method can handle finite Reynolds number flows.

During FY1999, we developed parallel LB simulation capabilities to study stationary and mobile solutes in bounded domains. Our studies included calculating (1) the hydrodynamic force and torque acting on stationary, spherical particles in bounded flows; and (2) the hydrodynamic force and torque acting on mobile particles convecting down a rectangular conduit in a pressure-driven flow [Fig. 1(b)]. Our benchmark simulation results exhibit excellent agreement with existing theory and with well-accepted results from published alternative methods. Our results to date do indeed show that the LB method accurately solves relevant, nontrivial flow problems. Furthermore, we developed relevant physical models to simulate external fields and built them into the LB capability.

In FY2000, we will continue studying complex fluid systems relevant to microfluidic efforts at LLNL. Specifically, we will (1) complete our studies of colloidal capture caused by external fields, (2) characterize the hydrodynamic lift phenomena in bounded domains, and (3) incorporate the additional physics that are necessary to study and characterize particulate behavior in microfluidic devices into our LB simulation capability.

(a)

(b)
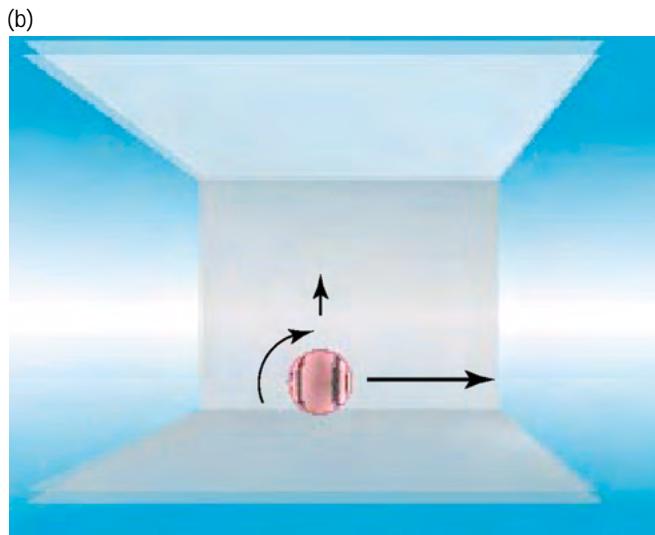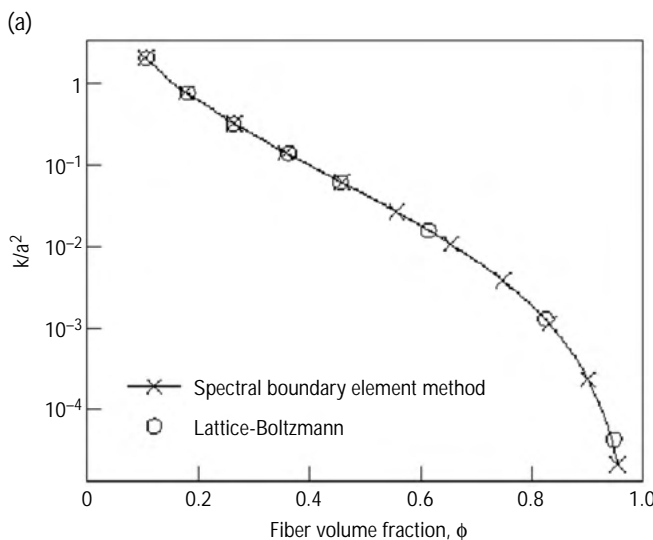
Figure 1. Early results from lattice-Boltzmann (LB) simulations: (a) compared with spectral boundary element methods (SBEM) for pressure-driven flow through fibrous media—where k is the hydraulic permeability, and a is the radius of the cylinders—the LB results are in nearly exact agreement with SBEM for a very wide range of solids fractions; and (b) a translating and rotating sphere in a pressure-driven flow in a bounded, rectangular channel—the sphere experiences a small lift velocity caused by inertial effects.

Improved Implicit Finite-Element Dynamics

M. A. Puso, E. Zywicz

99-ERD-018

Implicit, nonlinear, structural analysis has been used for many years; nevertheless, for a variety of numerical issues it can be difficult to perform on many problems. Implicit finite-element analysis has been most often used for determining the quasi-static response of a structural model, whereas explicit finite-element codes have typically been used for nonlinear dynamics problems. However, many structural-dynamics problems occur over time spans that are too long for explicit analysis because of the inherently small time steps required. On the other hand, these same problems may be too nonlinear for implicit dynamic analysis. Long-term, highly nonlinear dynamics problems in this "gray area" include seismic, reentry-vehicle, and transportation-container vibration analysis.

The purpose of our project is to research and implement new implicit finite-element algorithms capable of modeling these gray-area dynamics problems. We will accomplish this by solving the numerical problems inherent in the implicit method.

The two main difficulties for implicit analysis are stability and contact nonlinearities. That is, (1) for nonlinear problems, the standard implicit integration methods (e.g., Newmark's method) are not, in general, unconditionally stable; and (2) convergence of the nonlinear-solution algorithm is severely affected by the presence of unilateral constraints on the contact surface.

For general nonlinear dynamic analysis, the classic implicit methods can become numerically unstable, and often do so in the presence of large, rigid-body rotations or severe contact impact. For example, if you were to model a space vehicle spinning in orbit, Newmark's method would be unable to model the long-term dynamics because of the numerical instability.

With linear analysis, the spectral method is used to determine the stability of an algorithm. These algorithms are considered "A" stable. In the nonlinear regime, we cannot exploit spectral methods; here, enforcement of "algorithmic energy" conservation (or dissipation) can enforce stability. This has been shown for nonlinear elasticity, where the "algorithmic energy"

is conserved by making the appropriate adjustments to the nonlinear strain evaluation. By conserving algorithmic energy, velocity and displacements are bounded, and stability is ensured.

In our work, we generalize the energy-conservation method to include (1) coupled, rigid-flexible body systems; (2) contact with friction; and (3) plasticity. Because friction and plasticity are dissipate, we deem the new, unconditionally stable technique to be the "algorithmically energy-consistent method."

Contact surfaces are used to interface disconnected objects that may impact during analysis. This contact interaction is highly nonlinear and is the biggest culprit for convergence problems. Much of the problem stems from the non-smooth nature of the contact surface. The finite-element contact surface is comprised of bilinear facets. This discretization causes jumps in contact forces at facet edges and vertices—making it very difficult to achieve global convergence of the Newton Raphson nonlinear solution algorithms. To alleviate this problem, we have used 3-D bi-Hermitian patches to interpolate the bilinear surface mesh. This provides C1 (smooth) continuity between facets. This smoothing has been shown to provide a vast improvement in the convergence of the contact algorithm on problems such as thermal cycling of weapons components.

In summary, during FY1999 we developed state-of-the art implicit algorithms that are more robust, efficient, and accurate than those previously available. For example, we can now use the implicit method to simulate spinning, rigid-flexible space structures that impact at contact surfaces, and we obtain good, long-term dynamics results without the problems of numerical instability.

In FY2000, we will focus on improving the FY1999 work and in addition implement (1) new, nonlinear complementary methods for Lagrangian multiplier contact; and (2) constitutive models for plasticity that ensure numerical stability by algorithmically accounting for energy dissipation.

A Laser-Driven Photocathode Injector and Femtosecond-Scale Laser–Electron Synchronization for Next-Generation Light Sources

G. P. Le Sage

99-ERD-026

The next generation of high-brightness, tunable x-ray light sources, advanced free-electron laser (FEL) applications, and ultrahigh-gradient accelerators will require advances in the technology of low-emittance, relativistic electron beams that are synchronized to short-pulse laser systems. These short-pulse x-rays enable time-resolved characterization of shock dynamics and the examination of materials under extremes of pressure and temperature. Examples of their use include equation-of-state characterization on high-density materials; crystal disorganization and regrowth in shocked and heated materials; and measurement of short-time-scale, phase-transition phenomena. Single-shot evaluation, requiring high peak flux, is important for complex experiments such as the probing of laser-shocked actinides required for the Stockpile Stewardship Management Program (SSMP).

To achieve the single-shot x-ray flux demanded by these experiments, an electron beam with bunch charge between 1 and 10 nC, a pulse length of 1 ps or less, and diameter of order 20 μm is required, synchronized within 1 ps or less to an intense laser pulse. The combination of these requirements for high peak electron current, short pulse length, low emittance, and subpicosecond synchronization necessitates a specialized type of electron injection source known as a photoinjector. In this project, we developed a state-of-the-art photoinjector. This injector, when combined with LLNL's 100-TW Falcon laser (35-fs pulse length) and LLNL's existing 100-MeV S-Band radio-frequency linear accelerator (rf LINAC), will enable x-ray pulse intensity five orders of magnitude higher than in previous demonstration experiments—thereby extending the range of applicability beyond repetitive, solid-state applications.

The primary goals of this project were to (1) develop a photoinjector capable of delivering high electron density within a focused laser spot, synchronized to the Falcon laser system; (2) synchronize the rf LINAC and the high-power Falcon laser system; and (3) develop the necessary electron-beam diagnostics for optimization of the laser–electron interaction.

During FY1999, we (1) delivered to the photoinjector laboratory a high-power rf system commissioned with 18 MW; (2) designed, cold tested, brazed, and installed a photoinjector cavity that met or exceeded all specifications; and (3) designed and implemented the photoinjector's test beamline, complete with optics and diagnostics. Innovations incorporated in the photoinjector cavity included a diamond-turned cathode, improved vacuum, and the use of high-isostatic-pressure annealed copper. In addition, we completed the ultraviolet laser system and synchronized the rf LINAC with the Falcon laser system. As part of this work, we proposed new techniques for meeting the synchronization requirements of the system in its final configuration. New diagnostic techniques developed at LLNL will enable characterization of the beam parameters and optimization of the laser–electron interaction.

The results of this project provide the basis for research to be performed during the LDRD project "Intense Laser–Electron Interaction Research for Future Light Sources" (00-ERD-032). Under the new project, our recently produced photoelectron beam will be used in FY2000 for Thomson scattering using the photoinjector independently of the rf LINAC. Photoinjector integration with the LINAC will follow these initial experiments.

Supernova Astrophysics in Three Dimensions

R. G. Eastman, S. E. Woosley

99-ERD-043

Supernovae (SNe) are among the brightest objects in the Universe. They produce nearly all the elements heavier than helium and leave behind some of the most exotic objects in nature, e.g., neutron stars and black holes. Progress towards understanding SNe has been impeded by a lack of the computer power needed to solve the full 3-D problem. However, the advent of the Accelerated Strategic Computing Initiative (ASCI) Teraflop computers gives us a unique opportunity to make significant progress on the most fundamental aspects of SNe, neutron stars, and black hole formation.

During the first year of this project, we made substantial progress in developing C-Prometheus 3-D (CP3D) into a full-featured astrophysics code suitable for performing highly accurate, full physics, parallel 3-D simulations of high energy astrophysical phenomena, such as supernovae explosions and black hole accretion. We enhanced the piecewise parabolic method-based hydrocode CP3D by building in scripting language with interactive graphics, parallel multigroup flux-limited diffusion, parallel and portable integrated-optical, equation-of-state routines, and many other capabilities.

We developed and incorporated into CP3D a parallel, embeddable interactive parser and problem generator, the grammar of which is the ANSI C programming language. Since it is ANSI C compliant, it can parse any C language application code and write its own compilable interface wrapper routines. It takes roughly five minutes to add an interactive front end to almost any application. This approach to incorporating scripting languages into application codes is an alternative to scripting languages that have their own grammar and require hand-coded interfaces to be written.

We developed and prototyped a new, adaptive angular mesh, constrained, second-order-accurate SN + variable Eddington factor transport method. This new algorithm uses quadratic interpolation to represent the angular variation of the specific intensity within an angle zone. With this interpolant, the amount of radiation within each quadrant of the zone (obtained by factor of 2 refinement of the angular zone) can be estimated and compared with the quantity obtained by integrating the transport equation on the refined grid. If the two estimates are to within a prescribed tolerance of each other, the current refinement level is either kept or reduced. Otherwise, the grid is refined. A 1-D spherical transport code was written to test the idea. The figure shows the exact and computed intensity variation with direction cosine at various distances from a light source of radius 1 and isotropic emergent intensity of 1. Typically, a SN transport algorithm would be unable to resolve the intensity in a problem such as this.

We performed 2-D test runs of the Rayleigh-Taylor instability produced in a 15-solar-mass red supergiant explosion as the shock runs down the density gradient between the oxygen and helium shells, and between the helium shell and the hydrogen envelope. This is an important problem, which relates to recent x-ray observations of a Type II SN with the Chandra X-ray Observatory, as well as to the use of Type II SN as probes of the cosmological distance scale.

In FY1999, we also looked into the observational consequences of mixing, especially at x- and γ-ray energies. We ran Monte-Carlo and deterministic transport calculations to determine the spectral evolution of various Type Ia SN models. This work resulted in predictions for the iron, cobalt, and nickel K-shell line flux that can be made with the X-Ray Multi-Mirror Mission x-ray observatory (launched December 1999), which will discriminate between the two most viable alternatives for the progenitor and explosion mechanism of Type Ia SNe.

The results of our research have been published, including four articles in *Astrophysical Journal*.
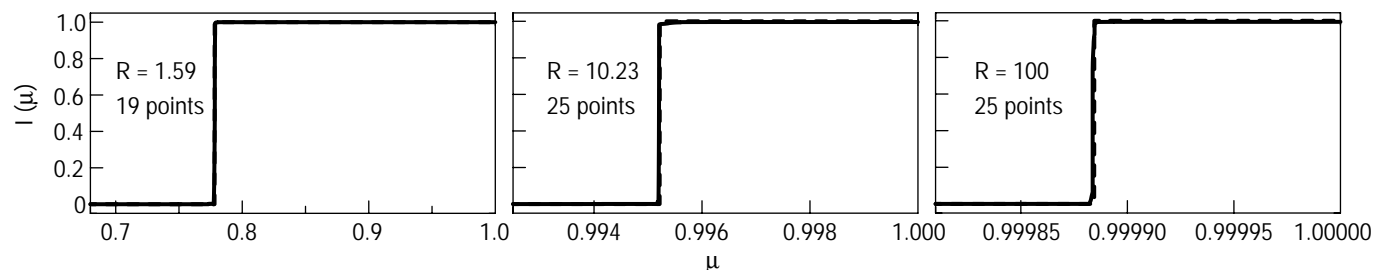
The variation in specific intensity as function of direction cosine at three distances from a spherical isotropic light source.

Optimizing Radiation Treatment Planning for Cancer: A Revolution in Radiation Therapy

C. Hartmann-Siantar, D. Garrett, R. House, S. May, R. Patterson, B. Yang

The PEREGRINE Monte Carlo Dose Calculation System provides accurate, 3-D Monte Carlo dose calculations fast and economical enough to be practical for widespread use in the radiation therapy community. By combining Monte Carlo transport methods with automated treatment planning and quantitative verification of dose delivered, we will provide tools that fully integrate the accuracy of 3-D Monte Carlo dose calculations into every aspect of cutting-edge radiation therapy planning and delivery. The PEREGRINE system, completed in FY1998, has been successfully licensed to the radiation therapy treatment planning community. It has been submitted to the Food and Drug Administration for premarket notification and is expected to be commercially available soon. In addition to the technical accomplishments, two postdoctoral fellows trained as part of this LDRD effort moved on to permanent positions in the national security program, taking with them many of the lessons learned in Monte Carlo transport, code design, and quality assurance.

In FY1999, we initiated PEREGRINE FALCON—a system for automatic radiation therapy planning that optimizes 3-D Monte Carlo dose calculations and beam delivery parameters to determine a physician's most effective treatment plan. Our method decouples the time-consuming processes of dose calculation, optimization, and assessment so that efficient algorithms can be used to rapidly explore different assessment criteria.

This system is designed to take advantage of new treatment-delivery hardware, computer-controlled multileaf collimators, which enable the practical delivery of radiation fields in which the beam intensity is varied across the beam. In this form of therapy, known as intensity modulated radiation therapy (IMRT), the increase in the number of the delivery parameters makes the treatment planning of IMRT too complex to optimize by manual trial-and-error. PEREGRINE FALCON provides the computer-optimization system necessary to achieve maximum therapeutic gains from computer-controlled delivery and IMRT.

In FY1999, we demonstrated the feasibility of separating the Monte Carlo calculation from the optimization. To this end, we modified PEREGRINE, and implemented a single-thread prototype version of the IMRT planning tool. We applied the prototype tool to a clinical prostate case and generated an excellent dose distribution shown in the figure. In this case, the plan-assessment criterion was to maximize the difference between the tumor and normal tissue dose. Comparisons with a manually optimized 3-D conformal therapy plan without intensity modulation shows a dramatic improvement in the conformal nature of the beam, including a significantly lower dose to the rectum, bladder, and lateral nerves.

In the process of developing and applying the prototype tool, we learned valuable lessons about calculation time, memory usage, and code architecture that will help us take advantage of the multi-thread architecture of the PEREGRINE hardware. These include understanding the dominant computationally intensive steps and resultant calculation times, optimal allocation of memory, and tradeoffs between various types of penalty functions and evaluation strategies. In addition, we began to investigate methods to speed up calculations.

To assess timing, we addressed two possible paths: optimization calculations using a quadratic penalty function and optimization with more general functions using iterative methods, taking advantage of gradients to speed up convergence. For calculations using a quadratic penalty function, we estimate the computation time to be less than 30 minutes on the PEREGRINE target hardware configuration. This will enable the first practical Monte Carlo-based optimization calculations. For a representative penalty function of a more general nature, we estimate that a calculation will take less than two hours on the PEREGRINE target hardware (assumes 1000 iterations, with gradient calculation). In FY2000, we intend to design and implement the planning tool on a multi-threaded platform and to modify PEREGRINE for faster dose calculations required by the planning tool. We also intend to improve user interface and start collaborations with the University of California at San Francisco.

| PEREGRINE: 3-D-CRT | PEREGRINE FALCON: Optimization, IMRT |
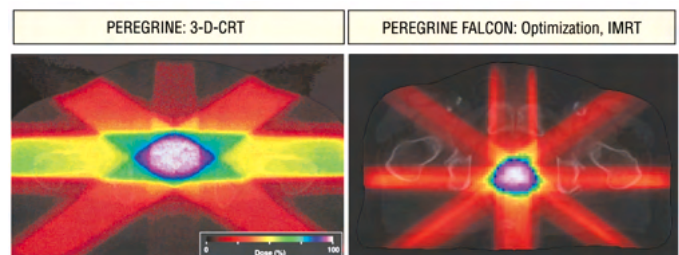
In the PEREGRINE FALCON calculation, prescription isodose lines precisely wrap around the prostate and avoid high doses to healthy tissue and critical nerves.

Combined Simulation, System Identification, and Sensing for Enhanced Evaluation of Structures

D. B. McCallen, G. C. Burnett, G. A. Clark, C. R. Noble

99-ERD-057

Monumental structures in the United States are all vulnerable to damage or failure when stressed by abrupt, large-scale natural or human-generated events. In recent years, the design and damage analysis of these large structural systems have become increasingly reliant on computational simulation; as computational speeds increase and massively parallel simulations become commonplace, this reliance will likely become even more pervasive. With the increase in fidelity of simulation models, there are great expectations that simulations will provide improved understanding and insight into the way in which structures respond to various loading conditions. However, in many respects our ability to discretize and compute has outpaced our ability to test and verify our computational models.

The ever-larger models that are being constructed must be actually representative of the systems being simulated. To meet this need, our goals in this project are to (1) develop algorithms that rigorously compare the simulated and measured system responses of large structures, (2) quantify the shortcomings of the simulation models, and (3) prescribe appropriate perturbations to the simulation models that will result in their improvement.

The technical approach to this problem revolves around a signal-processing scheme (see figure) in which the computed and measured responses of a structure are compared for known structural loadings. The model-based signal-processing algorithms utilize the system-simulation model, developed from finite-element discretizations of the structure, modified to a first-order, state-space-equations form. The measured structural response provides the second element of input to the signal-processing algorithms. The model-based signal processor first compares simulated and measured structural response to determine if the structural model is adequate (i.e., if the simulation model and the actual structure match). If there is a model mismatch, a least-squares-based system identification is performed to determine the appropriate simulation-model parameters to ensure correlation between the simulation model and the actual structure. On the basis of the system identification, the matrices of the simulation model can be modified and updated. For example, in a model of a building structure, the model-based signal processing can determine how the stiffnesses of the structural elements (e.g., of the individual beams and columns) should be modified in order to arrive at a more accurate model.

An important corollary to the system identification of the structure is the fact that the model-based signal-processing algorithm can be used to detect and locate damage in a structure. If system identification has been performed on a structure before an event such as an earthquake, changes associated with damage in the structure can be determined by retesting the structure after the event.

During FY1999, we successfully developed the model-based signal-processing algorithms and addressed some practical considerations of observability with a reduced set of sensor locations. In blind studies—in which we compared a computational model of a building structure and a "measured" structure (which consisted of a perturbed model of the structure)—the signal-processing algorithms correctly determined a mismatch between the simulation model and the "measured" structure. Even more importantly, the signal processing correctly identified discrepancies between the stiffnesses of individual elements in the simulated and "measured" structure. We also performed a carefully controlled experiment on a scale-model structure.

In FY2000, we plan to analyze an existing, large structure and to continue the development and validation of our model-based signal-processing algorithms.

Measurement and communication

Measured input & response

Model-based signal processor

Simulator

Difference detector

Difference identifier

Finite-element-based, numerical simulation model

$[M]$
$[K]$
$[C]$

System matrices

$[M]\{\ddot{x}\} + [C]\{\dot{x}\} + [K]\{x\} = \{f(t)\}$

Identify discrepancies between model and actual structure

Characterize the nature of the discrepancies

Information feed-back loop

Damage assessment
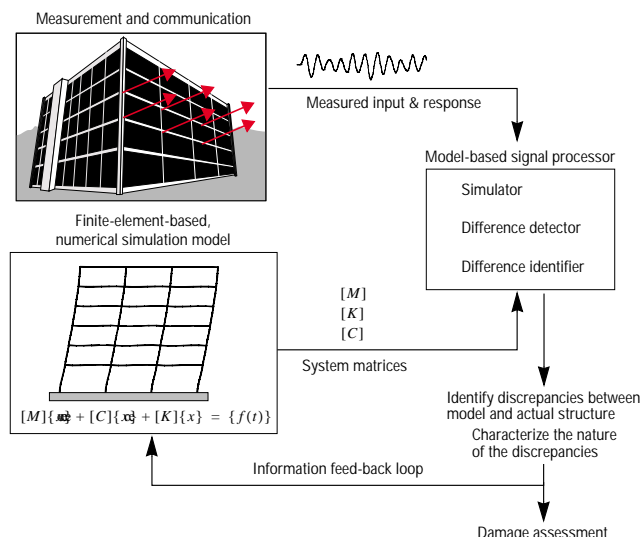
Model-based signal processing for the determination of system parameters.

Long-Range Weather Prediction Technologies

A. Ledebuhr, A. Grossman

Advanced numerical weather-prediction (NWP) models are being used with ever increasing spatial resolution. For these models to provide the anticipated improvement in forecast accuracy and range, major advances are needed in the atmospheric observation system. High-resolution global observations are required for model initialization, data assimilation, and validation of weather forecasts. A proposal has been made to establish a high-density global network of atmospheric microtransponders to record both temperature and wind data at high spatial resolution. These data would then be used in conjunction with new weather-prediction models to increase the reliability of long-range weather forecasts.

In addition to major advances in the data-collection technology required to provide the proposed high-resolution data-collection network, systems studies must be undertaken to (1) determine the density and frequency of the observations; and (2) understand the insertion requirements, spacing, and evolution of the global transponder ensemble that will enable long-range weather predictions using the next generation of NWP models.

The goal of this project was to perform these studies utilizing numerical models that provide realistic simulations of global weather patterns. This required us to use a global circulation model (GCM) to provide atmospheric wind-flow patterns coupled to a transport model to provide transponder trajectories. Transponder-insertion scenarios can then be studied to provide optimal insertion locations and rates, as well as resulting ensemble distribution and spacing data.

During FY1999, the first major issue we addressed was whether transponders released daily at predetermined levels and locations would provide a reasonable global distribution after a 35-day period. Our initial studies used the National Center for Atmospheric Research (NCAR) CCM3 global climate model (GCM) (a 2.8-deg-latitude by 2.8-deg-longitude by 18-vertical-level global grid) and the Naval Research Laboratory NOGAPS GCM (with T159/L42 resolution, 240/480 latitude/longitude grid points, i.e., 0.75 deg, and 24 vertical levels) to provide the horizontal wind fields at each grid point at 4-h intervals for 35 days. These wind fields were used to drive LLNL's GRANTOUR chemistry-transport model. GRANTOUR is a Lagrangian parcel model in which the atmosphere is treated as a set of constant-mass air parcels advected by GCM wind fields.

For our simulations, each parcel was taken to be a transponder. We envisioned each transponder in the constellation as a small (~10-cm diam), free-floating, neutrally buoyant balloon. For the initial simulations, we assumed that the balloons were constrained to fixed pressure levels, and we neglected vertical motions.

A launch scenario consisted of 300 launch sites distributed evenly in the Northern and Southern Hemispheres, in which one transponder was launched per day for 35 days at each of ten atmospheric pressure levels. The figure shows the number of levels within each vertical column that contains at least one transponder at day 35. The columns represent equal horizontal areas of approximately 250 km on a side. For those columns that contain at least four levels with transponders, a vertical sounding is possible. The plot shows that a reasonable global coverage of transponders will result from this launch scenario.

We also investigated two methods for remotely interrogating the transponders. One possibility was that an earlier conceptual design of a laser infrared radar (lidar) instrument mounted on a satellite could support the interrogation of the transponders—our analysis confirms its ability to do so. Alternately, in an active radio-frequency (rf) transponder system concept, rf satellite platforms would interrogate the transponders—this system also appears capable of providing the required data set.

This project has shown that, in principle, the transponder constellation discussed here could provide a relatively uniform global data set for incorporation into advanced numerical weather-prediction models.
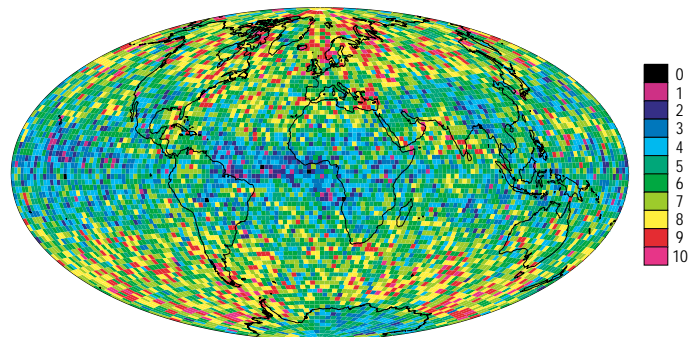
Simulated scenario 35 days after "transponders" (small, neutrally buoyant balloons) have been launched at 10 atmospheric pressure levels and their distribution calculated by a global circulation model. Colors show the layers with one or more balloons in vertical columns 250 km on each side. Four or more transponders in a column would provide adequate resolution of temperature and wind data in that column.

Rapidly Reconstructing Releases of Biological Agents in Urban Areas

J. H. Shinn, C. H. Hall, J. I. Daniels, L. Neher

99-ERD-069

Our goal was to test algorithms for reconstructing the time and release of a biological agent from information about the activity patterns of victims, dose-response functions for pathogenic organisms, disease latency, and meteorology. We believe we have successfully designed a system that meets this goal.

Significant challenges included (1) an unannounced release in which time, place, source term, and method of dispersal are not known; (2) the lengthy latency between exposure and onset of anthrax symptoms; (3) symptoms that mimic common influenza and cold symptoms; (4) the unfamiliarity of medical personnel with bioagent symptoms; and (5) our highly mobile population.

Our project had two major components: we developed (1) algorithms based on current epidemiological anthrax research to set up and test scenarios to simulate infected individuals in a mobile population; and (2) scripts and algorithms for BIOURBAN—an Internet-accessible, Web-based geographic information system (GIS)—to "back-calculate" the point of origin of a clandestine anthrax release in an urban area in the U.S.

BIOURBAN is a technology development for a GIS-based information synthesis and analysis produced solely on this project. In concept, BIOURBAN will be available as a password-protected Web page where information about specific events, victims, victim time-and-location clusters, and meteorological data can be accessed, entered, updated, and analyzed. It contains data describing population locations at various times; street and freeway networks; public places such as large arenas and auditoriums, prominent public buildings, schools, hospitals, and transit systems; and categories of land use. It is designed to access meteorological data and dispersion models and can support incident-response systems such as LLNL's Atmospheric Release Advisory Center (ARAC). BIOURBAN is written with commercial GIS software (using a combination of Visual Basic, C++, html, and Java). Data entered by the user are transmitted to a server running the GIS software; the data are processed, and the output is returned to the user.

The input page we designed for BIOURBAN is an expansion of the FBI system called Rapid Start. The primary data needed are the locations of victims at specific times during the past 10 to 20 days. (In a real event, these data would be obtained by FBI interviews with victims, relatives, friends, or coworkers.) BIOURBAN analyzes the most likely routes between locations. In our algorithm, the route lines or points are color-coded to represent possible periods of victim exposure. These are searched in telescoping time periods to find the likely common-exposure period.

To test BIOURBAN, we simulate a clandestine anthrax release (see figure); we locate a plume over a presumed population at a scenario-determined time and place and specify the source term. The GIS software in BIOURBAN colocates the plume and population using a common projection system. Individuals are "exposed" and "infected" using our probabilistic algorithms, which embody current epidemiological research on anthrax. One of the most important features is the anthrax-specific estimate of time-to-onset of symptoms—this determines the days before even a first indication of the attack. After the individuals are infected statistically, BIOURBAN incident response can be simulated.

In emergencies, BIOURBAN would be implemented with the first confirmed anthrax case. Under the Victim tab on the BIOURBAN Web page, information on each victim would be entered at the user site. Information from our algorithms would be entered and made accessible under the Event tab on the BIOURBAN Web page. Agencies could then provide timely action to reduce further infection and to interdict terrorists.
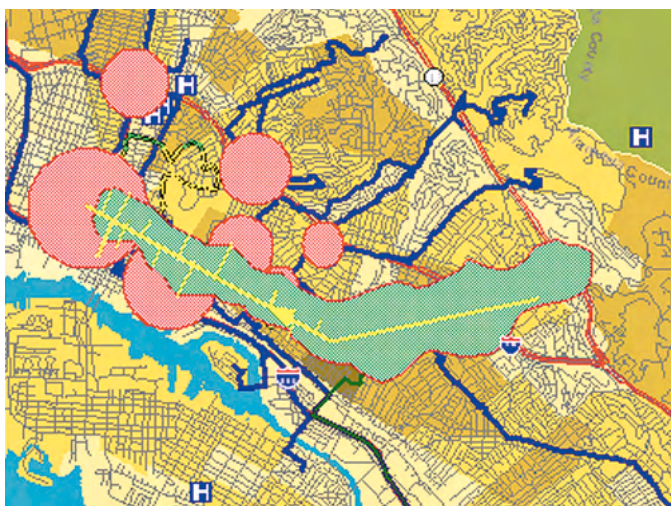
Reconstruction of a clandestine biological agent attack using algorithms developed in this project. Streets and hospitals ("H") are shown. Blue lines represent the reconstructed pathways of victims; pink circles represent clusters of victims who shared common paths. The light-green area is the actual plume released during a bioterrorist attack; yellow lines represent attempts to determine the dimensions of the plume based on observed medical information and the locations of the victims.

Semi-Automated Image Analysis

U. G. Goldstein, S. K. Sengupta

99-ERD-075

Although imagery has made invaluable contributions to map-making, the generation of spatial databases, and intelligence analysis, it has never been fully exploited. This problem is growing because the amount of imagery available is increasing and the number of analysts available to look at it is decreasing. A further complication is that advanced imagery systems, such as multispectral Landsat or Canadian Radarsat, require more sophisticated analysis than a simple visible-light image.

To address these shortfalls in imagery exploitation, there has been considerable interest in developing computer algorithms for image understanding (IU) so that the more routine imagery analysis tasks can be assigned to a computer. Although there have been some major successes in this area, a significant gap exists between these successes and what is actually being used.

This project seeks to find solutions to the image exploitation problem by matching promising IU research to national security applications, filling in research gaps, testing algorithms on real problems with real data, and working out man-machine interaction problems. Its goal is to provide proof-of-principle for new IU methods as applied to intelligence analysis and other spatially related national security problems while enriching the technology base at the Laboratory. During FY1999, we concentrated our efforts in two areas: (1) matching promising IU methods to real national security applications, and (2) researching the problem of finding vertical obstructions on monoscopic images.

We are building collaborations with leaders in this field. With Science Applications Incorporated (SAIC), we are exploring whether their automatic target monitoring (ATM) methods could be modified to help a weapons of mass destruction (WMD) image analyst prioritize imagery that he receives on a daily basis. We started this work by surveying the needs of WMD analysts, both at LLNL and at the National Imagery and Mapping Agency.

Finding vertical obstructions such as towers, buildings, and hanging wires is an important part of generating up-to-date maps or related spatial databases. It is also an integral part of the process of defining a knowledge base of all man-made structures on the face of the Earth. We addressed the problem of automatically detecting vertical obstructions by using methods derived from pattern recognition theory and morphological image processing. The dataset used for this research consisted of a set of synthetic aperture radar (SAR) images collected by Sandia National Laboratory with an aircraft-based sensor. Hanging wires approximated by low curvature parabolas were detected by a modified version of the Randomized Hough Transform. Towers, buildings, and other bright or dark objects were detected by clustering pixels in a feature space consisting of neighborhood statistics of pixels. Towers were localized from among the bright objects using their shape features. Possible locations of buildings were detected using the morphological features of their shadows obtained from clustering. A classified report will document this work and will be completed in FY2000.

Scientific Software Component Technology

S. Kohn, N. Dykman, G. Kumfert, B. Smolinski

99-ERD-078

We are developing software component technology for high-performance parallel scientific computing that will enable the rapid development of laboratory simulation software and the interoperability of scientific and mathematical software across the DOE complex. This essential new technology will address issues of complexity, re-use, and interoperability for laboratory software. Component technology enables cross-project code re-use, reduces software development costs, and provides additional simulation capabilities for massively parallel laboratory application codes. The success of our approach will be measured by its impact on DOE mathematical and scientific software efforts. Thus, we are collaborating closely with library developers and application scientists in the Common Component Architecture (CCA) forum, the Equation Solver Interface (ESI) forum, and other DOE mathematical software groups to gather requirements, write and adopt a variety of design specifications, and develop demonstration projects to validate our approach.

Numerical simulation is essential to the science mission at the Laboratory. However, it is becoming harder to manage the complexity of modern simulation software. For instance, several Laboratory code groups are currently exploring similar directions; there is no standardization—and thus no leverage—across the efforts. Software groups for the National Ignition Facility and for some national security programs are using common-object request-brokering architecture (CORBA) technology. One Accelerated Strategic Computing Initiative (ASCI) code team has developed its own component-like scripting language infrastructure based on Python and C++. Computational scientists develop complex, 3-D, massively parallel, full-physics simulations that require the integration of diverse software packages written by outside development teams. Currently, the integration of a new software package, such as a new linear solver library, can require several months of effort.

Current industry component technologies, such as CORBA, JavaBeans, and COM (Microsoft's standard component interface), have all been used successfully in the business domain to reduce software development costs and increase software quality. However, these existing industry component infrastructures will not scale to support massively parallel applications in science and engineering. In particular, they do not address issues related to high-performance parallel computing on ASCI-class machines, such as fast in-process connections between components, language interoperability for scientific languages such as Fortran, parallel data redistribution between components, and massively parallel components.

Since the mid-year start of this project in FY1999, we have focused on the needs of seamless language interoperability in a high-performance environment. Computational scientists are routinely hindered in code re-use by differences in programming languages: for example, a solver library written in C++ can be difficult to call from an applications code written in C or Fortran. Our approach adopts the industry practice of using an interface definition language (IDL) to describe component interfaces in a language-independent manner. We have developed an IDL for scientific applications (SIDL) that focuses on the unique needs of the scientific domain as compared to the business world. We have also created tools that use SIDL descriptions of software components to automatically generate language bindings and code that allows the component to be called easily from different languages.

As a demonstration project, we worked with the *hypre* team at LLNL, which develops scalable, high-performance linear solvers, to create Fortran bindings for their linear solver preconditioning library. Previously, because *hypre* did not support a Fortran calling interface, Fortran programmers did not have access to its advanced solver capabilities. In an afternoon, we were able to define SIDL interfaces for the *hypre* structured-grid preconditioning routines and generate the appropriate Fortran calling interface. Performance measurements on the ASCI Blue Pacific platform demonstrate that the overhead of our unique approach is less than a percent of the overall run-time.

In FY2000, we will continue to develop our component interoperability tools and focus on the needs of communication between distributed components running in different processor spaces. We will also provide language support for Python, a popular scripting language for scientific simulations at the laboratory. Finally, we will continue our collaborations with the CCA and ESI forums to help deploy our software component technology across the DOE complex.

SAVAnTS: Scalable Algorithms for Visualization and Analysis of Terascale Science

M. A. Duchaineau

We are devising multiple-resolution representations and algorithms that enable scientists to examine the results of large-scale scientific data with orders-of-magnitude higher efficiencies in speed and storage than with previous best practices. In stockpile stewardship, scientists make frequent computations, each involving thousands of processors producing terabytes of data, which overwhelms the disk drives, tape drives, and visualization processors devoted to the analysis of the output. Scientists studying climate change, waste repository safety, or molecular chemistry will soon face these same challenges. When developed, our methods could give scientists more efficient means to extract, store, retrieve, and display the most critical information they need.

To understand their data, scientists use information from dozens of variables—such as pressure, density, and velocity—which are typically defined on a grid covering some region of 3-D space for some period of time. We address the most critical and challenging extraction and display methods: looking at one variable at a time on a slice or volume projection, or looking at a variable as a color on a surface extracted from other variables, such as material-fraction interfaces or density contours. This focus leads to two essential enabling technologies: (1) wavelets for storing and retrieving slices and volumes, and (2) surface hierarchies for accelerating the display of extremely complex interfaces.

Our first research focus is in sparse wavelet transforms—methods whose work scales as the tiny output size rather than the high sampling density required in previous approaches. We combine this approach with similar speedups in the fundamental arithmetic coding step and selective-access data services (see figure). For one Accelerated Strategic Computing Initiative (ASCI) application, this led to a hundred-fold speedup of storage and slice display, and a hundred-fold reduction in data space for slice and projected-volume display, when compared to previous best practice.

Our second focus is on surface hierarchies, both in the fundamental representations and in fast algorithms for optimal display adaptation. Our new representations follow two distinct approaches: (1) an implicit, adaptive means of storing surfaces using sparse wavelet compression of the distance field of a surface, exploiting our success with volume wavelet methods; and (2) wavelets that explicitly store unstructured surface geometry, a difficult extension from traditional regular-grid wavelets. These representations promise efficient compression of surface data, and form the basis for our further developments in view-dependent optimization, where the best possible display grid is computed to adapt continuously to a scientist's changing point of view, potentially yielding two or more orders-of-magnitude speedups. In FY1999, we devised a testbed and began extending our theoretically optimal methods from a limited domain to the difficult surface morphologies in major LLNL applications.

In the fall of 1999, the SAVAnTS team collaborated on a LLNL effort that won the prestigious *Gordon Bell Prize*, a major award in supercomputing, at the *SuperComputing'99* Conference in Portland, Oregon. The LLNL team applied advanced compression and visualization techniques developed under the LDRD Program to enable full-detail, interactive analysis of the record-breaking Richtmeyer-Meshkov instability computation. The results were resolved with 64 times more numbers stored than the team had originally thought feasible.

The ultimate goal of this effort is fully optimized post-processing, storage, and display for the complete range of large-scale computational grids. While we have begun proving the basic concepts, two urgent challenges remain in order to meet the orders-of-magnitude gains needed by laboratory scientists. First, performance on highly adaptive volumetric grids must be increased ten-fold through adaptation of our sparse wavelet transform. Second, we must generalize wavelets and display optimization for the topologically complex scientific surfaces of the major laboratory applications, giving a hundred-fold speedup. Beyond these two goals for FY2000, the primary long-term challenge is time-dependent data, which requires fundamental advances in output-sensitive methods over the coming years.
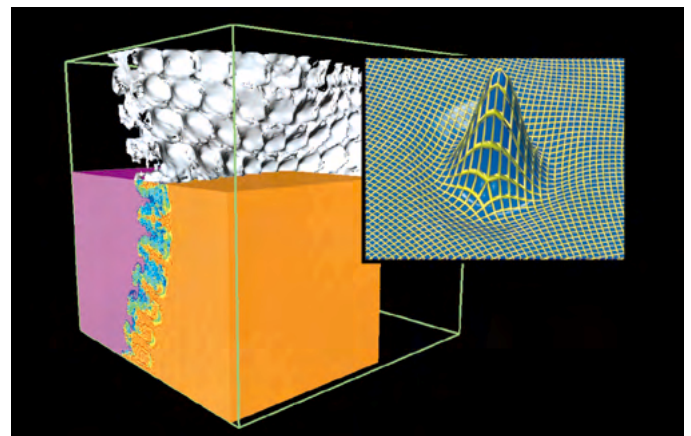
A novel wavelet for an irregular neighborhood (inset) is a building block for compression and display acceleration of large-scale data, such as this turbulence simulation.

Sapphire: Scalable Pattern Recognition for Large-Scale Scientific Data Mining

C. Kamath

99-ERI-010

Our ability to collect data through simulations, observations, and experiments far exceeds our ability to explore, analyze, and understand the data. This problem of data overload is becoming a serious impediment to the Laboratory's scientific advancement in areas as diverse as counterproliferation, the Accelerated Strategic Computing Initiative (ASCI), astrophysics, and climate modeling. To address this problem, we are developing a new generation of tools and techniques to automate the exploration and analysis of scientific data. We are developing scalable data mining algorithms for the interactive exploration of large, complex, multidimensional data sets. Our research enables Laboratory scientists to easily extract useful information from their data. For example, our work helps astrophysicists to look for galaxies of interest using objective, semi-automated techniques instead of a subjective, manual approach.

These data mining techniques that enable the semi-automated discovery of patterns, associations, anomalies, and statistically significant structures in data consist of two steps: (1) in *data pre-processing*, we extract high level features from raw data; and (2) in *pattern recognition*, we use these features to discover and characterize patterns in the data. Our focus is on image processing algorithms for extracting features from image data, and decision trees and neural network techniques for pattern recognition. Our research objective is to design and develop parallel algorithms and software that are scalable, robust, accurate, and interpretable. To demonstrate these techniques, we are collaborating with scientists at LLNL and the Institute of Geophysics and Planetary Physics (IGPP) to (1) identify galaxies with bent-double morphologies in the faint image of the radio sky at twenty centimeters (FIRST) data set, and (2) identify asteroids in the massive compact halo objects (MACHO) data set.

Our initial step in mining the FIRST data was to understand the problem and the data itself. Extracting relevant features was made easier by using the FIRST catalog, which contains information obtained by fitting 2-D Gaussians to each galaxy. After grouping the Gaussians that formed a galaxy, we calculated features representing the spatial relationship between them. These were input to a decision tree algorithm that was trained using examples of known bent and non-bent doubles. When this decision tree was applied to galaxies with unknown morphology, it found several bent-doubles. More importantly, it found at least one bent-double that was overlooked during a manual search of part of the data, revealing the true potential of data mining techniques (see figure). These bent-doubles that were found using the decision tree were validated by the astronomers on the FIRST project.

We designed the Sapphire system architecture to address the diverse data mining needs of Laboratory scientists. For example, not all applications require the entire data mining process, and different algorithms work well on different data sets. We must handle growing data sets from different domains while ensuring portability of our software across various machines. Our algorithms are designed using object-oriented techniques. Each class of algorithms, developed as a library, is linked using the scripting language Python. Intermediate data are stored in a database to allow simple queries. Parallel implementation is done using the message passing interface (MPI) and OpenMP standards to ensure portability.

We surveyed several approaches for scaling image processing and decision trees algorithms, collected a list of requirements, and are currently designing our software. We investigated ways to extract robust features that are invariant to scaling, translation, and rotation. We showed that thresholding of wavelet coefficients is an effective tool for de-noising image data. Our software design includes several wavelets, threshold selectors, and de-noising policies.

In FY2000, we will complete the design of parallel image processing and decision tree algorithms, implement key parts to investigate scalability issues, refine the detection of bent-doubles, and work on the MACHO data set and neural network algorithms.
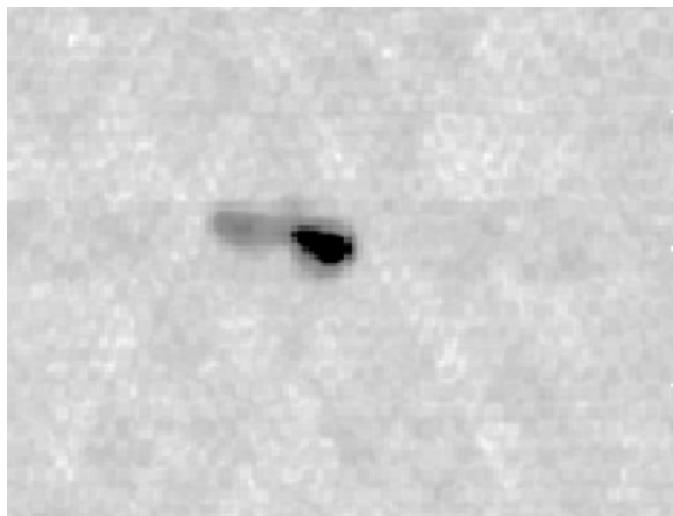
A bent-double galaxy that was overlooked in a manual search, but detected using data mining techniques

Modeling and Simulation for Critical Infrastructure Protection

J. C. Smart, D. E. Sackett, R. R. Johnson, T. G. Brandt, B. E. Anderson, R. G. Hartley, K. J. SooHoo, S. E. Gentry, E. W. Wheelock

99-SI-005

With the rapid growth of global computing and communications, information assurance is a crucial underpinning of United States national security strategy and of the security at DOE facilities. To address this important issue requires the ability to predict, recognize, and react in real time to potential intrusions. This gives rise to a number of complex technical challenges, including automated characterization of computer networks, modeling of networks, analysis of network structure, identification of vulnerabilities, simulation of network behavior, and assessment of the consequences of intrusions.

Our objective in this project is to develop a modeling and simulation environment for the Information Operations, Warfare, and Assurance (IOWA) environment. IOWA was created at LLNL to determine how information systems may be vulnerable to intrusion, what actions can be taken to successfully defend against these intrusions, and what are the consequences of such intrusions if they do occur. The figure shows the IOWA tool set.

In FY1999, we focused on (1) mapping LLNL's Open LabNet as a pilot use of IOWA's tools and utilizing the results to better understand network behavior, (2) simulating network behavior and analyzing the sensitivity of this behavior to various parameters, (3) simulating the dependencies between Internet protocol (IP) networks and other infrastructure systems and the resulting vulnerabilities, and (4) beginning a cost-benefit analysis of various computer security measures.

In our Open LabNet mapping effort, we have collected a great deal of information about LLNL's unclassified network and how it interacts with the Internet. For example, we found that (1) within a 2-week period of listening to traffic going in and out of LLNL, we can identify almost all the 12,300 hosts that regularly communicate with external systems; (2) within a 1-week period, we can identify over 90% of these 12,300 hosts; (3) about 2,500 hosts on Open LabNet do not normally communicate outside but respond to an outside probe; and (4) about 75% of LLNL's network messages represent World Wide Web interactions.

When assessing power-distribution and other supervisory-control and data-acquisition (SCADA) systems (these are telecommunications, processing, and monitoring infrastructure systems), we found that these systems are very manually oriented and that the dependencies on IP networks are fewer than expected. Therefore, we have focused our network-simulation effort on verifying the IP network simulation and on isolating critical parameters to which network behavior is very sensitive. The results of this in-depth study are being documented.

Statistics from LLNL, DOE, and other organizations are helping to develop heuristics to predict types and frequencies of computer intrusions. We collected data to use in estimating probable damage from these intrusions, and we are using this information to better characterize the trade-offs related to implementing computer security measures for a particular organization.

We also completed a proof-of-concept demonstration showing the relationships and interdependencies of a computer network and a power-distribution system.

A primary focus of our FY2000 activities will be on characterizing vulnerabilities and potential intrusion scenarios; preliminary analysis has already determined a highly promising approach to this complex problem. We will also be working with Stanford University's Knowledge Systems Laboratory to develop a set of ontologies to accurately characterize vulnerabilities and the pre- and postconditions of exploitations of the vulnerabilities. (An ontology is a knowledge representation that can be manipulated with inference engines and other tools customized for our purposes.) We will attempt to tie the representation and inferencing capability in with a rule-based intrusion-detection approach and with our unique network-characterization technology. We believe our work will provide the next major leap in vulnerability characterization and intrusion-detection technology. We will also continue to characterize and generalize LLNL's network.
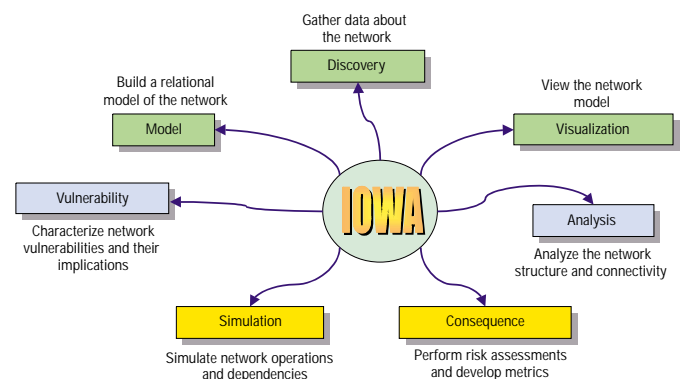
Architecture diagram of the IOWA integrated tool suite. This model uses integrated graphical and relational-database representations to enable high-performance visualization, analysis, and information retrieval.

Energy and Environmental Technologies

5
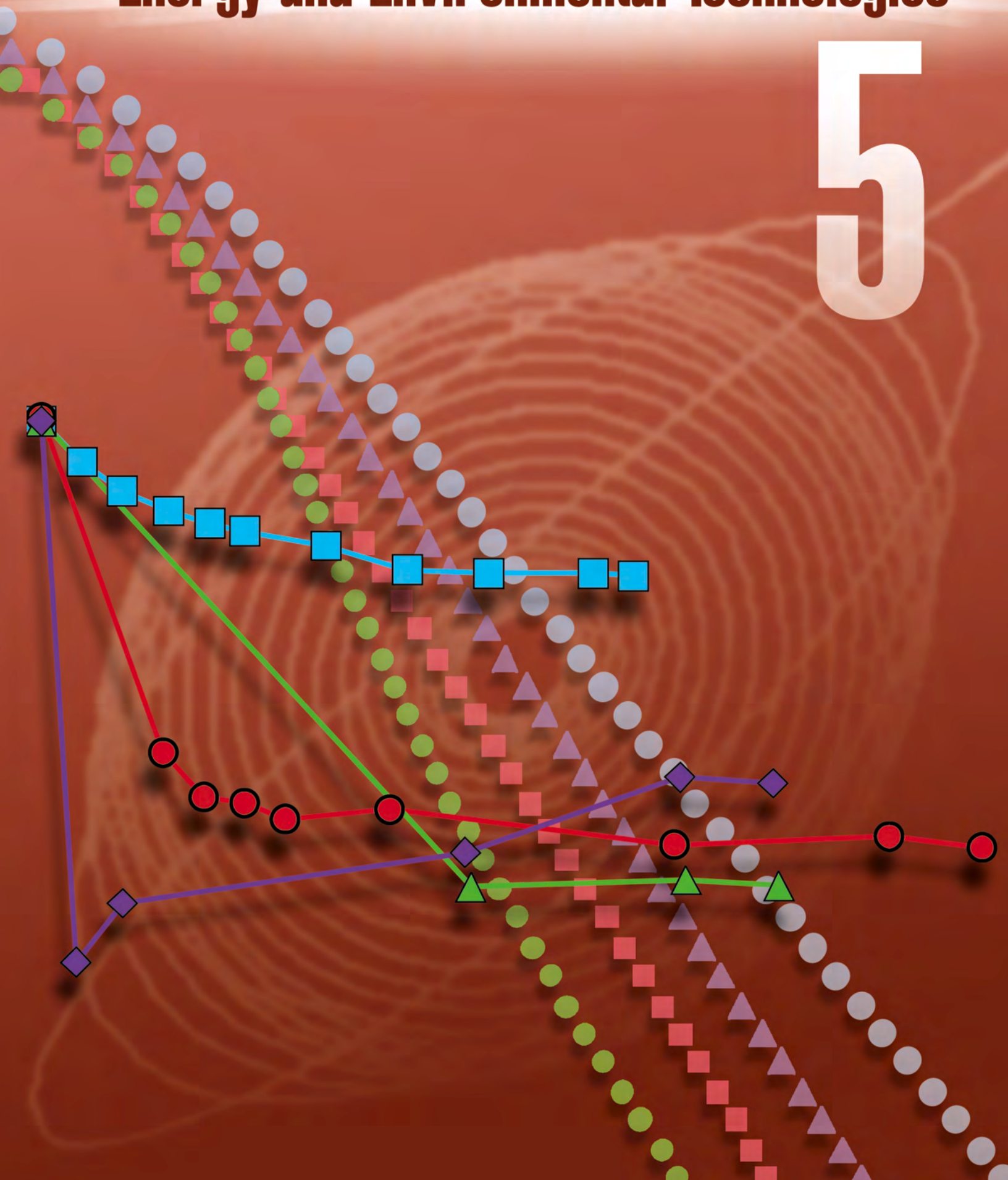
Energy and Environmental Technologies

Optimization and Monitoring of an In-Situ Biodegradative Process

A. M. Happel, J. M. Horn, T. C. Legler, S. R. Kane

97-ERD-030

Trichlorethylene (TCE) is a widely used industrial solvent that has contaminated numerous groundwater sites, including those at LLNL. The presence of TCE in drinking water represents a public-health hazard because of its toxicity and suspected carcinogenicity. Methanotrophs—bacteria found in subsurface environments that use methane for carbon and energy—contain soluble methane mono-oxygenase (sMMO) enzymes that have a very broad substrate specificity. That is, sMMO catalyzes not only the conversion of methane to methanol, but also oxidizes TCE, forming an epoxide that eventually degrades to carbon dioxide. Methanotrophs have been shown to have the highest rates of TCE oxidation in comparison to bacteria with alternative TCE oxidative enzyme systems—which degrade TCE at only one-fiftieth the rate.

In this study, we have been investigating the control of sMMO synthesis in two methanotrophs, *Methylosinus trichosporium* OB3b and *M. sporium*, with the goal of optimizing its production to better utilize this enzyme for in-situ remediation of TCE at polluted sites. In particular, we have studied the effect of growth substrate (methane vs methanol) and growth phase on sMMO production and TCE degradation. We grew cells on methane or methanol, harvested them at different growth phases, and assayed for TCE degradation. In addition, we evaluated the regulation of sMMO production by analyzing the amount of sMMO messenger RNA (mRNA) produced under various growth conditions.

We found that TCE degradation rates were increased when cells were transferred through several batch cultures grown on methane. In general, *M. sporium* showed slightly higher degradation rates than *M. trichosporium* OB3b at similar phases of growth. Comparable rates of TCE degradation were observed for methanol-grown cells, even though sMMO is not required for growth on methanol. Furthermore, analysis of sMMO gene expression showed a similar trend to TCE degradation assays: signals corresponding to the presence of sMMO mRNA were observed for cells grown on methanol as well as for cells grown on methane.

These findings imply that both methane and methanol can be used as growth substrates for production of sMMO. Methanol offers the advantage of simple and cost-effective in-situ application to encourage the production of sMMO (and subsequent TCE degradation). Methane gas, on the other hand, is more difficult and costly to apply in subsurface environments. Initial studies showed that the strains grew on low concentrations of methanol (0.001%) and were not inhibited in their ability to degrade TCE at these methanol concentrations. Therefore, it may be possible to feed subsurface methanotrophic populations on low levels of methanol and enhance TCE degradation in situ.

In FY1999, we developed monitoring techniques for sMMO production that will allow biodegradative enzymatic activities to be directly measured in situ. We fused green fluorescent protein (GFP)—a "reporter gene" whose product is easily measured—to the genetic regulatory region of the sMMO genes. GFP was placed under the same genetic control as sMMO; thus, under conditions where sMMO is expressed, the reporter-gene product, GFP, is produced. GFP can be directly measured online, nondestructively, and in real time using fluorescence spectroscopic methods. Using this system, the expression of sMMO can be followed by measuring the production of light from the fused GFP–gene product. Alternatively, individual cells may be visualized by fluorescence microscopy.

We constructed reporter strains in both methanotrophic strains; at year's end, we were evaluating these strains for their response to various potential inducers and inhibitors of sMMO production.

Methanotroph cells containing the GFP reporter gene will be useful for (1) further investigating the regulation of sMMO production; (2) evaluating environmental conditions favorable for sMMO production; and (3) monitoring and quantifying TCE degradation in subsurface, field applications.

Neptunium Solubility: Kinetic or Thermodynamic Control

T. J. Wolery, C. E. A. Palmer, K. E. Roberts

97-ERD-047

The Department of Energy (DOE) is pursuing the establishment of a permanent disposal site for high-level nuclear waste at Yucca Mountain, Nevada. The potential future radiation dose to humans is a key consideration. Neptunium (Np) concentrations observed in short-term experiments yielded calculated doses in excess of proposed regulatory limits. Though the actual regulatory limits (yet to be adopted) may apply to only the first 10,000 years, a longer-term safety hazard is nonetheless implied. However, short-term data may grossly exaggerate the long-term reality in an actual repository by ignoring the role of certain insoluble Np solids that may form only at very slow rates.

Thermodynamic data at 25°C show that experimentally observed, approximately 10^{-3} M Np(V) concentrations at pH 6 are supersaturated with respect to solid NpO_2. However, the observed solids were Np(V) solids, both $NaNpO_2CO_3$ and Np_2O_5. Thermodynamic calculations confirmed equilibrium with these phases, but cannot show why NpO_2 was not obtained instead. The reaction that should occur shows NpO_2+ (the principal dissolved Np species) reacting with water to produce solid NpO_2, molecular oxygen, and protons.

We have been testing the hypothesis that NpO_2 is slow to form on the time scale of the earlier experiments by studying the precipitation of NpO_2 at higher temperatures, where rates should be faster—as implied by the concept of the Arrhenius activation energy. Under these conditions, the formation of this solid should be observable.

During FY1997 and FY1998, we conducted solubility experiments at elevated temperature and analyzed our results. In FY1997, after two weeks of reaction time at 200°C the aqueous Np(V) concentration decreased, and a small amount of precipitate was collected. During FY1998, we analyzed the solids by x-ray powder diffraction (XRD) and conducted additional solubility experiments in which we monitored the aqueous Np concentration over time. The solids from these experiments, analyzed by XRD, x-ray absorption spectroscopy (XAS), and scanning electron microscopy (SEM), were identified as crystalline NpO_2. This was the first time that crystalline NpO_2 had been observed to precipitate from an aqueous solution of Np(V). Changes in pH correlated, as expected, with the changes in dissolved Np.

During FY1999, we conducted additional solubility experiments at 200°C to investigate the effect of pH on the precipitation of solid NpO_2 from aqueous solution. After a few months of reaction time, we observed steady-state pH values (ranging from 4 to 9) and significant decreases in the aqueous Np concentrations. The latter are shown in Fig. 1(a) as a function of time. Solids were collected from each of the experiments and analyzed by XRD. In all cases, the solids obtained were identified as crystalline NpO_2 [see Fig. 1(b)].

Our hypothesis is that a rate law very similar to that for silica (SiO_2), controls the growth rate of NpO_2. The rate would depend mainly on the surface area of the precipitate and the concentration of $Np(OH)_4(aq)$, a form of Np(IV). Our experiments were conducted under oxidizing conditions, so nearly all the Np in solution was the NpO_{2+} species (or at higher pH, one of its complexes). However, there was a very small amount of Np(IV) species in equilibrium with the Np(V). This implies that the rate will increase with increasing Np(V) and increasing pH and, to a lesser degree, with decreasing oxygen fugacity. The predicted effect on the rate of increasing pH is quite evident in Fig. 1(a).

Precipitation of NpO_2 should occur at low temperatures over very long times, thus leading to significantly lower aqueous Np concentrations and eliminating any long-term dose problems due to Np release from a waste repository.

Figure 1. Results of elevated-temperature experiments designed to test the hypothesis that NpO_2 would be slow to form at ambient temperatures: (a) aqueous Np concentrations as a function of time in solubility experiments conducted at 200°C, and (b) representative x-ray powder-diffraction pattern of our precipitated solid NpO_2 and the reference NpO_2 pattern.
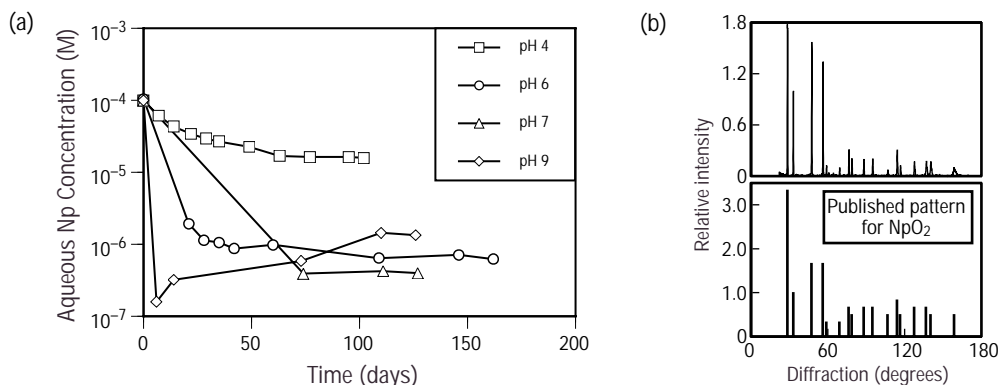
A Study of the Basic Properties of Gas Hydrates and Kinetics of their Formation, with an Emphasis on Methane Clathrate

W. B. Durham

98-ERD-008

Gas hydrates (clathrates) are compounds with an ice-like crystalline framework that encages "guest" gas molecules, and methane clathrate is the most commonly occurring gas hydrate in nature. Although it has several potentially important applications related to its extraordinary properties and widespread presence in Earth's near-surface environment, methane hydrate has received only occasional and unsystematic laboratory investigation in the several decades since it was discovered. Our project integrates recent research breakthroughs with our current expertise and capabilities to advance our general knowledge of the synthesis, basic properties, and behavior of gas hydrates—particularly methane clathrate. Our improved understanding of this material will position the Laboratory to play a significant role in serving the nation's future environmental and energy needs. In FY1999, we made important progress at LLNL's experimental geophysics laboratory and in our coinvestigator's laboratory at the U.S. Geological Survey in Menlo Park, California.

We discovered that methane hydrate is an exceedingly strong material compared to water ice, which is often taken as a model for the hydrate. The strength difference with respect to ice is a factor of roughly 20. To put this into perspective, the strength contrast between hydrate and water ice is approximately the same as that between stainless steel and hydrate. Because water ice is often found as a contaminant in hydrate samples, the extreme strength contrast presented a challenging experimental problem, and required us to take extraordinary steps to remove water from the samples.

In our continuing studies of hydrate metastability, we established that the "anomalous preservation" that occurs when the hydrate is depressurized can continue for a very long time—up to 24 hours or more—if depressurization takes place at temperatures just below the melting temperature of water ice. If there is a possibility of exploiting hydrates as an energy resource, we obviously will have to deal with the matter of extraction of the gas phase. In particular, we will need to find combinations of pressure and temperature change that do not encounter severe anomalous preservation. We have also now documented the breakdown of hydrate (to water plus methane gas) at temperatures above 0°C, where we see signs of formation of an intermediate phase, which may help us understand the anomalous preservation effect.

In addition, we completed an exhaustive series of measurements of sonic wave speeds (both shear and compressional) of methane hydrate using an apparatus built during the first year of the project. For the fully dense material, our measurements have now allowed publication of the first full set of elastic parameters for methane hydrate. We also measured the effect of porosity on wave speeds, establishing that measurement as a probe of a state of the hydrate in the lab and possibly in the field as well.

Finally, we performed the first measurements of thermal conductivity on pure methane hydrate, and completed construction and testing of an experimental configuration for measuring thermal diffusivity of hydrate at elevated pressure. Both measurements are still at the preliminary stage. We carried out the conductivity measurements at low confining pressure, and the samples were therefore somewhat porous. The next step is to put the samples under elevated pressure so that we can observe the intrinsic value of thermal conductivity. We successfully tested the diffusivity apparatus with a pure ice sample; it is now ready for hydrate measurement.

In FY1999, we presented our findings at the *3rd International Conference on Gas Hydrates* and published our results in two journals, *Energy & Fuels* and the *Journal of Physical Chemistry B.*

High Power Density Solid-Oxide Fuel Cells

A. Q. Pham, B. Chung, R. S. Glass

98-ERD-031

A solid-oxide fuel cell (SOFC) is a solid-state electrochemical device that converts the chemical energy in fuels directly into electricity. Since they are not limited by the Carnot cycle, SOFCs can have energy efficiency as high as 60%, or even more than 80% when used in combination with gas turbines. The SOFCs can operate on a variety of fuels without an expensive external fuel reformer, yet they generate very low emissions; thus, they are an attractive option for clean and efficient power generation for the 21st Century. However, despite many successful demonstrations by Siemens-Westinghouse, the SOFC commercialization is still not envisioned for the near future because of excessively high fabrication costs. In this project, we are developing high-performance, low-cost SOFCs. Our strategy is based on the development and demonstration of low-cost thin film processing techniques and on the optimization of the material and stack designs to increase fuel cell power density.

Lower operating temperature has been recognized worldwide as the key point for low-cost SOFCs because cheap alloys can then be used as interconnect materials instead of the expensive all-ceramic components. In order to lower the operating temperature without compromising the fuel cell power density, it is necessary to decrease the cell resistance by using thin-film

technology. Previously, we successfully developed a novel low-cost thin-film deposition technique, for which we filed a U.S. Patent. This technique is very simple, yet highly versatile, and can produce high quality thin films of thickness ranging from one to several hundred microns.

In FY1999, we focussed on developing and optimizing the remaining components of the fuel cell, i.e., the anode, the cathode, and the interconnect. Our goal was to demonstrate power density of 1 W/cm^2 at 800°C. Using the multilayer-graded electrolyte developed earlier, we have been able to incorporate a high performance cathode, $La_{0.6}Sr_{0.4}Fe_{0.8}Co_{0.2}O_3$, in the cell. Such a structure is not possible with conventional single-component electrolyte layer based on yttria-stabilized zirconia (YSZ) because of the chemical incompatibility between YSZ and the present cathode material. The multilayer cell showed a significant decrease in electrical loss when compared to conventional cells.

Using a three-electrode-polarization technique, we identified that the performance of the current fuel cell anode is limited by the removal of water vapor produced by the anodic reaction. We then developed a bilayer anode structure with a thick, highly porous layer covered by a thin layer. The former serves mainly as support structure for the whole cell, and the high porosity allows an easy water removal. The thin layer is the actual active component for the electrochemical anodic reaction. The overall cell is thus an all thin-film system on a porous support.

The figure shows the electrochemical performance of the optimized cell with the new cathode and anode structures. Using humidified hydrogen as fuel, a high power density of 0.92 W/cm^2 has been obtained at 800°C. For comparison, the Siemens-Westinghouse fuel cell has a power density less than 0.3 W/cm^2 at 1000°C. Under certain favorable conditions, power density close to or even higher than 2 W/cm^2 has been observed. However, it is unlikely that such a high power density can be maintained in a fuel cell stack.

In FY2000, we plan to build a 50-W prototype fuel cell stack. To date, we have only single cells that deliver a few watts output at most. We will also continue to optimize the fuel cell components.
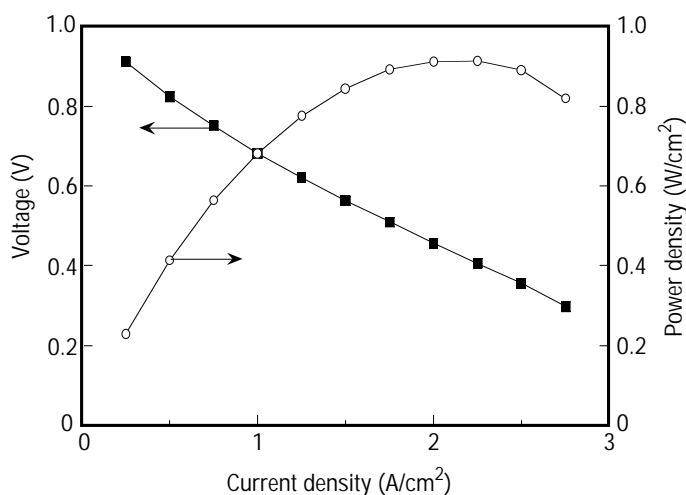
Electrochemical performance of a thin-film solid-oxide fuel cell operated in air/hydrogen at 800°C.

Stability Issues in Passive Magnetic Bearings: Experimental Tests

R. F. Post, D. D. Ryutov, W. H. Kent, D. L. Podesta, M. G. Fowler

Work performed over the last several years at the Laboratory has resulted in the invention of a new type of magnetic bearing system: the ambient-temperature passive magnetic bearing. When fully developed, such bearings could find many important applications in our nation's technology. While the principles on which these bearings operate have been thoroughly proven both theoretically and experimentally, certain practical issues must also be addressed if these bearings are to be employed in general applications. Foremost among these problems is that of ensuring that rotor–dynamic instabilities can be controlled in situations of practical interest.

Our goal during FY1999 was to elucidate important aspects of this issue, through extension of the theory and through the design and construction of test stands that could be used to measure the critical constants of bearing elements. These critical constants could then be inserted in the theoretical equations that define the conditions for avoiding the onset of rotor–dynamic instabilities.

The main instability that is of concern here is the so-called "transverse whirl" instability, one which is stimulated by displacement-dependent drag forces that may act on the rotating body being levitated by the passive bearing system. By "displacement-dependent drag force" there is meant any situation where a transverse displacement of the rotating body results in an increased drag on the leading side of the displacement, with an accompanying decreased drag on the following side. The result is a net force on the center of mass that stimulates an exponentially growing whirling motion of the center of mass. (Squealing, poorly lubricated bearings in rotating machinery are a common symptom.) Displacement-dependent drag forces can arise either from the passive bearing elements themselves or from exterior sources, such as aerodynamic-drag forces. If drag increases nonlinearly with the displacement, then a new situation can arise—one in which the system is stable only for a limited range of displacements. However, beyond that limit instability sets in, and the displacement grows "explosively" (i.e., more rapidly than exponentially). This situation must be understood theoretically, so that it can be predicted and overcome.

In pursuit of these, during FY1999 we built a test to measure the velocity-dependent damping coefficient of eddy-current-type dampers and took measurements over a wide range of velocities and damper-plate thicknesses. We observed a nonlinear effect that we believe should be incorporated in stability analyses. We also built a test to measure the displacement-dependent drag of permanent-magnet bearing elements. In measurements performed with two annular magnets in the attractive mode, we found that the drag force was far less than predicted by an over-simplified theoretical estimate.

Following our analysis, we also set up and solved numerically the nonlinear differential equations describing the center-of-mass motion of a rotor suspended by passive magnetic elements with given characteristics. A result (that we believe to be new) is that we can now show directly and quantitatively the effect of anisotropic bearing stiffness in limiting the onset of "explosively" growing rotor-dynamic instabilities. Figure 1 illustrates this effect: Fig. 1(a) shows an unstable case; in Fig. 1(b), the system has been stabilized by the introduction of a small amount of anisotropy into the bearing system.

In FY1999, a follow-on patent on our passive bearing was issued, and our passive magnetic bearing concept was selected by *Popular Mechanics* for a "2000 Design" award.
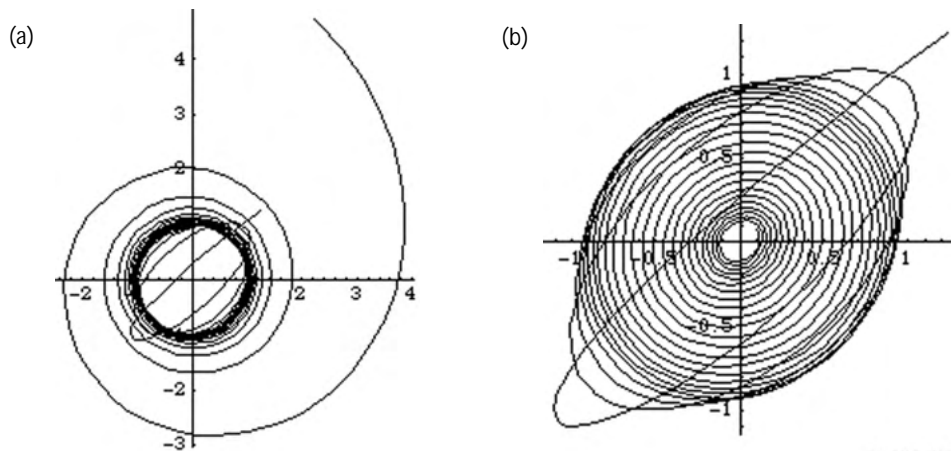
Figure 1. Effect of anisotropic stiffness in stabilizing a nonlinear transverse whirl instability, for example, as it could be encountered in a magnetically suspended rotor: (a) the center-of-mass motion of the rotor is seen to be unstable beyond a critical amplitude, and (b) the motion has the same initial amplitude, but it has been stabilized by introducing an anisotropy of 2% into the bearing stiffness (note change of amplitude scale between the two graphs).

Evaluation of Electro-Osmotic-Aided Remediation of Dense, Non-Aqueous Phase Liquid Contaminated Aquitards

T. Pico, N. Cherepy, A. Elsholz, R. Ruiz, D. Wildenschild

98-ERD-038

We are developing a technology base to address a major environmental problem at DOE sites, DoD facilities, and industrial sites across the U.S. and around the world: groundwater contamination by chlorinated solvents. Cleanup of aqueous-phase contaminant plumes in ground water is limited by our inability to remediate fine-grained soils in the contaminant source areas. These contaminated fine-grained soils become secondary sources of contamination, slowly diffusing dissolved contaminants into adjacent high-permeability zones. This diffusion extends the time to reach cleanup standards that prevents site closure.

Electro-osmotic-aided remediation is the only known technology that shows promise for cost-effective and efficient remediation of chlorinated solvent contamination in fine-grained sediments. When an electrical potential is applied across a saturated soil mass, cations, positively charged ions that are present in quantity at the negatively charged clay surface, are attracted to the cathode, or negative electrode. As the cations migrate, they carry their water of hydration and dissolved contaminants toward the cathode. This electric field-driven movement of a liquid phase through a porous matrix is called electro-osmosis.

Currently, the restoration strategy for removal of chlorinated solvents from deep (~100 ft) fine-grained soil zones at LLNL is the combined deployment of pump and treat technology and electro-osmotic pumping. This LDRD project focuses on (1) assessing the effectiveness of electro-osmotic pumping on contaminated soils, (2) optimizing processing conditions, and (3) rapidly screening contaminated soils for applicability of electro-osmotic-aided remediation prior to deployment. Bench-scale tests provide the site-specific information needed for effective and cost-efficient deployment of electro-osmotic-aided remediation.

During FY1999, we developed an LLNL-designed bench-top cell to study electro-osmotically induced flow, hydraulically induced flow, electrical currents, and voltage distributions in soil cores. We simulated in-situ conditions by subjecting the core to a confining pressure matching the underground stresses of its original location. Presently, we are measuring electro-osmotic and hydraulic conductivity on soil cores taken from a field site at LLNL, where pilot-scale electro-osmotic pumping feasibility tests are in progress. Figure l(a) shows hydraulic conductivity measurements (kh) of a clay core yielding kh = $2.15 \pm 0.35 \times 10^{-10}$ m/s. Figure 1(b) shows the electro-osmotic conductivity, ke = $0.94 \pm 0.28 \times 10^{-9}$ m^2/s–V. Therefore, under a potential gradient of 1 V/cm, the equivalent hydraulic conductivity of this sediment is 1×10^{-7} m/s, about 500 times greater than without an imposed electric field. Further advantages of electro-osmotic pumping include (1) electro-osmotic flow preferentially passes through finer-grained, clay zones, due to their high electrical conductivity; and (2) flow is directed along the electric field lines allowing easy collection of pumped water. Power efficiency improves with slower processing; electro-osmotic pumping on this core at 1 V/cm requires 0.15 kWh/L pumped, while 3 V/cm will increase flow rate by a factor of 3, but energy use climbs to 1.4 kWh/L.

During FY2000, we plan to study soil dynamics during electro-osmotic pumping, such as changes in resistivity and structure, as well as electro-osmosis mass removal efficiency from contaminated cores. We will also explore a variety of enhancement technologies including pH and ionic strength control, surfactants, and steady-state vs pulsed voltage loading. We will develop reactive transport simulation software to aid in establishing relationships between macroscopic flow and microscopic surface interactions based on input soil characteristics, electrical gradients and geometries.
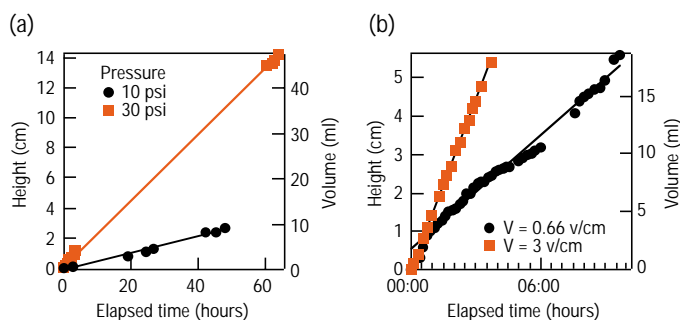
Figure 1(a) shows hydraulic conductivity of a soil core from a sediment zone 120 feet below surface; (b) shows electro-osmotic conductivity of same core.

MEMS-Based Fuel Cells for Micropower Conversion

J. D. Morse, A. F. Jankowski

98-ERD-091

We have been developing a new, miniature fuel cell that is based on an LLNL-developed technology that combines thin-film expertise with microfabrication and microelectromechanical systems (MEMS). This fuel cell offers a highly compact, lightweight, long-lasting power source with high specific energy compared to existing battery technologies. It would be scalable over a broad range, easily recharged, and compliant with all environmental and safety requirements.

During FY1999, we concentrated on demonstrating the fabrication and initial operation of both solid-oxide and proton-exchange membrane (PEM) electrolytes in fuel cells that were monolithically integrated on silicon chips having micromachined manifold systems. In developing the fabrication process, we addressed several issues associated with the integration and performance of a fuel-cell stack, micromachined fuel manifold, and flow-field structure. We did this by using photolithographic and etching techniques to create a thin-film, porous-anode structure and then micromachining silicon to form a free-standing fuel-cell membrane. Using comparable means, similar structures were formed in the cathode layer. The porous electrode structures enable the rapid diffusion of fuel and oxidant through the electrode structures to the electrolyte interface, as well as the exhaust of reaction byproducts (water).

To enable manifolding of fuel and oxygen to the anode and cathode, respectively, we constructed a test fixture to position the entire assembly in a furnace. Thus, the fuel-cell structure on the micromachined silicon chip was mechanically stabilized as the temperature increased. We measured the performance of the fuel cell by sweeping the voltage applied across the electrodes and measuring the current drawn from the power supply. The current–voltage characteristics for both PEM and solid-oxide fuel cells at various temperatures of operation were measured using dilute hydrogen fuel.

The PEM thin-film fuel cell was tested over the temperature range from 50 to 90°C, with a cell overpotential being exhibited at room temperature. The resulting output current–voltage characteristics are illustrated in Fig 1(a). The overall shape of these curves is typical for PEM fuel cells. The low current output is partially a result of using dilute (4% hydrogen in argon) fuel. This is the first demonstration of a monolithically integrated PEM fuel-cell structure.

Perhaps more compelling is the operation of a solid-oxide, thin-film fuel cell over the temperature range 250 to 320°C. The solid-oxide fuel cell (SOFC) had a porous nickel anode, an yttria-stabilized zirconia electrolyte, and a silver cathode, all deposited using vacuum sputter-deposition techniques. The free-standing SOFC membrane was tested using dilute (4%) hydrogen fuel; the result was the lowest operating temperature reported to date for a solid-oxide fuel cell. The resulting current–voltage characteristics are illustrated in Fig. 1(b). This low temperature is the advantage offered by utilizing thin-film components for the electrode and electrolyte materials.

In FY2000, we plan to fabricate and evaluate additional electrolyte materials, fabricate manifolding systems with a substrate that will deliver hydrogen-based fuel from a common reservoir to electrode–electrolyte membranes, and evaluate fuel storage and delivery systems.
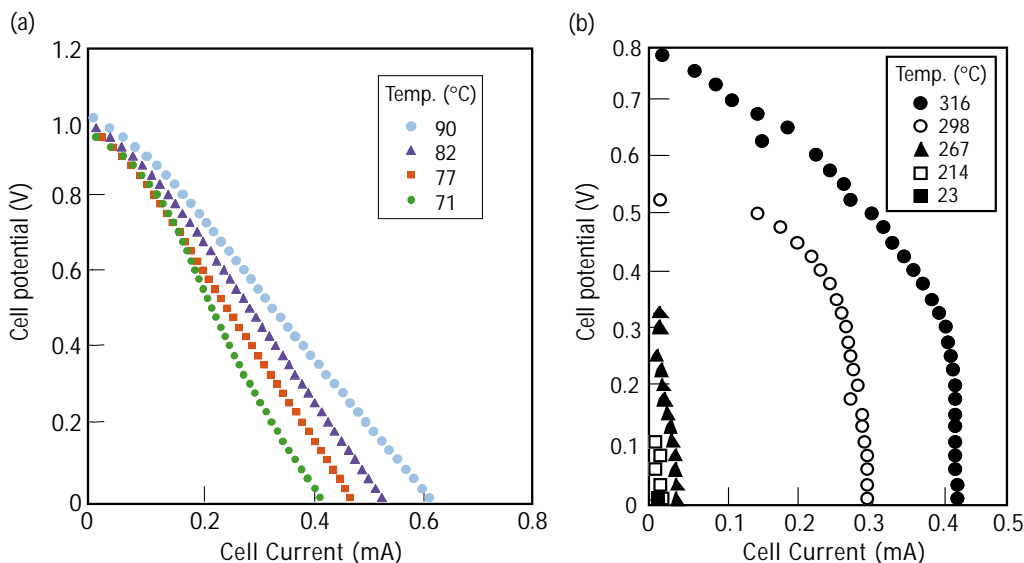
Figure 1. Output current–voltage characteristics for a (a) proton-exchange membrane (PEM) fuel cell, and (b) solid-oxide fuel cell (SOFC).

Chemical Aspects of Actinides in the Geosphere: Towards a Rational Nuclear Materials Management

P. G. Allen, E. R. Sylwester

98-ERD-094

This research project focuses on developing actinide x-ray absorption spectroscopy (XAS) to complement existing LLNL core capabilities for studying actinide environmental chemistry. Synchrotron-based XAS is an element-specific, in-situ structural probe that determines the oxidation state and local structure of metal atoms in non-crystalline systems. It is particularly useful for characterizing the chemical form or speciation of actinide elements (U, Np, and Pu) in complex environmental matrices. Since an element's speciation directly dictates physical properties such as toxicity and solubility, this information is critical for evaluating and controlling the evolution of actinides through the environment. Specific areas within DOE nuclear and environmental management programs where speciation is important are (1) waste processing and separations; (2) wasteform materials for long-term disposition; and (3) aqueous geochemistry. Because of its non-invasive and species-selective approach, XAS can provide information on the environmental fate and transport of actinides, which is unattainable by other analytical methods. As a result, XAS is a vital characterization tool for basic research on actinide materials.

Our approach has been to design and implement actinide XAS instrumentation and to demonstrate, evaluate, and improve the capability through specific actinide experiments that are applicable to research areas within DOE and LLNL (i.e., Yucca Mountain, Pu disposition). During FY1999, we successfully performed XAS experiments for Np sorption on cementitious materials, U sorption on geologic materials, Pu complexation with chelating agents, and actinide metal alloys. In addition to improving our knowledge on the chemistry of actinides in the environment and nuclear materials, the results of this work are serving to refine the actinide XAS methodology for more general use.

In the area of Np sorption on cementitious materials, concrete structures will be present in significant amounts in the proposed nuclear waste repository at Yucca Mountain. Over the long term, leaching from waste forms may lead to actinide interactions with the surrounding cementitious materials. As a result, it is important to understand the nature and level of interactions of actinides with these materials in order to evaluate, predict, and control transport. During FY1999, we investigated the behavior of the Np(V) ion in the presence of these materials using XAS. We performed measurements at the Stanford Synchrotron Radiation Laboratory (SSRL) by probing the Np L_{III} absorption edge for Np-loaded cement samples in-situ. We observed strong interactions with the cement materials, suggesting that the concrete structures will act as an additional barrier to actinide migration at high pH. In addition, we observed a chemical reduction of Np(V) to Np(IV) over time. Since tetravalent Np species are significantly less soluble than pentavalent Np species, this may be a fundamental controlling condition for decreased mobility of Np within the repository.

We also addressed U sorption on alumina, silica, and montmorillonite. With respect to migration in the far field, actinide ions may have the propensity to interact with certain minerals and clays. During FY1999, we studied the behavior of the hexavalent uranium species, UO_2^{2+}, in the presence of SiO_2, Al_2O_3, and the alumino-silicate clay mineral montmorillonite. Experiments were performed on U-loaded wet mineral samples under acidic and near-neutral pH conditions. Depending on the pH and ionic conditions, U L_{III}-edge XAS experiments determined the presence of mononuclear surface complexes (inner sphere), ion-exchanged (outer-sphere) surface complexes, and surface precipitated solids. Due to the different binding characteristics (both kinetic and thermodynamic), the identification of such species using XAS as shown in the figure is crucial from a mechanistic standpoint for accurately modeling the migration of actinide species in the environment.

In FY2000, we plan to continue our development of the actinide XAS capability using a custom designed Ge x-ray fluorescence detector. The systems we plan to investigate include (1) U and Pu in zirconolite ceramic waste forms for high level waste disposition, and (2) Pu adsorbed on colloidal silicate minerals representative of systems found in the vicinity of the Nevada Test Site. Determining the oxidation state and structure of the actinides elements in these systems is crucial for understanding their fate and transport in the environment.

Principal mechanisms of actinide sorption at mineral surfaces. Outer sphere is an ion-exchange process, whereas inner-sphere involves formation of chemical bonds.
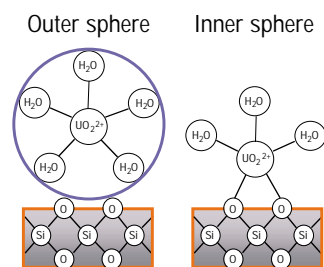
Mechanisms of Entry for Inhaled Metals into the Central Nervous System

G. Bench, P. G. Grant, J. L. Lewis, T. Carlsen, J. Woollett, K. Divine

98-ERI-004

DOE sites requiring environmental restoration are characterized by various mixtures of inorganic and radionuclide constituents, some of which present human health risks. However, risk evaluation is hindered to the extent that environmental exposure conditions deviate from controlled laboratory studies. Laboratory studies are often not validated through analysis of tissues from subjects environmentally exposed to these contaminants. To improve risk evaluation, a method that can perform spatial, quantitative, multi-element analyses of biological matrices is desirable. Field verification using such methods should allow better extrapolation of laboratory data and better prediction of ecological and human health impacts in situations where contaminant exposures occur.

We are assessing the capability of microbeam proton-induced x-ray emission (m-PIXE) to provide such analyses by investigating, as a demonstration project, factors controlling the central nervous system (CNS) transport and toxicity of inhaled metals. In FY1999, we used laboratory rats to study inhaled manganese uptake into the CNS. We have shown that manganese chloride entered the CNS of animals via deposition in the olfactory bulbs, while control animals showed no evidence of manganese above ambient levels.

We also started to assess whether the uptake and distribution of inhaled metals in field animals can be predicted from information on the exposure medium and laboratory data on biological uptake and distribution. We performed the fieldwork on ground squirrels collected at LLNL's Site 300. We selected this species of ground squirrel because it burrows and inhales soil particulates. We have collected ground squirrels from a reference area and an area near a firing table with elevated manganese soil content. The reference area had a Mn soil content of 200 ± 20 mg/kg, while the area near the firing table had manganese content of 400 ± 20 mg/kg. We are now conducting PIXE analysis of olfactory bulb tissue sections from the collected animals (two reference area animals and two animals from the firing table area have been analyzed). The figure shows manganese content versus position in analyzed olfactory bulbs.

We recognize the difficulties of interpreting data from multiple exposure pathways in these field studies. However, we can discriminate olfactory Mn contents between groups of animals with tissue manganese content related to soil manganese content. Furthermore, olfactory bulb manganese contents are higher than liver manganese contents and the shape of the olfactory bulb manganese profiles suggest olfactory uptake. We can characterize differences in our field sites and potentially utilize that information to interpret any differences in results both between sites and between field and laboratory data, which should provide us with valuable tools to define future research.

In FY2000, we intend to conclude the ground squirrel analyses and to analyze laboratory rats exposed via nose-only inhalation to cadmium. In a similar vein to the Mn data, we will compare Cd data from laboratory rats to Cd data from the ground squirrels.
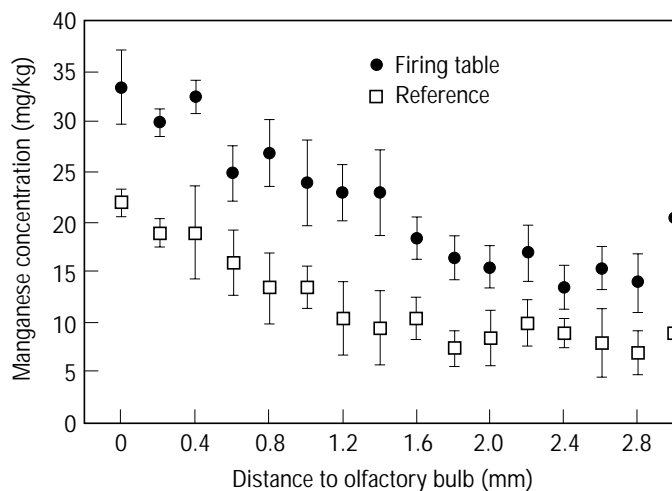
Manganese content versus position in the analyzed olfactory bulbs from ground squirrels collected at LLNL's Site 300.

Evaluation of an Expedient Terrorist Vehicle Barrier

D. B. McCallen, W. Wattenburg

98-FS-003

The potential for terrorist attacks on critical facilities presents a major national security issue for the United States. The terrorist attacks on building structures in Oklahoma, Africa, Lebanon, and Saudi Arabia—which have resulted in the loss of hundreds of lives, thousands of casualties, and extensive building destruction—have demonstrated the vulnerability of typically constructed buildings to vehicle-delivered bombs. The ability of terrorists to construct a destructive bomb from readily available materials, coupled with the fact that our buildings have not been designed to resist the extreme dynamic loads generated by vehicle-delivered bombs, will continue to put critical structures at risk.

When attempting to mitigate bomb damage, distance is one of the best allies; the further a vehicle can be kept away from a facility, the better the chance that the facility can survive the blast-wave loading. Past experience has shown that armed guards can not stop a determined terrorist driving a speeding vehicle. An effective, passive, physical barrier is necessary to ensure that a speeding vehicle can not drive up to, or in some cases directly into, a critical facility.

In this recently completed feasibility study, we investigated a design for an expedient barrier to

Field test of a simple, expedient barrier to terrorist vehicles, showing how a moving vehicle was disabled upon its impact with an anchored barrier made from standard steel pipes strung together with a taut steel cable.

terrorist vehicles. The proposed barrier is constructed from common, readily available steel pipes and steel cable. The steel pipes are laid end-to-end on the ground, with the cable strung through the pipes. The cable is anchored at the ends of the barrier to a mass, which can consist of concrete blocks, sand-filled barrels, or any other massive object.

We field tested this barrier at a remote dry-lake bed at DOE's Nevada Test Site (NTS). Two surplus trucks, each fitted with a remote-control system, were crashed into the barrier at high speed to assess the ability of the barriers to (1) stop the forward progress of the vehicles, and (2) render the vehicles inoperable after impact.

In the first field test, a 3/4-ton truck loaded with about 500 lb of sand was rammed into the barrier at 35 mph. The vehicle's impact on the barrier was quite violent—our analysis of a slow-motion video sequence and inspection of the vehicle after the impact revealed that the truck motor was completely sheared from its mounts, the rotor translated into the radiator of the vehicle, and the drive-shaft assembly was completely severed on initial impact. However, although the vehicle was completely disabled, it was able to hop the barrier before coming to a halt.

For the second field test, which was performed with a speeding 1-ton truck, the cables within the pipes were brought to a more taut condition. The impact of the second vehicle with the barrier, which occurred at a vehicle speed of 42 mph, exhibited nearly identical damage (the engine was completely sheared off, and the drive train was broken); however, because of the tauter cable, the second truck was caught on the barrier and flipped after impact (see figure).

The tests demonstrated that this flexible barrier system is very efficient in absorbing the kinetic energy of a speeding vehicle (stopping and disabling it), without itself being destroyed in the process. This barrier can be rapidly built—without specialized construction skills or equipment—from common and readily available materials. It could be particularly useful where threats to U.S. assets or troops arise quickly and an expedient barrier is required on short notice. As such, it provides antiterrorist planners with an additional mitigation device.
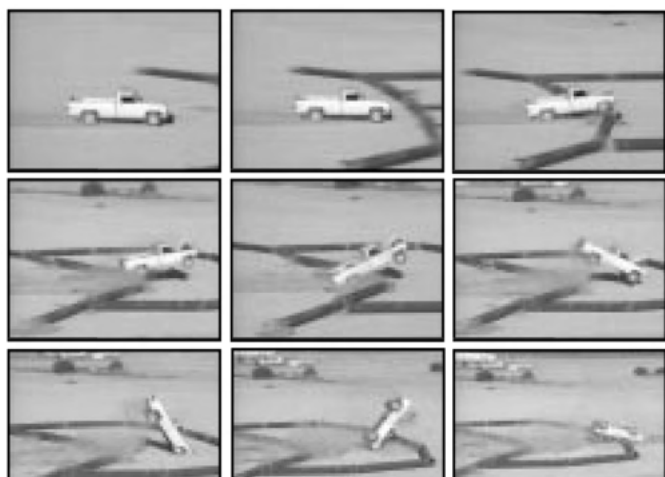
Modeling Generation of Strong Plasma Currents with Application to Spheromaks

T. D. Rognlien, M. E. Rensink

99-ERD-029

Magnetic fusion energy (MFE) research is increasingly focused on assessing the potential of compact confinement devices for commercial power production—instead of relying on the comparatively large tokamak reactor. This shift has resulted in a need for new computational tools to both interpret present experiments and efficiently design larger follow-on devices. One alternate device that has a good potential for such a compact reactor is the spheromak, and a small-scale version of this configuration, the Sustained Spheromak Physics Experiment (SSPX), is now being developed at LLNL (LDRD Project 00-SI-008).

A crucial feature of the spheromak is that the confining magnetic configuration (and for present experiments, the energy input to the plasma) are both injected via electrical current produced by a plasma gun operating between biased electrodes at the edge of the device. One of the key questions to be answered by the LLNL experiment is whether or not the spheromak can be sustained for long-period operations by the high-current plasma gun. Such current injection has applications to other types of MFE devices as well.

The goal of this research project is to develop a comprehensive, 2-D computational model of the plasma-gun operation and its effect on the edge and core plasmas. Heretofore, the theoretical understanding of the plasma-gun operation for the spheromak has been quite primitive. Our work here has unified a number of important physical processes into the detailed simulation code UEDGE, which has the additional benefit of allowing realistic device geometry. We previously used the 2-D UEDGE transport code to study edge plasmas in tokamak devices. This project thus fits well with our expertise in large-scale computer modeling. Furthermore, the SSPX device allows us to benchmark these models, aid experimental optimization, and design future devices.

In FY1999, we began by generalizing UEDGE, which runs on workstations and supercomputers, to include the spheromak configuration that has biased gun electrodes. However, because of the active nature of the electrically biased edge plasmas in spheromaks, we have added models of new physical processes. These models now include the ratio of current to voltage in the plasma sheath (which allows consistent secondary electron emission from the surface), plasma heating caused by the current flowing through the resistive plasma, enhanced plasma resistivity from turbulence, and gas recycling from electrodes.

We have made good progress toward our goal of understanding the basic operation of the plasma gun to explain the measured large edge currents. Specifically, in spheromak experiments, the gun voltage is a few kilovolts, and the current is approximately 200 kA. Our initial simulations with classical resistivity and standard sheath conditions at the gun electrodes showed that the edge-plasma current is limited to the ion-saturation current, which is much lower than the observed spheromak current. Furthermore, the gun voltage producing this current is about a factor of 10 lower than the observed gun voltage. Although enhanced resistivity can produce higher gun voltages, it can not produce the observed current.

We think that strong secondary-electron emission from the cathode is the likely cause of the large gun currents. When such an emission is included in our simulations, the calculated current is within a factor of two of that observed; we believe the remaining discrepancy may be caused by excessive emission from thermal "hot-spots" on the cathode. The secondaries form a beam of electrons in the plasma after accelerating through the electode voltage. We are now analyzing instabilities from this beam-plasma systems with a particle-in-cell (PIC) code to calibrate a simplified model of the heating caused by the instability within UEDGE.

In FY2000, we plan to extend the present model to include the effect of magnetic turbulence on the radial transport of current and energy in spheromaks. Here, we will use reduced models that are being developed and which will be calibrated with a detailed 3-D plasma- and magnetic-turbulence code.

Transmutation of Radioactive Nuclear Waste

A. Toor

99-FS-008

Lack of a safe disposal method for radioactive nuclear waste (RNW) is a problem of staggering proportion and impact. The total RNW produced by France and Canada amounts to hundreds of tons per year. Disposition of these materials represents a health hazard to the world's population and particularly to people in the vicinity of temporary storage facilities. Because societal awareness of the hazards associated with RNW has delayed development of U.S. nuclear fission reactors, we do not benefit from the large investment of resources in this industry. Instead, we rely on nonreusable energy sources (coal, oil, and natural gas), a practice that adds to other unresolved global problems such as air pollution, acid rain, and global warming.

One solution to RNW is to transmute the radioactive elements into other radioactive isotopes with much shorter half-lives. Transmutation using neutrons has been discussed and studied for the past four decades. We suggest an alternative approach that has not been considered to date: the transmutation of RNW elements using gamma rays.

In this feasibility study, we examined the photon-mediated transmutation of ^{137}Cs and ^{90}Sr, two major components of RNW with half-lives of about 30 years. At 14 MeV, both species undergo (gamma,n) reactions, producing daughter isotopes with half-lives of 13 and 50 days, respectively. At higher energies, photo-fission in addition to the (gamma,n) reactions takes place. The fission products (fission fragments and secondary neutrons) cause further transmutation of the RNW.

The LLNL COG code is a multiparticle 3-D Monte Carlo transport code that includes all of the relevant gamma-ray cross sections. It does not, however, have the capability at present to create and track the fission products and account for their subsequent interactions.

We have therefore reduced the scope of this study to use COG to simulate only the (gamma,n) reactions due to a 14-MeV photon beam stopping in a target that was either pure ^{137}Cs or ^{90}Sr.

The (gamma,n) reaction rate in ^{137}Cs for a 100,000-particle run at the surface and at 5 cm depth is 1.2×10^{-06} and 8.0×10^{-07} reactions per cm^3-source particle, respectively. We find the majority of gamma-ray interactions are atomic reactions, namely Compton scattering and pair-production. These electrons are the major source of energy loss limiting the gamma ray-induced transmutation efficiency. Even if more detailed simulations that include photo-fission show factors of 4–5 improvement in the transmutation rates, hope for this technological solution to RNW will require the development of a capability to recover a significant fraction (~10%) of the energy carried by the Compton electrons. For certain applications, inverse klystrons have been developed that convert to electricity, approximately 30% of the energy carried by the electrons. We have used COG to evaluate the transmutation rate in geometries that contain a stack of thin (few cm) plates of RNW separated by gaps containing inverse klystrons. The results of these calculations look promising if 10% of the electron energy can be recycled.

We conclude that the physics of the proposed gamma-ray transmutation scheme is sound and the development of an inverse klystron or similar device to capture a significant fraction of the energy carried by the Compton electrons is required to make the scheme energetically feasible. With the operational parameters for such a device, optimization of the RNW plate thickness and the overall transmutation efficiency could be calculated accurately enough to determine if this approach is competitive with neutron transmutation of RNW.

Lasers/Electro-optics/Beams

6

Supernovae to Supersolids: Science for the National Ignition Facility

B. A. Remington

97-ERD-022

In collaboration with several universities, we have been developing experiments on intense lasers such as Nova, Falcon, and Gekko and also planning for the scientific use of the National Ignition Facility (NIF) as a test bed for compressible radiative hydrodynamics relevant to astrophysics and condensed-matter physics. In FY1999, we concluded this 3-year project with three series of experiments: a supernova (SN) hydrodynamics series, a supernova-remnant (SNR) series, and an experiment to establish the response of materials in a region of extremely high strain rates.

Experiments using intense lasers were developed to answer specific questions about hydrodynamic instabilities relevant to the evolution of core-collapse SNs. For example, the high velocities of the core elements in SN1987A are still unexplained and may have a bearing on the observed light curve. To (1) test the hydrodynamics of the supernova code PROMETHEUS, and (2) address the validity and limitations of laser experiments for supernova research, we completed a series of experiments on LLNL's Nova laser. Planar experiments were carried out, and a more "star like" cylindrically divergent experiment was done on Nova.

A second set of experiments was motivated by the SNR now developing around SN1987A. The ejecta from this supernova is on a collision course with its circumstellar ring nebula, with impact expected just about now. The first laser experiments—which were conducted in 1D on Nova—were designed to observe ejecta plasma flowing into a low-density ambient plasma, where it would form a classic forward-shock—reverse-shock system, much like in the astrophysical SNR. Proof-of-principle 2-D experiments were also conducted to study the predicted hydrodynamic instabilities thought to occur at the contact discontinuity between the forward and reverse shocks.

Radiative shocks and blast waves occur throughout our galaxy—typically triggered by past supernova explosions. During FY1999, we began developing experiments to create a radiative blast wave in the laboratory, using the Falcon laser at LLNL. To examine the properties of a radiative shock, we conducted an initial experimental study on blast-wave propagation in a low-density, gas-cluster target. Our results indicate that ionization is generated ahead of the shock wave because of radiative preheat. The radiative precursor was more significant for higher-Z gases. We modeled the radiative blast wave using the 1-D hydrodynamics code HYADES, plus astrophysics codes. The high Mach numbers (M = 5 to 20) are similar to astrophysical shocks. However, because the laboratory gas was at a much higher density, the radiation was coupled to the hydrodynamics, giving a radiative precursor—as opposed to simply cooling the plasma.

We also conducted high-Mach-number, radiative-jet experiments on Nova and on the Gekko laser at Osaka University. Benchmarking the radiative-hydrodynamics codes used to model protostellar jets such as HH47 against relevant laboratory data is of great interest to the astrophysics community. A radiatively collapsed, high-Mach-number (M = 15), narrow, hot jet of gold plasma was observed in experiments on Nova. Numerical simulations suggested that the effects of radiative cooling on the hydrodynamics of the jet were very large. The jet temperature was initially hot (electron temperature = 1 to 2 keV), but cooled rapidly (within 0.5 ns) to 100 eV through radiative losses which triggered the collapse of the jet on axis. A subsequent series of experiments was performed on the Gekko laser where the Z of the jet was varied. The high-Z jets (Au, Fe) radiatively collapsed on axis, but the low-Z jets (Al, CH) did not. These results are being used to test the radiation-hydrodynamics code ZEUS.

During this project, we have demonstrated that (1) properly scaled, dynamically evolving astrophysical subsystems can be recreated in the laboratory on intense lasers; and (2) new regimes of solid-state physics st extreme pressures and extremely high strain rates can be experimentally accessed. This unique, very visible work has led to many invited talks, colloquia, and publications. It also attracts top young scientists to LLNL.

Technologies for Advanced Induction Accelerators

M. A. Hernandez, C. W. Williams, G. W. Kamin, G. A. Duncan

97-ERD-086

This project, one component of the inertial fusion energy (IFE) research at LLNL, aimed at developing the technologies necessary for a commercial fusion energy source. It has focused on the concept of indirect drive targets using a heavy ion accelerator and has utilized the Heavy Ion Fusion (HIF) Small Recirculator as a test bed. A "recirculator" is exactly what its name implies—an accelerator, in which the beam travels around a ring-shaped configuration, repeatedly passing through each accelerating element.

We attained some notable achievements in several important areas. For example, acceleration of the recirculating beam requires high efficiency induction core materials driven by high repetition rate, programmable pulse waveforms. As the beam is accelerated, it gains both kinetic and electrical energy; in addition, our acceleration scheme calls for compressing the beam to help reduce emittance effects. The induction core modulators must thus be able to produce precise, fast rise-time waveforms with varying shapes, amplitudes, and widths.

During FY1999, we installed four stages of modulator circuits, which were developed under a separate small business collaboration. Once installed, these were used to conduct experiments to determine the accelerator cell and magnetic material characteristics. The cells containing ferrite material were able to sustain 500-V pulses for 5 μs, while those built with the Metglas material sustained 1000-V pulses for 5 μs. The modulator pulse rise-time was not fast enough to provide the necessary beam longitudinal confinement because of the larger than expected cell capacitance. The beam was maintained within 1 mm of the accelerator centerline throughout the 90-deg bend.

During FY1998, we installed and tested a prototype unipolar Bending Dipole Pulser on the Small Recirculator. The performance of this pulser was marginal. During FY1999, we extended the design of the prototype pulser to better meet the recirculator requirements. The Pulser was re-built to (1) provide matching bipolar outputs and (2) drive twice as many dipole plates (10 vs 5). Shot-to-shot repeatability was improved to 0.2% within a specified output range (up to 20 kV at 35 V/μs slope). The timing and triggering circuits were re-worked to better integrate with the existing recirculator pulsed-power and diagnostics systems. These specifications successfully met the requirements for coordinated bending and acceleration in the initial 90-deg bend of the recirculator.

Our research was successful in two additional areas in FY1999. We initiated design efforts intended to integrate and re-package the beam position sensors (C-probes) and their associated acquisition and analysis components. We also completed a significant portion of the mechanical design for a new HIF source injector.

While the accomplishments of this LDRD project were different from those originally proposed, we were still able to materially increase our understanding of the recirculator accelerating and steering components and the beam transport dynamics. This heightened knowledge will serve to enhance LLNL's technology base in future accelerator development efforts.

Aluminum-Free Semiconductors and Packaging

M. A. Emanuel

97-ERD-111

Using laser diodes instead of flash lamps to pump solid-state lasers generally results in improved efficiency and reliability. The goal of this project was to develop and investigate the use of high-power laser diodes for pumping solid-state lasers.

Common solid-state laser systems such as yttrium-aluminum-garnet doped with neodymium or ytterbium (Nd:YAG, Yb:YAG) require pump light in the 800- to 1000-nm range, and such laser diodes have typically been fabricated in the AlGaInAs material system on a GaAs substrate. Unfortunately, the presence of aluminum near the light-generating (active) regions in these devices appears to limit their high-power performance and reliability.

To circumvent the apparent limitations of aluminum in these laser diodes, attention has turned to device structures with the Al-free material system of InGaAsP in and around the active region. Laser diodes in this system offer wavelength coverage similar to those in the AlGaInAs/GaAs material system, and early research results suggested that they might offer improved, high-power performance. However, Al-free diodes also bring with them difficulties compared to AlGaInAs devices—such as more challenging wafer-growth techniques and a greater performance degradation at high temperatures.

In FY1999, we evaluated the data of other researchers as well as our own experimental results and those of our industrial collaborators, and we have drawn some tentative conclusions about the usefulness of diodes with Al-free active regions.

When devices with uncoated facets are compared, diodes with Al-free active regions generally exhibit greater maximum output power before damage (catastrophic optical damage thresholds) and also longer-term reliability than their counterparts with AlGaInAs active regions. This is consistent with the simple model in which aluminum at the facets reacts with oxygen and water and thus degrades the electrical and optical properties of the facets. Much of the early enthusiasm for Al-free devices was based upon this observation. However, useful laser diodes have facet coatings (high reflectivity on the back and low reflectivity, typically 5 to 15%, on the output facet); thus, test comparisons involving uncoated facets—although they might illuminate interesting physical processes—are not conclusive.

It has been found by several researchers that judicious treatment and facet coating of AlGaInAs lasers can bring their performance and reliability to levels comparable to those exhibited by Al-free devices. The technical details of these treatments are almost always held proprietary, but they appear to be simple and inexpensive—as evidenced by the fact that the price of treated AlGaInAs devices is comparable to that of devices with Al-free active regions that have recently come to market.

In summary, it would appear that early suggestions of an inherent superiority of Al-free diodes over their AlGaInAs-based counterparts have not been borne out; in fact, the performances of these diodes appear to be comparable.

High Average Power Intracavity Frequency Conversion

C. A. Ebbers, K. I. Schaffers

97-ERD-138

A solid-state, high average-power, long-lifetime, visible (515–532 nm) laser source is of interest in materials processing and as a useful pump source for other systems such as Ti:Sapphire lasers. By utilizing $KTiOPO_4$ and LiB_3O_5 (KTP and LBO, respectively) as an intracavity frequency conversion crystal, we have produced over 300 W of high-reliability second-harmonic light. The critical element with the highest risk of failure within such a solid-state laser is the frequency doubling crystal. To increase the availability and reliability of these crystals, we are

evaluating the efficiency and utility of the new nonlinear optical crystals $GdCa_4O(BO_3)_3$ (gadolinium calcium oxyborate or GdCOB), which are capable of replacing KTP and LBO for the frequency doubling element.

We have demonstrated that GdCOB, a crystal whose nonlinear optical properties have only been recently discovered, has the nonlinear and thermal-mechanical properties necessary to potentially replace LBO or KTP in an intracavity-doubled laser. However, the birefringence—the difference between the refractive indices of the crystal—is currently too large to allow efficient frequency conversion of an intracavity doubled laser. In a direct comparison of intracavity frequency conversion performance, we demonstrated that a GdCOB crystal produced one-half the optical power produced by a similar length LBO crystal. The difference in the optical power generation is due to the smaller angular acceptance of the GdCOB crystal compared to the LBO crystal. A key to the research this year was the recognition that the birefringence (or angular acceptance) can be altered through modification of the basic chemical formula of GdCOB. The GdCOB structure is unique in that many different modifications can be made to the lattice—potentially allowing the crystal to be "engineered" for noncritical phase-matching (dramatically increasing the angular acceptance). There are three potential modification paths: (1) substitution of one lanthanide for another (e.g., La for Gd); (2) substitution of the alkaline earth (Sr or Ba for Ca); and (3) fluorination (substitution of CaF_2 for Gd_2O_3). We have grown over 30 derivatives of the "COB" structure using the Czochralski method. This effort has yielded high quality crystals for nonlinear measurements. It is significant to note that high quality crystals of the LaCOB and derivatives were grown at LLNL for the first time; previously, it was believed that these crystals could not be grown.

As illustrated in the figures, direct measurements on these new crystals show that, as predicted, the angular acceptance increases for 1,064 nm, doubling as the lanthanide ion in the crystal is changed (yttrium, gadolinium, and lanthanum). With further modification, as described above, it may be possible to reach noncritical phase-matching for this wavelength. However, modeling of the birefringence suggests that LaCOB is noncritically phase-matched for 1,030 nm. The addition of LaCOB and mixed $Gd_xLa_{(1-x)}COB$ crystals adds a new crystal capable of noncritically phase-matched harmonic generation for wavelengths between 970 and 1,030 nm, an important addition to the relatively few available nonlinear optical crystals for this important wavelength region.
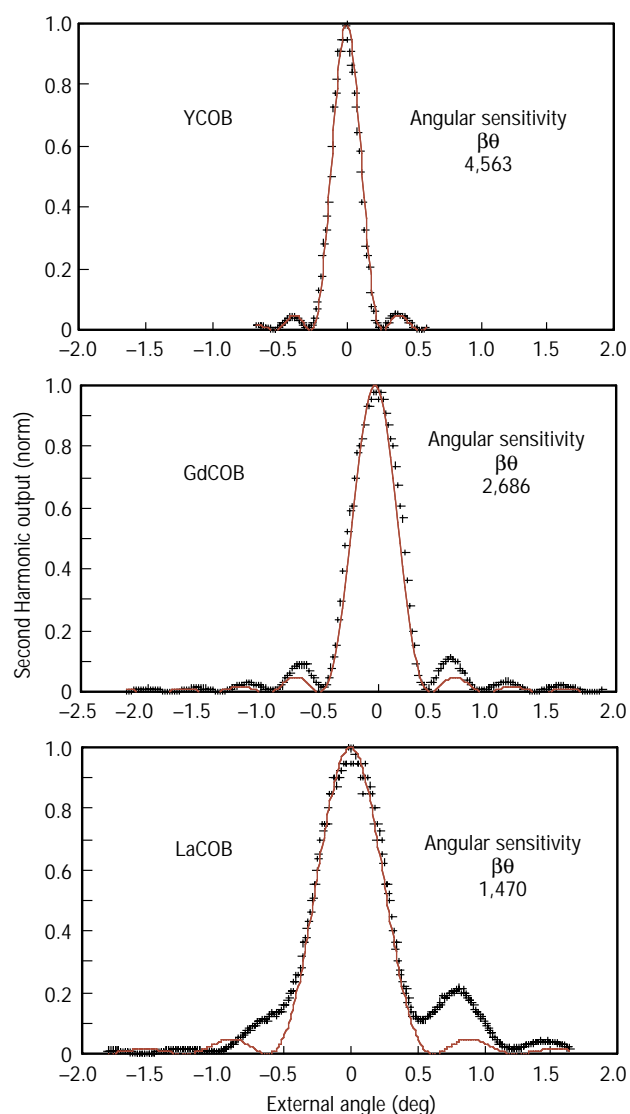
The measured angular acceptance of LaCOB, GdCOB, and YCOB. The angular acceptance increases as the larger ion (La) is substituted in the crystal.

Mercury: Next-Generation Laser for High-Energy Density Physics

C. Bibeau, R. Beach, M. Emanuel, C. Orth, S. Payne, K. Schaffers, J. Skidmore, S. Sutton, S. Fulkerson, C. Ebbers, S. Telford, L. Zapata

97-SI-014

Mercury is the first in a planned series of diode-pumped, solid-state lasers (DPSSLs) of interest to inertial confinement fusion (ICF) applications. Primary performance goals for Mercury include 10% efficiencies at 10 Hz and a 1- to 10-ns pulse with 1ω energy of 100. Achieving high energy and good beam quality while operating at repetition rates up to 10 Hz within an architecture that allows scaling to megajoule class systems makes Mercury a technically challenging project.

Our design for the Mercury laser simultaneously incorporates several novel technologies (diodes, crystals, and gas cooling) in a robust architecture capable of kilowatt average power operation. The laser design uses a Yb-doped crystalline gain media, $Yb^{3}+:Sr_5(PO_4)_3F$ (Yb:S-FAP), that offers 1-ms storage lifetime, and 900-nm laser diodes that offer both high efficiency and reliability (10^8 shots). The laser is amplified by four passes of the beam through two, gas-cooled, amplifier-head assemblies.

During FY1999, we completed the laboratory plumbing, electrical, and clean room upgrades; assembled one of the four pump-delivery arms; constructed one gas-cooled, amplifier-head diagnostics laser system to measure wavefront and gain; began building and testing components for the Mercury laser system; and worked on techniques for growing Yb:S-FAP crystals.

The pump-delivery arm seen in the figure consists of a copper, water-cooled support structure in which the diodes (up to 160 kW) can be mounted; a hollow, reflective-light concentrator; a hollow-metal, parallel-plate light guide called a homogenizer (which smooths the spatial profile of the diode light); and a set of lenses that relays the diode light exiting the homogenizer to the seven crystalline amplifier slabs mounted in aluminum vanes. The efficiency of the pump-transport system was measured to be 78%, in line with prediction from the OPTICAD ray trace model.

We connected the amplifier head to its utility system, which provides closed-loop recirculation and cooling of the helium gas. For initial testing of gas-flow dynamics at 0.1 Mach, we used a solid seven-vane cassette. The gas enters the amplifier head from the bottom, passes through an acceleration stage, and then crosses the slabs for heat removal. This is followed by gradual deceleration stages in order to prevent mechanical vibrations in the amplifier head. Accelerometer

measurements determined that the vibrations caused by gas flow were negligible, and the design for cooling the amplifier gas was judged a success.

For the diagnostics laser system, we inserted Nd-glass slabs in the amplifier head to serve as surrogates because the seven Yb:S-FAP crystals were not ready. We measured the wavefront distortions caused by the flow of pressurized gas in the amplifier head; results indicated that, as expected, the distortions were negligible ($<0.005 \lambda$). In addition, one quarter of the diode array was assembled (10 tiles = 40 kW), and one quarter of the slabs' aperture was pumped with diode light. The low-order thermal distortions caused by thermal loading were measured to be about 1.4 waves/pass for Nd-glass slabs.

During FY1999, we fabricated the first 10 tiles for the laser-diode array. Each tile consists of forty 900-nm laser bars, procured from an outside vendor, that are packaged internally on BeO heatsinks. Although the tiles meet all specifications, difficulties in procuring an adequate number of the BeO heatsinks led us to choose a silicon alternative that is also expected to meet all specifications.

In our crystal-growth efforts, we concentrated on eliminating four major defects by adopting a new, smaller-diameter growth technique. We are encouraged by this technique because small sections of grown boules were defect-free. However, during FY1999 we continued to concentrate on producing half-size crystals that can be bonded together to form a full 4- by 6-cm slab. Interferometry on bonded samples showed no compromise to the optical quality.
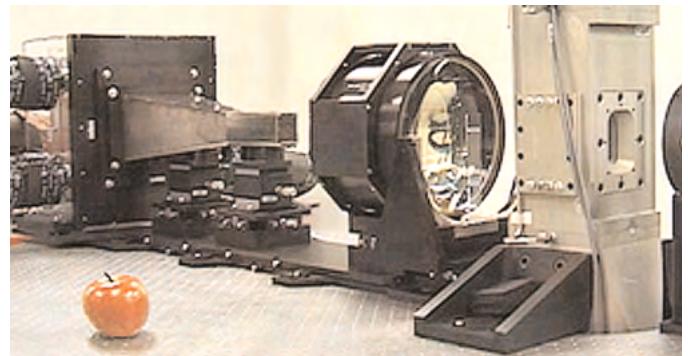
Pump-array assembly of Mercury, a prototype, high-repetition-rate laser for use in inertial confinement fusion applications. Shown are (left to right) the diode array, the pump-delivery system, and the gas-cooled amplifier head. The apple is included to indicate scale.

Advanced Wavefront Control Techniques

J. M. Brase, S. S. Olivier, K. Avicola, R. G. Hartley, M. W. Kartz, C. A. Thompson, S. E. Winters

98-ERD-061

Programs at LLNL that involve large, high-power laser systems—ranging from energy-research applications such as the National Ignition Facility (NIF) to new concepts in tactical laser weapons—depend on the maintenance of good beam quality. In such laser systems, control of time-varying aberrations in the beam requires precise control of the laser wavefronts.

Deformable mirrors can be used to control up to a few tens of phase-control points. However, high-spatial-frequency aberrations that require controlling up to thousands of corrective points make the cost of the mirror system prohibitive. New phase-control technologies such as adoptive optics (AO) offer control of many phase points with small, low-cost devices. Over the past two decades, LLNL has developed a broad capability in AO technology for both laser-beam control and high-resolution imaging. However, as requirements increase, the existing technology base for wavefront control becomes inadequate.

The goals of this project are thus to expand our wavefront-control capabilities by (1) increasing our understanding of the performance of these optical systems via improved modeling tools, (2) studying novel approaches to controlling low-order wavefronts that offer reduced cost and complexity, and (3) improving the control of high-resolution wavefronts by applying new AO technologies.

In FY1999, our work advanced in four areas: (1) advanced modeling tools for deformable mirrors; (2) low-order wavefront correctors with Alvarez lenses; (3) a direct, phase-measuring-heterodyne wavefront sensor; and (4) high-spatial-frequency wavefront control using spatial light modulators.

Our advanced modeling tool for deformable mirrors uses the finite-element method to predict the response of the mirror surface to input forces or displacements on the back of the mirror. We experimentally validated our finite-element method on a prototype NIF deformable mirror—its residual error prediction is significantly improved over that provided by earlier Gaussian methods.

In our work with Alvarez lenses, we are seeking to develop a wavefront corrector that (1) has only two or three degrees of freedom, (2) potentially costs less than conventional AO systems, (3) has greater reliability, and (4) imparts fewer intensity variations in the intermediate field. We fabricated Alvarez lenses using two different methods and tested the lenses using interferometry, beam propagation, and far-field imagery. Our data confirmed that both sets of lenses met design and manufacturing specifications and also theoretical performance expectations.

Conventional wavefront-control systems use a Hartmann sensor to measure local wavefront slopes. In contrast, a heterodyne sensor not only would directly measure phase and potentially reduce the cost and complexity of the AO system, but also would perform at a much higher speed than the Hartmann sensor. In FY1999, we designed, fabricated, and tested a two-channel, pulsed, heterodyne demonstration system and verified that heterodyne signals were obtained when a phase-modulated pulsed laser was used. We also designed a sensor array appropriate for controlling a 39-actuator deformable mirror.

The primary technology for high-spatial-frequency wavefront control is a new generation of spatial light modulators (SLMs) based on either liquid-crystal (LC) or microelectromechanical systems (MEMS) technology. These SLMs can provide wavefront correction at high spatial frequencies at relatively low unit cost. In FY1999, we (1) characterized the optical-wavefront control capability of these devices using interferometry; (2) assembled and aligned a laboratory testbed system; (3) designed, implemented, and tested a high-spatial-frequency wavefront sensor and control algorithm, and (4) performed initial wavefront-control experiments in the laboratory testbed.

Initial tests have shown that LC-SLMs are a promising technology for wavefront control. In FY2000, we plan to fully characterize their performance and apply the full set of technologies to improve wavefront quality for a short-pulse laser application.

3ω Damage: Growth Mitigation

M. R. Kozlowski, S. G. Demos, Z. Wu

Laser-induced damage to optical materials limits the design, performance, and operational cost of high-power laser systems, including the National Ignition Facility (NIF). The laser damage process consists of two primary steps. The first is the initiation of damage at a pre-existing absorbing defect present in the raw material or because of the manufacturing process. The second is growth of the damage site as a result of subsequent illumination. Through the use of diagnostic techniques, such as total internal reflection microscopy (TIRM), and collaboration with the optical finishing industry, the density of initiation sites on polished fused silica optics has been decreased by several orders of magnitude in the past few years. In spite of these improvements, it is clear that some damage to optical surfaces is still likely to occur. The operational lifetime of the optics is then limited by the growth of the damage sites under further illumination.

The focus of our research in FY1999 was to develop a physical model for damage growth that would (1) provide an understanding of the laser-system parameters that affect the growth rate, and (2) suggest potential routes for the reduction or mitigation of damage growth. Fused silica is the preferred material for transmissive optics in the near ultraviolet because of its low absorption coefficient at those wavelengths. The proposed model for damage growth suggests that the high-temperature plasma created by the damage-initiating defect modifies the surrounding, non-absorbing silica to produce an absorbing by-product. Energy from the next pulse is then absorbed by the modified material leading to growth of the initial damage site.

Evidence supporting the creation of absorbing material has been provided by two optical techniques: photoluminescence (PL) spectroscopy and photothermal microscopy (PTM). The PL measurements show that the intensity and the spectrum of photoemission from silica surfaces is modified at damage sites, as shown in the figure. The damaged areas show at least three characteristic luminescence bands. The bands at 650 nm and 560 nm are attributed to well-known SiO_2 defects associated with broken Si–O bonds and oxygen vacancies, respectively. These defects can result from either mechanical or radiation damage to the silica. The nature of the third peak at 560 nm in not clear. One possible explanation for the peak is the presence of silicon nanoparticles resulting from the decomposition and subsequent phase separation of the plasma-damaged silica. The creation of absorbing SiO_2 by-products is also supported by PTM measurements that show increased absorption-related heating within the damage sites.

Based on our understanding of the nature of the absorbing layer we have attempted to eliminate the layer using either a chemical etch to remove the material or a high-temperature anneal to re-oxidize or repair the material. The PL and PTM measurements indicate that both the chemical etch and thermal anneal help to reduce the levels of absorbing material created at damage sites.

In FY2000, our activities will continue to focus on the identification and removal of the modified absorbing layer at damage sites on fused silica. Areas of local heating detected using PTM will be directly correlated with specific luminescent defects. Transmission electron microscopy cross-sectioning and luminescence-decay studies will clarify the layered nature of the absorbing layer including the possible presence of silicon nanoparticles. Etch and thermal treatment parameters will be optimized based on PTM, PL, and damage growth-rate studies.
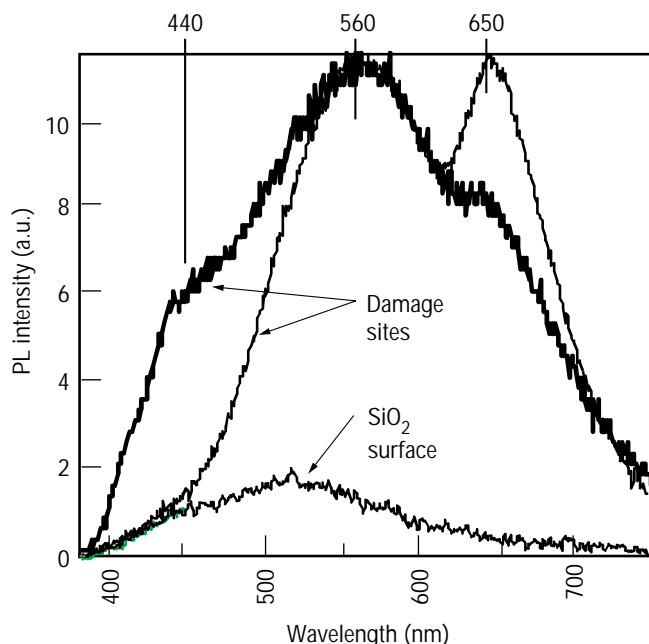
Photoluminescence spectrum (351-nm continuous-wave laser excitation) of fused silica surfaces before and after laser damage with 355-nm pulses.

All-Solid-State Tunable Laser Source using Sum-Frequency Mixing

R. H. Page, R. J. Beach, C. A. Ebbers, S. A. Payne

98-ERD-078

Tunable, narrow-band visible laser light finds many applications in spectroscopy, process monitoring, isotope separation, and other fields. Traditionally, dye lasers have generated such tunable visible light; however, it is inherently difficult to design, operate, and maintain a reliable, precisely tuned dye oscillator. Last year, we undertook a project whose main goal was to create a "replacement"—a solid-state laser system that produces continuous-wave (CW) tunable visible light. Among other things, it was to exhibit a clear pathway to deployment as an improved alternative to a pulsed dye laser master oscillator for isotope separation. Our secondary goal was to establish a core competency in high-power fiber lasers.

Our FY1998 project was successful, since it included the demonstration of an integrated breadboard system that generated nearly 100 mW of 589-nm light. This system used efficient sum-frequency-mixing of lasers at 1319 nm and 1064 nm. It was based largely on commercially available, telecommunications-style components, and was comprised of four main building blocks: (1) a narrow-band 1319-nm Nd:YAG laser; (2) a distributed-feedback Yb:silica fiber oscillator, tuned to 1064 nm; (3) a home-built high-power, cladding-pumped Yb:silica fiber amplifier; and (4) a periodically poled lithium niobate frequency-summing crystal. The oscillator design proved so successful that it has been adopted in the front-end portions of large Nd:glass laser systems for inertial confinement fusion, e.g., the National Ignition Facility. While building the cladding-pumped amplifier that delivered 2 W at 1064 nm, we developed expertise in high-power fiber lasers and began a computer model for designing fiber lasers and amplifiers.

In FY1999, we saw progress in several areas. For some applications, the source's linewidth must be increased from its nominal value (under 50 MHz) to several GHz. We obtained and tested commercial fiber-pigtailed phase modulators that work well with the Yb:silica fiber oscillator and amplifier. Modulator performance (i.e., modulation index) scaled as expected with radio-frequency (rf) drive power and frequency, and we showed that GHz bandwidths could be generated at satisfactory duty cycles. In addition, we assembled special housings for the Yb:silica distributed feedback fiber oscillators, which allow temperature tuning. Tests showed that the visible light wavelength could, given a suitable reference wave-meter, be held reliably and stably at a given value.

Our FY1998 cladding-pumped Yb:silica fiber amplifier made inefficient use of the pump light. We obtained and tested some double-clad fibers with a different aspect ratio (of cladding to core area) and doubled the output power, to over 4 W. Although we had good results with our "home-made," cladding-pumped fiber amplifiers, we also tested a fiber-pigtailed commercial unit. We obtained roughly 3-W output, a satisfactory power for this project.

In order to establish a scientific basis for the design of active fiber components, we refined our fiber-amplifier computer model to include the effects of amplified spontaneous emission and distributed scatter loss. The model now has significant predictive capability and has reproduced some (but not all) of the experimental data from our fiber amplifiers.

In anticipation of in-situ tests of our visible-light system, we performed further integration, resulting in a "brassboard" (shown in the figure) whose significant components are all from commercial vendors, suggesting the possibility of out-sourcing. This prototype assembly, which is clearly compact, "turn-key," and "stand-alone," could be produced for less than $100,000. It provides for wavelength tuning and phase modulation, and, in principle, it is ready to use.

Single-frequency, tunable orange (589-nm) light beam emerging from the integrated solid-state visible light source. Electricity is the only utility required.

Petawatt Laser Data Analysis and Technology Development

M. Key

98-ERD-079

The Petawatt (PW) laser—with 1-PW pulses of 500-fs duration and capable of being focused to intensities reaching 3×10^{20} W·cm^{-2}— opened a new regime of experimental physics, where electrons in the light wave are strongly relativistic. It produced a wealth of novel scientific data.

The primary objective of this project during FY1999 was a systematic analysis of these data. A second objective was to establish a key new technology for creating the large-transmission gratings needed for the next step in PW-laser development.

Our analysis of the PW data has yielded widely reported, outstandingly interesting scientific results. The most exciting discovery was the least expected. In studies aimed at characterizing the relativistic electrons generated by irradiating solid targets in vacuum, we observed that an intense, highly collimated beam of protons with energies up to 55 MeV was emitted perpendicular to the rear surface of the target. As much as 7% of the laser energy was converted to greater than 20-MeV protons. The proton spectrum showed a sharp, high-energy cut-off, with the cut-off decreasing away from the beam's axis. We identified and modeled the acceleration mechanism: The relativistic electrons form a Debye sheath at the solid–vacuum interface, thus creating electric fields of many MV/μm. The ion beam has significant applications potential, which we are now exploring.

We also found that bremsstrahlung by the electrons generated an intense continuum of multimegavolt x-ray photons in high-Z targets. Gold targets 1-mm thick emitted x rays in a broad (~100°) forward cone. Doses to 2 rads at 1 m were recorded, implying a greater than 40% conversion to relativistic electrons. We obtained radiographs of submillimeter resolution through 15 cm of Pb. Exciting new byproducts of this work included the study of laser-induced nuclear processes and pair production. Photons at energies greater than 10 MeV induce (γ,xn) nuclear activation (where x is the number of neutrons ejected in the photoneutron process), seen in Au for $x \leq 7$ and used to measure the photon spectrum up to 70 MeV; photofission of uranium was similarly induced.

In fast-ignition physics, a key problem is the electron transport of energy from the laser beam into solid-density material. We measured electron heating in solid targets in two ways. A narrow deuterium–deuterium (DD) thermonuclear fusion peak in neutron spectra from CD_2 targets, with front layers of CH or Cu, implied temperatures of 0.5 to 1 keV. X-ray emission spectra from Al sensor layers buried up to 20 μm deep in CH targets gave temperatures of 300 eV at densities of 0.6 g/cm^3. Pinhole-camera images of the buried-layer x rays showed an annular pattern of heating (~80-μm diam) to depths greater than 100 μm, giving evidence of the collimation predicted for magnetically guided energy flow. Observation of spot heating at depths more than ten times the diameter of the focal spot is new and significant progress.

The development at LLNL of 1-m-diam, reflective diffraction gratings for pulse compression was the key technology enabling the PW laser. The power-limiting factor is damage to the gold coating on the gratings. Fused-silica transmission gratings can operate at much higher energy fluence; high-diffraction efficiency should enable generation of 3-kJ laser-pulse energies, four times the present PW limit. This requires grooves in the diffraction gratings with 0.75-mm spacing and great depth relative to their width. A significant technology step addressed in this project was the adaptation of the reactive ion-beam etching process (used to create the required groove depth in the final manufacturing steps) with the objective of obtaining a spatially uniform etch rate at large aperture. Optical tests on a 65-cm substrate that was put through the full process showed that in some areas high-efficiency diffraction was obtained, but that overall the efficiency was low and not spatially uniform. We identified gas-feed control as the (rectifiable) problem.

Development of Subpicosecond X-Ray Pulses for Measuring Dynamics in Heated and Shocked Materials

T. Ditmire, K. Wharton, J. Zweiback, T. E. Cowan, M. D. Perry, B. A. Remington

99-ERD-036

Advances in the development of high-repetition-rate (>1 Hz), very high-peak- power (>10 TW) short-pulse lasers are now making possible a wide range of basic, high-accuracy experiments that are relevant to LLNL's Science-Based Stockpile Stewardship (SBSS) mission. One particularly important possibility is that these high-energy, ultrafast lasers can be used to generate bright, short, x-ray pulses that can be utilized to time-resolve the dynamics of high-Z materials subject to laser-driven shock waves. Using x rays as ultrafast probes makes possible a number of diagnostic techniques beyond the optical probes commonly used. For example, Bragg and Laue diffraction of x rays from crystals provides detailed information about the long-range crystalline order of the material. With these short-pulse x-ray probes coupled to a laser-driven shock wave, detailed studies of shocks at the microscopic, atomic lattice level are now possible. Phenomena such as the transition from elastic to plastic flow, solid-to-solid phase transitions, and melting can be diagnosed in shocked metals.
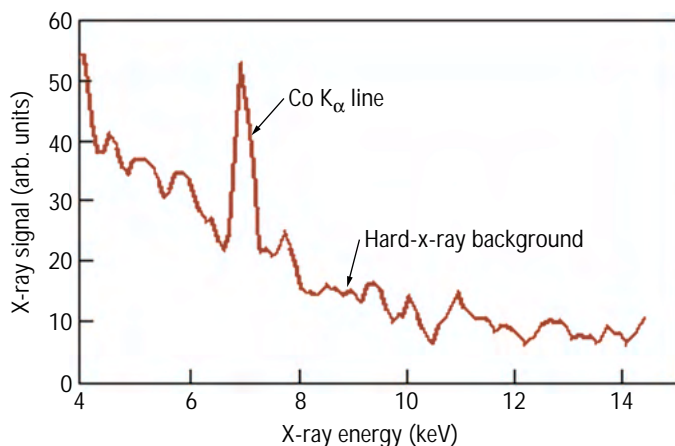
X-ray spectrum obtained from the irradiation of Co by 35-fs pulses, showing strong Co K_α radiation at 6.9 keV. These x rays are produced by the acceleration of electrons by the strong laser field into the bulk Co target. The multi-keV electrons excite K-holes in the Co atoms, which emit the K_α radiation upon decay.

The goal of this project is to develop the technology of short-pulse x-ray generation and to pursue applications that will support the SBSS effort.

In FY1999, we began developing the x-ray sources and diagnostic techniques to make such measurements possible. The emphasis in this phase is on developing sources using laser-driven plasmas. We developed and characterized a short-pulse, laser-driven, pulsed source of x rays with a pulse width of about 1 to 10 ps and sufficient flux per pulse to permit single-shot, time-resolved studies.

Our laser-plasma source generates characteristic x-ray radiation in a material with a short, focused, intense, near-infrared, 35-fs laser pulse. In our experiments, we focused these pulses onto Co or Ti targets at intensities of up to 5×10^{17} W/cm^2. These high intensities produce a plasma on the surface of the target and accelerate electrons at high energy into the target. The electrons produce bright, K_α x-ray emission. The emission from this process is very fast (under a picosecond) because the electrons that produce the x rays have a duration that is comparable to that of the laser pulse itself. The spectrum from such an experiment is shown in the figure. During FY1999, we demonstrated a conversion efficiency of up to 10^{-5} of the laser energy into Ti K_α radiation, which should be sufficient to yield good, single-shot diffraction measurements from single crystals of Si or Al.

With the successful development of such a K_α source, during FY2000 we intend to begin using this source as a probe on shock waves in Al. We will diffract these x rays from Al shocked with a second laser pulse. Since the angle of diffraction is directly related to the spacing between atomic planes in the crystal, such an experiment will allow us to examine the time history of the compression and relaxation of the lattice as a shock wave passes through the material. This information should provide important information to aid in modeling the propagation of shock waves in metals.

Ultimately, our use of these K_α sources to develop the pump-probe diagnostic techniques will lead to experiments at much higher x-ray fluxes using the Falcon-laser, linear-accelerator-based Thomson x-ray source, which is now under development.

Fundamental Studies for High-Brightness, High-Average-Power Laser Design

E. Honea, L. E. Zapata, R. Beach

99-ERD-037

A laser of high average power up to 100 kW and more and with high beam quality is of great current interest. It can be used in a wide range of applications—from point-defense systems involving aircraft and ships to welding, drilling, and cutting thick plates. It is estimated that at least 20 kW of continuous-wave (CW) power is needed to defeat an incoming missile; power output exceeding a megawatt is necessary to confront heavy armor.

Our goal in this project is the design and development of a scaleable, diode-pumped, solid-state laser with the required average power and beam quality. We believe that solid-state laser technology will ultimately be able to outperform chemical laser systems—we plan to show that the compactness and associated energy density are unavailable from any other approach.

The new approach incorporates several innovations not presently used in solid-state lasers. One is a thin, low-thermal-impedance, ytterbium-doped, yttrium–aluminum–garnet (Yb:YAG) gain disk that is diffusion bonded to an index-matched, undoped "cap." The gain disk has the dual purpose of preventing the trapping of amplified spontaneous emission while facilitating optical pumping. Another innovation is the use of optical "horns" at the edges. These horns couple the diode-pump light into the composite structure while coupling out the amplified spontaneous emission (ASE) generated within. A third innovation is a high-performance, microchannel-cooled back-plane capable of dissipating a heat flux up to 1 kW/cm^2. This back-plane is indium-soldered to the thin gain disk—it rejects the heat generated in the thin gain medium while the laser beam is extracted in the parallel but opposite direction to the heat flow.

During FY1999, our in-depth analysis of pumping schemes revealed that introducing the pump light through the edges of the device has the advantage of trapping the diode-pump light in the composite structure, thus multipassing it through the gain medium. This implies that commercially available Yb:YAG material with moderate Yb concentrations can be used for the gain medium—thereby eliminating the need for the fully stoichiometric ytterbium–aluminum–garnet (YbAG) material required for other pumping schemes. Because of the extremely thin gain elements, operation is possible at very high thermal power densities before stress ruptures the material. The novelty of our approach is that it exploits the high radiance of a diode-laser array to inject pump light through the small edge dimension of a disk. We have filed a patent disclosure.

In FY1999, we completed the analysis and details for a design (see figure) that will prove the most important ideas above. We received most of the ordered parts and tested components.

For FY2000, we will (1) test our first-generation device; (2) demonstrate the use of index-matched, diffusion-bonded horns to manage ASE and improve pump delivery; (3) implement a low-thermal-impedance highly reflective coating for true CW operation at high heat loading; and (4) investigate resonators for producing optical beams of high quality. During our tests, we expect to extract 500 W. This result will demonstrate that efficient optical pumping through the edges of the device is possible; it will be used to bench-mark our calculations for pumping and ASE depumping.

With the information obtained from our tests, it will be possible to better design a module for eventual scaling to truly high average outputs measured in tens of kilowatts—or even megawatts.
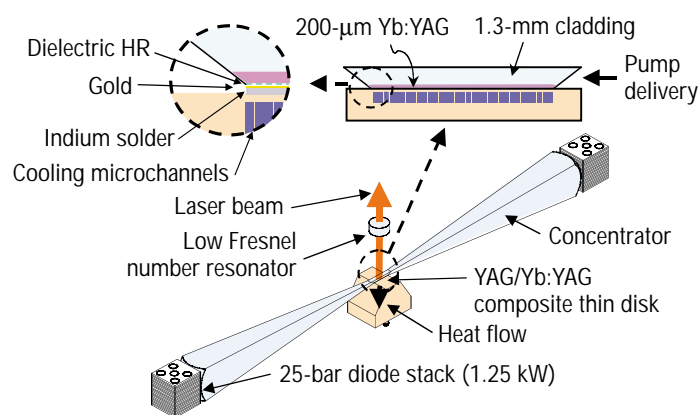
Major components of our first-generation, high-average-power, solid-state laser. The device consists of a 6- by 3- by 1.5-mm slab with wedged ends through which it will be pumped by two 25-diode bar stacks of 1.25-kW output each.

Ion-Beam-Control Experiments

T. C. Sangster

99-ERD-052

Ion beam induction accelerators are the leading driver candidates for inertial fusion energy production. Intense ion beams are focussed onto a deuterium–tritium capsule to initiate a tiny thermonuclear burn; the fusion energy is captured for power generation by a flowing liquid metal wall. This project utilized an existing scaled beam facility to study the effects of active beam control on a space-charge-dominated ion beam with parameters similar to an ion driver. The specific goals of this project were (1) to successfully coordinate the acceleration and bending of the ion beam while minimizing the emittance growth, and (2) to study in detail the effects of a beam phase space mismatch between the ion source and the transport lattice. These issues are critically important for the design of a full-scale ion beam driver. Beam emittance will determine the final focus spot size; subsequently, this spot size determines, in large part, the final energy gain of the fusion energy target.

The experiments were conducted using an 80-keV, 2-mA potassium beam matched into a strong

The in (X) and out-of-bend-plane (Y) beam positions track the nominal centerline under full acceleration when coordinated with the bending dipole voltage ramp.

focussing, 90-deg.-bend transport lattice consisting of ten permanent magnet quadrupoles, ten electrostatic dipoles, ten capacitive probe position monitors (0.1 mm position resolution) and five MetGlas induction cores. We developed a customized electrostatic dipole pulser to provide a precise voltage ramp of 35 V/µs with a pulse-to-pulse accuracy of 0.1% to compensate for the 500 V of acceleration at each induction core (i.e., as the beam velocity increases so must the dipole bending voltage). The induction core pulsers, developed by First Point Scientific, Inc., met stringent waveform requirements including 0.1% voltage ripple, >kHz repetition rate and a variable pulse height. The primary project milestone, graphically illustrated in the figure below, was the demonstration of 100% beam current transport through the 90-deg.-bend with the acceleration pulses coordinated with the correct dipole voltage ramp and the beam position within 1 mm of the nominal centerline at each of the quadrupole magnets (the beam position probes are located inside the quadrupoles). Despite the impressive 0.1% waveform accuracy on the electrostatic dipoles, the stability of the beam position at the end of the 90-deg. bend was not adequate to reliably measure the beam emittance with parallel slits. Furthermore, because it was not possible in this experiment to delay the ramped voltage pulse from dipole to dipole to compensate for the beam propagation time, other diagnostics indicated a slight twist in the beam longitudinal profile that would have likely caused the beam emittance to grow appreciably.

Another significant effort involved studying the effect of matching the ion beam from the source into the transport lattice. This was done using an array of electrostatic focussing and steering quadrupoles (referred to as the match section). If the phase space is not matched properly in this section, significant beam loss can occur, which would be disastrous for a driver-scale beam. By varying the match conditions and steering the beam on and off the nominal axis, it was possible to improve (or degrade) the beam emittance through the matching section by over 40%. This simple study underscores the importance of proper beam control throughout the entire accelerator when dealing with space-charge-dominated ion beams.
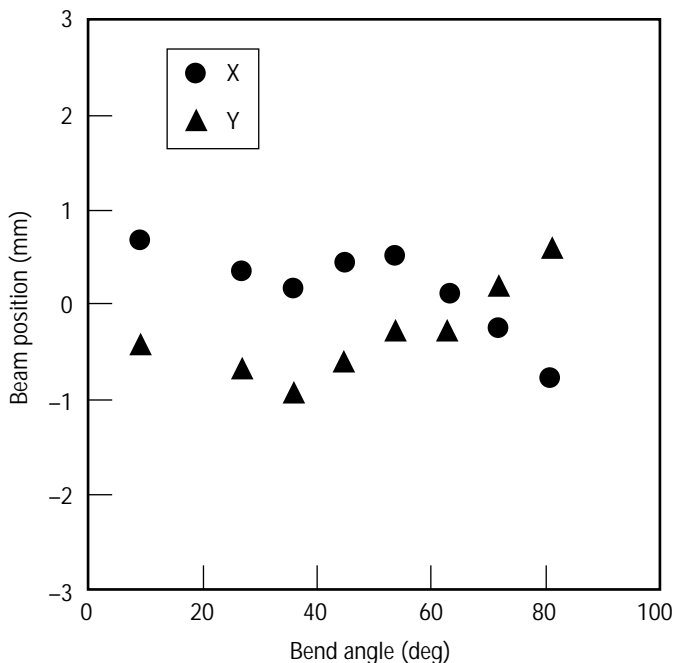
Model Development for the Interaction of Ultrahigh-Intensity Lasers with Matter

A. B. Langdon, S. P. Hatchett, D. E. Hinkel, B. F. Lasinski, C. H. Still, S. C. Wilks

99-ERD-063

Analyses of recent experiments at LLNL on the Petawatt and other ultrahigh-intensity ($>10^{20}$ W/cm^2) lasers have made possible real advances in our fundamental understanding of the interaction of a pulse from such lasers with high-density matter. Specifically, during FY1998 a number of highly productive experiments conducted on the Petawatt laser were designed to elucidate this complex interaction and to provide an extensive database for future model development (see work performed in project 98-ERD-079, p. 6–9).

Our goal in this project is to accurately model this interaction and the associated physical phenomena. This model will enable LLNL to fully exploit these phenomena in several areas, including radiography, novel ignition methods, equation-of-state studies, and opacity physics.

Accurately modeling the interaction between an ultrahigh-intensity laser and high-density matter is a fundamentally difficult, nonlinear problem. Laser energy is absorbed by collisionless processes that generate relativistic electrons. A description of the transport of the hot electrons must include, in a self-consistent way, the very large electrostatic and magnetic fields produced by the hot-electron current. These large fields affect both the background plasma and the high-energy electron beam.

Faced with this complexity, and rather than attempting to create a single overarching simulation, we are approaching the modeling problem by developing and extending codes and theories that model parts of the problem well. Thus, we will obtain sufficient overlap to enable a complete, integrated picture. Here, we discuss our FY1999 work on these models and on their application to Petawatt experiments.

We added relativistic mass shift and electron "cavitation" effects—which lead to self-focusing—to the new, massively parallel version of the laser–plasma interaction code, F3d. When this code is provided plasma profiles from LLNL's LASNEX code and from experimental data, plus a detailed description of the aberrated laser beam from the experiments referred to earlier, F3d would model propagation of the laser beam through the low-density plasma corona of the plasma target.

We also implemented a massively parallel, 3-D particle-in-cell (PIC) code that provides the most complete description of the laser–plasma interaction in under-and over-dense plasma at densities both below and above the "critical" electron density (10^{21} cm^{-3}), the maximum for which the laser light can classically propagate. This code is in early production in the parameter regime of ultrahigh-intensity experiments.

We modeled the production of bremsstrahling within the laser targets and its interaction with detectors. This allows us to calibrate those detectors and to determine key parameters of the hot electrons generated by the laser–plasma interaction, that is, the conversion efficiency, the average energy of the electrons, and the velocity distribution of these electrons within the target.

To determine the properties of the very energetic electrons and ions emitted from the target, we designed and modeled the response of charged-particle detectors. In particular, we identified an extraordinarily intense, collimated ion emission from the back of the target. We developed a theory, confirmed by our supporting PIC simulations, explaining the generation of the ion beam. Our theory shows how the high density of energetic electrons produced by petawatt–kilojoule lasers will generate electric fields of order MV/μm on the target surfaces. These fields accelerate ion beams, and the relative power of the beams depends on the scale length of the plasma density on the surface of the target. Our discovery and physical explanation have enabled us to establish a record of invention and to submit a patent application.

In FY2000, we will continue to analyze and exploit the Petawatt-laser database, and we will further develop and apply the new and extended codes.

Generalized Homodyne Sensor

E. T. Rosenbury

99-ERD-073

Motion sensing, vibration sensing, and point-of-closest-approach sensing capabilities are required by many U.S. government agencies. Micropower impulse radar (MIR) and narrow-band radars can be used for these purposes; however, pulsed homodyne radar sensors (HRSs) would offer many advantages over both technologies. For example, HRSs (1) offer increased sensitivity and an improved possibility for certification by the Federal Communications Commission (FCC) because of a narrowed energy bandwidth; (2) are single-antenna devices by default—impulse sensors normally require two antennas; and (3) offer greater range sensitivity, improved noise immunity, and lower cost per unit than narrow-band radars. A homodyne sensor could also enable new capabilities in speech sensing and mine detection.

The goal of this project was to develop a robust HRS system capable of detecting distant motion and measuring close-in, minute vibrations. Features would include swappable output filters, functionality over frequencies ranging from 950 MHz to 5 GHz, and the potential for FCC certification because of a filter installed at the antenna.

During FY1999, we (1) designed and built a prototype HRS, (2) fabricated a first-cut circuit board, (3) performed initial debugging, and (4) began working with an improved design.

To establish the basic board parameters and establish the operating characteristics of the actual circuit, we modeled the HRS circuit using ICAP4 (a commercial circuit-analysis package). With this modeling, we were able to obtain a fairly accurate representation of the actual waveform. However, modeling also established the fact that the component values did not have a great overall effect on the actual operating frequency of the burst signal.

We tested the original board design and verified the model's performance characteristics [Fig. 1(a)]. At the same time, we determined that the actual operating frequency might be a result of stray board values and field-effect transistor (FET) inter-element values.

When we tested the original design using 21 different FETs, we found that the overall frequency could be varied over a frequency spectrum of 1.8 to 6 GHz. With this in mind, we changed the board substrate to a material that has better broadband characteristics and more stable dielectric constants.

By the close of the year, the new board design had arrived and testing had begun. This initial testing seemed to prove out (1) the design ideas established while we were testing the original board design, (2) the concept that the FET and the board material were the frequency-determining elements [Fig. 1(b)], and (3) that the new board material results in significant improvements in noise and board stability. We have tested two FET's with the new board—one operating at 2.2 GHz and the other at 3.7 GHz—and we are awaiting the arrival of FET samples believed to operate at the lower end of the desired spectrum. Final debugging and final board fabrication remain to be completed. A large build might then be accomplished, enabling future projects to explore the various application areas cited earlier.

(a)

(b)
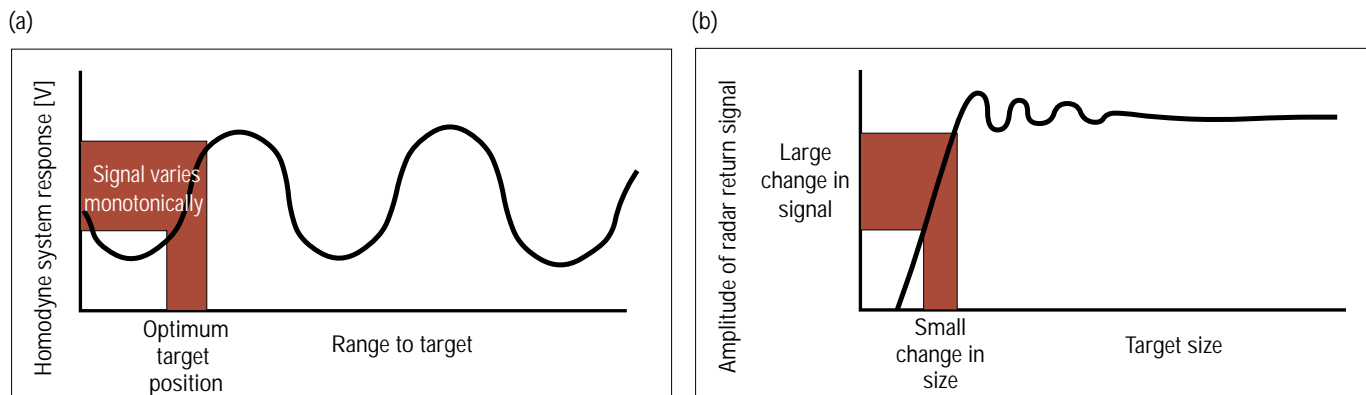
Figure 1. Results of tests of circuit boards for the new homodyne radar sensor, showing how signal sensitivity can be maximized by (a) adjustable phase, and (b) swappable transmission frequency.

Microwave Detection of Hematomas

W. S. Haddad, J. Chang, E. T. Rosenbury, G. Dallum, P. Welsh, D. Scott, D. Duarte, V. Acevedo-Bolton

In the United States, 2 million people are treated for head injuries every year in the civilian sector alone. It is well known that with any intracranial hemorrhage, the time lapse between the instance of injury and the positive identification of the hemorrhage must be minimized in order to maximize the likelihood of full recovery by expediting the delivery of proper care.

A recent advance in device technology at LLNL—the micropower impulse radar (MIR)—has made it possible to produce extremely compact, low-power, ultrawide-bandwidth radars that could be used in the microwave detection of epi- and subdural hemorrhages (hematomas). This application of the MIR technology could produce a device that would significantly improve the prognosis for head-injury patients and simultaneously reduce the economic burden on both the patient and the health-care provider.

The goals of this project were thus to (1) apply LLNL's MIR technology to the development of a noninvasive microwave device for the detection of hematomas, (2) develop a clinical-trial-ready hematoma-detector prototype, and (3) initiate human trials.

Our design is based on the following: An ultrafast pulse having a width on the order of 100 ps is transmitted by the MIR and directed into the head via a specialized antenna. The pulse is absorbed and reflected from the various tissues in the head and their interfaces, and is subsequently received by the antenna. Computer processing of the received signal can then be used to characterize the tissue variations. Because the incident pulse width is short, it will be possible to differentiate thin structures on a millimeter scale. For example, an epidural hematoma results in the separation of the aura from the meningeal wall; this will be observed in the delayed echo of the signal reflected by the interfaces at skull and aura.

During FY1999, we (1) performed a preliminary experimental demonstration of our concept; (2) developed an estimate of the dimensions of the smallest detectable hematoma; (3) built and characterized a prototype of the specialized antenna for the hematoma detector that confines the transmitted radiation to a small (~2 in. diam) region of the head and reduces noise and clutter in the received signal by suppressing the effects of patient/operator motion; (4) developed a procedure for constructing phantoms (physical models) of the head that are designed to have properties similar to a human head in the microwave regime, and which are used for laboratory tests and experimentation as part of the device development process; (5) nearly completed building a fully modular, instrument-based impulse radar system that will serve as a laboratory test and development tool by providing full control of the device parameters such as the range resolution, scanning rate, range-gate width and distance, and antenna testing capability; (6) adapted a pre-existing MIR device (a dual-antennae version) for use in laboratory tests using phantoms; (7) wrote a LabView-based data-acquisition driver that runs on a laptop PC; and (8) submitted a patent disclosure.

By the end of FY1999, we were poised to continue with our development of the prototype device suitable for use in trials with human subjects. Future work would include completing the instrument-based system, creating robust numerical signal-analysis tools, refining the design of the specialized antenna, developing custom MIR electronics, and arranging for human trials in collaboration with a world-class medical institution.

Critical Density Interaction Studies

P. E. Young, C. T. Hansen, H. A. Baldis

99-ERI-007

High-intensity laser–plasma interactions are important for numerous efforts at the Laboratory, including the Fast Igniter project, direct-drive studies for the National Ignition Facility (NIF), and studies involving x-ray radiography research, high-energy x-ray backlighters, and laser cutting. For many years, the interaction of high-intensity electromagnetic (EM) waves with the coronal plasma surrounding ignition targets has been of interest to programs such as these.

Understanding laser propagation through underdense plasmas is important because in many laser–target experiments, the laser beam can filament or self-focus—this can change the laser intensity at the target from what one would measure in a vacuum. A secondary effect of filamentation is that levels of the stimulated Brillouin and Raman scattering instabilities (SBS and SRS, respectively) can change because filamentation changes the laser intensity, the density, and the density gradients on which the growth of SBS and SRS depend. These instabilities may be important because SBS can also modify the amount of light coupling into the target, and SRS can generate hot electrons that can heat the target.

The goal of this project is to develop and calibrate a predictive capability for the interaction of EM waves with plasma densities near the critical density, n_c. To perform this work, we combine a set of unique tools: (1) a laboratory experiment using a high-repetition-rate laser and detailed plasma diagnostics for quantitative measurements of laser propagation and background plasma parameters, and (2) nonparaxial wave-interaction codes to model laser filamentation and SBS in plasmas throughout the coronal plasma.

Our experimental program provides an opportunity to test and verify theoretical models over a wide range of plasma parameters—for example, plasma density varying from well underdense to the critical density region, a wide range of laser intensities (up to 5×10^{16} W/cm^2), and different laser-illumination geometries. For the first time, we are able to explore the physics of laser-beam propagation at higher densities ($n_e / n_c > 0.5$), where n_c is the critical electron density, in the well-controlled conditions of the preformed plasmas—we tested nonparaxial physics of beam propagation, different mechanisms of anomalous laser light absorption, and effects of Langmuir turbulence.

In FY1999, we developed a novel laser experiment to investigate the interaction of intense laser light with the critical density. Experimental investigation of processes near the critical density have previously been hampered because n_c is normally within a few micrometers of the target; diagnostic access is therefore extremely difficult. In our laser–plasma interaction experiments, plasmas are formed by the irradiation of a solid target so that there is a steep density gradient at the critical surface. This has important physical consequences; for example, the Spitzer approximation for electron-energy transport breaks down because the electron mean free path is larger than the temperature scale length, and nonlocal heat transport must be considered. By using two different wavelengths for the plasma formation and interaction beams, one can form a critical density that is far removed (~100 μm) from the solid target. Replacing the solid target with an exploding foil allows one to create a parabolic density profile with a peak density near n_c, permitting detailed investigation of plasma-induced smoothing, hole boring, and forward-accelerated electrons.

Work during FY1999 included implementing new diagnostics required for the experiments and evaluating the effect of the pulse shape on channel formation. Our theoretical work has expanded the modeling of SBS and filamentation to high densities.

During FY2000, we plan to finish our analysis of data showing the dependence of channel formation and guiding on the shape of the laser pulse and submit it for publication.

Development of a Compton X-Ray Source and a Vacuum Laser Accelerator

H. A. Baldis, F. V. Hartemann

99-ERI-008

Tabletop, laser-based light sources hold the promise to radically transform advanced biomedical applications, including innovative cancer research. For example, 33.1-keV x rays are used for high-contrast angiography by imaging the K-edge of iodine; at 1 Å (12 keV), protein crystallography is revolutionizing the pharmaceutical industry by allowing the design of new drugs—as exemplified by the protease inhibitors used to decrease the viral load in HIV patients. Also, a Compton light source based on 200-MeV electrons would create 4-MeV gamma rays that would penetrate deeply into high-Z materials—these would be extremely useful for defect imaging of manufactured components and for high-resolution flash radiography.

We are conducting an experimental and theoretical analysis of the interaction between high-brightness, relativistic electron beams and femtosecond, ultrahigh-intensity laser pulses. The two most important geometrical configurations under investigation correspond to Compton backscattering and high-gradient, vacuum laser acceleration.

Within this context, we are developing two prototype X-band (8.548 GHz) radio-frequency (rf) photoinjectors [see Fig. 1(a)] that are capable of producing high-quality, relativistic electron beams with extremely low emittance and very high peak currents (typically, 1 nC of charge generated within 1 ps, producing 1 kA of peak current).

The first rf gun produces 5-MeV beams, which can generate x rays around 2 to 4 nm, capable of propagating through the so-called "water-window" via Compton backscattering. The second system—a plane-wave transformer (PWT) linear accelerator (LINAC) developed in collaboration with David Yu—will generate 25-MeV electrons that are capable of producing 1-Å radiation.

One of the most important experimental results achieved during FY1999 was the precise, controlled tuning of the 5-MeV rf structure, using a novel rf circuit.

With this technique, we have simultaneously achieved balanced pi-mode operation of the gun—which is crucial for producing high-quality beams—and critical coupling (with a reflection coefficient smaller than 1/10,000,000). In the pi-mode, the full cell and 1/2 cell are 180 deg out of phase, thus compensating for the transit time of electrons in the 1/2 cell.

The development of a laser oscillator specifically designed to meet the stringent requirements of ultrahigh-intensity Compton backscattering, including extremely low timing jitter (<100 fs) and excellent spatial and temporal beam quality and control, has resulted in the demonstration of a quantum-well AlGaAs semiconductor laser that produces pulses with 7 nm of optical bandwidth at repetition rates between 0.595 and 1.462 GHz and that is externally mode-locked to the rf gun fields. We have also commissioned a 10-fs titanium:sapphire laser oscillator [Fig. 1(b)], and we are working on the laser pre-amplifier, which will produce 1 mJ at a repetition rate of 1 kHz.

Our main theoretical results for FY1999 include the (1) development and benchmarking of a 3-D laser-focus code; (2) demonstration of vacuum laser acceleration by coherent dipole radiation; (3) demonstration of vacuum ponderomotive scattering by a 3-D electromagnetic field distribution that exactly satisfies the Lorentz–Coulomb gauge condition; (4) description of coherence in Compton scattering in terms of a stochastic electron gas model; and (5) invention of a new concept for vacuum laser acceleration — the chirped-pulse inverse free-electron laser (IFEL).

In FY2000, we plan to demonstrate the first table-top, water-window, advanced, laser-driven x-ray source. This represents an important milestone in the development of table-top Compton x-ray sources for advanced biomedical applications, including K-edge phototherapy using tagged monocloal antibodies and protein crystallography.
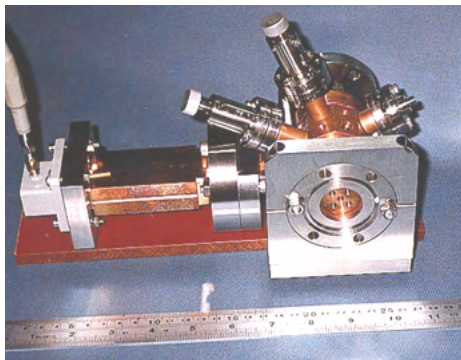
(a) (b)

Figure 1. This X-band, 5-MeV gun (a) is the highest-frequency photoinjector currently in operation; the 10-fs laser oscillator (b) is the front end of a TW-class laser system used for producing Compton x rays.

Self-smoothing of Laser Light in Plasmas

H. A. Baldis, W. Rozmus, C. Labaune, R. Berger, B. Cohen

99-ERI-018

The modification of the optical characteristics of a laser beam by a plasma is a key issue in laser–plasma coupling. It is critical to understand how this takes place, if we are ever to understand the interaction processes in the plasma corona as well as the coupling at super-high intensities—as when laser pulses approach Petawatt intensities. Interpreting and understanding parametric instabilities in laser-produced plasmas has been a problem of increasing complexity. Improvements in diagnostic capabilities in experimental studies, as well as refinements in the modeling (using different numerical techniques), are showing a complex scenario: strong interplay among instabilities, modification of the plasma conditions caused by the instabilities, and modification to the initial distribution of laser intensity inside the plasma. Of particular interest are stimulated Brillouin scattering (SBS) and stimulated Raman scattering (SRS), instabilities which have been studied extensively during the past 20 years, both theoretically and experimentally. Until now, most studies—mainly driven by requirements associated with inertial confinement fusion (ICF)—have concentrated on backscattering instabilities. The role of forward instabilities has not received much attention, despite having the potential for strongly modifying the overall laser–plasma interaction region.

The objective of this project is to study numerically the nonlinear enhancement of large-angle, forward scattering of two identical laser beams propagating in a preformed plasma. It is known that filamentation instability and self-focusing are capable of modifying laser-beam geometry, altering the electromagnetic-field distribution and spectral properties. These instabilities, combined with forward SBS, apparently cause a plasma-induced smoothing (self-smoothing) of the laser light as it propagates through the plasma. The final effect may have consequences similar to the temporal smoothing introduced intentionally in many laser systems. We do not propose this phenomenon as a smoothing technique; however, we claim that the understanding of this effect is crucial to the interpretation of experimental results on parametric instabilities.

Figure 1 shows the numerical spectra that we obtained during FY1999 from 2-D simulations in which a system of nonparaxial electromagnetic and ion acoustic-wave equations was solved in Cartesian geometry. The two incident beams are symmetric with regard to the x-axis. The transmitted light is collected along different angles q in the near-field domain and analyzed spectrally. The electron temperature, T_e, and electron density, N_e used in our numerical simulations were: $T_e = 0.5$ keV, $N_e = 0.3 \, n_{cr}$ where n_{cr} is the critical density for the laser light. The simulations were carried out over 300 ps. To account for the laser time-history used in experiments, the laser-beam intensities were ramped in time. Figure 1(a) shows the spectra of the transmitted light as a function of time for the case of a single-beam indication; Fig. 1(b) shows the same, but for the case of the two-beam irradiation geometry, at an angle of 22 deg.

Our results correspond well to observed features in recent experiments. In the simulations, the onset of this red-shifted component can be clearly identified as occurring at the moment when the average intensity of the beam speckles (high-intensity regions) reaches the critical value for self-focusing. Thus, at this moment a large number of speckles are unstable with respect to self-focusing and to the subsequent instabilities of a light trapped in a filament. It is important to notice that it is approximately at the same moment that a broad, red-shifted component appears in the single-beam spectra.

The work performed under this project helps explain features observed in experiments based on the modification of the laser field due to the growth of forward scattering. This is an important step towards our future understanding of parametric instabilities on laser-produced plasmas.
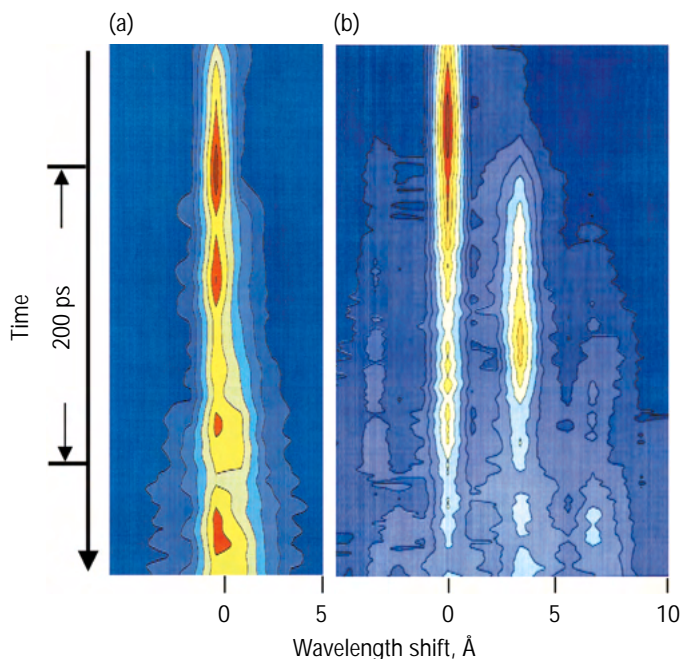
Figure 1. Frequency spectra of the transmitted light from 2-D simulations for (a) single-beam irradiation, and (b) two equal-intensity beams crossing at 22 deg. Results correspond closely to experimental observations under similar beam-crossing configurations.

Laser Satellite Communications

F. Dowla, J. Brase, S. Olivier

Wireless laser communication systems are expected to provide gigabit-per-second line-of-sight links and to play a critical role in defense and civilian communication systems. Our objective was to explore specific benefits of employing adaptive optics for free-space laser communications. The unpredictable nature of the propagation media—the atmosphere—might be a potential problem for free-space laser communication, where gigabits of data are transmitted through the air interface by sending and receiving short-duration light pulses. However, LLNL has unique capabilities in high spatial resolution adaptive optical devices that potentially can be used to reduce the scintillation in optical carriers. The Laboratory is developing microfabrication and microelectromechanical systems- (MEMS-) based wavefront control devices with hundreds of actuators, which are expected to drive down the cost of the transceivers for high-bandwidth optical communication systems and advance the technology of adaptive optics for communication applications. In this feasibility study, we developed a performance model for MEMS adaptive optics communication systems, focusing on horizontal path applications.

We determined that the use of adaptive optics would definitely increase the reliability of optical communications by increasing the signal-to-noise ratio (SNR) at the receiver—thus allowing the system to perform well with acceptable bit-error rates. Problems caused by atmospheric turbulence are particularly difficult in ground-to-ground communications over long distances. Based on our modeling, an adaptive optic system employing a few hundred actuators should be sufficient for improved and reliable communication.

Adaptive optics system parameters can be determined by application-specific modeling of atmospheric turbulence. For horizontal atmospheric propagation within several meters above ground and for path lengths longer than 1 km, a laser beam experiences multiple scatterers, i.e., "strong turbulence" propagation. Such propagation broadens the beam width and causes intensity scintillation at the detector. This effect worsens with increasing range and, for a detector of fixed size, results in a loss of SNR. Clearly, adaptive optics would be most effective for long distances, where there is a requirement for low-power operation. We investigated existing models and made preliminary attempts to extend them to strong turbulence.

Another method to improve SNR is to use a large aperture on the detector. Several methods have been proposed to model the signal variance, based on the strong turbulence model. The detector aperture size plays an important role in calculation of the actual intensity incident on the receiver. As the size of the aperture grows larger than the transverse coherence length of the laser beam, the superposition of fields at the receiver element becomes partially coherent. The scintillation will be less pronounced because of the incoherent superposition of the field on the detector plane. We determined that aperture averaging might be useful for reducing fluctuations in SNR.

Finally, it might be highly beneficial to utilize diverse techniques, such as spatial and temporal redundancy, and wideband signals in the optical system. It is unlikely that adaptive optics can compensate for all extreme atmospheric conditions. We feel that further improvement is possible by incorporating advances in error correction coding (e.g., Turbo-coding) into our system for improved performance at very high data rates.

LiInS$_2$: A Superior Material for Mid-Infrared Nonlinear Frequency Conversion

C. A. Ebbers

99-LW-024

Tunable laser sources with wavelengths in the mid-infrared (3–11 μm) are useful for remote sensing applications such as wind-shear lidar, atmospheric monitoring, and chemical-biological agent detection. In particular, long range (>1 km), remote sensing must be performed at wavelengths with favorable atmospheric transparency. Mid-infrared (IR) atmospheric transparency windows exist in the range of 2–2.5, 3.3–4.3, 4.5–5, 8–9, and 10–12 μm. In the absence of a laser source, which can directly tune across the desired wavelength regions, a solid-state laser pumping an optical parametric oscillator (OPO) is utilized. The key element within such an OPO is the nonlinear optical crystal. In particular, it is desirable to utilize the existing, mid-IR, robust solid-state laser sources for the pump laser (i.e., Nd:YAG). While several crystals exist for producing tunable mid-IR light with wavelengths as long as 4.5 μm, there exists only one nonlinear optical crystal capable of utilizing Nd:YAG to produce light at 5–11 μm. Typically, in order for the efficient and robust Nd:YAG pump laser to be converted to the 5 to 10-μm wavelength, a two-stage nonlinear device is utilized, requiring two nonlinear optical crystals.

Lithium thioindate (LiInS$_2$) is a nonlinear optical crystal discovered in 1972. Due in part to difficulties in growing the crystal, the largest crystals grown at the time were on the order of 3 mm per side and further development faltered in favor of other nonlinear optical crystals. However, this crystal has the distinct advantage of a large transparency range (0.4–8 μm), allowing direct mid-IR generation via pumping with a near-IR solid-state lasers (such as Nd:YAG). We characterized the LiInS$_2$ crystals grown via more modern growth techniques and determined the necessary parameters to evaluate this "re-discovered" crystal for mid-IR pump sources. We measured the parameters necessary for evaluating the utility of this crystal for average power, mid-IR OPOs. Because of our effort, crystals of LiInS$_2$ with apertures up to 5 mm × 5 mm × 10 mm are now commercially available.

In addition to characterizing the linear and nonlinear optical properties of these crystals, we measured their thermal conductivity, thermal birefringence, and thermal tuning. The thermal conductivity of LiInS$_2$ along the *x, y,* and *z* axes is 62, 60, and 76 mW/(cm-K). For reference, this is nearly 2 times higher than lithium niobate. We have directly measured the Type II noncritical phase-matching wavelength for propagation down the *x* axis, 2.320 ± 0.002 μm, and determined that the change in noncritical wavelength with temperature to be less than 0.01 nm/C. These measurements indicate that LiInS$_2$ is highly suitable for use as a high average-power OPO. Unfortunately, small scattering defects, similar to those present in the development stage of other sulfide nonlinear optical crystals (AgGaS$_2$), prevent us from directly obtaining OPO oscillation with a 1-μm pump source at this time. The presence of these scattering sites indicates that further refinement of the growth technique is required. Through annealing of the crystals, it may be possible to eliminate this type of defect; we are examining this approach. Finally, we have also obtained crystals of LiInSe$_2$. As expected, the selenide crystals have a longer wavelength transparency than the sulfide crystals, extending the useful range of this class of nonlinear optical crystals to 8.5 μm.

An Inner-Shell Photo-Ionized X-Ray Laser at 45 Å

F. A. Weber, P. M. Celliers, S. J. Moon, L. B. Da Silva

A long standing goal of Laboratory x-ray laser research is the realization of x-ray lasers working at wavelengths close to or even below the water window (26–44 Å) with a table-top energy source. Although a number of tabletop-sized schemes have been demonstrated recently, they work at wavelengths beyond 100 Å and are difficult to scale to shorter wavelengths.

In this project, we adopted one very attractive approach to short wavelength x-ray lasers—the inner-shell photo-ionization (ISPI) scheme. In this scheme, the laser transition is pumped by an incoherent x-ray source. Using carbon for the lasant material as an example, the underlying concept is based on the fact that the photo-ionization cross section is much larger for the tightly bound inner shell electrons (i.e., the 1s electrons) than for the more loosely bound outer shell electrons (i.e., the 2p and 2s electrons). This requires photon energies at least high enough to photo-ionize the K-shell, ~286 eV, in the case of carbon. As a consequence of the higher cross section, the inner-shell are "selectively" knocked out, leaving a hole state $1s2s^2 2p^2$ in the singly charged carbon ion. This generates a population inversion to the radiatively connected state $1s^2 2s^2 2p$ in C+, leading to gain on the 1s-2p transition at 45 Å. The resonant character of the lasing transition in the single ionization state intrinsically allows much higher quantum efficiency compared to other schemes.

Competing processes that deplete the population inversion include auto-ionization, Auger decay, and in particular collisional ionization of the outer-shell electrons by electrons generated during photo-ionization. These competing processes rapidly quench the gain. Consequently, the pump method must be capable of populating the inversion at a rate faster than the competing processes. This can be achieved by an ultra-fast, high intensity laser that is able to generate an ultra-fast, bright x-ray source. Our calculations to date indicate that for the C 2p-1s lasing transition an ultra-fast x-ray burst (on the order of 40 fs) is needed to generate gain of ~10 cm^{-1} with a duration of 50 fs. Although the basic concept of the ISPI laser was proposed 30 years ago, it has never been demonstrated because such pumping sources have not been available. With the advent of advanced chirped-pulse amplification techniques, we only now have been able to install our experiment at LLNL's Falcon laser, which can deliver powerful pulses of light in the petawatt regime.

During FY1999, we completed the target design and launched a series of x-ray spectroscopy investigations in order to optimize the absorber/x-ray converter–filter package. The most promising configuration consists of a 200 Å gold absorber coated with 1 k of titanium for soft x-ray attenuation. Figure 1(a) depicts predicted target performance and shows integrated output intensity versus energy for various times. Figure 1(b) shows a representative pinhole image taken at best focus (*f*/2, 100 mJ, 35 fs) from the front (gold) side of the target assembly. The soft x-ray spot size is about 50 μm and the estimated conversion efficiency is 10^{-4}.

For FY2000, we plan to complete the spectroscopic investigation with a time-resolved measurement of the target output and implement a traveling wave pumping system. Our ultimate goal is to demonstrate a prototype ISPI x-ray laser at a wavelength of 45 Å. If realized, ISPI x-ray lasers hold significant promise as useful tools in biology, microbiology, biomedical imaging, materials science, and high-density plasma diagnostics.

(a)

(b)
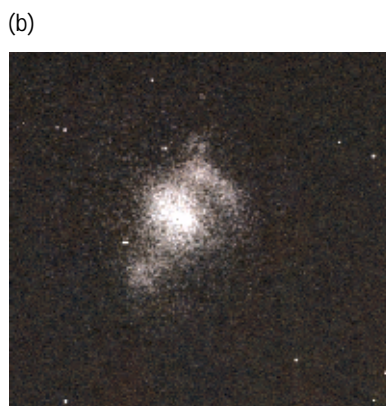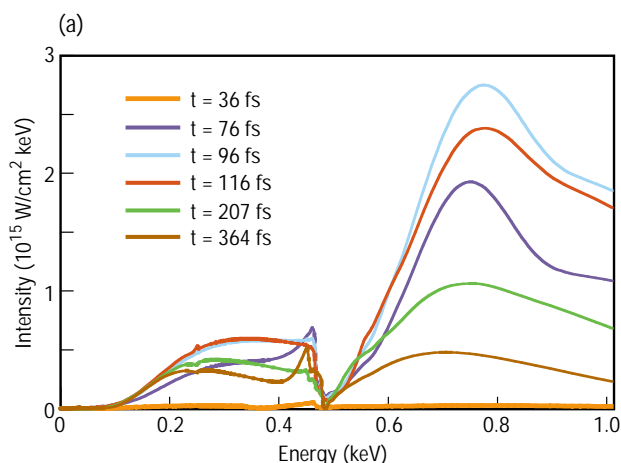
Figure 1(a) shows predicted x-ray absorber/filter performance; (b) shows a pinhole image of front side emission at best focus (*f*/2).

Manufacturing Processes and Technologies

7
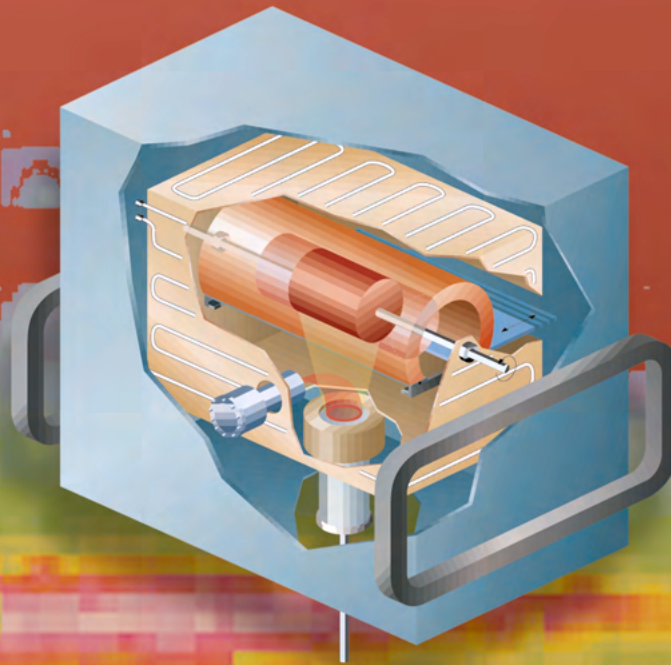
Section 7

Manufacturing Processes and Technologies

Improved Printed Circuit Board Fabrication through Etch Rate Control

M. P. Meltzer

97-ERD-032

The intent of the project is to lower environmental and human health risks associated with printed circuit board (PCB) manufacture and to redesign the process for greater efficiency and profitability. The major technical challenge was to develop a "compositionally modulated" electroplating approach, in which either of the two metals is deposited from the same bath. Compositionally modulated plating offers significant environmental and cost advantages. It can (1) eliminate the need for lead, an extremely toxic material, from several manufacturing steps, and (2) shorten the manufacturing process.

The new plating approach is based on deposition of either copper or nickel from the same bath. Through control of bath chemistry and rectification, we can select the particular metal to be deposited. Copper is plated first to the desired thickness of the PCB's circuitry (typically 0.5 mil or 0.0005 inch). Next, a nickel layer is deposited as an "etch resist" to protect the copper circuitry. This layer is left in place rather than stripped (as etch resists generally are); it serves as a finish coat to the board onto which components are soldered. Testing has demonstrated that this nickel layer, which contains a small percentage of copper due to the chemistry of the process, provides a good solderable surface.

Production advantages arise from the elimination of several steps in the manufacturing process: First, the deposition of copper circuit traces and of the etch resist layer are combined into one operation. Any need for rinsing between these two steps is also eliminated.

Next, the nickel etch resist layer does not have to be stripped, eliminating a costly, labor intensive operation that also generates significant hazardous waste. Unlike the nickel layer, the tin and tin-lead etch resists in current use are not durable enough to be employed as finish coats.

Finally, hot air solder leveling (HASL), the most common method of finishing PCBs, is no longer needed because the nickel serves as both an etch resist and a finish coat. In addition, HASL is one of the main uses of lead in traditional PCB manufacturing. Its elimination has both production and environmental advantages.

The modulated plating technology was adapted from layered electroforming techniques used to build up copper-nickel composite materials of high tensile strength. These materials typically have many alternating, extremely thin layers of each metal. Our modulated plating approach altered process parameters in order to deposit the thicker layers of metal required for PCB circuitry and etch resist layers.

Our plans for FY2000 focus on improvements to the deposit properties (in particular, its elongation, plating rate and throwing power) in order to render the technology more viable for industrial applications. An electrochemical manufacturer, currently examining the technology for its commercialization application, potentially a source of future development.

Radiation Hardening of CMOS Microelectronics

T. W. Sigmon, A. M. McCarthy

97-ERD-066

The objective of this project was to investigate and develop novel microtechnologies with advanced functionality—specifically, radiation-hard electronics—that will have a profound impact on the surety of nuclear weapons that are subject to radiation-intense environments. LLNL's radiation-hard technology provides a unique means of forming radiation-hard, thin-film silicon microelectronics on almost any material—metal, glass, plastic, etc. It allows innovative applications of microchips both in radiation-hard electronics and in flexible, lightweight electronics.

In this procedure, the microelectronics are transferred by (1) bonding a fully fabricated silicon wafer of microelectronics devices, circuit face down, on a holding substrate; and (2) removing the silicon substrate so that only thin-film silicon is left in the transistor-device areas. The devices are held in place by the combined action of the holding substrate, the matrix of interconnecting metal, and surface dielectrics.

In FY1999, we successfully applied this technology to the transfer of n-channel metal oxide semiconductors (MOSs). In the figure, we show a optical micrograph of an array of n-MOS transistors that have been thinned, along with an enlargement of a single device.

During FY1999, we performed 3-D calculations jointly with Sandia National Laboratories (SNL) on the effect of substrate thickness on the single-event upsets

Single transistor island

Arrays of thinned n-MOS transistors

Example of a array of thinned n-MOS devices. An enlargement of a single transistor is shown for clarity (where G stands for gate, S for source, and D for drain).

(SEUs) of SNL's CMOS6 16K SRAM cells. (An SEU is an upset of the charge on a device resulting from the passage of a high-energy charged particle such as an alpha particle.) Simulated and measured results on the effect of substrate thinning on the current–voltage characteristics of a device were found to correlate—no increase in subthreshold leakage was either predicted or observed. We also simulated charged-particle strikes into the gate (G) and drain (D) regions of n-channel devices. The thinned structures showed a major increase in the upset threshold (the point where the charge state on the drain changes) for strikes into the drain—a silicon thickness of 0.5 μm performed as well as the standard silicon thickness of SNL's silicon-on-insulator (SOI), radiation-hard devices. Gate strikes showed improved thresholds, again essentially emulating those of the SOI devices.

An interesting, unforeseen result of these simulations is that we discovered a limit to the radiation hardness of present-day radiation-hard structures that had not been previously predicted; that is, gate strikes do not improve from the use of either thinned silicon or SOI devices. Verification of this result could have a direct impact on the future development of scaled, SOI, radiation-hard devices.

As a result of these predictions, we began to develop a process for thinning SNL's CMOS6 wafers. We developed an approach in which KOH is used for bulk removal of the silicon; this is followed by a high-low doping, selective wet-chemical etch to remove the heavily p-doped substrate from the low-doped, epitaxially grown material. The selective-etch solution giving the best results was 1:3:8 HF(49%): HNO_3(30%): CH_3COOH(100%) (in volume). In this solution, the etch rate of the silicon doped with a boron concentration greater than $7 \times 10^{13}/cm^3$ is 2 μm/min, decreasing to about 0.02 μm/min at boron concentrations of $3 \times 10^{17}/cm^3$.

In future work, the bonding process will be changed to render our procedure compatible with standard silicon-fabrication techniques. This will be achieved by using a combination of chemical-mechanical planarization (CMP) and low-temperature bonding. It will be important to verify the simulation results mentioned above.
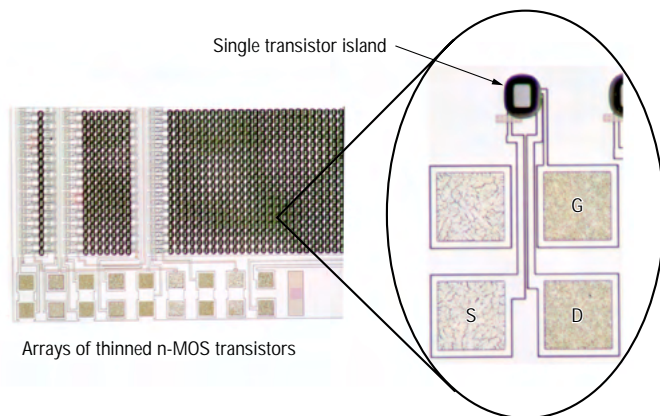
A Spatial-Frequency-Domain Approach to Designing Precision Machine Tools

D. Krulewich Born

Currently, many tolerances are specified in terms of the spatial-frequency content of residual errors on the surface of a machined part. During the design of a new machine tool, we typically use an error budget as a sensitivity-analysis tool to ensure that the parts manufactured by the machine tool will meet the tolerances specified for the finished component. Thus, error budgets provide the formalism whereby we account for all sources of uncertainty in a process, and we sum them to arrive at a net prediction of how "precisely" a manufactured component can meet a target specification. However, the conventional error-budgeting procedure provides no formal mechanism for designing machines that can produce parts with spatial-frequency-based specifications.

The objective of this project was to develop a new error-budgeting methodology for designing precision machine tools and motion-control systems that can meet the increasingly stringent tolerances required by LLNL's programs. During this project, we developed a new error-budgeting methodology to aid in the design of new machines used to manufacture parts with spatial-frequency-based specifications.

Our new methodology has six steps. The first step is to identify the physical influences that generate dimensional errors on the surface of a machined part, including thermal gradients and temperature variability, bearing noise, and fluid turbulence in cooling passages. The next step is to determine how these physical influences couple to the machine, and then convert them into "elemental errors," that is, into displacements that have a direct influence on machine performance. The third step is to convert the elemental errors into the frequency domain; the fourth step is to then sum them in the frequency domain. At this point in our procedure, we have a completely new algorithm with a statistical foundation that allows us to place error bounds around the sum of the elemental errors.

The fifth step considers the machining process. During the machining process, the removal of material during machining creates "cutting forces." These cutting forces combine with forces induced by the machine errors. The structure of the machine responds to these forces with vibratory displacements that ultimately result in additional errors on the machined part. The ratio between the cutting force and the amount of material removed is the "material-removal transfer function." In our procedure, the combined errors then go through the material-removal transfer function, which accounts for the dynamics of both the material-removal process and the machine. The sixth step is to transform the errors into the coordinate system of the part. The output from this process is the continuous spectrum of errors at all spatial frequencies on the part.

During FY1999, we completed our experiments and validated each step in our new error-budgeting procedure. We first measured the contributing errors and then machined parts on a T-based lathe. We used our procedure to predict the frequency content of the errors on the machined parts and compared the results to actual measurements of the errors in the parts. The predicted mean error was close to the measured mean error for four sets of test measurements. Furthermore, the measured errors stayed below the 99th percentile confidence limit for all but one single point, which exceeded the confidence limit by about 1 microinch at a frequency of 1 cycle/in. This variation may have been caused by an unaccounted-for thermal condition that existed during either the machining or the measurement process. It may also have resulted from some simplifications that were made while we were mapping the tool geometry onto the part. We had predicted that the cycling of the environmental control would cause an error at about 2 cycles/in.; however, we did not significantly observe it on the measured part. We believe that the cutting lubricant that we used during the machining probably supplied thermal control at the tool/part interface, thereby minimizing any thermal growth caused by environmental cycling.

In summary, we demonstrated that this new procedure can be used to predict the spatial-frequency content of errors on the surface of a machined part. Our procedure will be used at LLNL to select and design new machines used to manufacture parts with frequency-based specifications.

High-Precision, Droplet-Based Net Form Manufacturing of Advanced Materials

A. B. Shapiro

98-ERD-085

In collaboration with the University of California, Irvine (UCI), we have been working on a new technology that relies on the precise deposition of nanoliter molten-metal droplets that are targeted onto a substrate by electrostatic charging and deflection. This way, 3-D structural materials can be manufactured microlayer by microlayer. Because the droplets have small volumes, they rapidly solidify on impact, bringing forth a material component with the fine grain structures that lead to enhanced material strength. Rapid solidification also leads to high geometric fidelity because there is no macroscopic fluid flow of the deposited droplets.

If successful as an industrial practice, this technology would provide significant economic benefits and enhance material quality; it could revolutionize manufacturing in this country. Immediate applications at LLNL would include (1) rapid prototyping of metal parts and manufacture of new alloys by co-jetting different metals, and (2) manufacture of hybrid microelectromechanical systems (MEMS) by fabricating 3-D structures on etched substrates. Possible future applications include fabrication of micro-optic arrays, and the ability to precisely control the trajectory of a droplet can be used for biological separation (e.g., directing droplets into microscale test tubes).

To develop a useful technology, we must understand the transient thermal behavior of a droplet during time of flight, the mechanical deformation and solidification of a droplet on impact with a substrate, the deformation and thermal interaction of an incoming partially liquid droplet with the previously deposited and solidified material, and how the microstructure is formed.

UCI has been responsible for the experimental investigation of the manufacturing feasibility of this process and for corroborating the predictions of our numerical models. We have contributed LLNL's unique expertise in the computational modeling of 3-D heat transfer and solid mechanics and the large-scale computer resources necessary to model this system.

In FY1999, we modeled the liquid-metal splatting on a substrate with DYNA3D, a Lagrangian solid-mechanics finite-element code, and ALE3D, an arbitrary Lagrangian Eulerian code. The Eulerian part of ALE3D was better able to model the very large deformation and flow of the liquid metal on impact with the substrate.

We developed an analytical model that predicts the spread of a liquid-aluminum droplet striking a substrate. Solidification and its effect on the flow of the liquid was included in the model. Our model showed good agreement with experimental data in the literature; however, neither DYNA3D nor ALE3D successfully matched either the analytical model or data in the literature. At present, both codes lack the physics to model surface tension, which is a major physical force that arrests the spreading of the liquid.

We also developed a computer code, HOTDROP, that could model the overall system and predict the impact velocity and temperature of a droplet. This code calculated (1) overall energy and momentum balances on a liquid droplet during time of flight, (2) generation impact velocity and temperature of a droplet, (3) the effect of the wake from a leading droplet on the velocity of a trailing droplet, and (4) the effect of the environmental chamber's temperature, pressure, and gas type (e.g., N_2, CO_2) on a droplet's temperature drop during time of flight.

During FY1999, UCI moved the technology forward from using solder droplets to using more interesting materials with higher melting points, such as aluminum. A manufacturing problem associated with the reduction of oxides in the fabricated parts was solved by designing and incorporating a filter pack in the liquid stream. Tensile tests of fabricated parts were promising—the measured yield stresses (8,900 psi) were greater than both the yield stress for the starting aluminum ingot (6,816 psi) and published handbook values for aluminum (6,800 psi).

Manufacturing U-6 wt% Nb Parts by E-beam Physical Vapor Deposition

K. W. Westerberg, T. C. Meier, T. M. Anklam

Electron-beam physical vapor deposition (EBPVD) is a viable method for producing near-net shape U-6 wt% Nb (U6Nb) parts. In this process, vapor produced by e-beam evaporation is deposited on the surface of a moving substrate (mandrel). Because of the atom-by-atom nature of the deposition process, we can produce fully dense vapor deposits with high fidelity replication of mandrel details, precise dimensional control, and correct alloy composition and metallurgical properties. Following heat-treatment, vapor deposited material exhibits mechanical properties similar to those of wrought U6Nb material. Vapor deposits on the order of millimeters in thickness can be produced quickly because of the high vapor rates achievable with e-beam evaporation. Such EBPVD processing to manufacture U6Nb parts produces significantly less waste, with fewer process steps than does the conventional manufacturing technology. Near-net shape parts require less machining, and scrap material is amenable to recycle via e-beam processing. This manufacturing technology offers the potential for significant cost savings in the DOE's manufacturing missions.

This project builds on previous work in U6Nb vapor deposition. We have produced U6Nb tensile test specimens by means of EBPVD that meet specifications for yield strength, ultimate tensile strength, and elongation to failure after heat-treatment. We have also produced a 1-in.-diam. cylinder with wall thickness near that required for hydrodynamic (hydro) testing. The goal of this project is to use a sub-scale experimental facility to develop the technology needed to make full-scale U6Nb parts by EBPVD. This requires (1) a size-scalable mandrel, (2) maximized vapor utilization, and (3) mandrel manipulator motions to produce all part features. A high deposition temperature (about 90% of the absolute melting temperature) is required to produce a quality deposit. This combined with the high thermal expansion of uranium makes it necessary to use a mandrel that yields (crushes) during cool-down. The challenge is to develop a mandrel with good dimensional control and surface finish that survives uranium exposure at high temperatures. We selected a coated alumina insulating foam that crushes during cool-down. The foam is commercially available in a range of sizes including those needed to produce full-size parts. The material can be machined to tight dimensional tolerances with excellent surface finish using a diamond-tool lathe (diamond-turning). A thin tantalum metal coating is sputter-deposited on the surface to protect the alumina from uranium attack.

The vapor deposition process is designed to maximize the fraction of produced vapor that lands on the mandrel while maintaining the correct mandrel temperature to make a quality deposit. Both the vapor flux and the thermal energy caused by reflected electrons arriving at a surface increase as the surface approaches the vapor source. This leads to a trade-off between high vapor utilization and the management of heat as the mandrel is moved closer to the vapor source. The "skip" energy is sufficient to overheat and melt a vapor deposit. We took care to select e-beam parameters that provide correct deposition temperature at the mandrel for a given standoff. The manipulator moves the mandrel in the vapor stream such that the desired coating thickness is achieved on all features of the part.

In FY1999, our hardware demonstrated the reliability, range of motion, and stability required for this process. In addition, we produced a sub-scale part with the desired features and a significant wall thickness that exhibited minimal distortion during cool-down. The mandrel design is scalable to full-sized parts, and we demonstrated deposition at a standoff necessary to rapidly produce parts. We demonstrated the technology needed to produce near net shape U6Nb parts by EBPVD.
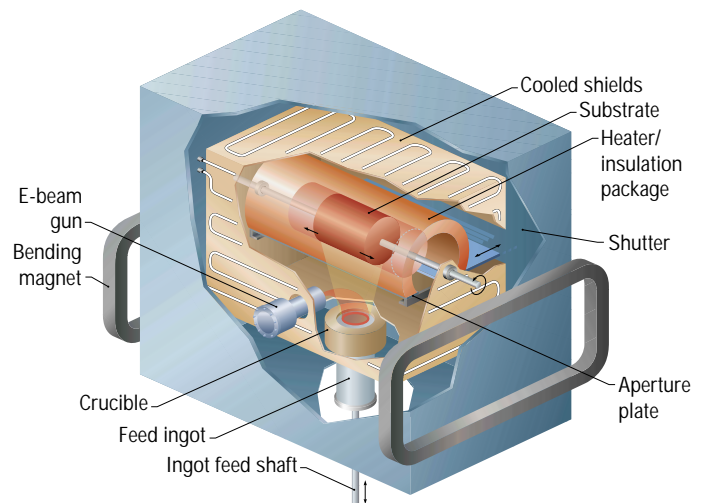
E-beam vapor deposition system to produce near net shape metal alloy shells. A magnetically guided electron beam is used to evaporate metal from the feed ingot. The vapor is deposited just below its melting point on the outer surface of the rotating cylindrical substrate (mandrel) that is machined to match the inner contour of the desired part. After cooling, the crushable mandrel is easily removed yielding a near-net shape part. A wall thickness of several millimeters can be achieved in a 20-hour deposition run.

Microrelay Strong Links for Caltrap

A. Bernhardt, G. Cooper, V. Malba

99-ERD-051

A miniature, integrated weapon safing and arming device requires a reliable, innovative switch whose behavior in abnormal environments such as fire can be predicted. Our goals in this project were to (1) develop a new design concept for a high reliability microrelay, (2) build a prototype, and (3) demonstrate high-force relay closure in the prototype.

We designed a microrelay to meet commercial specifications: 3-g (or 0.03 N) closure force and 30-mA actuation current at less than 0.5 V. Our microrelay not only occupies less than 1 mm^3—about 1% of the volume of the smallest commercial part—but also, its fabrication takes advantage of semiconductor processing, which has the potential to automate microrelay production.

Reliable metal-to-metal contacts require sufficient contact force to plastically deform contact surfaces at asperities—thereby increasing the contact area. On the other hand, contact metallurgy and the gaseous environment must be controlled to prevent contact welding, contamination, oxidation, and other effects that change contact resistance over time. A contact force of 3 g is commonly used with gold/gold-alloy contacts in a sealed relay. In this way, more than 10 million closures can be achieved with a resistance of less than 100 mΩ. Our prototype relay preserves the contact metallurgy of commercial relays.

The fundamental innovation in the fabrication of our microrelay is the use of a 3-D lithographic process to create a "winding" around a discrete magnetic core. To achieve sufficient inductance to generate the desired contact force, we chose a discrete core of substantial cross section (about 0.3 mm^2). Because of the core thickness, thin films deposited around it cannot be patterned by conventional lithography, but they can be patterned by our 3-D process.

The microrelay is formed on a single substrate so that critical core-to-armature distance can be precisely defined using a thin sacrificial layer. The initial separation of the core and armature is about 10 μm. The issue of greatest significance to the performance of the relay is the dimensional precision of relay closure—the electrical contacts should touch when the armature and the core (which define the magnetic circuit) are separated by only about 1 μm. Defining a manufacturable process that can achieve this goal has been the triumph of this year's development effort.

To define the design of our prototype microrelay, we performed both 1-D analytic and 3-D numerical modeling. The prototype differed in a number of ways from the design primarily because of problems in fabricating the iron core. The prototype served its purpose, however, verifying the design concept and demonstrating the closure forces required. Measurements of the force generated by the microrelay, as a function of the separation of the armature from the pole pieces of the core are shown in the figure. The data are consistent with a force of 3 g at a separation of 1 μm using 0.03 A with the larger core of the design. This force can also be achieved at larger separation by increasing the number of turns in the winding.

In conclusion, we have designed a microrelay that meets commercial specifications and can be sufficiently reliable for weapons applications. We fabricated a prototype that provides concept verification. The fabrication process produces the required micrometer-scale tolerances in the separation of the armature and the core and lends itself to simultaneous fabrication of thousands of microrelays on the same substrate.
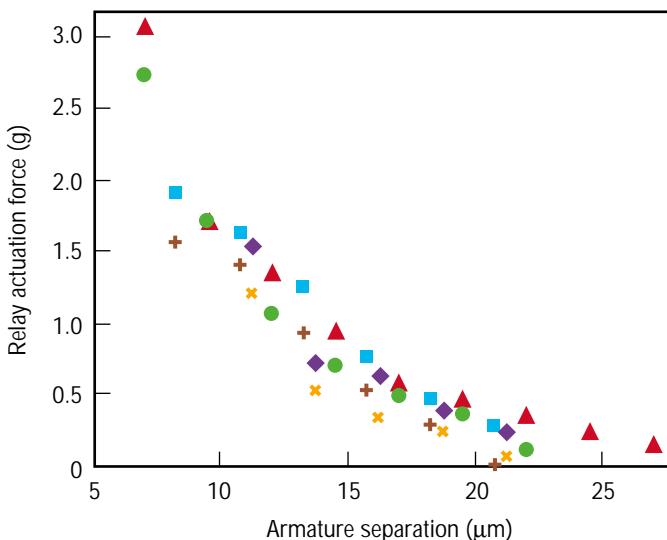
Force measured between the armature and the actuator of the microrelay, shown as a function of the separation between them. Current was 0.5 A, to allow force to be measured at large separation. Data from 6 runs are shown in various colored shapes. Uncertainty in position is ±3 μm because of the presence of particles that prevent perfect contact. Surface flatness was approximately ±1 μm. The data are consistent with a contact force of 3 g at a separation of 1 μm using an actuation current of 0.03 A with a larger core.

Development of a Magnetic Random-Access Memory Device

C. Cerjan

99-ERD-059

Random-access memory (RAM) is one of the most important components of a computer system. In large part, the bit density and access time of this memory determines the overall performance of the entire system. Almost all personal computers use dynamic RAM (DRAM) technology because of its very favorable cost-to-performance ratio. This type of fast memory depends upon semiconductor-based, doped-silicon materials; hence, it is relatively inexpensive to manufacture. As memory size increases, however, storage-bit size must be reduced—resulting in significant technological obstacles that might preclude further development of DRAM technology. The primary obstacle to bit-size reduction is widely recognized to be the dielectric material used in the device. This material holds the charge until an applied voltage activates it. That is, the device's capacitance must rise significantly; otherwise, individual bits will no longer operate reliably.

The use of magnetic materials in place of semiconductor materials for RAM (MRAM) has become feasible with the advent of a new class of magnetoresistive materials—the so-called giant magnetoresistive (GMR) multilayer stacks. These materials were initially investigated for their use in magnetic sensors, where they have successfully replaced the older generation of inductive read heads, providing 5- to 10-fold increases in areal density. The introduction of this technology to RAM applications would have several natural advantages: nonvolatility, intrinsic radiation hardness, and higher bit densities than projected DRAM devices. The outstanding technical obstacle confronting MRAM development is the relatively slow access time of an individual element. Introducing GMR materials with higher sensitivity can significantly reduce this access time.

The critical issue of increased field sensitivity was directly confronted in this half-year investigation. We initially concentrated our research on the optical patterning of an optimized, high-GMR-response, ternary alloy (NiFeCo) previously developed at LLNL.

This alloy had originally been investigated for use in magnetic read-head applications where its high thermal stability—its retention of high GMR response after heat treatment—made it an attractive candidate for manufacturing processes. During the course of our research, we discovered that an anomalous field response occurred during patterning. That is, when a sheet of this material was patterned by electron lithography into small, submicrometer-sized cylindrical dots, the magnetoresistance jumped tenfold or more, especially at the smallest feature sizes.

We then focused on critical verification experiments that would confirm or refute the earlier incomplete observations of enhanced response at small feature sizes. If this trend were verified, then another set of experiments would be devoted to the elucidation of the underlying mechanism controlling this unusual behavior.

A high-performance optical stepper located at LLNL had sufficient dynamic range to provide a useful test of the field response at somewhat larger feature sizes. We began a careful set of scaling experiments in which we fabricated cylindrical dots of varying radius. These experiments included features ranging from a 2- to a 0.35-μm radius.

The largest features did indeed display a scaling response similar to that observed earlier, but a severe problem arose in one of the necessary processing steps that destroyed the smaller (less than 0.5-μm radius) devices. We traced the experimental problem to an overly aggressive planarization step that removed more material than expected from the patterned arrays.

Thus, it appears that our previous observations of enhanced magneto-resistive response were not experimental artifacts and that partial oxidation of the exposed multilayer surface was its primary cause. Furthermore, identification of the difficulties with the polishing procedure has provided important process information. Indeed, these results suggest another series of experiments that modify the chemical composition of the slurry and the duration of its application.

Development of Echelle Immersion Gratings for Very High Resolution Infrared Spectroscopy

D. R. Ciarlo, J. Ge, P. J. Kuzmenko

99-FS-004

Infrared spectroscopy is becoming the most exciting field in astronomy. The goal of this feasibility study was to develop silicon immersion gratings that promise a major impact in this area. Silicon gratings in immersed reflection mode, called silicon immersion echelles, offer high efficiency and very high spectral resolving power (R >100,000) in the infrared (IR) for the first time. Silicon gratings in transmission mode, called grisms (grating on a prism), promise a very convenient and inexpensive way to implement intermediate and high spectral resolution in any existing IR camera. This will free up resources at major observatories that would otherwise be spent developing traditional large and expensive IR spectrographs. Both the silicon immersion echelle and grism promise to play a critical role in space and airborne missions to significantly reduce the size and weight of spectroscopic instruments.

We developed the world's first etched silicon grisms. Researchers worldwide have tried for more than three decades to develop such a device without success. The grisms have a 10×10 mm^2 etched area, 66-μm groove spacing, and a 46-deg. wedge angle. We measured the surface figure of these grisms. For the three best grisms the rms wavefront error is 0.035 wave in reflection at 0.6328 μm. This corresponds to 0.027 wave in transmission at 1.0 μm, which is diffraction limited.

We installed one of the silicon grisms in a UC Berkeley near-IR camera, IRCAL, and tested it with starlight at the Lick 3-m telescope. One of the first light spectra of a nearby young star binary, T Tauri, is shown in the figure. With the 5-mm-diam. pupil size of the IR camera, this grism provides R = 5,000 with a 0.2-arcsec slit at 2.2 μm. This spectral resolution is the highest ever obtained with grisms. When a cross disperser is added, the entire K band (2.0 μm < λ < 2.4 μm) will be covered by the 256×256 HgCdTe array. The details of the testing and initial exciting scientific observation results were released at the American Astronomical Society meeting in Atlanta in January 2000.

Other silicon grisms with silicon nitride antireflective coatings and different wedge angles were tested in the lab later in 1999. Preliminary measurements show that the nitride coatings can provide better than 97% transmission in the K band, while uncoated silicon transmits only 54%.

During FY1999, our silicon grating development has drawn favorable attention from the Stratospheric Observatory for Infrared Astronomy (SOFIA) and the Next Generation Space Telescope (NGST), both large, high-profile National Aeronautics and Space Administration (NASA) projects. The project scientists have requested that we submit proposals to them for further grating development. We are forming an official collaboration between NASA Goddard Space Flight Center (headquarters for NGST), NASA Ames (headquarters for SOFIA) and LLNL to develop silicon gratings for NGST and SOFIA missions. Our results have been presented at five international conferences and workshops. Two journal articles (one in astronomy and one in optics) are being prepared.

Silicon grism spectra of T Tauri binary stars. One of the first light spectra with the silicon grism at the Lick 3-m telescope taken on the night of October 28, 1999. Two spectra are from the primary and secondary stars of the T Tauri binary with only 0.65-arcsec separation. The measured spectral resolution with a 0.2-arcsec slit is R = 5,000 at 2.2 μm, as expected.
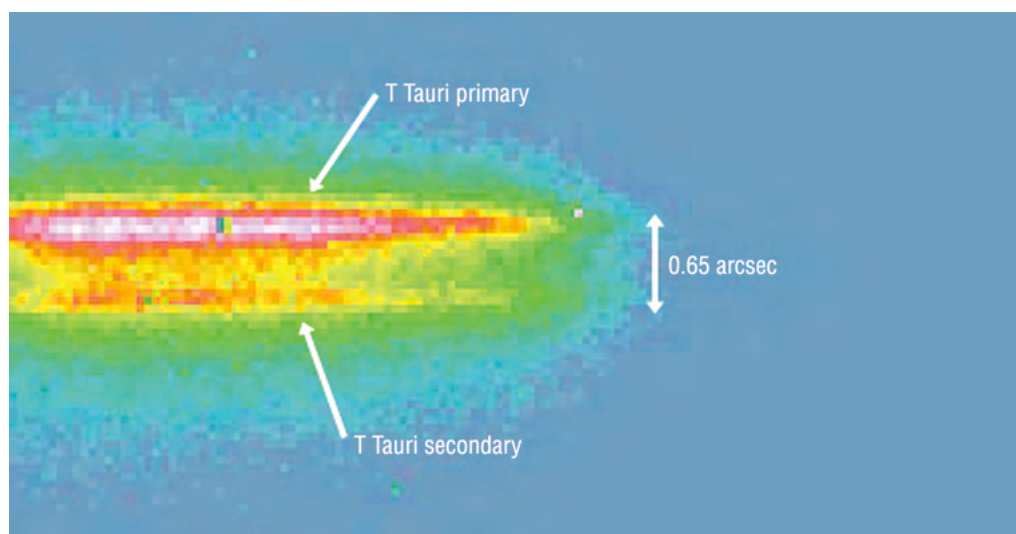
Materials Synthesis and Characterization

8
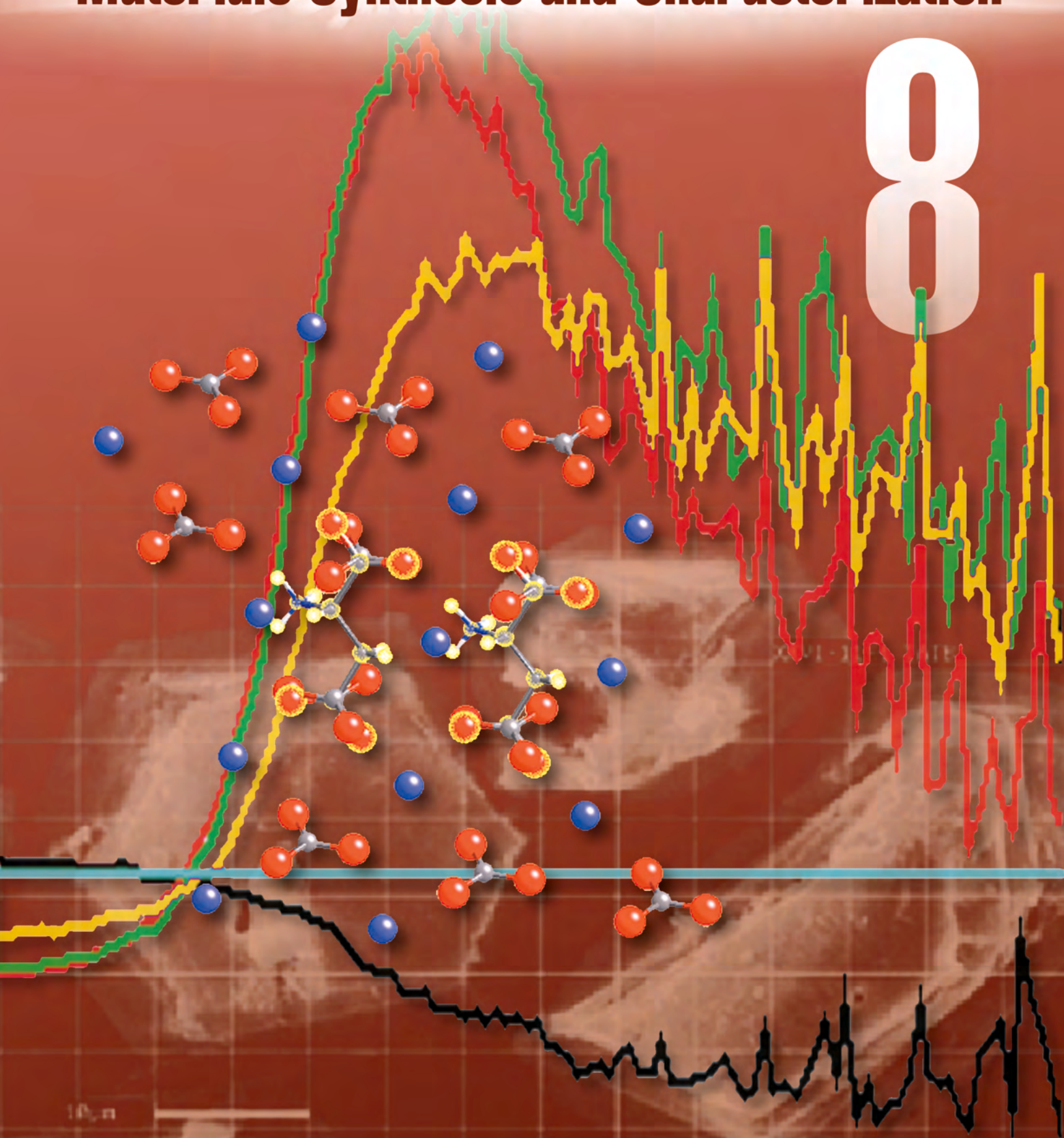
Materials Synthesis and Characterization

Defect Studies of Optical Materials using Near-Field Scanning Optical Microscopy and Spectroscopy

M. Yan, J. McWhirter, T. Huser, W. Siekhaus, J. De Yoreo

Understanding the properties of materials at the nanometer scale has become a key issue in programmatic and basic research at the Laboratory. We have developed near-field scanning optical microscopy (NSOM) to optically characterize materials with a spatial resolution about one order of magnitude better than conventional microscopy. Combining scanning probe and optical fiber technologies, NSOM simultaneously provides optical (e.g., spectroscopic properties) and topographic information with 50-nm resolution. This project has resulted in the development of two NSOM instruments, which have been used to perform research on the characterization of surface and sub-surface defects in optical materials, including fused silica, potassium dehydrogen phosphate (KDP), and gratings. This research using NSOM directly addresses the issue of laser-induced damage in optical materials, which is typically initiated by a local variation in optical properties at sub-micron scale.

Our work during FY1999 focused on the detection of the local laser field associated with the defects, using evanescent-wave NSOM techniques. The detection of the local laser field is achieved by measuring the near-field evanescent wave produced by a laser beam that is totally internally reflected at the sample surface. The near-field evanescent wave signal, collected by NSOM fiber probe, is proportional to the intensity of the electrical field at the sample surface. The figure shows pairs of NSOM images for samples of fused silica, a grating, and a KDP crystal. In the figure, the top image of each pair shows the surface topography, and bottom image is the evanescent wave NSOM image. Figure 1(a) shows the topography and local laser intensity (by NSOM) of damage sites on fused silica. The high intensity in the NSOM image is associated with a surface crack generated during the laser irradiation. Subsequent in-situ laser damage was observed to be spatially correlated with the high laser intensity observed in the NSOM image. This demonstrates that the local field enhancement mechanism is important for predicting the growth of laser-induced damage on fused silica. Figure 1(b) shows the local field enhancement for an optical grating from the LLNL diffractive optics group. In the NSOM image, the high intensity regions are associated with the edge of the grating line structure, as seen in the topographic image. This measurement provides a fundamental understanding for the cause of laser damage and a quantitative analysis of field enhancement. Figure 1(c) shows etching defects on a KDP crystal that lie below a 70-nm sol-gel coating on the surface. The top image shows the flat surface of the sol-gel coating. The bottom image shows the optical image of the etch pits, which occur at the interface of the sol-gel coating and the KDP crystal. These results show that NSOM provides a unique non-destructive method for sub-surface detection of defects. During FY1999, we also developed an integrated NSOM/confocal microscopy system that is sensitive enough to detect fluorescence from single molecules and to measure their properties spectro-scopically. This capability opens new avenues for detecting chemical and biological species at the molecular levels.

In summary, we have developed a new metrology to detect defects in optical materials below the diffraction limit of light. We have (1) measured the growth of laser-induced damage in fused silica due to field enhancement, (2) measured local laser-intensity variations due to the structures of an optical grating, and (3) identified the etch pits of KDP crystal due to sol-gel coatings. Thus, NSOM technology provides an optical method to identify and characterize nano-scale materials needed for research and programmatic developments at LLNL.

(a)   (b)   (c)
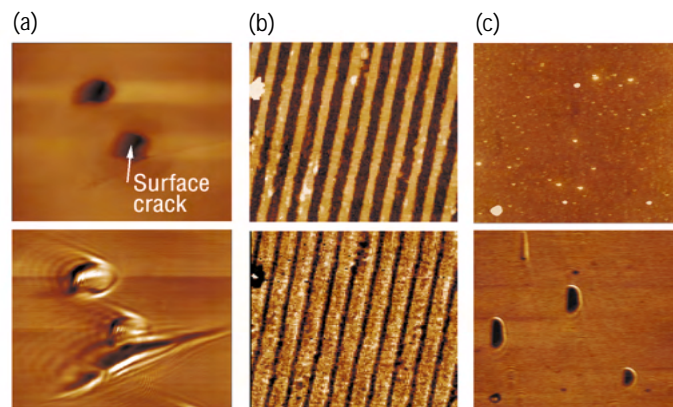
Figure 1. The topographic (top) and evanescent-wave NSOM (bottom) pairs of NSOM images for samples of (a) fused silica, (b) a grating, and (c) a KDP crystal. The image size is 20×20 μm.

High-Performance Polyimide Coating Technology

S. A. Letts, C. C. Roberts, R. C. Cook

97-ERD-016

Polyimide is a leading candidate as an ablator for inertial confinement fusion experiments on the National Ignition Facility (NIF). In this project, we have been developing techniques for fabricating high-strength capsules by (1) developing monomer, vapor-deposition techniques for fabricating polyimide shells; (2) demonstrating flat polyimide films with adequate properties for the NIF; and (3) applying these techniques to shell-coating technology. The original impetus for investigating the fabrication of polyimide shells was the need for high-strength shells that would enable the capsules to be transported at room temperature. Because the tensile stress on the capsule under these conditions will be 120 MPa, the essential issue is whether the polyimide shell would survive such a stress, catastrophically burst, or balloon to a larger diameter.

In early FY1999, we had demonstrated the production of NIF-scale (about 2-mm i.d., with 160-µm-thick walls) polyimide shells by codepositing pyrometallic dianhydride (PMDA) and 4,4'-oxydianiline (ODA) from vapor phase; unfortunately, the surfaces of these shells were quite rough. Hence, our efforts during most of FY1999 were focused on finding the sources of these defects and improving surface finish.

We limited our experiments to shell coatings with thicknesses ranging from 20 to 30 µm. After investigating a number of possible defect sources, we found that the defect density correlates with the starting mandrel mass and is a linear function of the thickness of the PMDA/ODA coating. We investigated various pan designs and agitation methods and deposition parameters such as coating rate and distance. In summary, we found that (1) contact phenomena are the primary drivers for defect generation, (2) deposition rate (or time of agitation) is the strongest processing handle for agitated shells, and (3) simple changes in agitation technique do not eliminate the defects. Mixing of monomers may have a secondary role in generating defects.

In our study of ways to improve surface finish, we investigated smoothing polyimide monomer-coated shells. The gas-levitation technique involves suspending a PMDA/ODA-coated shell in a stream of gas and solvent vapor with the expectation that the vapor-deposited coating will become plasticized by the solvent—the result would be surface-energy-induced flow and smoothing. The solvent vapors are then removed, and the shell is heated to the curing temperature of the polyimide. Our preliminary results indicated that an order-of-magnitude improvement in surface finish is easily achievable.

Previously, we had demonstrated the production of Kapton-like films with a tensile strength of approximately 100 MPa (or about 40% the strength of commercial Kapton). Commercial Upilex films have a tensile strength of 400 MPa. In FY1999, we prepared Upilex-like coatings in a high-vacuum chamber followed by thermal treatment to 300°C. At year's end, we were mapping the effects of processing conditions on the tensile strength, film stress, molecular weight, and surface finish.

During FY1999, we also performed tensile-creep testing on a number of commercial polyimide films. In these tests, we applied a constant tensile stress of 17 to 210 MPa to the films. Depending on the load, we observed strains of 0.5 to 40% and 0.3 to 5.5% for Kapton and Upilex, respectively. At 120 Mpa (the tensile-stress specification for NIF), Kapton yields to about 15% strain, whereas a strain of only 2% is observed for Upilex. In the case of Upilex, little permanent deformation is observed.

During this project, we made extensive progress toward producing a suitable polyimide capsule for NIF. We demonstrated the production of NIF-scale polyimide capsules, but the surfaces were extremely rough.

Origins of Laser Damage in KDP Crystals

J. J. De Yoreo, S. G. Demos, M. Yan, T. A. Land, M. Staggs

The ability of optical materials to withstand high-power ultraviolet (UV) laser irradiation without sustaining irrevocable damage is critically important in two areas central to LLNL: laser fusion and UV lithography. In particular, the output fluence of the National Ignition Facility (NIF) is limited by the 351-nm laser damage thresholds of the KH_2PO_4 (KDP) frequency-conversion crystals. Increasing the laser output would maximize the odds of achieving ignition, allow target physicists to assess target performance at higher drives, and provide higher temperature–density conditions for studies of the physics of stellar interiors. Moreover, to meet design criteria for fusion-laser systems, KDP crystals must be conditioned by illumination with low-fluence laser irradiation to increase the damage threshold by about a factor of two. Although previous work indicated that damage was caused by extrinsic defects, little of the basic science needed to understand either the processes of damage or conditioning or the defects responsible for damage has been performed.

During the initial years of this project, we showed that damage is accompanied by temperatures in excess of 1000 K in regions with diameters less than 100 nm. The results required the presence of either submicrometer inclusions of highly absorbing species or, at a minimum, submicrometer clusters of such species. In both cases, we hypothesized that, during laser irradiation, localized heating due to absorption by the inclusion results in its vaporization, followed by damage to the crystal through local melting as well as fracture from thermal stresses. Low-fluence laser conditioning should then reduce the probability of damage by heating the inclusions to temperatures below the vaporization point—increasing the solubility and diffusivity of the inclusions so that they become more dispersed and less absorbing. Likely candidates for the damage precursors include transition metal phosphates—particularly suspect because they are highly insoluble, are present in the starting materials, and have high UV absorption coefficients.

During FY1999, we focused on (1) identifying precursor composition by either postdamage elemental analysis of damage sites or by optical spectroscopy during damage, and (2) observing precursor incorporation during growth using atomic force microscopy (AFM).

To look for atomic emission lines during damage, we used time-resolved emission spectroscopy on the initial damage "fireball." Although the spectra revealed high-temperature radiation from the bulk, we saw no clear atomic emission signatures. Through careful chemical etching, we brought sites that had been laser damaged

near the surface of the crystal. We then investigated these sites by ion sputtering through them and performing secondary ion mass spectrometry on the ejecta. Our measurements (see figure) revealed submicrometer regions that were rich in Ca, Fe, Cr, and Cu. Some of these species, particularly Fe, are strong UV absorbers when in the form of phosphates. Our measurements provide the strongest evidence to date that metallic phosphate particles or metallic ion clusters serve as the precursors to damage. As a result of these experiments, (1) efforts to improve the damage threshold of KDP and KD_2PO_4 (DKDP) crystals during growth are now focused on reducing metallic impurities on the starting materials and on better solution filtration, and (2) the NIF Project has incorporated our experimental approaches into the development of optical materials.

Finally, we investigated the growth of KDP in the presence of Fe, Cr, and Al using in-situ AFM. Our results (1) provide the first microscopic picture of impurity–step interactions, (2) show that the growth of KDP surfaces in impurity-bearing solutions occurs on close bunches of elementary steps known as macrosteps (individual elementary steps are immobilized by the impurities), and (3) suggest that macrosteps play an important role in determining the distribution of the impurities and their clusters that are the source of laser damage.
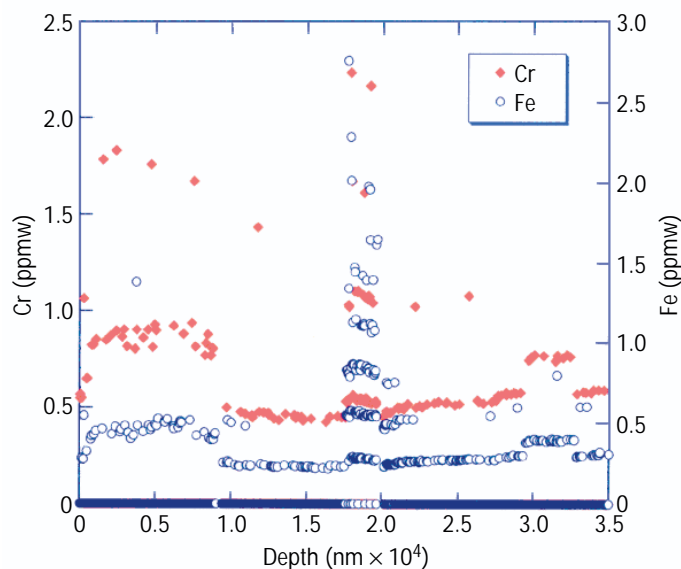
Secondary ion mass spectra collected while sputtering through a damage site, showing the dependence of impurity concentration on depth. The data show a spike in the concentrations of Cr and Fe over a micrometer-sized region that includes the damage site.

High Performance Explosive Molecules

L. E. Fried, C. J. Wu, M. R. Manaa, P. F. Pagoria, G. Fox

97-ERD-101

In this project, which has now completed its third year of funding, we have been seeking to substantially accelerate the development of new, high-performance and enhanced-safety explosive molecules. By combining state-of-the-art quantum-chemistry calculations with the aggressive, synthetic pursuit of promising candidate molecules, we have substantially advanced the state of the art in the synthesis of high-explosive molecules.

Our approach has been based on the tight linkage of theory with chemical synthesis. That is, we (1) established a high-explosive, performance-prediction code by linking the thermochemical code CHEETAH with the ab-initio, electronic-structure code GAUSSIAN and the molecular-packing code MOLPAK; and (2) used first-principles calculations of electronic structures to predict the stability of target compounds found through this extensive computational search.

In FY1999, we concentrated our theoretical efforts on obtaining a better understanding of the stability of energetic materials. Our theoretical calculations of performance had been very reliable throughout this project; however, the determination of material stability

We have calculated the mechanism for the decomposition of the TATB high-explosive molecule into the shown furoxan molecule under high temperature. The calculations show that intramolecular hydrogen transfer can be important in the decomposition of energetic material.

proved to be less accurate. Previous stability calculations of our target molecules had been based on the assumption that molecular decomposition occurs through simple bond fission. Then, during FY1999 we synthesized the high-energy target molecule TNBP, but found that it was not as stable as expected. Although it is stable for periods of several hours, TNBP's chemical reaction with most simple liquids complicates its handling and isolation. (We verified, however, that TNBP is a powerful, energetic material by exploding a very small quantity of the material with a hand-held hammer. The load retort indicated complete reaction and substantial power.)

We therefore decided to undertake a more comprehensive study of decomposition in TATB, a material of direct interest in LLNL's national security mission. We determined that decomposition in TATB occurs through an intramolecular hydrogen transfer, rather than through simple bond dissociation. The result of the hydrogen-transfer decomposition mechanism is shown in the figure. Hydrogen bonding plays an important role in the mechanism, which helps to explain why stability calculations for hydrogen-bonded materials appear to be more difficult than those for materials without hydrogen bonding. The results of this study have been submitted for publication.

The most promising material synthesized in this project was DNBP; we believe that DNBP may find future application in the DOE as a material with a superior combination of safety and performance. The performance predicted for DNBP is nearly equal to that of HMX, but DNBP has much better thermal and impact stability. During FY1999, we obtained a quantitative measure of the energy content of DNBP using a calorimeter. The measured energy content was in close agreement with theoretical predictions. We also optimized the synthesis of DNBP, so that large quantities could be made economically. In our initial synthetic path, we achieved a factor of two improvement in the yield, which allowed us to make several grams of the material.

In FY1999, we began a research collaboration with Dr. J. Bottaro of SRI to investigate the possibility of higher-energy, fluorinated versions of the DNPB molecule. Dr. Bottaro is expert in the chemistry of fluorine, and his laboratory is equipped to deal with the special handling precautions necessary for fluorine. Dr. Bottaro successfully synthesized mono- and di-fluoro analogues of DNBP. These analogues have not yet been fully characterized.
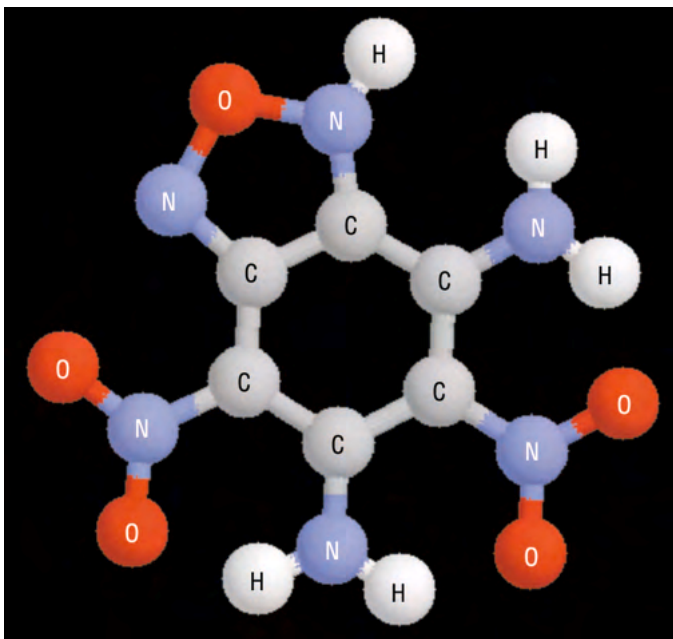
Novel Approaches to Surface Analysis and Materials Engineering using Highly Charged Ions

A. V. Hamza, T. Schenkel, A. V. Barnes, D. H. Schneider

97-ERD-102

Complex problems in materials science require very sensitive, high spatial resolution (<50 nm) determination of chemical structures in near-surface volumes. Slow, highly charged ions (HCIs) provide new, unique tools for probing chemical structure on a nanometer scale. We are exploring the potential of these new techniques in studies of materials with programmatic significance such as high explosives and actinide surfaces. Specifically, we are studying HCI-based surface analysis techniques (such as secondary ion mass spectrometry or SIMS), which are capable of achieving sensitivity of less than 109 atoms/cm^2. In addition, this technique can determine chemical structure and hydrogen concentration. These attributes make this technique especially important to Laboratory research in enhanced surveillance and nonproliferation.

The unique advantage of HCIs over singly charged ions is the extreme energy density that is deposited into a nanometer-sized near-surface volume at the impact of a single HCI. This high energy density causes the emission of large numbers of secondary electrons, ions, neutral atoms, and clusters from surfaces.

The high secondary ion yield produced by HCIs enables the use of coincidence counting in SIMS. By accumulating time-of-flight cycles event by event, we can differentiate among impact events by the presence of characteristic "fingerprint" ions. We recently demonstrated chemical structure determination on a length scale of 25 nm. We analyzed silicon (Si) wafers with sub-micron copper (Cu) lines. A tantalum (Ta) diffusion barrier surrounds the copper lines and separates them from the silicon and silicon dioxide. The TaO^+ fingerprint ion was shown to be anticorrelated to both Cu^+ and Si^+ secondary ions. Chemical analysis of the 25-nm Ta barrier layer was possible.

The high yield of low energy secondary electrons upon surface impact coupled with the high secondary ion yield also enables HCI based spectromicroscopy. By accelerating secondary electrons and ions with an electrostatic lens, an image of the surface is obtained. Contrast can be based on both secondary electron and secondary ion emission, since all secondary particles are collected via time-of-flight.

The figure shows a series of images collected with the HCI-spectromicroscope from a ^{238}U sample. The primary ion was Xe^{44+}. The sample was sputter cleaned, then exposed to hydrogen at 5×10^{-2} Torr for 19 hours. Panel (a) shows an H- contrast image of a carbon inclusion (~40 μm wide and ~400 μm long) after hydrogen exposure. Areas with high concentration of H^- are red and yellow; areas of low H^- concentration are violet and blue. Some areas of the carbon inclusion have a very low hydrogen concentration, whereas areas outside the carbon inclusion have uniform hydrogen coverage. Panel (b) shows the H^- contrast image after a second sputter cleaning. Hydrogen was removed from most of the sample, except for a few micrometer-sized areas at the edge of the carbon inclusion. Panel (c) shows a secondary ion contrast image of the panel (a) image. The blue colored area corresponds to O^-, F^-, and UO^{3-} emission; the yellow colored area corresponds to Cn^- emission. The high yield of carbon cluster ions strongly suggests that the carbon feature is not simply a carbon island but a carbon inclusion. Panel (d) shows an H^- contrast image of the sample exposed to a second hydrogen exposure of 5×10^{-2} Torr for 12 hours. The hydrogen concentration is strongly associated with the edges of the carbon, as if the hydrogen not removed from the previous exposure nucleates the growth of a hydrogen island on the surface. These measurements have application to the aging of the nuclear stockpile.

We have published 17 journal articles and filed 2 patents on our research for this LDRD project.
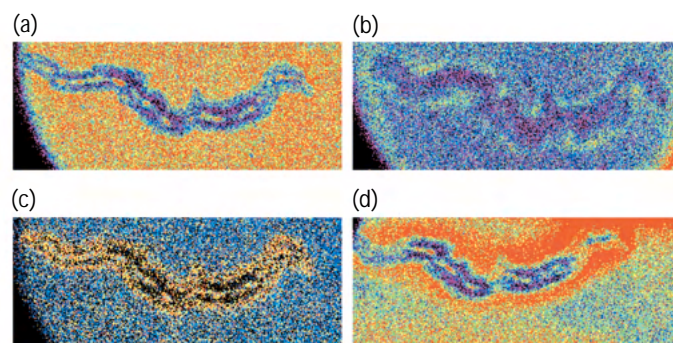
Highly charged ion (Xe^{44+}) spectromicroscope images of a carbon inclusion on a polycrystalline ^{238}U surface. Panels (a), (b), and (d) are H^- contrast images, and Panel (c) is a carbon cluster ion contrast image.

Experimental Validation for Atomistic Simulations of the Deformation of Tantalum

G. H. Campbell, J. Belak, J. A. Moriarty, S. L. Weinland

97-ERD-117

Atomistic simulations are an increasingly important means of understanding the behavior of materials under a variety of conditions. With this technique, atoms in an assembly of thousands, or even millions, are defined and allowed to interact according to certain rules and boundary conditions. Because these boundary conditions include temperature and states of stress, properties such as the equation of state or ideal shear strength can be calculated. To speed computation, the rules of interaction are often simplified. This simplification requires approximations about the physics of the interacting atoms. Therefore, the development of models of interatomic interactions requires an evaluation of whether the essential physics has been incorporated in the model. The models are tested by comparing their predictions with experimental observations.

Recently developed models of interatomic interactions incorporate angularly dependent contributions to model materials with directional bonding—such as the body-

centered-cubic (bcc) transition metals in which the d–bands participate in bonding. The strength of the directional component of the bonding has a major influence on the structure of crystal defects. In this project, we have been testing the accuracy of a model of interatomic interactions with angular dependence developed here at LLNL—the model generalized psuedopotential theory (MGPT)—by comparing its predicted grain boundaries to experimentally determined boundaries. Our results for Mo were reported last year. This year, we report our results for Ta.

The MGPT-predicted structure for the $\sum5(310)/[001]$ symmetric-tilt grain boundary in Ta is shown in Fig. 1(a,b). This boundary has the [001] crystal direction as the common tilt axis, and Fig. 1(a) views the structure along this direction. A notable feature in the view perpendicular to the tilt axis [Fig. 1(b)] is that the crystal planes are not perfectly aligned; rather, there is a shift of one crystal with respect to the other. This shift depends critically on the strength of the angularly dependent terms in the model; without directional bonding, no shift is predicted.

To experimentally investigate the structure of the Ta grain boundary, we fabricated it by diffusion bonding precisely oriented single crystals of high-purity Ta in LLNL's ultrahigh-vacuum diffusion-bonding machine. We then used LLNL's new, state-of-the-art, field-emission transmission electron microscope (TEM) to investigate the actual atomic structure of the boundary.

The images acquired, shown in Fig. 1(c,d), are projections of the structure in the two directions shown by the models in Fig. 1(a,b). The top image is a view of the Ta grain boundary along the tilt axis; the bottom image is acquired in the direction perpendicular to the tilt axis. When the structure is viewed in the latter direction, only one set of atomic planes can be resolved in the microscope; thus, only a single set of fringes is visible in the Fig. 1(d) image. If this image is viewed at a glancing angle, so as to sight down the fringes, a shift is seen as the fringes cross the position of the grain boundary. The fringes in the top half of the image do not align with the fringes on the bottom half of the image. Thus, the shift between the crystals predicted by the MGPT is confirmed by this experiment.

These FY1999 results, combined with the previous year's results for Mo, supply a strong validation of the theory that the angularly dependent interatomic interactions incorporated in models such as the MGPT are a necessary component in the accurate atomistic modeling of bcc metals.
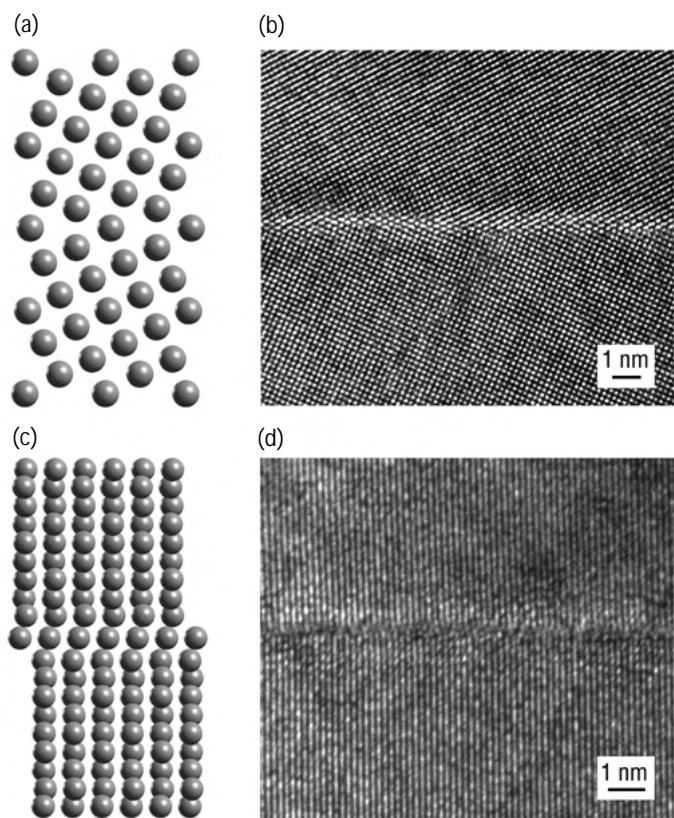
Figure 1. Comparison between predicted and observed grain boundaries in Ta: (a,b) two views of predicted atomic structure (see text), and (c,d) high-resolution electron micrographs that view the boundary in the same directions as (a,b).

Physical Basis for Materials Synthesis using Biomineralization

J. J. De Yoreo, C. A. Orme

97-LW-069

Calcium carbonate (calcite) crystals grown under most solution conditions are rhombohedral structures (rhombs) formed by the six symmetrically related, lowest-energy, {104} faces of calcite. Calcite crystals found in living systems such as mollusk shells, however, are not restricted to these simple calcite rhombs; rather, they show structures with (1) higher-energy faces expressed, and (2) the higher-energy polymorphs being utilized. Biomineralized structures also often employ chemical species that exhibit right and left handedness (chirality) and sometimes exhibit symmetry that is less than the crystal symmetry of calcite. It remains a challenge for material scientists to understand how biological systems can use the same materials to build such varied structures. A common motif not only for the calcite systems that compose shells but also for the calcium phosphate systems that compose mammalian bones and teeth is the use of organic materials in the form of proteins to guide the inorganic crystal growth.

Our goal has been to understand how organic species interact with the growing crystal to alter its polymorphic expression and symmetry. Such knowledge has wide-reaching implications, not only for biology but also for material synthesis.

In most biological systems, acidic proteins are associated with the crystallization process. Because these proteins are rich in aspartic acid, we have looked at how the individual amino acids—particularly aspartic acid—interact with the elemental steps as a first step towards understanding the more complicated protein interactions.

During FY1999, we used the atomic force microscope (AFM) to image the interaction of calcite atomic steps with various amino acids during both growth and dissolution. Pure calcite grows by the motion of elemental steps in polygonal spirals around a dislocation to form what is referred to as a growth hillock. Two of the steps form an obtuse angle and two form an acute angle with respect to the cleavage plane. The obtuse steps are mirror images of one another, as are the acute steps. When achiral glycine is added to the growth solution, the acute steps become rounded and lose their original facet directions; the obtuse steps are unaffected. The hillock remains symmetric about the glide plane. When aspartic acid is added, again both acute steps become curved, and the obtuse steps remain unperturbed. However, the mirror symmetry is now broken. Figure 1(a,b,c,d) shows the effect of aspartic acid: the chiral amino acids bind to calcite steps in a preferential way, and the right-handed (D) and left-handed (L) forms bind to opposite steps that are mirror images of one another. Thus, the chiral nature of the amino acids breaks the crystal symmetry and leads to a chiral configuration of the growth steps.

During calcite dissolution, the addition of aspartic acid changes the pit geometry from the rhombohedral symmetry associated with pure calcite to a trapezoidal shape. Three of the new facets are independent of the handedness of the amino acid, but the fourth reverses about the glide plane depending on whether the D or L form is added. This suggests two different binding mechanisms—one that can be explained by an electrostatic attraction between the negative residue and the positive calcium ions, and one that involves two sites on the calcite so that the glide symmetry can be broken. To describe this new effect, we developed a simple crystallographic model that relates the shape of the amino acid structure to the surface atomic structure of calcite.

During this project, we developed unique AFM instrumentation to allow (1) flowing solutions over our sample surface at controlled temperature, pH, and CO_2 content, and (2) changing solution composition while collecting images of the sample surface. Our results have been presented in a number of talks and publications.
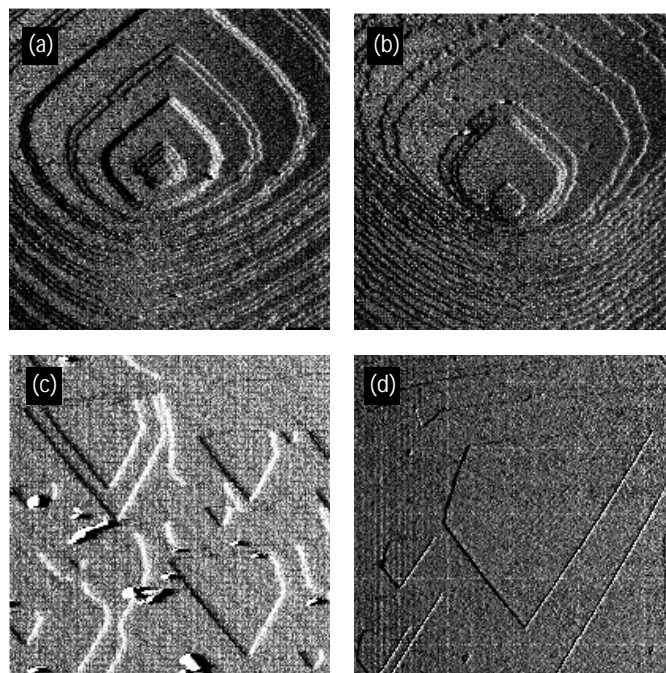
Figure 1. Atomic force microscopy images of calcite atomic steps modified by aspartic acid: (a) and (c) show the growth and dissolution pit, respectively, of D-asp; (b) and (d) show the growth and dissolution pit, respectively of L-asp.

Micromechanics of Highly Filled Polymers

S. E. Groves, S. J. DeTeresa, B. J. Cunningham

98-ERD-015

We are attempting to characterize the micromechanical response of highly filled polymers. In this class of materials, the continuous binder that bonds the highly filled material dominates the observed viscoelastic response. Our goal with this suite of tools and models is to predict the long-term mechanical response. Because of the domination of the binder, realistic lifetime analysis must account for its contribution. For FY1999, we divided this project into four tasks: characterization of the local microstructure, in-situ property measurement, binder constituent properties, and micromechanical modeling.

Characterizing the local microstructure of highly filled polymers proved to be extremely difficult. Our goal is to determine what the 3-D structure looks like so that a representative local volume element can be constructed for constitutive modeling. Highly filled polymers are very difficult to polish and suffer from lack of contrast between filler and binder. In FY1998, we explored several methods, including computed x-ray tomography and atomic force microscopy. X-ray tomography lacked the necessary resolution to clearly distinguish the binder material—the best resolution available at this time are from 3–5 mm, which falls short of the requirement by better than an order of magnitude. Atomic force microscopy (AFM) suffered from having incompatible tip designs for probing and identifying soft binder between the grains of high explosive. However, AFM was believed to be a useful tool, provided an appropriately designed high aspect ratio probe could be fabricated. A new probe was fabricated at LLNL having a diameter of 0.1 μm, a shaft length of 2 μm, and a tip radius of ~1.5 nm. This tip was installed in a traditional AFM, producing very encouraging high resolution scans on mock high explosives.

In order to improve our ability to image microstructure, this project acquired a new scanning electron microscope (SEM) that can image organic-based materials without the need to apply a thin layer of conductive coating, such as gold. With regard to coating, our concern has been that the conductive coating would mask some of the microstructural features of interest. The SEM purchased was a LEO 438 Variable Pressure System, see Figure 1(a). (LEO is the new name of Cambridge Instruments, the developer of the first commercial SEM.) Figures 1(b) and 1(c) are images of energetic materials. Figure 1(c) represents our first good attempt at imaging a polished surface of the LX17 explosive. A key to getting this image was that we hand-lapped this material in an ice water bath. The ice bath was used to keep the LX17 temperature well below its glass transition temperature of ~28°C. This facilitates the polishing process by preventing the soft binder from smearing across the surface. In Figure 1(c), we believe the brighter-colored material to be the KELF binder, which appears brighter because of selective electron charging. (KELF-800 is the trade name of chlorotrifluoroethylene/vinylidene fluoride.) The TATB explosive particles probably have a higher electrical conductivity than the binder does and thus by selectively varying the SEM chamber pressure we can enhance the contrast of the KELF binder by allowing it to charge.

Laboratory applications of materials include plastic bonded explosives, propellants, specialized filled organic materials for stockpile systems, and highly filled epoxy dielectric materials for the National Ignition Facility. In particular, this project has helped identify and develop technologies in support of the DOE Enhanced Surveillance Program—for prediction of main charge lifetimes. This project has significantly improved our micromechanical tool set for highly filled polymers.

(a) (b) (c)
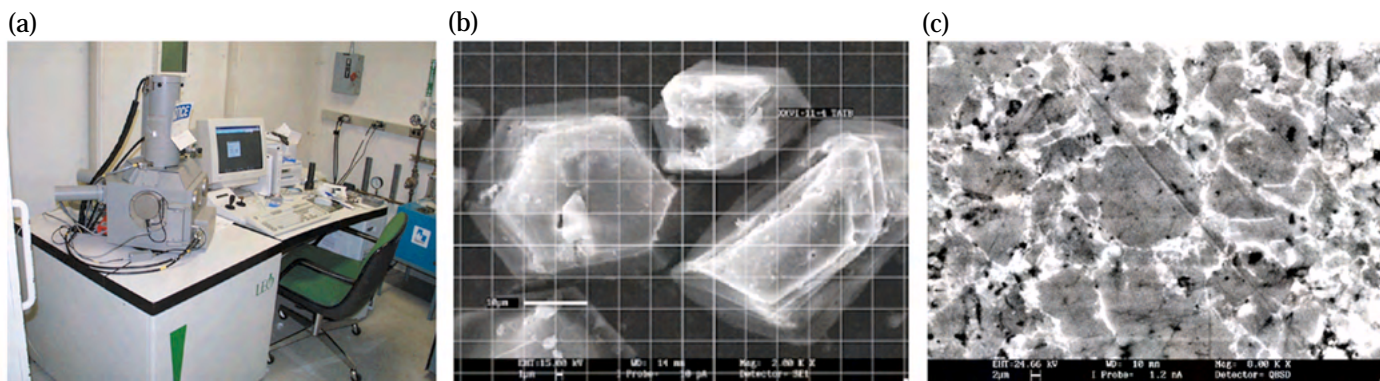
Figure 1. The panels show (a) the new LEO variable pressure scanning electron microscope, (b) individual TATB explosive particles in LX17, and (c) polished surface image of LX17-1.

Fundamental Aspects of Radiation-Induced Microstructural Evolution in Plutonium–Gallium

M. J. Fluss, T. Diaz de la Rubia, B. Wirth, M. Wall, T. Felter

When Pu decays, it produces an alpha particle (~5 MeV) and a uranium atom (~85-keV). Plutonium atoms are displaced from their lattice sites at a rate of once every ten years. The vacancies, interstitials, helium atoms (the stopped alpha particles), and possible radiation-induced segregation may result in microstructural evolution that could lead to unacceptable dimensional and density changes in Pu alloys. The ability to predict such changes is essential to the security and reliability of our nation's nuclear weapons stockpile.

Addition of Ga, Al, or In is known to stabilize Pu in the face-centered-cubic (fcc) delta phase and to give the materials desirable metal properties. Our goal is to understand how and why the composition and microstructure of Pu–Ga might change over time.

A sophisticated modeling capability (using molecular dynamics and kinetic Monte Carlo methods) had been developed at LLNL earlier in this project, we tested it on high-Z, low-melting-point materials. However, our model requires both experimental validation and parametric data specific to the Pu–Ga alloy system. Thus, in FY1999 we used molecular dynamics to describe the radiation-damage process and the subsequent rapid relaxation of the damage cascade that takes place in a 10- to 50-ps time frame. We applied the kinetic Monte Carlo technique to model the subsequent tracing of the microstructural evolution as defects (atomic vacancies, interstitials, and their aggregates) diffuse and interact in the material's lattice over a period of decades.

Special equipment was required to achieve the high signal-to-noise ratio for measuring small resistance changes and accurately and quickly controlling temperature. This equipment was designed and built at LLNL and tested in FY1999 by irradiating and annealing high-purity Pb foils. We observed distinct annealing stages: Stage I—interstitial migration, II—detrapping of interstitials from impurities and migration of small interstitials clusters, III—vacancy migration, and IV–V—dissociation of vacancy clusters. The handling of Pu-metal samples at our 4-MeV accelerator facility requires special care—we designed and fabricated a unique irradiation vacuum chamber (see figure) so that we could safely handle the small Pu–Ga foils.

During FY2000, we will be irradiating 10-μm-thick Pu–Ga foils with 43.8-MeV protons at liquid-helium temperature (4.2 K), thereby producing a large population of stable but noninteracting defect pairs (a vacancy and an interstitial). Then, we will anneal the foils—reducing the number of defects—and track changes in defect concentration with four-point resistometry. We will use the annealing curves for proton-irradiated Pu–Ga as a function of radiation dose to deduce the Stage I–V temperatures and give us a sense of (1) the annealing consequences arising from the complexity of the Pu–Ga alloys, and (2) the role of Ga-vacancy binding and the influences of other constituents. Subsequently—to deduce both the activation energies and, where possible, the chemical order of the annealing kinetics—we will perform detailed differential thermal annealing experiments at the relevant temperatures. We will compare the details of the annealing kinetics to predictions of the modeling codes and use self-consistency between experiment and calculations to tune the models.

The intimate connection between theory and experiment should result in one of the best systematic studies of radiation damage in metals; more importantly, our results will have direct application to science-based stewardship as it applies to Pu alloys.
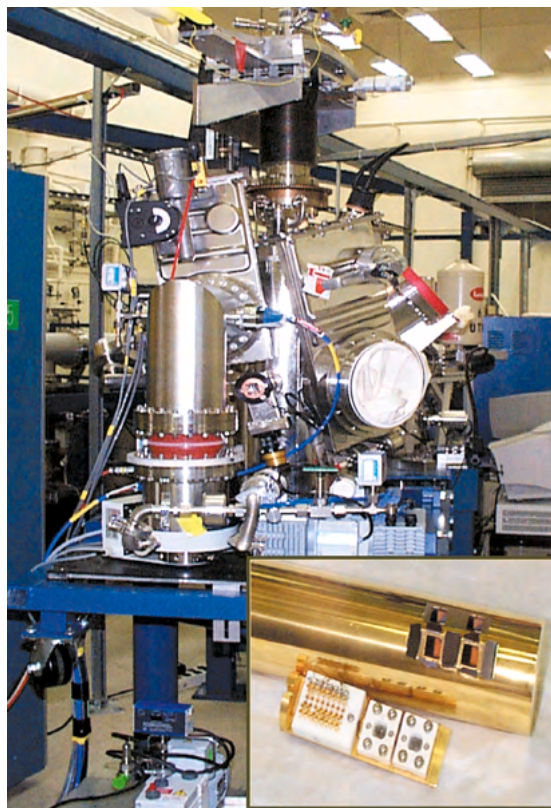
Specialized, unique vacuum chamber for radiation and annealing studies of Pu-alloy specimen is (1) both an accelerator chamber and a glove box, and (2) movable between the accelerator and a safe-handling area. The inset shows the specimen holder and the cryostat's heat shield, where holes allow entry of the proton beam and ceramic shields (white rectangles) define the irradiation area.

Solid-State Physics of Transuranics

L. J. Terminello, P. G. Allen, D. K. Shuh, J. Terry

98-ERD-040

An important aspect of LLNL's science-based stockpile stewardship mission is the experimental validation of first principles calculations of plutonium and its alloys, which are the basis of many weapons systems and materials models. This project focussed on first principles calculations of U, Pu, and their alloys by measuring the electronic structure of a material using soft x-ray spectroscopies—including valence band photoemission spectroscopy (VBPES), soft x-ray fluorescence (SXF), and x-ray absorption spectroscopy (XAS).

Current approaches to modeling the electronic structure of Pu, its alloys, and other transuranics rely on the local density approximation (LDA). This approach has been useful in modeling many other metals and alloys, but suffers from the limitation that it does not include enough of the electron correlation needed to accurately describe heavy elements (i.e., the strong relativistic effects). Various attempts to overcome this limitation with an adjustable "correlation" parameter in the LDA have led to fairly accurate interatomic distances for alpha-Pu and delta-Pu, albeit with a somewhat unphysical adjustable parameter. Our goal in this project was to measure the electronic structure of U, Pu, and their alloys to compare to the current state-of-the-art calculations and pending calculations on alloys.

One interesting phenomenon that we are looking for experimentally is the localization of the 5f electrons in the alloys of Pu that should have intermediate electronic properties between itinerant (delocalized) 5f electrons in Pu and lower actinides and localized 5f (Kondo effect) electrons in americium. Earlier photoemission research on U, Pu, and Am observed the localization in Am, but saw itinerant behavior in the alpha-Pu. The degree of localization for the 5f electrons in Pu alloys has direct bearing on the macroscopic properties of these materials (such as heat capacity) and thus underlies the importance of this project to measure the electronic structure of these materials as a means of model validation. Our program was the first to do a combined SXF–XAS probe of any of the actinides and provide coulomb interaction information useful for theorists to refine the correlation correction to their models.

We successfully performed XAS experiments on the alpha and delta phase of plutonium in FY1999. Initial interpretation of these results indicates that our sample preparation methods are producing unreacted surfaces that remain pristine throughout the experiment. These results also indicate that we can see evidence for charge transfer in the alloy that will be critical for accurate interpretation of the coulomb effects in Pu and its alloys. The figure shows a comparison of the core level photoabsorption near edge structure from alpha- (lower curve) and delta- (upper curve) Pu. The difference in near edge structure is a direct sampling of the difference in empty electronic states in the two phases of Pu and can be interpreted as evidence of charge transfer in select phases of Pu. These results are consistent with our earlier work on U and Nb–U alloys, where we observed a similar charge transfer.
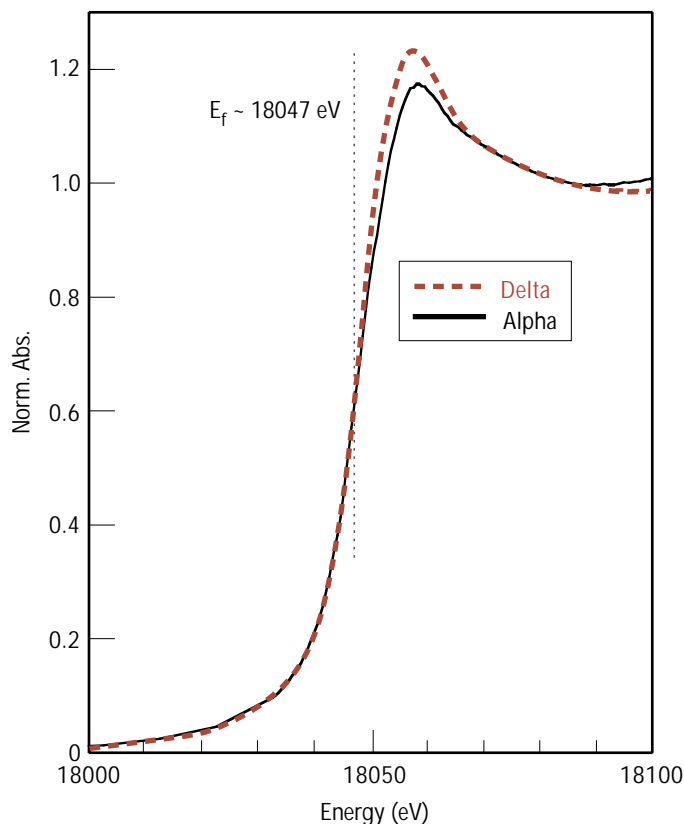
The x-ray absorption near-edge structure (XANES) of alpha- (broken line) and delta- (solid line) Pu.

Nanostructure High Explosives using Sol-gel Chemistry

T. M. Tillotson, R. L. Simpson, L. W. Hrubesh

98-ERD-048

Energetic materials such as propellants, explosives, and pyrotechnics are substances that store energy chemically. Since the invention of black powder, 1000 years ago, the technology for making solid energetic materials has remained either the physical mixing of solid oxidizers and fuels (e.g., composites), or the incorporation of oxidizing and fuel moieties into one molecule (e.g., trinitrotoluene, TNT). In this project, we bridge the length scale between these two approaches by preparing nanostructured energetic materials using sol-gel methodologies.

Sol-gel chemistry involves the reactions of chemicals in solution to produce nano-sized primary particles, called "sols," which can be linked to form a 3-D solid network, a "gel," with the remaining solution residing within open pores. Solution chemistry determines the resulting nanostructure and composition, which in turn determines material properties. Controlled evaporation of the liquid phase results in a dense porous solid, "xerogel," while supercritical extraction eliminates the surface tension of the retreating liquid phase, producing highly porous "aerogels." A typical dried gel structure is uniform because the particles and the pores between them are on the nanometer scale. In addition to providing fine microstructural and compositional control needed to produce materials that have both high energy density and extremely fast release rates, sol-gel offers other advantages of safety and stability in energetic material processing, e.g., eliminating the need for hazardous machining.

In FY1999, we focused our research on the synthesis and characterization of energetic nanocomposites. Nanocomposites are multicomponent materials in which at least one of the component phases has one or more dimensions (length, width, or thickness) in the nanometer size range, usually defined as 1 to 100 nm. Energetic nanocomposites are a class of material that (1) has both a fuel and oxidizer component, and (2) has at least one of the component phases that meets the size definition.

We synthesized a prototype nanocomposite by crystallizing ammonium perchlorate (AP) within the pores of an organic gel in FY1998. In this composite, the AP acts as an oxidizer with the hydrocarbon gel skeleton serving as the fuel. In FY1999, small angle neutron scattering (SANS), a non-destructive method for characterizing nanostructures, was conducted at the National Institute of Standards and Technology on both the energetic nanocomposites and the fuel-only samples. Results for the fuel-only specimens were consistent with other SANS data for gels, which typically give average primary particle sizes of a few nanometers. By comparison, results from the energetic nanocomposite, in addition to displaying the typical structure, also showed extremely small (~1 nm) AP particles and >10 nm particles, which are presumed to be agglomerates of the small AP crystals. A dynamic molecular model suggests that these small nanometer size crystallites of oxidizer can easily fit within the microporosity of the fuel's primary particles, thereby providing mixing of fuel and oxidizer at levels unattainable by state-of-the-art production methods. Differential scanning calorimetry (DSC) of this energetic nanocomposite showed an exotherm at ~260°C, indicating that it is indeed energetic, whereas the trace for neat AP shows no exothermic reaction in the absence of the fuel skeleton.

In addition, we developed a new synthesis route for preparing inorganic oxidizing gel networks from inexpensive hydrated iron salts. By adding a metal fuel (e.g., aluminum) to the sol prior to gelation, we were successful in synthesizing pyrotechnic nanocomposites (thermites, as shown in the figure) with fuel/oxidizer components reversed from the fuel nanocomposites described above. Thermitic reactions are extreme exothermic reactions that involve a metal reacting with a metallic oxide to form a more stable oxide and the corresponding metal of the reactant oxide. Production of thermites by this wet chemical process reduces the fire hazards associated with conventional processing and allows more intimate mixing of the fuel/oxidizer components with precise stoichiometric control. Early performance results are quite promising; in future research, we will explore compositional control to tailor the temperature and rate of burn.

Burning iron oxide/aluminum sol-gel derived thermite atop a silica aerogel.

Elastic Constants of Metals at High Pressures and Temperatures

H. Cynn, C. S. Yoo

98-ERD-059

We measured single crystal elastic constants, C_{ij}, of tantalum powder samples to 1.05 Mbar, using stress and angle-resolved synchrotron x-ray diffraction (SAX) and a modified SAX-LLNL diamond anvil cell (DAC). These elastic properties at high pressure are fundamental to our understanding of atomistic potential, equation-of-state (EOS), melting, anharmonicity, and phase transition of solid material. Aggregate elastic and mechanical properties are also obtained from averaging the measured single crystal elastic constants. This new SAX technique has several advantages over the conventional experimental methods to determine elastic constants by acoustic scattering of light or ultrasonic wave, which are applicable to transparent single crystal and limited to relatively low pressure below 0.1 Mbar; these methods are not applicable to metals due to optical opacity and polycrystalline powder. The elastic EOS data for metals at high pressure and high temperature are important to DOE defense programs, where they are required for hydrodynamic simulations of the performance of conventional and nuclear weapons. The purpose of this project is to develop a new experimental technique-stress- and angle-resolved SAX that can accurately determine single-crystal elastic constants from opaque and polycrystalline metals at high pressure and temperature. Tantalum is a critical programmatic material whose elastic properties are needed to verify empirical models in current weapon's design codes.

With regard to the C_{ij} of tantalum, we performed three separate measurements. The first required an accurate determination of EOS of tantalum using angle-resolved x-ray diffraction: The current EOS of tantalum has been accurately measured to 1.74 Mbar, using angle-dispersive SAX. The EOS is in excellent agreement with the 300-K reduced isotherm from shock-wave data using zero-point energy from the calculation. The best agreement is also shown in comparison with ultrasonic data for the bulk modulus and for the pressure derivative of bulk modulus. Secondly, in-situ deviatoric stress was determined from the x-ray transmission measurements of the sample thickness and from the pressure gradient across the sample. We measured deviatoric stress to 0.65 Mbar and linearly extrapolated over a Mbar to improve the accuracy of the determination of C_{ij} data. The sample thickness was measured and calibrated by micro-probing x-ray tomography of the sample in a DAC using the third-generation synchrotron sources at Lawrence Berkeley National Laboratory's Advanced Light Source. This allows us to understand mechanical yielding (or flow stress) of material in quantitative way over a Mbar pressure range. Finally, we determined lattice strain as a function of stress angle, i.e., an angle between the compression axis and the normal to the lattice plane. The SAX method is now mature and able to determine the elastic constant of tantalum above 1 Mbar at the Stanford Synchrotron Radiation Laboratory. In the figure below, the C_{ij} are compared with ultrasonic data to 0.1 Mbar (10 GPa). C_{44} shows a very good agreement between the two data, although C_{11}–C_{12} deviates at high pressure. However, the aggregate properties—such as bulk and shear moduli—show very good agreement with ultrasonic data.

Our capabilities to measure accurate EOS, elastic constants, and materials strength in an extended pressure range over 1 Mbar have crucial implications for validating the Steinberg-Guinan model used in current weapon design codes and theoretical developments of constitutive materials models. The EOS and elastic data of actinides are also fundamental to understanding high-pressure behavior of highly correlated systems of 5F-band electrons. The present SAX technique is capable of obtaining single-crystal elastic constants at the pressure-temperature conditions well above other conventional methods. It provides important elastic data for science as well as for various Laboratory programs, e.g., the elastic properties of iron at Mbar pressures are keys to understand the geodynamics and seismic anisotropy at the Earth-core. The elastic properties of actinides are also of interest to the Stockpile Stewardship Program. This LDRD project has enabled a new Laboratory program to investigate mechanical properties of actinides at high pressures and temperatures.
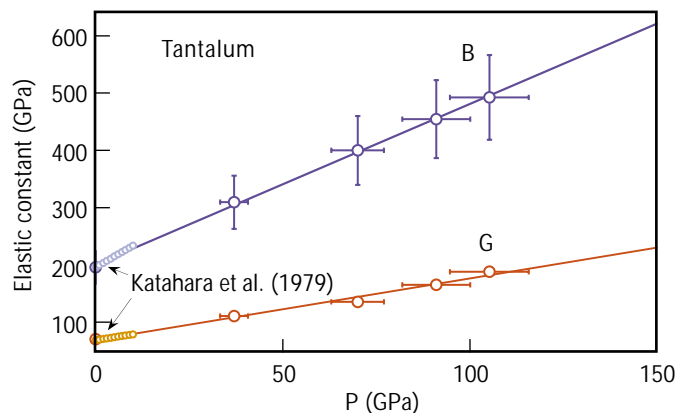
Elastic constants, bulk (B) and shear (G) moduli, are shown as averaged from the measured elastic constants, C_{11}, C_{12}, and C_{44} of tantalum. Katahara, et al. reference shows ultrasonic velocity measurements at relatively low-pressure ranges.

Grain-Boundary Engineering for Improved and Predictable Materials Properties

A. J. Schwartz, W. E. King, M. Kumar

98-ERD-080

Grain-boundary engineering is an emerging field within the materials-science community in which significant material-property improvements have been reported through modifications to the grain-boundary network. Grain boundaries are often categorized as "special" or random with reference to the coincident site lattice (CSL) model, whereas the grain-boundary network is characterized by the grain-boundary character distribution (GBCD) and triple-junction distribution (TJD). Grain-boundary engineering has been enabled by orientation imaging microscopy (OIM), which is a relatively new scanning electron microscopy (SEM) technique that allows the GBCD and TJD to be characterized in a time-efficient manner. Sequential thermomechanical processing (deformation followed by annealing) has been shown to produce significant improvements in material properties such as corrosion resistance, stress-corrosion cracking, creep, total elongation to failure, and fracture, as well as to alter the morphology and type of grain-boundary precipitates.

We are focusing on understanding the underlying mechanisms of property improvements achieved by modifying the grain-boundary network. Our investigation couples to LLNL's interests in (1) understanding nucleation, growth, and coalescence of voids during dynamic failure; (2) determining the influence of grain boundaries on deformation for application to the multiscale modeling of materials; (3) improving the performance of shape-charge liners; and (4) enhancing corrosion resistance for long-term waste storage.

During FY1999, we focused on Inconel 600, a widely used, commercial Ni-base alloy. Our starting material was plate stock that—while being reduced to rolled plate from the cast ingot— underwent extensive deformation and annealing. By reducing the thickness of the plate stock an additional 80% with intermediate anneals, we realized factor-of-two improvements in the GBCD and nearly a 90% reduction in the detrimental triple junctions [Fig. 1(a)]. We also made substantial progress toward elucidating the underlying mechanisms of grain-boundary engineering though coupled transmission electron microscopy (TEM) and OIM characterization. TEM of the deformed material strained to 5, 15, 25, and 45% indicated an inhomogeneous distribution of dislocations that is largely dependent on the orientation of the grain relative to the stress axis. The partially recrystallized Inconel 600 revealed boundary-decomposition reactions that form the basis for a proposed mechanism for the disruption of the random grain-boundary network. In Fig. 1(b), an immobile boundary is decomposing into two, lower-energy boundaries, one of which is mobile.

Previous research indicated that improvements in the GBCD are necessary but not sufficient to ensure improvements in properties. The connectivity of random grain boundaries is probably the critical factor in determining the improvements. We developed software routines to calculate the TJD based on the number of special CSL boundaries coming together at a triple point and modeled these distributions on the basis of geometrical requirements of the triple-junction crystallography; model results correlate quite well with percolation thresholds.

We have begun dynamic property measurements of grain-boundary-engineered Cu and electrochemical corrosion measurements of Inconel 600.

In FY2000, we will employ microstructural characterization with OIM and TEM to (1) further understand the critical stages in the microstructural optimization process, and (2) correlate these microstructural changes with improvements in properties. We will develop software routines to calculate and analyze the lengths of random boundaries through the microstructure.

(a)

(b)
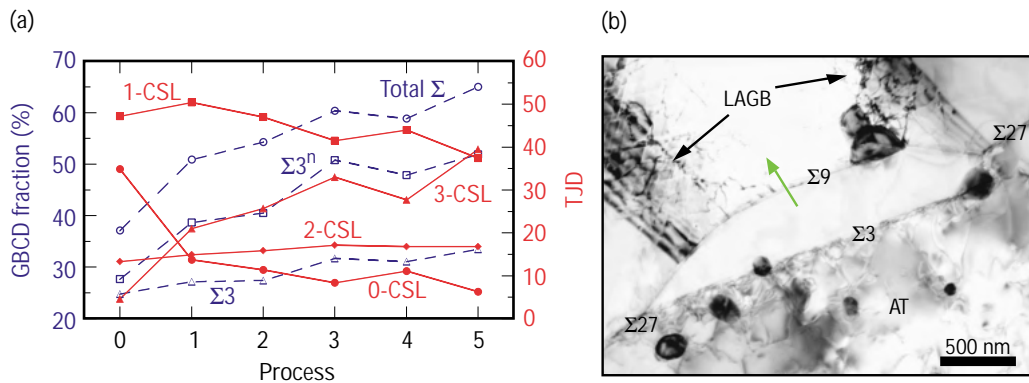
Figure 1. Work with Inconel 600: (a) grain-boundary character distributions defined as the relative fractions of "special" (Σ) and "random" boundaries (dashed lines), and triple-junction distributions (TJD) relative to the coincident site lattice (CSL) model (solid lines); and (b) transmission electron microscopy (TEM) image of the $\Sigma3$–$\Sigma9$–$\Sigma27$ triple junction (LAGB: low-angle grain boundary; AT: the annealing twin).

New Si-Based Compound Clusters and Their Application in Field-Emission Devices

M. Balooch, L. N. Dinh, W. McLean II

98-LW-006

The work function of materials, defined as the minimum energy required to remove an electron from the material into the vacuum, plays a major role in the efficiency, durability, and economic viability of field-emission devices. Field emission is defined as the emission of electrons from the surface of a condensed phase into a vacuum under high electrostatic fields. The emission current is exponentially dependent on the work function of the surface as well as on the applied field; the field strength can be enhanced by reducing the radius of curvature of the electron-emitting surface (typically a "tip" with radius of curvature ~10 nm). Field-emitting devices will become economically and technologically attractive for flat-panel displays if materials with stable- and low-work functions are used to realize extraction voltages of <15 V in a gated structure. This is especially true if one wishes to fabricate low-cost planar emitters.

The purpose of this project is to produce and investigate the properties of the silicon/alkali metal/oxygen compounds films consisting of small clusters with low work function (down to 1.2 eV). The small radii of curvature inherent to these clusters provide an easy path for emission of electrons in an electrostatic field. This, in turn, means that the conventional gated field-emission structures could be drastically simplified, and the required sharp tips, which are extremely hard to make, could either be relaxed or eliminated.

In FY1998, we employed pulsed laser deposition (PDL) and physical thermal vaporization techniques to produce films with nano- to micrometer-scale

<100-nm-thick Si/Cs/O (PLD) film [4.5 months]

1000-nm-thick CsI [4 months]

CsI [7 months]

<100-nm-thick Si/Cs/O (PVD) film [4.5 months]

2500-nm-thick CsI [4 months]

Electron emission of Si/Cs/O and CsI-coated microchannel plate under x-ray (1–2 keV) irradiation. Months of air exposure are indicated in brackets.

constituent clusters. The structure and size distribution of the clusters has been obtained by scanning probe microscopy. The elemental and chemical compositions of the clusters were monitored with Auger electron spectroscopy and x-ray photoelectron spectroscopy. The electronic density of states near the Fermi level, the absolute and temporal-spatial work function study of the clusters, and their derivative films were examined by ultraviolet photoelectron spectroscopy and photoelectron emission microscopy. The resulting films have shown I-V characteristics needed for good cold-cathode emitters.

In FY1999, we have shown by transmission electron microscopy and electron diffraction that, under certain deposition conditions, the Cs/Si/O nanoclusters are crystallites and have random orientation. Crystallites of $Cs_2Si_2O_5$ have been routinely obtained by physical vapor deposition (PVD) technique. We successfully built field-emission diode displays that exhibited turn-on voltage in the range of 10–20 V and did not require the fabrication of any complicated sharp structure. This could dramatically reduce the manufacturing cost of field-emission display. In addition, the technique has been applied on microchannel plate (MCP), used as a diagnostic tool for x-ray detection. The MCPs coated with thin (<100 nm) films of nanoclusters with proper ratios of Cs/Si/O were comparable in sensitivity to detectors coated with many micrometer thick CsI films currently used at the Laboratory. However, unlike CsI coatings that degrade in time if exposed to ambient environment, our Cs/Si/O coatings stand the test of time and ambient air exposure. The figure shows a MCP x-ray detector coated with CsI, Cs/Si/O of different thicknesses and under x-ray (1–2 keV) irradiation. The gray scale in the picture is proportional to the electron emission intensity. The superior stability of the Cs/Si/O nanocluster films with respect to air exposure can be clearly seen in this image. In the course of building the field emission displays, we have also succeeded in depositing highly sticking, low-voltage phosphor screen with the right stoichiometry by PDL onto glass.

We have filed three patent applications and have published results in *Physical Review B* and the *Journal of Applied Physics*. Presently, we are collaborating with Etec Corporation to produce an enhanced emission photo cathode for the future lithography application. We also plan to further improve the sensitivity of LLNL x-ray detectors using our optimized nanocluster thin-film coating.
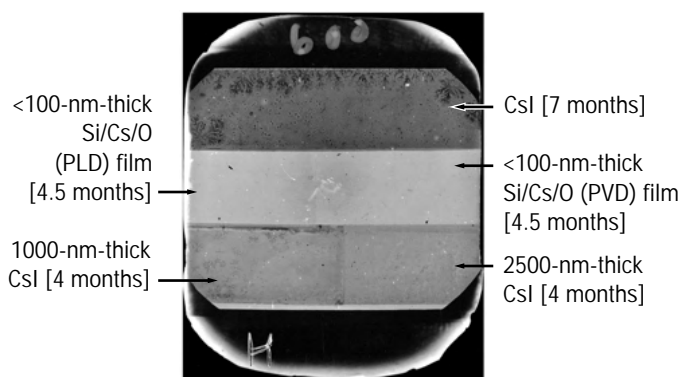
Semiconductor Quantum Dots for Advanced Blue Light-Emitting Devices and Laser Diodes

H. W. H. Lee

98-LW-058

That blue light-emitting-devices (LEDs) are rapidly becoming an increasingly important technology is underscored by intense world-wide research and development. Blue-emitter technology is the cornerstone for crucial applications such as full-color, flat-panel displays; ultrahigh-density optical memories and data storage; back lighting; and chemical and biological sensing. Currently, the GaN material system dominates the field of blue emitters. However, critical obstacles remain for this material system. Growth-related defects, which arise from lattice-matching problems, degrade the device and limit the operational lifetime.

For light-emitting applications, semiconductor quantum dots (QDs) provide an innovative and potentially superior alternative to the GaN system. QD properties are size-dependent because of quantum confinement (QC) of electrons and holes. In particular, QC causes the energy gap of QDs to change with their size. Therefore, changing the QD size enables broad tunability of the output color within a single material system. Other advantages of QC include high luminescence efficiency, long lifetime, reduced sensitivity to traps and defects, simplicity of processing, and lower cost.

During FY1999, we uniquely demonstrated that Si and Ge QDs can be made to emit light from the red to the ultraviolet when the QD size is changed. This represents a significant advancement in the understanding of the light-emission properties of these QDs. As a result, electroluminescent (EL) devices made from these materials may also have this broad spectral tunability.

In view of this, during FY1999 we developed an extremely versatile EL material system for QD light-emitting devices (QD–LEDs). The EL material consists of Si or Ge QDs embedded in a thin-film (~100 nm) host matrix with a larger bandgap than the QDs (e.g., in polymers and sol-gels). Advantages of this nanocomposite are (1) ease and low cost of producing high-quality, thin, conformal, and flexible EL films by spin coating or vapor deposition; (2) integration of thin EL material into a large variety of optoelectronics systems; (3) control of the EL color by controlling QD size; and (4) robust devices—because the active material (Si or Ge) can tolerate extreme conditions.

Our QD–LED operates via radiative recombination of carriers injected into the EL material. The QDs act as radiative recombination centers within the host matrix. This matrix serves several functions: it (1) disperses the QDs in the appropriate concentration, (2) enables low-cost and simple processing of the EL nanomaterial into flexible and conformal thin films, (3) enables integration into optoelectronics systems, and (4) assists in carrier transport to the QDs. Electrons and holes are injected via a cathode and an anode, respectively. The QD–LED consists of the EL material sandwiched between a cathode and anode. Other carrier-transport layers were used to assist in the transport of carriers to the QDs. Forward electrical bias results in blue-light emission. We successfully demonstrated the first and only blue-emitting QD–LED using Si and Ge QDs. The QD-LED produces bright and tunable blue electroluminescence, which changes with QD size in a manner consistent with QC.

In FY1999, we also explored the use of QDs for blue lasers. For this application, blue photoluminescence from the active material is insufficient. A critical prerequisite for lasing is the more demanding requirement of optical gain. During FY1999, we performed femtosecond-resolved measurements of the optical gain from Si and Ge QDs and demonstrated the first and only measurement of optical bleaching and gain in these QDs. This is a critical and significant development; by demonstrating that lasing is possible with these QDs, we opened the door to a new class of blue lasers. A blue QD laser will enable many future photonics technologies important to both the private sector and DOE missions.

Beryllium Materials for National Ignition Facility Targets

A. F. Jankowski

99-ERD-002

A promising inertial confinement fusion target for the National Ignition Facility (NIF) is a coated polymer shell filled with a hydrogen-based fuel. Be coatings offer the potential for improved performance as an ablating material because of their lower opacity, a greater ablation rate, higher initial mass, and greater bulk strength than polymer coatings.

For optimum performance, the Be-coated capsules require a smooth surface finish, uniform coating thickness, microscopic homogeneity, and high strength. The coatings must allow for filling of the capsule with gaseous, hydrogen-based fuels. These demanding requirements can be met through a synthesis method with a focus on the control of microstructure. It is postulated that with sputter deposition the surface roughness would decrease through a designed decrease of grain size in the coating.

The material properties of sputter-deposited coatings are sensitive to their microstructure and growth morphology. To meet the requirements for Be-coated capsules, the goal of this project is to optimize (1) the microstructure—through control of composition, and (2) the growth morphology—through control of the deposition-process parameters.

Prior experimental studies of evaporation and sputter deposition revealed that grain size of 99.8 at.% pure Be can be reduced by adding metal impurities such as Fe or Ti. These higher atomic weight elements can replace the requirement of adding 1 at.% Cu to the Be for stability. Grain size can also be reduced by using additives that are metallic-glass formers. For example, boron is a glass-forming additive that can replace Be because both elements have equal mass density-to-molecular weight ratios.

During FY1999, development of the Be–B–(X) alloy—where X is Fe and/or Cu—was successful in refining the grain size of sputter-deposited coatings from micrometers to nanometers. We achieved a capsule surface with 1-nm root-mean-square (rms) roughness for a 10-μm-thick Be–B–(X) coating, whereas the previous best for either Be or Be–Cu coatings was greater than 100 nm.

The conditions of the sputter-deposition process affect both the energetics of the sputtered atoms in the vapor flux and their mobility (i.e., the incident angle of approach). The application of a negative substrate bias induces a bombardment of ionized, sputter-gas species onto the substrate. The ion-assisted deposition process results in a more dense columnar growth (i.e., less porosity) and a reduced grain size. The effect on mechanical strength is favorable. Biased deposition results with an increase fracture stress from less than 40 MPa to greater than 200 MPa for Be–Cu-coated capsules. The effect on the surface finish on 10-μm-thick coatings has been to reduce the roughness from greater than 150-nm rms to less than 30-nm rms.

A coarsening of the surface finish was modeled for columnar coatings at glancing angles of incidence in the vapor flux. We achieved a reduction in the roughness of 10-μm-thick Be coatings to less than 20-nm rms by introducing an aperture to shield the capsule from glancing angles of deposition.

In FY2000, we will formulate and execute a matrix of experiments to optimize the effects of the composition and deposition conditions; this will lead to a set of recommendations for materials and process methods to produce Be-based capsules.

Chemistry and Processing of Nanostructured Materials

G. A. Fox, T. F. Baumann, A. L. Vance

99-ERD-004

This research combines dendrimer chemistry with LLNL's expertise in organic aerogels for the design of novel nanostructured materials. Organic aerogels are typically prepared by means of sol-gel polymerization, a process which transforms monomers into nanometer-sized clusters that then cross-link to form the 3-D network or gel state. While sol-gel chemistry provides the opportunity to synthesize new material compositions, it cannot separate the process of cluster formation from gelation. This limitation results in structural deficiencies in the gel state that have an impact on the physical properties of the dried xerogel, aerogel, or nanocomposite. In order to control the properties of the resulting gel, one should be able to regulate the formation of the clusters and their subsequent crosslinking.

We are utilizing dendrimer methodology to separate the cluster formation step from the gelation process so that new nanostructured materials with controlled topologies can be produced. Dendrimers are 3D, highly branched macromolecules that are prepared in such a way that their size, shape, and surface functionality are readily controlled. Consequently, the incorporation of dendrimers into sol-gel synthesis should allow for greater control over both the composition and topology of the resultant nanostructured materials. In FY1999, we focused our efforts in three main areas: (1) synthesis of new multifunctional dendritic precursors, (2) preparation of organic gels based on dendrimers and (3) predictive computational analysis for the prudent selection of candidates for sol-gel polymerization.

Since the building block for many organic aerogel systems is resorcinol (1,3-dihydroxybenzene), we are functionalizing dendrimers with resorcinol derivatives to yield novel precursors of known size that are reactive under sol-gel conditions. We performed computational studies to guide our selection of resorcinol derivatives for the functionalization of the dendrimers. Electron density calculations on a variety of resorcinol derivatives show that prudent selection and placement of the substituent yield new monomers that retain the reactivity of the parent molecule. To verify the computational studies, we prepared new organic aerogels based on these resorcinol derivatives. For example, the sodium salt of 2,4-dihydroxybenzoic acid was reacted with formaldehyde in the presence of a catalyst, followed by supercritical extraction, to yield a novel organic aerogel containing ion exchange (carboxylate) sites. We are currently functionalizing a series of small molecules, such as ethylenediamine, and dendrimers with these resorcinol derivatives.

Since many of these derivatives and functionalized dendrimers may not be soluble in water, we are investigating alternative solvent systems for the sol-gel reaction (see figure). We have prepared resorcinol-formaldehyde (RF) aerogels using a non-aqueous solvent as the gelation medium. The transmission electron micrograph (TEM) of a RF aerogel produced in N,N-dimethylformamide shows that the nanostructure of these materials is retained despite the fact that water was not used in the sol-gel polymerization. The resulting aerogels, however, were significantly more dense than the formulation predicted (target density = 150 mg/cm^3, actual density = 300 mg/cm^3). Non-aqueous sol-gel synthesis could significantly reduce processing time and allow the incorporation of new and unique monomers in the sol-gel process.

We have also prepared organic gels, termed *dendrigels*, through the condensation of amine-terminated dendrimers with formaldehyde. The dendrigels were prepared with various equivalents of formaldehyde to investigate the impact that the degree of crosslinking has on the gel structure. The dendrigels became significantly more dense during the drying process, indicating the flexible cores of the dendrimers collapse when the solvent is removed. In FY2000, we will investigate alternative dendrimer frameworks to improve the structural integrity of the resultant materials. Concomitantly, we will utilize computational methods to model solvent interactions with dendrigels.

70 nm
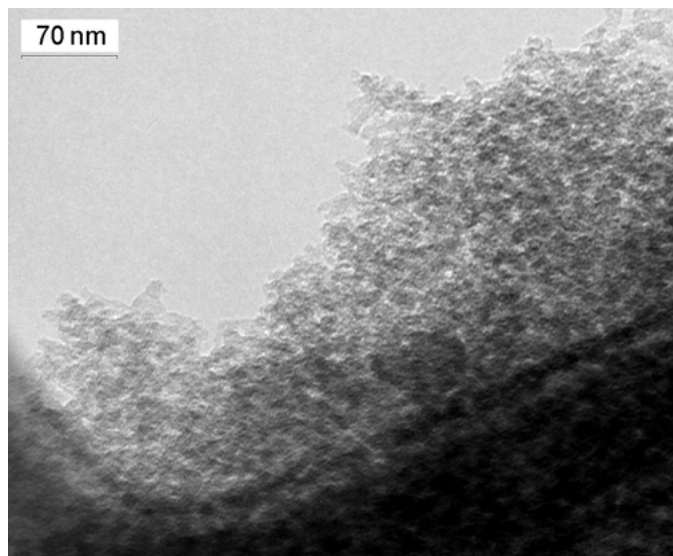
Resorcinol-formaldehyde aerogel produced in a non-aqueous medium exhibits features of materials prepared by conventional aqueous techniques.

Kinetics of Solid Phase Reactions at High Pressure and Temperature

J. M. Zaug, C. M. Tarver, J. W. Forbes

99-ERD-007

Time-resolved measurements of phase transition and chemical reaction rates of solid phase materials at high pressures and temperatures are insufficient in the published literature. Knowledge of such rates is essential for understanding geological phenomena, high-pressure chemical synthesis, and planetary physics. High-pressure chemistry is also fundamental to the understanding of combustion and detonation processes. The basic kinetic processes governing detonation in condensed phase energetic materials are not completely understood. Some of these ultra-fast chemical processes can be understood by developing phase stability fields and corresponding transition rates for unreacted solid phase materials. When considering shock initiation of detonation, it is essential to determine solid phase transition and reaction rates along the melt line. Without such data, interpretation of dynamic, low impact pressure experiments on solid phase materials is difficult.

This project will provide accurate high-pressure experimental data (e.g., solid phase stability fields, kinetics, intermediate product rate laws, etc.) of molecular constituents relevant to Defense Program computational efforts. We are developing computer algorithms that predict dynamic and often violent events. Since mathematical algorithms alone are not sufficient to create predictive models, such models must be normalized to experimental data taken in the correct pressure–temperature regimes. Combustion, planetary evolution, nuclear events, plasma physics, and biomechanics are but a few of the processes we attempt to simulate with these algorithms.

In FY1999, we designed and constructed high-pressure diamond-anvil cell tools to be used in conjunction with available optical diagnostics. We set out to learn what pressure and temperature conditions lead to a solid phase symmetry change in an energetic material, tetranitro tetrazacyclo-octane (HMX). Published literature accounts indicate that if the β-HMX polymorph is pressurized to 3 kbar then heated, the solid phase β-δ transition will not occur and indeed, β-HMX decomposes. Figure 1(a) shows our experimental setup. While the hydrothermal diamond-anvil cell is compressed (at elevated temperatures) using a hydraulically actuated piston cylinder, the sample is illuminated by a train of 1064-nm laser pulses. The HMX frequency converts the beam to 532 nm, a process called second harmonic generation (SHG). The SHG intensity dramatically increases when the HMX changes phase and thus allows us to track this change in real time. Figure 1(b) shows SHG intensity when a preheated HMX sample is pressurized from 0 to 5 kbar in 60 seconds [region 1 of Fig. 1(b)]. The SHG intensities in regions 2–3 are the result of shifting the δ-HMX polymorph with respect to the incoming beam. We dropped the voltage (region 4) in order to stop photomultiplier tube saturation. The SHG intensity then reduces back to β-HMX levels, indicating that a reversible transition has occurred. In addition, we produced a video showing the 7% HMX volume expansion that occurs during this transition.

In our future research, additional studies of the pressure-induced β-δ HMX transitions along different isotherms will quantify the known phase diagram and stability field curves.

(a)

(b)

Figure 1(a) SHG/x-ray diffraction diagnostic block diagram; and (b) 150°C pressure-induced β <–> δ SHG intensity as a function of time.
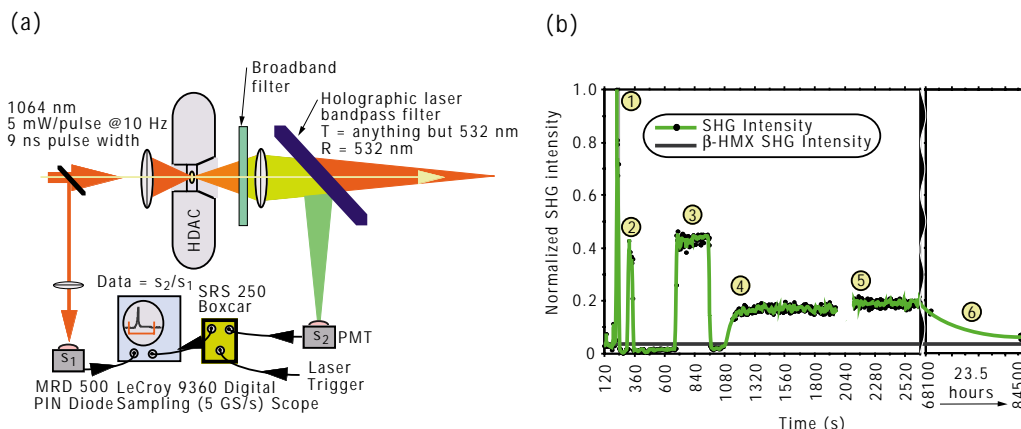
Role of Impurities in Mechanically Induced Defects

R. H. Howell, P. Asoka-Kumar, J. Hartley, P. A. Sterne

99-ERD-047

The mechanical properties of metals are controlled primarily by dislocations. We are performing a program of measurements of dislocations and associated defects using positron annihilation spectroscopy. We have completed experiments on fatigued and stressed samples and installed in-situ capabilities. An improved understanding of dislocation dynamics and interactions, an outstanding problem in multiscale modeling of materials, is the current focus of major theoretical efforts at LLNL. Our project satisfies the need for a non-destructive, in-situ experimental microscopic defect probe. Measurements are coupled to theory to give an atomistic view of defects including their impurity interactions. Probing impurity interactions is a unique contribution not addressed by other LLNL efforts. We established positron spectroscopy on deformation defects and completed two experiments in metals that clearly identify elemental impurity interactions with defects.

This capability is enabled by our MeV positron beam, which serves basic research and programmatic experiments and is ideally suited for in-situ measurements of samples using positron annihilation spectroscopy. To determine impurity interactions, we installed a new spectrometer that measures the momentum of orbital electrons and provides identification of elements surrounding defects that trap positrons. We developed corresponding theoretical calculations to further enhance this analytical tool.

We measured a catalog of pure elements to establish an experimental orbital electron momentum database and validate theoretical models. This system was then tested by measuring the elements surrounding the open volume in a five component (Zr, Ti, Al, Ni, Cu) amorphous metallic alloy (see figure). For each state of the alloy, the data were described by a unique linear combination of reference spectra. From this analysis, we were able to provide the first evidence that the distribution of the elements around the open volume was highly non-uniform and strongly favored Zr and Ti. These data have motivated R. Dauskardt of Stanford University to collaborate on effects of compressive stress in metallic glasses.

We completed experimental and theoretical analysis of stainless steel samples fatigued in small steps to total failure and for the first time directly observed a long-suspected correlation between carbon and fatigue-induced defects. Positron lifetimes established the growth of two defects: One lifetime was typical of vacancy clusters in iron and trapped 80% of the positrons at high fatigue levels; the second trap lifetime was typical of dislocation cores or grain boundaries. Orbital electron momentum measurements showed a combination of carbon and steel that matched the trapping fraction of the vacancy cluster defect. Our calculations show that vacancy cluster carbon decoration must be nearly complete to match the observed lifetime and momentum data. Measurements are in progress on a series of samples, including Al for in-situ measurements, Ta obtained from the dislocation dynamics project (see page 4–5) and deformed Cu.

We have developed new calculational methods to predict positron behavior in complex defect geometries. Using a novel finite element-based electronic structure program, we have calculated positron distributions and lifetimes on systems with as many as 2160 atoms. We have used atomic positions from molecular dynamics calculations obtained from the Accelerated Strategic Computing Initiative to calculate positron lifetimes for a catalog of defects in elemental copper and silver, obtaining very close agreement with experiment for vacancies, collapsed vacancy loops, and stacking fault tetrahedra. We have also developed an atomic-based code for calculating orbital electron momentum spectra. This code has been validated against experiment and is now used to analyze experimental data for which reference systems are unavailable.
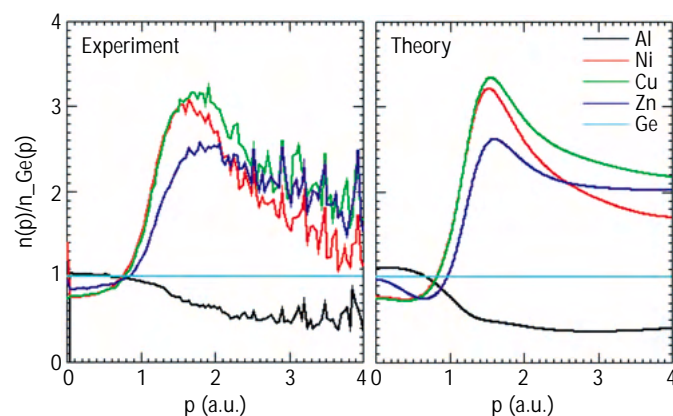
Measurements and calculations of orbital electron momenta determine properties of defect-impurity interactions by identifying the elements that surround the defects.

Nanolaminate Structures for BioElectroRecognition

W. D. Wilson, T. Barbee, Jr., H. Ackler, B. Rupp, A. Shestakov, M. Surh, D. Wilson

99-ERD-066

The development of integrated biotechnology devices is a rapidly expanding field, limited by manufacturability constraints and an incomplete understanding of processes on the nanoscale. We seek to apply Laboratory capabilities in materials synthesis and numerical simulation to the design and fabrication of probes to manipulate, detect, or characterize molecular and nanoscale pathogens.

Our specific goal in this project is to apply well-understood nanolaminate structures to this purpose by making these structures dimensionally commensurate with molecular and biologically significant species (i.e., making them significantly smaller than microlithographic-length scales). The synthetic compositional control in these structures combined with biochemical linker molecules should yield new knowledge and technology that would advance the development of chemical/molecular sensors. Atomic/chemical-force microscopy (AFM) enables us to visualize—for the first time—a charged surface of a nanolaminate in a fluid. Computational methods developed here permit the design and simulation of complex static and dynamic electrical effects in the vicinity of these structures in fluid environments.

Our nanolaminate structures are synthesized using physical vapor deposition at up to 0.7% uniformity over 10- by 20-cm areas. They are constructed from oxides and elemental or alloyed metals with variable thickness vs either depth or lateral position. This provides a wide

From top to bottom: the calculated electrostatic potential (Φ) vs lateral position (ranging from ± 20 mV), an atomistic model of the surface, and a measured atomic force microscopy (AFM) friction map of the nanolaminate in water.

design range for dimensional commensuration and varied surface chemistry.

In FY1999, we constructed a uniform nanolaminate of alternating 500-Å SiO_2 and Al_2O_3 layers. By adjusting the fluid pH, we made the surface charge negative for stripes of SiO_2 and positive for Al_2O_3. A charged AFM probe was scanned over the surface. The resulting friction-force map (see figure, bottom image), which clearly identifies regions of different charge coincident with the multilayers, is the first direct visualization of surface charge in an artificial structure.

We also simulated nanolaminates at atomic levels (see middle image in figure). Troughs, wedges, cylinders, and holes were allowed as possible design elements to be fabricated in the nanolaminate structures. A solvent-accessible boundary surface was then constructed on the surface. This was employed in a Green's function solution to the linearized Poisson–Boltzmann equation, which included dielectric discontinuities between the heterolayers and between solid and fluid. The calculated variation in potential (top image in the figure) yielded large electric fields that polarize particles near the surface. Subsequently, we determined the free energy of a nearby, charged, spherical particle using a double-boundary Poisson–Boltzmann calculation that included all surface and induced image charges and the energy of solvation. We found that the interaction energy was chemically significant across 50-Å distances in water.

High electric fields (e.g., those associated with DNA) were addressed with the LLNL code ICF3D. The elliptic Poisson equation was transformed to a nonlinear diffusion equation for the desired potential. When we applied the method to planar geometries, we found excellent agreement with our analytical results. Our spherical-particle calculations have yielded a database for developing simple, approximate algorithms.

Alternating fields imply complex dielectric constants or conductivities. We developed a finite-difference method in which the motion of the co- and counter-ions in the fluid is explicitly included. The solution includes linear and nonlinear terms. The resulting, frequency-dependent dipole moments and energies may be useful for molecular recognition.

In FY2000, we will manufacture and simulate nanolaminates with novel geometries (e.g., trough structures) and begin testing their interactions with solvated molecules. This will provide guidance for the design of devices for particle manipulation or templates for growth of protein crystals.
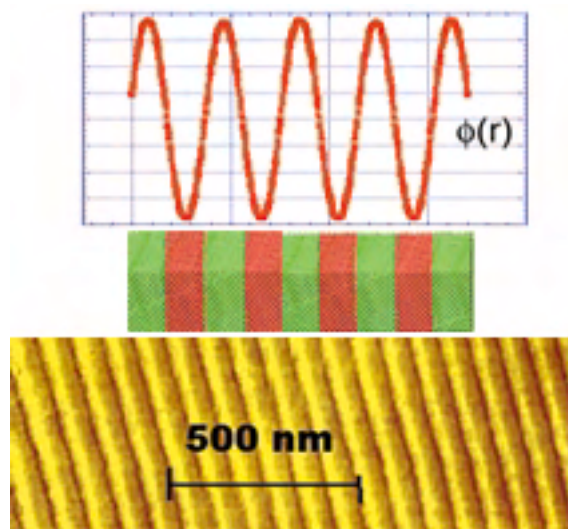
Determining the Structure of Biomaterials Interfaces using Synchrotron-based X-Ray Diffraction

M. T. McBride, J. J. De Yoreo

Many organisms exhibit control over biomineralization processes, resulting in exquisitely tailored crystalline architectures. Control may involve the introduction of acidic macromolecules that interact with growing crystals, or carefully timed introduction of ions, the removal of trace elements, the introduction of specific enzymes, etc. These processes, which occur at crystal surfaces, are mediated by atoms at the solid/solution interface. Understanding such processes requires tools for probing surfaces and near-surface atomic structure in fluids.

Surface x-ray diffraction (SXRD) techniques have recently been used to determine the atomic ordering of crystal surfaces in liquids and the near-surface ordering of the liquid phase. Because it can be applied in situ, SXRD provides a dynamic picture of the system under study, giving crystal structure, surface molecular structure, the stereochemistry of adsorbates, and the stereospecifity of binding sites. This method provides a crucial link between experimental surface techniques, such as scanned probe microscopy, and theoretical tools, such as kinetic Monte Carlo and molecular dynamics—all of which are playing increasing roles in detection, identification, and characterization of biological molecules and materials. This project has two main goals: (1) to build a competency for LLNL in x-ray analysis of fluid/solid interfaces; and (2) to establish the feasibility of using SXRD to determine the interface structure of biomaterials by applying it to simple model biomineral systems and comparing the measured interface structure with predicted structures based on crystallographic modeling. Our collaborators are Dr. Elias Vlieg, et al. at the University of Nijmegen in The Netherlands and Drs. Paul Fenter and Neil Sturchio at Argonne National Laboratory (ANL).

We have chosen as our model systems calcium carbonate and calcium phosphate in aspartic and glutamic acid-bearing solutions. The calcium compounds are ubiquitous among biomineral structures, while the two acidic amino acids—both as simple and poly-amino acids—are the dominant constituents of protein mixtures implicated in the control of biomineralization. We performed three initial experiments to become proficient in data collection, data analysis, and interpretation. The first two served primarily as training exercises, while in the third, we looked for changes in calcite structure upon addition of aspartic acid. These latter measurements showed clear evidence for the presence of an organic thin film on the (104) face, but because of beam-induced damage of the film, which led to significant intensity variations, we were not able to draw conclusions about the ordering of the film.

We grew calcite crystals in D- (right-handed) and L- (left-handed) aspartic acid. Crystals became elongated in the (001) directions and expressed an unequal mixture of (110) and (1-10) facets. The new facets are stereospecific. These results indicate that (1) aspartic acid adsorbs to the surface, (2) the adsorption is stereospecific, and (3) future SXRD should be applied to the (110) and (1–10) faces, not the (104) face expressed in the aspartic acid-free system. Efforts to model amino acid interactions with calcite using crystallographic software and Cerius2 modules are ongoing; we have recently begun molecular dynamics simulations. Published adsorbate binding models suggest that adsorbate carboxylates substitute for calcite carbonate anions on the (1–10) facets. Figure 1(a) shows that aspartic acid cannot bind the (1–10) face without causing severe lattice deformations, but that aspartic acid is easily accommodated in a binding interaction involving two steps on (104) symmetry-equivalent faces, as shown in Fig. 1(b). This model is consistent with our atomic-force microscopy results. Finally, we are establishing independent investigator beam time at ANL synchrotron facility.

In FY2000, we intend to (1) complete the study of surface modification in the calcite-aspartic and calcite-glutamic acid systems; (2) examine a calcite-aragonite phase transformation, which occurs in the presence of acidic macromolecules extracted from abalone; and (3) complete the modeling of both aspartic and glutamic acid interactions with calcite, using frustrated total internal reflection techniques to look for differences in those bonds.
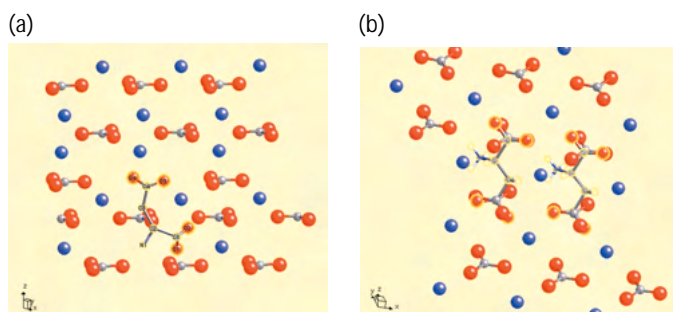
(a)   (b)

Figure 1(a) shows L-aspartic acid (highlighted) on the (1–10) calcite surface, and (b) shows L-aspartic acid fits without deformation on (104) symmetry-equivalent calcite faces.

A Study of Spatially Resolved Temperature Diagnostics for High Explosives

H. W. H. Lee

99-ERI-017

The next generation of 2-D and 3-D weapon-simulation codes will require marked advances in the spatial and temporal resolution of the various diagnostics to verify the complex physics predicted from these calculations. This is particularly true for the complicated physics of high-explosive (HE) detonation and burn, of which a detailed understanding is crucial to nuclear-weapons performance and integrity.

The processes involved in the detonation of HEs occur very rapidly and lead to extremely high pressures (several GPa) and temperatures (several thousand kelvin). A key diagnostic that has so far eluded experimentalists is a temperature diagnostic for burning HE. Temperature is a basic thermodynamic property that enables a fundamental understanding of important HE physics such as the chemical processes involved in the shock-to-detonation transition and the thermal part of the equation-of-state of the detonation products. Accurate, spatially localized temperature measurements with high temporal resolution are thus crucial, but are unfortunately lacking. Our work addresses this important problem.

During FY1999, we demonstrated several important physics principles that support a new spatially resolved temperature diagnostic for HE burns and shock fronts. Our diagnostic provides (1) a 2-D spatial resolution of 10 to 100 μm (the critical length scale needed for useful modeling of HE burns), (2) single-shot measurement capability, and (3) temporal resolution.

Our diagnostic determines temperature through the population distribution between two appropriately spaced atomic-energy levels. Temperature is deduced from the population distribution (e.g., Boltzmann), which can be determined with a variety of techniques, including luminescent and holographic methods. The population distribution is related to the ratio of the luminescence intensity from the two energy levels, which gives the temperature.

Two requirements for the energy levels are (1) the energy difference between the levels must approximate the average thermal energy; and (2) to mitigate background interference (e.g., blackbody radiation), luminescence must occur in the blue or ultraviolet. Requirement (2) will allow background emission subtraction to minimize interference.

On the basis of these requirements, during FY1999 we performed spectroscopic measurements on several atomic systems and succeeded in identifying two rare-earth ions (Tm^{3+} and Tb^{3+}) as promising candidates for the atomic system. Our luminescence measurements indicate that with these ions (1) the difference in energy levels will allow temperature measurements of a few thousand kelvin, (2) interference from Doppler and collisional broadening are not limiting problems, and (3) the required number density of atoms for useful signal levels is reasonable.

In FY1999, we also designed and constructed an experimental system to implement our temperature diagnostic. In this design, (1) the luminescence is collected either with free-space optics or with a 2-D imaging fiber, (2) the design of the collection optics determines the area and spatial resolution of the measurement, and (3) an excitation laser initially populates the excited states and enters through the collection optics. Then, (1) a fraction of the collected light from the HE burn is directed to a 2-D detector array—which provides a background emission spectrum to allow its subtraction and thus minimizes its interference with the atomic luminescence; and (2) the remainder of the luminescence is directed to two other 2-D detector arrays, where optical filters separate the spatial image of the luminescence from each atomic level. Information from all three detector arrays is computer-processed into a 2-D temperature image, which, with proper design of the imaging optics, permits a spatial resolution of 10 to 100 μm.

With 2-D detector arrays such as we have designed, single-shot information is obtained, along with time-resolved 2-D temperatures. This represents critical capabilities that presently do not exist.

Atomic Structure and Deformation Behavior of Bulk Amorphous Alloys

T. G. Nieh, L. M. Hsiung, B. W. Choi

Bulk amorphous alloys (BAAs) constitute a new and exciting class of metallic glasses for structural and functional use. These materials not only have unusual properties (e.g., high strength and excellent resistance to wear), but also exhibit many peculiar behaviors (e.g., they deform elastically and exhibit very limited plasticity in uniaxial tension).

The objective of this project was to gain a basic understanding of the atomic and defect structure of BAAs and of how structural stability affects their deformation behavior. We placed particular emphasis on understanding (1) shear-band formation, which is the dominant deformation mode at ambient temperature; and (2) Newtonian plastic flow, which is expected to be the dominant deformation mode at supercooled-liquid temperatures in BAAs. Such understandings would allow suppression of shear instability, promotion of homogeneous deformation at low temperatures, and improved formability at supercooled-liquid temperatures.

Examining the atomic structure of BAAs is difficult because only limited advanced equipment is available. As our first attempt during FY1999, we conducted positron-annihilation experiments using LLNL's newly installed, two-detector coincidence system. In contrast to conventional positron measurements—which provide information on positron lifetime and the Doppler broadening of the annihilation gamma rays—the two-detector system can use the momentum part of the Doppler-broadened annihilation spectra to distinguish different elements around an annihilation site. Our experimental results showed that there was more Ti, at the expense of Ni and Cu, around volumetric defects in a cast Zr–10Al–5Ti–17.9Cu–14.6Ni bulk metallic glass. Annealing of the cast sample at 200°C appeared to have no affect on the atomic structure.

During FY1999, we also investigated the deformation behavior of a Zr–10Al–5Ti–17.9Cu–14.6Ni metallic glass at temperatures above the glass transition temperature, that is, in the supercooled-liquid region. As expected, the alloy was observed to exhibit a large tensile elongation in this region; a maximum tensile elongation of over 600% was recorded at 425 to 440°C at a high strain rate of 10^{-2} s^{-1}. We found that both the flow stress and tensile elongation were very sensitive to testing temperature. Surprisingly, experimental results indicated that the alloy does not behave like a Newtonian fluid (m = 1, where m is the strain-rate sensitivity exponent). Microdiffractions from deformed samples revealed the crystallization of the amorphous structure. We suggest that the non-Newtonian behavior was caused by the concurrent crystallization of the amorphous structure during deformation; thus, we actually tested a mixed crystalline-plus-amorphous structure. At the present time, we don't know whether the in-situ crystallization phenomenon, which leads to the observed non-Newtonian behavior, also occurs in other BAA systems. At temperatures above the crystallization temperature, in spite of having a nanocrystalline structure, the amorphous Zr–10Al–5Ti–17.9Cu–14.6Ni alloy exhibited limited ductility. This is a result of poor strain accommodation at grain triple junctions.

In this project, we provided preliminary observation for non-Newtonian behavior in a metallic glass in the supercooled-liquid region and offered a possible explanation for the observation. However, additional experiments at a higher annealing temperature are needed to clarify the dynamics of atomic structure. Other techniques such as atomic probe microscopy, high-resolution transmission electron microscopy, and neutron scattering also have great potential for studying the structure of BAAs.

Synthesis and Characterization of Nanowires

R. G. Musket, T. E. Felter, A. Quong

99-LW-026

With the dimensions of components in micro-electronic circuits shrinking, the fundamental phenomena associated with electronic conduction through wires and with device operation can be expected to change. For example, as the length of electrical conductors is reduced, ballistic transport will become the main mode of conduction. Sufficient reduction in the cross-sectional area of conductors can lead to quantum confinement effects. Prior knowledge of the phenomena associated with decreasing size should help guide the designers of future, smaller devices in terms of geometries and materials.

However, prior knowledge requires the availability of sufficiently small nanowires for experiments. To date, the smallest nanowires that have been fabricated and investigated had diameters of 8 nm. We have proposed and initiated the unprecedented study of these size-related phenomena. This study consists of synthesizing, using a novel version of nuclear track lithography, and characterizing, physically and electrically, nanowires with diameters of 1 to 5 nm and lengths of 2 to 250 nm.

For our coordinated theoretical and experimental study of nanowires, we first require the creation of the unprecedented nanowires. We identified three different potential sources for the atomic species to be infiltrated into the latent nuclear tracks: (1) solid-state coatings applied either before or after nuclear tracking, (2) liquids with atomic and/or ionic species, and (3) dynamic sub-monolayer surface layers with the atoms having very high mobility. In each of these three cases, both thermally driven diffusion of atomic species and electric field enhanced diffusion of ions were deemed viable options.

Our initial approaches were concentrated on the solid-state coating sources. We performed infiltration experiments using metallic coatings of Ag, Au, and Pd with thicknesses of 0.5 to 60 nm applied by sputter deposition either before or after the nuclear tracking step. The substrates studied were thermal oxides on Si, bulk silica, bulk mica, and bulk quartz. The irradiation conditions were 15- to 17-MeV Xe ions uniformly rastered over half of each sample to a total fluence of 1×10^{11} Xe/cm^2.

The major goal of these initial studies was to determine the heating conditions (temperature, environment, and time) that lead to infiltration of the nanowire species into the latent track. The infiltration, or diffusion, of the atomic species into the latent tracks must occur prior to the annealing of the damage (atomic vacancies and interstitials) existing in the latent tracks.

Although we had several apparent successful infiltrations, careful follow-up studies showed that we really had only one truly positive result. For 25-nm-thick gold deposited on tracked quartz and heated at 650°C for 2 h in vacuum, there was Rutherford backscattering (RBS) evidence that diffusion into the tracked quartz half of the sample was substantially greater than that into the non-tracked half.

In addition, we designed, fabricated, and assembled a capability for electric field enhanced diffusion of ions from solid state coatings. This capability includes the ability to heat up to eight samples simultaneously in very high vacuum or in the presence of gases with applied electric fields.

Unfortunately, we were notified that our LDRD project will not be funded in FY00, so we do not have the resources to complete this unprecedented and challenging study. However, our studies provided insights that allowed us to refine our patent application on the process for fabrication of nanowires. Finally, we believe that one of the many options we have identified will lead to the desired nanowires, and we will continue to seek funding to continue this work.

Nuclear/Atomic Science and Technology

9

Section 9

Nuclear/Atomic Science and Technology

Proton Radiography for the Advanced Hydrotest Facility

E. P. Hartouni, M. Aufderheide, P. D. Barnes, Jr., R. Bionta, D. Fujino, H. Park, R. A. Soltz, D. Wright

Proton radiography is a technique for studying the dynamics of imploding systems. High-energy protons illuminate an object and are absorbed and scattered by it. They are brought to a focused image by a magnetic-lens system, then detected by a set of integrating, imaging detectors. The many advantages offered by proton radiography, including mature source technology, long interaction lengths, high detection efficiency, and multiple types of radiographic information, lead to its potential use in the proposed proton Advanced Hydrotest Facility (AHF). This facility, which would be located at Los Alamos National Laboratory (LANL), would be used as part of LLNL's Stockpile Stewardship Program to determine primary yield, study weapons safety, and provide data on various physics experiments. Our purpose in this project has been to assess the science of proton radiography as a tool for studying the time-dependent hydrodynamics of imploding systems.

During FY1999, our primary focus was on acquiring data and developing techniques for proton radiography. Data related to the fundamental aspects of proton–nucleus collisions (essential as input to simulation and analysis codes) were provided by Brookhaven National Laboratory (BNL) experiments E910 and E943. These experiments led to the submission to Fermi National Accelerator Laboratory (Fermilab) of proposal P907 to continue a series of experiments at beam energies of interest to the proposed AHF. A third major experiment at BNL, E933, used BNL's high-energy primary proton beam to radiograph static objects of relevance to systems interesting to hydrotesting.

Data analysis of BNL E910 has focused on particle production in proton–nucleus (p–A) collisions in the 7- to 19-GeV energy range. These data have been instrumental in assessing the possible high-energy backgrounds in proton radiography. In particular, we used measurements of pion momentum and angular distributions to tune empirical models of particle productions. These models are used as input to simulation codes of proton radiography experiments for the purpose of predicting radiographs. In addition to the studies relevant to proton radiography, the results of BNL E910 have contributed to the body of knowledge of p–A physics that will be important to understanding the results of BNL's Relativistic Heavy Ion Collider (RHIC) when it begins data collecting data in mid-FY2000.

Cross sections of particle interactions in p–A physics provide important input to simulation codes as well as checks on the analysis of radiographic information (e.g., as provided by step wedge data). In BNL E943, we collected data on six nuclei (Be, C, Al, Cu, W, and Pb) at ten beam energies (0.538, 0.814, 1.09, 1.38, 1.66, 2.65, 3.50, 4.35, 6.07, and 7.80 GeV). These data (1) provide, for the first time, a comprehensive view of data around the production threshold for pions; (2) will be used to discriminate between various models of the p–A absorption cross sections; and also (3) will be used, directly, in various simulation codes and data libraries.

Proton radiography at 25 GeV was the topic of BNL E933. This experiment, which ran for 14 days in August 1999, was the collaborative effort of 50 physicists from LLNL and LANL. In a series of experiment to measure the limits of proton radiography as a quantitative tool, over 1000 images of various objects [e.g., step wedges, spatial calibration plates, the French Test Object (FTO), etc.] were obtained on both phosphor image plates and charge-coupled-device (CCD) cameras (provided by both laboratories).

At year's end, our quantitative data analysis of data from E933 was in process; results will be presented and published during FY2000. It appears that the E933 data set will provide definitive answers to the limits of quantitative radiography with high-energy proton beams. Proposals for additional experiments based on E933 will be submitted to BNL's Program Advisory Committee (PAC) for consideration for the FY2000 run period.

Uncharted Frontiers in the Spectroscopy of Highly Charged Ions

P. Beiersdorfer

97-ERD-103

The Laboratory is at the forefront of producing and trapping ions of any element and charge state. In this project, we have been developing novel spectroscopic capabilities regarding highly charged ions. We have systematically created new research tools tailored to LLNL's novel ion sources that enable entirely new classes of measurements. We have developed instrumentation capable of unprecedented precision that enables definitive tests of fundamental theories—including tests of nuclear structure theory, quantum electrodynamics, and magnetic interaction among free and bound electrons in scattering theory. We have also established the basis for developing new diagnostic techniques for high-temperature plasmas, such as those generated with the National Ignition Facility (NIF), and for understanding the spectral line emission from the astrophysical plasmas surrounding cataclysmic variables and the interstellar medium by observing spectral radiation never before seen in the laboratory.

During the past year, we implemented novel, high-precision techniques for measuring radiative lifetimes, opened the 15- to 400-Å wavelength to scientific scrutiny with the development of highly efficient, soft-x-ray grating spectrometers, and demonstrated the use of absolutely calibrated monolithic crystals as reliable x-ray standards. The development of new spectrometers and techniques in FY1999 has added to our implementation of several high-resolution soft- and hard-x-ray spectrometers that we developed in FY1998.

Our implementation of novel methods for determining accurate radiative transition probabilities has put us on the forefront of this area of research. We now hold the record in the accuracy with which radiative rates of metastable levels with lifetime less than 1 ms can be measured. This adds to the capabilities that we developed during FY1998, making LLNL the only laboratory in the world capable of measuring radiative lifetimes in the femtosecond regime.

Two monolithic crystals manufactured from a large, silicon-crystal block were successfully tested to yield new standards in the x-ray region. Each monolith has two reflecting surfaces [see Fig. 1(a)] that produce a double image of the spectral lines of interest. The spacing of the crystalline layers was absolutely calibrated in a comparison with laser frequency standards by our collaborators at the University of Jena, Germany. From the spacing of the double image and the distance between the front and back reflecting surface, absolute x-ray wavelengths were determined for the Lyman-alpha transitions of hydrogenic Si^{13+} and Ar^{17+}, proving that new x-ray standards can be developed this way.

The extreme ultraviolet (EUV) and soft-x-ray region from 15- to 400-Å contains radiation from many charge states of elements such as W and Au—which are important to the radiative power balance in magnetic fusion and inertial confinement fusion (ICF). We have opened this wavelength band to scientific scrutiny by implementing two soft-x-ray spectrometers. To illustrate our new capabilities, we reexamined spectral measurements performed on Nova and Omega. Our new data, shown along with Nova/Omega data in Fig. 1(b), has three times the accuracy of the earlier data and reveals much better agreement with theory than before.

The capabilities created under this project have significantly strengthened LLNL's core competencies in basic atomic physics and our readiness for evolving programmatic needs by opening up large areas to scientific scrutiny and propelling the Labotatory to a leadership position. This project has been the basis for nearly two dozen scientific publications, including two Ph. D. theses. Scientific results produced with the new capabilities have revised atomic scattering theory and have tested fundamental theories with unprecedented accuracy. The results of this LDRD project will have a lasting impact on atomic theory, spectral modeling, and diagnostic development.

Figure 1. Novel spectrographic techniques and results: (a) an Si(220) monolith carved from a single block of silicon that has two reflection surfaces—the resultant double image enables new x-ray standards, and (b) spectral measurements in the extreme ultraviolet obtained from our experiments shown with that obtained earlier using the Nova/Omega laser—our results are much closer to theoretical values.
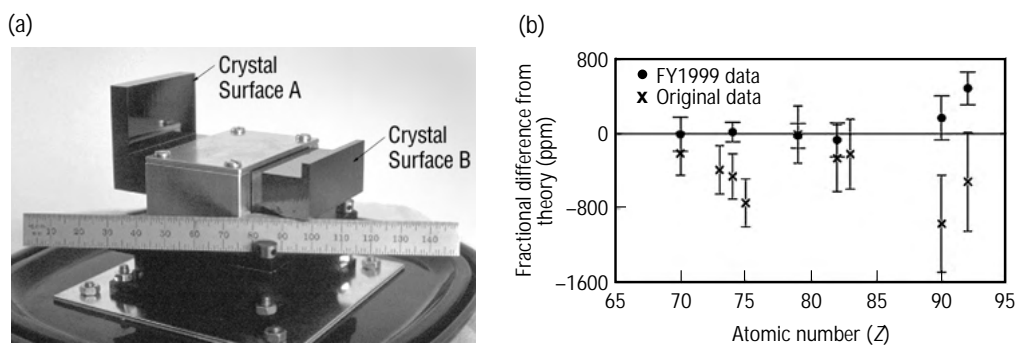
Development of Short-Pulse, Laser-Pumped X-Ray Lasers

J. Dunn, A. L. Osterheld

97-ERD-105

We have successfully developed a tabletop x-ray laser based on the transient collisional excitation (TCE) scheme. Transient x-ray lasers have substantially higher efficiency than previous collisional schemes and can be driven by a high power, picosecond, small laser system at a high repetition rate. These x-ray lasers are ultra-bright x-ray sources because of the high output, narrow divergence, high monochromaticity, and short-pulse duration. As such, they have applications in imaging and diagnostics of high-density plasmas, in chemistry and material science, and in x-ray lithography. This type of experiment can also validate codes used in the Stockpile Stewardship Program because of the unique transient conditions in the high temperature plasma used to generate the x-ray laser.

The improved efficiency of a TCE x-ray laser is achieved by using a long pulse to form the plasma amplifier medium and a short pulse to pump the inversion. The tabletop Compact Multipulse Terawatt (COMET) laser is a chirped pulse amplification system that supplies both the long, 600-ps plasma forming beam and the short, 1-ps excitation beam. The two-pulse configuration allows the optimization of the separate processes to generate the x-ray laser. This takes typically 5–10 J of laser energy, which is significantly less than the kilojoules of energy required previously. Also, the fast-excitation process with the 1-ps pulse produces very high transient gains of 35–65/cm that are typically 10 times higher than quasi-steady state schemes. We have modeled these results with a one-dimensional hydrodynamics and atomic kinetics code coupled to a transient ray tracing post-processor. The experimental characterization and theoretical analysis performed in FY1998 allowed us to better understand the x-ray laser conditions.

In FY1999, we developed numerous x-ray lasers with wavelengths between 119–326 Å by producing plasmas with a closed-shell electron configuration of either low-Z neon-like ions (elements ionized until they have 10 electrons remaining) or nickel-like ions (with 28 electrons remaining). Studies of the plasma ionization on one of our Ne-like ion x-ray lasers, using keV high-resolution x-ray spectroscopy of L-shell Fe resonance lines, demonstrated that Ne-like ionization was created by long pulse heating only. This confirmed that the optimum pre-conditions were being created by the long pulse before the arrival of the excitation pulse.

We have maximized the output of the x-ray lasers by driving them into the saturation regime and have carefully measured some of their properties. We achieved a major milestone in FY1999 when we implemented a traveling wave irradiation scheme that matched the arrival of the optical pulse with the propagation of the x-ray laser along the plasma. This kept the picosecond gain high for the x-ray laser beam and increased the x-ray output by 20–100 times. We presently extract 12 μJ of x-ray laser energy from the plasma. Other experiments, with our collaborators, involved the use of high quality multilayer optics to image the x-ray laser as it exited the plasma. We found that we could control the spatial dimension of the gain region by varying the optical laser parameters.

The project has achieved its main goal of creating a tabletop x-ray laser. We are currently investigating a range of applications for this ultra-bright source. Experiments using the x-ray laser to probe a plasma are in progress and will be used to test predictions from hydrodynamics codes. This will demonstrate the potential of the short pulse and short wavelength properties of this x-ray laser as a diagnostic probe for high-density plasmas created by the National Ignition Facility.
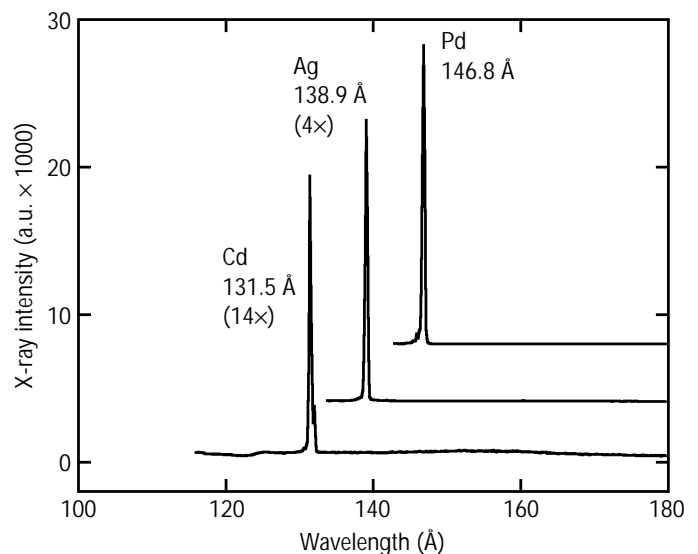
Single shot spectra from the Ni-like ion sequence shows strong 4d-4p x-ray laser line of Cd, Ag, and Pd.

Intense Laser–Electron Beam Interactions

T. E. Cowan, T. Ditmire, G. P. Le Sage

97-SI-001

The integration of advanced short pulse laser technology with conventional radio-frequency (rf) accelerators is an important new direction in advanced accelerator research in the 21st century. This has been particularly apparent in the planning for the next generation of x-ray light sources beyond present, third-generation synchrotrons. The leading candidate for a major facility is a x-ray free electron laser, which is made possible by an ultra-high brightness laser-generated electron beam. The scientific motivation for a fourth-generation light source also arises largely from research within the laser community on ultrafast time-resolved measurements, e.g., solid-state dynamics in laser-heated crystals. It is expected that these types of pump-probe experiments—which use laser-generated, sub-picosecond pulses of radiation to stroboscopically probe the structural changes of a laser-heated or shocked sample—should be applicable to a variety of physical, chemical, and biological systems; further, they will revolutionize our understanding of dynamic phenomena on a time scale characteristic of atom motions.

In this project, we are taking a lead in the development of next-generation light sources in two ways. First, we are identifying and solving the key technology issues in combining laser and accelerator systems by integrating the Falcon Ti:sapphire short pulse laser with a high-brightness electron beam from the LLNL 100-MeV electron linear accelerator. Second, we will use this system to produce an interim short-pulse x-ray capability, orders of magnitude more intense than presently available, at which we will develop the new experimental capabilities needed for future ultrafast measurements. In addition, we could perform some of the seminal ultrafast experiments that will help strengthen the scientific case for a 4th generation light source.

We have made considerable progress towards integrating the Falcon short pulse laser with the 100-MeV linac electron beam in FY1999. The ultimate performance figure of merit will be to overlap at the collision point, a tightly focussed (~10 μm), picosecond-long electron bunch with a high intensity laser pulse, synchronized to less than ~0.5 ps. Relativistic Thomson scattering of the laser light by the electrons will produce an extremely bright, ~ps pulse of hard x-rays, which can then be used for ultrafast experiments.

The stringent electron beam requirements dictate the use of a low-emittance rf photocathode injector as the electron source for the linear accelerator. In FY1999, we have completed the construction of the low emittance, rf photocathode injector, which will provide our initial degree of synchronization of the laser, electron, and x-ray beams. Developed in collaboration with the Particle Beam Physics Group at UCLA, the 1.6-cell S-band rf gun has been conditioned to 5 MeV with dark current beams, and should provide exceptional beam emittance characteristics with photo-electrons from a new photocathode laser system. We have also designed and fabricated much of the beam switchyard system required to integrate the rf photogun with the existing linear accelerator. We have developed new high-resolution electron beam diagnostics, based on optical transition radiation, for measuring the emittance characteristics of the new beam.

Independently, we completed the Falcon laser system to the 20-TW level in FY1999. It operates routinely at 10 Hz and has been used successfully for several independent experiments. In FY1999, we also designed and constructed the optical transport system from the Falcon laboratory to the below-ground electron beam vault and installed the grating compressor chamber.

Sustained Spheromak Physics Project

E. B. Hooper, D. N. Hill, H. S. McLean, R. W. Wood, S. Woodruff

97-SI-009

The Sustained Spheromak Physics Experiment (SSPX) began operating in FY1999 in order to study the performance of an important alternate to the tokamak. In the spheromak, the toroidal magnetic field configuration (donut shaped) is produced by internal currents in the plasma, rather than by external magnets, as in the tokamak (also a toroidal configuration). These internal plasma currents result from relative motion between the plasma fluid and fluctuating internal magnetic fields in a self-consistent manner by means of dynamo action. Our current experiments on SSPX will determine if the magnetic turbulence associated with the dynamo can be made weak enough so that the associated energy losses are acceptably small for a fusion reactor.

Our work in FY1999 focussed on learning how to produce spheromak plasmas reliably, determining the internal magnetic configuration from external measurements, and developing hardware for a new magnetic configuration which should lead to improved performance. The basic SSPX was completed in November 1998, after which we began testing the main power systems. In parallel with the testing, we completed installation of a basic set of startup diagnostics. First plasmas were obtained in April 1999.

During the initial operating period, which lasted until mid-August, we mapped out the basic operating space for spheromak formation in the SSPX device. The spheromak is formed when we puff hydrogen gas into the injector region and apply high voltage (3–8 kV to date) between the electrodes to produce an electrical discharge (currents as high as 400 kA, so far). When the discharge current exceeds a threshold value, the magnetic field lines can bulge out of the injector region and fill the main chamber (bounded by a copper shell flux conserver). Figure 1(a) shows the cross section of the SSPX device with representative plasma surface contours included. Our results show that the threshold current for spheromak formation agrees with theory, though with modifications to account for the particular magnetic field geometry in SSPX (the field gets weaker moving down and out of the injector region).

The basic characteristics of the spheromak—internal magnetic field shape and strength, along with the toroidal and poloidal plasma currents—has been determined using external magnetic field measurements coupled with the magneto hydrodynamic (MHD) equilibrium solver code CORSICA. We measure the poloidal and toroidal magnetic field components as a function of time at 14 locations around the flux conserver shell, as shown in Fig. 1(a). We then compare these data with the fields calculated by CORSICA and adjust the plasma current profile until we obtain a reasonable match, as shown in 1(b). In this case, the data are consistent with 500-kA toroidal plasma current.

During FY1999, we also designed and built a set of bias field coils, which will allow us to produce spheromak plasmas using currents flowing down the machine axis as opposed to across the injector gap. Such configurations should have lower threshold currents and consequently lower magnetic turbulence levels compared to the present configuration. In the next phase we plan to install these coils to see if improved performance (hotter plasmas) results. In addition, we will continue adding (1) plasma diagnostics, such as Thomson scattering, to measure electron temperature, (2) ultra-short-pulse reflectometry, which measures the plasma density profiles, (3) bolometers to measure radiated power, and (4) a transient internal probe to directly measure the internal magnetic field profiles.
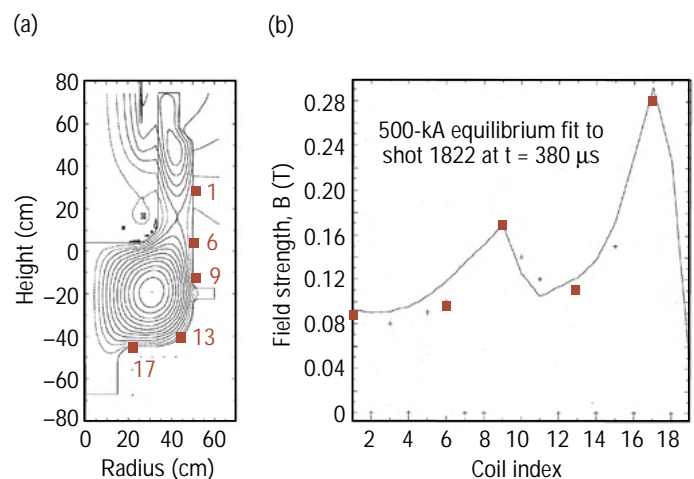
(a) (b)

Figure 1(a) SSPX plasma cross section showing selected magnetic probes; (b) a comparison between measurement and the CORSICA code. Magnetic coils measure the field at discrete locations on the wall.

Mapping of Enhanced Nuclear Stability in the Heaviest Elements

K. J. Moody, J. F. Wild, N. J. Stoyer, M. A. Stoyer, R. W. Lougheed

98-ERD-050

Predictions of the properties of nuclides near the extreme limits of nuclear stability provide a measure of our understanding of the fundamental properties of matter and the fission process. Predictions of an "island of stability" of long-lived superheavy elements beyond the limits of the known nuclides date back more than 30 years; during this time, there have been many unsuccessful searches for these nuclei. During the last decade, there has been a large effort by our group and others to systematically discover and characterize the properties of the intervening unstable nuclei. Starting 8 years ago, in an on-going collaboration with Russian scientists at the Joint Institute for Nuclear Research (JINR) at Dubna, Russia, we have observed the decays of previously unknown isotopes of elements 106, 108, and 110 whose properties are determined by subtleties in the nuclear structure caused by the shell effects that are predicted to result in the island of stability in the heavier elements. The resulting data have been successfully reproduced by the theoreticians, whose refined predictions of the decay modes and production rates of the superheavy elements have enabled us to design experiments with the sensitivity to locate these elusive nuclides.

In this LDRD project, we are continuing our collaboration with the Russian scientists at JINR. We are performing experiments to discover and characterize the superheavy isotopes around the magic nucleon numbers $Z = 114$ and $N = 184$, produced in the bombardment of ^{244}Pu targets with ^{48}Ca ions. Products of the complete fusion of the two nuclei recoil out of the target and into the Dubna Gas-Filled Separator, which isolates any element 114 atoms from beam particles and the unwanted products of side reactions. The superheavy-element recoils impact a position-sensitive detector array; the impact and any subsequent alpha- and spontaneous-fission (SF) decays are tagged with times and positions that allow the decay sequence to be reconstructed.

In FY1999, we performed two long irradiations; in the resulting data, we isolated the signatures of the decays of two atoms of element 114, constituting the discovery of the element. One decay sequence (see figure) we have attributed to the mass-289 isotope, which alpha decays with an amazingly long 30-s lifetime. Two subsequent alpha decays and a spontaneous fission, which occur over a span of 30 min, chart the progress of the decay away from the island of stability into species that are unstable to SF decay. The second decay sequence is due to the mass-288 isotope, which also alpha decays, but with a 0.8-s lifetime. A second alpha decay and a SF decay follow the initial decay, the total sequence spanning 25 s.

Along with the observation of a third element-114 isotope by another Dubna group, and still another isotope of element 114 as part of the decay chain of the recent element-118 discovery by the Lawrence Berkeley National Laboratory group, we feel we have made an excellent start at mapping the extent and strength of the nuclear shell effect that results in the island of stability.

In FY2000, we will perform a third irradiation of ^{244}Pu, after which we will irradiate ^{248}Cm; this experiment should result in the production of element-116 isotopes that should alpha decay to the element-114 isotopes that we have already discovered.
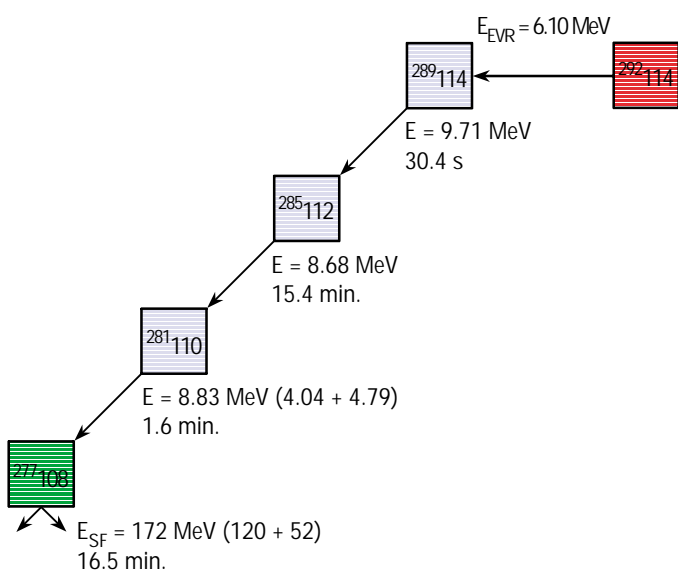
The first observed decay sequence for element 114. The initial nucleus formed by the fusion of the ^{48}Ca and ^{244}Pu nuclei de-excited by emitting three neutrons, leaving the evaporation residue 114–289. This product passed through the separator and impacted the detector array with an observed kinetic energy of 6.1 MeV. Subsequently, three alpha decays and a spontaneous fission at the times and energies indicated occurred at the same position in the detector, indicating their correlation with one another.

Development of High-Velocity Launcher Technology

R. G. Finucane, T. W. Alger,

98-ERD-055

Conventional, two-stage light-gas launchers do not efficiently apply their high breech pressures to the projectile. Our objective in this project was to carry out the analysis, design, construction, and testing of a new class of launchers. We hoped to expand the pressure range of the conventional, two-stage gas launcher to overlap and validate the pressure regimes previously attainable only with shock waves generated by nuclear explosions, lasers, or multistage conventional explosions. That is, these launchers would have the capability to conduct—in a laboratory setting—high-velocity-impact, equation-of-state (EOS) measurements at up to 2-TPa (20 Mbar) pressure levels in high-Z materials.

Our design entailed a new class of distributed-injection, gas-dynamic launchers that are designed to use a boat-tail projectile to overcome the fundamental gas-expansion phenomenon known as escape velocity (the Riemann limit).

In the first year of this project (FY1998), we focused on demonstrating some of the crucial technical advances required for our new concept. We designed and tested two fast diaphragm-opening techniques, deciding on the basis of these tests to use an exploding bridge wire (EBW) driven by a high-voltage capacitor discharge. We designed and built a gas-release test fixture to study the rate of rise of pressure at a fixed distance from the EBW-fired bursting diaphragm. In parallel with this work, we designed and built a first-stage helium launcher, consisting of a pressure intensifier used to boost the helium-bottle pressure from 10 to 100 MPa, a 100-MPa gas breech, and a new, 5-m-long, 20-mm-diam barrel. We also designed a distributed-injection acceleration section and assembled a target chamber and associated velocity-measurement equipment (a velocity interferometry system for any reflector, or VISAR) into a complete launcher system.

Our program included analytical, numerical, and experimental studies of the fast gas-release flow technique that is central to the success of our approach. The analyses led us to believe that, in a typical configuration, the pressure will be effectively applied to the projectile in a time short relative to its few-microsecond traverse time; the experimental program we conducted during FY1999 supported these estimates. In addition, our program revealed some dramatic, increased efficiencies in this process that were completely unexpected and previously unknown to the launcher community.

The most fundamental practical restrictions on the performance of any gas launcher are the ability of the launcher to (1) contain pressure in a reservoir, and (2) effectively apply that pressure to the base of a moving projectile. Our gas-release test-fixture experiments serendipitously revealed that our design was capable of applying nearly twice the pressure to the projectile that is initially contained in the reservoir. We later confirmed this result analytically and related it to an obscure type of direct energy exchange between unsteady fluid flows. (This physical approach was the basis for the German V-1 "buzz bomb" of World War II; it has been applied to a limited number of commercial applications.) However, direct fluid-energy exchange has not previously been applied to gas-launcher technology.

As a result of these discoveries, we estimate that a practical, 15 km/s, high-velocity launcher could be built using our direct-energy-exchange, distributed-injection approach. However, the radical nature of the results, the lack of confirming or allied work being carried out anywhere else, and the fact that it would take extensive time and resources to demonstrate targeted performance precluded further development. We plan to submit the results to a refereed journal to ensure that the results of this research are well documented.

New Physics at the B Factory: Search for CP Violation

D. M. Wright

An asymmetry in the decay of particles and their corresponding antiparticles (charge-parity or CP violation) is a crucial problem for both particle physics and cosmology. In fact, CP violation is one of the last major components of the Standard Model of particle physics that is not thoroughly understood. CP violation is also a necessary ingredient in cosmological models that explain the predominance of matter over antimatter in the universe. Particle physics can not yet explain the source of this effect in the evolution of the early universe, but this project plays an important role in one of the leading efforts to explore this fundamental physics question.

The Standard Model of particle physics has been extremely successful at explaining data from particle-physics experiments over the past 50 years; however, the theory's explanation for CP violation has never been stringently tested. In the late 1980s, it was realized that by studying the decay of B mesons (a heavy form of matter that can be produced in accelerators), a definitive set of experiments could be conducted to test the model. Every major accelerator laboratory in the world has a high-priority experimental program to search for CP violation in B mesons.

With two other DOE laboratories, LLNL played a major role in constructing the B Factory at the Stanford Linear Accelerator Center (SLAC)—the B Factory is an accelerator that produces large quantities of B and anti-B mesons. This project supports a major role for LLNL in the international collaboration of physicists that has assembled the BaBar detector, the one and only one detector at the B Factory. In May 1999, BaBar became the first CP-violation experiment to come online. By September 1999, the experiment had achieved high luminosity running; it continues to set world-record levels of event production.

The most sensitive tests of CP violation at BaBar can be made from the K^0_S decay channel of the neutral B meson. This mode is relatively easy to detect. Equally sensitive, but more challenging to detect, is the K^0_L decay channel. To make a convincing discovery, the experiment should see a signal in both channels. From the very beginning, LLNL has been involved in the design and construction of the K^0_L-detection system and its associated software. The ultimate goal of this project is to shed light on the mystery of CP violation, specifically by focusing our physics effort on the important K^0_L decay channel.

In FY1999, we got our detector systems up and running and began analyzing their performance in preparation for CP-violation measurements. We have (1) completed—with our BaBar colleagues—the commissioning of the readout and monitor electronics for the entire K^0_L-detector system; (2) begun testing the K^0_L-detector using data from both cosmic-ray and colliding-beam events; (3) completed the first analysis of the LLNL-built portion of the K^0_L-detector, to measure the individual detector efficiencies and alignment parameters; (4) developed software to monitor and track chamber-performance characteristics as a function of time; and (5) studied chamber behavior and developed operating procedures for colliding-beam injection and stable running modes.

Simulations of tens of millions of colliding-beam events are required to develop the physics-analysis algorithms and to calibrate the detector-hardware systems. Since FY1998, we have been applying LLNL's symmetric parallel-processor resources to the production of Monte Carlo simulations for BaBar. In FY1999, we made major changes to the simulation software and architecture: all software was converted to an object-oriented framework; an elaborate, semi-automated processing system was implemented; and a distributed database system was added to store all input and output data. LLNL was the first site to implement these changes and is the single largest source for these simulations outside SLAC.

In FY2000, BaBar will achieve stable running at high luminosity, and we will begin collecting statistically significant data sets. We will (1) completely calibrate the K^0_L detector systems, (2) build the software tools to reconstruct the K^0_L decay channel from the data, and (3) begin a search for the CP-violation signal in the K^0_L channel. In the next few years, the BaBar collaboration expects to discover or rule out CP violation in B-meson decay; we are well-positioned to play a crucial role in producing evidence for a convincing discovery.

Exploratory Research for a Proton Radiography Demonstration Experiment

E. Hartouni, O. Alford, P. D. Barnes, Jr., A. Chargin, J. Hochman

98-ERD-088

Continuing certification of the safety and reliability of the U.S. nuclear weapons stockpile will require a major new radiographic facility, one that will provide multiple radiographic pulses on multiple axes. A high-energy proton beam is one of the radiographic probes being considered.

The purpose of this project was to determine whether it is possible to build a 20-GeV proton synchrotron suitable for a hydrotest experimental program (1) as quickly as possible (say within 2 or 3 years), and (2) as economically as possible (of order $100M).

The result of our work is that, indeed, such a synchrotron is technically feasible and can be built within the cost and schedule constraints. However, to meet the schedule and cost goals, this synchrotron (nicknamed "Scrounge-atron") relies heavily on the availability of components from the decommissioned Fermi National Accelerator Laboratory (Fermilab) Main Ring.

During FY1999, we examined schedule, costs, and component availabilities. We determined that we could meet the schedule and cost goals by adopting the following design procedure. First, we would use existing parts where available and appropriate. Second, if the parts were not available, we would use existing designs. Last, only if neither parts nor designs were available would we design and construct the required part. This procedure minimizes the design effort required for the accelerator. It is possible because—for most of the accelerator systems—the characteristics required for radiography are far below the capabilities of current state-of-the-art accelerators.

We based our analysis of component availability on the decommissioning of the Fermilab Main Ring, which has made a large variety of parts available for reuse. Our Scrounge-atron is designed around the B1-type dipole magnets and the Q4-type quadrupole magnets from the Main Ring. In January 1999, 120 of the dipoles and 40 of the quadrupoles were moved from Fermilab to a storage area at the Nevada Test Site (NTS) for possible use in a proton radiography facility. In addition to these magnets, correcting sextupole, octupole, and regular and skew quadrupole magnets are also available. Because the vacuum pipe is already epoxied into the dipoles, only short sections of new pipe would be required. All the power supplies for the magnets are available. Most of the diagnostic equipment is available (e.g., beam monitors and the associated readout electronics).

Other systems—such as the ion source, a radio-frequency quadrupole (RFQ), radio-frequency cavities for accelerating the beam (originally from the Princeton-Penn Accelerator [PPA]), modulators, and associated power supplies—are also available. Although steering dipole magnets are not available, Fermilab has designs and fabrication capabilities that are quite adequate for producing magnets.

We found that many of the major linear-accelerator components also exist. These include the ion source—at Brookhaven National Laboratory (BNL), parts of the RFQ—at Lawrence Berkeley National Laboratory (LBNL), a 20-MeV drift-tube LINAC (DTL)—also at LBNL, a section of 100- to 200-MeV DTL—at Fermilab, and various designs for additional components—at Fermilab.

Our analysis showed that these components could be assembled into an accelerator capable of providing a beam of 20-GeV protons with intensities of 1011 protons per pulse, for 10 pulses of 20-ns duration that are spaced 250 ns apart. As required, this particular accelerator could be upgraded (1) in energy to 50 GeV, (2) in intensity, and (3) in the number of lines-of-sight for radiography. The accelerator's duty cycle would be 1 min.

We conclude that such a demonstration experiment, located at NTS, would have an estimated project cost of $167M. Construction could be completed in a 3-year time frame, assuming that construction is the time-limiting factor (not project management decision milestones, as would likely be the case). This facility would provide a radiography capability for the national hydrotest program and would be relevant to the Stockpile Stewardship Program.

The Fundamental Nucleon–Nucleon Interaction: Probing Exotic Nuclear Structure using GEANIE at LANSCE/WNR

L. A. Bernstein, J. A. Becker, P. E. Garrett, K. Hauschild, C. A. McGrath, D. P. McNabb, E. Tavukcu

98-LW-051

We have been using the Germanium Array for Neutron Induced Excitations (GEANIE) spectrometer at the Los Alamos Neutron Science Center/Weapons Neutron Research (LANSCE/WNR) to study the structure of neutron-deficient nuclei from ^{80}Zr to ^{100}Sn using the techniques of gamma-ray spectroscopy.

Our initial goal was to study exotic nuclei that are at the limits of being bound with respect to spontaneous proton emission. However, the most interesting result has been the plethora of data for exotic nuclear reactions. The ^{92}Mo and ^{112}Sn data sets yielded a wealth of information regarding reaction dynamics in more than a dozen nuclei each (see figure). These data have provided the most rigorous test to date of neutron-induced nuclear-reaction modeling over this wide (1 to 250 MeV) energy range.

During FY1999, we compared our experimental data from the ^{92}Mo and ^{112}Sn experiments to calculations from two state-of-the-art reaction models: HMS-ALICE and GNASH. Although the models succeeded in reproducing some aspects of the data, we observed several notable discrepancies.

Our ^{92}Mo data suggest an incorrect treatment of (n,n'γ) over the entire range of excitation energies. This is a particularly surprising result because naively one would assume that the (n,n'γ) reaction, which yields the same initial and final nucleus, would be the one best understood. One possible interpretation for this deviation is a simplistic treatment of the nuclear structure effects in the compound system. However, another interpretation is that the shape of the nucleus is incorrectly treated. Furthermore, there is a systematic failure of the models to accurately predict the cross sections of negative parity states in any of the reaction products.

In addition to the deviation between experiment and theory for the (n,n'γ) reaction, there is a systematic failure of both models to predict the (n,αxnγ) reactions that lead to neutron-deficient Zr nuclei. These reactions are of particular concern because they are important to stellar nucleosynthesis via the s-process (slow neutron capture near the line of stability). The ^{112}Sn data also show regions of disagreement with the model codes. In particular, the lighter Sn and Cd isotopes are produced far less strongly than predicted.

At the end of FY1999, we were preparing these results for discussion at the October 1999 Division of Nuclear Physics Meeting of the American Physical Society; they will also be the subjects of two journal papers.

In addition to the studies of nuclear reactions, we undertook a systematic study of nuclear structure in ^{92}Mo. We assigned on the order of a dozen new levels to ^{92}Mo and observed gamma rays depopulating isomeric states. Finally, a follow-up experiment on our FY1998 study of reaction dynamics in ^{196}Pt produced a similar amount of new structure information. At the close of FY1999, we were also preparing an article on both of these studies.

Nuclei formed following neutron-induced reactions on ^{92}Mo (left) and ^{112}Sn (right) targets. Reaction products observed in-beam are in gray. The arrows indicate nuclei observed following β^{+} and electron-capture decay. Black corners indicate stable nuclei.
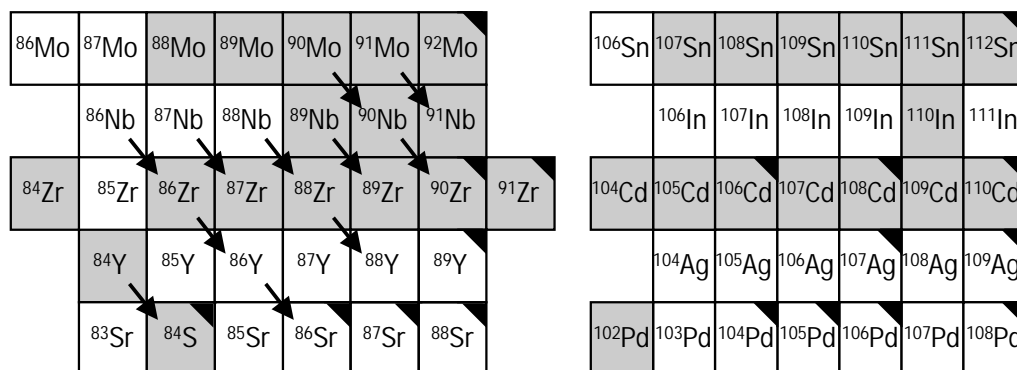
Laboratory Simulations of Accretion-Powered X-Ray Sources

M. E. Foord

99-ERD-044

Accretion—the dominant energy-conversion process in the universe—involves the flow of material down the deep, gravitational potential well of a massive compact object, such as a neutron star or black hole. The potential energy is converted into thermal radiant energy. Because the radiation is generated in a compact region, its temperature can be tens of millions of degrees.

This scenario describes a class of objects known as accretion-powered x-ray sources. In our Milky Way galaxy, the most important examples of accretion-powered objects are x-ray binaries and cataclysmic variables, in which material from a normal star is captured by the gravitational field of a closely orbiting compact star, neutron star, or white dwarf. On a vastly larger scale, active galactic nuclei are powered by the accretion of material onto a supermassive black hole, where the source of material is the host galaxy itself.

The goal of this project is to experimentally validate models that are used to interpret emission spectra from accretion-powered x-ray sources. With the upcoming launch of three major x-ray observatories, the astrophysics community is about to take a dramatic step towards understanding these x-ray sources. The new satellites—Chandra (NASA), the X-Ray Multi-Mirror Mission (European Space Agency) and Astro-E (Japanese Space Agency)—will, for the first time, observe x-ray sources with sufficiently high spectral resolution to uncover details of the physical processes underlying these objects. However, current photoionization and spectral-synthesis models used for interpreting such x-ray spectra are still being developed and are untested in the laboratory. Thus, our major objective is to provide the first benchmark data for validating and improving these models.

The Z-pinch facility at Sandia National Laboratories provides an ideal source of x rays for simulating the effects of accretion on astrophysical plasmas. During FY1999, we undertook initial experiments to (1) measure absolute x-ray fluxes from the Z-pinch, and (2) determine the degree of ionization in a low-density Fe sample positioned a few millimeters away from the source. For these initial plasma characterization and emission experiments, we developed a Johann x-ray spectrometer to cover the energy range of the L-shell Fe spectrum. Absorption spectra, sensitive to the charge-state distribution of the sample, were obtained by backlighting samples with the pinch emission. Emission measurements were obtained from a second sample positioned to the side of the pinch. Sandia's instrumentation was used to characterize the pinch emission. Our test setup is shown in the figure.

Our initial results indicate that the radiation pulse from the Z-pinch ionizes the Fe sample well into the L-shell. At year's end, we were comparing our results to predictions from various astrophysical codes developed by different groups from around the world. Such comparisons should help improve these codes at a critical time when new discoveries concerning high-energy processes in the Universe are about to unfold. Our initial results were presented at the Atomic Data Needs for X-ray Astronomy Workshop at Goddard and have received widespread publicity due to their relevance to the recent Chandra launch, (*Science*, December 10, 1999; *Popular Science*, March 2000).

During the next year, we will continue with experiments designed to measure the sample density using back-light imaging. We are also planning to measure—as an electron-temperature diagnostic—the recombination emission continuum and line emission from dopants in the samples. Finally, as results from the satellites become available, we will have the unique opportunity to compare the overall spectral properties of an x-ray-photoionized plasma with spectra from cosmic x-ray sources.
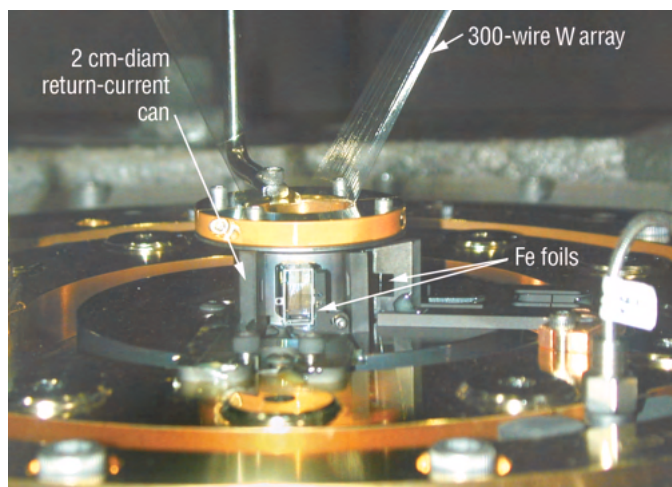
Foils containing 200-Å layers of Fe are radiated by the x-ray emission from the Sandia Z-pinch, simulating photoionized plasmas found near accretion-powered objects.

Upgrade of the Large-Scale, Dark-Matter Axion Search

C. Hagmann, D. Kinion, W. Stoeffl, K. van Bibber

99-ERD-045

Relic axions produced in the Big Bang are a promising candidate for the dark matter in the universe. If axions exist, they would be a major constituent of the dark halo within and around our galaxy. Although very weakly interacting with ordinary matter, axions can theoretically be detected by their conversion into photons in a cavity permeated by a strong magnetic field.

A search experiment at LLNL has been scanning for an axion signal for several years. The apparatus used in this search has three basic building blocks (1) a 200-L, low-loss tunable microwave cavity; (2) a superconducting (80-kG) magnet; and (3) a low-noise microwave receiver coupled to the cavity. Both the cavity and the front-end transistor amplifier are cooled to 1.5 K by pumped liquid helium, while the magnet is held at 4.2 K. The experimental signature of the axion would be a narrow peak (with a width ~1 kHz) at the frequency $f = m_a c^2 / h$, where c is the speed of light, h is Planck's constant, and m_a is the axion mass. Unfortunately, the axion mass—and hence the signal frequency—is poorly constrained, thus requiring a repetitive and time-consuming frequency tuning and averaging process. This equipment has been used to search for axions in the 550- to 810-MHz band, without success—thereby ruling out one of two major axion models [the Kim-Shifman-Vainshtein-Zakharov (KSVZ) axion] in the mass range 2.3 to 3.3 μeV. However, the signal could lurk anywhere between about 100 MHz and many GHz, and be somewhat weaker than what is now detectable.

Our goal in this project has been to maximize the likelihood of finding the axion by increasing the sensitivity of the search and the scanning speed by lowering the present system noise temperature by an order of magnitude.

To this effect, our collaborators at the University of California, Berkeley (UCB), have designed and demonstrated a superconducting quantum interference device (SQUID), shown in the figure, for use as a low-noise radio-frequency amplifier. SQUID uses a resonant strip-line coil input, thereby increasing its frequency range to over 1 GHz. The amplifier frequency of the SQUID is determined by the strip-line length and is chosen prior to manufacture. A voltage-controlled capacitor in parallel with the strip line is used for additional, in-situ fine tuning of the amplifier. The noise temperature of the SQUID drops linearly with the physical temperature—at least down to 0.1 K, where hot-electron effects in the resistive shunts cause the electron temperature to level off. To date, the best system noise temperature measured at UCB is 0.12 K at a frequency of 440 MHz—at a physical temperature of 0.5 K. This already represents a factor of about ten improvement over conventional transistor amplifiers.

In parallel, we redesigned the existing experimental apparatus at LLNL in preparation for the upgrade. First, this includes a superconducting bucking coil to create a low magnetic-field region (a volume of a few liters) for housing the SQUID and associated hardware. Second, the cryogenic hardware requires substantial modification for accommodating a commercial dilution refrigerator for cooling both SQUID and cavities to 100 mK.

In FY1999, we also commissioned a new microwave cavity array consisting of a pack of four identical cavities of about 35-L volume. Their resonance frequencies are higher because of their smaller size, and they will be used for axion searches in the 800- to 2000-MHz band. Each cavity has a single (metal or ceramic) tuning rod, which is moved by a piezo-electric motor. During data taking, all four cavities are kept ganged together at the same frequency, effectively acting as a single cavity with four times the volume.
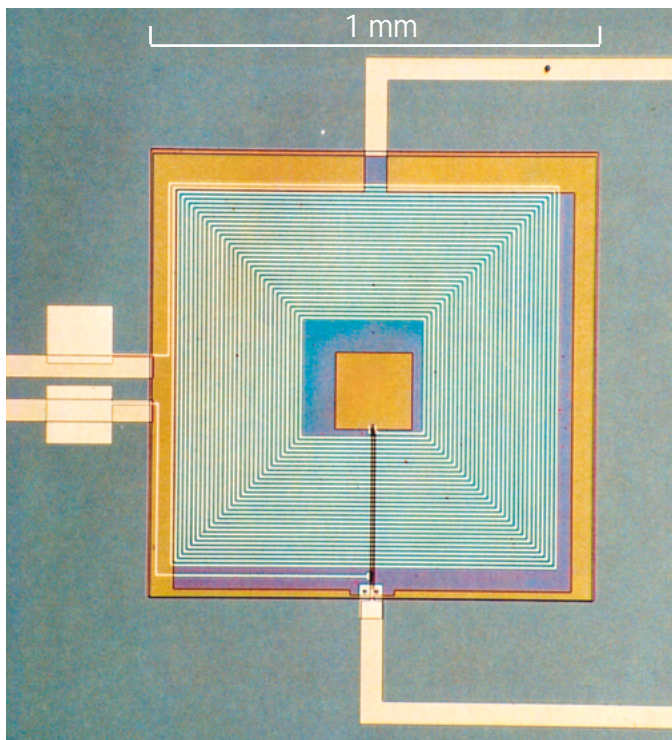
The thin-film superconducting quantum interface device (SQUID) amplifier designed at the University of California, Berkeley, for LLNL's axion-search experiment. The two input leads on the left are connected to the multiturn primary coil. Underneath it, and separated by an insulating layer, is the single-turn secondary coil and two Josephson junctions.

100-Gbar Shock Heating with 100-TW JanUSP

*P. T. Springer, P. A. Patel, D. F. Price, S. C. Wilks*

99-ERD-049

The focus of the project is to determine if short pulse laser technologies can produce 100-Gbar shocks in the laboratory, which could heat targets to energy densities rivaling those produced in stars and nuclear weapons and allow experiments to test their radiative models with direct measurements. While such shocks are 1,000 to 10,000 times stronger than those produced by radiative ablation on the world's largest lasers or by gas guns, they are predicted to be produced by the pondermotive pressure of a 10^{21} W/cm^2 focal intensity laser interacting with solid density targets. Experiments are conducted to test this possibility using the world's brightest laser, the 200-TW JanUSP (Janus ultra-short pulse) laser, which operates at focal intensities above 10^{21} W/cm^2. Methods for prepulse control sufficient to allow the creation of 100-Gbar shocks are being implemented. Understanding conditions at 10^{21} W/cm^2 offers significant challenges in both science and technology. This LDRD project (1) explores the high intensity laser matter interaction in new regimes, (2) addresses the science of high field laser atom interaction, and (3) tests weapons plasma radiative models and ion stopping models with direct measurements. The project also offers significant advancements in science and technology of interest to other Laboratory research relevant to national security.

In FY1999, we demonstrated 200-TW operation of JanUSP at focal intensities of 2×10^{21} W/cm^2, producing the world's brightest laser. This key milestone was accomplished using large aperture Ti:sapphire crystals, pumped by a 150-J beam from the Janus laser, then compressing and focusing the 15-J, 75-fs beam to near the diffraction-limited performance. The laser was characterized for power and focal spot size. In FY1999, we took initial steps to reduce the level of the amplified spontaneous emission to 10^{-7}. This will be further reduced to the 10^{-11} level using either saturable absorber technologies or laser frequency doubling. We conducted 2-D particle-in-cell (PIC) simulation of target experiments. Initial experiments characterize the laser matter coupling using photonuclear activation of gold, proving the laser field was of sufficient intensity to produce 20-MeV gamma rays through the electrons accelerated in the intense field. We applied a simultaneous measurement of the plasma density using Doppler techniques to test the PIC predictions for target coupling and the resulting electron spectrum. We implemented diagnostics to investigate the production and heating with ion shocks, including an ion time-of-flight spectrometer and a 500-fs resolution streaked x-ray spectrometer. Target energetic experiments and heating range experiments will use Doppler shifts of line radiation from the emitted plasma and ion time of flight spectroscopy to characterize ion heating and stopping powers in plasma.

In FY2000, we plan to continue exploring the physics and applications of 100-Gbar ion shock generation. Laser prepulse will be reduced to the 10^{-11} level to permit the high intensity laser interaction with solid targets. This should greatly increase the thermal plasma energy densities, while suppressing the harmful effects of hot electrons on the plasma equilibrium. We will complete target energetics and heating range experiments, which were begun in FY1999, with the highest contrast pulses. Experimental focus will then shift to ion energetics optimization and studies of thermalization in targets. X-ray spectral measurements will determine the brightness temperature and the degree of ionization in high-Z targets.
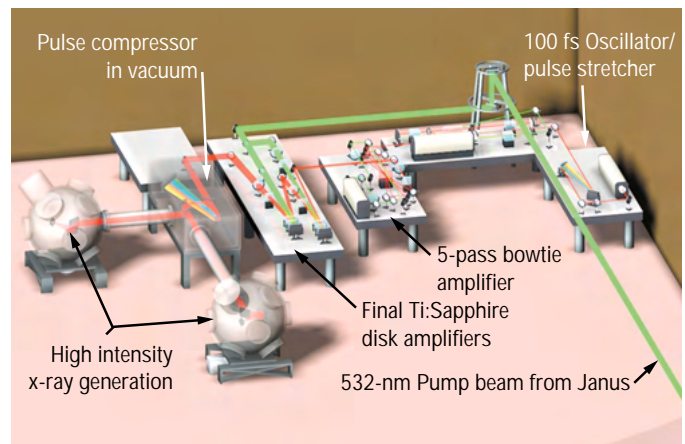
In FY1999, the 200-TW JanUSP, the world's brightest laser, attained focal intensities of 10^{21} W/cm^2 at 10 J.

Science and Applications of Low-Emittance Electron Beams

K. van Bibber, D. Ball, E. Cook, J. Elmer, J. Gronberg, J. Hill, J. Klingmann, G. Le Sage, C. Landram, B. Merritt
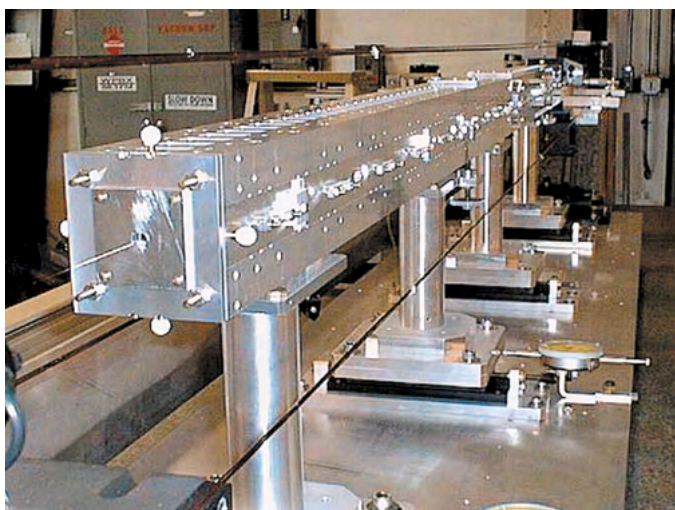
99-ERD-055

The capability of making very low-emittance electron beams of temporally short, high charge bunches has opened exciting new possibilities in basic and applied science. Progress in creating and accelerating ultra-low emittance electron beams is central to the future of accelerator physics. Two proposed applications driving an intense worldwide R&D effort are a TeV electron-positron linear collider, and a linac-driven free-electron laser (FEL) as a fourth-generation synchrotron light source. In addition, high-energy accelerators have become a cornerstone of the nuclear weapons stockpile stewardship effort.

In collaboration with the Stanford Linear Accelerator Center (SLAC) and the Japanese High Energy Accelerator Research Organization (KEK), we prototyped and tested an X-band (11.4 GHz) linear collider accelerator structure. The principal challenge for a real linear collider is to find a fabrication strategy that (1) ensures the required micron-level tolerances and (2) can be mass-produced economically. LLNL developed the procedure for precision machining of the copper accelerating cells for this structure, 206 in total, complex in shape and all different in critical dimensions. Over the 10 km that the electrons (and positrons) will be accelerated, irregularities in machining or alignment would lead to beam blow-up, and preclude its being squeezed down to the few nanometers spot size needed

to achieve design luminosity. The goal of this work was to demonstrate a successful prototype, then compare the measured and calculated wakefields with beam at the SLAC linac.

The experiment was carried out by shooting a high-energy electron bunch through the accelerator structure, launched deliberately off-axis to excite the transverse wakefield. This leader bunch is then followed by an on-axis witness bunch at a variable time-delay. By noting the sideward deflection of the second bunch, we measured the wakefield as a function of delay time. The measured and calculated wakefields were in good agreement most everywhere in time, with discrepancies corresponding to known out-of-tolerance features for a small group of cells. The structure was also shown to work as its own beam-position monitor. By measuring the power and frequency of the transverse mode coupled out by quadrant damping manifolds, we measured the cell-to-cell deviation of the structure from absolute straightness. They agreed in absolute value with those from a coordinate measuring machine at the micron level, all along the length of the structure.

In this LDRD project, we also designed a precision permanent-magnet undulator for a test of the underlying physics of linac-driven FELs. Electron bunches of sufficiently small emittance open up the possibility of an entirely new regime of FEL operation, self-amplified spontaneous emission (SASE). This prototype, shown in the figure, will be tested with 70-MeV electrons at Brookhaven National Laboratory (BNL) in FY2000, producing first-harmonic SASE light at 800 nm. We expect to observe, for the first time ever, saturation of the gain curve for SASE radiation. This experiment is a collaboration of LLNL, SLAC, Los Alamos National Laboratory, the University of California at Los Angeles, and BNL. Should this experiment prove successful, it could lead to a major demonstration project utilizing 15-GeV electrons from the SLAC linac and a 100-m-long undulator. Such a facility could produce fully coherent 1.5-Å x-rays 10 billion times brighter than current third-generation synchrotron light sources, such as the Advanced Photon Source at Argonne National Laboratory. This would open the possibility of single-shot holography of proteins and time-resolved studies of chemical reactions and phase changes of materials at the femtosecond level.

A prototype permanent-magnet undulator to be tested at the Brookhaven 70-MeV Accelerator Test Facility.

Gamma Watermark: A New Means of Tagging Valuable Objects

M. Y. Ishikawa, L. L. Wood, K. J. Moody, R. W. Lougheed, W. E. Parker, T. F. Wang

Law enforcement officials have long searched for a way to solve the frequently vexing problems of determining the rightful ownership of everything from paintings to computer software to combating increasingly sophisticated counterfeiters. Because of its low cost, miniscule size, ease of use, and safety, the Gamma Watermark represents a significant advance over commercially available means of watermarking, such as digital, paper, and embedded-silicon-chip technologies. It is expected to establish indisputable links between owners and their property.

Such a very low-level gamma-ray emitting tag is made possible by the exquisite single-photon sensitivity and very high-energy resolution of modern, commercial gamma-ray detectors, which can record a single nuclear beta decay with high efficiency and precision. The amount of radioactivity required to continuously express a unique digital signature that can be quickly read out using this instrumentation is about 1 nCi.

In an initial feasibility study ("Gamma Watermark," 99-FS-001), we determined the feasibility of a gamma watermark that would contain a very small fraction (1/1000) of the radioactivity of a typical smoke detector. Our goal in the present project was to develop and demonstrate a microscopic-scale, very low-level (i.e., nCi) gamma-ray-emitting tag consisting of a unique, precisely metered combination of radioisotopes with appropriately long half-lives. None of these isotopes would occur naturally (at nCi levels) in the object to be tagged.

Special features of our Gamma Watermark include its near-microscopic size and its very low-level radiation emission. These attributes effectively preclude its being swept from the tagged object by instrument-supported inspection of the object, even if ordinary gamma-ray detectors (e.g., scintillation counters) are employed. Because each radioisotope emits gamma rays in a different wavelength, different combinations of radioisotopes in different ratios produces a gamma-ray signature equivalent to an electronic bar code.

In addition to the unique gamma-ray signature, the watermark contains a built-in "clock" that provides a date stamp of its creation. This clock is initially set to a 1:1 ratio of the intensities of two radioisotopes of different half-lives. The observed ratio of these two isotope intensities indicates how much time has elapsed since the watermark's creation. The usual lifespan of a Gamma Watermark is anticipated to be a few decades, although a mixture of radioisotopes could be selected that would last for centuries.

During FY1999, our prototype "bead format" tags demonstrated both sweep-resistance and unique signature recovery(see fig.); they have been tested on CD-ROMS and museum-provided test specimens. A Record of Invention, Provisional Patent Application, and final Patent Application have been filed for this work.

We developed a different application of the Gamma Watermark during FY1999—that of a watermark token generated directly by an ink-jet printer. The development of the ink-jet-produced token makes possible the mass production of uniform Gamma Watermarks at exceedingly low unit cost. This development is potentially of great importance—our Gamma Watermark tokens avoid the limitations of commercially available tagging methods, while fulfilling the needs of national security, law enforcement, museums, paper instruments-of-value, and other applications.

In July 1999, the Gamma Watermark won a prestigious *R&D 100 Award* as one of the 100 most technologically significant new products of 1999.

The miniscule Gamma Watermark can be applied to a bead that is then deposited on or inside an object. Here, such beads have been circled in red and are shown on a dime for scale.

Gamma Watermark

M. Y. Ishikawa, L. L. Wood, R. W. Lougheed

99-FS-001

The purpose of this Gamma Watermark feasibility study was to examine the possibility of creating a microscopic scale, very low-level, i.e., nanocurie (nCi), gamma-ray emitting "barcode" (or watermark) comprised of a unique combination of appropriately long half-life radioisotopes—none of which occurs naturally at nCi levels in the object to be tagged. The ratios of the amounts of radioisotopes selected to comprise any given tag could be made to be unique, at least among the class of objects ever to be tagged this way. Other special features of the Gamma Watermark include its near-microscopic physical size and its very low-level radiation emission. This new type of watermark could represent a radical departure from the industry-standard approaches and, if successful, would introduce a novel new technology into everyday use.

Early on, it became clear that the potential applications of gamma watermarking included (1) establishing provenance for highly valued art objects, (2) documenting site-of-origin of archaeological and paleontological materials for paleoenvironmental and paleoecological data, (3) validating paper instruments of value, and (4) performing national security-specific tasks. The final stage of the project aimed to develop and demonstrate gamma watermarking with prototype tags used with real high-value objects, including sweep-resistance and unique signature recovery. In September 1998, a Record of Invention (LLNL File No. IL-10391, 9/9/98) was filed on the Gamma Watermark by the LLNL Patent Office.

This feasibility study utilized theory, computation, and experiment to explore fundamental issues encompassing the Gamma Watermark concept.

Emphasis was placed on computational Monte Carlo-based simulations of detector/signal response for a generic Gamma Watermark barcode, utilizing experimental data obtained in the laboratory and using a high-efficiency, high-purity crystalline germanium detector. The computationally simulated cases of the Gamma Watermark were based on a cocktail of two "keying" radioisotopes in nCi quantities at 1- and 10-year checkpoints. The background radiation levels used in these simulations were supplied by laboratory measurements on what were considered potentially worst case background radioactivity levels. Because the resulting analyses were promising, it appears that the Gamma Watermark, as proposed, works and could be useful for decades.

We calibrated suitable solutions of radionuclides in the laboratory for later use in Gamma Watermark barcodes. We also examined in detail the amount of information that could be actually stored in a practical manner within a watermark signature of this kind. We also investigated different deployment methodologies for the Gamma Watermark (e.g., bead-based, ink-jet so-called tokens, etc.).

Based on the results of this feasibility study, the Gamma Watermark effort was continued as an exploratory research LDRD project (99-ERD-070). In 1999, the Gamma Watermark was awarded a *1999 R&D 100 Award* by *R&D Magazine* as one of the 100 most technologically significant products in the world to come to fruition that year. Please refer to the previous page in this *FY1999 LDRD Annual Report* ("Gamma Watermark: a New Means of Tagging Valuable Objects") for a more detailed discussion of the results for the Gamma Watermarking ERD project.

Monte Carlo Simulations for Mine Detection

A. Toor, A. Marchetti

In 1998, LLNL arranged for the testing and evaluation of Russian-developed technology for detecting antitank mines at the Buried Objects Detection Facility (BODF) located at the Nevada Test Site (NTS). BODF is a 30-acre facility with about 300 live antitank mines, each containing 6 to 12 kg of high explosive (HE). The mines are buried at depths up to 15 cm. The Russian system scored higher than any other technology tested to date. Our goal was to conduct Monte Carlo (MC) simulations to (1) gain better understanding of the Russian system, and (2) determine if improved sensors and algorithms could be scaled to detect antipersonnel mines containing 30 g of HE.

The Russian system combines information from two separate sensors. One sensor detects anomalous concentrations of hydrogen in a rapid process based on neutron scattering—a handheld instrument can scan a large area at 4 to 5 m^2/min. Once the hydrogen anomalies have been located, a second sensor measures the thermal-neutron-excited gamma-ray spectrum to determine whether that location also contains high concentrations of nitrogen. The second process is slower; each locations requires 3 to 5 min. Information from both sensors is then used to determine if the anomaly is a buried antitank mine.

During FY1999, we conducted 3-D MC simulations of the Russian system using COG and TART (developed at LLNL) and MCNP [developed at Los Alamos National Laboratory (LANL)]. The simulations included the soil composition and the geometry and response functions for the neutron source and sensors used in the field tests. All codes gave essentially the same results.

For hydrogen detection, we calculated signals for typical antitank mines buried 2.5- to 10-cm deep. When we compared the detected neutrons backscattered from the soil with the signal from a mine containing 5 kg of TNT (20-cm diam, 10-cm high) buried 2.5-cm deep, we found the signal-to-background ratio exceeded 2 throughout the thermal region of the spectrum; the fraction of neutrons scattered from the TNT reaching the detector was about 0.1%. This showed that the hydrogen concentration for 5 kg of TNT would be easily detected using this technique. Comparisons of our simulations with the field data were limited due to our lack of knowledge of the Russian pulse-forming circuits, neutron-energy thresholds, and integration time constants. Nevertheless, the simulations were in qualitative agreement with the field data in that they predicted measurable signals for all the detected mines.

Our nitrogen-determination simulation used the same 5 kg of TNT antitank mine buried 10-cm deep. The gamma-ray detector (100 cm^2, 6-cm high) was displaced radially 15 cm from a shielded, ^{254}Cf neutron source (1×10^7 n/s). The detector and source were positioned 5 cm above the soil surface. Figure 1 compares the simulated gamma-ray spectra for the soil only [Fig. 1(a)] and the soil plus TNT [Fig. 1(b)]. These data assume 100% detection efficiency at all energies. The photon peak at 10.8 MeV corresponding to the (n,γ) reaction in nitrogen is clearly seen when the TNT is present. Although the signal is weak (9 counts per 20 million source neutrons) natural background in this spectral region is extremely low. With a detection efficiency of 1×10^{-2}, a statistically significant signal (3σ) would be obtained in about 3 min.

Our data indicate that successful scaling of the Russian mine-detection system to detect antipersonnel mines containing 30 g of high explosive is not practical. Because of the low signal-to-background ratio for backscattered neutrons, there would be many false positives arising from natural sources of hydrogen concentrations in the soil. Also, the (n,γ) signal from 30 g of TNT would be about 10 photons per 4 billion neutrons—necessitating many hours of integration time to obtain a statistically significant signal.
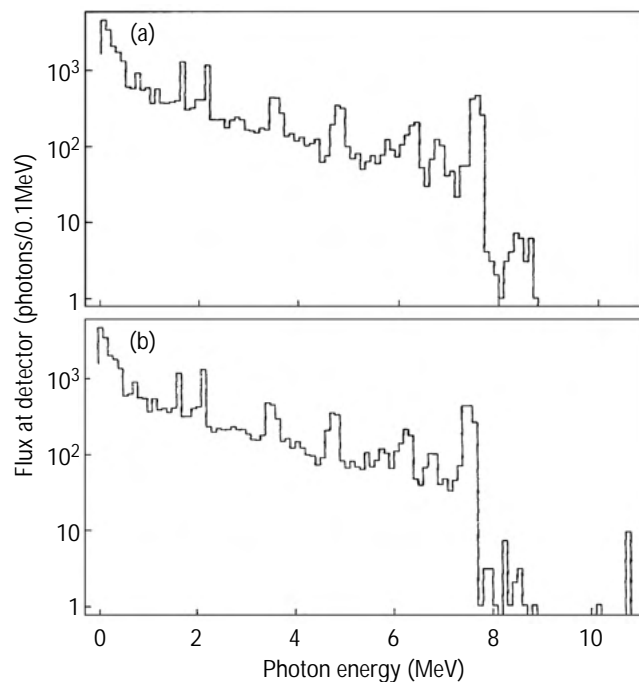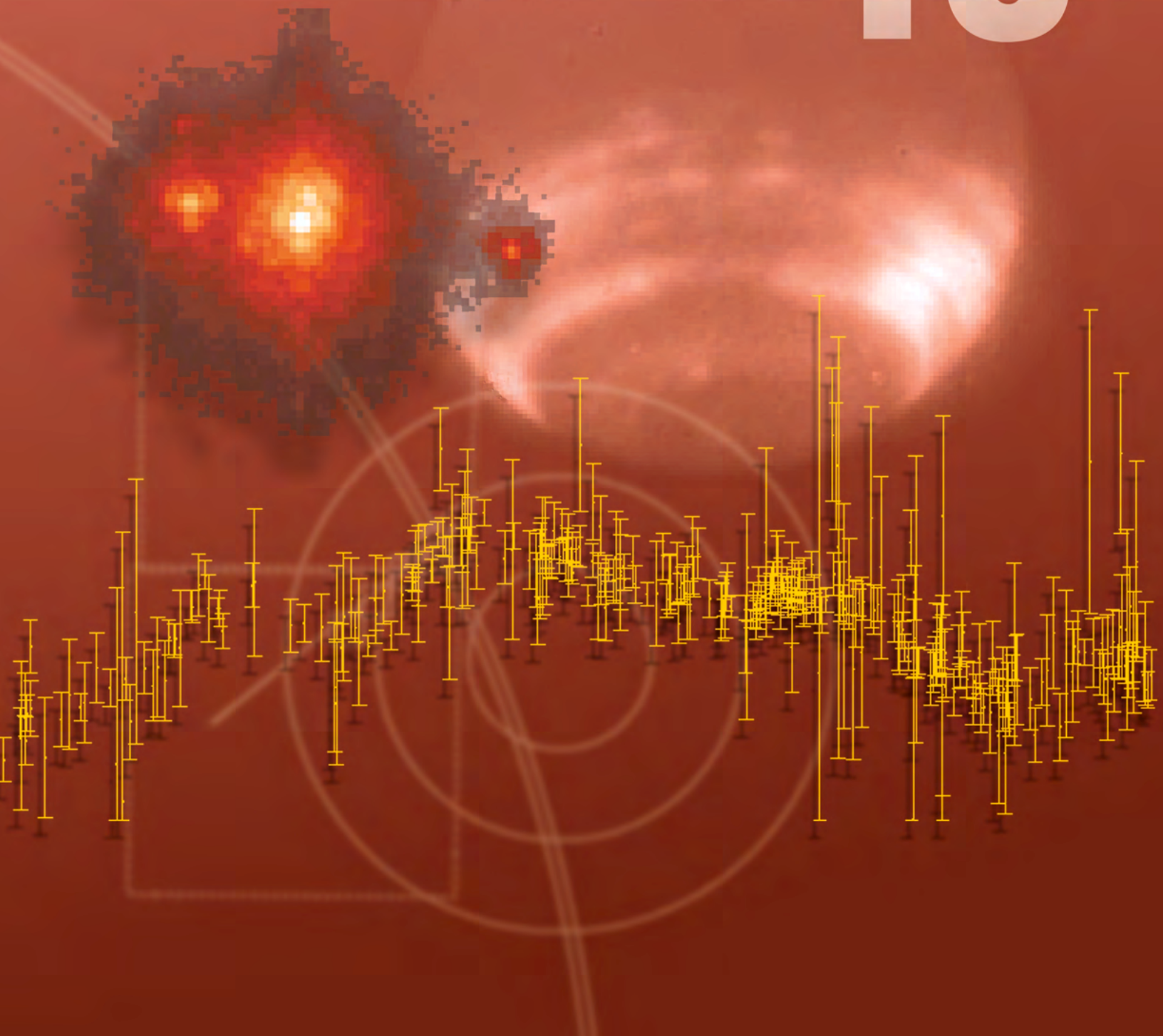

Figure 1. Monte Carlo simulations of (n,γ) spectrum (20 million neutron histories) run during evaluation of Russian-developed technology for the detection of buried mines, showing (a) soil only, and (b) soil plus 5 kg of TNT buried 15 cm below the surface. Photon peak at 10.8 MeV in (b) shows presence of TNT.

Space Science and Technology

10

Space Science and Technology

Laser Guide-Star-Based Astrophysics at Lick Observatory

C. Max, K. Avicola, J. Brase, H. Friedman, D. Gavel, S. Olivier, B. Macintosh

The resolution of ground-based telescopes is typically limited to about 1 arcsec because of the blurring effects of atmospheric turbulence. Adaptive optics (AO) technology senses and corrects for the optical distortions caused by turbulence hundreds of times per second, using high-speed sensors, computers, and deformable-mirror and laser technologies similar to those originally developed for the atomic vapor laser isotope separation (AVLIS) program.

The goal of this project has been to make AO systems widely useful astronomical tools that provide resolutions up to an order of magnitude better than current, ground-based telescopes.

In previous years, we designed, built, and tested our AO system and laser on the 3-m Shane Telescope at the University of California's (UC's) Lick Observatory. Our AO system contains a laser that can produce an artificial beacon for sensing and correcting the atmospheric turbulence in regions of the sky where natural guidestars are not available. In our system, a 20-W dye laser, mounted on the side of the Shane Telescope, produces the equivalent of a 9th-magnitude artificial guidestar at any direction the telescope points. The dye laser is tuned to the 589-nm resonant line of atomic sodium so that it causes the sodium in the Earth's mesospheric layer at a 90-km altitude to fluoresce. In engineering tests, we had shown excellent results using natural guidestars as dim as 12th magnitude; with AO correction, we were able to achieve the diffraction-limited resolution of the Shane Telescope at near-infrared (IR) wavelengths.

During FY1999, we improved the Shane Telescope's AO system so that it better accommodates routine science observations. We (1) incorporated a new IR science camera with higher sensitivity and spatial resolution; (2) modified the optical layout of the AO bench to allow wide-field observations where the natural guidestar (usually a bright, nearby star in our galaxy) is separated from the science object of interest (for example, an extragalactic object such as a quasar); and (3) upgraded the software interface and optical-bench automation so that the system can now be set up, calibrated, and operated by one person from a computer workstation.

We used this newly improved AO system for astronomical observations in a sequence of science programs feasible only with the high resolution provided by this instrument. A number of UC faculty and graduate-student observers participated in these dedicated science-observation runs. Astronomy projects included imaging newly-forming stars (see figure); searching for dim, binary-star companions; measuring the mass density of nearby galaxies; and imaging galaxies containing active nuclei.

To make the laser-guidestar system on the Shane Telescope a routinely usable instrument, in FY1999 we improved and tested a number of laser-subsystem components. In particular, we (1) improved procedures for aligning the pump lasers, making them more stable in power output; (2) installed temperature control in the laser room housing the master oscillator, which improved the wavelength stability of the oscillator; and (3) improved procedures and alignment of diagnostic systems in the laser beamline.

Most extragalactic astronomy—and even a large fraction of the study of galactic objects such as young stellar regions, nebular remains of supernovea, etc.—will benefit greatly by use of the laser guidestar because most targets are not near natural guidestars that are 12th magnitude or brighter. On the basis of our work at Lick, laser-guidestar systems have been installed on or are being planned for a number of other telescopes around the world, including the Keck 10-m telescope on Mauna Kea in Hawaii.
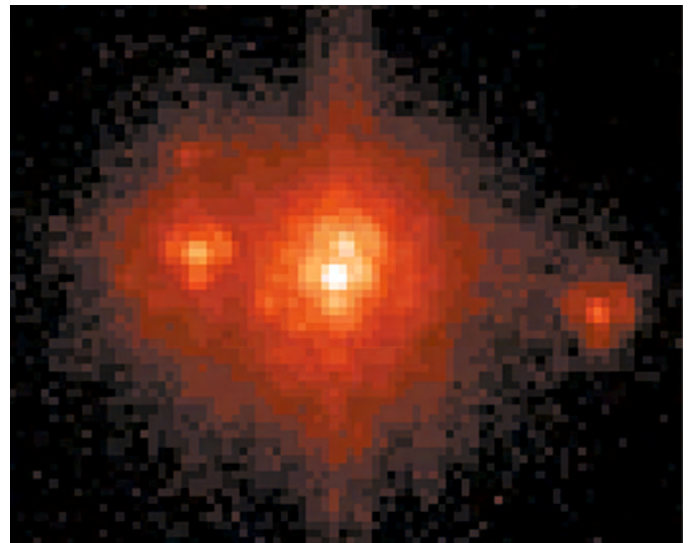
Adaptive optics (AO) image of LkHa 234, showing five stars in a young stellar system. Previous, non-AO observations identified this object only as a binary. Such multistar systems are usually dynamically unstable, so eventually several of these stars will be ejected from the system. The "ring" around each star is a characteristic of diffraction-limited resolution (the Airy ring). The bright "halo" is scattered light resulting from incomplete AO correction of the atmospheric turbulence.

A Comprehensive X-Ray Spectral Code for High-Energy Astrophysics

D. A. Liedahl, K. Fournier, C. W. Mauche

97-ERD-057

Hot cosmic plasmas cool by emitting x rays. When plasma temperatures exceed about one million Kelvin, highly ionized species of several elements radiate in a set of discrete spectral lines over the 1- to 200-Å range. The wavelength distribution of this radiation can be used to infer temperatures, densities, velocities, and chemical compositions of the emitting plasmas—information that can then be used to constrain models of the structure of the sources being studied.

X-ray spectroscopy is about to become a major focus of astrophysical research. Launches of three major "facility-class" observatories are scheduled for 2000: National Aeronautics and Space Administration's (NASA's) Chandra X-ray Observatory, the European Space Agency's (ESA's) X-Ray Multi-Mirror Mission (XMM), and Astro-E, a joint Japan–U.S. project. Instruments aboard these spacecraft will achieve order-of-magnitude improvements in spectral resolving power. With projected lifetimes of up to ten years, these missions are expected to return data of very high quality from hundreds of celestial targets.

The aim of this project has been to develop a spectral-analysis tool with a level of quality commensurate to that expected in the data. Our project has had three primary tasks: (1) generation of the bulk of the atomic database using LLNL's computer codes, (2) compilation, critical assessment, and incorporation of atomic data that cannot be generated at LLNL in a timely manner, and (3) design of a user interface that will allow rapid access to and manipulation of the database. Our overall package is called the Livermore X-Ray Spectral Synthesizer (LXSS).

The essentials of the first two tasks were completed during the first two years of this project. The database was generated using the HULLAC (Hebrew University–Lawrence Livermore Atomic Code) suite. Atomic data, which include structure calculations, radiative transition rates, and electron–ion collisional excitation rate coefficients, were stored in FITS (Flexible Image Transport System) format, for easy interface with fitting packages provided by NASA centers. We wrote several "pipeline processing" codes in interactive data language (IDL) to facilitate uniform data conversion and storage. During FY1999, an extensive IDL graphical user interface—which will allow access to a number of simulation and display functions—and a database query function became operational. At year's end, we were addressing the issue of benchmarking through close collaboration with LLNL's electron beam ion trap (EBIT) team, with various tokamak groups in the U.S. and Italy, and with an LLNL–Sandia project at Sandia National Laboratory's (SNL's) Z-machine.

Members of our team are re-analyzing spectroscopic data from the Advanced Satellite for Cosmology and Astrophysics (ASCA), using the more sophisticated spectral models being developed for LXSS. Our focus has been on the study of two massive X-ray binary systems, Vela X-1 and Centaurus X-3. We have provided compelling evidence that x-ray irradiated stellar winds may be fundamentally inhomogeneous, and have shown that, surprisingly, the wind velocity and density profiles appear to be little affected by x-ray irradiation.

We have been funded to participate in the Chandra Emission Line Project, a unique spectroscopic survey of three hot stellar coronae. LXSS spectral models are now being used to help analyze Chandra "first-light" spectra from the binary star system Capella. Continuum and line-opacity models included in LXSS are being used in the interpretation of the Chandra absorption-line spectrum from the Seyfert 1 galaxy NGC 5548. For the near future, based largely upon the strength of our modeling capabilities, we have been awarded Guest Observerships on Chandra, XMM, and Astro-E, and we are participants in the XMM Guaranteed Time program. We foresee that the next few years will bring many opportunities to exercise the full capability of LXSS.

Asteroids and Comets: Completing the Inventory of the Solar System

C. R. Alcock

The observed frontier of the Solar System has progressed from only 10 AU when Kepler deduced his laws of planetary motion in the early 1600s (then, only six planets were known to orbit the Sun), to about 50 AU today, with the detections of solid objects in the region just outside the orbit of the planet Neptune. Progress is much more difficult beyond Neptune, because the objects are small, and the brightness in reflected sunlight declines as the inverse fourth power of distance. However, deep surveys using charge-coupled devices (CCDs) have revolutionized the study of this region. Exploiting their ability to search for moving objects much fainter than were visible in the earlier photographic surveys, astronomers have discovered over 200 trans-Neptunian objects (TNOs).

Imaging surveys can detect relatively large objects. The smallest seen to date is probably 50 km in diameter (this is an estimate based upon its brightness and an assumption about how much sunlight is scattered back into the inner solar system). On the other hand, the comets seen in the inner solar system are much smaller, typically a few kilometers in diameter. Such objects cannot be seen in the imaging surveys because they are much too faint. Even the largest telescopes in the world, at the Keck Observatory on Mauna Kea, Hawaii, do not have sufficient sensitivity to detect objects this small in the trans-Neptunian region.

An alternative way to detect small TNOs is to monitor bright stars and to detect the rare occultation of these stars by the objects in question. Using this technique, one can work with bright objects (the background stars), which are readily seen even with modest telescopes. However, there are great challenges to face; that is, the occultations (1) are expected to be rare (fewer than one per star-year with continuous monitoring), and (2) will be brief (less than 1 s long). One must therefore be very alert to the possibility of false positives—stars may blink out for a fraction of a second for a variety of prosaic reasons, including scattering of the starlight by atmospheric turbulence, or even obscuration by high-flying birds!

The purpose of this project was to design a system that could perform a survey for small TNO's. Our specific goal for FY1999 was to complete a specific design, establish a collaboration to perform the project, and select a site for the operation.

During FY1999, we completed the design of a system that we believe will make the measurements needed for this purpose, while controlling the false positives. The system will comprise three small (50-cm aperture) astronomical telescopes, which will image the same star field simultaneously. The data will be collected with CCD cameras, which will be operated in an innovative mode that we invented for this purpose. Data will be processed at the telescopes; automated processes will make the occultation detections and log the results.

The possibility of false positives will be controlled by requiring simultaneous detection at all three telescopes. The telescopes will initially be located meters apart; the separation can be increased to kilometers if this proves desirable. We anticipate that false positives will be eliminated by this operation.

In FY1999, we entered into a collaboration with scientists at the University of California, Berkeley; at the National Aeronautics and Space Administration (NASA) Ames Research Center; and also at two institutions in Taiwan—the Institute of Astronomy and Astrophysics and the National Central University. Our Taiwanese collaborators will shoulder two thirds of the capital costs for the survey; more significantly, they have accepted full responsibility for the site and operation of the facility. This is a great saving in cost and effort to LLNL.
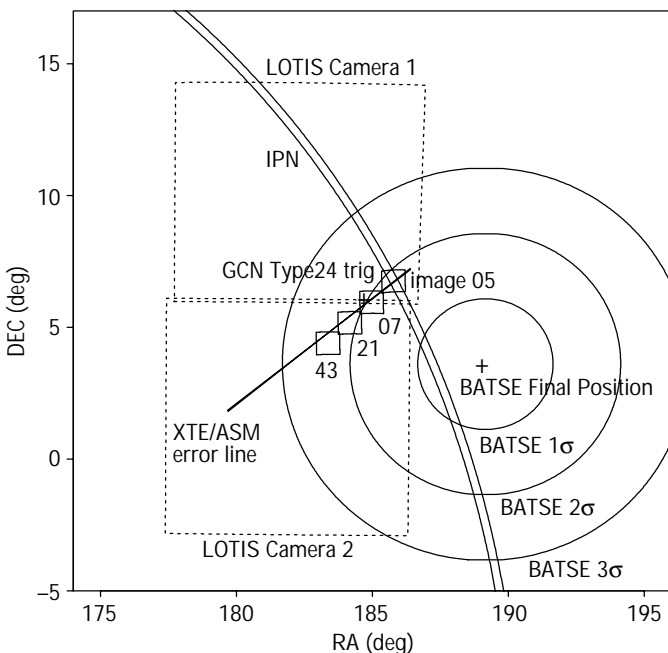
We expect the survey system will be installed in Taiwan in the middle of calendar year 2000.

A Search for Simultaneous Optical Counterparts of Gamma-Ray Bursts

H. S. Park, R. A. Porrata, R. M. Bionta, G. G. Williams

97-LW-019

Gamma-ray bursts (GRBs)—brief bursts of gamma-ray radiation that appear randomly in the sky—remain among the least understood of all observed astronomical phenomena. GRBs are difficult to study because of their short duration (from 1 to ~1000 s) and the poor angular resolution of gamma-ray detectors (a 1s error of 1 to 10 deg). During the last two years, nearly 30 years after the discovery of GRBs, optical afterglows have been observed for a dozen bursts. Follow-up, ground-based observations finally determined that GRBs are at significant cosmological distances. Some GRB parameters such as energy, ambient environment, and dynamics have been obtained from the optical and radio follow-up observations. However, the nature of the GRB progenitors is still poorly understood. On January 23, 1999, one GRB (GRB990123) was detected by a group in New Mexico with a prompt optical signal. However, this observation was inconsistent with the brightness and spectrum of the later-time afterglows. We will need more such observations to understand the physical process of GRB progenitors.

The goal of this project has been to measure optical emissions while GRBs are still emitting gamma-rays, thereby gaining insight into the processes that produce the GRBs.

To measure simultaneous optical signals from GRBs, we constructed the Livermore Optical Transient Imaging System (LOTIS) at LLNL's Site 300. Our collaborators included NASA; Clemson University, South Carolina; California State University, Hayward; and the University of California. LOTIS is an unconventional and innovative automatic instrument that consists of a 2 by 2 array of wide-field-of-view (17.6- by 17.6-deg) telescopes that can respond to real-time GRB triggers within about 10 s. LOTIS receives real-time GRB triggers from NASA's Goddard Space Flight Center over the Internet. While the GRBs are emitting gamma rays, LOTIS attempts to detect optical transients associated with the GRB. During FY1999, LOTIS accumulated over 3500 observing hours and recorded images for over 40 GRB events with response times of 6 to 15 s. Unlike data from the January 23 event mentioned above, our data show no prompt optical counterpart related to GRBs, down to the limiting sensitivity of our instrument.

The inconsistency between our observations and the GRB990123 constrains the gamma-ray burst model, particularly the relativistic blast-wave model parameters such as density of the surrounding medium and the Lorentz factor of the ejecta from the gamma-ray bursts. Our results, which constrain various GRB models, have been reported at conferences and published in refereed journals and in *Gamma-Ray Coordinate Network Circulars.*

In response to new NASA and European GRB satellite missions (HETE2, INTEGRAL, and SWIFT) we are refurbishing a 0.6-m telescope (Super-LOTIS) capable of responding to satellite-initiated GRB coordinate triggers within 30 s at about 19-mV levels. In FY1999, we concentrated on constructing this telescope and automating the data-acquisition process. The tasks included motorizing the mount, designing and constructing optical elements that correct for color aberration, installing a charge-coupled-device (CCD) camera, and writing on-line software to operate the system. First light was seen on February 25, 1999. Although Super-LOTIS is still located at an LLNL site that is not ideal, it has already responded to many GRB triggers (see figure). Super-LOTIS results have also been published and reported. We expect the system will improve its performance when we move it in early 2000 to its permanent, darker site at Kitt Peak National Observatory—being prepared by our NASA collaborators.

Livermore Optical Transient Imaging System (LOTIS) coverage of gamma-ray burst event GRB990308. The burst is most likely located in the overlapping region observed by three satellites: BATSE (circles represent 1 to ~3σ errors), IPN (shown as a long arc), and XTE/ASM (thin line in the middle). The big rectangular boxes represent the coverage by the LOTIS telescope at 132 s after the burst; the small boxes represent that by Super-LOTIS telescopes at 28 min. We searched for optical counterparts in the burst location (image 05 area) at these prompt times and detected no signal that constrains theoretical gamma-ray burst models.

Stellar Velocimetry with a Novel High Efficiency Interferometer

D. J. Erskine, J. Ge

98-ERD-054

One of the hottest topics in astronomy today is the search for planets outside our solar system by measuring the extremely small Doppler shifts on starlight created by the planet as it tugs the star during its orbit. Jupiter and Saturn-like planets would create 12 and 3 m/s velocity wobbles, respectively. The extra-solar planets discovered to date however have been very different from our own solar system, many as massive as Jupiter and yet orbiting many times closer. These have produced large velocity signatures of order 50 m/s. This begs the question: Is our solar system unique? In order to better answer this question, the current Doppler measuring instruments need to be improved to have finer velocity resolution (i.e., 1 m/s or better). The current instruments based on diffraction gratings have complicated instrument responses, which limit current Doppler velocity resolutions to ~3 m/s.

We have developed a new instrument called a fringing spectrometer, or spectrally dispersed interferometer. The Doppler shift is detected by change in phase of fringes created by an interferometer, whose visibility are enhanced by being splayed out in a spectrum by a low-resolution disperser. Because the interferometer has a mathematically simpler behavior than a grating, the velocity resolution is improved.

Previously, we developed prototype hardware and obtained initial fringing spectra. In FY1999, we (1) developed the software for extracting the phase of the fringes to yield velocities, (2) added hardware to improve system stability, (3) built a second-generation instrument optimized for telescope operation, and (4) developed optical fiber feeding systems for the FY2000 tests. At the end of FY1999, we successfully passed starlight from the nearby Leuschner 30-in. Telescope at the University of California, Berkeley into a thin optical fiber, which will soon lead to our fringing spectrometer.

Our novel hybrid approach combining interferometry and dispersive spectroscopy has enabled us to reach a new phase measurement precision of $1/20,000^{th}$ of a fringe, an order of magnitude improvement for interferogram analysis. This allowed us to break the 1 m/s barrier for the first time, compared to the current limit of about 3 m/s for grating instruments. The figure below shows a velocity repeatability test using a stationary bromine lamp, which simulates the stellar spectrum. The standard deviation in first 16 minutes is 0.76 m/s. Although the long-term drift is larger, it is already competitive with conventional instruments (comparison data on a planetless star by leading planet-finding astronomers Geoff Marcy and Paul Butler). This data was taken with the preliminary instrument prior to late FY1999 improvements. We expect these to improve long-term stability in FY2000 to the 1 m/s level.

This technique promises many benefits in other areas of spectroscopy and metrology. Our project will enhance LLNL's capabilities in advanced diagnostics essential to the Stockpile Stewardship Management Program and the nonproliferation effort. The mathematical tools we developed enabled more than 100 times faster extraction of velocities from spectra compared to current planet searches, using an instrument that is also inexpensive and compact. In FY2000, we will test our instrument on starlight at observatory telescopes to verify its abilities to detect smaller mass planets. In addition, the ~1 m/s resolution will be useful for measuring real time radial velocity oscillations of stellar photospheres analogous to the Sun's solar oscillations, which has been tried unsuccessfully by others. This can lead to better understanding of the internal structure of stars and help distinguish small mass planet tugging effects from photosphere behavior.
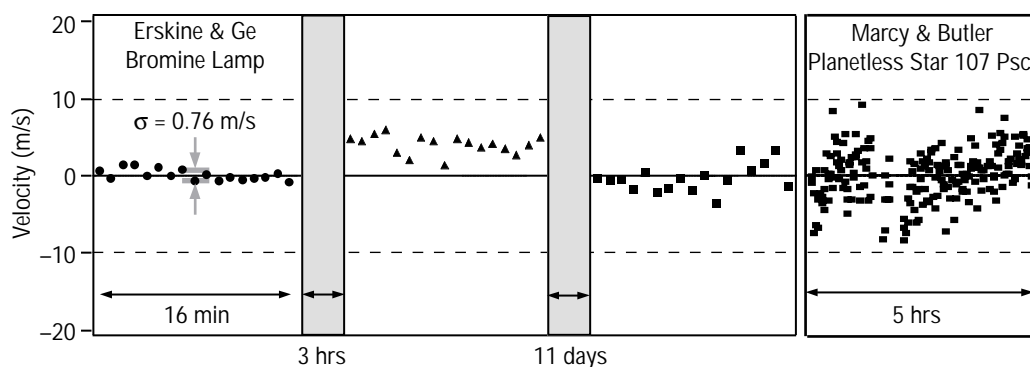
Velocity repeatability test using a stationary spectral source (bromine lamp), compared to Marcy and Butler's repeatability test on a planetless star.

The Study of the Hydrodynamics of Single-Bubble Sonoluminescence

R. W. Lee, P. E. Young, W. Moss, D. Chambers, M. Schnittker, D. Solis

98-ERD-081

Sonoluminescence (SL) is the production of visible light by a gas bubble that is suspended in a fluid (normally water) by an acoustic standing-wave field. Present understanding of the phenomenon suggests that SL may result in temperatures of over 10^5 K (which approaches the temperature found in the solar corona), pressures of over 10^{12} Pa (close to the pressure at the center of the planet Jupiter), light emission of less than 10^9 s duration, and concentration of mechanical energy of up to 10^{12}. In SL, a 10-μm-diam bubble (i.e., a bubble with a diameter of about 1/10 the width of a human hair) oscillating in an audiofrequency (25 kHz), ultrasonic field synchronously emits on the order of a million photons in a short pulse each acoustic period. The process by which the acoustic energy is converted into electromagnetic energy is not completely understood and is being investigated by numerous research groups around the world.

In this project, we are addressing several important topics of general interest to LLNL, including a detailed study of the hydrodynamics in spherical geometry, the properties of matter at extreme conditions, and the source of the light flash. Our methods include (1) experiments that look at the hydrodynamic collapse of a bubble; (2) simulations of the spherical nature of the collapse—the details of the simulations that must be exercised can be rigorous tests of the hydrodynamic codes; (3) studies that have impact on the equation of state of the gases, in the bubble as well as that of the water at extreme conditions—necessary because there was no reasonable solution of the source of the emissivity from the bubble; (4) unique techniques such as ultrafast-laser probing of the collapsed bubble—which will provide basic information on the ability of codes to map out the implosion phase correctly; and (5) studies aimed at understanding the light emission—

these may provide a path for the use of this rather interesting phenomenon.

We have successfully engaged high-quality students in our project. These young, bright individuals are attracted to LLNL to participate in research in which they become fully involved. This project has been an exceedingly effective method for introducing researchers to LLNL and for gaining public awareness.

Our experiments and simulations during FY1999 essentially confirm that the light flash is caused by plasma formation. To reach this conclusion, we studied the behavior of the light emission from a well-characterized cell. We (1) set up a laser-probing system to obtain images of the bubble with 10-ns time resolution—this is used to measure the maximum and ambient bubble radii during the acoustic cycle, (2) assembled a thermoelectric system to allow control of the water temperature—this temperature is critical to the amount of light emission from the bubble, (3) used an optical streak camera to measure the duration and time shape of the light emission from the bubble, and (4) investigated the pulse duration as a function of water temperature, driving pressure, and gas concentration—we observed 50- to 300-ps duration pulses. Our measurements provided data that rigorously tested the hydrodynamic models.

At the end of the year, we were studying the spectrum of the SL emission for comparisons with models of spectra from warm, dense matter in order to set constraints on the temperature and density of the plasma inside the collapsed bubble.

In FY2000, we plan to develop a bubble-radius vs. time relationship, attempt to measure the bubble temperature and electron density (in both visible and near-infrared light), model the high-quality data from noble-gas bubbles, and improve our spectral-synthesis model to allow studies of the bubble in the initiation stage.

Primordial Quasars and Starbursts in Protogalaxies

W. van Breugel

98-ERI-005

Within standard cosmological models, the formation of galaxies is a hierarchical process. Large galaxies are thought to grow through the merging of smaller systems; the most massive objects form in over-dense regions, which will eventually evolve into the large clusters of galaxies seen today. It has also been suggested that the first massive black holes either may have grown in similar hierarchical fashion, together with their parent galaxies, or that they may have preceded galaxy formation and be primordial.

It is therefore of great interest to find the progenitors of the most massive galaxies and their active galactic nuclei (AGN)—or active, massive black holes—at the highest possible redshifts (an astronomical measure of distance) and to study their properties and cosmological evolution. Our goal in this project is to find and study these first-forming massive galaxies and (active) black holes.

Previous work by our group at LLNL's Institute of Geophysics and Planetary Physics (IGPP), performed in collaboration with colleagues from the University of California at Berkeley and at Davis (UCB and UCD, respectively), the California Institute of Technology; and Leiden Observatory (The Netherlands), had already shown that powerful radio sources are amazingly good beacons for massive galaxies.

In this project, during FY1999 we combined two techniques to build a very efficient sample for finding such radio sources at the highest possible redshifts. The first method is to select radio sources with ultrasteep spectra (USS) at radio wavelengths, or very red "radio color." Most powerful radio galaxies have radio spectral-energy distributions that steepen with frequency. Therefore, at fixed observing frequencies more distant sources exhibit steeper spectra.

The second method relies upon the well-known magnitude–redshift relationship at infrared (IR) wavelengths for powerful radio galaxies. At low redshifts, such radio galaxies are uniquely associated with massive galaxies. The well-behaved IR-magnitude–redshift diagram then suggests that such galaxies can be found through IR identification.

Our first chance to apply these methods was in December 1998 using the Keck Telescope. During these observations, we discovered a radio galaxy, TN J0924-2201, at a record-shattering redshift $z = 5.19$. This discovery has broken the distance record for objects powered by super-massive black holes which, until now, had been held for 36 years by quasars. It was reported by CNN Headline News on June 17, 1999, and also by other major news sources. A Keck near-IR image of the radio galaxy is shown in the figure. The radio source associated with the galaxy is shown by contours overlaid on the galaxy.

Black holes powering radio galaxies such as TN J0924-2201 are thought to be a billion times more massive than our sun. Because of its high redshift, the black hole must have formed within the first one billion years after the Big Bang. One of the main challenges now is to understand how such massive black holes could have formed in such a short time.

For FY2000, we plan to continue our search for even higher-redshift radio galaxies and quasars. Several promising new candidates have been identified, and observing time at the largest telescopes in the world (the Keck 10-m Telescope, and the European Southern Observatory's 4- $\times$ 8-m Very Large Telescope) has been awarded. Several of the highest-redshift objects will be observed with narrow-band and tunable filters to study their gaseous halos, which may provide kinematic information about the first stages of galaxy and black-hole formation. Observations at submillimeter wavelengths to search for the presence of dust and cold gas, which must accompany large-scale star formation in young galaxies, will also be pursued.
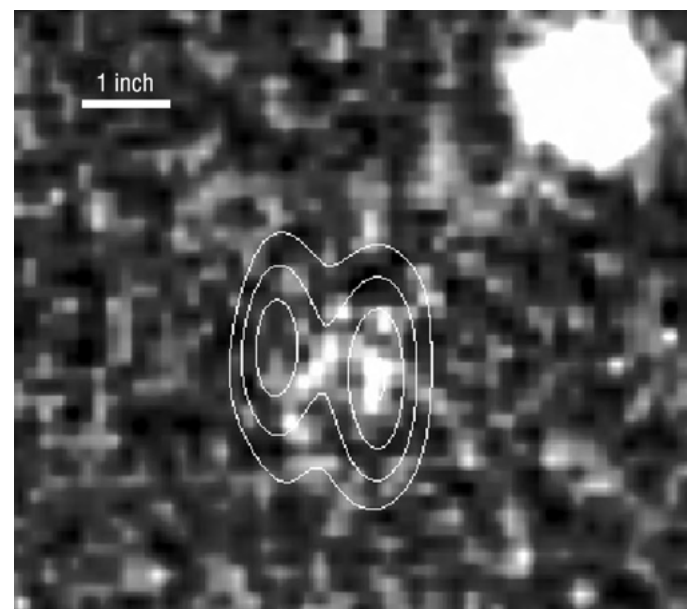
Keck near-infrared image of the radio galaxy TN J0924-2201 at redshift $z = 5.19$, with radio contours superposed.

Feasibility Study for Analyzing Plasma-Aerodynamic Effects

B. M. Penetrante, J. W. Sherohman

98-FS-002

Plasma-aerodynamic experiments to modify shock wave behavior have generated much interest in the United States and the international aerodynamic communities. Experiments conducted by the U.S. Air Force Research Laboratory (AFRL) at Wright-Patterson Air Force Base have verified two major Russian claims that could help provide a significant breakthrough in supersonic/hypersonic flight technologies. Weakly ionized electrical discharge plasmas have been observed to cause "anomalous relaxation" of the bow shock wave and result in a major reduction in drag for an object moving at supersonic/hypersonic speed. These plasmas have been observed to increase the speed of the shock wave, disperse the shock structure, and dissipate the shock wave amplitude. Although verified experimentally, the phenomena are not understood. We conducted preliminary calculations that utilize plasma physics and computational fluid dynamics modeling capabilities at LLNL to help understand the AFRL experiments. If the plasma-aerodynamic effects can be understood, controlled, and made to occur in an efficient, large-scale way, there is potential for high-payoff, both commercially and militarily.

We chose to address the propagation of a shock wave through a weakly ionized plasma in a shock tube. Here, a longitudinal direct-current plasma is generated with a pair of electrodes inside a Pyrex tube. An acoustic shock wave is generated by a spark gap. Photo-acoustic deflection waveform signals are simultaneously recorded at two or more locations in the shock tube. The first notable observation is the acceleration of the shock upon entry into the plasma region from the neutral gas. The other interesting effect is the change in the shock structure; the shock splits into several separate shocks and the shock waves are damped significantly as the current is increased. Controversy remains about what physical mechanism is responsible for these effects. Some have suggested that the energy exchange between the shock wave and the excited state atoms/molecules in the non-equilibrium plasma is important. Others have suggested that a strong space charge field is formed at the shock boundaries, causing the acceleration of ions and, by charge exchange collisions, the transfer of energy and momentum to neutrals in front of the shock wave. Gas temperature gradients due to heating by the plasma have also been invoked to explain the shock behavior; however, even this simple explanation has not been carried out rigorously in a model that can be validated by experiment.

We modeled the plasma kinetics to obtain the gas temperature distribution in the discharge as a function of the electrical current. We used this gas temperature distribution as input to the arbitrary Lagrange-Eulerian grid technology code ALE3D, which then calculated the propagation of the shock wave through the gas.

Our calculations demonstrate the shock wave characteristics that are observed experimentally. As the gas temperature in the plasma region is increased, the shock velocity increases, as noted from the decrease in arrival time. The shock breaks up into multiple shocks as it encounters the temperature gradient between the plasma and the neutral gas. The amplitude of the leading shock decreases as the temperature in the plasma region is increased. The 3D simulations show that thermal gradients can explain most of the experimentally observed effects, including the dispersion and extreme damping of the shock wave structure. The gas temperatures required to quantitatively explain the experimental observations are consistent with those that are produced by the electrical currents used in the experiment.

The modeling capabilities at LLNL have provided significant insights into the physics controlling plasma-aerodynamic effects. Further research is required to determine how the effects can be utilized to benefit the commercial and military aerodynamic industry.

ALE3D calculation of the shock signals in a 30-Torr argon discharge plasma. The peak gas temperature on axis produced by the plasma is indicated.
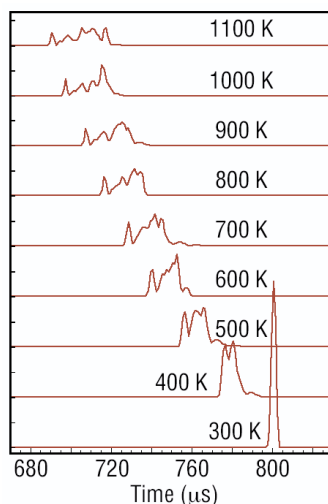
The Size, Shape, and Composition of the Milky Way

C. R. Alcock

99-ERD-041

The objective of this project is to exploit our new dataset comprising the photometric histories of tens of millions of stars to determine the size, shape, and composition of the Milky Way. After decades of effort, astronomers do not know how large the Milky Way is, how much it weighs, or what it is made of. At LLNL, we have exploited the gravitational microlensing effect and established that MACHOs (massive compact halo objects) make up 20–100% of the dark matter in the Milky Way, and thus are the dominant identified component of the Galaxy. The primary limitation on the interpretation of the gravitational microlensing data is not small-number event statistics, but the inadequate model for the large-scale structure of the Milky Way.

The primary limitation on the determination of the extent, shape, and mass of the Milky Way is the small number of "tracers" in the outer region of the galaxy for which we can determine the distance, radial velocity, and transverse velocity. For those few objects which are known, distances can usually be estimated with precision ~10%. Radial velocities can be determined spectroscopically with great precision (typically much better than 1%, which is more precise than needed for this purpose). The real problem is the transverse component of the velocity. There are no good estimates of the transverse velocity for any object more than 15 kpc (kiloparsec) from the center of the Milky Way.

Two of the target regions for our gravitational microlensing work are promising tracers: these are the Large and Small Magellanic Clouds (LMC and SMC). Both are located well away from the center of the galaxy (45 kpc and 55 kpc, respectively, from the Solar System), and both are clearly bound into the gravitational potential well of the galaxy. Distances and radial velocities are well known for both the LMC and the SMC, and a preliminary, but inadequate estimate of the transverse velocity of the LMC has been made.

The transverse component of velocity is obtained by measuring the angular motion (proper motion) of the object on the sky, and multiplying this by the distance to that object. The angular motion is very small, and can only be revealed by comparing images taken decades apart in time. Reliable reference point sources that are far behind the LMC are needed to determine the proper motion. The only promising candidates for this purpose are quasars, which are extremely bright, point-like objects located at enormous distances. It has not been possible, until now, to find the quasars needed for this work.

Many quasars exhibit erratic variability of a kind not seen in stars, and we used this to identify the approximately 20 quasars out of the approximately 20 million objects in the database. It is not trivial to identify one object in a million, but in FY1999, we succeeded, using a combination of color information and erratic variation with time. Three quasars were confirmed spectroscopically. One example is shown in the Fig. 1 below.

In addition to locating quasars for this purpose, it is essential that we be able to measure the positions of objects with adequate precision to determine the motion across the sky. The expected displacement of the LMC during the history of the MACHO Project is ~80 nanoradians. We have demonstrated the needed precision with a careful analysis of the data for one of our gravitational microlensing events.

In FY2000, we propose to complete our sampling of approximately 20 quasars, using the full survey of the Macho Lightcurve Database. We intend to initiate systematic proper motion determination. The first step in this process will be to assemble the library of high quality image data. This work will lead to a more accurate model for the Milky Way.
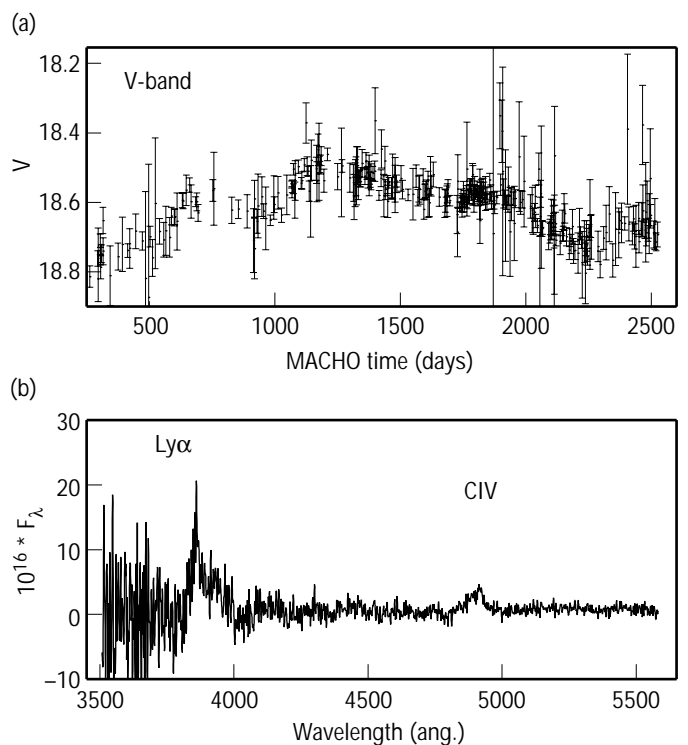
(a)

(b)

Figure 1. (a) shows the time variation of the flux from a confirmed quasar; (b) shows the spectrum of the quasar.

An Imaging Fourier Transform Spectrometer for Astronomy

K. H. Cook, J. R. Graham, C. L. Bennett, J. Bixler, E. H. Wishnow, R. Wurtz

99-ERD-065

The Next Generation Space Telescope (NGST) is designed to be an 8-m, infrared (IR)-optimized astronomical telescope with an orbit far from the radiation of Earth. NGST will be able to observe currently unseen sources in the high-redshift universe and (currently) dark matter. Because the spatial distribution and spectral signatures of the most interesting unseen objects are not well known, NGST's instruments must include a spectrograph of flexible resolution that obtains simultaneous spectra of the greatest number of objects across the telescope's focal plane. An imaging Fourier transform spectrograph (IFTS) best meets NGST's requirements because it can deliver a spectrum for every pixel—a "spectral datacube."

We are part of a collaboration proposing an IFTS named the Fourier transform infrared spectrometer (IFIRS) for NGST. The goals of this LDRD project are to (1) develop a ground-based, facility-class visible/IR IFTS because only one ground-based, astronomical IFTS has previously been fielded; and (2) show the feasibility of flying IFIRS on NGST. With this instrument, we will demonstrate the utility and versatility of an IFTS for astronomy in the signal and noise regimes comparable to those of NGST.

In FY1999, we demonstrated an astronomical IFTS using bench-top technology. All the demonstrations described below were presented at the NGST Science and Technology Symposium in September 1999.

Our first-generation, ground-based instrument follows the IFIRS design: a four-port (two input and two output) Michelson interferometer with two imaging detector arrays. Metrology from a laser interferometer placed in parallel with the optical beam maintains optical-path stability. The instrument was operated in the laboratory for a few weeks, then disassembled, crated, shipped, and re-assembled at a remote observatory—thus demonstrating the design's relative ease of alignment.

Our experiments at Kitt Peak National Observatory during FY1999 included (1) demonstrating the wide-field, multi-object photometry capability of our instrument; and (2) obtaining simultaneous imaging in multiple, widely separated emission lines. For the first, we obtained a series of frames of a field containing a globular cluster [Fig. 1(a)]. Even though the field drifted during the series of observations, we were able to extract interferograms for individual stars from nonreregistered frames [Fig. 1(b)]. In deep NGST observations, this would be the mode for extracting the spectra of moving objects, such as objects in the Kuiper Belt. For the second experiment, we observed the Orion Nebula, computed the line center of two emission lines, and extracted the corresponding channels as slices from the spectral datacube. With the panchromatic image, these observations are equivalent to three-filter imaging—two narrowband and one broad—but they were acquired simultaneously, with the corresponding multiplex advantage.

We performed further demonstrations in the laboratory at LLNL, including (1) hybrid disperser-interference spectroscopy, and (2) common-mode noise rejection. One remedy for source-noise-limited observations is to cut down the bandwidth per pixel by dispersing the image of the object across several pixels using a low-dispersion prism and the IFTS together in a hybrid configuration. To demonstrate this, we made hybrid IFTS observations of Polaris. High-resolution spectroscopy of bright cluster giants will benefit from hybrid IFTS observations. The second demonstration involved observing Polaris through a small telescope and taking short-exposure, two-output images. The images exhibited signal drifts arising from atmospheric scintillation. We removed the drift using common-mode rejection. Two-output data will also provide a direct method of identifying cosmic-ray hits (a likely problem in NGST datacubes).

In FY2000, we will build a facility-class, ground-based optical IFTS prototype around a new interferometer. This IFTS is intended to perform searches for high-redshift galaxies with an efficiency higher than with existing filter techniques. Further, the design of this new interferometer allows it to be reconfigurable as a mid-IR IFTS.
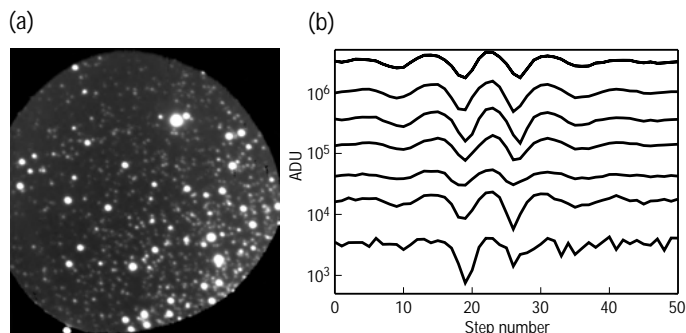
(a)

(b)

Figure 1. Results obtained with our ground-based Fourier Transform Infrared Spectrometer (FTIRS): (a) panchromatic image of the southeastern edge of the globular cluster M4, and (b) extracted interferograms of stars from the M4 datacube, a representative series across 7.5 magnitudes (ADU = arbitrary data).

Advancement and Refinement of HyperSoar Modeling and Feasibility Issues

P. H. Carter

In response to our nation's security needs for global reach and for rapid access to orbit, we invented a revolutionary concept for a hypersonic vehicle that is notably different from, and more efficient than, conventional aircraft. HyperSoar flies at ten times the speed of sound, skipping upon the atmosphere like a rock thrown upon the surface of a lake—turning its engines on each time it skips upon the air and turning them off while its coasts between skips. With its revolutionary design, a HyperSoar aircraft could fly between any two points on the globe in less than two hours. A HyperSoar bomber the size of a B-52 could take off from the U.S. and deliver its payload, equipment, or personnel to any point on the globe—from an altitude and at a speed that defies all current defensive measures—and return to the U.S. without the need for refueling or for bases on foreign soil. In terms of space lift, HyperSoar could be employed as the first stage of a two-stage-to-orbit space launch system. Our research shows this approach will allow approximately twice the payload-to-orbit as today's expendable launch systems for a given gross takeoff weight.

We are developing the computational tools and modeling required to advance the principles incorporated in the concept. We accomplished our primary objective to develop a more detailed vehicle design with the associated aerodynamics and propulsion modeling. This "waverider" vehicle design is illustrated in the figures below. We defined a preliminary aerodynamic model, and the National Aeronautics and Space Administration (NASA) Ames Research Center is collaborating with us to develop an even higher fidelity model. Another collaborator, Aerojet Corporation, has provided a model of a rocket-based combined-cycle (RBCC) engine for our propulsion model.

HyperSoar flies a periodic hypersonic cruise (PHC) trajectory. The use of period control in an airplane's trajectory is a relatively new topic. The mathematical foundations of periodic control are still being constructed and the intuitive physical understanding of why these trajectories work are still being argued. In part, our current research strives to provide some preliminary insights as to why PHC trajectories are fuel optimal. From a survey of research on this topic and in our investigations, it appears that PHC trajectories attempt to strike a balance between aerodynamic and propulsion efficiency. This involves an exchange between kinetic and potential energy to ensure that the total energy of the vehicle remains approximately constant over a cycle. Such PHC trajectories achieve a more optimal balance in this exchange of kinetic and potential energy than is achieved by steady cruise trajectories. It has been shown mathematically that steady cruise trajectories can violate the second-order sufficient conditions for the existence of a local minimum. While a similar proof does not exist currently for periodic cruise trajectories, it does rule out steady cruise as a fuel-optimal solution.

Our improved vehicle design and the associated modeling will allow us to develop more complete simulations and numerical analyses of these trajectories. We have begun the simulation of PHC trajectories on NASA's POST (Program to Optimize Simulated Trajectories) software code. Our successful simulation of PHC trajectories with POST is an important step towards the wider acceptance of these trajectories by the technical community. In FY2000, we will investigate additions to POST that will allow it to simulate PHC trajectories in a more accurate and efficient manner. This will advance the understanding of PHC trajectories and encourage their use in a broad spectrum of military and civil applications.
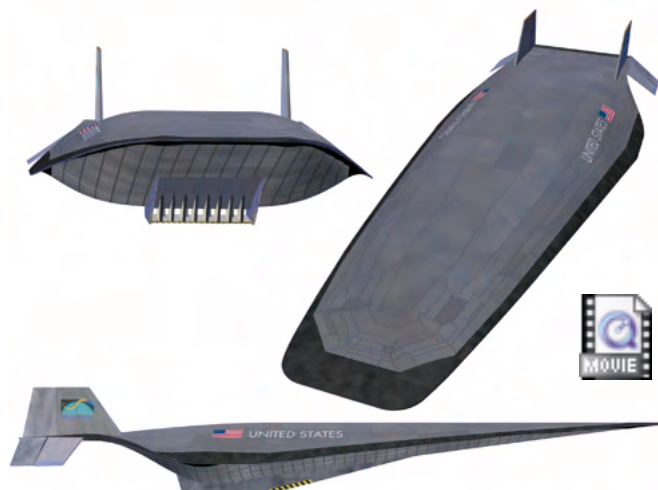
The HyperSoar vehicle uses osculating cone "waverider" aerodynamic design methodology to integrate hypersonic aerodynamics with rocket-based combined-cycle engines, thermal protection, and flight controls.

Primitive Planetary Systems via the Keck Telescope

B. Macintosh, S. Gibbard, C. Max

99-ERI-003

Adaptive optics (AO) uses high-speed sensors, computers, and mirrors to cancel out optical aberrations. LLNL has a long history of using this technology for applications as diverse as correcting internal aberrations in laser beams to astronomy; AO is a key technology for developing ultraprecise optical systems operating under difficult conditions. Astronomical AO can cancel out the distortions in an image caused by rapidly-moving turbulence in the Earth's atmosphere, allowing Earth-based telescopes to reach their fundamental diffraction-limited resolution. The largest ground-based telescopes, such as the 10-m Keck II Telescope, can in this way achieve resolutions higher even than the Hubble Space Telescope, particularly at near-infrared (IR) wavelengths.

The Keck AO system was jointly built by LLNL and the Keck Observatory. The high-speed software that controls the system and integrates the shape-changing "deformable mirror" used to cancel the atmospheric turbulence was written at LLNL. We have been using this system to study the origins of planetary systems like our own. Initially, we are studying objects in our own solar system that may contain information about primitive conditions on the early Earth or the formation of the planets; ultimately, we will image the circumstellar disks around young stars in which planets are thought to form.

During FY1999, we used the Keck AO system to map the surface of Titan, Saturn's largest moon. Methane in Titan's atmosphere is broken down by ultraviolet (UV) light into ethane and other complex hydrocarbons, shrouding Titan's surface in a thick, smog-like haze. Neither the Voyager spacecraft nor the visible-light cameras on the Hubble Space Telescope have been able to produce quantitative maps of Titan's surface. However, near-IR imaging at Keck allows us to measure the properties of this haze and simultaneously produce a reflective albedo map of Titan's surface. The results of our initial observations were published in *Icarus*.

We then extended our observations to produce a complete map of Titan's surface—which shows large, dark regions that may represent "seas" of liquid hydrocarbons at a resolution far beyond that available from conventional systems. The complex organic chemistry involving these hydrocarbons is a good analog for the prebiotic Earth—in many ways, Titan is the most Earth-like body in our solar system. We also began observations using the advanced, near-IR spectrograph on the Keck Telescope to study the chemistry of Titan's atmosphere and surface.

During FY1999, we also used the Keck AO system to observe Neptune [Fig. 1(a,b)], the outermost large planet in our solar system, and one with complex weather systems driven by heat retained from its formation. By using different narrow-band filters, we probed different altitudes in Neptune's atmosphere. Working with our collaborators at the University of California, Berkeley, we developed atmospheric models to fit our observations, deriving the properties of Neptune's stratospheric and tropospheric cloud layers.

We participated in early testing of the Keck AO system to determine its sensitivity to the protoplanetary systems that we will be looking for. In early FY2000, we will have our first observing run on the Keck Telescope that is dedicated to studying circumstellar disks; this will be our first opportunity to probe the conditions under which planets form.

(a)

(b)

Figure 1. Advantage of using adaptive-optics (AO) on an Earth-based telescope to study objects in our solar system, as shown by (a) a conventional, near-infrared (IR) image of Neptune, and (b) a high-resolution, near-IR image of Neptune taken using the Keck Telescope's AO system.
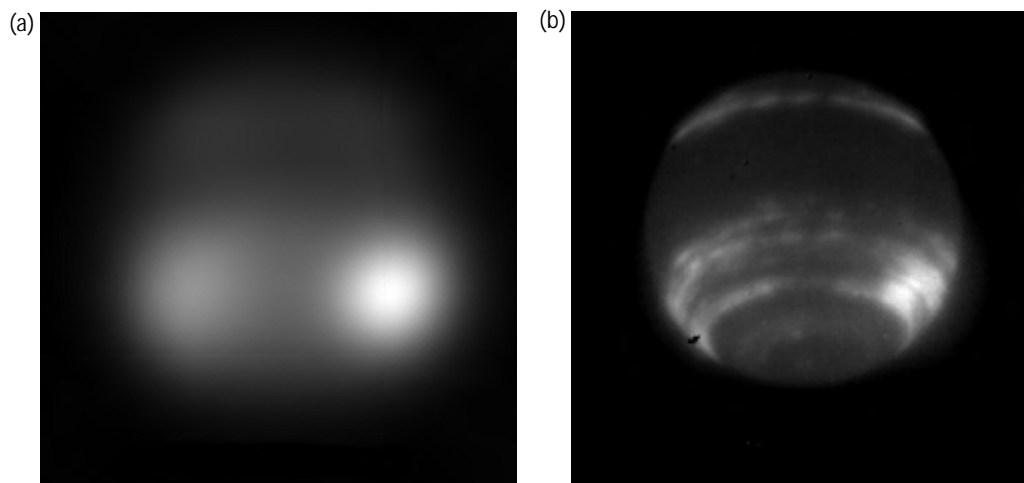
Application of Laboratory and Modeling Capabilities to Extreme Ultraviolet Spectroscopy of Astrophysical Sources

C. W. Mauche, D. A. Liedahl, P. Beiersdorfer

99-LW-053

As evidenced by the x-ray emission of our Sun, the cosmic x-ray background, and the more than 180,000 catalogued cosmic x-ray sources, the Universe is proficient at producing high-temperature plasmas. Diagnostics of the physical conditions of these cosmic plasmas is provided by spectra in the extreme ultraviolet (EUV; 912–100 Å) and x-ray (0.1–10 keV) wavebands obtained with such facilities as the Extreme Ultraviolet Explorer (EUVE) and the Chandra X-ray Observatory. The interpretation of these spectra requires large sets of atomic data and sophisticated spectral modeling capabilities, but all too often the atomic data required to develop these capabilities does not exist. To help remedy this situation, we have undertaken a project which combines experimental data from the Livermore Electron Beam Ion Trap (EBIT) facility with theoretical data generated with Livermore atomic physics codes to develop reliable spectral models of highly-charged ions in the EUV. These efforts indirectly validate spectroscopic diagnostics for weapons experiments on lasers and pulse-power facilities and strengthen the Laboratory's core competency in atomic physics.

Because of its high cosmic abundance and persistence over a wide range of temperatures, iron (Fe) is an important diagnostic of the plasma conditions in cosmic sources. For example, fully one third of the lines in the Solar EUV Rocket Telescope and Spectrograph catalog of an average solar active region are due to Fe IX–XVII and provide coverage of the temperature range from 600,000 K to 4 million K. Unfortunately, atomic models of these ions calculated with the HULLAC (Hebrew University/Lawrence Livermore Atomic Code) atomic physics package are affected by electron–electron interactions. These do not seriously affect calculations of radiative and collisional rates, but they do affect wavelengths at the few percent level. Because of the high line density and line blending, these errors seriously compromise our ability to interpret the EUV spectra of cosmic sources. To remedy this situation, we have performed a series of EBIT measurements of the line emission from iron in the 60- to 140-Å waveband. The spectral resolution of these measurements is 0.3 Å, comparable to that of EUVE, and the electron density is 5×10^{11} cm^{-3}, comparable to that of the corona of the Sun and other late-type stars.

These efforts have produced several results. We developed a comprehensive catalog of EUV lines from M-shell iron (Fe IX–XVI) in the 60- to 140-Å waveband. In addition, we revised the estimate of the radiative cooling of high-temperature plasmas by iron, which dominates the cooling in cosmic-abundance plasmas from 400,000 K to 10 million K. Next, we produced laboratory data to correct theoretical atomic models and develop reliable spectral models of M-shell iron in the EUV. Finally, we developed a solution of the origin of the quasi-continuum in the EUVE spectra of late-type stars, which has been variously ascribed to a high-temperature tail on the emission measure distribution of stellar coronae, reduced metal abundances, resonant scattering (destruction) of emission lines, and incompleteness of atomic models.

Appendix

Publications

Principal Investigators Index

Tracking Code Index

FY1999 Annual Report Publications

These documents reporting LDRD research in FY1999 were published under the auspices of the Department of Energy and denote DOE publication numbers in compliance with contract W-7405-Eng-48.

Aceves, S., A. B. Shapiro, V. Sahai, *An Accuracy Evaluation for the Madejski Splat Quench Solidification Model*, UCRL-JC-133757, 98-ERD-085.

Adijiwaya, I., T. Critchlow, R. Musick, "Detecting data and schema changes in scientific documents," submitted to *International Conference on Data Engineering*, UCRL-JC-134444, 97-ERD-033.

Ahle, L. A., et al., "Current Status of the Recirculator Project at LLNL," *Proc. PAC99 Conference*, to be published, UCRL-JC-132273, 99-ERD-052.

Ahle, L. E., and H. S. Hopkins, "Gated Beam Imager for Heavy Ion Beams," *AIP Conference Proceedings*, **451**, 507–513, UCRL-JC-130010, 99-ERD-052.

Ahle, L., "Heavy Ion Fusion Experiments at LBNL and LLNL," *Proc. LINAC98 Conference*, to be published, UCRL-JC-131792, 99-ERD-052.

Albala, J. S., et al., "From Genes to Proteins: High-throughput Expression and Purification of the Human Proteome," submitted to *J. Cell. Biochem.*, UCRL-JC-132485, 99-ERD-039.

Albala, J. S., et al., "From Genes to Proteins: High-throughput Expression and Purification of the Human Proteome," UCRL-JC-132485abs, 99-ERD-039.

Albala, J. S., et al., "High-throughput Expression and Purification of the Human Proteome," UCRL-JC-13557abs, 99-ERD-039.

Albala, J. S., I. R. McConnel, F. Farrahi, J. E. Lamerdin, "Characterization of RAD51B and its role in genomic stability and DNA repair," UCRL-JC-132399abs, 99-ERD-039.

Alcock, C., "The Dark Halo of the Milky Way," submitted to *The Global Weekly of Research Science*, UCRL-JC-136828, 99-ERD-041.

Alford, O., et al., "Scrounge-atron: a phased approach to the Advanced Hydrotest Facility utilizing protons," *Proc. Particle Accelerator Conference 1999*, New York, March 29–April 2, 1999, UCRL-JC-133131, 98-ERD-088.

Alford, O., et al., *The Scrounge-atron, A Proton Radiography Demonstration Accelerator*, UCRL-LR-134107, 98-ERD-088.

Allen, P. G., E. R. Sylwester, E. A. Hudson, *The Structure of Uranium (VI) Sorption Complexes on Silica, Alumina, and Montmorillonite*, UCRL-JC-134461, 98-ERD-094.

Arav, N., et al., "Hubble Space Telescope Observations of the Broad Absorption Line Quasar PG 0946+301," *The Astrophys. J.*, **516**, 27, UCRL-JC- 233180, 98-ERI-005.

Arav, N., et al., "What Determines the Depth of BALs? Keck HIRES Observations of BALQSO 1603+300," *The Astrophys. J.*, **524**, 566, UCRL-JC- 236102, 98-ERI-005.

Armstrong, R., et al., "Toward a Common Component Architecture for High-Performance Scientific Computing," submitted to *High Perform. Distrib. Comp.*, UCRL-JC-134475, 99-ERD-078

Ashby, S., T. Critchlow, M. Ganesh, R. Musick, T. Slezak, "Genomics Data Warehousing Forum Slides," UCRL-MI-132847, 97-ERD-033.

Asoka-Kumar, P., R. Howell, W. Stoeffl, D. Carter, "High Intensity Positron Program at LLNL," *Applications of Accelerators in Research and Industry '98*, J. Duggan, ed., North Holland, Amsterdam, to be published, UCRL-JC-132024, 99-ERD-047.

Athreya, R. M., V. K. Kapahi, P. J. McCarthy, W. van Breugel, "Large Rotation Measures in Radio Galaxies at z > 2," *Astronomy and Astrophysics*, **329**, 809, UCRL-JC-129387, 98-ERI-005.

Aufderheide, M. B., et al., "High energy proton radiography as a means of material identification," *Proc. 9th International Symposium on Nondestructive Characterization of Materials*, Sydney, Australia, June 28–July 2, 1999, UCRL-JC-133273, 97-ERD-058.

Azevedo, S. G., "Preliminary Detection Experiments with the NU-designed Parabolic Reflector Antenna," Lawrence Livermore National Laboratory, UCRL-VG-135432, 97-SI-013.

Baldis, H. A., C. Labaune, W. Rozmus, A. Maximov, *Forward Scattering as a Potential Self-Smoothing Phenomena*, UCRL-MI-133230, 99-ERI-018.

Baldwin, C., P. Brown, R. Falgout, F. Graziani, J. Jones, "Iterative Linear Solvers in a 2D Radiation-Hydrodynamics Code: Methods and Performance," *J. Comp. Phys.*, **154**, 1–40, UCRL-JC-130933, 98-ERD-022.

Balhorn, R., L. Brewer, M. Corzett, "DNA Condensation by Protamine and Arginine-rich Peptides: Analysis of Toroid Stability using Single DNA Molecules," accepted by *Mol. Reprod. & Dev.*, UCRL-JC-136025, 99-LW-057.

Barsky, D., E. T. Kool, M. E. Colvin, "Interaction and Solvation Energies of Nonpolar DNA Base Analogues and Their Role in Polymerase Insertion Fidelity," *J. Biomolecular Structure and Dynamics*, **16**, 1119–1134, UCRL-JC-132590, 98-SI-008.

Barsky, D., M. E. Colvin, "Guanine-cytosine base pairs in parallel-stranded DNA: An ab initio study of the keto-amino wobble pair versus the enol-imino tautomer pair," *J. Phys. Chem. B*, in press, UCRL-JC-134817, 98-SI-008.

Barth, A. J., et al., "Polarized Narrow-Line Emission from the Nucleus of NGC 4258," *The Astron. J.*, **118**, 1609, UCRL-JC- 235667, 98-ERI-005.

Barton, I. M., et al., "Diffractive Alvarez Lens," submitted to *Opt. Lett.*, UCRL-JC-135583, 98-ERD-061.

Battersby, C. L., L. M. Sheehan, M. R. Kozlowski, "Effects of wet etch processing on laser-induced damage of fused silica surfaces," *Laser Induced Damage in Optical Materials: 1998*, SPIE **3578**, 446, UCRL-ID-131224, 98-ERD-063.

Bauman, B., et al., "New optical design of adaptive optics system at Lick Observatory, *Proc. SPIE*, **3762**, 194–200, UCRL-JC-134970, 97-ERD-037.

Bedrossian, P. J., A. J. Schwartz, M. Kumar, W. E. King, "Observation of Localized corrosion Properties of Ni and Ni-based Alloys using Coupled Atomic Force Microscopy and Orientation Imaging Microscopy," *MRS Proceedings,* UCRL-JC-135219abs, 98-ERD-080.

Beiersdorfer, P., et al., "Polarization of K-shell x-ray transitions of Ti^{19+} and Ti^{20+} excited by an electron beam," submitted to *Phys. Rev. A*, UCRL-JC-134527, 97-ERD-103.

Beiersdorfer, P., et al., "Spectral Catalogue of the Intermediate Ionization States of Iron in the Extreme Ultraviolet," *Proc. NASA Workshop on Laboratory Space Science*, UCRL-JC-130832, 97-ERD-057.

Beiersdorfer, P., J. K. Lepson, G. V. Brown, D. A. Liedahl, C. W. Mauche, S. B. Utter, S. M. Kahn, "Quasi-Continuum Line Emission from Fe VII-X in the Extreme Ultraviolet Region below 120 Angstroms," *Bull. Amer. Astro. Soc.*, **31**, 706, UCRL-JC-133902abs, 99-LW-053.

Beiersdorfer, P., et al., "Observation of Quasi-Continuum Line Emission from Fe VII to Fe X in the Extreme Ultraviolet Region Below 140 Angstroms," *Astrophys. J.* **519**, L185, UCRL-JC-133895, 99-LW-053.

Beiersdorfer, P., J. R. Crespo Lopez-Urrutia, P. Springer, S. B. Utter, K. L. Wong, "Spectroscopy in the extreme ultraviolet on an electron beam ion trap," *Rev. Sci. Instruments*, **70**, 276, UCRL-JC-131082, 97-ERD-103.

Bell, J., P. Duffy, C. Covey, C., L. Sloan, *Comparison of temperature variability in observations and sixteen climate model simulations*, UCRL-JC-134554-rev. 1. 99-SI-001.

Benedict, L., et al., "Dielectric function of wurtzite GaN and AlN thin films," *Solid State Comm.*, **112**, 129, UCRL-JC-134679, 98-ERD-052.

Bennett, C. L., "A Comparison of Imaging Spectrometers," *ASP*, UCRL-JC-137081, 99-ERD-065.

Bennett, C. L., "Critical Comparison of 3-D Imaging Approaches for NGST," *PASP*, UCRL-JC-135320, 99-ERD-065.

Bennett, C. V., and B. H. Kolner, "Parametric temporal imaging," in *Ultrafast Electronics and Optoelectronics*, J. Bowers and W. Knox, Eds., book chapter in vol. 28 of *Trends in Optics and Photonics*, 53–62, OSA, August 1999, UCRL-JC-133872, 98-ERD-027.

Bennett, C. V., and B. H. Kolner, "Principles, performance and demonstration of an up-conversion time microscope," paper UWC6 in *Proc. Ultrafast Electronics and Optoelectronics'99*, Aspen, Colorado, April 12–16, 1999, UCRL-JC-132648, 98-ERD-027.

Bennett, C. V., and B. H. Kolner, "Subpicosecond Single-Shot Waveform Measurement using Temporal Imaging," paper ThBB0001 presented at *LEOS'99* in San Francisco, CA, Nov. 8–11, 1999, UCRL-JC-135110, 98-ERD-027.

Bennett, C. V., and B. H. Kolner, "Temporal imaging system demonstrates 103¥ magnification and 300-fs resolution," submitted to *Conference on Lasers and Electro-Optics*, Baltimore, MD, May 23–28, 1999, UCRL-JC-132413, 98-ERD-027.

Bennett, C. V., and B. H. Kolner, "Up-conversion time microscope demonstrates 103¥ magnification of ultrafast waveforms with 300-fs resolution," paper PD2.2 in *Proc. LEOS '98,* Dec. 1–4, 1998, UCRL-JC-132458, 98-ERD-027.

Bennett, C. V., and B. H. Kolner, "Up-conversion time microscope demonstrating 103¥ magnification of femtosecond waveforms," *Opt. Lett.*, **24**, 783, UCRL-JC-132458, 98-ERD-027.

Benson, L. V., J. W. Burdett, M. Kashgarian, S. P. Lund, F. M. Phillips, R. O. Rye, "Climatic and hydrologic oscillations in the Owens Lake Basin and the adjacent Sierra Nevada, California," *Science*, **274**, 746, UCRL-JC-125154, 97-ERI-009.

Bibeau, C., et al., "Diode-Pumped Solid-State Lasers for Inertial Fusion Energy and High Energy Density Plasma Physics," *EII International Symposium*, UCRL-JC-130687, 97-SI-014.

Bibeau, C., et al., "Diode-Pumped Solid-State Lasers: Next Generation Drivers for Inertial Fusion Energy and High Energy Density Plasma Physics," *IEEE J. Quant. Electron.*, UCRL-JC-129614, 97-SI-014.

Bibeau, C., et al., "High Average Power 1-μm Performance and Frequency Conversion of a Diode-End-Pumped Yb:YAG Laser," *IEEE J. Quant. Electron.*, UCRL-JC-129612, 97-SI-014.

Bonlie, J., F. G. Patterson, D. Price, W. E. White, P. Springer, "Production of >10^{21} W/cm^2 from a Large Aperture Ti:sapphire Laser System," presented at *Ultrafast Optics '99* in July 1999, Ascona, Switzerland, UCRL-JC-134914abs, 99-ERD-049.

Brewer, L. R., M. Corzett, R. Balhorn, "Protamine-Induced Condensation and Decondensation of the Same DNA Molecule," *Science*, **286**, 120–123, UCRL-JC-134078, 99-LW-057.

Brotherton, M. S., B. J. Wills, A. Dey, W. van Breugel, R. Antonucci, "Spectropolarimetry of 3CR 68.1: A Highly Inclined Quasar," *The Astrophys. J.*, **501**, 110, UCRL-JC-129159, 98-ERI-005.

Brotherton, M., et al., "A Spectacular Poststarburst Quasar," *The Astrophys. J.*, **520**, 87, UCRL-JC-235640, 98-ERI-005.

Brotherton, M., et al., "Discovery of Radio-Loud Broad Absorption Line Quasars using Ultraviolet Excess and Deep Radio Selection," *The Astrophys. J.,* **505**, 7, UCRL-JC- 233710, 98-ERI-005.

Brown, G., P. Beiersdorfer, D. Liedahl, S. Kahn, S., K. Widmann, "Laboratory Measurements and Modeling of the Fe XVII X-Ray Spectrum," *The Astrophys. J.*, **502**, 1015, UCRL-JC-128877, 97-ERD-057.

Brown, P., B. Chang, F. Graziani, C. Woodward, "Implicit Solution of Large-Scale Radiation-Material Energy Transfer Problems," *Proc. Fourth IMACS International Symposium on Iterative Methods in Scientific Computation*, Austin, TX, Oct. 18–20, 1998, UCRL-JC-132831, 98-ERD-022.

Brown, P., B. Chang, M. Dorr, U. Hanebutte, C. Woodward, "Performing Three-Dimensional Neutral Particle Transport Calculations on Tera Scale Computers," *High Performance Computing '99* (part of the *1999 Advanced Simulation Technologies Conference*), April 11–15, 1999, San Diego, CA, UCRL-JC-132006, 98-ERD-022.

Brown, T. A., P. D. Quay, R. C. Francis, D. Holmgren, "Radiocarbon time-histories for subpolar North Pacific surface waters spanning the last 50 years," *EOS, Transactions of the AGU*, **79** (17), 167, UCRL-JC-130385abs, 97-ERD-052.

Burrows, A., T. Young, P. Pinto, R. Eastman, T. Thompson, "Supernova Neutrinos and a New Algorithm for Neutrino Transport," accepted by *Astrophys. J.*, UCRL-JC-135429, 99-ERD-043.

Caffee, M. W., G. B. Hudson, C. Velsko, G. R. Huss, E. C. Alexander, A. R. Chivas, "Primordial Noble Gases from the Earth's mantle: identification of a primitive volatile component," *Science*, **285**, 2115–2118, UCRL-JC-132371-rev. 1, 99-ERI-005.

Caldeira, K., and B. Goviindasamy, *Geoengineering Earth's radiation balance to mitigate anthropogenic climate change*, UCRL-JC-135617abs, 99-SI-001.

Campbell H. L., S. R. Visuri, L. B. Da Silva, "Effects of Stress Waves on Cells," *Proc. SPIE*, **3254**, 92–96, UCRL-JC-130131, 98-LW-030.

Campbell, E. W., B. J. Bauman, D. R. Sweider, S. S. Olivier, "High-accuracy calibration of an adaptive optics system using a phase shifting diffraction interferometer," *Proc. SPIE,* **3762**, 1999, 237–244, UCRL-JC-134805, 98-ERD-036.

Campbell, E., B. Bauman, D. Swieder, S. Olivier, "High-accuracy calibration of an adaptive optics system using a phase-shifting diffraction interferometer," *Proc. SPIE,* **3762**, 237–244, UCRL-JC-134805, 97-ERD-037.

Campbell, G. H. W. E. King, S. M Foiles, D. Cohen, "Determination of Grain Boundary Atomic Structure Using Quantitative High Resolution Electron Microscopy," *Materials Science Forum,* **294–296**, 35–42, UCRL-MI-131167, 97-ERD-117.

Campbell, G. H., J. Belak, J. A. Moriarty, "Atomic Structure of the ∑5 (310)/[001] Symmetric Tilt Grain Boundary in Molybdenum," *Acta Materialia*, in press, UCRL-JC-132639, 97-ERD-117.

Candy J. V., R. D. Huber, D. H. Chambers, G. H., Thomas, "Matched-Field Imaging of Laser Ultrasound using a Novel Correlation Cancelling Approach," *JASA*, **105**, (2), 1252, UCRL-JC-133397, 99-LW-045.

Carle, S. F., A. Ramirez, Daily, R. Newmark, A. Tompson, "High-performance computational and geostatistical experiments for testing the capabilities of 3-D electrical resistance tomography," *Proc. the Symposium on the Application of Geophysics to Engineering and Environmental Problems*, March 14–18, 1999, Oakland, CA, UCRL-JC-132943, 98-ERD-005.

Carle, S. F., A. Ramirez, W. Daily, R. Newmark, A. Tompson, "A geostatistical approach to obtaining geologically plausible ERT inversions," *Fifth Society of Industrial and Applied Mathematics Conference on Mathematical and Computational Issues in the Geosciences*, San Antonio, TX, March 24–27, 1999, UCRL-JC-132053abs, 98-ERD-005.

Carle, S. F., A. Ramirez, W. Daily, R. Newmark, A. Tompson, "Integration of geologic interpretation, geostatistics, parallel computing, and electrical resistance tomography for characterization of 3-D aquifer system heterogeneity," *American Geophysical Union Fall Meeting*, San Francisco, CA, December 6–10, 1998, UCRL-JC-13155abs, 98-ERD-005.

Carle, S. F., and A. Ramirez, "Integrated subsurface characterization using facies models, geostatistics, and electrical resistance tomography," submitted to *J. Environ. and Eng. Geophys.*, UCRL-JC-136739, 98-ERD-005.

Caturla, M. J., et al., "Comparative Study of Radiation Damage Accumulation in Cu and Fe," accepted by *J. Nuc. Mat.*, UCRL-JC-135256, 98-ERD-090.

Chemakin, I., et al., "Centrality dependence of p minus production and stopping in p-A collisions at 18 GeV/c," *Phys. Rev. Lett.*, UCRL-JC-133113, 97-ERD-058.

Chemakin, I., et al., "Measuring centrality with slow protons in proton-nucleus collisions at the AGS," *Phys. Rev. C*, **60**, UCRL-JC-133327, 97-ERD-058.

Cherepy, N. J., W. W. McNab, "Electro-osmotic-aided Remediation of Organic Solvent Contaminated Sediments," *J. Electrochem. Soc.*, UCRL-JC-134325sum, 98-ERD-038.

Circone, S., L. A. Stern, S. H. Kirby, J. C. Pinkston, W. B. Durham, "Methane hydrate dissociation rates at 0.1 MPa and temperatures above 272 K," *Proc. 3rd International Conference on Gas Hydrates*, in press, UCRL-JC-136097, 98-ERD-008.

Clague, D. S., "Lattice Boltzmann Modeling of Spherical Solutes in Confined Domains," *1998 Engineering Thrust Area Report*, UCRL-LR 53868-98, 99-ERD-016.

Clague, D. S., "Lattice Boltzmann Simulation of Complex Fluids," *1999 Engineering Thrust Area Report,* UCRL-LR-53868-99, 99-ERD-016.

Clague, D. S., P. J. Cornelius, "The Hydrodynamic Force and Torque on a Bounded Sphere in Poiseulle Flow," *International J. Num. Meth. in Fluids*, UCRL-JC-136255, 99-ERD-016.

Cohen, B. I., et al., "Modeling of ultra-short pulse reflectometry," *Phys. Plasmas*, **6**, 1732, UCRL-JC-132452, 97-SI-009.

Colvin, M. E., J. C. Sasaki, N. L. Tran, "Chemical Factors in the Action of Phosphoramidic Mustard Alkylating Anticancer Drugs: Roles for Computational Chemistry," *Current Pharmaceutical Design*, **5**, 645–663, UCRL-JC-135223, 98-SI-008.

Cowan, T. E., et al., "High energy electrons, nuclear phenomena and heating in petawatt laser-solid experiments, *Lasers and Particle Beams*, **17**, (4), UCRL-JC- 235187, 97-SI-001.

Critchlow, T., "An approach to scientific data integration," presentation at *IBC Bioinformatics*, UCRL-VG-135612, 97-ERD-033.

Critchlow, T., *DataFoundry Web Pages*, located at http://www.llnl.gov/CASC/datafoundry/, UCRL-MI-132541, 97-ERD-033.

Critchlow, T., K. Fidelis, M. Ganesh, R. Musick, T. Slezak, "Information management for scientific data," submitted to *ITAB Information Technology and Applications in Biotechnology*, UCRL-JC-133640, 97-ERD-033.

Critchlow, T., R. Musick, *DataFoundry Overview for Collaborators*, UCRL-MI-132993, 97-ERD-033.

Critchlow, T., R. Musick, T. Slezak, "Experiences using a metadata based integration infrastructure," submitted to *Biomolecular Informatics*, UCRL-JC-134854, 97-ERD-033.

Cynn, H., and C. S. Yoo, "Elastic constants of Ta measured using a diamond anvil cell and stress and angle resolved x-ray diffraction," AIRAPT-17, **146**, UCRL-JC- 903710, 98-ERD-059.

Cynn, H., and C. S. Yoo, "Equation of state of tantalum to 174 GPa," *Phys. Rev. B*, **59**, 8526, UCRL-JC-130367, 98-ERD-059.

De Breuck, C., M. S. Brotherton, H. D. Tran, W. van Breugel, H. J. A. Röttgering, "Discovery of an Ultra-Steep Spectrum, Highly Polarized Red Quasar at z = 1.462," *The Astronom. J.*, **116**, 13, UCRL-JC-129737, 98-ERI-005.

de Supinski, B., and J. May, "Benchmarking Pthreads Performance," *Proc. 1999 International Conference on Parallel and Distributed Techniques and Applications*, UCRL-JC-133263, 99-ERD-009.

De Yoreo J. J., C. Orme, H. Teng, P. Dove, "Physical controls on crystal growth during biomineralization," *Association for Crystallization Technology*, UCRL-JC-128976abs, 97-LW-069.

De Yoreo, J. J., et al., "Characterization of optical performance and defect structure of rapidly grown crystals of KDP and DKDP," *American Conference on Crystal Growth West*, UCRL-JC-130623abs, 97-ERD-098.

De Yoreo, J. J., "From small molecules to macromolecules: assessing the trends in surface dynamics," *AACGE-11*, UCRL-JC-135057abs, 97-LW-069.

Demos, S. G., et al., "Temperature and spectral investigation of bulk KDP below damage using 355nm laser irradiation," *SPIE Proc. 29th Annual Boulder Damage Conference*, **3244**, 223, UCRL-JC-128357, 97-ERD-098.

Demos, S. G., M. Staggs, M. Yan, H. B. Radousky, J. J. De Yoreo, Microscopic fluorescence imaging of bulk defect clusters in KH_2PO_4 crystals, *Opt. Lett.*, **24**, 268, UCRL-JC-131085, 97-ERD-098.

Demos, S. G., M. Staggs, M. Yan, H. B. Radousky, J. J. De Yoreo, "Investigation of optically active defect clusters in KH_2PO_4 under laser photoexcitation," *J. Appl. Phys.*, **85**, 3988, UCRL-JC-132646, 97-ERD-098.

Demos, S. G., M. Yan, G. Staggs, J. J. De Yoreo, H. B. Radousky, "Raman scattering investigation of KH_2PO_4 subsequent to high fluence laser irradiation," *Appl. Phys. Lett.*, **72**, 2367, UCRL-JC-129340, 97-ERD-098.

Demos, S. G., Staggs, M. Yan, H. B. Radousky, J. J. De Yoreo, "Observation of photo-excited emission clusters in the bulk of KDP and laser conditioning under 355-nm irradiation," *SPIE*, **3578**, 509, UCRL-JC-131411, 97-ERD-098.

Diaz de la Rubia, T., M. J. Caturla, M. Fluss, *Dimensional Stability and Microstructure Evolution in Irradiated Systems with Complex Kinetics*, UCRL-ID-136235, 98-ERD-028.

Dinh, L. N., M. A. Schildbach, M. Balooch, W. McLean II, "Pulsed laser deposition of ZnO nanocluster films by Cu-vapor laser," *J. Appl. Phys.*, **86**, 1149, UCRL-JC-132913, 98-LW-006.

Dinh, L. N., W. McLean, II, M. A. Schildbach, M. Balooch, "Synthesis and Characterization of Si/Cs/O nanocluster thin film with negative electron affinity," *Phys. Rev. B.*, **59**, 15513, UCRL-JC-130945, 98-LW-006.

Ditmire, T., J. Zweiback, V. P. Yanovsky, T. E. Cowan, G. Hays, K. B. Wharton, "Nuclear Fusion from Explosions of Femtosecond Laser Heated Clusters," *Nature*, **398**, 492, UCRL-JC-135040, 99-ERD-036.

Divine, K. K., J. L. Lewis, P. G. Grant, G. Bench, "Quantitative Particle Induced X-ray Emission Imaging of Rat Olfactory Epithelium Applied to the Permeability of Rat Epithelium to Inhaled Aluminum," *Chemical Research in Toxicology*, **12**, 575-581, UCRL-JC-130665, 98-ERI-004.

Divine, K. K., J. L. Lewis, P. G. Grant, G. Bench, "Quantitative Particle Induced X-ray Emission Imaging of Rat Olfactory Epithelium applied to the Permeability of Rat Epithelium to Inhaled Aluminum," *Proc. 216 American Chemical Society Meeting*, **1**, Toxi 66, UCRL-JC-130665-abs., 98-ERI-004.

Duchaineau, M. A., "Prepare, Browse and Select for Terascale Visualization and Analysis," invited presentations at LBNL NERSC and UC Davis CIPIC, UCRL-MI-134356, 99-ERI-009.

Duffy, P. B., and K. Caldeira, "Sensitivity of Simulated Salinities in a Three-Dimensional Ocean General Circulation Model to Vertical Mixing of Destabilizing Surface Fluxes," *Climate Dynamics*, **15**, 81–88, UCRL-JC-129901, 99-SI-001.

Duffy, P. B., M. Eby, A. J. Weaver, "Effects of Sinking of Salt Rejected During Formation of Sea Ice on Results of a Global Ocean-Atmosphere-Sea Ice Climate Model," *Geophys. Res. Lett.*, **26**, 1739–1742, UCRL-JC-131721. 99-SI-001.

Duffy, P., J. Bell, C. Covey, L. Sloan, *Effect of flux adjustments on temperature variability in climate models*, UCRL-JC-134153abs, 99-SI-001.

Dunn, J., A. L. Osterheld, Y. Li, J. Nilsen, V. N. Shlyaptsev, "Transient collisional excitation x-ray lasers with 1 ps tabletop drivers," accepted by *J. Selected Topics in Quant. Electron.*, UCRL-JC- 136568, 97-ERD-105.

Dunn, J., et al. "Demonstration of x-ray amplification in transient gain nickel-like palladium scheme," *Phys. Rev. Lett.*, **80**, 2825, UCRL-JC-128707, 97-ERD-105.

Dunn, J., et al. "Tabletop transient collisional excitation x-ray lasers," *SPIE Proceedings*, **3776**, in press, UCRL-JC-136567, 97-ERD-105.

Dunn, J., et al., "High gain x-ray lasers pumped by transient collisional excitation," *AIP Conference Proceedings*, **443**, 106, UCRL-JC-130019, 97-ERD-105.

Dunn, J., et al., "Progress in table-top transient collisional excitation x-ray lasers at LLNL," *IOP Conference Proceedings*, **159**, 51, UCRL-JC-133238, 97-ERD-105.

Dunn, J., et al., *Determination of transient gain lifetime for a 1-ps driven nickellike palladium 14.7 nm x-ray laser*, Internal Report, UCRL-JC-131413, 97-ERD-105.

Dunn, J., J. R. Hunter, B. O. Sellick, Y. Li, "Reflection echelon optic for traveling wave, transient gain soft x-ray laser," submitted to *Appl. Optics*, UCRL-JC-136566, 97-ERD-105.

Dunn, J., Y. Li, A. L. Osterheld, J. Nilsen, J. R. Hunter, V. N. Shlyaptsev, "Gain saturation regime for laser-driven tabletop, transient, Ni-like ion x-ray lasers," submitted to *Phys. Rev. Lett.*, UCRL-JC-136566, 97-ERD-105.

Dunn, J., Y. Li, J. Nilsen, V. N. Shlyaptsev, A. L. Osterheld, "Demonstration of transient gain x-ray lasers near 20 nm for nickellike Y, Zr, Nb, and Mo," *Opt. Lett.*, **24**, 101, UCRL-JC-132041, 97-ERD-105.

Eastman, R. G., et al., "Laboratory Measurements for Supernovae Expansion Opacities," UCRL-JC-904193, 99-ERD-043.

Elmer, J., J. Klingmann, M. Mugge, K. van Bibber, et al., "Accelerator Structure R&D for Linear Colliders," *Proc. 1999 Particle Accelerator Conference*, New York, 1999, **5**, 3423, UCRL-JC-136456, 99-ERD-055.

Emanuel M., J. Skidmore, N. Carlson, "High efficiency AlGaAs based laser diode at 808 nm with large transverse spot size," *IEEE Photon. Tech. Lett.*, UCRL-JC-124003. 97-SI-014.

Erskine, D. J., and J. Ge, "Novel Interferometer Spectrometer for Sensitive Stellar Radial Velocimetry," submitted to *Astr. Soc. Pacific*, UCRL-JC-134314, 98-ERD-054.

Erzberger, J. P., and D. M. Wilson III, "The role of Mg_{2+} and specific amino acid residues in the catalytic reaction of the major human abasic endonuclease," *J. Mol. Biol.*, **290**, 447–457, UCRL-JC-132629, 97-ERD-002.

Erzberger, J., D. Barsky, O. Scharer, M. Colvin, D. Wilson, "Elements in abasic site recognition by the major human and *Escherichia coli* apurinic/apyrimidinic endonucleases," *Nucleic Acids Res.*, **26**, 2771–2778, UCRL-JC-130481, 97-ERD-002.

Farley, D. R., et al., "Radiative Jet Experiments of Astrophysical Interest Using Intense Lasers," *Phys. Rev. Lett.*, **83**, 1982, UCRL-JC-133046, 97-ERD-022.

Feit, M. D., A. M. Komashko, A. M. Rubenchik, J. Larsen, "Modeling of pressure evolution produced by ultrashort laser pulses," *AIRAPT-17*, UCRL-JC-133578, 97-LW-074.

Feit, M. D., A. M. Rubenchik, F. Y. Genin, S. Schwartz, L. M. Sheehan, "Extrapolation of damage test data to predict performance of large area NIF optics at 355 nm," *Laser Induced Damage in Optical Materials: 1998*," SPIE **3578,** 226, UCRL-ID-131222, 98-ERD-063.

Feit, M. D., B. C. Stuart, A. M. Rubenchik, M. D. Perry, L. B. Da Silva, J. Neev, "Ultrashort laser pulse ablation of hard tissue," *OSA Trends in Optics and Photonics*, **17**, 173, UCRL-JC-129002, 97-LW-074.

Fellers, R. S., D. Barsky, F. Gygi, M. E. Colvin, "An ab initio study of DNA base pair hydrogen bonding: a comparison of plane-wave versus Gaussian-type function methods," *Chem. Phys. Lett.*, in press, UCRL-JC-134815, 98-SI-008.

Felton, J. S., M. G. Knize, F. T. Hatch, M. J. Tanga, M. E. Colvin, "Heterocyclic amine formation and the impact of structure on their mutagenicity," *Cancer Lett.*, **143**, 127–134, UCRL-JC-132719, 98-SI-008.

Fodor, I., P. Duffy, C. Kamath, C. Baldwin, *Effect of missing data on the apparent trend in the Earth's surface temperature since 1860*, UCRL-JC-135586abs, 99-SI-001.

Fournier, K., M. Cohen, M. May, W. Goldstein, "Radiative Cooling Rate and Charge State Distribution for Argon in a Low Density Plasma," *Atomic Data and Nuclear Data Tables*, UCRL-JC-129529, 97-ERD-057.

Fournier, K., M. Cohen, W. Goldstein, "Dielectronic Recombination Rates in H-like Ar^{17+} to Ne-like Ar^{8+}," *Phys. Rev. A,* **56**, 4715, UCRL-JC-127789, 97-ERD-057.

Fournier, K., M. May, D. Pacella, B. Gregory, M. Finkenthal, W. Finkenthal, "Calculated Radiative Power Losses from Mid- and High-Z Impurities in Tokamak Plasmas," *AIP Conference Proc.*, **443**, 73, UCRL-JC-130183, 97-ERD-057.

Froula, D. and P. Young, *Sonoluminescence for the Undergraduate Laboratory*, UCRL-JC-129336. 98-ERD-081.

Galli, G., A. Catellani, F. Gygi, "Wetting silicon carbide with nitrogen: a theoretical study," *Phys. Rev. Lett.*, **83**, 2006, UCRL-JC-133955, 98-SI-008.

Galli, G., F. Gygi, A. Catellani, "Quantum mechanical simulations of micro-fracture in a complex material," *Phys. Rev. Lett.*, **82**, 3476, UCRL-JC-132096, 98-SI-008.

Garcia, M., *The 2D Electric Field above a Planar Sequence of independent Strip Electrodes*, UCRL-JC-136248, 99-ERD-016.

Garrett, P. E., et al., "^{92}Mo(n,xnypz\alpha) reactions studied with GEANIE at LANSCE/WNR, *Bull. Am. Phys. Soc.*, **44**, (5), 63, UCRL-JC-134769abs, 98-LW-051.

Gavel, D. T., B. Bauman, E. W. Campbell, C. Carrano, S. Olivier, "Practical comparison of phase diversity to interferometry in measuring the aberrations in an adaptive optics system," *Proc. SPIE*, **3762**, 1999, 266–268, UCRL-JC-134805, 98-ERD-036.

Gavel, D., H. Friedman, B. Bauman, "Lick sodium laser guide star: performance during the 1998 LGS observing campaign," *Proc. SPIE*, **3762**, 20–27, UCRL-JC-135002, 97-ERD-037.

Ge, J, et al. "Next generation ground-based very high resolution optical and infrared spectrographs for extra-solar planet searches," (1999) *BAAS*, **194**, 903, UCRL-JC-133965abs, 99-FS-004.

Ge, J, et al., "Adaptive optics high resolution spectroscopy: present and future direction," (1999), *SPIE*, **3762**, 174, UCRL-JC-132672, 99-FS-004.

Ge, J., D. Ciarlo, P. Kuzmenko, B. Macintosh, C. Alcock, K. Cook, "Etched silicon grating for next generation space telescope (NGST)," (1999), *NGST Science and Technology Exposition*, UCRL-JC-135357, 99-FS-004.

Ge, J., et al. "The First Light of the World's First Silicon Grisms," (2000), *BAAS,* **195,** UCRL-JC-136251abs, 99-FS-004

Ge, J., et al., "Adaptive optics high resolution spectroscopy: present and future direction," (1999), *IMAGING THE UNIVERSE IN THREE DIMENSIONS: Astrophysics with Advanced Multi-wavelength Imaging Devices*, UCRL-JC-132672abs, 99-FS-004.

Genin, F. Y., J. H. Campbell, A. Salleo, "Nano-second rear surface laser drilling of fused silica in the IR and the UV," *Gordon Research Conference on Laser Interactions with Materials*, UCRL-MI-130967, 98-ERD-063.

Gibbard, S. G., et al., "Titan: High Resolution Speckle Images from the Keck Telescope," *Icarus*, **139**, 189, UCRL-JC-128848, 99-ERI-003.

Goldstein, P., and D. Dodge, "Fast and Accurate Depth and Source Mechanism Estimation Using P-Waveform Modeling: A Tool for Special Event Analysis, Event Screening, and Regional Calibration," *Geophys. Res. Lett.* **26**, 2569–2572, UCRL-JC-132139, 99-ERD-034.

Govindasamy, B., M. F. Wehner, C. R. Mechoso, P. B. Duffy, "The Influence of a Land Surface Scheme on Simulated Climate by LLNL/UCLA AGCM," *Global and Planetary Change*, **20**, 67–86, UCRL-JC-130941. 99-SI-001.

Grossman, A. S., and C. R. Molenkamp, *Atmospheric Test Models and Numerical Experiments for the Simulation of the Global Distribution of Weather Data Transponders*, UCRL-ID-135526, 99-ERD-061.

Grossman, A. S., and C. R. Molenkamp, *Atmospheric Test Models and Numerical Experiments for the Simulation of the Global Distribution of Weather Data Transponders II: Vertical Motion of the Transponders*, UCRL-ID-135526 Pt. II, 99-ERD-061.

Gu, M. et al., "Laboratory Measurements of Resonant Contributions to Fe XXIV Line Emission," *Physica Scripta*, UCRL-JC-132214, 97-ERD-057.

Guilderson, T. P., D. P. Schrag, "Abrupt Shift in Subsurface Temperatures in the Eastern Tropical Pacific Associated with Recent changes in El Niño," *Science*, **281**, 240, UCRL-JC-133997, 98-ERI-002.

Guilderson, T. P., D. P. Schrag, J. Southon, M. Kashgarian, "High Resolution Coral D^{14}C Records from the Tropical and Sub-tropical Pacific: Reconstructing Ocean Dynamics," meeting abstract, UCRL-JC-135321abs, 98-ERI-002.

Guilderson, T. P., K. Caldiera, P. B. Duffy, "Radiocarbon as a diagnostic tracer in ocean and carbon cycle modeling," *Global Biogeochemical Cycles*, accepted for future publication, UCRL-JC-134783, 98-ERI-002.

Hadjiconstantinou, N., *Estimating the Maximum Splat Diameter of a Solidifying Droplet*, UCRL-JC-133712, 98-ERD-085.

Hagmann, C., S. Chang, P. Sikivie, "Axions from string decay," *Nucl. Phys. Proc. Suppl.*, **72**, 81, UCRL-JC-131307, 99-ERD-045.

Hakem, N., P. G. Allen, E. R. Sylwester, *Sorption and Diffusion Studies of Pu(IV) and PU(IV)-EDTA onto and through Hanford Soil*, UCRL-JC-135799, 98-ERD-094.

Hamza, A. V., T. Schenkel, A. V. Barnes, "Dependence of Cluster Ion Emission from Uranium Oxide Surfaces on the Charge State of the Incident Slow Highly Charged Ion," *European Phys. J. D*, **6**, 83, UCRL-JC-131620, 97-ERD-102.

Hansen, C. T., S. C. Wilks, P. E. Young, "Spectral evidence for collisionless absorption in sub-picosecond laser-solid interactions," submitted to *Phys. Rev. Lett.*, UCRL-JC-134197, 99-ERI-007.

Harrison, T. M., A. Yin, F. J., Ryerson, "Orographic evolution of the Himalayan and Tibetan Plateau," in *Tectonic Boundary Conditions for Climate Reconstructions* (ed. T. Crowley and K. C. Burke), Oxford University Press, *Oxford Monographs on Geology and Geophysics*, **39**, 39–72, UCRL-JC-126356. 97-ERI-003.

Hartemann, F. V., "Stochastic electron gas theory of coherence in Compton scattering," submitted to *Phys. Rev. E*, UCRL-JC-133229, 99-ERI-008.

Hartemann, F. V., and J. R. Van Meter, "Vacuum propagation of a near-critical electromagnetic wave," submitted to *Phys. Rev. Lett.*, UCRL-JC-135083, 99-ERI-008.

Hartemann, F. V., et al., "High-field electron-photon interactions," *Proc. Lasers '98*, UCRL-JC-133349, 99-ERI-008.

Hartemann, F. V., et al., "RF characterization of a tunable, high-gradient, X-band photoinjector," *IEEE Trans. Plasma Sci.*, UCRL-JC-134498, 99-ERI-008.

Hartemann, F. V., et al., "The chirped-pulse inverse free-electron laser: a high-gradient vacuum laser accelerator," *Phys. Plasmas*, **6**, 4104, UCRL-JC-134073, 99-ERI-008.

Hartemann, F. V., et al., "Ultrahigh-intensity holographic electron beam modulation and coherent harmonic generation," submitted to *Phys. Rev. E*, UCRL-JC-134907, 99-ERI-008.

Hartley, J. H., et al., "Positron annihilation studies of fatigue in 304 stainless steel," *Applied Surface Science*, **149**, 204, UCRL-JC-126768, 99-ERD-047.

Hartley, J. H., R. H. Howell, P.A. Sterne, "Bulk Defect Analysis with a High-Energy Positron Beam," *Applications of Accelerators in Research and Industry '98*, J. Duggan, ed., North Holland, Amsterdam, to be published, UCRL-JC-131480, 99-ERD-047.

Hartzell, S., S. Harmsen, A. Frankel, S. Larsen, "Calculation of broadband time histories for ground motion; validation using strong-ground motion from the 1994 Northridge Earthquake," *Bull. Seismological Society of America*, **89**, in press, UCRL-JC-134317, 98-LW-028.

Hatch, F. T., F. C. Lightstone, M. E. Colvin, "QSAR of Flavonoids for Inhibition of Heterocyclic Amine Mutagenicity," submitted to *Environmental and Molecular Mutagenesis*, UCRL-JC-134708, 98-SI-008.

Hatchett, S. P., Electron, Photon and Ion Beams from the Relativistic Interaction of Petawatt Laser Pulses with Solid Targets, submitted to *Bull. Am. Phys. Soc.*, UCRL-JC-904898, 99-ERD-063.

Hattass, M., et al., "Charge Equilibration Time in Solids," *Phys. Rev. Lett.*, **82**, 4795, UCRL-JC-133795, 97-ERD-102.

Heeter, R. F., et al. "X-ray photoionized plasmas in the laboratory," UCRL- JC-137022, 99-ERD-044.

Heeter, R. F., *X-ray photoionized plasma in the laboratory*, a viewgraph presentation, UCRL-VG-137493, 99-ERD-044.

Heller, A., "From Dinosaur Bones to Software, Gamma Rays Protect Property," *Science and Technology Review* (October 1999), UCRL-52000-99-10, 99-ERD-070.

Hilgenfeldt, S., D. Lohse, W. Moss, "Water-Temperature—Dependence of Single Bubble Sonoluminescence," *Phys. Rev. Lett.*, **80**, 1332, UCRL-JC-131347. 98-ERD-081.

Hill, D. N., et al., "The SSPX experimental plan," *Bull. Amer. Phys. Soc.,* **43**, 1769, UCRL-JC-131418abs, 97-SI-009.

Hoffert, M. I., K. Caldeira, C. Covey, P. B. Duffy, B. Santer, "Solar variability and the Earth's climate," *Nature*, in press, UCRL-JC-134549, 99-SI-001.

Hooper, E. B., et al., "Overview of SSPX Physics," *Bull. Amer. Phys. Soc.*, **43**, 1768, UCRL-JC-131418abs, 97-SI-009.

Horn, J. M., T. C. Legler, A. M. Happel, "Optimization of TCE Degradation by Methylosinus Strains," *Abstracts of the 97th General Meeting of the American Society for Microbiology*, **Q102**, 472, UCRL- JC-132817, 97-ERD-030.

Howell, R. H., P. A. Sterne, J. Hartley, T. E. Cowan, "High energy beam lifetimes analysis," *Applied Surface Science*, **149**, 103, UCRL-JC-126786, 99-ERD-047.

Howell, R. H., P. Asoka-Kumar, W. Stoeffl, J. H. Hartley, P. A. Sterne, "Materials Analysis using Positron Beam Lifetime Spectroscopy," *Proc. International Workshop on Advanced Techniques of Positron Beam Generation and Control, JAERI*, **93**, UCRL-JC-132819, 99-ERD-047.

Hunt, A. W., et al., "In-flight Annihilation of Fast Positrons: Spatial Sampling of Crystal Electrons," accepted by *Nature*, UCRL-JC-134796, 99-ERD-047.

Huser, T., M. Yan, C. Collison, L. J. Rothberg, B. R. Hsieh, "Microscopic imaging of photoluminescence from PPV related polymers," *American Physical Society March 1999 Meeting*, UCRL-JC-133153abs, 97-ERD-013.

Hutcheon, I. D, A. J. R. Kent, R. J. Ryerson, "The Temperature of Formation of Carbonate Minerals in Martian Meteorite ALH84001: Constraints from Cation Diffusion," *EOS (Transactions of the American Geophysical Union)*, **79**, F967, UCRC-JC-131679abs, 98-ERD-042.

Hyde, R. A., "Eyeglass: 1. Very Large Aperture Diffractive Telescopes," *Appl. Optics* **38**, 4198, UCRL-JC-131624, 97-ERD-060.

Iota, V., C. S. Yoo, H. Cynn, "Quartzlike Carbon Dioxide: An Optically Nonlinear Extended Solid at High Pressures and Temperatures," *Science*, **283**, 1510, UCRL-JC- 903844, 98-ERD-059.

Ishikawa, M., L. Wood, J. Kirkland, K. Carpenter, "Gamma Watermarking of High-Value Specimens for Robust Establishment of Provenance," *J. Vertebrate Paleontology*, **19**, 54A, UCRL-JC-133899abs, 99-ERD-070.

Joy, K. I., M. A. Duchaineau, "Boundary Determination for Trivariate Solids," *Pacific Graphics '99 Conference*, UCRL-JC-134275, 99-ERI-009.

Kahn, S., et al., "Laboratory X-Ray Spectroscopy Experiments in Support of NASA's X-Ray Satellite Missions," *Proc. NASA Workshop on Laboratory Space Science*, UCRL-JC-130129, 97-ERD-057.

Kallman, J. S., E. Ashby, D. Ciarlo, G. Thomas, *Novel Ultrasound Scintillator*, UCRL-ID-133154, 98-LW-035.

Kane, J. O., et al., "Scaling Supernova Hydrodynamics to the Laboratory," *Physics of Plasmas*, **6**, 2065, UCRL-JC-132438, 97-ERD-022.

Kane, S., J. Horn, T. Legler, A. Happel, "Expression of soluble methane monooxygenase (sMMO) in *Methylosinus trichosporium* OB3b and *M. sporium*," *Abstracts of the 99th General Meeting of the American Society for Microbiology,* **Q340**, 599, UCRL-JC-132782, 97-ERD-030.

Kartz, M. W., et al., "High Resolution Wavefront Control of High-power Laser Systems," *Proc. Workshop on Adaptive Optics for Industry and Medicine*, Durham, England, July 12–16, 1999, UCRL-JC-235980, 98-ERD-061.

Kent, A. J. R., I. D. Hutcheon, F. J. Ryerson, D. L. Phinney, "The temperature of formation of carbonate in Martian meteorite ALH84001: Constraints from cation diffusion," *Lunar and Planetary Science Conference*, **30**, 38, UCRL-JC-133070, 98-ERD-042.

Kim, B.-M., et al., "Plasma luminescence feedback control system for precise ultrashort pulse laser tissue ablation," *SPIE*, **3255**, 92, UCRL-JC-130596, 97-LW-074.

Kim, B.-M., et al., "Shockwave generation on biological tissue using ultrashort laser pulses," *OSA Annual Meeting*, UCRL-JC-133977abs, 97-LW-074.

Kim, B.-M., M. D. Feit, A. M. Rubenchik, C. B. Darrow, L. B. Da Silva, "Medical applications of ultrashort pulse lasers," *Laser Medicine and Biophysics*, UCRL-JC-133470abs, 97-LW-074.

Kim, B.-M., M. D. Feit, A. M. Rubenchik, D. M. Gold, B. C. Stuart, L. B. Da Silva, "Ultrashort pulse laser ablation of biological tissue," *SPIE*, **3254**, 203, UCRL-JC-130595, 97-LW-074.

Kim, B.-M., M. D. Feit, A. M. Rubenchik, E. J. Joslin, L. B. Da Silva, "Optimal ultrashort pulse laser parameters for effective hard tissue ablation," *BiOS'99*, UCRL-JC-131437abs, 97-LW-074.

Kim, B.-M., M. D. Feit, A. M. Rubenchik, L. B. Da Silva, "Medical applications of ultrashort pulse lasers," *PR/CLEO'99*, **1**, 43, UCRL-JC-133470. 97-LW-074.

Kim, B.-M., N. A. Gentile, K. B. Trauner, R. A. London, "Three Dimensional Monte Carlo Modeling of Laser-Tissue Interaction," *Proc. SPIE*, **3601**, 320, UCRL-JC-133637, 97-ERD-056.

King, W. E., M. Kumar, A. J. Schwartz, "Triple Junction Distributions in Polycrystals," *TMS*, UCRL-JC-134234, 98-ERD-080.

King, W. E., M. Kumar, A. J. Schwartz, Evolution of the Triple Junction Distribution in Polycrystals with Sequential Thermomechanical Processing, *MRS Proceedings*, UCRL-JC-134726abs, 98-ERD-080.

Kinion, D., and K. van Bibber, "Large scale US dark matter search," *Nucl. Phys. Proc. Suppl.*, **72**, 117, UCRL-JC-131603, 99-ERD-045.

Klingman, J., J. Elmer, M. Mugge, K. van Bibber, et al., "Fabrication of DDS-3, an 11.4 GHz Damped-Detuned Structure," *Proc. 1999 Particle Accelerator Conference*, New York, 1999, **2**, 777, UCRL-JC-13351, 99-ERD-055.

Kohn M. J., L. R. Riciputi, D. Stakes, D. L. Orange, "Sulfur isotope variability in biogenic pyrite: Reflections of heterogeneous bacterial colonization?," *American Mineralogist*, **83**, 1454–1468, UCRL-JC-129907, 97-ERI-003.

Kohn, M. J., "Why Most 'Dry' Rocks Should Cool 'Wet,'" *American Mineralogist*, **84**, 570–580, UCRL-JC-127725, 97-ERI-003.

Kohn, M. J., and J. W. Valley, "Effects of cation substitutions in garnet and pyroxene on equilibrium oxygen isotope fractionations, *J. Metamorphic Geol*, **16**, 625–639, UCRL-JC-130556, 97-ERI-003.

Kohn, M. J., and J. W. Valley, "Oxygen isotope geochemistry of the amphiboles: Isotope effects of cation substitutions in minerals, "*Geochim. Cosmochim. Acta*, **62**, 1947–1958, UCRL-JC-128107, 97-ERI-003.

Kohn, M. J., M. J. Schoeninger, W. W. Barker, "Altered states: Effects of diagenesis on fossil tooth chemistry," *Geochimica et Cosmochimica Acta*, **83**, 2737–2747, UCRL-JC-128120, 97-ERI-003.

Komashko, A. M., M. D. Feit, A. M. Rubenchik, M. D. Perry, P. S. Banks, "Simulation of material removal efficiency with ultrashort laser pulses," *Conference on Laser Ablation*, UCRL-JC-133744, 97-LW-074.

Krulewich, D., and H. Hauschildt, "Spatial Frequency Domain Error Budget," *Proc. American Society for Precision Engineering 1998 Annual Meeting*, **18**, 49–52, UCRL-JC-131681, 97-ERD-084.

Kumar, M., A. J. Schwartz, W. E. King, "Modifications to the Microstructural Topology in FCC Materials through Thermomechanical Processing," *Proc. Twelfth International Conference on Textures of Materials* (J. Szpunar, Ed.), Canadian National Research Council Press (1999), 180, UCRL-JC-135761, 98-ERD-080.

Kumar, M., A. J. Schwartz, W. E. King, "The Role of Twinning in the Optimization of the Grain Boundary Character Distribution," *Advances in Twinning* (S. Ankem and C. S. Pande, eds.), **13**, UCRL-JC-131664, 98-ERD-080.

Kumar, M., W. E. King, A. J. Schwartz, "Microstructural Evolution in FCC Materials During Sequential Thermomechanical Processing—Implications for Grain Boundary Engineering," *MRS Proceedings*, UCRL-JC-134724abs, 98-ERD-080.

Kumar, M., W. E. King, A. J. Schwartz, "Modifications to the Microstructural Topology in FCC Materials through Thermomechanical Processing," *Acta Materialia,* UCRL-JC-135761, 98-ERD-080.

Labaune, C., et al., "Enhanced forward scattering in the case of two crossed laser beams interacting with a plasma," UCRL-JC-135653, 99-ERI-018.

Land, T. A., J. J. De Yoreo, T. L. Martin, G. T. Palmore, "A comparison of growth hillock structure and step dynamics on KDP {100} and {101} surfaces using atomic force microscopy," *Krystallografia*, **44**, 655, UCRL-JC-132645, 97-ERD-098.

Land, T. A., T. L. Martin, S. Potapenko, G. T. Palmore, J. J. De Yoreo, "Recovery of crystal surfaces from impurity poisoning," *Nature*, **399**, 442, UCRL-JC-133063, 97-ERD-098.

Landahl, E. C., and F. V. Hartemann, Chirped pulse Compton backscattering at relativistic intensities," UCRL-JC-132047, 99-ERI-008.

Langdon, A. B., et al., "Models for ultra-intense short pulse laser beam propagation in underdense plasmas," submitted to *Bull. Am. Phys. Soc.*, UCRL-JC-904892, 99-ERD-063.

Larsen, S. C., J. Grieger, "Elastic modeling initiative: 3-D computational modeling," *Proc. Soc. Expl. Geophys. Confer.*, **68**, 1803–1806, UCRL-JC-130224, 98-LW-028.

Larsen, S. C., M. Antolik, D. Dreger, C. Stidham, B. Romanowicz, "3-D simulations of scenario earthquakes in the San Francisco Bay Area," *EOS Trans.*, **78**, 437, UCRL-JC-128458, 98-LW-028.

Larson, M. C., et al., "Multiwavelength VCSEL transmitter for WDM parallel optical fiber interconnects," *12th Annual Meeting of the Institute for Electrical and Electronics Engineers Lasers and Electro-Optics*, San Francisco, CA, November 8-11, 1999, UCRL-JC-134719-rev. 1, 98-ERD-057.

Lasinski, B. F., A. B. Langdon, S. P. Hatchett, M. H. Key, M. Tabak, "Particle-in-cell simulations of ultra intense laser pulses propagating through overdense plasma for fast-ignitor and radiography applications," *Phys. of Plasmas*, **6**, 2041, UCRL-JC-131245, 99-ERD-063.

Lasinski, B. F., et al., "Parallel PIC simulations of ultra-high intensity laser plasma interactions," submitted to *Bull. Am. Phys. Soc.*, UCRL-JC-904879, 99-ERD-063.

Le Sage, G. P., T. E. Cowan, R. B. Fiorito, D. W. Rule, "Transverse phase space mapping of relativistic electron beams using Optical Transition Radiation," *Phys. Rev. ST Accel. Beams*, **2**, 122801, UCRL-JC-135566, 97-SI-001.

Lee, B. I., and D. M. Wilson III, "The RAD2 domain of human exonuclease 1 exhibits 3' to 5' exonuclease and flap structure-specific endonuclease activities," *J. Biol. Chem.*, in press, UCRL-JC-13567, 97-ERD-002.

Lee, B.-I., M. Shannon, L. Stubbs, D. M. Wilson III, "Expression specificity of the mouse exonuclease 1 (mExo1) gene," *Nucleic Acids Res.,* **27**, 4114–4120, UCRL-JC-134081, 97-ERD-002.

Lehnert, M., et al., "Hubble Space Telescope Imaging of the Host Galaxies of High-Redshift Radio-loud Quasars," *Astroph. J. Suppl.*, **124**, 11, UCRL-JC- 235600, 98-ERI-005.

Lemoff, A. V., A. P. Lee, R. R. Miles, C. F. McConaghy, "An AC Magnetohydrodynamic Micropump: Towards a True Integrated Microfluidic System," *Transducers'99*, **2**, 1126–1129, UCRL-JC-132466, 98-ERD-089.

Lepson, J. K., P. Beiersdorfer, G. V. Brown, D. A. Liedahl, C. W. Mauche, S. B. Utter, S. M. Kahn, "Cataloguing the Lines from the Intermediate Charge States of Iron, Fe VII through Fe XXIV, in the Extreme Ultraviolet Below 150 Angstroms," *Bull. Amer. Astro. Soc.* **31**, 706, UCRL-JC-133800abs, 99-LW-053.

Li, Y., et al., "Wavelengths of the Ni-like 4d 1S0 - 4p 1P1 x-ray laser line," *Phys. Rev. A*, **58**, R2668, UCRL-JC-130928, 97-ERD-105.

Li, Y., J. Dunn, J. Nilsen, A. L. Osterheld, V. N. Shlyaptsev, "Near field imaging of a saturated table top x-ray laser," *SPIE proceedings*, **3776**, in press, UCRL-JC-134717, 97-ERD-105.

Liedahl, D. A., "Spectroscopy With the New Generation of X-ray Observatories," submitted to *Physica Scripta*, UCRL-JC-132424, 97-ERD-057.

Liedahl, D. A., "The X-Ray Properties of Photoionized Plasmas and Transient Plasmas," *X-Ray Spectroscopy in Astrophysics*, **189**, UCRL-JC-132453., 97-ERD-057.

Liedahl, D., et al., "A Synergistic Approach to Modeling X-Ray Spectra," *Proc. of the NASA Workshop on Laboratory Space Science*, UCRL-JC-131403, 97-ERD-057.

Logan, C. M., A. Schach von Wittenau, E. Alexis, "Effects of Back Shield Albedo on Imagery with a dpix FLashscan 20 Using 9-MV Bremsstrahlung Spectrum: Measurements and Monte Carlo Simulations," submitted to *Materials Evaluation*, UCRL-JC-136055, 99-ERD-015.

London, R. A., V. Esch, D. Papademetriou, "Numerical Simulations of a Diode Laser BPH Treatment System," *Proc. SPIE*, **3601**, 141, UCRL-JC-131237, 97-ERD-056.

Makarewicz, A. J., S. R. Visuri, R. A. London, "Modeling optically generated focused shock-waves," *Proc. SPIE*, **3601**, 207–211, UCRL-JC-132990, 98-LW-030.

Manaa, M. R., and L. E. Fried, "DFT and ab initio study of the unimolecular decomposition of the lowest singlet and triplet states of nitromethane," *J. Phys. Chem.*, **102**, 9884, UCRL-JC-130489, 97-ERD-101.

Manaa, M. R., and L. E. Fried, "Intersystem Crossings in Model Energetic Materials," accepted by *J. Phys. Chem.*, UCRL-JC-132787, 97-ERD-101.

Marcy, G. W., R. P. Butler, S. S. Vogt, D. Fischer, M. C. Liu, "Two new candidate planets in eccentric orbits," *Astrophys. J.*, **520**, 239–247, a UC Berkeley publication, collaborating on 98-ERD-036.

Marion II, J. E., and B.-M. Kim, "Medical applications of ultra-short pulse lasers," *BiOS'99*, 3616, UCRL-JC-133470-rev. 1, 97-LW-074.

Mattioli, M., "Experimental and Simulated Neon Spectra in the 10-nm Wavelength Region from Tokamak and Reversed Field Pinch Plasmas," *Phys. Rev. E*, **60**, 4760, UCRL-JC-134074, 97-ERD-057.

Matula, T., I. Hallaj, R. Cleveland, L. Crum, W. Moss, R. Roy, R., "The Acoustic Emissions from Single-Bubble Sonoluminescence," *J. Acoustic Soc. of America*, **103**, 1377, UCRL-JC-131348. 98-ERD-081.

May, J., and B. de Supinski, "Experience with Mixed MPI/Threaded Programming Models," *Proc. 1999 International Conference on Parallel and Distributed Techniques and Applications*, UCRL-JC-133213, 99-ERD-009.

May, M., et al., "Benchmarking Atomic Physics Models for MCF Plasma Physics Experiments," *Rev. Sci. Instrum.*, UCRL-JC-132593, 97-ERD-057.

McAninch, J. E., and T. F. Hamilton, *Measurement of plutonium and other actinides by accelerator mass spectrometry: a comparative assessment of competing techniques,* UCRL-ID-133118, 98-ERD-100.

McAninch, J. E., et al., "Plutonium measurements by accelerator mass spectrometry at LLNL," accepted for publication in *Nuc. Instr. & Meth. B* as part of the proceedings of the *8th International Conference on Accelerator Mass Spectrometry*, UCRL-JC-136204, 98-ERD-100.

McAninch, J. E., T. F. Hamilton, *Measurement of plutonium and other actinides by accelerator mass spectrometry: a comparative assessment of competing techniques*, UCRL-ID-133118, 98-ERD-100.

McCallen, D., A. Astaneh-Asl, S. Larsen, "Seismic studies of the San Francisco-Oakland Bay Bridge," *12th World Conference on Earthquake Engineering*, UCRL-JC-135386, 98-LW-028 and 99-ERD-057.

McWhirter, J., A. Noy, W. Siekhaus, M. Yan, "Observation of field enhancement and laser induced damage near surface defects in fused silica using evanescent wave microscopy," *American Physical Society March 1999 Meeting*, UCRL-JC-133155abs, 97-ERD-013.

Miller, W. O., *HOTDROP Operation Guidelines*, UCRL-MA-135167, 98-ERD-085.

Mirin, A. A., et al., "Very High Resolution Simulation of Compressible Turbulence," *SuperComputing'99 Conference,* UCRL-JC-134237, 99-ERI-009.

Molenkamp, C. R., and A. S. Grossman, *1999: Atmospheric Test Models and Numerical Experiments for the Simulation of the Global Distribution of Weather Data Transponders III: Horizontal Distributions.* LLNL Report UCRL-ID-135526 Pt. III, 99-ERD-061.

Moon, S. J., et al. "Characterization of a high-gain Ne-like Fe transient x-ray laser," *SPIE Proceedings*, **3776**, in press, UCRL-JC- 135728, 97-ERD-105.

Morse, J. D., and A. F. Jankowski, "Testing of Solid Oxide Fuel Cells for Micro to Macro Power Generation," submitted to *Proc. Electro Chem Soc.*, UCRL-JC-134198, 98-ERD-091.

Moss, W. C., et al., "Computed Optical Emission from a Sonoluminescing Bubble," *Phys. Rev. E*, **59**, 2986, UCRL-JC-131765. 98-ERD-081.

Moss, W. C., J. L. Levatin, A. Szeri, "All good oscillations must come to an end," submitted to *Science*, UCRL-JC-134371. 98-ERD-081.

Musick, R., K. Fidelis, T. Slezak, M. Thelen, *Advanced data exploration tools for bioinformatics*, UCRL-PROP-134462, 97-ERD-033.

Musick, R., *Supporting large scale computational science*, UCRL-ID-129903, 97-ERD-033.

Musick, R., T. Critchlow, "Practical lessons in supporting large scale computational data," submitted to *Sigmod Record*, UCRL-JC-135606, 97-ERD-033.

Nicholson, D. M. C., P. A. Sterne, J. C. Swihart, J. Tran, Y. Wang, "Electron and positron states in amorphous Ni0.4Pd0.4P0.2," accepted by *Modelling and Simulation in Materials Science and Engineering*, UCRL-JC-135778, 99-ERD-047.

Nieh, T. G., T. Mukai, C. T. Liu, J. Wadsworth, "Superplastic Behavior of a Zr–10Al–5Ti–17.9Cu–14.6Ni Metallic Glass in the Supercooled Liquid Region," *Scripta Materialia*, **40**, 1021–1027, 1999. UCRL-JC-236984, 99-LW-001.

Nikkel, D. J., A. A. Brown, J. Casey, "Modeling of Anisotropic Inelastic Behavior," *Engineering Research, Development, and Technology*, **6-1**, UCRL-JC-53868, 98-ERD-020.

Nilsen, J., et al., "Measuring the wavelengths of the Ni-like 4d 1S0 - 4p 1P1 x-ray laser line," *IOP Conference Proceedings*, **159**, 135, UCRL-JC-130946, 97-ERD-105.

Nilsen, J., J. Dunn, A. L. Osterheld, Y. Li, "Lasing on the self-photopumped nickel-like 4f 1P1 - 4d 1P1 x-ray transition," *Phys. Rev. A.*, **60**, R2677, UCRL-JC-134368, 97-ERD-105.

Nilsen, J., Y. Li, J. Dunn, A. L. Osterheld, "Modeling short-pulse-driven collisional x-ray lasers and other new schemes, *SPIE Proceedings*, **3776**, in press, UCRL-JC-132649, 97-ERD-105.

Nilsen, J., Y. Li, J. Dunn, A. L. Osterheld, "Progress in understanding the short pulse driven collisional x-ray lasers," *IOP Conference Proceedings*, **159**, 123, UCRL-JC-130948. 97-ERD-105.

Nitao, J. J., and W. E. Glassley, "Modeled porosity modification in the near-field environment due to coupled thermal-hydrological and geochemical processes," *Scientific Basis for Nuclear Waste Management XX*, UCRL-JC-131163, 98-SI-004.

Noy, A., C. Orme, M. McBride, J. De Yoreo, "Morphological Changes in Calcite Induced by Amino Acids: Emergence of Chirality," *Material Research Society*, December 1999, UCRL-JC-135308abs, 97-LW-069.

Oganessian, Y. T., et al., "Synthesis of Superheavy Nuclei in the Ca-48 + Pu-244 Reaction," *Phys. Rev. Lett.*, **83**, 3154, UCRL-JC-133388, 98-ERD-050.

Olivier, S. S., et al., "High-resolution wavefront control using liquid crystal spatial light modulators, *Proc. SPIE*, **3760**, UCRL-JC-134900, 98-ERD-061.

Olivier, S., et al., "Improved performance of the laser guide star adaptive optics system at Lick Observatory," *Proc. SPIE*, **3762**, 2–7, UCRL-JC-134956, 97-ERD-037.

Orme, C., H. Teng, P. Dove, J. De Yoreo, A. Hina, G. Nancollas, "In Situ Studies of Calcite and Brushite," *AACGE-11*, UCRL-JC-134022abs, 97-LW-069.

Osterheld, A. L., et al., "Modeling of Laser Produced Plasma and Z-Pinch X-ray Lasers," *IOP Conference Proceedings*, **159**, 353, UCRL-JC-130951, 97-ERD-105.

Osterheld, A. L., J. Dunn, V. N. Shlyaptsev, "Characterization of transient gain x-ray lasers," *IOP Conference Proceedings*, **159**, 131, UCRL-JC-133237, 97-ERD-105.

Owens, T. J., G. Zandt, "The implications of crustal property variations on models of Tibetan Plateau evolution," *Nature*, **387**, 37–43, UCRL-JC-126608, 97-ERI-003.

Pacella, D., et al., "Measurement of the Radiative Cooling Rate for Krypton and Argon and Their Profiles in the FTU Plasma," *Proc. 25th European Conference on Controlled Fusion and Plasma Physics*, UCRL-JC-130884, 97-ERD-057.

Park, H.-S., et al., "LOTIS: GRB follow-up observations at early time," *Astronomy & Astrophysics*, **577**, UCRL-JC-132114, 97-LW-019.

Pask, J. E., B. M. Klein, C. Y. Fong, P. A. Sterne, "Real-space local polynomial basis for solid-state electronic-structure calculations: a finite-element approach," *Phys. Rev, B*, **59**, 12352, UCRL-JC-132360, 99-ERD-047.

Patel, P. K., F. Patterson, D. F. Price, K. Widmann, S. C. Wilks, P. T. Springer, *Initial Experiments on the JanUSP Laser at Focal Intensities $>10^{21}$ W/cm^2*, UCRL-JC-134911, 99-ERD-049.

Patel, R. R., et al., "Compact, low-crosstalk, WDM filter elements for multimode ribbon fiber data links," *Electronic Components and Technology Conference*, San Diego, CA, June 1-4, 1999, UCRL-JC-132974, 98-ERD-057.

Patel, R. R., et al., "Multi-mode fiber coarse WDM grating router using broadband add/drop filters for wavelength re-use," *12th Annual Meeting of the Institute for Electrical and Electronics Engineers Lasers and Electro-Optics*, San Francisco, CA, November 8-11, 1999, UCRL-JC-134637, 98-ERD-057.

Patel, R. R., et al., "WDM filter modules in compact, low-cost plastic packages for byte-wide multimode fiber ribbon cable data links," *Electronic Lett.*, **35**, (10), 840–842, May 1999, UCRL-JC-132640, 98-ERD-057.

Patience, J., et al., "A high-resolution search for stellar companions to stars with planets," *Bull. Amer. Astronomical Soc.,* **193**, 97.08, UCLA publication collaborating on 98-ERD-036.

Patterson, F. G., J. Bonlie, D. Price, W. E. White, "Suppression of Parasitic Lasing in Large Aperture Ti:sapphire Laser Amplifiers," *Opt. Lett.* **24**, 963–965, UCRL-JC-133239, 99-ERD-049.

Patterson, F. G., J. Bonlie, D. Price, W. E. White, "$>10^{21}$ W/cm^2 Laser Based Upon Large Aperture Ti:sapphire Disk Amplifiers," *Post-Deadline CLEO 99*, UCRL-JC-134912abs, 99-ERD-049.

Patterson, F. G., J. Bonlie, D. Price, W. E. White, P. Springer, "Development of Large Aperture Ti:sapphire Disk Amplifiers for Chirped Pulse Amplification," presented at *Ultrafast Optics '99* in July 1999, Ascona, Switzerland, UCRL-JC-134915abs, 99-ERD-049.

Payne S., "Picosecond Nontadiative Processes in Neodymium-doped Crystals & Glasses: Mechanism for the Energy Gap Law," *TOPS ASSL 98*, UCRL-JC-128623, 97-SI-014.

Peng, H., Asztalos, S., et al., "Cryogenic cavity detector for a large-scale cold-dark-matter axion search," accepted by *Nucl. Instrum. Meth.*, UCRL-JC-134709, 99-ERD-045.

Pentericci, L., et al., "HST Images of the Extremely Clumpy Radio Galaxy 1138-262 at z =2.2," *Astr. Astroph.*, **504**, 139, UCRL-JC- 235005, 98-ERI-005.

Perry, M. D., B. C. Stuart, P. S. Banks, M. D. Feit, J. A. Sefcik, "Ultrashort-pulse laser machining," *LIA Lasers Materials Processing Handbook,* UCRL-JC-132159, 97-LW-074.

Perry, M. D., B. C. Stuart, P. S. Banks, M. D. Feit, V. Yanovsky, A. M. Rubenchik, "Ultrashort-pulse laser machining of dielectric materials," *J. Appl. Phys.*, **85**, 6803, UCRL-JC-132156. 97-LW-074.

Pham, A. Q., T. H. Lee, B. Chung, R. S. Glass, "Colloidal Spray Deposition Technique for the Processing of Thin Film Solid Oxide Fuel Cells," *Electrochemical Society*, **99-19**, 172, UCRL-JC-135760, 98-ERD-031.

Phillips, T. W., et al., Diagnosing hot electron production bu short pulse high intensity lasers using photonuclear reactions," *Rev. Sci. Instr.*, **70**, 1213, UCRL-JC-129813, 98-ERD-079.

Pinto, P. A., R. G. Eastman, "Physics of Type Ia Supernova Lightcurves: II. Opacity and Diffusion," *Astrophys. J.*, **530**, UCRL-JC-234205,99-ERD-043.

Pinto, P. A., R. G. Eastman, "Physics of Type Ia Supernova Lightcurves: I. Analytic Results and Time Dependence," *Astrophys. J.*, **530**, UCRL-JC-132022, 99-ERD-043.

Pizzagalli, L., A. Catellani, G. Galli, F. Gygi, A. Baratoff, "Theoretical study of the 3x2 reconstruction of beta-SiC," *Phys. Rev. B*, **60**, R5129, UCRL-JC-134424, 98-SI-008.

Post, R. F., D. D. Ryutov, "Ambient-Temperature Passive Magnetic Bearings: Theory and Design Equations," *Proc. 6th International Symposium on Magnetic Bearings*, **109**, UCRL-JC-129214, 98-ERD-035.

Purtirka, K., "Plumbing the depths of mantle heterogeneity," submitted to *Nature*, UCRL-JC-135322, 99-ERI-005.

Putirka, K. D., "Clinopyroxene plus liquid equilibria to 100 kbar and 2450 K," *Contributions to Mineralogy and Petrology*, **135**, 151–163, UCRL-JC-131481, 99-ERI-005.

Putirka, K. D., "Melting depths and mantle heterogeneity beneath Hawaii and the East Pacific rise: constraints from Na/Ti and REE ratios," *J. Geophys. Res.*, **104**, 2817–2829, UCRL-JC-131482, 99-ERI-005.

Remington, B. A., et al., "Modeling Astrophysical Phenomena in the Laboratory with Intense Lasers," *Science*, **284**, 1488, UCRL-JC-131535, 97-ERD-022.

Rice, J., et al. "The Rydberg Series of Helium-like Cl, Ar, and S and their High-n Satellites in Tokamak Plasmas," *New J. Phys.*, **1**, 19.1–19.27, UCRL-JC-135505, 97-ERD-057.

Roberts, C. C., S. A. Letts, M. D. Saculla, E. J. Hsieh, R. C. Cook, "Polyimide Films from Vapor Deposition: toward high strength NIF capsules," *Fusion Technology*, **35**, 138, UCRL-JC-132194, 97-ERD-016.

Roberts, C., S. A. Letts, M. D. Saculla, R. C. Cook, *High Performance Polymide Coating Technology*, UCRL-ID-129313, 97-ERD-016.

Roberts, K. E., C. E. A. Palmer, T. J. Wolery, "The Precipitation of Crystalline Neptunium Dioxide from Near-Neutral Aqueous Solution," presented at the *Seventh International Conference on the Chemistry and Migration Behavior of Actinides and Fission Products in the Geospher,* September 26 to October 1, 1999, Incline Village, Nevada, UCRL-VG-135393, 97-ERD-047.

Rome, C. A., A. Noy, M. McBride, J. De Yoreo, "Selective Binding of Chiral Amino Acids to Atomic Steps of Calcite," *Material Research Society,* December 1999, UCRL-JC-135307abs, 97-LW-069.

Röttgering, H. J. A., R. van Ojik, G. K. Miley, K. C. Chambers, W. J. M. van Breugel, S. de Koff, "Spectroscopy of Ultra-Steep-Spectrum Radio Sources: A Sample of z > 2 Radio Galaxies," *Astronomy and Astrophysics*, **326**, 505, UCRL-JC-123261, 98-ERI-005.

Rozmus, W., et al., "Calculations of thermal transport and enhanced ion-acoustic fluctuations from Thomson scattering measurements in the high-Z laser produced plasmas," UCRL-JC-131460, 99-ERI-018.

Rozmus, W., et al., "Theory of SBS and Filamentation growth in high density plasma," *Phys. of Plasmas*, UCRL-JC-900683, 99-ERI-007.

Ruggiero, A. (LLNL) and R. J. Lang (SDLI), *Remotely-Interrogated High Data Rate Free Space Laser Communications Link*, response to DARPA BAA 99-25 STAB solicitation, UCRL-ID-136276, 99-ERD-011.

Ruggiero, A., J. D. Cooke, R. Ratowsky, "Optical Frequency Conversion Using Nondegenerate Four-Wave Mixing in Broad Area Angled Grating (a-DFB) Lasers," submitted to *CLEO*, UCRL-JC-136458, 99-ERD-011.

Ryerson, F. J., J. Van Der Woerd, P. Tapponnier, X. Xiwei, B. Meyer, A. S. Meriaux, "Rapid active thrusting and river incision of the tanghenan shan, a consequence of transfer of sinistral slip from the Altyn Tagh fault," *Tectonics*, in press, UCRL-JC-134629, 97-ERI-003.

Ryerson, F. J., T. M. Harrison, A. Yin, M. Murphy, "The Gangdese and Renbu-Zedong Thrust systems: Lateral extent and thrust history," *Tibet-Himalaya-Karakorum Workshop*, UCRL-JC-126611abs, 97-ERI-003.

Ryutov, D. D., et al., "Similarity Criteria for the Laboratory Simulation of Supernova Hydrodynamics," *Astrophys. J.*, **518**, 821, UCRL-JC-130956, 97-ERD-022.

Salleo, A., R. R. Chinsio, J. H. Campbell, F. Genin, "Crack propagation in fused silica during UV and IR ns-laser illumination," *Laser Induced Damage in Optical Materials: 1998*, SPIE **3578**, 456, UCRL-ID-131218, 98-ERD-063.

Sankaran, V., D. J. Maitland, J. T. Walsh, Jr., "Polarized light propagation in turbid media," *Proc. SPIE*, **3598**, 158, UCRL-JC-131122, 99-LW-011.

Sankaran, V., J. T. Walsh, Jr., D. J. Maitland, "Polarized light propagation through tissue and tissue phantoms," *OSA Annual Meeting*, UCRL-JC-135239abs, 99-LW-011.

Sankaran, V., K. Schoenberger, D. J. Maitland, "Polarization discrimination of coherently propagating photons in turbid media," *Appl. Optics,* **38**, 4252, UCRL-JC-132681, 99-LW-011.

Sankaran, V., M. J. Everett, D. J. Maitland, J. T. Walsh, "Comparison of polarized light propagation in biologic tissue and phantoms," *Optics Lett.*, **24**, 1044–46, UCRL-JC-133624, 98-ERD-062.

Sankaran, V., M. J. Everett, D. J. Maitland, J. T. Walsh, Jr., "Propagation in Biologic Tissue and Phantoms," *Optics Lett.*, **24**, 1044, UCRL-JC-133624, 99-LW-011.

Santer, B. D., et al., "Interpreting Differential Temperature Trends at the Surface and in the Lower Troposphere," accepted by *Science*, UCRL-JC-135694, 99-ERD-056.

Santer, B. D., et al., "Statistical Significance of Trends and Trend Differences in Layer-Average Atmospheric Temperature Time Series," accepted by *J. Geophys. Res.* (Atmospheres), UCRL-JC-133622,99-ERD-056.

Santer, B. D., et al., "Uncertainties in Observationally Based Estimates of Temperature Change in the Free Atmosphere," *J. Geophys. Res.* (Atmospheres), **104**, 6305–6333, UCRL-JC-128790, 99-ERD-056.

Sathyam, U. S., B. W. Colston, L. Da Silva, M. J. Everett, "Evaluation of optical coherence quantitation of analytes in turbid media using two wavelengths," *Appl. Optics*, **38**, 2097–2104, UCRL-JC-131433, 98-ERD-062.

Savin, D., et al., "Simulations of a Maxwellian Plasma Using an Electron Beam Ion Trap," *Physica Scripta*, UCRL-JC-131735, 97-ERD-057.

Schenkel, T., A. V. Hamza, A. V. Barnes, D. H. Schneider, "Interaction of Slow Highly Charged Ions with Surfaces," *Progress in Surface Science*, **61**, 23, UCRL-JC-133730, 97-ERD-102.

Schenkel, T., et al., "Analysis of Sub-Micron Cu-Ta-SiO$_2$ Structures by Highly Charged Ion SIMS, *J. Vac. Sci. & Tech. B*, **17**, 2331, UCRL-JC-133731, 97-ERD-102.

Schenkel, T., et al., "Deposition of Potential Energy in Solids by Slow, Highly Charged Ions," accepted by *Phys. Rev. Lett.*, UCRL-JC-132793, 97-ERD-102.

Schenkel, T., et al., "Surface Analysis by Highly Charged Ion Based Secondary Ion Mass Spectrometry," *Physica Scripta*, **T80**, 73, UCRL-JC-132033, 97-ERD-102.

Schmidt, J., and C. A. Ebbers, *Thermally Insensitive Propagation Direction in LiInS$_2$,* UCRL-MI-135826, 99-LW-024.

Schrag, D. P., T. P. Guilderson, "Abrupt Shift in Subsurface Temperatures in the eastern Tropical Pacific associated with recent changes in El Niño," *Mineralogical Magazine*, **62A**, 1353, UCRL-JC-134000, 98-ERI-002.

Schwartz, A. J., J. S. Stölken, W. E. King, G. H. Campbell, "Lattice Rotations During Compression Deformation of a [011] Ta Single Crystal," *Mat. Sci. & Eng.*, in press, UCRL-JC-134189, 97-ERD-117.

Schwartz, A. J., M. Kumar, W. E. King, "Influence of Processing Method on the Grain Boundary Character Distribution," *MRS Proceedings*, UCRL-JC-134727abs, 98-ERD-080.

Schwartz, A. J., W. E. King, G. H. Campbell, J. S. Stolken, D. H. Lassila, S. Sun, B. L. Adams, "Orientation Imaging Microscopy Investigation of the Compression Deformation of a [011] Ta Single Crystal," *ASME J. Eng. Mater. Tech.*, **121**, 178–181, UCRL-JC-133390, 97-ERD-117.

Schwegler, E., G. Galli, F. Gygi, "Water under pressure," submitted to *Phys. Rev. Lett.,* UCRL-JC-134297, 98-SI-008.

Shapiro, A. B., *High Precision Droplet Based Net-Form Manufacturing,* UCRL-ID-135740, 98-ERD-085.

Shi, F. G., T. G. Nieh, Y. T. Chou, "A Free Volume Approach for Self-Diffusion in Metals," accepted by *Scripta Materialia*, UCRL-JC-136119, 99-LW-001.

Shigemori, K., et al., "Observation of the Transition from Hydrodynamic to Radiative Shocks," submitted to *Ap. J. Lett.*, UCRL-JC-134470, 97-ERD-022.

Shlyaptsev, V. N., et al. "Modeling of tabletop transient inversion and capillary x-ray lasers, *SPIE Proceedings*, **3156**, 193, UCRL-JC-130197, 97-ERD-105.

Shlyaptseva, A. S., R. C. Mancini, P. Neill, P. Beiersdorfer, "Polarization properties of dielectronic satellite lines in the K-shell x-ray spectra of B-like Fe XXII," *J. Physics B*, **32**, 1041, UCRL-JC-131409, 97-ERD-103.

Simpson, R. L., R. W. Swansiger, D. M. Hoffman, R. S. Lee, T. M. Tillotson, L. W. Hrubesh, "New Formulations and Material Characterization," *Joint DoD/DOE Munitions Technology Development Program*, 11–15, UCRL-ID-103482, 98-ERD-048.

Skidmore, J., et al., "High power operation of InGaAsP/InP laser diode array at 1.73 mm," *IEEE Photon. Tech. Lett.*, UCRL-JC-127615, 97-SI-014.

Smolinski, B., S. Kohn, N. Elliott, N. Dykman, "Language Interoperability Mechanisms for High-Performance Parallel Scientific Components," *International Symposium on Computing in Object-Oriented Parallel Environments*, UCRL-JC-134260, 99-ERD-078.

Stanford, S. A., P. R. Eisenhardt, M. E. Dickinson, "The Evolution of Early-Type Galaxies in Distant Clusters," *The Astrophys. J.*, **492**, 461, UCRL-JC-126384, 98-ERI-005.

Stern, L., D. Hogenboom, W. Durham, S. Kirby, I. Chou, "Optical-Cell Evidence for Superheated Ice under Gas-Hydrate-Forming Conditions," *J. Phys. Chem. B*, **102**, 2627, UCRL-JC-132369, 98-ERD-008.

Stern, L., S. Kirby, W. Durham, "Polyscrystalline Methane Hydrate: Synthesis from Superheated Ice, and Low-Temperature Mechanical Properties," *Energy & Fuels*, **12**, 201, UCRL-JC-132370, 98-ERD-008.

Sternberg, M. G. Galli, T. Frauenheim, "NOON—a non-orthogonal localised orbital order-N method," *Computer Phys. Comm.*, **118**, 200, UCRL-JC-132141, 98-SI-008.

Sterne, P. A., J. E. Pask, B. M. Klein, Calculation of Positron Observables Using a Finite-Element-Based Approach," *Applied Surface Science*, **149**, 238, UCRL-JC-131338, 99-ERD-047.

Stidham, C., D. Dreger, M. Antolik S. Larsen, B. Romanowicz, "Three-dimensional structure influences on the strong motion wavefield of the 1989 Loma Prieta earthquake," *Bull. Seismological Society of America*, **89**, in press, UCRL-JC-132602., 98-LW-028.

Strauss, M., et al., "Self-Consistent Evolution of Tissue Damage Under Stress Wave Propagation," *Proc. SPIE*, **3601**, 178, UCRL-JC-132925, 97-ERD-056.

Strauss, M., et al., "Two-Dimensional Rayleigh Model of Vapor Bubble Evolution," *Proc. SPIE*, **3601**, 212, UCRL-JC-132924, 97-ERD-056.

Summers, J. S., D. Roe, P. D. Boyle, M. Colvin, B. R. Shaw, "Structural Studies of a Borane-Modified Phosphate Diester Linkage: Ab Initio Calculations on the Dimethylboranophosphate Anion and the Single-Crystal X-ray Structure of its Diisopropylammonium Salt," *Inorg. Chem.*, **37**, 4158, UCRL-JC-132589, 98-SI-008.

Surh, M., T. Barbee, L. Yang, "Theory of the equation of state of hot dense matter," *Proc. AIRAPT*, in press, UCRL-JC-133454, 98-ERD-052.

Tavukcu, E., K. Hauschild, et al, "Gamma-Ray Spectroscopy of ^{196}Pt and Reaction Dynamics Using GEANIE at LANSCE/WNR," *Bull. Am. Phys. Soc.*, **44**, (5), 77, UCRL-JC-134833abs, 98-LW-051.

Teller, E., et al., *Long-Range Weather Prediction And Prevention of Climate Catastrophes: A Status Report*, Erice Seminar paper, UCRL-JC-135414, 99-ERD-061.

Teng, H., P. M. Dove, J. J.De Yoreo, "Kinetics of calcite growth: Surface processes and relationships to macroscopic rate laws," *Geochim. et Cosmochim.*, in press, UCRL-JC-137199, 97-LW-069.

Teng, H., P. M. Dove, J. J.De Yoreo, "Reversal of calcite morphologies induced by microscopic growth kinetics: insight into biomineralization," *Geochim. et Cosmochim.*, **63**, 2507 (1999), UCRL-JC-137039, 97-LW-069.

Thelen, M., C. Venclovas, K. Fidelis, "Sliding Clamp Model for the Rec1 Family of the Cell Cycle Checkpoint Proteins," *Cell*, **96**, 769–770, UCRL-JC-132395, 98-SI-008.

Thompson, S., *A simple climate model to aid understanding of thermohaline collapse*, UCRL-JC-135587abs, 99-SI-001.

Tillotson, T. M., L. W. Hrubesh, R. L. Simpson, R. S. Lee, R. W. Swansiger, L. R. Simpson, "Sol-Gel Processing of Energetic Materials, *J. Non-Crystalline Solids*, **225**, 358, UCRL-JC-127539, 98-ERD-048.

Träbert, E., et al., "Improved EBIT Lifetime Measurements of the Ne8+ 1s2s 3S1 Level," *Phys. Rev. A*, **60**, 2034, UCRL-JC-133906, 97-ERD-103.

Träbert, E., P. Beiersdorfer, S. B. Utter, "The EBIT Quest for Better Transition Probabilities of Forbidden Lines," *Physica Scripta*, **T80**, 450, UCRL-JC-131737,97-ERD-103.

Tran, H. D., M. H. Cohen, P. M. Ogle, R. W. Goodrich, S. D. Alighieri, "Scattered Radiation from Obscured Quasars in Distant Radio Galaxies," *The Astrophys. J.*, **500**, 660, UCRL-JC-128461, 98-ERI-005.

Tran, H., et al., "A Polarimetric Search for Hidden Quasars in Three Radio-Selected Ultraluminous Infrared Galaxies," *The Astrophys. J.*, **516**, 85, UCRL-JC- 234604, 98-ERI-005.

Troha, A. L., et al., "Vacuum electron acceleration by coherent dipole radiation," *Phys. Rev. E*, **60**, 926, UCRL-JC-132048, 99-ERI-008.

Ullom, J. N., M. Frank, J. M. Horn, S. E. Labov, K. Langry, W. H. Benner, "Identification of Microorganisms Using Superconducting Tunnel Junctions and Time of Fight Mass Spectrometry," accepted by *Nuc. Instr. and Meth. A*, UCRL-JC-134432, 98-ERD-097.

Utter, S. B., G. V. Brown, P. Beiersdorfer, E. J. Clothiaux, N. Podder, "Grazing-incidence measurements of L-shell line emission from highly charged Fe in the soft x-ray region," *Rev. Sci. Instruments*, **7**, 284, UCRL-JC-131315, 97-ERD-103.

Utter, S. B., P. Beiersdorfer, J. R. Crespo López-Urrutia, E. Träbert, "Implementation of a normal incidence spectrometer on an electron beam ion trap," *Rev. Sci. Instruments,* **70**, 288, UCRL-JC-129794, 97-ERD-103.

van Bibber, K. A., J. M. Hill, G. P. Le Sage, et al., "Photon Beam Diagnostics for VISA FEL," *Proc. 1999 Particle Accelerator Conference*, New York, 1999, **4**, 2480, UCRL-JC-136457, 99-ERI-055.

van Bibber, K., et al., "Recent Developments in the Design of the NLC Positron Source," *Proc. 1999 Particle Accelerator Conference*, New York, 1999, **5**, 3450, UCRL-JC-136449, 99-ERI-055.

van Bibber, K., et al., "The NLC Injector System," *Proc. 1999 Particle Accelerator Conference*, New York, 1999, **5**, 3447, UCRL-JC-136450, 99-ERI-055.

van Breugel, W. J. M., S. A. Stanford, H. Spinrad, D. Stern, J. R. Graham, "Morphological Evolution in High Redshift Radio Galaxies and the Formation of Giant Elliptical Galaxies," *The Astrophys. J.*, **502**, 614, UCRL-JC-128464, 98-ERI-005.

van Breugel, W., et al., "A Radio Galaxy at Z = 5.19," *The Astroph. J.*, **518**, 61, UCRL-JC- 235005, 98-ERI-005.

Van der Woerd J., et al., "Holocene left slip-rate determined by cosmogenic surface exposure dating on the Xidatan segment of the Kunlun Fault (Qinghai, China)," *Geology*, **26**, 695–698, UCRL-JC-128338, 98-ERI-013.

Van der Woerd, J., et al., "Strain-Styles, Large-Scale Morphology and Post-Glacial Slip-Rates along the Active Kunlun Fault," *EOS*, **77**, F687, UCRL-JC-126614abs, 97-ERI-003.

Van Meter, J. R., et al., "Radiative corrections in symmetrized classical electrodynamics, Phys. Plasmas," UCRL-JC-135844, 99-ERI-008.

Van Meter, J. R., et al., "Reflection of plane waves in Rindler space," UCRL-JC-134497, 99-ERI-008.

Venclovas, C., K. Ginalski, K. Fidelis, "Addressing the Issue of Sequence-to-Structure Alignments in Comparative Modeling of CASP3 Target Proteins," *Proteins: Structure, Function, and Genetics*, **3**, 73–80, UCRL-JC-134550, 98-SI-008.

Visuri, S. R., R. A. London, L. B. Da Silva, "Stress Wave Focusing Transducers," *Trends in Optics and Photonics*, **22**, 330–332, UCRL-JC-130697, 98-LW-030.

Waite, W. F., M. B. Helgerud, A. Nur, J. C. Pinkston, L. A. Stern, S. H. Kirby, W. B. Durham, "Laboratory measurements of compressional and shear wave speeds through methane hydrate," *Proc. 3rd International Conference on Gas Hydrates*, in press, UCRL-JC-136096, 98-ERD-008.

Wang, H., P. Duffy, M. Eby, A. Weaver, E. Wiebe, *Importance of water vapor transport to the hydrological cycle in an atmospheric energy-moisture balance model coupled to an OGCM*, UCRL-JC-135361abs, 99-SI-001.

Wang, J. G., B. W. Choi, T. G. Nieh, C. T. Liu, "Nano-Scratch Behavior of a Zr-Based Bulk Amorphous Alloy,", accepted by *J. Materials Research*, UCRL-JC-135381, 99-LW-001.

Wang, L., M. Yan, W. Siekhaus, U. Mohideen, J. Yang, "Imaging of stress fields around nano-indents in fused silica by near-field scanning optical microscopy," *Solid State Lasers for Application to Inertial Confinement Fusion Third Annual International Conference*, UCRL-JC-129458abs, 97-ERD-013.

Wargelin, B., P. Beiersdorfer, D. Liedahl, S. Kahn, S. von Goeler, "Observation and Modeling of High-n Iron L-Shell Lines From Intermediate Ion Stages," *The Astrophys. J.*, **496**, 1031, UCRL-JC-128010, 97-ERD-057.

Warrick, A. L., S. G. Azevedo, J. E. Mast, "Prediction of Buried Mine-like Target Radar Signatures using Wideband Electromagnetic Modeling," *SPIE—The International Society for Optical Engineering*, **3392**, 776–83, UCRL-JC-130338, 97-SI-013.

Weaver, A. J., P. B. Duffy, M. Eby, E. C. Wiebe, "On the Evaluation of Ocean and Climate Models using Present-day forcing, Atmosphere-Ocean," *Atmosphere-Ocean*, in press, UCRL-JC-133962, 99-SI-001.

Weiss, O., and J. S. Albala, "Development of a Functional Chip for High-throughput Screening of Protein-DNA Interactions," UCRL-JC-135580abs, 99-ERD-039.

Westmacott, G., F. Zhong, M. Frank, S. Friedrich, S. Labov, W. H. Benner, *Investigating Ion-Surface Collisions with a Niobium Superconducting Tunnel Junction Detector in a Time-of-Flight Mass Spectrometer*, UCRL-JC-136629, 98-ERD-097.

Wilhelmsen, J., and C. A. Thompson, "An Adaptive Optic for Correcting Low-Order Wavefront Aberrations," UCRL-ID-135689, 98-ERD-061.

Wilks, S. C., et al., "Ion acceleration in ultra-intense, laser-plasma interactions," *Bull. Am. Phys. Soc.*, UCRL-JC-904894, 99-ERD-063.

Williams, G. G., "LOTIS Search for Early Time Optical Afterglows: GRB971227," *Astrophys. J. Lett.*, **519**, L25, UCRL-JC-133882, 97-LW-019.

Williams, R. V., M. E. Colvin, N. Tran, R. N. Warrener, D. Margetic, "Exceptionally Pyramidalized Olefins: A Theoretical Study of the Cyclopropenyl Fused Tricycles-Tricyclo[3.2.1.0]oct-2(4)-ene, Tricyclo[3.2.1.0]octa-2(4),6-diene, Tricyclo[3.2.2.0]non-2(4)-ene and Tricyclo[3.2.2.0]nona-2(4),6-diene," submitted to *J. Org. Chem.*, UCRL-JC-135854, 98-SI-008.

Wilson, D., J. Carney, M. Coleman, A. Adamson, M. Christensen, J. Lamerdin, "HEX1: A new human nuclease family member with homology to Saccharomyces cerevisiae exonuclease I," *Nucleic Acids Res.*, **26**, 3762–3768, UCRL-JC-130499, 97-ERD-002.

Wirth, B. D., V. Bulatov, T. Diaz de la Rubia, "Atomistic Simulation of Stacking Fault Tetrahedra Formation in Cu," accepted by *J. Nuc. Mat.*, UCRL-JC-136398, 98-ERD-090.

Wood, R. D., et al., "Initial operation of the SSPX Experiment," *Bull. Amer. Phys. Soc.*, **43**, 1769, UCRL-JC-131418abs, 97-SI-009.

Woods, B. W., M. Runkel, M. Yan, M. Staggs, N. Zaitseva, M. Kozlowski, J. J. De Yoreo, "Investigation of damage in KDP using light scattering techniques," *SPIE Proc. 28th Annual Boulder Damage Conference*, **2966**, 20, UCRL-JC-125368, 97-ERD-098.

Woosley, S. E., R. G. Eastman, B. P. Schmidt, "Gamma Ray Bursts and Type Ic Supernovae: SN 1998bw," *Astrophys. J.*, **516**, 788, UCRL-JC-132203, 99-ERD-043.

Wruck, D. A., A. Brachman, E. Sylwester, P. G. Allen, C. E. A. Palmer, *Sorption of Np(V) by U(VI) Hydroxide Solids*, UCRL-JC-135791, 98-ERD-094.

Wu, C. J., and L. E. Fried, "Ring closure mediated by intramolecular hydrogen transfer in the decomposition of a push-pull nitroaromatic: TATB," submitted to *J. Phys. Chem.*, UCRL-JC-135864, 97-ERD-101.

Wu, Z., M. D. Feit, M. J. D. Natoli, A. M. Rubenchik, L. M. Sheehan, M. Yan, "Single-beam photothermal microscopy-a new diagnostic tool for optical materials," *Laser Induced Damage in Optical Materials: 1998*, SPIE 3578, 604, UCRL-ID-131212, 98-ERD-063.

Wurtz, R., et al., *First Observations with the LLNL Optical Imaging Fourier Transform Spectrometer*, UCRL-MI-136948, 99-ERD-065.

Wurtz, R., K. H. Cook, C. L. Bennett, J. Bixler, D. Carr, E. H. Wishnow, "Ground-Based Demonstration of Imaging Fourier Transform Spectrometry and Techniques," *ASP*, UCRL- JC-136953, 99-ERD-065.

Yan, M., et al., "Impurity and laser-induced damage in the growth sectors of rapidly grown KDP crystals," *SPIE Proc. 28th Annual Boulder Damage Conference*, **2966**, 11, UCRL-JC-126804, 97-ERD-098.

Yan, M., et al., Impurity segregation and its effects on the optical properties of KH_2PO_4, *SPIE: Solid State Lasers for Application to ICF*, UCRL-JC-123594abs-rev. 2, 97-ERD-098.

Yan, M., L. Westin, R. A. Torres, J. J. De Yoreo, L. Carman, N. P. Zaitseva, "Molecular defects in KDP crystals," *International Conference on Crystal Growth*, UCRL-JC-129022abs, 97-ERD-098.

Yan, M., P. Santiago, M. Staggs, J. J. De Yoreo, L. Carman, N. Zaitseva, "Optical properties of doped KDP crystals," *Bull. Amer. Phys. Soc.*, **42**, 97, UCRL-JC-125972abs, 97-ERD-098.

Yan, M., R. Torres, I. Hutcheon, J. J. De Yoreo, N. P. Zaitseva, Z. U. Rek, "Impurity segregation and its effects on the optical properties of KH_2PO_4," *American Conference on Crystal Growth West*, UCRL-JC-123594abs, 97-ERD-098.

Yan, M., S. K. Oberhelman, W. J. Siekhaus, Z. Wu, L. M. Sheehan, M. R. Kozlowski, "Characterization of surface and sub-surface defects in optical materials using near field evanescent wave," *Laser Induced Damage in Optical Materials: 1998*, SPIE 3578, 718, UCRL-ID-131225, 98-ERD-063.

Yoo, C. S., et al., "Crystal structures of carbon dioxide at high pressures: 'superhard' polymeric carbon dioxide," submitted to *Phys. Rev. Lett.*, UCRL-JC-134573, 98-SI-008.

Zaug, J. M., D. L. Farber, I. M. Craig, L. L. Blosch D. K. Shuh, D. W. Hansen, C. M. A-Ruddle, Quasi-dynamic Pressure and Temperature Initiated b to d Solid Phase Transitions in HMX, (AIP Press, New York), *Proc. 1999 AIP Conference*, Snowbird, UT, June 27–August 2, 1999, in press, UCRL-JC-134654, 99-ERD-007.

Zemla, A., C. Venclovas, J. Moult, K. Fidelis, "Processing and Analysis of CASP3 Protein Structure Predictions," *Proteins: Structure, Function, and Genetics*, **3**, 22–29, UCRL-JC-135299, 98-SI-008.

Zemla, A., C. Venclovas, K. Fidelis, B. Rost, "A Modified Definition of Sov, a Segment Based Measure for Protein Secondary Structure Prediction Assessment," *PROTEINS: Structure, Function, and Genetics*, **34**, 220–223, UCRL-JC-129140, 98-SI-008.

Zhao, P., P. G. Allen, E. R. Sylwester, B. E. Viani, *The Sorption of Uranium(VI) and Neptunium(V) onto Hydrothermally Altered Concrete*, UCRL-JC-135790, 98-ERD-094.

FY1999 Annual Report Principal Investigators Index

Name	Page
Post, R. F.	5-5
Puso, M. A.	4-18
Putirka, K. D.	2-14
Quong, A. A.	4-10
Remington, B. A.	6-1
Rognlien, T. D.	5-11
Rosenbury, E. T.	6-14
Ruggiero, A. J.	1-12, 1-22
Rupp, B.	3-8
Ryerson, F. J.	2-2
Sangster, T. C.	6-12
Santer, B. D.	2-13
Satcher, J. H.	1-24
Schwartz, A. J.	8-13
Shapiro, A. B.	7-4
Shinn, J. H.	4-24
Sigmon, T. W.	1-19, 7-2
Smart, J. A.	4-29
Sommargren, G. E.	1-17
Southon, J. R.	2-3
Springer, P. T.	9-13
Steich, D.	4-1
Terminello, L. J.	8-10
Tillotson, T. M.	8-11
Tittiranonda, P.	3-2
Toor, A.	5-12, 9-17
Trebes, J. E.	1-16
Van Bibber, K. A.	9-14
Van Breugel, W.	10-7
Visuri, S. R.	3-9
Vogel, J. S.	3-7
Weber, F. A.	6-21
Westbrook, C. K.	4-14
Westerberg, K. W.	7-5
Wilson, D. M.	3-1, 3-12
Wilson, W. D.	8-20
Wolery, T. J.	5-2
Wright, D. M.	9-8
Yan, M.	8-1
Young, P. E.	6-16
Zaug, J. M.	8-18
Ziock, K.-P.	1-4

FY1999 Annual Report Tracking Code Index